Matthew S. Allen · Randall L. Mayes
Daniel Jean Rixen   *Editors*

Dynamics of Coupled Structures, Volume 4

Proceedings of the 35th IMAC, A Conference and Exposition on Structural Dynamics 2017

SEM

_⚞_ Springer

Conference Proceedings of the Society for Experimental Mechanics Series

Series Editor

Kristin B. Zimmerman, Ph.D.
Society for Experimental Mechanics, Inc.,
Bethel, CT, USA

Matthew S. Allen • Randall L. Mayes • Daniel Jean Rixen
Editors

Dynamics of Coupled Structures, Volume 4

Proceedings of the 35th IMAC, A Conference and Exposition
on Structural Dynamics 2017

Editors
Matthew S. Allen
Department of Engineering Physics
University of Wisconsin
Madison, WI, USA

Randall L. Mayes
Structural Dynamics Department
Sandia National Laboratories
Albuquerque, NM, USA

Daniel Jean Rixen
Technical University of Munich
Garching, Germany

Preface

Dynamics of Coupled Structures represents one of ten volumes of technical papers presented at the 35th IMAC, A Conference and Exposition on Structural Dynamics, organized by the Society for Experimental Mechanics and held in Garden Grove, California, January 30–February 2, 2017. The full proceedings also include the following volumes: *Nonlinear Dynamics*; *Dynamics of Civil Structures*; *Model Validation and Uncertainty Quantification*; *Sensors and Instrumentation*; *Special Topics in Structural Dynamics*; *Structural Health Monitoring and Damage Detection*; *Rotating Machinery, Hybrid Test Methods, Vibro-Acoustics, and Laser Vibrometry*; *Shock and Vibration, Aircraft/Aerospace, and Energy Harvesting*; and *Topics in Modal Analysis and Testing*.

Each collection presents early findings from experimental and computational investigations on an important area within structural dynamics. Coupled structures or substructuring is one of these areas.

Substructuring is a general paradigm in engineering dynamics where a complicated system is analyzed by considering the dynamic interactions between subcomponents. In numerical simulations, substructuring allows one to reduce the complexity of parts of the system in order to construct a computationally efficient model of the assembled system. A subcomponent model can also be derived experimentally, allowing one to predict the dynamic behavior of an assembly by combining experimentally and/or analytically derived models. This can be advantageous for subcomponents that are expensive or difficult to model analytically. Substructuring can also be used to couple numerical simulation with real-time testing of components. Such approaches are known as hardware-in-the-loop or hybrid testing.

Whether experimental or numerical, all substructuring approaches have a common basis, namely, the equilibrium of the substructures under the action of the applied and interface forces and the compatibility of displacements at the interfaces of the subcomponents. Experimental substructuring requires special care in the way the measurements are obtained and processed in order to assure that measurement inaccuracies and noise do not invalidate the results. In numerical approaches, the fundamental quest is the efficient computation of reduced order models describing the substructure's dynamic motion. For hardware-in-the-loop applications, difficulties include the fast computation of the numerical components and the proper sensing and actuation of the hardware component. Recent advances in experimental techniques, sensor/actuator technologies, novel numerical methods, and parallel computing have rekindled interest in substructuring in recent years leading to new insights and improved experimental and analytical techniques.

The organizers would like to thank the authors, presenters, session organizers, and session chairs for their participation in this track.

Madison, WI, USA   Matthew S. Allen
Albuquerque, NM, USA   Randall L. Mayes
Garching, Germany   Daniel Jean Rixen

Contents

Chapter 1
Techniques for Verification of Structural Acoustic Models

Hasan G. Pasha and Rajendra Gunda

Abstract When designing mechanical structures, the desired acoustic performance and efficiency are often achieved by employing upfront CAE driven design and development process. The advantages of this approach are multi-fold compared to a purely testing based approach. However, making key design decisions based solely on the results obtained from these CAE models requires that the models be verified and validated by comparing the model predictions with known solutions of simple sources and experimental data respectively. The boundary element method is typically used for modeling and predicting the radiated sound-field from a vibrating structure. This involves discretizing the surface of the vibrating structure with discrete boundary elements, applying the appropriate boundary conditions and solving the Helmholtz integral equations to predict the sound-field. The theoretical background is presented along with verification examples involving simple and complex sound sources.

Keywords Model verification • Code verification • Solution verification • Boundary element method • CHIEF • Burton-Miller formulation • Gear whine predictions

Notation

$\lvert \epsilon_{rel} \rvert$	Relative error, %
λ	Wavelength, m
ρ	Density, $kg\,m^{-3}$
ω	Circular frequency, $rad\,s^{-1}$
Ω	Solid angle
c	Sound wave propagation velocity, $m\,s^{-1}$
j_m	Spherical Bessel function of the first kind of order m
k	Wavenumber, m^{-1}
n	Outward normal vector
$p(r,t)$	Time dependent acoustic pressure, Pa
$\bar{p}(r,\omega)$	Frequency dependent acoustic pressure, Pa
r	Receiver point location
r_0	Source point location
v_n	Normal velocity, $m\,s^{-1}$
$C(r)$	Integration constant of the Kirchoff-Helmholtz Integral Equation
D	Domain of wave propagation
∂D	Boundary of the domain of wave propagation
$G(r,r_0)$	Free-field Green's function

H.G. Pasha (✉)
Lucid Motors USA, Inc, Menlo Park, CA, USA
e-mail: pashahg@mail.uc.edu

R. Gunda
Advanced Numerical Solutions, Inc, Columbus, OH, USA

$H_0^{(1)}$ Hankel function of the first kind of order zero
$H_0^{(2)}$ Hankel function of the second kind of order zero
J_m Bessel function of the first kind of order m
N Number of nodes

Abbreviations

Symbol	Description
BEM	Boundary Element Method
CAE	Computer Aided Engineering
FEM	Finite Element Method
FMM	Fast Multipole Method
SPL	Acoustic Pressure Level
V&V	Verification and Validation

1.1 Background

1.1.1 Introduction

Characterizing the sound-fields due to mechanical or acoustic (internal sources) excitation is a critical part of designing mechanical structures. These sound-fields are complicated functions of geometry, source distribution and noise control treatment. Hence, these cannot be computed in closed form. The desired acoustic performance and efficiency are often achieved by employing upfront CAE driven design and development process.

Typically CAE techniques such as, *boundary element method (BEM)* and *finite element method (FEM)*, are used in structural acoustic analysis. A detailed account on BEM and its application to acoustics can be found in [1–4]. In both FEM and BEM the problem domain is divided into finite elements. However, in FEM the *entire problem domain* is divided into elements, but in BEM only the *bounding surface* of the domain is discretized.

The advantages of a CAE driven approach are multi-fold compared to a purely testing based approach. However, making key design decisions based solely on the results obtained from these CAE models requires that the models be verified and validated by comparing the model predictions with known solutions of simple sources and experimental data respectively.

The verification and validation (V&V) methods and procedures were originally developed to improve the credibility of simulations in several high-consequence fields, such as nuclear technology. This was driven by a ban on nuclear testing for safety purposes [5]. Although there may not be safety concerns in many other engineering applications, conducting extensive testing as part of product development may be very expensive and time consuming. In addition, it may not be possible to conduct testing in certain configurations. Applying V&V to improve the credibility of CAE models for structural design can potentially address these concerns.

1.1.2 Verification and Validation

AIAA [6] and Oberkampf and Trucano [7] in the context of assessing the accuracy and reliability computer models, verification and validation are defined as:

Verification: refers to process of determining that a model implementation accurately represents the developer's conceptual description of the model and the solution to the model. Frequently, the verification portion of the process answers the question *"Are the model equations correctly implemented?"* and deals with mathematics.

Validation: refers to the process of determining the degree to which a model is an accurate representation of the real world system from the perspective of the intended uses of the model. Frequently, the validation process answers the question *"Are the correct model equations implemented?"* and deals with physics.

Verification should always precede validation. The discussions in this paper are limited to the verification part of the V&V process. The mathematical model for structural systems can be defined by a set of partial differential or integro-differential equations, along with the required initial and boundary conditions. The mathematical model is then translated in to a computational (discrete-mathematics) model and solved by a computer implementation of relevant algorithms. The goals as part of the verification process are to identify, quantify and reduce errors caused by the mapping of the mathematical model to a computer implementation.

The verification process can be further classified as *code verification* and *solution verification*. Code verification deals with assessing the reliability of the software coding, whereas solution verification deals with assessing the numerical accuracy of the solution to a computational model.

1.1.3   Mathematical Models

1.1.3.1   The Acoustic Wave Equation

Sound is a *vibrational* transmission of mechanical energy that propagates through matter as a wave (as a compression wave through fluids and as both compression and shear waves through solids).

The equation for the transmission of a sound wave in a *homogeneous isotropic fluid* can be evolved by deriving the relationship between the pressure variations within the fluid and the deformation of the fluid. This can be achieved by using the thermodynamic properties of the fluid and law of conservation of mass. The linear acoustic wave equation in homogeneous isotropic medium at rest is,

$$\nabla^2 p(r, t) - \frac{1}{c^2} \frac{\partial^2 p(r, t)}{\partial t^2} = 0. \tag{1.1}$$

1.1.3.2   The Helmholtz Equation

In the *steady-state* case, the acoustic pressure fluctuation is *time harmonic* as expressed in Eq. (1.2), the time dependence, $e^{-i\omega t}$, is *suppressed*.[1]

$$p(r, t) = \text{Re}\left(\bar{p}(r, \omega) e^{-i\omega t}\right) \tag{1.2}$$

The Helmholtz equation (1.3) is obtained by substituting Eq. (1.2) in the wave equation (1.1).

$$(\nabla^2 + k^2)\bar{p}(r, \omega) = 0, \tag{1.3}$$

where, the constant k, is termed as the *wavenumber*,

$$k = \frac{\omega}{c} = \frac{2\pi}{\lambda}. \tag{1.4}$$

For a complete solution, the wave equation is written as a series of Helmholtz problems by expressing the boundary conditions as a Fourier series with components of the form of Eq (1.2). For each wavenumber and its associated boundary condition, the Helmholtz equation is then solved. The time-dependent acoustic pressure, $p(r, t)$, can then be constituted from the separate solutions.

---

[1] Alternatively, the Helmholtz equation can be obtained by applying *Fourier transform* to the acoustic wave equation (1.1).

1.1.3.3   The Free-Field Green's Function: Fundamental Solution of the Helmholtz Equation

The *fundamental solution* of the Helmholtz equation in 3D (interior), $G(r, r_0)$, is the sound-field due to a Dirac delta excitation, $\delta(r - r_0)$, due to a *monopole source* present at r_0. $G(r, r_0)$ is also termed as the *free-field Green's function*, which means that it is the (unique) solution, the sound-field generated by a point source excitation in free space.

$$(\nabla^2 + k^2)G(r, r_0) = -\delta(r - r_0) \tag{1.5}$$

$$G(r, r_0) = \frac{e^{-ik|r - r_0|}}{4\pi |r - r_0|}; \;\; r, \; r_0 \; \in \; R^3 \tag{1.6}$$

The fundamental solutions of the Helmholtz equation in 3D for exterior boundary value problems are given by Eq. (1.7).

$$G(r, r_0) = \frac{e^{ik|r - r_0|}}{4\pi |r - r_0|}; \;\; r, \; r_0 \; \in \; R^3. \tag{1.7}$$

1.2   BEM Formulation and the Computational Model

Acoustic problems can be formulated as *boundary integral equations* (BIE). BEM is a numerical method used for obtaining approximate solutions to BIE. This work concerns with the application of BEM to *time-harmonic* acoustic radiation problems.

The formulation of a boundary value problem into a BIE representation has several advantages as compared to FEM. The most important of these is the *reduction of the problem dimension*; three-dimensional problems are solved on two-dimensional surfaces enclosing the domain. In addition, for exterior problems, the *Sommerfeld radiation condition* is automatically incorporated in the integral formulation.

Copley [8] applied the BIE formulations to acoustics to predict sound-fields. There are two fundamental approaches to derive the boundary integral equation formulation for acoustic problems.

Direct Boundary Integral Formulation: It is based on the *Kirchoff-Helmholtz integral equation*. When at least one closed surface is present, direct formulation is possible. The acoustic problem is solved directly to yield the primary variables – *acoustic pressure* and *particle velocity*, on one side of the domain.

Indirect Boundary Integral/Simple-source Formulation: It is adapted from potential theory where the potential (acoustic pressure) is represented as being due to a *distribution of simple sources* over a surface represented by an integral of an unknown source-density function. The indirect formulation is applicable to both closed and open boundary problems. Both the sides of the of the boundary surface can be considered. The acoustic problem is solved to yield a secondary variable – *fictitious distribution of simple sources* at the boundary. The primary variables can then be obtained using a post-processing operation.

1.2.1   Direct BIE Formulation for Helmholtz Equation

The acoustic pressure or the particle velocity in a steady-state sound-field in a domain D, bounded by a closed surface ∂D, is governed by the Helmholtz equation and is subjected to the prescribed boundary conditions. Direct boundary integral formulation is based on deriving an equivalent integral equation – the *Kirchhoff-Helmholtz integral equation*, which is obtained using *Green's second identity* to the unknown field pressure and the fundamental solution.[2] Equation (1.8) can be used to evaluate the pressure at any point in the domain in interior or exterior problems.

$$C(r)p(r) = \int\int_S \left(i\rho ckG(r, r_0)v_n(r) - p(r)\frac{\partial G(r, r_0)}{\partial n} \right) dS \tag{1.8}$$

---

[2]Direct BIE formulation can also be obtained using the weighted residual technique.

$$C(r) = \begin{cases} 1, & \text{r in the fluid domain D} \\ \frac{1}{2}, & \text{r on smooth boundary } \partial D \text{ of the fluid domain D} \\ \frac{\Omega}{4\pi}, & \text{r on non} - \text{smooth boundary } \partial D \text{ of the fluid domain D} \\ 0, & \text{r outside the fluid domain D} \end{cases} \tag{1.9}$$

where, C is the integration constant of the Kirchhoff-Helmholtz integral equation, ρ is the density of the wave propagation medium, c is the wave propagation velocity, k is the wavenumber, $G(r, r_0)$ is the free-field Green's function, v_n is the normal component of the acoustic particle velocity, p is the acoustic pressure, $\frac{\partial}{\partial n}$ is the normal derivative and Ω is the solid angle.

1.2.2 Non-uniqueness and Regularization

The sound-field predicted in certain acoustic radiation problems (exterior domain) using integral equation approach is in error. For certain *characteristic frequencies/wavenumbers*, the straightforward formulation of the exterior problem in terms of a single integral equation using either of the formulations mentioned above yields a *non-unique* solution. Unique solutions for such problems exist and the anomaly is *non-physical*. This anomaly is purely due to the integral equation formulation.

Uniqueness can be restored by deriving another integral equation and combining it with the original equation. Schenck [9] proposed the *Combined Helmholtz Integral Equation Formulation* (CHIEF). In CHIEF, the integral equations for the *surface* and that for the *interior* are combined to form an *over-determined* system with which the deficiencies and the undesirable computational characteristics of the direct boundary integral formulation are overcome. Randomly distributed points (a.k.a. CHIEF points) are added inside the closed surface and the pressure is set to zero at these points.

Burton and Miller [10] suggested combining the integral equation and a multiple of its *normal derivative*, which addressed the non-uniqueness for the simple-source formulation. Although the Burton and Miller approach is computationally intensive compared to CHIEF, it is a more robust formulation.

1.2.3 Solution Schemes for the Boundary Integral Equation

For numerically approximating the Kirchhoff-Helmholtz integral equation, the surface is divided into a set of *distinct* boundary elements using standard boundary element procedures such as the *collocation scheme*, where the nodes of discretization represent the collocation points.

Let,

$$p^* = \frac{e^{-ik|r-r_0|}}{4\pi|r-r_0|}; \tag{1.10}$$

$$\frac{\partial p}{\partial n} \equiv q = i\rho ck v_n; \tag{1.11}$$

$$q^* = \frac{\partial p^*}{\partial n}; \tag{1.12}$$

where p^* is the fundamental solution.

It is assumed that the boundary variables, the acoustic pressure and particle velocity on each element, can be approximately represented by a linear combination of interpolation functions,

$$p(r) = \sum_{j=1}^{N} p_j \phi_j(r); \tag{1.13}$$

where, p_j is the pressure at a discrete boundary node and $\phi(r)$ are the shape functions. Also, the acoustic velocity at the boundary point can be represented as,

$$v_n(r) = \sum_{j=1}^{N} v_j \phi_j(r). \tag{1.14}$$

When the interpolations are used in Eq. (1.8), the integration over the surface is approximated by a sum of integrals over all the boundary elements such that,

$$C(r)\, p(r) = \sum_{j=1}^{N} p_j \int\!\!\int_S \phi_j(r) q^*(r, r_0) dS - \sum_{j=1}^{N} q_j \int\!\!\int_S \phi_j(r) p^*(r, r_0) dS. \tag{1.15}$$

This can be rewritten in a compact form as,

$$C(r)\, p(r) = \sum_{j=1}^{N} p_j a_j - \sum_{j=1}^{N} q_j b_j; \tag{1.16}$$

where,

$$a_j = \int\!\!\int_S \phi_j q^*(r, r_0) dS \tag{1.17}$$

$$b_j = \int\!\!\int_S \phi_j p^*(r, r_0) dS. \tag{1.18}$$

This formulation gives a system of N equations with N unknowns. The N imposed boundary conditions can be used to solve the system of equations to yield the unknown nodal acoustic pressure or particle velocity. When the nodal pressure or velocity for all nodes is known, the field pressure at any point in the domain D can be obtained using Eq. (1.15).

The boundary element method is considered as very promising for most of the acoustic problems as only the boundary needs to be meshed. Despite this advantage, BEM leads to dense non-symmetric complex valued linear systems. For N unknown field parameters this requires $O(N^2)$ storage and $O(N^3)$ computational costs. Use of iterative methods reduce the cost to $O(nN^2)$ operations, where n is the number of iterations required. As this is still quite large, a strategy that minimizes n is also needed.

Of the various techniques that have been proposed to increase the scalability of the BEM by accelerating the matrix-vector multiplication, the fast multipole method (FMM) is most widely accepted method in fast BEM implementations. The key idea in FMM is a multipole expansion of the kernel in which the connection between the collocation point and the source point is separated. By incorporating the FMM in a quickly convergent iterative scheme, rapid solution can be achieved with reduced computational and storage costs of the order, $O(nN \log N)$ [11].

1.3 Code Verification Examples

The *code verification* of the BEM implementation was performed by solving benchmarks problems that consisted of known analytical solutions. The results of code verification are presented in the following subsections [12].

1.3.1 Interior Pressure Due to a Circular Vibrator

This model problem consists of a *circular vibrator* of radius, $a = 1\,m$, which is vibrating with a uniform normal velocity, $v_n = 1\,ms^{-1}$, due to mechanical excitation. The boundary element mesh is uniform and consisted 16 constant elements (Fig. 1.1a). Numerical results of the interior surface pressure and the pressure at a location, $r = 0.5\,m$, are presented in Figs. 1.2 and 1.3 respectively up to $k = 20\,m^{-1}$.

The *characteristic wavenumbers* for the circular cavity are given as the roots or the *zero-crossings* of the Bessel function of order 0.

$$\begin{aligned} J_0(ka) &= 0 \\ k &= 2.4, 5.5, 8.7, 11.8, 15.0 \text{ and } 18.1. \end{aligned} \tag{1.19}$$

From Fig. 1.2 it is observed that the characteristic wavenumbers correspond to the values predicted in Eq. (1.19).
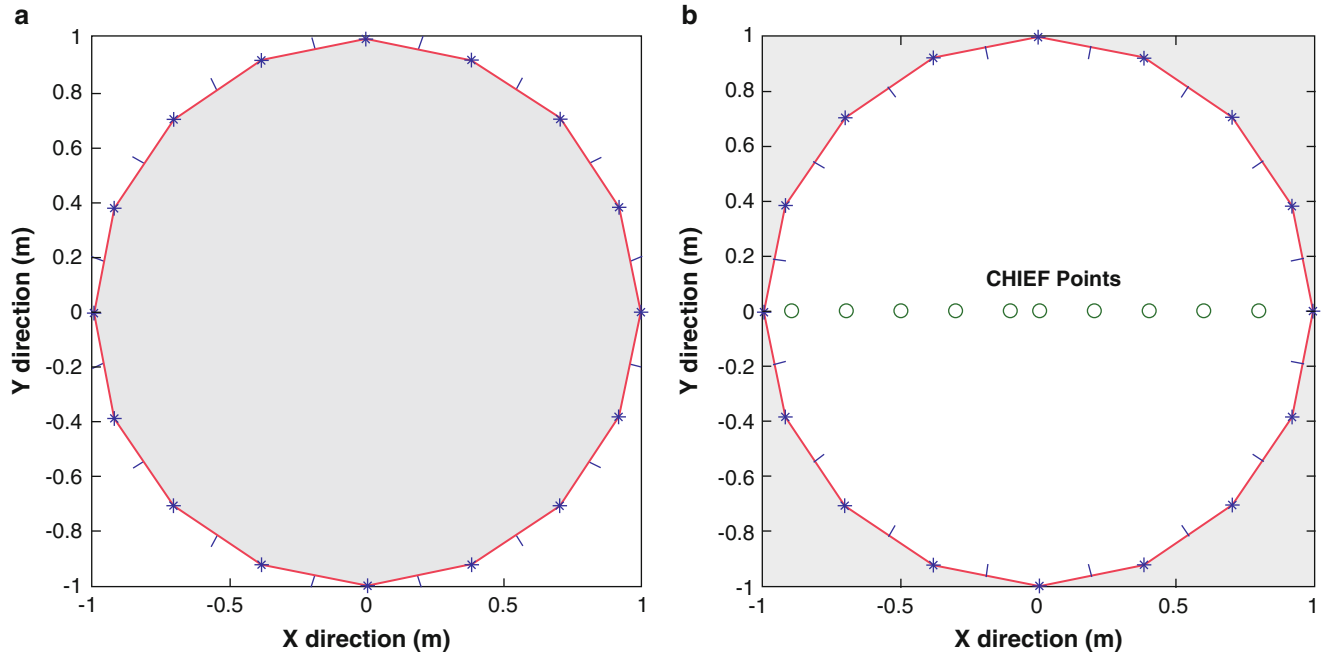
Fig. 1.1 Circular vibrator. (**a**) Interior domain. (**b**) Exterior domain – with 10 CHIEF points
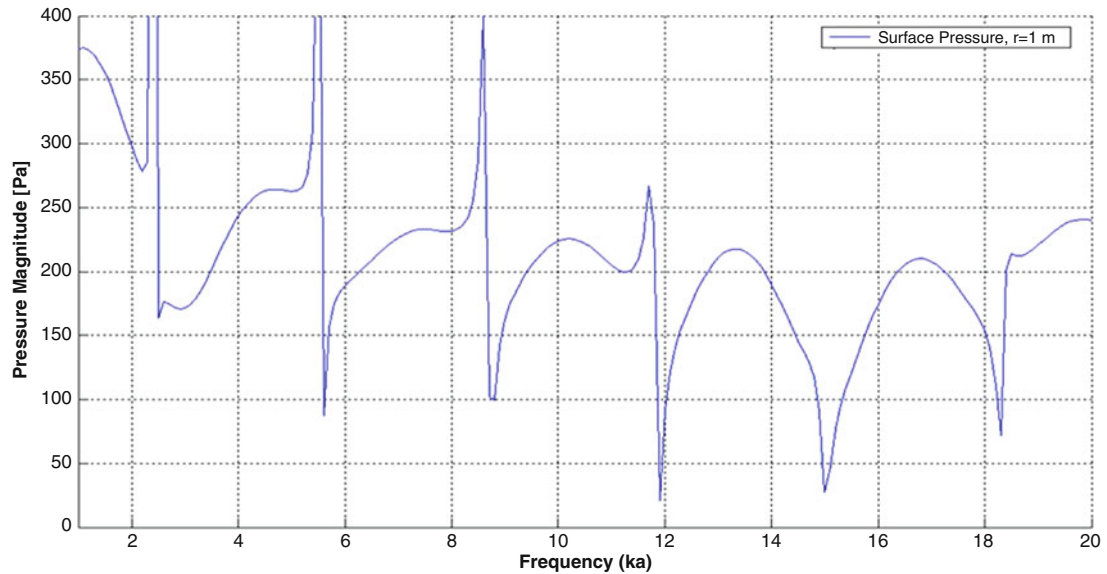
Fig. 1.2 Interior surface pressure due to a circular vibrator

1.3.2 Exterior Pressure Due to a Circular Vibrator

In exterior domain problems, for certain characteristic wavenumbers, unique solution is not possible as the boundary integral formulations are rendered incapable for numerical computation of valid solution. This is illustrated by the problem of predicting the sound-field radiated by a circular vibrator.

The sound radiated by a circular vibrator of radius, $a = 1$ m, in an infinite acoustic domain ($\rho = 1.2$ kg m^{-3} and $c = 343$ ms^{-1}) is predicted. The boundary element mesh consisted 16 constant elements (Fig. 1.1b). The exterior pressure is governed by the Helmholtz equation and it can be computed analytically using the following expression [2],

$$p(r) = i\rho c \frac{H_0^{(2)}(kr)}{H_1^{(2)}(ka)}. \tag{1.20}$$
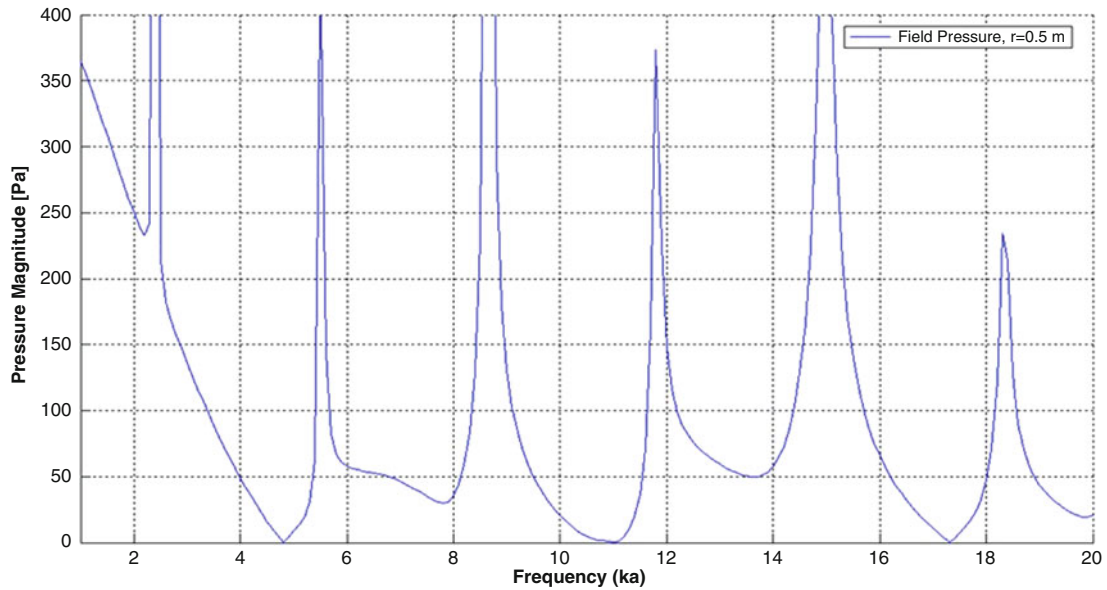
Fig. 1.3 Interior field pressure due to a circular vibrator
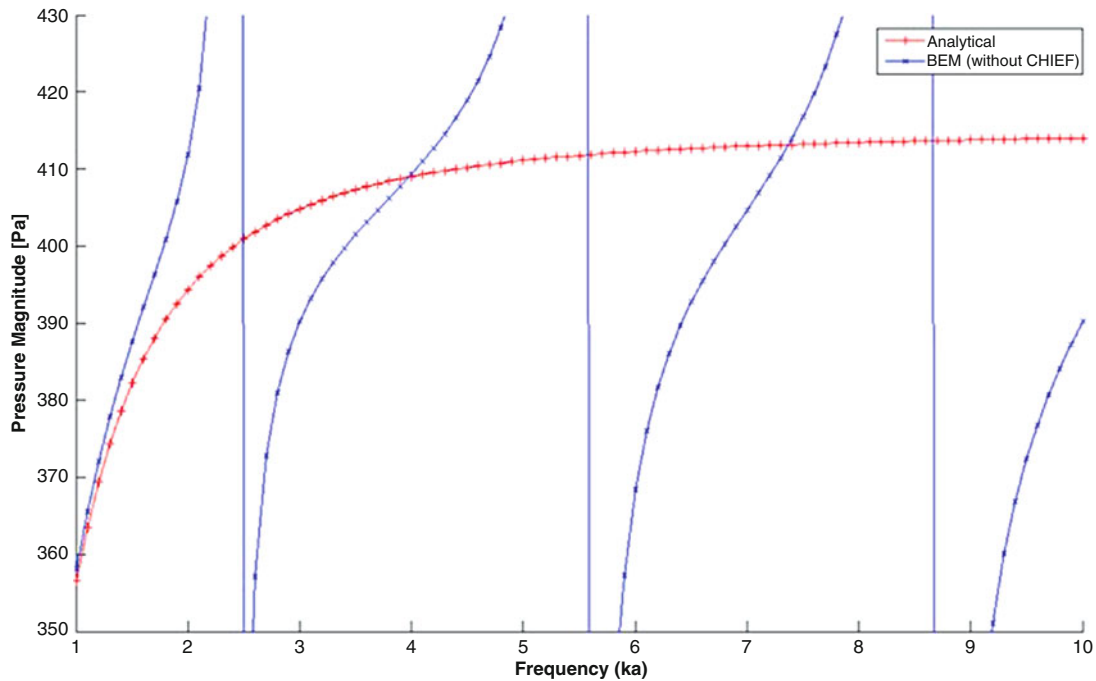
Fig. 1.4 Exterior pressure due to a circular vibrator

It is evident from Fig. 1.4 that the method of direct application of Eq. (1.8) fails to yield unique solution at critical wavenumbers that are given in Eq. (1.19). These wavenumbers match the characteristic wavenumbers of the corresponding interior problem. As mentioned in Sect. 1.2.2, this anomaly is purely due to the application of the BEM and does not have any physical significance.

The *Combined Helmholtz Integral Equation Formulation* (CHIEF) was applied for regularization. In this algorithm, the integral formulations for the *surface* and the *interior* are combined to form an *over-determined* system (substituting $C(r) = 1/2$ for the boundary nodes and $C(r) = 0$ for the interior CHIEF points, in the exterior domain BIE, Eq. (1.8)). Solving this over-determined system yields unique values for the field parameters – acoustic pressure and particle velocity.

While it is suggested that choosing just one CHIEF point would yield a unique solution, the effect of choosing more than one CHIEF point is also demonstrated. Sound-field predicted using an over-determined system with 1, 5 and 10 CHIEF points is shown in Figs. 1.5, 1.6 and 1.7 respectively.
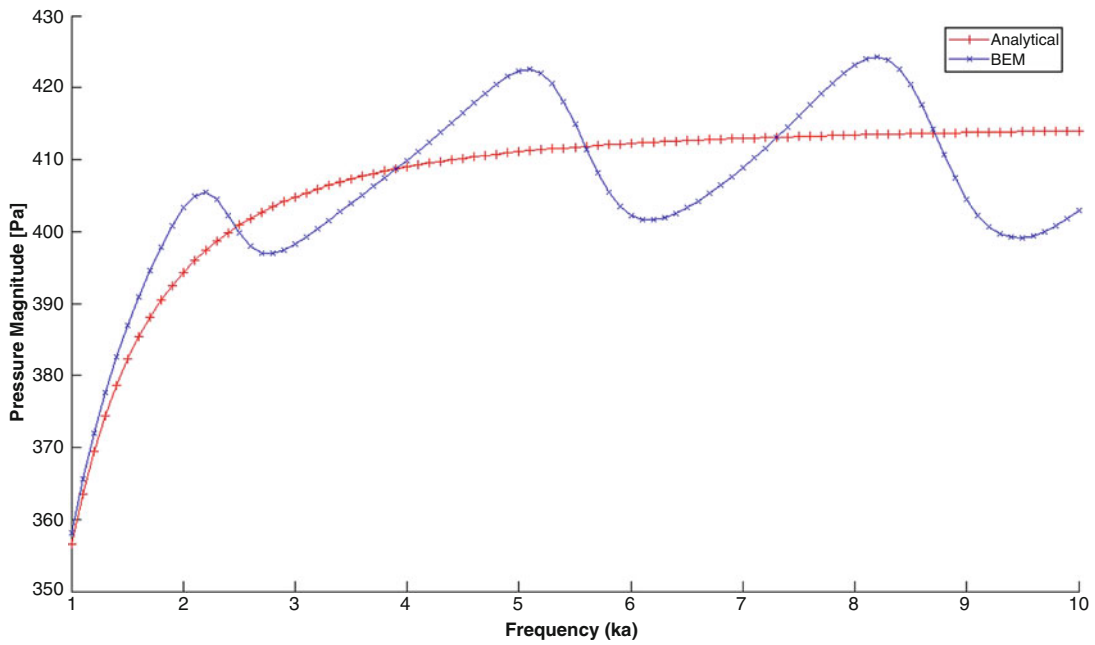
Fig. 1.5 Exterior pressure due to a circular vibrator, regularized with 1 CHIEF point
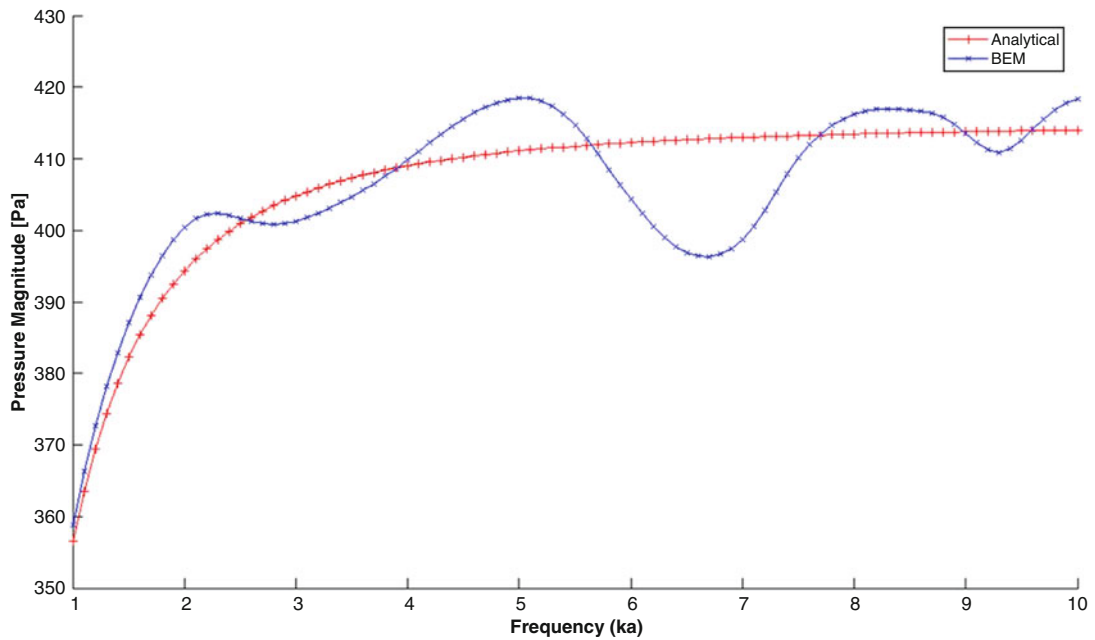
Fig. 1.6 Exterior pressure due to a circular vibrator, regularized with 5 CHIEF points
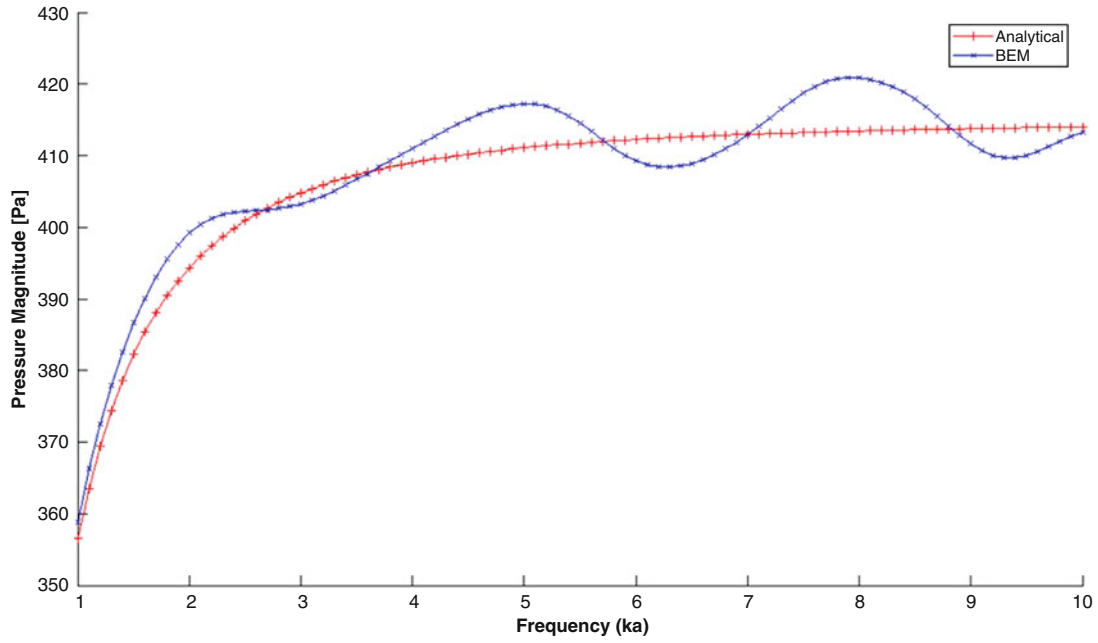
Fig. 1.7 Exterior pressure due to a circular vibrator, regularized with 10 CHIEF points
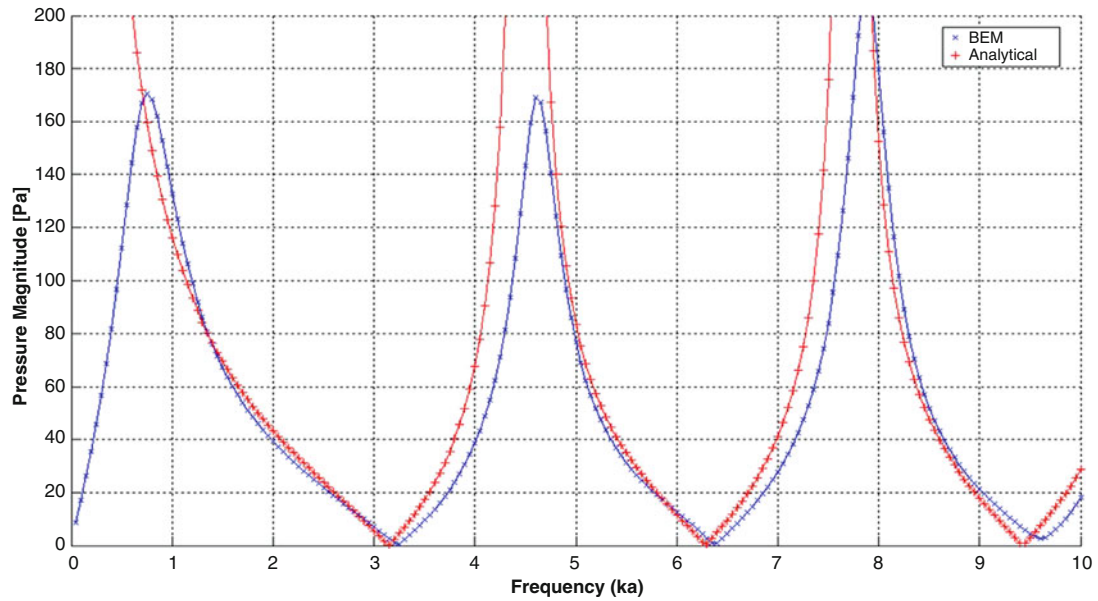
Fig. 1.8 Interior pressure due to a pulsating sphere

1.3.3 Interior Pressure Due to a Pulsating Sphere

A sphere of radius, $a = 1\,m$, pulsating with a uniform normal velocity, $v_n = 1\,m\,s^{-1}$, was analyzed in the frequency domain using the DBEM. The density of the acoustic medium and the wave propagation velocity were set as, $\rho = 1.2\,kg\,m^{-3}$ and $c = 343\,m\,s^{-1}$ respectively. Computations were performed with a wavenumber step of $0.01\,m^{-1}$.

The surface mesh of the sphere is shown in Fig. 1.9. As the sphere is symmetric about the three co-ordinate axes, it is sufficient to solve for the acoustic pressure using one octant of the sphere. The mesh consisted of 19 quadrilateral elements with linear interpolation functions. The predicted and analytical values of interior surface pressure are plotted in Fig. 1.8.
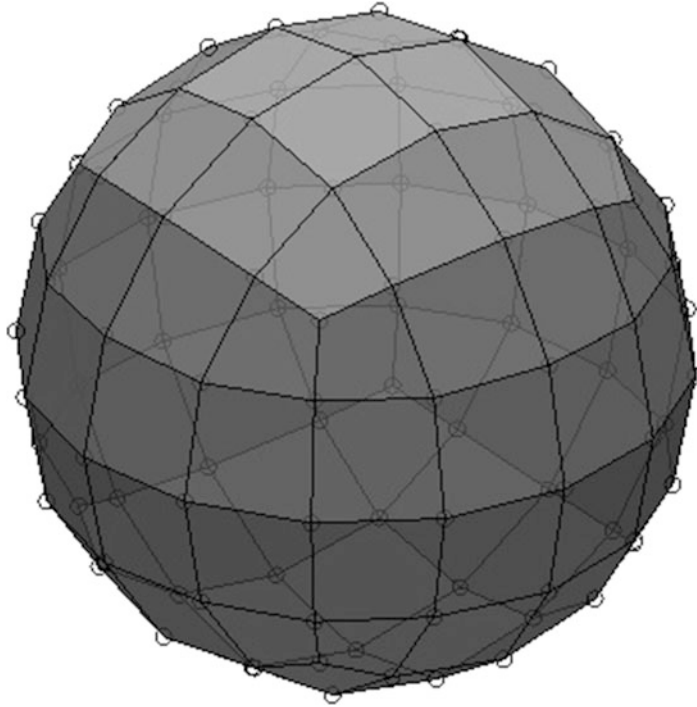
Fig. 1.9 Surface of a sphere meshed with quadrilateral elements

The pressure, p, at any location, $r \leq a$, inside the a pulsating sphere can be computed analytically using [13],

$$p(r) = -i\rho c \frac{j_0(kr)}{j_1(ka)} v_n, \tag{1.21}$$

where j_0 and j_1 are spherical Bessel functions of the first kind and order 0 and 1 respectively.

1.3.4 Exterior Pressure Due to a Pulsating Sphere

The sound-field radiated by a *pulsating sphere* of radius, $a = 1\,m$, and *uniform normal velocity*, $v_n = 1\,ms^{-1}$, prescribed on its surface, is predicted. The surrounding acoustic medium is air (density, $\rho = 1.2\,kg\,m^{-3}$ and wave propagation velocity, $c = 343\,ms^{-1}$). The computations are performed for a wavenumber step of $0.01\,m^{-1}$. The sphere is discretized as shown in Fig. 1.9. Due to axial symmetry it is sufficient to analyze just *one octant* of the sphere.

The analytical solution for the acoustic pressure, p, at a distance, $r \geq a$, from the center of the sphere of radius, a, pulsating with uniform radial velocity, v_n, is given by [13],

$$p(r) = \rho c v_n k a^2 \frac{ksa - i}{((ka)^2 + 1)\,r} e^{\left(\frac{ik(r-a)}{r}\right)} \tag{1.22}$$

The results of the analysis and the analytical solution are shown in Fig. 1.10. Several peaks occur, which coincide with the *eigenfrequencies* (also known as characteristic or irregular frequencies) of the inner volume of the sphere. As these peaks do not have any physical significance, they are eliminated by adding randomly distributed points inside the sphere at which the pressure is set to zero. The results obtained after regularization using CHIEF are shown in Fig. 1.11.
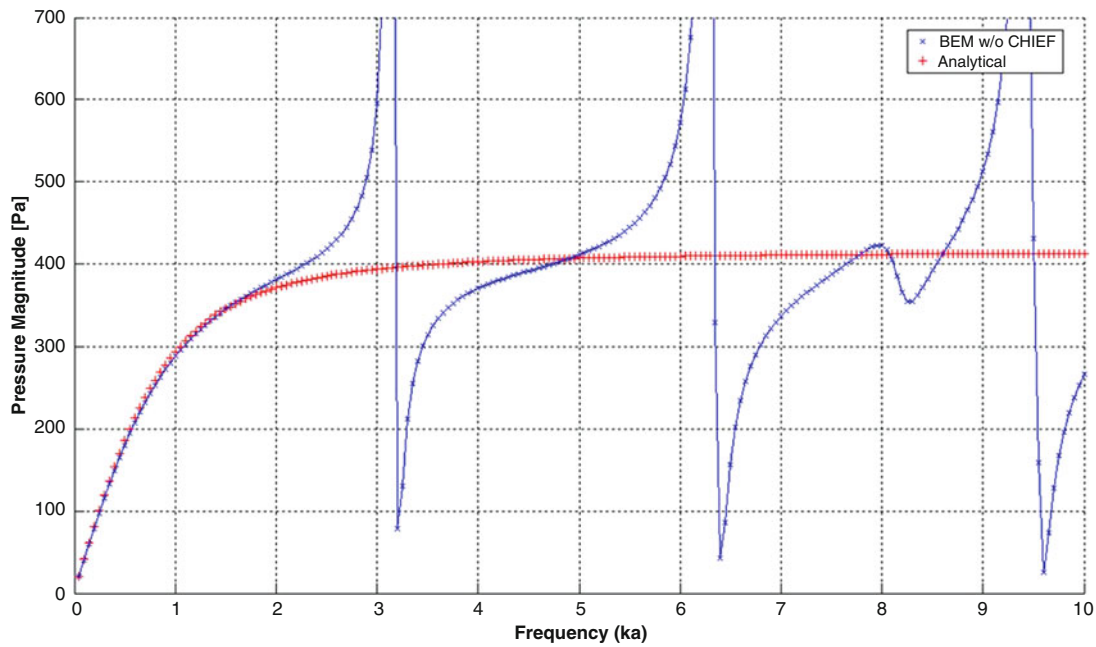
Fig. 1.10 Exterior pressure due to a pulsating sphere (without regularization)
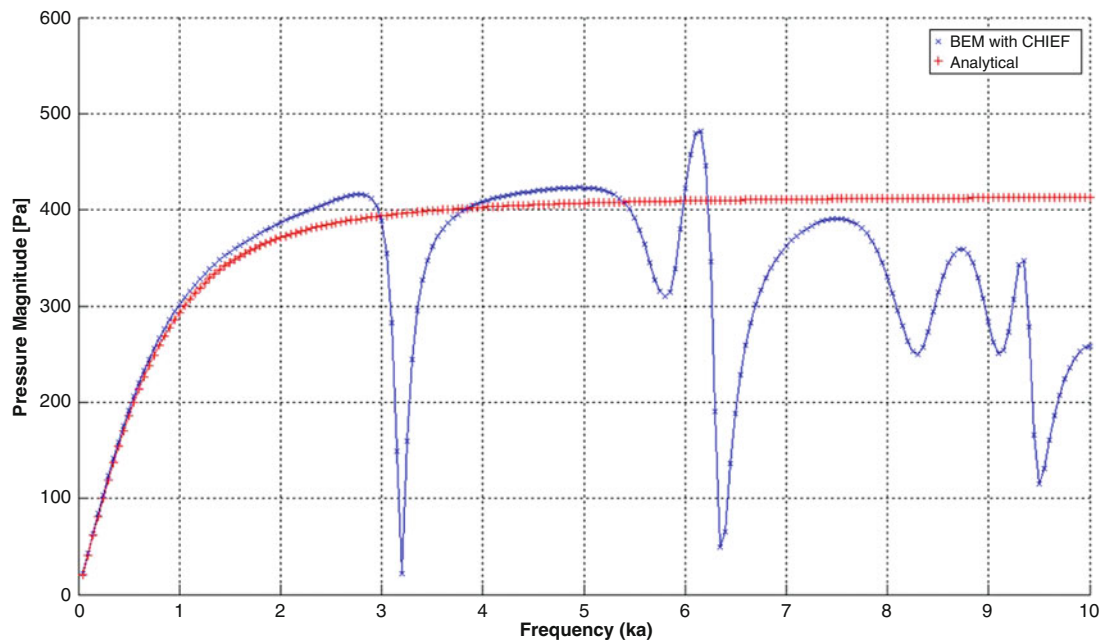
Fig. 1.11 Exterior pressure due to a pulsating sphere regularized with 1 CHIEF point

1.4 Solution Verification Examples

1.4.1 Gear Whine Prediction

Gear whine is one of the major noise sources in electric vehicle powertrains. It is theorized that gear whine is caused by static and dynamic transmission error, gear mesh stiffness variations, sliding friction, shuttling forces, etc. Gear whine is characterized by steady-state vibrations of the gear pairs. It manifests itself as modulated tones at gear mesh frequency, its harmonics, and the side bands of the gear mesh frequencies [14]. The gearbox housing structure vibration and its acoustic
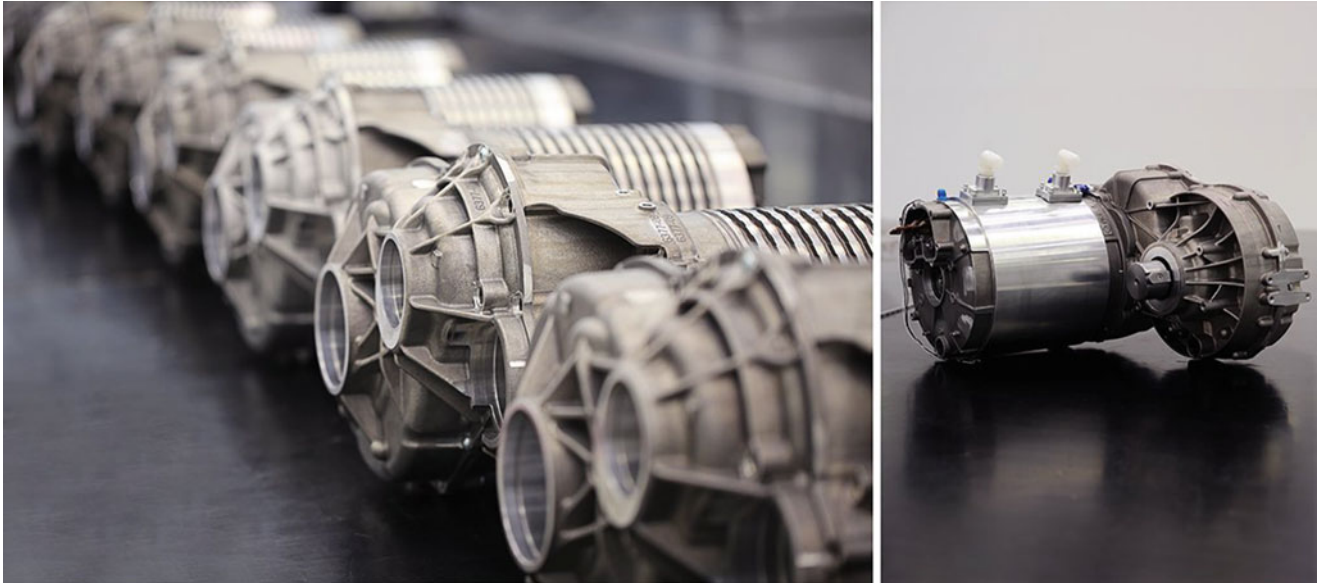
Fig. 1.12 Gearbox housing [www.lucidmotors.com]

sensitivity are critical in response to the gear whine excitations. The design objective is to optimize the gearbox housing for gear whine while achieving the desired structural efficiency by employing upfront CAE driven design and development.

The gearbox housing structure has a complicated geometry, as shown in Fig. 1.12. Closed form solution for such complicated geometries is not available. A *method of manufactured solutions* [7] using simple sound sources can be used to assist in the code and solution verification process. For example, the sound-field due to a monopole source in the far-field is given by Eq. (1.23). When the monopole source is bounded by the housing surface, the induced velocity on the housing surface due to the monopole source can be extracted. In a subsequent step, the induced velocity could be used as a boundary condition on the housing surface and the sound in far-field can be predicted. The sound predicted at a far-field point using the induced velocity boundary condition on the housing surface should be the same as that calculated using Eq. (1.23). This would serve as a code verification case. This process could be repeated for other simple sources, e.g. a dipole and quadrapole sound sources with known solutions, to generate additional code verification test cases.

$$p(r, \omega) = \frac{e^{ik|r-r_0|}}{4\pi|r - r_0|} \tag{1.23}$$

The number of elements in the computational model controls the solution time. It was desired to optimize the mesh size by studying the associated spatial discretization error. As previously discussed, the solution verification processes deals with obtaining an estimate of the error in the model predictions. By applying the method explained above, i.e. comparing the field pressure due to an induced velocity boundary condition with that calculated directly from the analytical expression. A family of surface meshes having different levels of mesh refinement were generated for the gearbox housing. An average element length of 7, 8, 10, 11 and 12 mm was chosen for the different surface meshes. The induced velocity on the housing surface due an enclosed monopole source was used to estimate the spatial discretization error. The results for the different meshes is shown in Fig. 1.13.

1.5 Results and Discussion

The goals as part of the verification process are to identify, quantify and reduce errors caused by the mapping of the mathematical model to a computer implementation. The code verification helps to identify errors due to spatial discretization and the choice of the BEM formulation. The solution verification process aided the quantification of the error associated with spatial discretization.
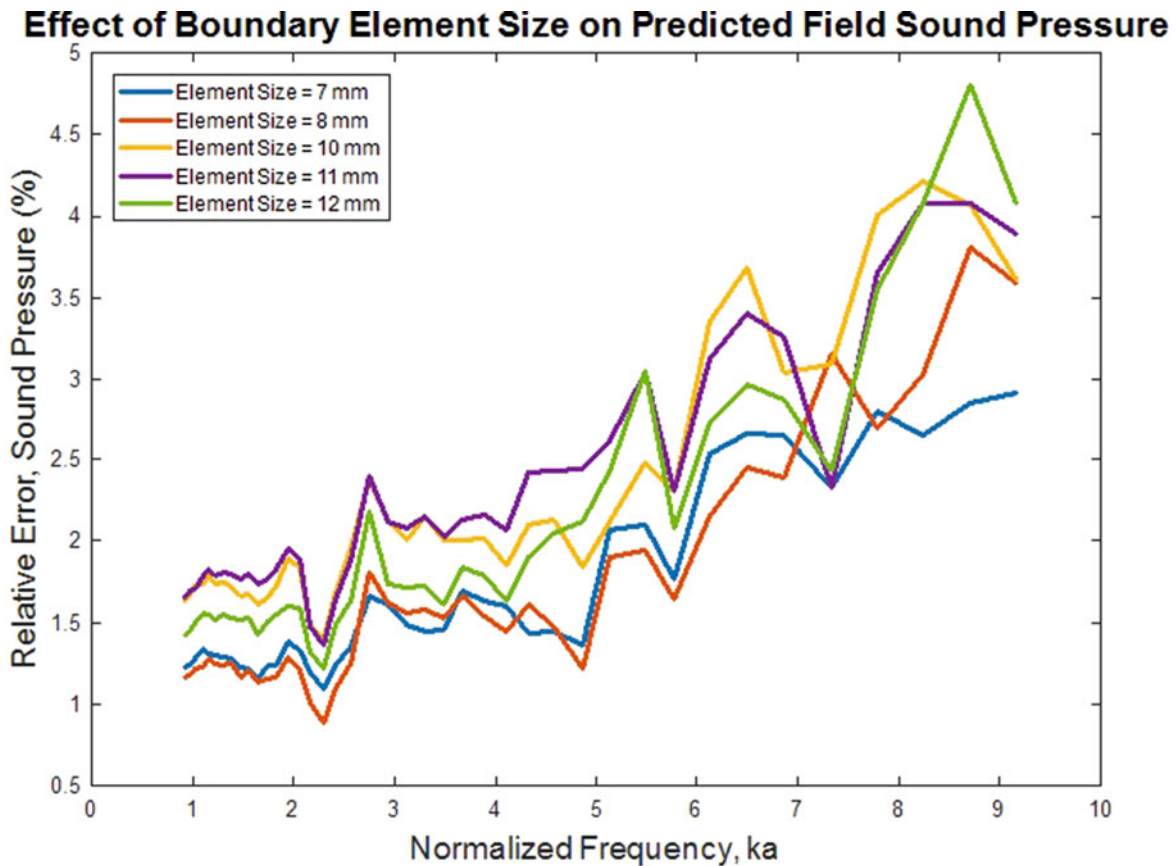
Fig. 1.13 Mesh sensitivity

The discretization requirements of BEM are dictated by low- and high-frequency thresholds. The low-frequency limit is dependent on the numerical integration technique used. The high-frequency limits are established by numerical integration technique, interpolation functions and most importantly the wavelength of sound. The predicted values of the interior acoustic pressure diverge from the analytical values for $ka > 9$ for the pulsating sphere case (Fig. 1.8). It is recommended to use six elements per wavelength are required to predict an acceptable solution.

Code verification for exterior domain problems helped in identifying the non-uniqueness issue associated with the direct implementation of the Helmholtz Integral Formulation. Particularly, the relative error was significantly high at certain frequencies for the gearbox housing structure. It could be attributed to the non-uniqueness in the solution at the characteristic frequencies of the complementary interior region bounded by the closed surface. This was ascertained by determining the eigenfrequencies of the complimentary interior problem.

The model set up for solving the interior domain problem was performed using the following steps:

1. Introduce a monopole source with volume velocity one at an interior point, e.g. at the origin (0,0,0)
2. Set the boundary condition on the surface to zero
3. Predict the acoustic pressure at interior field points

The peaks in the interior pressure (Fig. 1.14) correspond to the cavity resonances. As the Direct HIE Formulation resulted in non-unique solutions. The problem was solved by applying the Burton-Miller Formulation, which addressed this issue. The results are presented in Table 1.1.
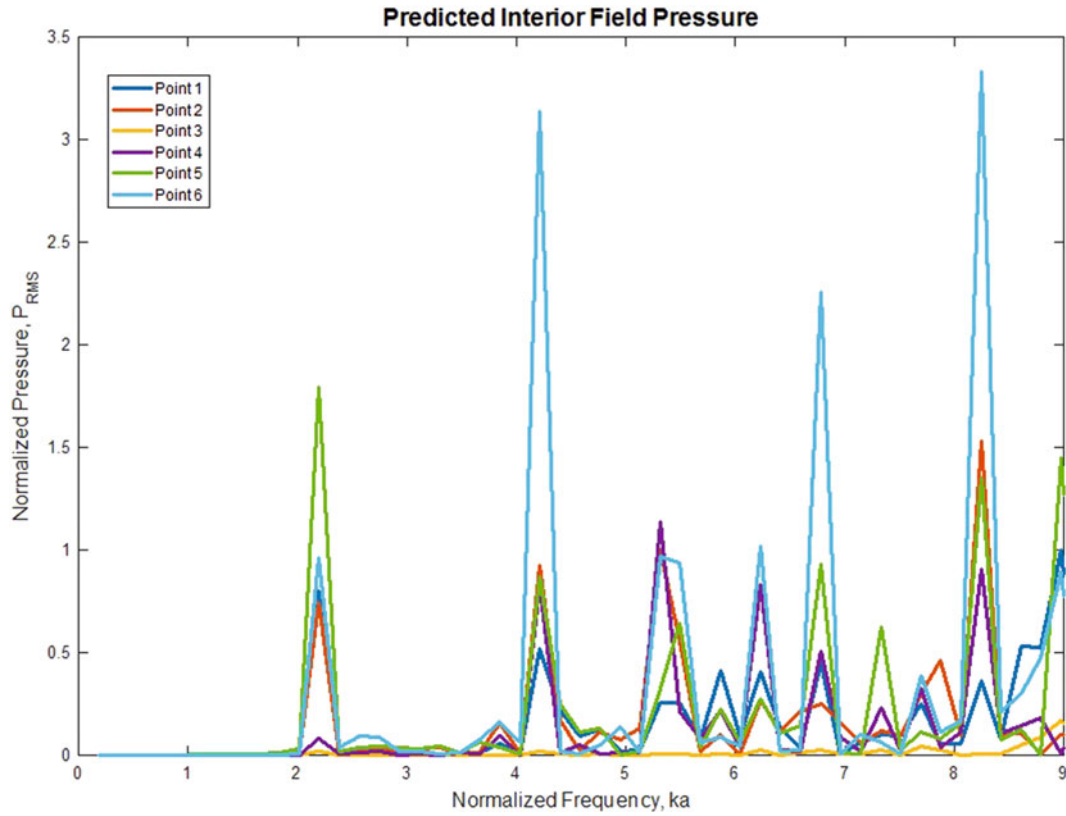
Fig. 1.14 Interior acoustic pressure

Table 1.1 Predicted exterior vs. analytical acoustic pressure

Field point	Location	Relative error $|\epsilon_{rel}|$ (%)	
		HIE	Burton-Miller
1	5a	35.30	0.94
2	10a	32.16	1.26
3	20a	30.04	1.28
4	50a	28.77	1.26
5	100a	28.04	0.84

1.6 Conclusions

Model verification and validation play a crucial role in building credibility in simulations. It is highly desirable to have a CAE lead product design and development process due to the associated time and cost advantages. Verification and validation of the models can be performed by comparing the model predictions with known solutions of simple sources and experimental data respectively. The boundary element method is applied in structural acoustics for sound-field predictions. In this paper, a background on the BEM formulations was provided. Model verification process was demonstrated with examples. The BEM implementation produced the desired results for interior domain problems. However, for exterior domain problems that have closed surfaces, the direct application of the BEM implementation failed to give unique solution at certain wavenumbers. These wavenumbers correspond to the eigenfrequencies of the complementary interior problem. This is non-physical and uniqueness can be restored using regularization techniques. Examples demonstrated the use of the Combined Helmholtz Integral Equation Formulation (CHIEF) and the Burton-Miller Formulation to restore uniqueness. In the case of complex geometries, the method of manufactured solutions to aid in the model verification was illustrated with examples.

References

1. Von Estorff, O.: Boundary Elements in Acoustics, Advances and Applications. WIT Press, Southampton (2000)
2. Wu, T.W.: Boundary Element Acoustics, Fundamentals and Computer Codes. WIT Press, Southampton/Boston (2000)
3. Chen, G., Zhou, J.: Boundary Element Methods. Academic, New York (1992)
4. Kythe, P.K.: An Introduction to Boundary Element Methods. CRC Press, Boca Raton (1995)
5. Thacker, B.H., Doebling, S.W., Hemez, F.M., Anderson, M.C., Pepin, J.E., Rodriguez, E.A.: Concepts of model verification and validation. Los Alamos National Lab, LA-14167-MS (2004)
6. AIAA: Guide for the verification and validation of computational fluid dynamics simulations. American Institute of Aeronautics and Astronautics, AIAA-G-077-1998 (1998)
7. Oberkampf, W.L., Trucano, T.G.: Verification and validation benchmarks. Sandia National Lab, SAND2007-0853 (2007)
8. Copley, L.G.: Fundamental results concerning integral representations in acoustic radiation. J. Acoust. Soc. Am. **44**(1), 28–32 (1968)
9. Schenck, H.A.: Improved integral formulation for acoustic radiation problems. J. Acoust. Soc. Am. **44**(1), 41–58 (1968)
10. Burton, A.J., Miller, G.F.: The application of integral equation methods to the numerical solution of some exterior boundary-value problems. In: Proceedings of the Royal Society of London. Series A, Mathematical and Physical Sciences. Royal Society of London (1971)
11. Gumerov, N.A., Duraiswami, R.: Fast Multipole Methods for the Helmholtz Equation in Three Dimensions. Elsevier Series in Electromagnetism. Elsevier Science, Burlington (2005). ISBN:9780080531595
12. Pasha, H.G.: Prediction of sound fields in closed and open cavities. Master's thesis, Indian Institute of Technology Madras (2008)
13. Williams, E.G.: Fourier Acoustics: Sound Radiation and Nearfield Acoustical Holography. Academic, San Diego (1999)
14. Singh, R.: Gear Noise: Anatomy, Prediction and Solution. In: Proceedings of Internoise (2009)

Chapter 2
Substructuring of Viscoelastic Subcomponents with Interface Reduction

Robert J. Kuether and Kevin L. Troyer

Abstract The Craig-Bampton approach for component mode synthesis in structural dynamics has been widely used to reduce the order of large, detailed finite element models made from linear elastic materials. This methodology separates the full order model into smaller subcomponents and reduces the equations of motion with a truncated set of fixed-interface modes and static constraint modes. A drawback of this approach is that the model has one constraint mode for every interface degree-of-freedom, which may result in a large and prohibitively costly superelement. Previous work has addressed this issue via characteristic constraint modes, which reduces the number of interface degrees-of-freedom by performing a secondary modal analysis on the interface partition. The current work extends the Craig-Bampton approach with interface reduction to include subcomponents with linear viscoelastic materials modeled using a Prony series. For substructures containing materials such as foams or polymers, the viscoelastic constitutive law more accurately represents the material energy dissipation compared to traditional viscous or modal damping. The new approach will be demonstrated on the assembly of two composite plates with fixed boundary conditions along one edge.

Keywords Viscoelasticity • Model reduction • Substructuring • Prony series • Structural dynamics

2.1   Introduction

Component mode synthesis (CMS), or dynamic substructuring, has long been used as a model reduction technique in structural dynamics. The idea is to separate a large scale finite element model into smaller, more computationally manageable subcomponents and reduce them with a set of component mode shapes. These lower order subcomponent models are then coupled to provide an efficient and accurate reduced order model of the original structure. Many techniques have been developed over the past 60 or so years and the interested reader is directed to the review papers in [1, 2]. Some variations of the substructuring approaches include the use of free- or fixed- interface modes (or other hybrid methods), dual or primal assembly, and frequency or physical domain coupling. Many of the common CMS strategies are for linear, undamped structures with linear elastic constitutive laws, but fewer works have been developed for models incorporating nonlinear or time-dependent materials.

The focus of this research is to develop a fixed-interface substructuring approach using primal assembly in the physical domain for finite element models with linear viscoelastic constitutive laws modeled as Prony series. The work by Qian et al. [3] presented a substructure synthesis method for the second-order form of finite element models with general forms of linear viscoelastic damping models. The CMS approach is formulated in the physical domain for the solution to transient problems, and each subcomponent is reduced using a Rayleigh-Ritz approach with a set of real, admissible trial vectors obtained from the eigensolution of the undamped equations. A frequency response function (FRF) based substructuring approach was developed by de Lima et al. in [4] where the frequency domain finite element model uses the complex modulus approach and frequency-temperature superposition to capture the frequency and temperature dependent linear viscoelastic behavior. They are concerned with modeling strategies to passively control mechanical vibrations of a main, linear elastic structure connected to linear viscoelastic mounts. The FRF representation allows either of the components to be represented either numerically

R.J. Kuether (✉) • K.L. Troyer
Sandia National Laboratories, P.O. Box 5800 MS 0346, Albuquerque, NM 87185, USA
e-mail: rjkueth@sandia.gov

or experimentally, however no reduction was performed at the subcomponent level. An improvement to the classical Craig-Bampton (CB) substructuring was adapted to viscoelastic finite element models in [5] by computing the fixed-interface and static constraint modes from the frequency independent stiffness and mass matrix, and enriching the basis with static residues associated with the viscoelastic damping forces and external forces. The method was developed for frequency domain responses, and uses a constant modal basis. Tran et al. [6] used a similar method for CMS of vibroacoustic problems, and a free-interface CMS scheme for viscoelastic subcomponents was proposed in [7].

The research presented in this paper develops a fixed-interface CMS approach using primal assembly in the physical domain for linear viscoelastic subcomponent models. Many existing approaches deal solely with frequency based substructuring which can only be solved for steady-state problems. A time domain approach allows the reduced model to be excited via transient inputs or steady state inputs if needed, allowing more flexibility in the types of solutions obtained from the model. Each subcomponent is reduced using a set of linearized complex fixed-interface modes, and a set of pseudo-static constraint modes; this is conceptually similar to the traditional Craig-Bampton approach in [8]. Since the number of interface degrees-of-freedom (DOF) can be prohibitively large, the assembled viscoelastic substructures are further reduced by performing a secondary modal analysis on the assembled boundary. The eigenvectors obtained from this analysis are referred to as linearized complex characteristic constraint modes, and were originally developed for undamped or proportionally damped systems [9, 10].

In Sect. 2.2, the fixed-interface CMS theory is developed for linear viscoelastic subcomponents along with the system-level interface reduction. Section 2.3 presents the results from a numerical example of two sandwich plates assembled at a shared interface. The results for the viscoelastic CMS models with and without interface reduction are presented and show how the results evolve with various bases. The final section draws conclusions from the theory and results.

2.2 Theoretical Development

A substructuring approach for large scale finite element analysis (FEA) begins by separating the semi-discretized model into smaller subcomponent models. The spatially discretized, N DOF equations of motion for a single subcomponent have the form,

$$\mathbf{M}\ddot{\mathbf{x}} + \mathbf{K}_K \int_0^t \zeta_K(t-\tau)\,\dot{\mathbf{x}}(\tau)\,d\tau + \mathbf{K}_G \int_0^t \zeta_G(t-\tau)\,\dot{\mathbf{x}}(\tau)\,d\tau + \mathbf{K}_e \mathbf{x} = \mathbf{f}_{ext}(t) \tag{2.1}$$

The coupled integro-differential equations have real, symmetric $N \times N$ matrices $\mathbf{M}$, $\mathbf{K}_K$, $\mathbf{K}_G$, $\mathbf{K}_e$, which correspond to the respective mass, viscoelastic bulk stiffness, viscoelastic shear stiffness, and elastic stiffness. The $N \times 1$ vectors $\mathbf{x}$ and $\mathbf{f}_{ext}(t)$ represent the physical displacements and externally applied forces, respectively, while the overdot is the time derivative. The integrals in Eq. (2.1) are separated into contributions from the shear and bulk relaxation functions whose constitutive law is represented by an exponential Prony series. The kernel function for the bulk relaxation modulus is written as

$$\zeta_K(t) = \sum_{i=1}^{N_K} K_{coeff,i} e^{-t/\tau_{K,i}} \tag{2.2}$$

where the leading coefficients must sum to unity

$$\sum_{i=1}^{N_K} K_{coeff,i} = 1 \tag{2.3}$$

The time-dependent function $\zeta_K(t)$ is a summation of N_K exponential functions that contain an amplitude coefficient $K_{coeff,i}$ corresponding to a particular time constant $\tau_{K,i}$. The shear relaxation kernel function, $\zeta_G(t)$, has the same form as Eqs. (2.2) and (2.3), with the exception that the coefficients ($G_{coeff,i}, \tau_{G,i}$) will be different and the Prony series may contain a different number of terms (N_G). In general, $\zeta_K(t)$ and $\zeta_G(t)$ are restricted to be continuous and monotonically decreasing, thus requiring that the coefficients and relaxation times be positive (e.g. $K_{coeff,i}$ and $\tau_{K,i}$). The integral terms have a simple functional form, such that the kernel functions are simply a constant matrix multiplied by a series of exponential functions.

Following the classical CB approach, the viscoelastic model in Eq. (2.1) is partitioned into interior and boundary DOF, respectively corresponding to x_i and x_b.

$$\begin{bmatrix} \mathbf{M}_{ii} & \mathbf{M}_{ib} \\ \mathbf{M}_{bi} & \mathbf{M}_{bb} \end{bmatrix} \begin{Bmatrix} \ddot{\mathbf{x}}_i \\ \ddot{\mathbf{x}}_b \end{Bmatrix} + \begin{bmatrix} \mathbf{K}_{K,ii} & \mathbf{K}_{K,ib} \\ \mathbf{K}_{K,bi} & \mathbf{K}_{K,bb} \end{bmatrix} \int_0^t \zeta_K(t-\tau) \begin{Bmatrix} \dot{\mathbf{x}}_i \\ \dot{\mathbf{x}}_b \end{Bmatrix} d\tau + \begin{bmatrix} \mathbf{K}_{G,ii} & \mathbf{K}_{G,ib} \\ \mathbf{K}_{G,bi} & \mathbf{K}_{G,bb} \end{bmatrix}$$

$$\int_0^t \zeta_G(t-\tau) \begin{Bmatrix} \dot{\mathbf{x}}_i \\ \dot{\mathbf{x}}_b \end{Bmatrix} d\tau + \begin{bmatrix} \mathbf{K}_{e,ii} & \mathbf{K}_{e,ib} \\ \mathbf{K}_{e,bi} & \mathbf{K}_{e,bb} \end{bmatrix} \begin{Bmatrix} \mathbf{x}_i \\ \mathbf{x}_b \end{Bmatrix} = \begin{Bmatrix} 0 \\ \mathbf{f}_{ext}(t) \end{Bmatrix} \tag{2.4}$$

These subcomponent equations appear conceptually similar to the undamped CB models with the exception of the two integral terms corresponding to the viscoelastic internal forces. The following subsections develop the reduction bases for each subcomponent, the primal assembly step and the interface reduction applied at the system-level.

2.2.1 Linearized Complex Fixed-Interface Modes

Due to the additional damping terms from the viscoelastic material, the dynamic, fixed-interface modes are obtained by formulating a linearized quadratic eigenvalue problem (QEVP) from the subcomponent model fixed at the entire set of boundary DOF. This is accomplished by retaining only the interior portion of the equations of motion in Eq. (2.4) as,

$$\mathbf{M}_{ii}\ddot{\mathbf{x}}_i + \mathbf{K}_{K,ii}\int_0^t \zeta_K(t-\tau)\dot{\mathbf{x}}_i d\tau + \mathbf{K}_{G,ii}\int_0^t \zeta_G(t-\tau)\dot{\mathbf{x}}_i d\tau + \mathbf{K}_{e,ii}\mathbf{x}_i = 0 \tag{2.5}$$

Taking the Laplace transform of this equation produces the QEVP,

$$\left(\lambda_r^2 \mathbf{M}_{ii} + \lambda_r \mathbf{K}_{K,ii} \sum_{j=1}^{N_K} \frac{K_{coeff,j}}{\lambda_r + 1/\tau_{K,j}} + \lambda_r \mathbf{K}_{G,ii} \sum_{j=1}^{N_K} \frac{G_{coeff,j}}{\lambda_r + 1/\tau_{G,j}} + \mathbf{K}_{e,ii} \right) \boldsymbol{\varphi}_{i,r} = 0 \tag{2.6}$$

The complex scalar λ_r is the eigenvalue while $\boldsymbol{\varphi}_{i,r}$ is the complex eigenvector. As proposed in [11, 12], an iterative approach is used to solve for each complex eigenvector by linearizing the Prony series in Eq. (2.6) about a prescribed complex value, λ_0,

$$\left(\lambda_r^2 \mathbf{M}_{ii} + \lambda_r \mathbf{K}_{K,ii} \sum_{j=1}^{N_K} \frac{K_{coeff,j}}{\lambda_0 + 1/\tau_{K,j}} + \lambda_r \mathbf{K}_{G,ii} \sum_{j=1}^{N_K} \frac{G_{coeff,j}}{\lambda_0 + 1/\tau_{G,j}} + \mathbf{K}_{e,ii} \right) \boldsymbol{\varphi}_{i,r} = 0 \tag{2.7}$$

By linearizing the Prony series about a fixed frequency, $\lambda_0 = i\omega_0$, Eq. (2.7) is iteratively solved for the rth linearized complex fixed-interface (LC-FI) mode until the residual between computed frequency and linearized frequency is sufficiently small (e.g. $|\mathrm{Im}(\lambda_r) - \omega_0|/|\omega_0| < 10^{-3}$). Due to the frequency dependence of the viscoelastic forces, this process is repeated for each fixed-interface mode of interest. Although there is additional upfront cost to solve the QEVP, the advantage to this approach is the fact that the imaginary part of the eigenvalues exactly corresponds to the oscillation frequency, so the number of fixed-interface modes can be truncated based on a cut-off frequency. The typical rule of thumb for substructuring is to include modes up to 1.5–2.0 times the frequency range of interest, and that rule is recommended for linear viscoelastic models as well.

The set of LC-FI modes are assembled into a complex matrix, $\boldsymbol{\Phi}_{ii}$. Since the basis for reduction in the physical domain is restricted to real vectors, the fixed-interface basis used to reduce Eq. (2.4) is defined as,

$$\boldsymbol{\Phi}_i^{LC} = \begin{bmatrix} \text{Re}\left(\boldsymbol{\Phi}_{ii}\right) & \text{Im}\left(\boldsymbol{\Phi}_{ii}\right) \\ 0 & 0 \end{bmatrix} \tag{2.8}$$

Including both the real and imaginary parts of the LC-FI modes essentially doubles the number of shapes, but results in a very efficient basis due to the fact that these account for the viscoelastic forces.

2.2.2 Pseudo-Static Constraint Modes

As defined by Craig in [13], a static constraint mode is "the static deformation of a structure when a unit displacement is applied to one coordinate of a specified set of constraint coordinates, while the remaining coordinates of that set are restrained, and the remaining degrees-of-freedom of the structure are force-free." For viscoelastic models with time-dependent material laws, the definition by Craig has been extended to the so-called pseudo-static constraint mode (PS-CM). Ignoring the inertia terms in Eq. (2.4), the frequency domain equations of motion become

$$\left(i\omega \begin{bmatrix} \mathbf{K}_{K,ii} & \mathbf{K}_{K,ib} \\ \mathbf{K}_{K,bi} & \mathbf{K}_{K,bb} \end{bmatrix} \sum_{j=1}^{N_K} \frac{K_{coeff\,j}}{i\omega + 1/\tau_{K,j}} + i\omega \begin{bmatrix} \mathbf{K}_{G,ii} & \mathbf{K}_{G,ib} \\ \mathbf{K}_{G,bi} & \mathbf{K}_{G,bb} \end{bmatrix} \sum_{j=1}^{N_G} \frac{G_{coeff\,j}}{i\omega + 1/\tau_{G,j}} + \begin{bmatrix} \mathbf{K}_{e,ii} & \mathbf{K}_{e,ib} \\ \mathbf{K}_{e,bi} & \mathbf{K}_{e,bb} \end{bmatrix} \right) \left\{ \begin{array}{c} \mathbf{X}_i \\ \mathbf{X}_b \end{array} \right\} = \left\{ \begin{array}{c} 0 \\ \mathbf{F}_{ext} \end{array} \right\} \tag{2.9}$$

A unit displacement at each boundary DOF while holding the others fixed is imposed by setting $\mathbf{X}_b = \mathbf{I}$, where $\mathbf{I}$ is the identity matrix. The interior DOF response to the unit deflection is computed from the top portion of Eq. (2.9),

$$\left(i\omega \mathbf{K}_{K,ii} \sum_{j=1}^{N_K} \frac{K_{coeff\,j}}{i\omega + 1/\tau_{K,j}} + i\omega \mathbf{K}_{G,ii} \sum_{j=1}^{N_G} \frac{G_{coeff\,j}}{i\omega + 1/\tau_{G,j}} + \mathbf{K}_{e,ii} \right) \mathbf{X}_i$$

$$= -\left(i\omega \mathbf{K}_{K,ib} \sum_{j=1}^{N_K} \frac{K_{coeff\,j}}{i\omega + 1/\tau_{K,j}} + i\omega \mathbf{K}_{G,ib} \sum_{j=1}^{N_G} \frac{G_{coeff\,j}}{i\omega + 1/\tau_{G,j}} + \mathbf{K}_{e,ib} \right) \tag{2.10}$$

In order to obtain a solution for the PS-CMs, an appropriate frequency, ω, must be chosen. When setting $\omega = 0$, the solution to $\mathbf{X}_i$ results in the classical static constraint mode ($\mathbf{X}_i = -\mathbf{K}_{e,ii}^{-1}\mathbf{K}_{e,ib}$). It is recommended using frequencies $\omega > 0$, which produce a complex-valued, pseudo-static shape $\mathbf{X}_i$. The real and imaginary parts of these vectors form the set of pseudo-static constraint modes,

$$\boldsymbol{\Psi}_c = \begin{bmatrix} \text{Re}\left\{ \begin{array}{c} \mathbf{X}_i \\ \mathbf{I}_{bb} \end{array} \right\} & \text{Im}\left\{ \begin{array}{c} \mathbf{X}_i \\ \mathbf{I}_{bb} \end{array} \right\} \end{bmatrix} = \begin{bmatrix} \text{Re}\left(\mathbf{X}_i\right) & \text{Im}\left(\mathbf{X}_i\right) \\ \mathbf{I}_{bb} & 0 \end{bmatrix} \tag{2.11}$$

2.2.3 Subcomponent Model Reduction

The reduced transformation matrix assembles the LC-FI modes from Eq. (2.8) and the PS-CM from Eq. (2.11) as,

$$\left\{ \begin{array}{c} \mathbf{x}_i \\ \mathbf{x}_b \end{array} \right\} = \begin{bmatrix} \text{Re}\left(\boldsymbol{\Phi}_{ii}\right) & \text{Im}\left(\boldsymbol{\Phi}_{ii}\right) & \text{Im}\left(\mathbf{X}_i\right) & \text{Re}\left(\mathbf{X}_i\right) \\ 0 & 0 & 0 & \mathbf{I}_{bb} \end{bmatrix} \left\{ \begin{array}{c} \mathbf{q}_k^r \\ \mathbf{q}_k^i \\ \mathbf{x}_b^i \\ \mathbf{x}_b^r \end{array} \right\} = \mathbf{Tq} \tag{2.12}$$

The generalized coordinates $\mathbf{q}_k^r$ and $\mathbf{q}_k^i$ correspond to the amplitudes of the real and imaginary parts of the LC-FI shapes, respectively, while $\mathbf{x}_b^r$ and $\mathbf{x}_b^i$ respectively represent the real and imaginary amplitudes of the PS-CMs. The basis in Eq. (2.12) is projected onto the subcomponent model in Eq. (2.4), producing a lower order model,

$$\widehat{\mathbf{M}}\ddot{\mathbf{q}} + \widehat{\mathbf{K}}_K \int_0^t \zeta_K (t - \tau)\, \dot{\mathbf{q}}(\tau)\, d\tau + \widehat{\mathbf{K}}_G \int_0^t \zeta_G (t - \tau)\, \dot{\mathbf{q}}(\tau)\, d\tau + \widehat{\mathbf{K}}_e \mathbf{q} = \mathbf{T}^{\mathrm{T}} \mathbf{f}_{ext}(t) \tag{2.13}$$

where

$$\widehat{\mathbf{M}} = \mathbf{T}^{\mathrm{T}} \mathbf{M} \mathbf{T}$$
$$\widehat{\mathbf{K}}_K = \mathbf{T}^{\mathrm{T}} \mathbf{K}_K \mathbf{T}$$
$$\widehat{\mathbf{K}}_G = \mathbf{T}^{\mathrm{T}} \mathbf{K}_G \mathbf{T}$$
$$\widehat{\mathbf{K}}_e = \mathbf{T}^{\mathrm{T}} \mathbf{K}_e \mathbf{T}$$

The real transformation matrix produces real reduced matrices.

2.2.4 Assembly

The reduced order viscoelastic models attach to adjacent models with a common interface using the primal formulation [2] to satisfy compatibility and equilibrium conditions at the boundary DOF. Without loss of generality, assume that two subcomponents are being coupled, denoted with superscripts (A) and (B). This is accomplished by satisfying the compatibility condition at the real-valued partition of the PS-CMs, such that $\mathbf{x}_b^{r,(A)} = \mathbf{x}_b^{r,(B)}$. This relationship enforces the two boundaries to have the same motion. Following standard assembly methods from finite element analysis [14], a direct coupling matrix $\mathbf{L}$ is defined as,

$$\begin{Bmatrix} \mathbf{q}^{(A)} \\ \mathbf{q}^{(B)} \end{Bmatrix} = \begin{Bmatrix} \mathbf{q}_i^{(A)} \\ \mathbf{x}_b^{r,(A)} \\ \mathbf{q}_i^{(B)} \\ \mathbf{x}_b^{r,(B)} \end{Bmatrix} = \begin{bmatrix} \mathbf{I} & 0 & 0 \\ 0 & 0 & \mathbf{I} \\ 0 & \mathbf{I} & 0 \\ 0 & 0 & \mathbf{I} \end{bmatrix} \begin{Bmatrix} \mathbf{q}_i^{(A)} \\ \mathbf{q}_i^{(B)} \\ \mathbf{x}_b^r \end{Bmatrix} = \begin{bmatrix} \mathbf{L}^{(A)} \\ \mathbf{L}^{(B)} \end{bmatrix} \mathbf{q}_u = \mathbf{L}\mathbf{q}_u \tag{2.14}$$

The vector $\mathbf{q}_u$ correspond to the unconstrained coordinates of the assembled system. The vectors $\mathbf{q}_i^{(A)}$ and $\mathbf{q}_i^{(B)}$ respectively represent the "interior" portion of the subcomponents (A) and (B) (i.e. those generalized coordinates not belonging to the real valued partition of the PS-CMs). For example, the interior portion of subcomponent (A) consists of $\mathbf{q}_i^{(A)} = \left[\mathbf{q}_k^{r,(A)\mathrm{T}} \;\; \mathbf{q}_k^{i,(A)\mathrm{T}} \;\; \mathbf{x}_b^{i,(A)\mathrm{T}} \right]^{\mathrm{T}}$. Using the coupling matrix in Eq. (2.14), the reduced order model of the assembled system becomes,

$$\mathbf{L}^{\mathrm{T}} \begin{bmatrix} \widehat{\mathbf{M}}^{(A)} & 0 \\ 0 & \widehat{\mathbf{M}}^{(B)} \end{bmatrix} \mathbf{L}\ddot{\mathbf{q}}_u + \mathbf{L}^{\mathrm{T}} \begin{Bmatrix} \widehat{\mathbf{K}}_K^{(A)} \int_0^t \zeta_K^{(A)} (t - \tau)\, \dot{\mathbf{q}}^{(A)}(\tau)\, d\tau \\ \widehat{\mathbf{K}}_K^{(B)} \int_0^t \zeta_K^{(B)} (t - \tau)\, \dot{\mathbf{q}}^{(B)}(\tau)\, d\tau \end{Bmatrix} + \mathbf{L}^{\mathrm{T}} \begin{Bmatrix} \widehat{\mathbf{K}}_G^{(A)} \int_0^t \zeta_G^{(A)} (t - \tau)\, \dot{\mathbf{q}}^{(A)}(\tau)\, d\tau \\ \widehat{\mathbf{K}}_G^{(B)} \int_0^t \zeta_G^{(B)} (t - \tau)\, \dot{\mathbf{q}}^{(B)}(\tau)\, d\tau \end{Bmatrix}$$

$$+ \mathbf{L}^{\mathrm{T}} \begin{bmatrix} \widehat{\mathbf{K}}_e^{(A)} & 0 \\ 0 & \widehat{\mathbf{K}}_e^{(B)} \end{bmatrix} \mathbf{L}\mathbf{q}_u = \mathbf{L}^{\mathrm{T}} \begin{Bmatrix} \mathbf{T}_{CB}^{(A)\mathrm{T}} \mathbf{f}_{ext}^{(A)}(t) \\ \mathbf{T}_{CB}^{(B)\mathrm{T}} \mathbf{f}_{ext}^{(B)}(t) \end{Bmatrix} \tag{2.15}$$

The form in Eq. (2.15) is convenient to solve since the integrals can be evaluated at the subcomponent level rather than at the assembly level.

2.2.5 System-Level Interface Reduction

In order to formulate the derivation for the reduction at the interface, Eq. (2.15) is rearranged such that the unconstrained coordinates, $\mathbf{q}_u$, enter into the integral functions of the viscoelastic forces,

$$
\begin{bmatrix} \widehat{\mathbf{M}}_{ii}^{(A)} & 0 & \widehat{\mathbf{M}}_{ib}^{(A)} \\ 0 & \widehat{\mathbf{M}}_{ii}^{(B)} & \widehat{\mathbf{M}}_{ib}^{(B)} \\ \widehat{\mathbf{M}}_{bi}^{(A)} & \widehat{\mathbf{M}}_{bi}^{(B)} & \widehat{\mathbf{M}}_{bb}^{(A)} + \widehat{\mathbf{M}}_{bb}^{(B)} \end{bmatrix} \begin{Bmatrix} \ddot{\mathbf{q}}_i^{(A)} \\ \ddot{\mathbf{q}}_i^{(B)} \\ \ddot{\mathbf{x}}_b^r \end{Bmatrix} + \begin{bmatrix} \widehat{\mathbf{K}}_{K,ii}^{(A)} & 0 & \widehat{\mathbf{K}}_{K,ib}^{(A)} \\ 0 & 0 & 0 \\ \widehat{\mathbf{K}}_{K,bi}^{(A)} & 0 & \widehat{\mathbf{K}}_{K,bb}^{(A)} \end{bmatrix} \int_0^t \zeta_K^{(A)}(t-\tau) \begin{Bmatrix} \dot{\mathbf{q}}_i^{(A)} \\ \dot{\mathbf{q}}_i^{(B)} \\ \dot{\mathbf{x}}_b^r \end{Bmatrix}
$$

$$
d\tau + \begin{bmatrix} 0 & 0 & 0 \\ 0 & \widehat{\mathbf{K}}_{K,ii}^{(B)} & \widehat{\mathbf{K}}_{K,ib}^{(B)} \\ 0 & \widehat{\mathbf{K}}_{K,bi}^{(B)} & \widehat{\mathbf{K}}_{K,bb}^{(B)} \end{bmatrix} \int_0^t \zeta_K^{(B)}(t-\tau) \begin{Bmatrix} \dot{\mathbf{q}}_i^{(A)} \\ \dot{\mathbf{q}}_i^{(B)} \\ \dot{\mathbf{x}}_b^r \end{Bmatrix} d\tau + \ldots
$$

$$
\begin{bmatrix} \widehat{\mathbf{K}}_{G,ii}^{(A)} & 0 & \widehat{\mathbf{K}}_{G,ib}^{(A)} \\ 0 & 0 & 0 \\ \widehat{\mathbf{K}}_{G,bi}^{(A)} & 0 & \widehat{\mathbf{K}}_{G,bb}^{(A)} \end{bmatrix} \int_0^t \zeta_G^{(A)}(t-\tau) \begin{Bmatrix} \dot{\mathbf{q}}_i^{(A)} \\ \dot{\mathbf{q}}_i^{(B)} \\ \dot{\mathbf{x}}_b^r \end{Bmatrix} d\tau + \begin{bmatrix} 0 & 0 & 0 \\ 0 & \widehat{\mathbf{K}}_{G,ii}^{(B)} & \widehat{\mathbf{K}}_{G,ib}^{(B)} \\ 0 & \widehat{\mathbf{K}}_{G,bi}^{(B)} & \widehat{\mathbf{K}}_{G,bb}^{(B)} \end{bmatrix} \int_0^t \zeta_G^{(B)}(t-\tau) \begin{Bmatrix} \dot{\mathbf{q}}_i^{(A)} \\ \dot{\mathbf{q}}_i^{(B)} \\ \dot{\mathbf{x}}_b^r \end{Bmatrix}
$$

$$
d\tau + \begin{bmatrix} \widehat{\mathbf{K}}_{e,ii}^{(A)} & 0 & \widehat{\mathbf{K}}_{e,ib}^{(A)} \\ 0 & \widehat{\mathbf{K}}_{e,ii}^{(B)} & \mathbf{K}_{e,ib}^{(B)} \\ \widehat{\mathbf{K}}_{e,bi}^{(A)} & \widehat{\mathbf{K}}_{e,bi}^{(B)} & \widehat{\mathbf{K}}_{e,bb}^{(A)} + \widehat{\mathbf{K}}_{e,bb}^{(B)} \end{bmatrix} \begin{Bmatrix} \mathbf{q}_i^{(A)} \\ \mathbf{q}_i^{(B)} \\ \mathbf{x}_b^r \end{Bmatrix} = \mathbf{L}^{\mathrm{T}} \begin{Bmatrix} \mathbf{T}_{CB}^{(A)\mathrm{T}} \mathbf{f}_{ext}^{(A)}(t) \\ \mathbf{T}_{CB}^{(B)\mathrm{T}} \mathbf{f}_{ext}^{(B)}(t) \end{Bmatrix} \tag{2.16}
$$

This equation is exactly the same as Eq. (2.15). The interface reduction corresponds to a secondary modal analysis applied to the boundary DOF partition of the assembly,

$$
\left(\widehat{\mathbf{M}}_{bb}^{(A)} + \widehat{\mathbf{M}}_{bb}^{(B)} \right) \ddot{\mathbf{x}}_b^r + \widehat{\mathbf{K}}_{K,bb}^{(A)} \int_0^t \zeta_K^{(A)}(t-\tau) \dot{\mathbf{x}}_b^r d\tau + \widehat{\mathbf{K}}_{K,bb}^{(B)} \int_0^t \zeta_K^{(B)}(t-\tau) \dot{\mathbf{x}}_b^r d\tau + \widehat{\mathbf{K}}_{G,bb}^{(A)} \int_0^t \zeta_G^{(A)}(t-\tau) \dot{\mathbf{x}}_b^r
$$

$$
d\tau + \widehat{\mathbf{K}}_{G,bb}^{(B)} \int_0^t \zeta_G^{(B)}(t-\tau) \dot{\mathbf{x}}_b^r d\tau + \left(\widehat{\mathbf{K}}_{e,bb}^{(A)} + \widehat{\mathbf{K}}_{e,bb}^{(B)} \right) \mathbf{x}_b^r = 0 \tag{2.17}
$$

Using the same iterative procedure to compute the LC-FI modes in Sect. 2.2.1, the complex modes computed from Eq. (2.17) produce a set of linearized complex characteristic constraint (LC-CC) modes, denoted as $\mathbf{\Psi}_{cc}$. As with the fixed-interface modes, these are also truncated based on frequency, although there is not a well establish rule for an appropriate cut-off frequency. This will be evaluated later in the results section. The LC-CC modes are used to reduce the number of boundary DOF, $\mathbf{x}_b^r$, in Eq. (2.16) via the transformation,

$$
\begin{Bmatrix} \mathbf{q}_i^{(A)} \\ \mathbf{q}_i^{(B)} \\ \mathbf{x}_b^r \end{Bmatrix} = \begin{bmatrix} \mathbf{I} & 0 & 0 & 0 \\ 0 & \mathbf{I} & 0 & 0 \\ 0 & 0 & \mathrm{Re}\,(\mathbf{\Psi}_{cc}) & \mathrm{Im}\,(\mathbf{\Psi}_{cc}) \end{bmatrix} \begin{Bmatrix} \mathbf{q}_i^{(A)} \\ \mathbf{q}_i^{(B)} \\ \mathbf{q}_{cc}^r \\ \mathbf{q}_{cc}^i \end{Bmatrix} = \mathbf{T}_{cc} \widehat{\mathbf{q}}_u \tag{2.18}
$$

Projecting the transformation matrix, $\mathbf{T}_{cc}$, onto Eq. (2.16) results in the reduced order model of the assembly with interface reduction,

$$\mathbf{T}_{cc}^{\mathrm{T}} \begin{bmatrix} \widehat{\mathbf{M}}_{ii}^{(A)} & 0 & \widehat{\mathbf{M}}_{ib}^{(A)} \\ 0 & \widehat{\mathbf{M}}_{ii}^{(B)} & \widehat{\mathbf{M}}_{ib}^{(B)} \\ \widehat{\mathbf{M}}_{bi}^{(A)} & \widehat{\mathbf{M}}_{bi}^{(B)} & \widehat{\mathbf{M}}_{bb}^{(A)} + \widehat{\mathbf{M}}_{bb}^{(B)} \end{bmatrix} \mathbf{T}_{cc}\ddot{\widehat{\mathbf{q}}}_u + \mathbf{T}_{cc}^{\mathrm{T}} \begin{bmatrix} \widehat{\mathbf{K}}_{K,ii}^{(A)} & 0 & \widehat{\mathbf{K}}_{K,ib}^{(A)} \\ 0 & 0 & 0 \\ \widehat{\mathbf{K}}_{K,bi}^{(A)} & 0 & \widehat{\mathbf{K}}_{K,bb}^{(A)} \end{bmatrix} \mathbf{T}_{cc} \int_0^t \zeta_K^{(A)}(t-\tau)\dot{\widehat{\mathbf{q}}}_u$$

$$d\tau + \mathbf{T}_{cc}^{\mathrm{T}} \begin{bmatrix} 0 & 0 & 0 \\ 0 & \widehat{\mathbf{K}}_{K,ii}^{(B)} & \widehat{\mathbf{K}}_{K,ib}^{(B)} \\ 0 & \widehat{\mathbf{K}}_{K,bi}^{(B)} & \widehat{\mathbf{K}}_{K,bb}^{(B)} \end{bmatrix} \mathbf{T}_{cc} \int_0^t \zeta_K^{(B)}(t-\tau)\dot{\widehat{\mathbf{q}}}_u d\tau + ...$$

$$\mathbf{T}_{cc}^{\mathrm{T}} \begin{bmatrix} \widehat{\mathbf{K}}_{G,ii}^{(A)} & 0 & \widehat{\mathbf{K}}_{G,ib}^{(A)} \\ 0 & 0 & 0 \\ \widehat{\mathbf{K}}_{G,bi}^{(A)} & 0 & \widehat{\mathbf{K}}_{G,bb}^{(A)} \end{bmatrix} \mathbf{T}_{cc} \int_0^t \zeta_G^{(A)}(t-\tau)\dot{\widehat{\mathbf{q}}}_u d\tau + \mathbf{T}_{cc}^{\mathrm{T}} \begin{bmatrix} 0 & 0 & 0 \\ 0 & \widehat{\mathbf{K}}_{G,ii}^{(B)} & \widehat{\mathbf{K}}_{G,ib}^{(B)} \\ 0 & \widehat{\mathbf{K}}_{G,bi}^{(B)} & \widehat{\mathbf{K}}_{G,bb}^{(B)} \end{bmatrix} \mathbf{T}_{cc} \int_0^t \zeta_G^{(B)}(t-\tau)\dot{\widehat{\mathbf{q}}}_u$$

$$d\tau + \mathbf{T}_{cc}^{\mathrm{T}} \begin{bmatrix} \widehat{\mathbf{K}}_{e,ii}^{(A)} & 0 & \widehat{\mathbf{K}}_{e,ib}^{(A)} \\ 0 & \widehat{\mathbf{K}}_{e,ii}^{(B)} & K_{e,ib}^{(B)} \\ \widehat{\mathbf{K}}_{e,bi}^{(A)} & \widehat{\mathbf{K}}_{e,bi}^{(B)} & \widehat{\mathbf{K}}_{e,bb}^{(A)} + \widehat{\mathbf{K}}_{e,bb}^{(B)} \end{bmatrix} \mathbf{T}_{cc}\widehat{\mathbf{q}}_u = \mathbf{T}_{cc}^{\mathrm{T}} \mathbf{L}^{\mathrm{T}} \left\{ \begin{array}{c} \mathbf{T}_{CB}^{(A)\mathrm{T}} \mathbf{f}_{ext}^{(A)}(t) \\ \mathbf{T}_{CB}^{(B)\mathrm{T}} \mathbf{f}_{ext}^{(B)}(t) \end{array} \right\} \quad (2.19)$$

2.3 Numerical Results: Composite Plate Assembly

The substructuring approach is now applied to a numerical example of the assembly of two sandwich plates with viscoelastic foam at the core. Figure 2.1 shows a schematic of the mesh along with the boundary conditions and interface location. Each plate is modeled with three layers of 20-noded hexahedral elements: the two outer layers correspond to elastic Aluminum 6061-T6 while the interior layer is a viscoelastic PMDI 20 foam. Subcomponent (A) has dimensions of 16 inches by 12 inches by 0.19 inches and a total of 4830 elements (73,605 DOF); subcomponent (B) has dimensions 8 inches by 12 inches by 0.19 inches and a total of 3780 elements (57,855 DOF). For reference, the assembled plate model has a total of 8610 elements or 130,305 DOF. Along the shared interface between the two sandwich plates, there are a total of 1155 DOF. As indicated in Fig. 2.1, the plates have fixed boundary conditions along the bottom edge and a point load is applied at the free end of the collinear interface.

2.3.1 Substructuring with Pseudo-Static Constraint Modes

This first subsection explores the substructuring approach without any reduction at the interface in order to demonstrate the method with the entire physical interface DOF included in the model (i.e. no interface reduction). The driving point FRF is computed for the point load shown in Fig. 2.1 over the range of 10 to 500 Hz with a frequency step of 1 Hz. These results are
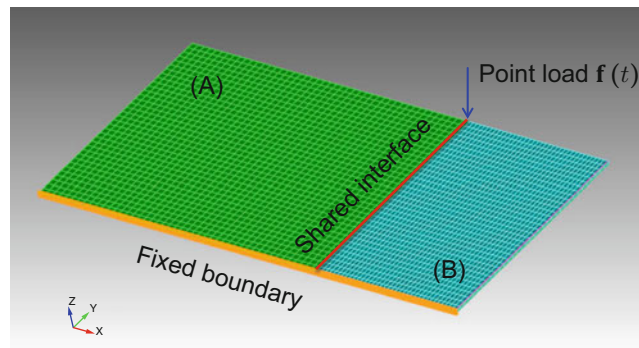
Fig. 2.1 Schematic of finite element mesh for composite sandwich plate with fixed boundary conditions
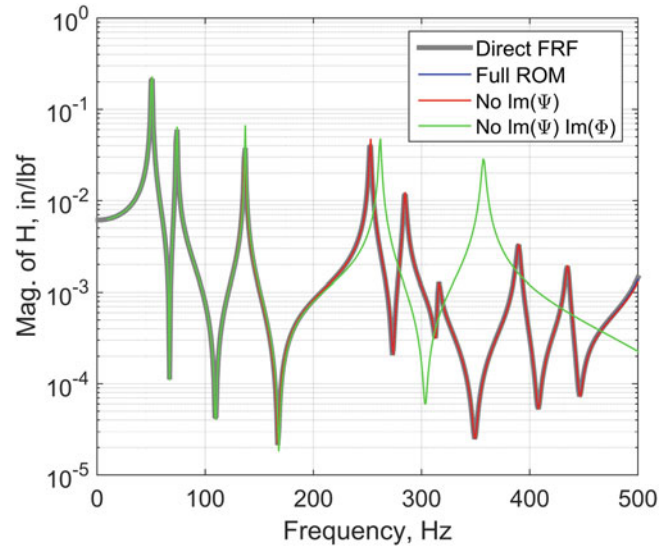
Fig. 2.2 Comparison of driving point FRFs for sandwich plate assembly

shown in Fig. 2.2. Each subcomponent was reduced with LC-FI modes up to 1000 Hz, two times the frequency bandwidth of interest. The three cases explored are as follows:

1. Each subcomponent preserves all real and imaginary parts in the reduction basis such that the transformation matrix in Eq. (2.12) remains as $\mathbf{T} = \begin{bmatrix} \text{Re}\,(\boldsymbol{\Phi}_{ii}) & \text{Im}\,(\boldsymbol{\Phi}_{ii}) & \text{Im}\,(\mathbf{X}_i) & \text{Re}\,(\mathbf{X}_i) \\ 0 & 0 & 0 & \mathbf{I}_{bb} \end{bmatrix}$.
2. The imaginary portion of the PS-CMs are removed from the transformation in Eq. (2.12) such that $\mathbf{T} = \begin{bmatrix} \text{Re}\,(\boldsymbol{\Phi}_{ii}) & \text{Im}\,(\boldsymbol{\Phi}_{ii}) & \text{Re}\,(\mathbf{X}_i) \\ 0 & 0 & \mathbf{I}_{bb} \end{bmatrix}$.
3. The imaginary portion of the PS-CMs and LC-FI modes are removed from the transformation in Eq. (2.12) such that $\mathbf{T} = \begin{bmatrix} \text{Re}\,(\boldsymbol{\Phi}_{ii}) & \text{Re}\,(\mathbf{X}_i) \\ 0 & \mathbf{I}_{bb} \end{bmatrix}$.

The legend in Fig. 2.2 labels these three cases respectively as "Full ROM", "No Im(Ψ)", and "No Im(Ψ) Im(Φ)".

In comparison to the direct FRF computed from the full order model, the "Full ROM" and "No Im(Ψ)" ROM agree very well at the resonances and anti-resonances. It is interesting to note that the imaginary part of the PS-CMs do not significantly improve the results and can be removed from the subcomponent's bases. On the other hand, further removing the imaginary part of the LC-FI modes ("No Im(Ψ) Im(Φ)") drastically worsened the accuracy of the ROM. Table 2.1 shows the order of the models used to compute the FRFs in Fig. 2.2, along with the required computational time in Matlab to obtain the results. The "No Im(Ψ)" ROM had 1155 fewer DOF than the "Full ROM" and cut the computational time down from 1070 s down to 70.4 s, which was one and three orders of magnitude less than the full model, respectively. As evidenced by the results in Table 2.1, the solution time does not scale linearly with model size due to the computational effort required to invert larger, dense matrices.

2.3.2 Substructuring with Interface Reduction

This subsection investigates the interface reduction technique applied to the "No Im(Ψ)" ROM from the previous subsection since this model accurately predicted the driving point FRF with the fewest number of DOF. A total of 13 LC-CC modes were computed from the boundary partition of the assembly in Eq. (2.17), with the largest natural frequency being 3993 Hz. This was eight times the frequency band of interest, and was significantly higher compared to the two times frequency rule for the LC-FI modes. Several ROMs with an increasing number of LC-CC modes (keeping both the real and imaginary parts) were created and used to compute the driving point FRFs.

Table 2.1 Model order and solution time for FRFs in Fig. 2.2

Model	Number of DOF	Solution time (s)
Full FEA model	130,305	24,050
Full ROM	3495	1070
No Im(Ψ)	1185	70.4
No Im(Ψ) or Im(Φ)	1170	67.8
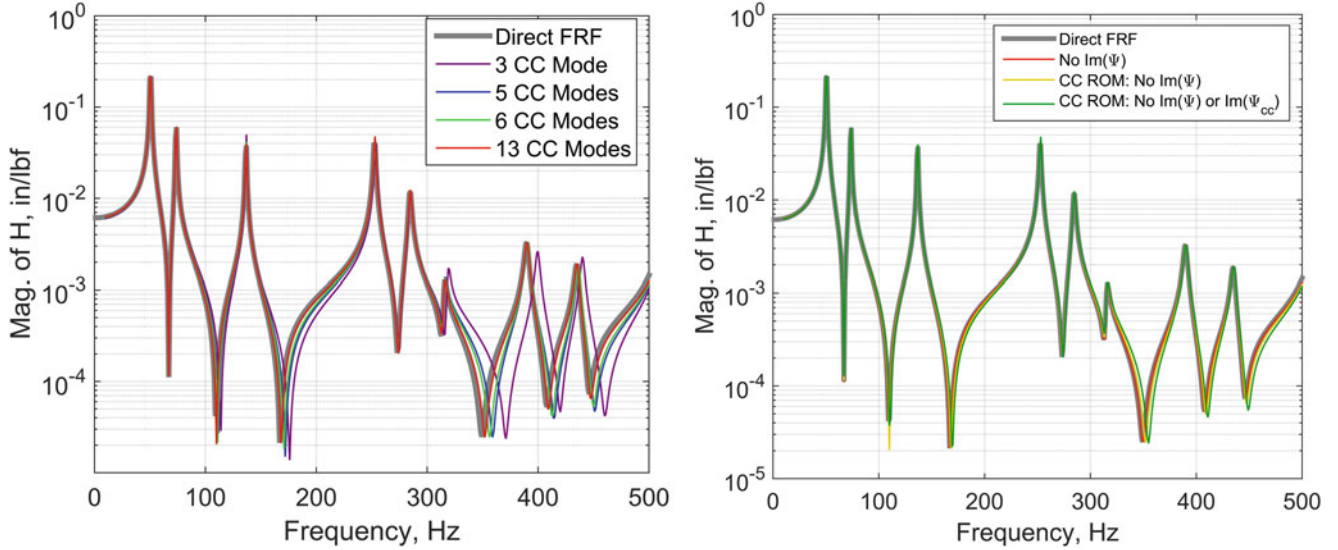
Fig. 2.3 Comparison of driving point FRFs for sandwich plate assembly with interface reduction for (*left*) varying number of LC-CC modes and (*right*) 13 LC-CC mode ROMs with and without the imaginary part

The left plot in Fig. 2.3 shows the convergence of the FRFs when reducing the interface with the following: 3 LC-CC modes up to 500 Hz, 5 LC-CC modes up to 1000 Hz, 6 LC-CC modes up to 2000 Hz and 13 LC-CC modes up to 4000 Hz. The results from the ROM with 3 LC-CC modes predicted the response well below 300 Hz, but the resonances and anti-resonances were not captured above this frequency. The rest of the ROMs agree quite well with the full order model ("Direct FRF") within 500 Hz, except at some of the anti-resonances. In fact, adding LC-CC modes to the subcomponent bases produced results that converged slowly at these frequencies. At least 13 LC-CC modes up to 4000 Hz were needed to obtain very good agreement between the ROM and the full order model.

The right plot in Fig. 2.3 shows a comparison of the driving point FRF for the "No Im(Ψ)" ROM from the previous subsection, along with two ROMs where the interface was reduced with all 13 LC-CC modes. Two cases of these latter models are as follows:

1. The "CC ROM: No Im(Ψ)" case includes both the real and imaginary parts of all 13 LC-CC modes.
2. The "CC ROM: No Im(Ψ) or Im(Ψ_{cc})" case is the same as (1) but removes the imaginary part of the LC-CC modes.

The results from the previous subsection showed that removing the imaginary part of the basis pertaining to the boundary DOF performed very well. This same observation holds true for the LC-CC modes as evidenced by the fact that the "CC ROM: No Im(Ψ)" and "CC ROM: No Im(Ψ) or Im(Ψ_{cc})" are practically indistinguishable. No difference between the models was observed at the resonant frequencies; however the FRF shifted slightly at the anti-resonances. The results in Table 2.2 show the size of the models used in Fig. 2.3b along with the solution time for each. Reducing the interface DOF gained two orders of magnitude in computational savings from the "No Im(Ψ)" ROM, resulting in a total of five orders of magnitude reduction compared to the full order FEA model.

2.3.3 Upfront Computational Cost

All model reduction techniques deserve a discussion of the upfront computational cost required to build the subcomponent models. The Sierra/SD finite element code was only used to compute the LC-FI modes, while a Matlab script was written to

Table 2.2 Model order and solution time for FRFs in Fig. 2.3b

Model	Number of DOF	Solution time (s)
Full FEA Model	130,305	24,050
No Im(Ψ)	1185	70.4
CC ROM: No Im(Ψ)	56	0.4
CC ROM: No Im(Ψ) or Im(Ψ_{cc})	43	0.3

Table 2.3 Upfront cost to compute reduction bases

Level	LC-FI modes	PS-CMs	LC-CC modes
$16'' \times 12''$ plate	621 s per iteration, per mode (22×621 s $= \sim$4 h)	37 min	N/A
$8'' \times 12''$ plate	542 s per iteration, per mode (9×542 s $= \sim$1.5 h)	29 min	N/A
Assembled boundary	N/A	N/A	562 s per iteration, per mode (44×562 s $= \sim$7 h)
Code	Sierra/SD	Matlab	Matlab

compute the PS-CMs and LC-CC modes. When computing complex modes and inverting relatively large matrices, Sierra/SD certainly outperforms Matlab in efficiency, so it makes it difficult to fairly compare the upfront cost. With that comment in mind, the computational effort of each basis is presented in Table 2.3. The reported values correspond to each code/solver running in serial. Sierra/SD is a massively parallel structural dynamics FEA code, so using this capability would reduce the computational burden. The upfront costs of these models represent the most upper bound and future work will explore ways to directly compute the PS-CMs and LC-CC modes within Sierra/SD on multiple processors.

2.4 Conclusion

This research developed a fixed-interface component mode synthesis strategy using primal assembly in the physical domain to reduce large-scale finite element models with linear viscoelastic materials. The subcomponent models are reduced using a set of linearized complex fixed-interface modes and pseudo-static constraint modes, each of which account for the internal viscoelastic forces in the equations of motion. Once the models are assembled, the boundary partition, which can be quite large for models with detailed meshes, a secondary complex modal analysis is performed to reduce the number of physical DOF at the interface. The viscoelastic CMS approach is demonstrated on a numerical example of two sandwich plates joined at a common interface. The results show that the ROMs without interface reduction are able to accurately compute the driving point FRFs when compared to the full order model results, as long as the basis includes the imaginary part of the LC-FI modes. The solution time for these models was reduced by three orders of magnitude. When applying the interface reduction with a sufficient number of linearized complex characteristic constraint modes, the ROM preserves the accuracy and lowers the computational cost by five orders of magnitude. It was observed that the frequency cut-off for the LC-CC modes was about eight times the bandwidth of interest, which is significantly higher in comparison to the two times frequency cut-off for the LC-FI modes.

References

1. Craig, R.R.: Coupling of substructures for dynamic analyses: an overview. In: Proceedings of AIAA/ASME/ASCE/AHS/ASC Structures, Structural Dynamics, and Materials Conference and Exhibit, pp. 1573–1584 (2000)
2. de Klerk, D., Rixen, D.J., Voormeeren, S.N.: General framework for dynamic substructuring: history, review, and classification of techniques. AIAA J. **46**, 1169–1181 (2008)
3. Qian, D., Hansen, J.S.: A time domain substructure synthesis method for viscoelastic structures. J. Appl. Mech.**62**, 407–413 (1995)
4. De Lima, A., Rade, D., Neto, F.L.: An efficient modeling methodology of structural systems containing viscoelastic dampers based on frequency response function substructuring. Mech. Syst. Signal Process. **23**, 1272–1281 (2009)

5. de Lima, A.M.G., da Silva, A.R., Rade, D.A., Bouhaddi, N.: Component mode synthesis combining robust enriched Ritz approach for viscoelastically damped structures. Eng. Struct. **32**, 1479–1488 (2010)

6. Tran, Q.H., Ouisse, M., Bouhaddi, N.: A robust component mode synthesis method for stochastic damped vibroacoustics. Mech. Syst. Signal Process. **24**, 164–181 (2010)

7. Ding, Z., Li, L., Hu, Y.: A free interface component mode synthesis method for viscoelastically damped systems. J. Sound Vib. **365**, 199–215 (2016)

8. Craig, R.R.J., Bampton, M.C.C.: Coupling of substructures for dynamic analysis. AIAA J. **6**, 1313–1319 (1968)

9. Castanier, M.P., Tan, Y., Pierre, C.: Characteristic constraint modes for component mode synthesis. AIAA J. **39**, 1182–1187 (2001)

10. Craig, R.R., Chang, C.J.: Substructure coupling for dynamic analysis and testing. NASA CR-2781 (1977)

11. Kuether, R.J., Troyer, K.L., Brake, M.R.W.: Time domain model reduction of linear viscoelastic finite element models. Presented at the ISMA2016 – International Conference on Noise and Vibration Engineering, Leuven, Belgium, 2016.

12. Sierra Structural Dynamics Development Team, "Sierra Structural Dynamics-User's Notes," Sandia Report SAND2016–3046 O (2016)

13. Craig, R.R.J., Kurdila, A.J.: Fundamentals of Structural Dynamics, 2nd edn. Wiley, New York (2006)

14. Cook, R.D., Malkus, D.S., Plesha, M.E., Witt, R.J.: Concepts and Applications of Finite Element Analysis, 4th edn. Wiley, New York (2002)

Chapter 3
Parameter Estimation of Joint Models Using Global Optimization

Robert J. Kuether and David A. Najera

Abstract Nonlinear joints and interfaces modeled with a discrete four-parameter Iwan element are defined by parameters that are often unknown a priori or require calibration to get better agreement with test data. While this constitutive model has been validated experimentally, its drawback lies in the difficulty of identifying the correct coefficients. This work proposes a parameter estimation approach using a genetic algorithm to minimize the residual between experimental and model data. Global optimization schemes have the ability to find global minima/maxima of a broad parameter space but require a very large number of function evaluations. This research focuses on decreasing the computational cost of the optimization scheme by developing a simplified model of the structure of interest and defining the objective function with amplitude dependent frequencies and damping ratios. A recently developed quasi-static modal analysis technique is used to determine these amplitude dependent properties of the model at a significantly reduced cost in comparison to solutions obtained with numerical time integration. This technique is demonstrated on a structure termed the Ministack which contains a foam-to-metal interface held together with a press fit joint.

Keywords Nonlinear joints • Parameter calibration • Global optimization • Nonlinear vibrations • Interfaces

3.1 Introduction

Common types of mechanical joints include bolted joints, compression fits, tape joints, and others. Joints maintain their strength via contact pressure and friction distributed over the contact surface, and at high enough load levels, they experience microslip or possibly full macroslip. The presence of frictional slip causes joints to have a nonlinear damping and a nonlinear stiffness, which makes their behavior difficult to model accurately. However, the ability to predict the nonlinear response of a structure with mechanical joints would greatly benefit a number of industries, including aerospace and defense where failure of critical systems can have grave consequences.

From a modeling perspective, a number of joint models have been developed to capture the phenomenological behavior of a mechanical interface, namely microslip, loss of stiffness, and nonlinear energy dissipation. One model of particular interest to this research is the four-parameter Iwan element developed by Segalman [1]. This one-dimensional element is a simplified whole joint model for use in structural dynamic simulations. Other simplified joint models include various Iwan type elements [2, 3] or the Bouc-Wen hysteresis model [4, 5]. Recently, a decoupled modal Iwan model was developed [6] to capture the nonlinear response of a mode assuming the mode shape is unchanged, and this modeling approach has been successfully applied to a realistic engineering structure [7].

One of the practical challenges involved with whole joint models, such as the four-parameter Iwan element, is the identification of the model parameters that capture the characteristic behavior of the interface. The four parameters of a modal Iwan model can be estimated by applying a modal filter to measured transient ring-down data and taking the Hilbert transform to estimate the nonlinear damping and frequency [6, 7]. A whole joint model can also be calibrated to test data

R.J. Kuether (✉)
Sandia National Laboratories, Albuquerque, NM 87185, USA
e-mail: rjkueth@sandia.gov

D.A. Najera
ATA Engineering, Inc., San Diego, CA 92128, USA

by using optimization techniques to minimize the residual between the data predicted by the numerical model and the measured data. Examples of this include the work by Charalampakis et al. [8, 9] who developed an identification method to determine the parameters of a Bouc-Wen hysteretic model using different global optimization schemes. Wang et al. [10] presented a joint model updating scheme using analytical mode decomposition to extract the instantaneous characteristics of the measured and numerically integrated response. These cost function metrics are used with a simulated annealing global optimization method to identify the optimal joint parameters.

The research presented here proposes to model the mechanical interface of a structural dynamic model with a four-parameter Iwan element and use the genetic algorithm implemented in [11] to calibrate the joint parameters. The genetic algorithm is a global optimization scheme that explores a broad parameter space and does not require an initial guess. Using global optimization over gradient based schemes is more computationally expensive since it demands more evaluations of the objective function, but has the advantage of finding global optimum. Because of this, quasi-static modal analysis [12] is used to estimate the amplitude dependent frequency and damping of the nonlinear mode of interest. Since this approach computes the instantaneous properties of the nonlinear model with a static solution, the proposed calibration scheme significantly reduces the computational effort needed to evaluate the objective function.

The sections of the paper are as follows. Section 3.2 briefly reviews the four-parameter Iwan formulation along with the optimization scheme developed to calibrate the parameters. Section 3.3 demonstrates the methodology on a simplified model of the "Ministack" hardware, which consists of a press fit joint of a metal slug within a foam encapsulant. The parameters of the nonlinear model are calibrated to experimental swept sine data of the real hardware. Section 3.4 discusses the conclusion.

3.2 Modeling and Calibration

3.2.1 Whole Joint Models

In structural dynamics, a whole joint modeling approach condenses a mechanical interface down to a discrete nodal location at which a pointwise constitutive model is used to describe the interface forces. This joint modeling approach reduces the time and length scales of the joint model for structural dynamics simulations requiring many time steps over a large period. Detailed interface models with Coulomb friction and node-to-node contact require detailed meshes not amenable to structural dynamics. The whole joint modeling philosophy relies on the assumption that the local kinematics at the interface do not significantly contribute to the response, since multi-point constraints (MPCs) are often used to tie a set of nodes on the contact surface down to a single point. Figure 3.1 shows an example of how MPCs tie to a surface to a single node to resemble the kinematics of three bolted joints in a beam.

One of the constitutive equations used within the whole joint model is the four-parameter Iwan element that was originally derived for lap-type joints [1]; the theory is briefly reviewed here. This constitutive model captures the microslip behavior
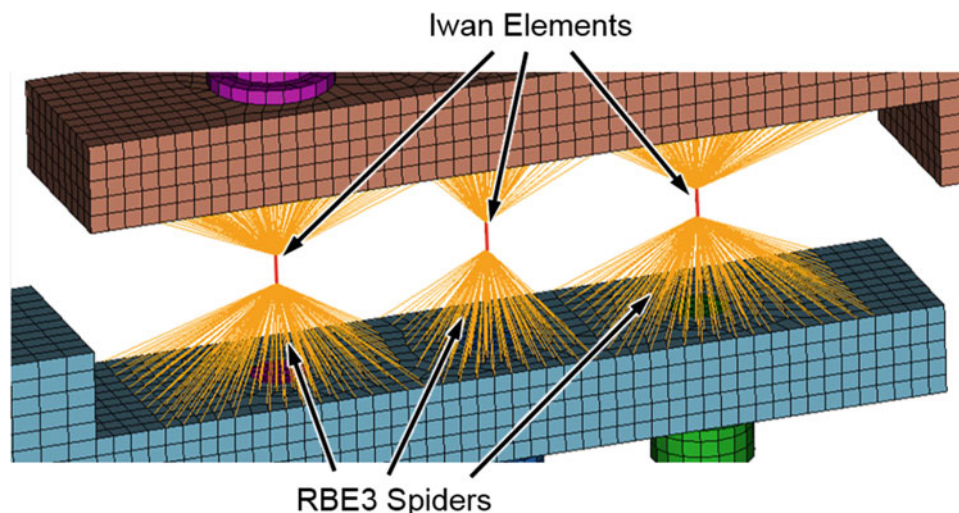
Fig. 3.1 Example of a whole joint model of three bolts in a lap-joint [13]
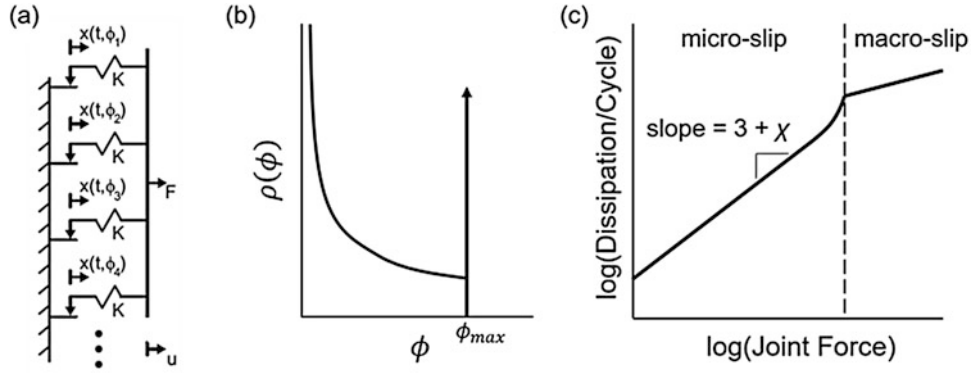
Fig. 3.2 Schematic of the (**a**) parallel-series Iwan element, (**b**) power-law population distribution, and (**c**) power-law energy dissipation versus force (Image from Gross et al. [13])

and nonlinear dependence of damping as the amplitude of the response increases, as well as a loss of stiffness at larger amplitudes. The force of a parallel-series Iwan model is written as,

$$F(t) = \int_0^{\infty} \rho(\varphi) [u(t) - x(t, \varphi)] \, d\varphi \tag{3.1}$$

with the stick/slip condition definitions,

$$\dot{x}(t, \varphi) = \begin{cases} \dot{u} & \text{if } \|u - x(t, \varphi)\| = \varphi \quad \text{and} \quad \dot{u}[u - x(t, \varphi)] > 0 \\ 0 & \text{otherwise} \end{cases} \tag{3.2}$$

The dimensionless values, $x(t, \varphi)$, are the displacement of the Jenkins elements with a slip displacement φ, $\rho(\varphi)$ is the population density of Jenkins elements of strength φ, and $u(t)$ and $F(t)$ are the joint displacement and applied force, respectively. The schematic in Fig. 3.2. shows the Iwan element as a set of Jenkins elements along with the population density and energy dissipation versus joint force.

Assuming a power-law population distribution that is terminated at a finite displacement,

$$\rho(\varphi) = R\varphi^{\chi} [H(\varphi) - H(\varphi - \varphi_{\max})] + S\delta(\varphi - \varphi_{\max}) \tag{3.3}$$

Substituting this equation into Eq. (3.1), the force-displacement relationship becomes,

$$F(t) = \int_0^{\varphi_{\max}} [u(t) - x(t, \varphi)] R\varphi^{\chi} d\varphi + S[u(t) - x(t, \varphi_{\max})] \tag{3.4}$$

where the parameters of the Iwan element are defined as,

$$R = \left(\frac{F_s(1 + \chi)}{\varphi_{\max}^{\chi+2}\left(\beta + \left(\frac{\chi+1}{\chi+2}\right)\right)} \right) \tag{3.5}$$

$$S = \left(\frac{F_s}{\varphi_{\max}} \right) \left(\frac{\beta}{\beta + \left(\frac{\chi+1}{\chi+2}\right)} \right) \tag{3.6}$$

$$\varphi_{\max} = \left(\frac{F_s(1 + \beta)}{K_T\left(\beta + \left(\frac{\chi+1}{\chi+2}\right)\right)} \right) \tag{3.7}$$

The Iwan element in Eq. (3.4) in conjunction with Eqs. (3.5), (3.6), and (3.7) is completely defined by the following parameters: F_s (slip force), K_T (joint stiffness when no slip occurs), χ (exponent describing slope of force-dissipation curve), and β (shape parameter of the force-dissipation curve near transition to macroslip). As discussed in [1], these parameters are preferred since they are "measureable" quantities. The slip force can be estimated from static calculations with an assumed Coulomb friction coefficient, while the low amplitude stiffness can be estimated by performing vibration tests at low excitation levels. Determining the values for χ and β is a bit more challenging and requires specific harmonically loaded experiments to calibrate.

3.2.2 Objective Function

Calibrating Iwan parameters (F_s, K_T, χ, β) can be difficult when the specific set of experiments are unavailable or too costly to run. Furthermore, finite element models with many joints, such as the one shown above in Fig. 3.1, could potentially have joint models with different parameters requiring calibration data. This section proposes a joint model calibration scheme that uses measured vibration data to identify the optimal parameters. First, a least squares objective function is defined in order to minimize the difference between the measured and predicted output,

$$\Gamma = \frac{1}{N} \sum_{i=1}^{N} \left(\frac{y - \tilde{y}(\mathbf{p})}{y} \right)^2 \tag{3.8}$$

The measured output, y, is obtained from test data and the predicted output, $\tilde{y}$, is the solution to the model for a given set of parameters, $\mathbf{p}$. A global optimization scheme makes numerous evaluations of this objective function so it is important to make the model simulations as inexpensive as possible.

Calibration algorithms for linear finite element models rely on invariant modal properties to define the residuals in the objective function in Eq. (3.8). Since the Iwan elements introduce nonlinear behavior, a new metric is sought to capture the important characteristics of the system. Recently Allen et al. [12] developed a quasi-static modal analysis technique that estimates the amplitude dependent natural frequency and damping ratio of a finite element model with Iwan elements. The approach works by applying a quasi-static force in the shape of the linearized mode and computing the nonlinear quasi-static response. From this force-displacement relationship, the secant of the loading curve provides an estimate of the amplitude dependent frequency, while the full hysteresis curve obtained using Masing's rules is used to estimate the effective damping for the given response amplitude. These two effective modal properties are used to define the objective function for the genetic algorithm described in the next subsection,

$$\Gamma_{\text{GA}} = \frac{\eta}{N} \sum_{i=1}^{N} \left(\frac{\omega_n(a_i) - \tilde{\omega}_n(a_i, \mathbf{p})}{\omega_n(a_i)} \right)^2 + \frac{(1-\eta)}{N} \sum_{i=1}^{N} \left(\frac{\zeta(a_i) - \left(\tilde{\xi}_{Iwan}(a_i, \mathbf{p}) + \tilde{\xi}_{viscous} \right)}{\zeta(a_i)} \right)^2 \tag{3.9}$$

Here the amplitude dependent natural frequencies, $\tilde{\omega}_n(a_i, \mathbf{p})$, and damping ratios $\tilde{\xi}_{Iwan}(a_i, \mathbf{p})$, are computed from the quasi-static approach for a set of model parameters, $\mathbf{p}$. The experimental data, $\omega_n(a_i)$ and $\zeta(a_i)$, can been estimated with either swept sine or transient ring-down tests as done in [14]. The scalar η is the weight coefficient used to give more or less importance to the frequencies or the damping ratios; a value of $\eta = 0.5$ gives equal weight to both properties.

Figure 3.3 shows a comparison of the amplitude dependent frequency and damping from simulated swept sine tests and the quasi-static modal analysis. The simplified model introduced later in Sect. 3.3.2 was used to generate this numerical data. Comparisons between the quasi-static modal analysis and transient ring-down data have been reported in [12]. The agreement between the frequency and damping estimates from both techniques suggests that the quasi-static approach can be used to simulate the model and obtain the same meaningful information as would be obtained from sine sweep data. Computing swept sine responses from a model would add significantly more computational effort per function evaluation of Eq. (3.8) and slow down the global optimization algorithm needed to explore the broad parameter space. Simulating the quasi-static analysis demands much less computational effort and hence is more desirable for use in the optimization algorithm.
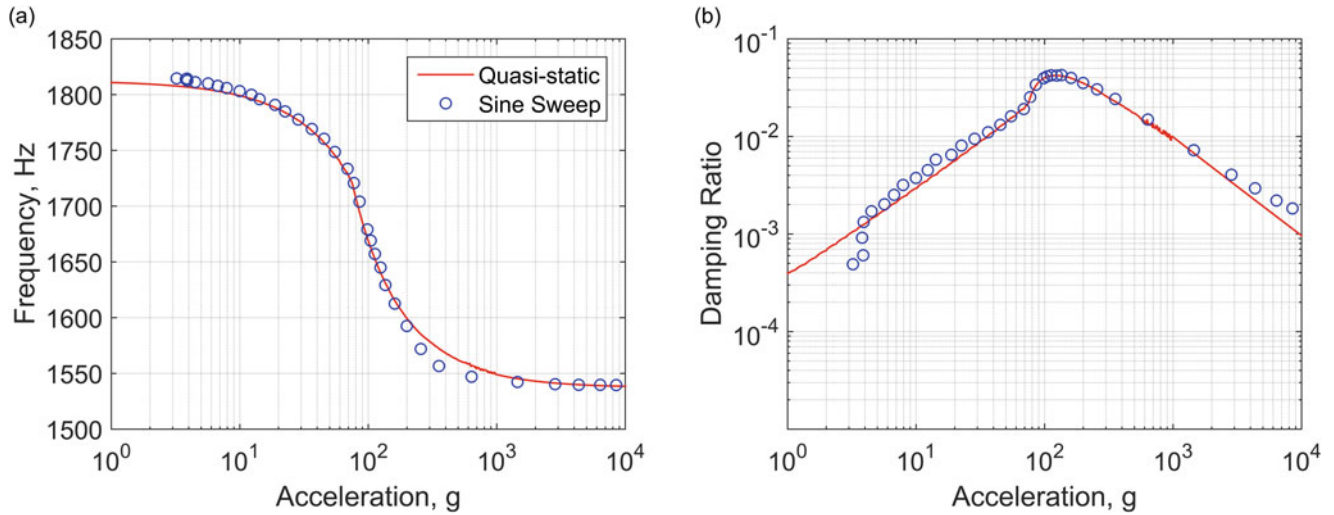
Fig. 3.3 Amplitude dependent (**a**) frequencies and (**b**) damping ratios for a simplified two degree-of-freedom model

3.2.3 Genetic Algorithm

A genetic algorithm (GA) is used to calibrate the Iwan parameters since it is a global optimization method that balances broad exploration of the parameter space with computational efficiency. It is usually better suited than gradient-based algorithms when multiple optima exist, but is more computationally expensive due to the number of function evaluations. GA is part of the family of evolutionary algorithms and relies on operators inspired by biological evolution. A random set of candidate solutions known as "individuals" are generated, forming a "population". At each generation, each individual has a set probability of "mutating", which is the main mechanism used for exploration of new solutions. In the case of joint model calibration, a Gaussian mutation operation is used. Individuals are also able to "mate" thus generating new solutions based on the combination of the fittest individuals in a given generation, where fitness is the value of the objective function. After mutation and mating, there is a selection process during which only the fittest individuals make it to the next generation. This process is repeated until convergence is reached and variance in the population is low. The GA algorithm used to calibrate the joint models is implemented in Python using the DEAP package [11].

3.3 Results

3.3.1 Experimental Hardware and Data

Test data was collected from a system termed the "Ministack" which consists of a solid aluminum 6061-T6 mass that fits into two 20 pounds per cubic foot closed cell PMDI foam cups. This subassembly is then inserted into an aluminum can, and a steel disk covering the top of the foam holds a nominal 700 lbf preload that is held in place with a threaded steel ring. The base plate of the can is then bolted to the shaker table for vibration testing. A schematic of the setup is shown below in Fig. 3.4. For reference, the solid aluminum mass (i.e. slug) is 4 inches high with a diameter of 3 inches. The foam cups each have an average inner depth of 2 inches, with an average inner diameter of 2.99 inches. As a result, the slug nominally fits tightly within the foam casing allowing for the preload to go through both the foam cups and the aluminum slug. In axial base excitation, the axial mode of the slug is expected to exercise the large foam-to-metal interface between the slug and foam cups and be the main source of nonlinear behavior.

A uniaxial control accelerometer was placed in a recess at the bottom of the base plate, and a triaxial accelerometer was attached to a cavity located on top of the slug (as seen in the left of Fig. 3.4). A series of sine sweep tests were carried out at various excitation levels to observe the nonlinear behavior near the resonance of the dominant axial mode. The test series is given below in Table 3.1. Prior to testing, the Ministack hardware was assembled by applying a preload via a press until the reading on the load cell was approximately the nominal value of 700 lbf. The retaining ring was tightened to maintain the preload, the press was released, and Ministack was then bolted to the shaker. The base plate of the can was accelerated
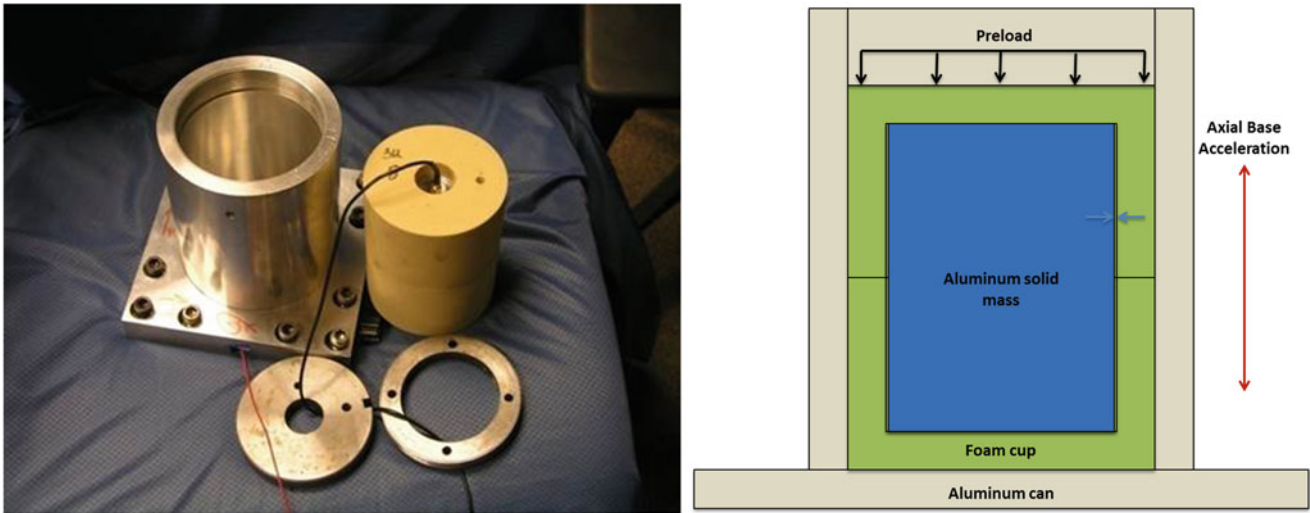
Fig. 3.4 Ministack hardware

Table 3.1 Sine Sweep test series for Ministack assembly

Test ID	Sweep series amplitudes
1	1 g up, 1 g down, 1 g up, 1 g down, 1 g up, 1 g down
2	2 g up, 2 g down
3	5 g up, 5 g down
4	10 g up, 10 g down

with a swept sine input between 700 and 2500 Hz at a linear rate. The first test was a sweep at 1 g amplitude from 700 to 2500 Hz (up), followed by a 1 g sweep from 2500 to 700 Hz (down). This was repeated two more times at a 1 g load level to allow the slug to "settle" within the foam cups. Following the 1 g sweeps, the Ministack was excited from 700 to 2500 Hz at a 2 g level, and then back down from 2500 to 700 Hz. The same upward and downward tests were then run at 5 g and 10 g levels, and the hardware was disassembled and reassembled, carefully noting the alignment as not to change the orientation of the components. The same tests were repeated for the reassembled hardware in order to observe any variability between two assembly processes.

The axial slug acceleration was processed using the short-time Fourier transform to estimate the envelope of the signal in the frequency domain. These results are shown below in Fig. 3.5 for all the downward sweeps (the 1 g sweep was the last of the three in the test series). There seemed to be some slight directional dependence of the sweep frequency (not shown here) but for the most part the upward and downward sweeps showed very similar responses. The envelopes of the response show that as the amplitude of the base acceleration increased, the resonant frequency decreased. This is consistent with the nonlinear behavior of microslip in mechanical joints. The resonant frequencies were determined from the swept sine test data by identifying the frequency at which the input and response were 90 degrees out-of-phase from one another. The effective damping was estimated via the half power bandwidth rule. The plots in Fig. 3.6 show the effective frequencies and damping ratios from the sine sweep data in Fig. 3.5 which served as the reference data of the objective function in Eq. (3.9) with which the model was calibrated.

3.3.2 Optimal Model Parameters

A simplified two degree-of-freedom system of equations was generated in order to model the dynamics of the Ministack hardware in Fig. 3.4. The schematic in Fig. 3.7 shows the discrete model of a slug mass, m_{slug}, connected to the can and the shaker mass, m_{can}, through parallel linear spring and Iwan elements. The mass of the aluminum slug was measured to be 2.65 lbf while the mass of the can plus shaker were assumed to be 386,000 lbf. The latter value was chosen in order to numerically apply a base acceleration as an external force.
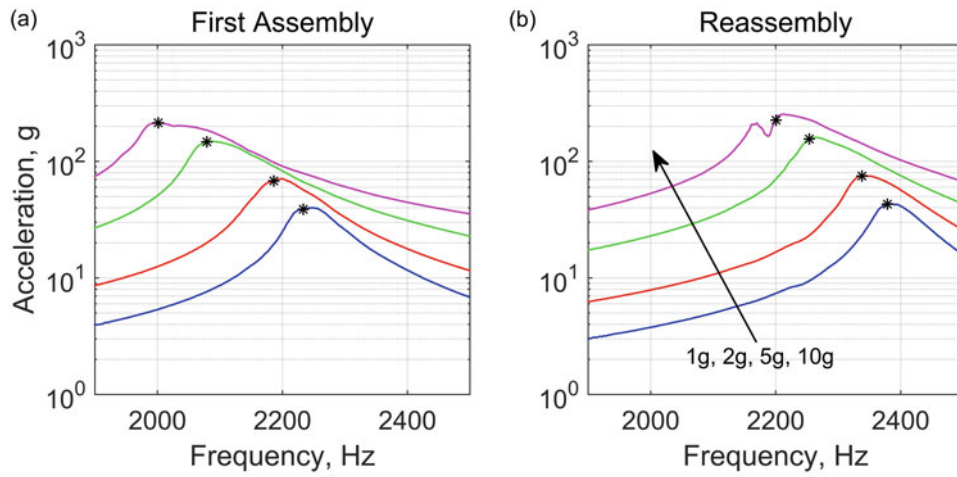
Fig. 3.5 Swept sine response envelopes for (**a**) initial assembly and (**b**) disassembly $+$ reassembly
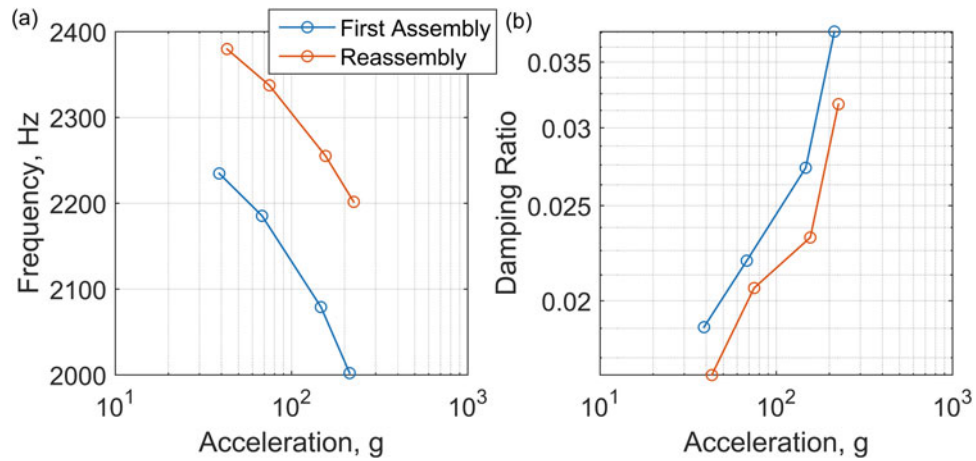
Fig. 3.6 Amplitude dependent (**a**) resonant frequencies and (**b**) damping ratios estimated from swept sine tests for initial assembly and disassembly $+$ reassembly
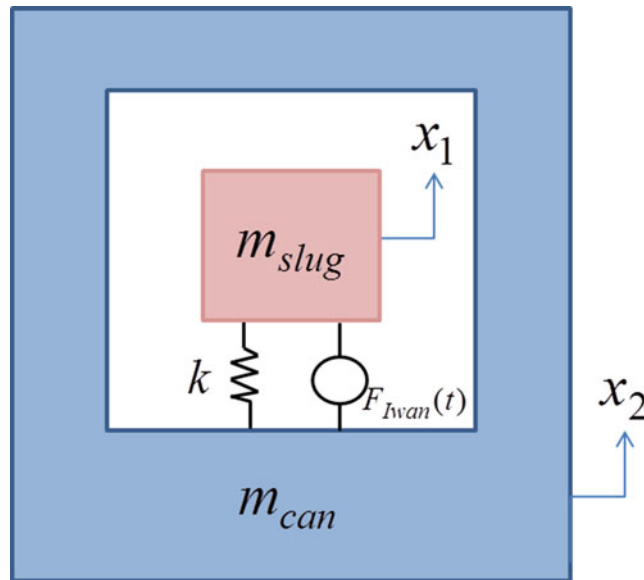
Fig. 3.7 Schematic of simplified Ministack model

Table 3.2 Optimal model parameters.

	Iwan parameters				Linear parameters	
	$F_s(lbf)$	$K_T(lbf/in)$	χ	β	$k(lbf/in)$	$\zeta_{viscous}$
First assembly	313	1.02×10^6	-0.65	0.004	6.12×10^5	0.0015
Reassembly	274	0.90×10^6	-0.61	0.025	8.56×10^5	0.0017
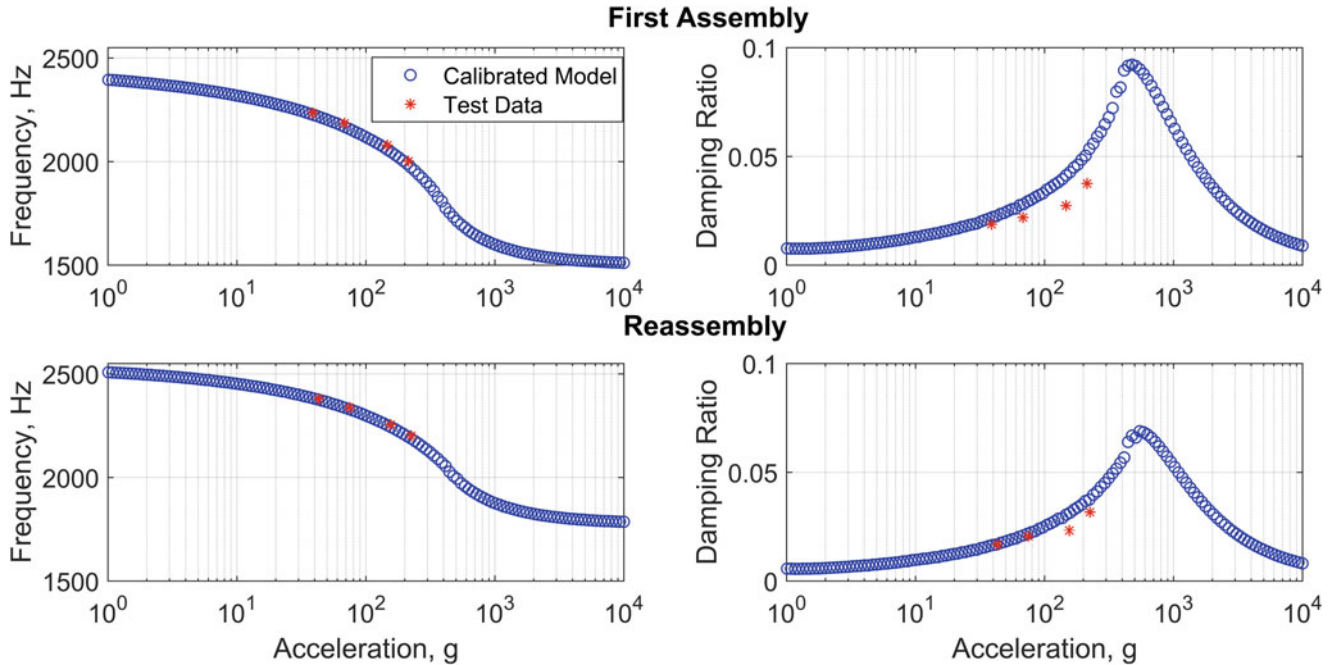
Fig. 3.8 Comparison of amplitude dependent frequencies and damping ratios from experiment and calibrated model for the (*top row*) initial assembly and (*bottom row*) disassembly + reassembly

The GA optimization and quasi-static modal analysis were applied to the simplified two degree-of-freedom model to estimate the four Iwan parameters (F_s, K_T, χ, β). In addition, the linear spring stiffness (k) and viscous damping ratio ($\zeta_{viscous}$) were also treated as unknowns. Due to the uncertainty of the damping ratios extracted from the test data, the weight coefficient, η, was set to 0.85 to more heavily weight the frequencies in Eq. (3.9). The resulting optimal model parameters found from the optimization routine are presented in Table 3.2 forthe initial assembly and disassembly + reassembly configurations. The linear viscous damping was effectively the same between the two configurations, but was lower than expected since the foam cups should introduce damping levels higher than ~0.1%. The linear spring stiffness shifted up when the system was reassembled and could be explained by the time dependent behavior of the foam under an uncertain level of preload. The Iwan parameters were in relatively good agreement between the two assemblies, with the exception of β. The slight change in slip force, F_s, and joint stiffness, K_T, could be explained by the change in load path between the can, foam and slug, as well as the relaxation of stresses within the foam. The slope of the energy dissipation curve, χ, agrees well between the two models suggesting that the power-law energy dissipation behavior is consistent for the press fit joint.

A comparison of the response obtained with the calibrated model using the quasi-static method and test data for initial assembly and disassembly + reassembly is shown in Fig. 3.8. The optimization algorithm was able to get the simplified model to predict frequencies that agreed very well with the test data and reasonably well for the damping ratios. The model was computed over a broad range of response amplitudes to show where the test data lies within the range of nonlinear stiffness and damping.

Figures 3.9 and 3.10 illustrate the design space explored by the GA. The scatter plots show the interactions between different model parameters and how they were explored. The plot in the last row and column show the value of the objective function as a function of the different parameters as they were explored. Plots along the diagonal are density plots showing
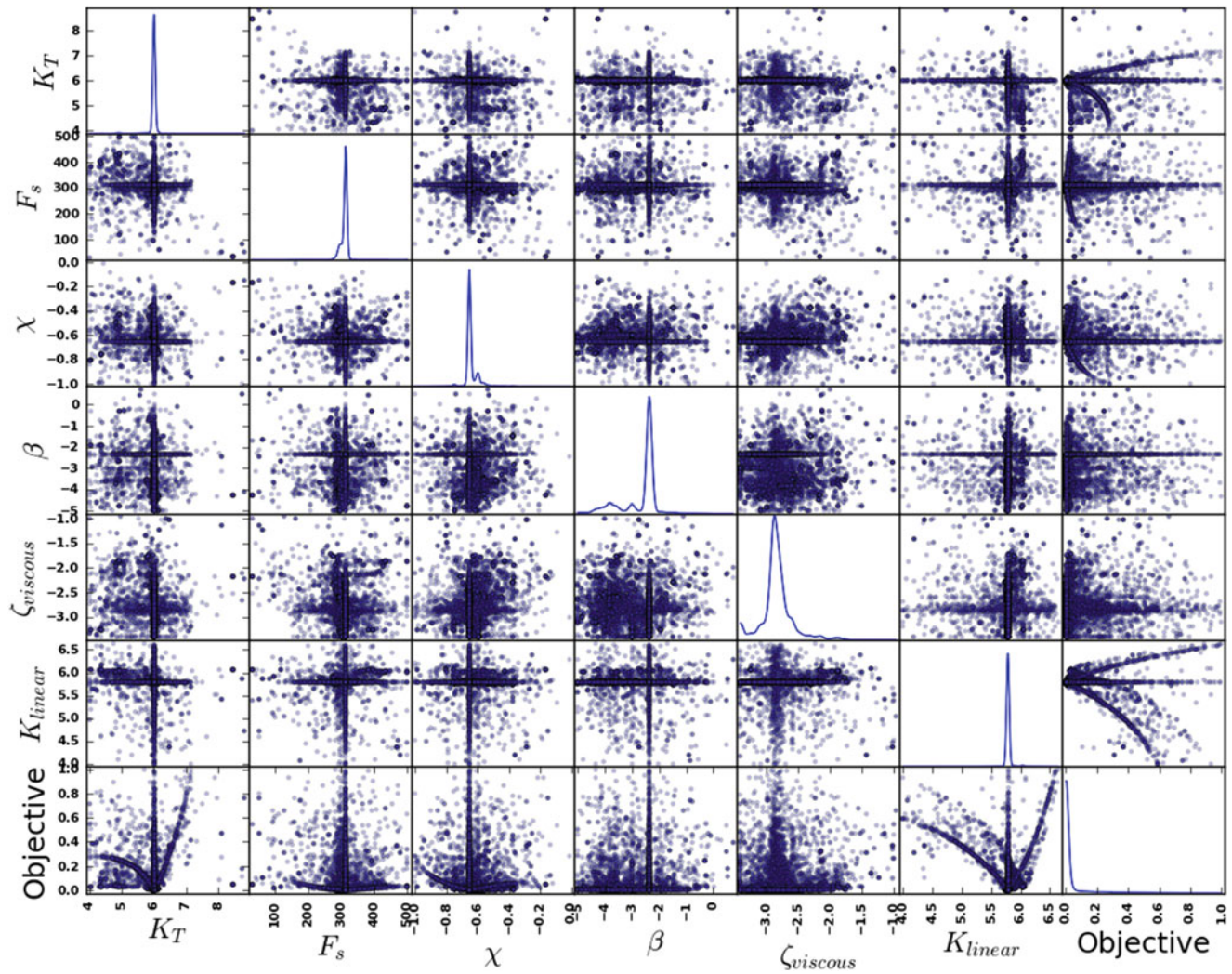
Fig. 3.9 Scatter plot matrix of GA exploration for initial assembly model parameters and objective function values

where the algorithm spent most of the time. The peaks of the density plots correlate with the optimal parameters ultimately chosen. These plots show that there was broad exploration of the parameter space and that a clear minimum emerged from the objective function.

3.3.3 Validation with Sine Sweeps

A final validation step was done to check how well the simplified, calibrated model could predict the experimental swept sine response. During testing, the axial base acceleration was measured with a control accelerometer and used as the input into the discrete model. Figure 3.11 shows the comparison between the experimentally measured response envelopes (solid lines) and the predicted envelopes (dashed lines) for the 1, 2, 5 and 10 g levels. The model under predicts the response amplitude for each input, however the resonant peaks appear to align with one another. It was observed in the control signal that the accelerometer had significant amplification as the shaker swept through the resonance. The input signal could have some significant coupling between the shaker and the Ministack that would not be captured by the model (the can and shaker were modeled as a rigid mass). Development of a higher fidelity model may better capture the flexibility of the Ministack and improve the ability of the model to predict the swept sine response.
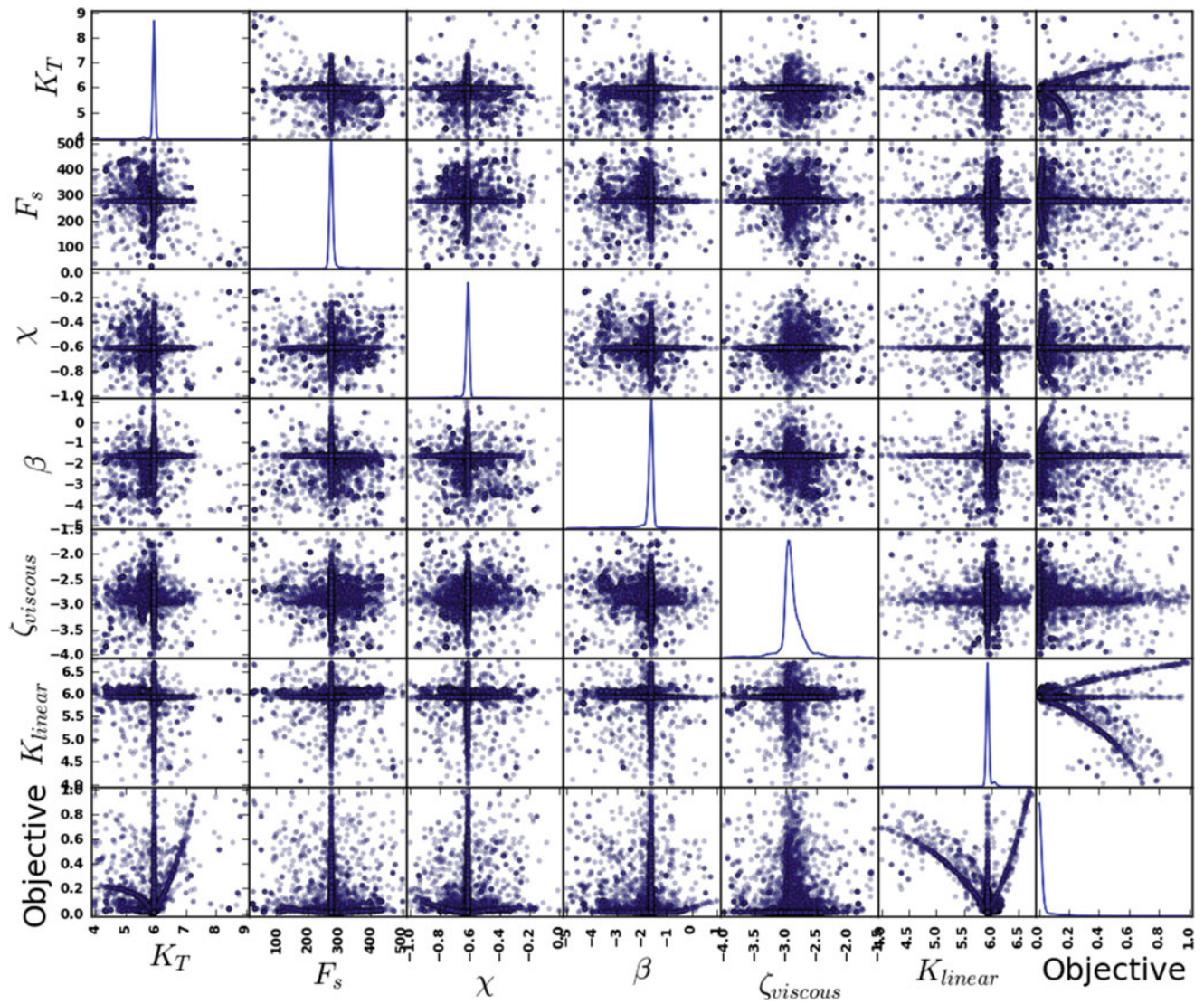
Fig. 3.10 Scatter plot matrix of GA exploration for disassembly + reassembly model parameters and objective function values

3.4 Conclusion

This research developed a joint model calibration scheme using global optimization and quasi-static modal analysis. A genetic algorithm was used due to its ability to search a broad parameter space and find global optimum. Since this approach typically requires an increased number of function evaluations, the quasi-static modal analysis was used to efficiently compute the amplitude dependent frequencies and damping ratios of the nonlinear model. These dynamic characteristics defined the least squares objective function used to evaluate the fitness of the parameters of the joint model. This method was demonstrated using the Ministack hardware, which consisted of a press fit joint of a metal slug within a foam encapsulant. A simplified two degree-of-freedom model was created to capture the dynamics of the fundamental axial vibration mode and the foam-to-metal interface was modeled with a four-parameter Iwan element. Experimental swept sine data taken from the Ministack hardware was used to determine the amplitude dependent frequencies and damping, and the model was calibrated to match this data. An optimal set of Iwan parameters were identified for two different assembly steps, and showed that the interface properties were only slightly affected by the reassembly. The validation step of the model unfortunately showed that the model was not in perfect agreement with the test data, and that the responses were under predicted. Development of a higher fidelity model could improve the ability to capture the experimental response.
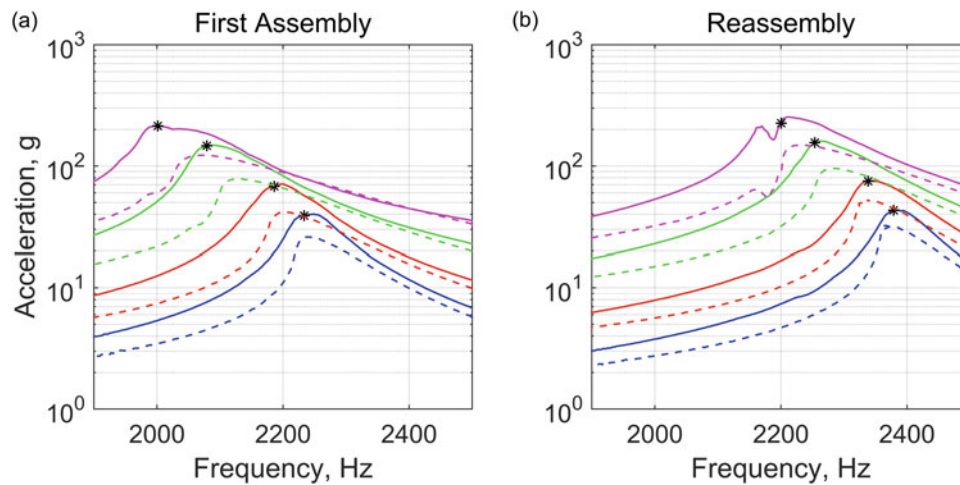
Fig. 3.11 Swept sine response envelopes for (**a**) initial assembly and (**b**) disassembly $+$ reassembly; (*solid lines*) test data (*dashed lines*) calibrated model

References

1. Segalman, D.J.: A four-parameter Iwan model for lap-type joints. J. Appl. Mech. **72**, 752–760 (2005)
2. Li, Y., Hao, Z.: A six-parameter Iwan model and its application. Mech. Syst. Signal Process. **68–69**, 354–365 (2016)
3. Mignolet, M.P., Song, P., Wang, X.Q.: A stochastic Iwan-type model for joint behavior variability modeling. J. Sound Vib. **349**, 289–298 (2015)
4. Bouc, R.: Forced vibration of mechanical systems with hysteresis. Presented at the Fourth Conference on Non-linear Oscillation, Prague, Czechoslovakia, 1967
5. Wen, Y.-K.: Method for random vibration of hysteretic systems. J .Eng. Mech. Div. **102**, 249–263 (1976)
6. Deaner, B.J., Allen, M.S., Starr, M.J., Segalman, D.J., Sumali, H.: Application of viscous and Iwan modal damping models to experimental measurements from bolted structures. J. Vib. Acoust. **137**, 021012 (2015)
7. Roettgen, D.R., Allen, M.S.: Nonlinear characterization of a bolted, industrial structure using a modal framework. Mech. Syst. Signal Process. **84B**, 152–170 (2017)
8. Charalampakis, A.E., Dimou, C.K.: Identification of Bouc–Wen hysteretic systems using particle swarm optimization. Comput. Struct. **88**, 1197–1205 (2010)
9. Charalampakis, A.E., Koumousis, V.K.: Identification of Bouc–Wen hysteretic systems by a hybrid evolutionary algorithm. J. Sound Vib. **314**, 571–585 (2008)
10. Wang, Z.-C., Xin, Y., Ren, W.-X.: Nonlinear structural joint model updating based on instantaneous characteristics of dynamic responses. Mech. Syst. Signal Process. **76–77**, 476–496 (2016)
11. Fortin, F.-A., Rainville, F.-M.D., Gardner, M.-A., Parizeau, M., Gagné, C.: DEAP: evolutionary algorithms made easy. J. Mach. Learn. Res. **13**, 2171–2175 (2012)
12. Allen, M.S., Lacayo, R.M., Brake, M.R.W.: Quasi-static modal analysis based on implicit condensation for structures with nonlinear joints. Presented at the ISMA2016 – International Conference on Noise and Vibration Engineering, Leuven, Belgium, 2016
13. Gross, J., Armand, J., Lacayo, R.M., Reuß, P., Salles, L., Schwingshackl, C.W., et al.: A numerical round robin for the prediction of the dynamics of jointed structures. Presented at the 34th International Modal Analysis Conference (IMAC XXXIV), Orlando, Florida, 2016.
14. Sumali, H., Kellogg, R.A.: Calculating damping from ring-down using Hilbert transform and curve fitting. In 4th International Operational Modal Analysis Conference (IOMAC), Istanbul, Turkey, May, 2011, pp. 9–11

Chapter 4
Real-Time Hybrid Simulation of an Unmanned Aerial Vehicle

Markus J. Hochrainer and Peter Schattovich

Abstract This work presents a real-time hybrid simulation for the analysis and optimization of the electronic control unit of a quadcopter. Therefore, the existing physical microcontroller hardware is coupled to a real-time computer model used to simulate the flight. This requires the numerical solution of nonlinear equations of motion including coordinate transformations. Knowing the flight dynamics, the simulated measurements of a virtual inertial measurement unit are determined and fed back to the physical flight control unit to calculate the required actuator response for a desired behavior, thereby closing the control loop. This type of hybrid simulation is currently the most efficient method to obtain a desired system performance before carrying out experimental tests with the entire physical system. Furthermore, a virtual reality module for real-time flight visualization was developed for better analysis of different flight scenarios. Since all results show excellent agreement with real flight testing, the work confirms the efficiency of the proposed system. During the tests it was e.g. possible to determine the effect of different inertia measurement unit sensors with specific noise characteristics on the overall flight dynamics and consequently, find the reason for rarely occurring engine failures. In addition, the project shows that complex real-time hybrid simulations on industrial level are possible even with low investment costs.

Keywords Real-time hybrid testing • Hardware in the loop • Real-time simulation • Quadcopter • Direction estimation

4.1 Introduction

Experimental techniques have developed significantly in the last decades, with a distinct focus on hybrid experimental-computational techniques. This process has been driven by a steady progress in model based design as well as physical modeling techniques together with powerful automatic code generation tools, which can be configured to generate fast C and C++ code for use on embedded processors, target rapid prototyping boards, microprocessors or real-time PC based systems. On the other side, there is a tremendous advance of cheap and very powerful embedded systems already including analog and digital interfaces and thus computing power is easily available for almost any level of real-time hardware. This reduces the additional costs for real-time hybrid simulation (RTHS) substantially, and, furthermore, the simulation model stays almost unaffected of the target hardware. As a consequence, hybrid simulation techniques have attracted increased research attention and they can be found in almost any field of experimental testing. This development is further supported by the fact, that modelling and simulation of multi-domain component oriented physical systems is supported by several modeling languages. In this context, all individual component models are based on physical connections, and the level of detail of the simulation can be changed just by exchanging simple components models to more complex ones. A hierarchy of different component models is often readily available from different component libraries.

Depending on the scientific discipline, the coupling of numerical and experimental techniques is known as (real-time) hybrid simulation, hybrid dynamic substructuring or hardware in the loop (HIL) testing. Although these new techniques have led to significant savings, faster product development and reduced design uncertainties, full scale experimental testing of the entire system cannot be eliminated completely. However, modern testing methods are even more demanding for the scientist due to the multidisciplinary nature of work integrating numerical and experimental methods. It requires advanced knowledge in the fields of modeling and simulation, real-time integration, model-order reduction, scalable numerical simulations, measurement and signal processing. Furthermore, since the coupled systems generally result in a closed loop structure, profound understanding of control theory, sensors and actuators is essential, see e.g. [1, 2]. Nevertheless, the research work of the last decade has resulted in a much deeper understanding of hybrid simulation and, consequently, many initial problems

---

M.J. Hochrainer (✉) • P. Schattovich
University of Applied Sciences, Johannes Gutenberg-Strasse 3, 2700, Wiener Neustadt, Austria
e-mail: markus.hochrainer@fhwn.ac.at

have been overcome leading to wide spread use of RTHS. From a historical perspective several hybrid techniques have been developed in the field experimental mechanics often with a distinct focus on earthquake engineering. Conventional experimental testing was either quasi-static or dynamic (shake table testing). Both types can be categorized as open loop, as all loads applied to the device under test (DUT) are predetermined, and feedback from the DUT is not required in the experiment. Quasi-static tests are based on the application of slowly varying loads to determine the nonlinear behavior of structural members, whereas shake table tests are required whenever a component shows a loading rate dependence. Since the loading capacity of quasi static test rigs is generally significantly higher than that of dynamic ones, quasi-static testing allows larger DUTs to be studied. If the loading is depending on the DUT's response (forces or displacements), the method is denoted hybrid simulation, since it combines both, numerical simulation of a substructure and physical testing. Typically, the behavior of the components tested physically is fairly complex and difficult to predict, whereas the numerical model is rather simple permitting highly reliable estimates. Hybrid simulations can be pseudo-dynamic or dynamic. Pseudo-dynamic hybrid simulations are typically displacement controlled with a feedback of measured physical forces to a numerical model which accounts for all dynamic effects like masses or (visco-) elastic components. The fact that all equipment necessary for hybrid simulation is available in a dynamics laboratory, is one of the salient feature of pseudo-dynamic hybrid simulation. If the DUT has dynamic properties which significantly influence the overall behavior, the hybrid simulation must be performed in real-time. This often requires complex control mechanisms and places high demands on equipment and simulation model (real-time simulation). The importance of hybrid simulation is strongly associated with experimental testing, which is, at the moment, the only reliable method to confirm, develop and improve numerical simulation models. Although well established in the field of civil engineering, RTHS has become very attractive for many other disciplines because it permits reliable testing of individual components while taking into account the complex interaction with the overall system. In automotive and aeronautic industry real-time hybrid simulation/testing is well established but known as hardware in the loop simulation/testing. The approval of components and modules is responsible for an ever increasing demand for this kind of testing in recent years. Depending on the actual application, the requirements and challenges of real-time hybrid simulations are very different. When testing mechanical systems quasi-static methods are often appropriate for nonlinear members of complex structures, however, in most other applications this type of time scaling is not possible and accordingly real-time hybrid testing is generally applied. This is particularly true if a system's electronic control unit (ECU) is tested because potential data transmission, digital interfaces, timing aspects, the control loop as well as possible analog filtering is hardly possible with quasi-static testing.

Apparently, the RTHS or HIL philosophy allows reliable component testing without any risk. This is a significant advantage in the development of aircrafts, because each test flight has the potential threat of aircraft crashes. However, as in any other discipline the computer models used for HIL-testing are a simplification of the real physical structure and therefore experiments and tests with the real system cannot be replaced completely yet. On the other side, the HIL philosophy enables investigations which are hardly possible with traditional methodologies, e.g. the repeatable injection of fault signals or the temporal/permanent failure of sensors if an ECU is selected as DUT. Therefore HIL currently seems to be the most versatile and efficient method for obtaining a desired system performance before performing experimental test with the entire physical system, see e.g. [3, 4] for aircraft applications. In the project presented, the copter was developed without proper simulation and since the performance did not meet the expectations, RTHS was used to analyze the system before redesigning it.

4.2 Concept

The primary prerequisite for any HIL testing is a complete separation of all physical components from the simulated numerical model. In case of the quadcopter the physical components include the control unit, power amplifier, BLDC engines and remote control. In the current project, the coupling between physical and simulated model is based on simulated sensor values and estimated aerodynamic lifting forces (rotor thrusts). The ECU position controller processes simulated accelerations and angular velocities generated by the real-time simulation of the quadcopter flight dynamics. The simulation model, on the other hand, receives the current engine speeds for individual rotor thrust determination. Thus, the HIL control loop is closed as illustrated in Fig. 4.1. The host-PC is primarily used for the configuration and control (HIL control/configuration) of the hybrid testing. However, since sufficient computational resources are available the host PC is also used for the online visualization (VR-model/data analysis) and analysis of the experimental results. Via a standard Ethernet interface the host PC communicates with the target PC, which performs all real-time simulations (flight dynamics) and derives the simulated measurements (IMU simulation). It is connected to the ECU, the physical section of the experiment, by a digital UART interface (RS232). The central component of the ECU is an embedded system based on a 16-bit microcontroller of type Microchip PIC 24FJ256GB106 which is already set up to perform both, the calculation of
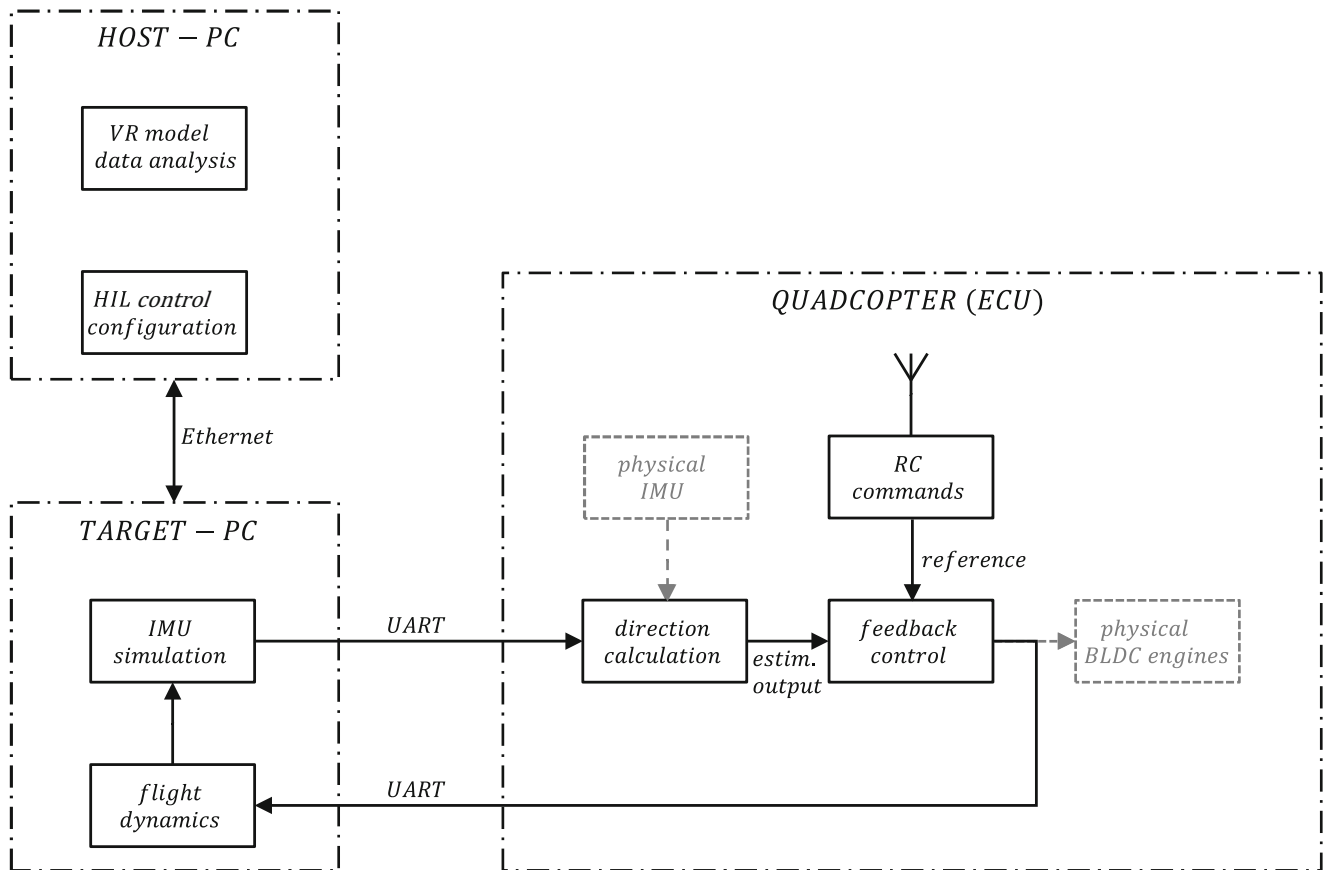
Fig. 4.1 Schematics of the HIL configuration applied

the direction in space (direction calculation) and the stabilization of the inherently instable quadcopter (feedback control). In addition the ECU is responsible for the communication with the RC-unit (RC commands) and the additional UART communication in the HIL setup.

4.3   System Modelling

When compared to helicopters, one outstanding advantage of quadcopters is the simple and robust design of entire drive line. The only requirement is that all rigid rotors can operate at different speeds. Although the number of rotors can vary, it is typically increased in pairs thereby generating redundancy and a higher level of reliability, e.g. in case of hexa- or octocopters. From all multirotor aircrafts available, the quadcopter is most popular and therefore a quadcopter setup was chosen for the original project. When compared to conventional helicopters, quadcopters have no moving parts, no cyclically adaption of the angle of attack, no governor and no need for a tail rotor. However, this is at the price of four engines, typically brushless DC (BLDC) drives, which are alternately rotating in opposite direction. When spinning at the same angular velocity, all reaction torques fully compensate, and the resulting lifting force is adjusted by the engine speed. Yaw (without a change of the cumulative thrust) results from a symmetric thrust-offset between the counter rotating blade pairs. Roll and pitch are adjusted by inversely changing the thrust of two opposing rotors, while keeping the total reaction moment and lifting force constant. The increasing popularity of quadcopters is also due to their simplicity with respect to control: Any complex flight maneuver results from superimposing the rotor speed adaptions of the corresponding basic flight operations (yaw, pitch, roll and altitude adjustment). It is important to recognize that the rotor thrusts always point in the direction of the local z-axis. Since the drive engines are directly connected to fixed pitch rotor blades, there are no moving parts, and consequently, the copter motion must be controlled by tilting the entire aircraft. Due to their geometric design, most quadcopter are inherently unstable unless the center of mass is located very low with respect to the distance of $2l$ between a pair of rotors. Therefore,
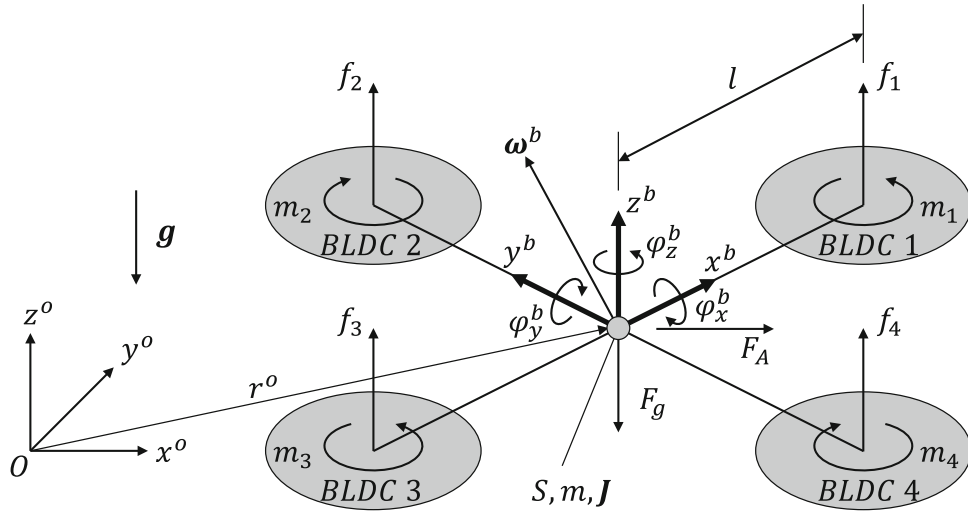
Fig. 4.2 Free body diagram of the quadcopter

a permanent feedback control stabilization is essential which is generally based on local IMU measurements. This inherit instability, on the other side, is the reason for the comparably fast flight dynamics. However, with rising copter and blade size, the rotor's moment of inertia is growing fast and rotor speed corrections take significantly longer, which negatively impacts control.

To obtain a mathematical model of the quadcopter motion, it is assumed rigid and fully symmetric with mass m, moments of inertia collected in the tensor J and the center of mass S. The forces acting on the rigid body are the four thrusts F_i, $i = 1 \ldots 4$, its corresponding reaction torques M_i, the aerodynamic drag force F_A and the gravitational force $F_g = mg$, with g denoting the constant of gravity, see Fig. 4.2 for the free body diagram.

Following the kinematics of rigid bodies, newton's law of inertia for moving reference frames renders an equation of motion in the moving reference frame (local coordinates superscript b)

$$m\dot{v}^b + m\omega^b \times v^b = \sum F_i^b + F_g^b + F_A^b, \tag{4.1}$$

where $\omega^b = \left(\dot{\varphi}_x^b, \ \dot{\varphi}_y^b, \ \dot{\varphi}_z^b\right)^T$ denotes the angular velocity vector. The conservation of angular momentum renders a nonlinear differential vector equation,

$$J^b\dot{\omega}^b + \omega^b \times J^b\omega^b = \sum M_i^b. \tag{4.2}$$

Defining the local coordinates by the principal axes of inertia, the inertia tensor becomes diagonal, $J = diag(J_x, \ J_y, \ J_z)$ and three nonlinear differential equations of motion with constant coefficient, known as Euler's gyroscopic equations are obtained, see e.g. [5, p. 420, 6]. From the equations of motion 1–2 the quadcopter dynamics is completely determined and for known individual engine thrust forces $F_i^b = (0, 0, f_i)^T$ together with the resulting moments $M_i^b = r_i^b \times F_i^b + (0, 0, m_i)^T$ the differential equations can be solved.

Apparently, the flight position must be given in absolute coordinates (superscript o) $O = (x^o, y^o, z^o)$, see Fig. 4.2. All rotations are based on the proper Euler angles $e^o = (\phi, \ \theta, \psi)^T$, which describe elemental rotations in a defined order: first the rotation ψ about the z-axis, then the rotation θ about the already rotated y-axis, and finally another rotation ϕ about the x-axis, see e.g. [7]. The transformation of vector quantities between different frames of reference is carried out by a matrix multiplication with the orthogonal rotation matrix $R(e)$, see again [7]. Since the equations of motion are given in local coordinates (moving frame of reference) the time dependent relation between the angular velocity vector ω^b and the Euler angles e^o

$$\dot{e}^o = \begin{pmatrix} 1 & \sin\phi\tan\theta & \cos\phi\tan\theta \\ 0 & \cos\phi & -\sin\phi \\ 0 & \sin\phi/\cos\theta & \cos\phi/\cos\theta \end{pmatrix} \omega^b = \Gamma(e)\,\omega^b \tag{4.3}$$
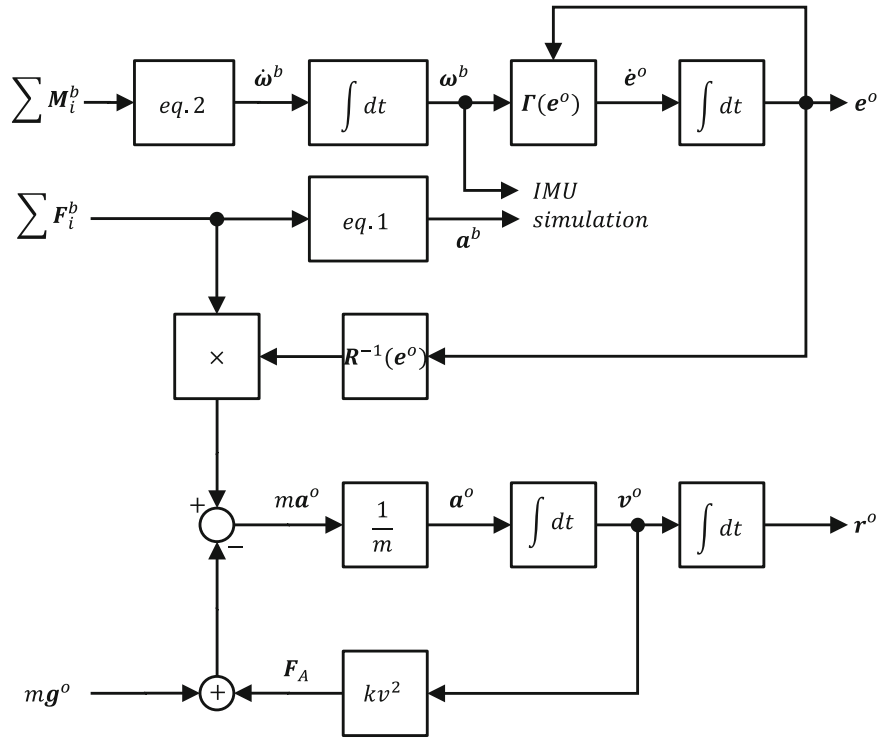
Fig. 4.3 Signal flow of real-time simulation

is required for the numerical integration of the equations of motion. For feedback stabilization the vast majority of quadcopters use IMU (gyro and accelerometer) measurements, which are predominantly processed by complementary filtering to determine the actual copter orientation. However, this measurement principle is only valid for stationary flight conditions, and this is the reason why it is essential to simulate the aerodynamic drag force $\boldsymbol{F}_A^0 = \boldsymbol{v}^o \, |\boldsymbol{v}^o| \, k$, with k describing the drag constant. An overview of the calculations necessary (signal flow) to obtain the actual position in global coordinates is given in Fig. 4.3. For simulated IMU measurements the determination of $\boldsymbol{\omega}^b$ is straightforward, the calculation of $\boldsymbol{a}^b$ requires the correction of the centrifugal forces, and both vector quantities must, of course, be scaled according to the datasheet's sensor hardware specification, see [8].

4.4   Implementation and Setup

Having derived the equations of motion and the signal flow diagram for solving them numerically, refer Fig. 4.3, it is straightforward to implement the numerical model in a signal flow based simulation environment. The numerical integration is performed using an explicit Runge-Kutta method of order four (RK4) with a constant integration step size (fundamental sample time) of $T_S = 5ms$. Within modern simulation environments the model can be compiled and transferred to the target computer hardware which is connected to the physical ECU system. Besides standard interfaces (Ethernet, RS232) there are no special hardware requirements in the current project, because the real-time ability is provided by the operating system. When the simulation is running on the target PC, the flight trajectories are determined from the four rotor speeds which are periodically transmitted from the physical ECU. Once the flight trajectory is known, the IMU sensor values can be derived directly from the local acceleration and angular velocity. Because the simulated sensor output represents a perfect measurement, it must be degraded by superposition of various sensor errors e.g. sensor noise, offset, temperature drift, nonlinearities, before transmitting it to the physical ECU for further processing. In the current project it was essential to keep the existing ECU firmware almost unchanged. However, minor modifications of the communication routines were required for data exchange with the real-time target PC. Before starting RTHS testing, it is, however, vital to identify all mechanical system parameter (mass, inertia tensor, geometric dimensions), as well as the drive characteristics at a high level of confidence. Consequently, all not directly measureable parameter were determined by experimental testing: The inertia
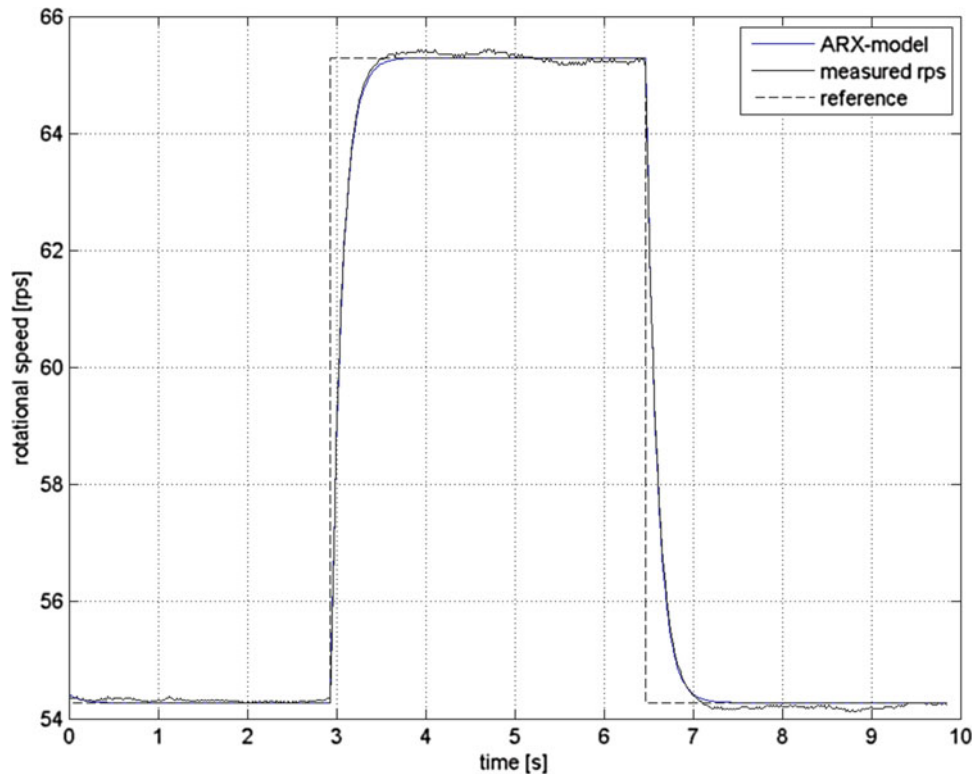
Fig. 4.4 Step response of the entire drive line

tensor by vibration tests, the speed-duty-cycle characteristics of the BLDC engine by rpm measurements and the quadcopter yaw using a pendulum type set-up. All experiments were repeated several times, with the desired parameter being identified using least squares methods. A rather important component of the entire identification process was the determination of the overall drive dynamics comprising of the power amplifier and the BLDC engine with rigidly attached rotors in the relevant rpm range, see Fig. 4.4. The overall drive line dynamics is obtained from an ARX model of first order, again, by least squares identification.

4.5 Experimental Results

The developed, calibrated and sufficiently tested HIL experiment allows to simulate, validate and analyze the dynamic performance of the quadcopter in any possible flight situation. Nevertheless, all experiments have shown, that the assessment of the system behavior is hardly possible using standard graphical interfaces like time-plots, time histories or numerical displays. Therefore, a flight animation was developed by linking 3D graphics objects of a virtual reality environment to the numerical simulation results. Only this way it was possible to develop a fundamental understanding of the system behavior, since a realistic visualization of the flight is essential if an operator is controlling the system using the standard RC control, see Fig. 4.5. Even in case of automated testing with predefined flight maneuvers, the visualization is crucial to correctly interpret the dynamic behavior.

Using the presented RTHS, the focus of the research and development work can again be put on the improvement of the IMU sensor measurements within the ECU firmware. Accordingly, the analysis concentrated on real physical flight situations which initially triggered the HIL testing: little stability margins during hovering, irregular crashes due to suspected engine shut down as well as firmware bugs in the processing of measured data. The inspection of the HIL flight stability has confirmed the shortcomings of the current ECU with respect to limit cycle vibrations around all axes during stationary hover flight. This deficient performance became even worse with increased simulated IMU sensor noise, see Fig. 4.6. The HIL experiment has proven undoubtedly, that this behavior was due to numerical effects when calculating the copter direction.
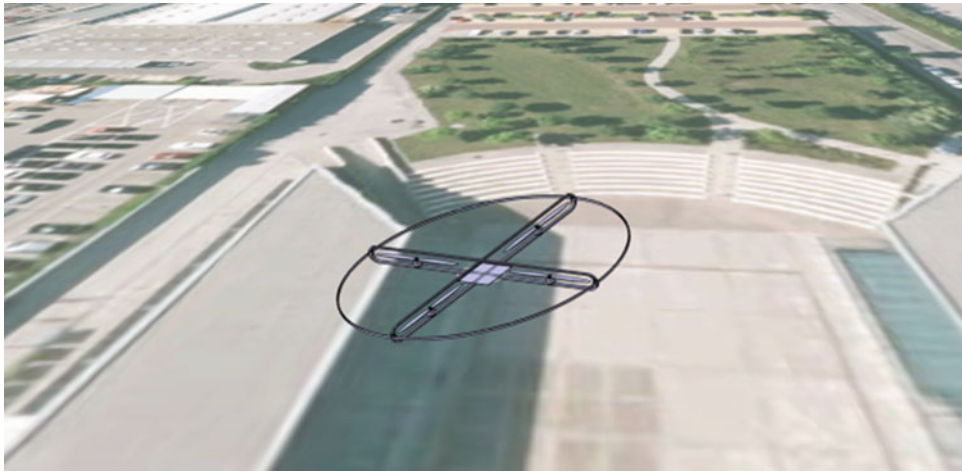
Fig. 4.5 Real-time visualization of a quadcopter flight at the university campus in the virtual reality environment, the copter is guided by a remote control
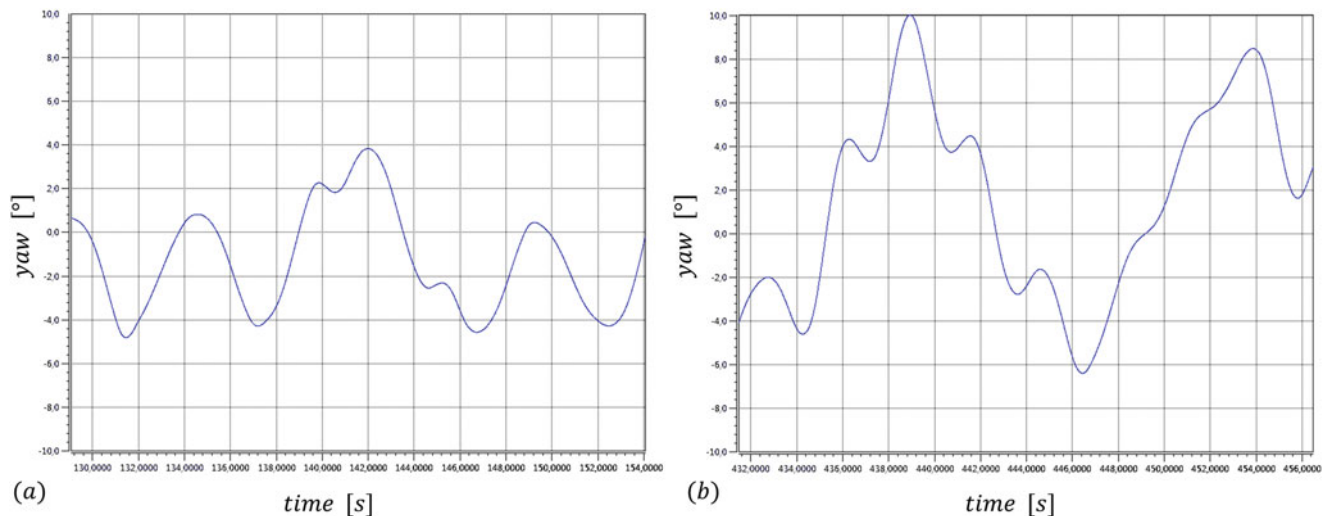
Fig. 4.6 Yaw vibrations during hovering for different IMU sensor configurations (**a**) low sensor noise (**b**) increased sensor noise

It is essential to note that the limit cycle behavior does not occur in a traditional simulation (model in the loop without HIL coupling). However, the effectiveness and reliability of the proposed set-up is confirmed, since undesired vibrations were clearly observed during real flights.

The hybrid simulation offers the possibility to rigidly attach the quadcopter in the laboratory while energizing the BLDC engines to activate all rotors during the experiment. Only this way the occasional engine stops could be reproduced, and systematic error tracking revealed an emergency shutdown triggered by the overcurrent protection module of the power amplifier unit. As expected, this behavior was directly dependent on the simulated sensor noise level and thus, the test has confirmed that sensor noise reduction by improved filtering is essential, because even under normal flight conditions the IMU is exposed to very high vibration and EMC levels. Similarly, the work has demonstrated that the firmware code segment for evaluating the angular velocity behaves improper when exceeding a critical gyro limit. Consequently, the implementation of either the numerical integration or the complementary filter is incorrect. Finally, the magnetic field sensor used to calculate the local yaw angle was tested, because it has always shown a moderate dependence on rotations about the other axes. So far, this effect has been attributed to interfering magnetic fields in the laboratory or EMC engine noise. The simulation of a perfect earth's magnetic field together with an ideal magnetic sensor, however, has revealed that the effect must again be attributed to the ECU data processing.

4.6 Conclusions

This work presents a real-time hybrid simulation for the analysis and optimization of the electronic control unit of a quadcopter, which was initially performed to analyze and understand the undesired dynamic flight performance. Hence, the existing physical ECU including the embedded system and firmware, the power amplifier and the BLDC engines are coupled to a real-time computer model used to simulate the flight. In summary, the HIL testing compares very well with real flight tests and the detected insufficient flight performance could be attributed clearly to shortcomings of the current firmware. A revision of the current sensor data processing is required with respect to noise and disturbance attenuation. With RTHS accurate testing of all firmware improvements is possible without real flight experiments. The hybrid simulation indicates, that instead of using improved IMU sensor units, a firmware tuning should be sufficient to achieve the desired flight behavior. The work confirms, that proper RHTS allows all flight maneuvers to be simulated and optimized at a very realistic level. Consequently, the HIL methodology opens opportunities and enables developments, which are hardly possible with traditional methods, or only with a significantly greater effort.

References

1. Saouma, V., Sivaselvan, M. (eds.): Hybrid Simulation: Theory, Implementation and Applications. Taylor & Francis Ltd (2008), London, UK
2. Bursi, O. S., Wagg, D.: Modern Testing Techniques for Structural Systems, Dynamics and Control. CISM International Centre for Mechanical Sciences, vol. 502, Springer, New York, Vienna (2008)
3. Gans, N.R., Dixon, W.E., Lind, R., Kurdila, A.: A hardware in the loop simulation platform for vision-based control of unmanned air vehicles. Mechatronics. **19**(7), 1043–1056 (2009)
4. Karpenko, M., Sepehri, N.: Hardware-in-the-loop simulator for research on fault tolerant control of electrohydraulic actuators in a flight control application. Mechatronics. **19**(7), 1067–1077 (2009)
5. Ziegler, F.: Mechanics of Solids and Fluids, 2nd reprint of second edition. Springer, New York, Vienna (1998)
6. Li, Z., Murray, R.M., Sastry, S.S.: A Mathematical Introduction to Robotic Manipulation. CRC Press, Boca Raton (1994)
7. Fu, K.S, Lee, C.S.G., Gonzales, G.C.: Robotics, Control, Sensing, Vision and Intelligence. McGraw-Hill International Editions (1987)
8. Schattovich, P.: Hardware in the Loop Studies of an Unmanned Aircraft, in German, Master Thesis, University of Applied Sciences, Wiener Neustadt, Austria (2016)

Chapter 5
An Integration of Mixed Contact Formulation with Model-Reduction Techniques

Blaž Starc, Gregor Čepon, and Miha Boltežar

Abstract A new method for efficient dynamics simulations of flexible systems with unilateral contacts is presented. The procedure is based on the Craig-Bampton model-reduction technique together with a contact formulation using single- and set-valued force laws. For the computation of system response, an event-driven integration scheme is proposed, which allows transitions among different contact states. An updating algorithm for derivation of the reduced-system matrices is developed as well as the formulation of new initial conditions. The applicability of the developed method is demonstrated on a simple structure with varying contact conditions.

Keywords Penalty method • System response • Time integration • Unilateral contacts • Dynamics

5.1 Introduction

The dynamic simulations of contacts between flexible bodies are usually conducted by applying a dense mesh and the use of the classical finite element method in combination with the penalty method [1]. This requires a large set of Degrees of Freedom (DoF) to represent the structure and the use of explicit analyses with small-time step-sizes to analyse the system response. This typically leads to long computation times and requires large computational resources. In this paper, a new method for efficient dynamics simulations of flexible systems with unilateral contacts is proposed. The procedure proposes the integration of single- and set-valued force laws together with the Craig-Bampton model reduction technique [2]. According to the contact state, an event-driven integration scheme is used, which allows the updating of reduced-system matrices as well as formulating new reduced-space initial conditions. The applicability of the developed method is demonstrated on a clamped-beam structure with a harmonic force on the free end and a varying contact condition.

5.2 Craig-Bampton Method

The classic finite-element approach requires a large number of nodes, which leads to large models and long computation times. In order to reduce the time, a coarser mesh needs to be applied, which is not always possible due to the convergence of the solution. A possible alternative is the Craig-Bampton [2] model-reduction technique. It retains the dense finite-element mesh, but replaces the physical DoF by a much smaller set of generalized DoF.

The model-reduction techniques are closely connected to the substucturing field, where a substructure dynamical model is defined as:

$$\mathbf{M}^{(s)}\,\ddot{\mathbf{u}}^{(s)}(t) + \mathbf{C}^{(s)}\,\dot{\mathbf{u}}^{(s)}(t) + \mathbf{K}^{(s)}\,\mathbf{u}^{(s)}(t) = \mathbf{f}^{(s)}(t) + \mathbf{g}^{(s)}(t), \tag{5.1}$$

The matrices $\mathbf{M}^{(s)}$, $\mathbf{C}^{(s)}$ and $\mathbf{K}^{(s)}$ represent the mass, the damping and the stiffness matrix of a substructure s, $\mathbf{u}^{(s)}(t)$ is the displacement vector, $\mathbf{f}^{(s)}$ is the external excitation vector and $\mathbf{g}^{(s)}$ is the vector of connection forces with the surrounding substructures. The Craig-Bampton method divides the physical DOF $\mathbf{u}$ into the internal $\mathbf{u}_i$ and the boundary DOF $\mathbf{u}_b$, which gives Eq. (5.1) the following shape:

B. Starc (✉) • G. Čepon • M. Boltežar
Faculty of Mechanical Engineering, University of Ljubljana, Aškerceva cesta 6, 1000, Ljubljana, Slovenia
e-mail: blaz.starc@fs.uni-lj.si

$$\begin{bmatrix} \mathbf{M}_{ii} & \mathbf{M}_{ib} \\ \mathbf{M}_{bi} & \mathbf{M}_{bb} \end{bmatrix} \begin{Bmatrix} \ddot{\mathbf{u}}_i \\ \ddot{\mathbf{u}}_b \end{Bmatrix} + \begin{bmatrix} \mathbf{K}_{ii} & \mathbf{K}_{ib} \\ \mathbf{K}_{bi} & \mathbf{K}_{bb} \end{bmatrix} \begin{Bmatrix} \mathbf{u}_i \\ \mathbf{u}_b \end{Bmatrix} = \begin{Bmatrix} \mathbf{f}_i \\ \mathbf{f}_b \end{Bmatrix} + \begin{Bmatrix} \mathbf{g}_i \\ \mathbf{g}_b \end{Bmatrix}, \tag{5.2}$$

where the index i denotes the internal DOF and b the boundary DOF. Note that the internal excitation forces $\mathbf{g}_i$ are assumed to be $\mathbf{0}$, since there is no contact with the neighbouring substructures.

The internal DOF are approximated as:

$$\mathbf{u}_i \approx \boldsymbol{\Psi}_c\,\mathbf{u}_b + \boldsymbol{\Phi}_i\,\boldsymbol{\eta}_i \tag{5.3}$$

Here, $\boldsymbol{\Psi}_c$ are the static constraint modes and $\boldsymbol{\Phi}_i$ are a reduced set of fixed interface vibration modes with the corresponding modal DOF $\boldsymbol{\eta}_i$. If Eq. (5.3) is inserted into Eq. (5.2) and the orthogonality between the vibration modes with respect to the mass or stiffness matrix [3] is taken into account, the following reduced equations of motion are obtained:

$$\begin{bmatrix} \mathbf{I} & \mathbf{M}_{\phi b} \\ \mathbf{M}_{b\phi} & \tilde{\mathbf{M}}_{bb} \end{bmatrix} \begin{Bmatrix} \ddot{\boldsymbol{\eta}}_i \\ \ddot{\mathbf{u}}_b \end{Bmatrix} + \begin{bmatrix} \boldsymbol{\Omega}_i^2 & \mathbf{0} \\ \mathbf{0} & \tilde{\mathbf{K}}_{bb} \end{bmatrix} \begin{Bmatrix} \boldsymbol{\eta}_i \\ \mathbf{u}_b \end{Bmatrix} = \begin{Bmatrix} \tilde{\mathbf{f}}_i \\ \tilde{\mathbf{f}}_b \end{Bmatrix} + \begin{Bmatrix} \mathbf{0} \\ \mathbf{g}_b \end{Bmatrix}, \tag{5.4}$$

where:

$$\begin{aligned}
\tilde{\mathbf{K}}_{bb} &= \mathbf{K}_{bb} - \mathbf{K}_{bi}\,\mathbf{K}_{ii}^{-1}\,\mathbf{K}_{ib} \\
\tilde{\mathbf{M}}_{bb} &= \mathbf{M}_{bb} - \mathbf{M}_{bi}\,\mathbf{K}_{ii}^{-1}\,\mathbf{K}_{ib} - \mathbf{K}_{bi}\,\mathbf{K}_{ii}^{-1}\,\mathbf{M}_{ib} + \mathbf{K}_{bi}\,\mathbf{K}_{ii}^{-1}\,\mathbf{M}_{ii}\,\mathbf{K}_{ii}^{-1}\,\mathbf{K}_{ib} = \\
&= \mathbf{M}_{bb} - \mathbf{M}_{bi}\,\boldsymbol{\Psi}_c - \boldsymbol{\Psi}_c^{\mathrm{T}}\,\mathbf{M}_{ib} + \boldsymbol{\Psi}_c^{\mathrm{T}}\,\mathbf{M}_{ii}\,\boldsymbol{\Psi}_c \\
\mathbf{M}_{\phi b} &= \boldsymbol{\Phi}_i^{\mathrm{T}}(\mathbf{M}_{ib} - \mathbf{M}_{ii}\,\mathbf{K}_{ii}^{-1}\,\mathbf{K}_{ib}) \\
\mathbf{M}_{b\phi} &= \mathbf{M}_{\phi b}^{\mathrm{T}} \\
\tilde{\mathbf{f}}_i &= \boldsymbol{\Phi}_i^{\mathrm{T}}\,\mathbf{f}_i \\
\tilde{\mathbf{f}}_b &= \mathbf{f}_b - \mathbf{K}_{bi}\,\mathbf{K}_{ii}^{-1}\,\mathbf{f}_i = \boldsymbol{\Psi}_c^{\mathrm{T}}\,\mathbf{f}_i
\end{aligned} \tag{5.5}$$

Here, $\boldsymbol{\Omega}_i^2$ represents a diagonal matrix of squared fixed-interface frequencies $\omega_{i,j}^2$.

5.3 Contact Formulation

The modelling of contacts between flexible bodies is usually formulated using the penalty method [1]. Using a large penalty stiffness may lead to an ill-conditioned stiffness matrix and consequently to a poor convergence. On the other hand, the method that imposes a non-penetration condition originates from the formulation between rigid-bodies [1, 4]. Here, a combination of single- and set-valued unilateral force laws is used as proposed in [5]. The proposed contact method models the contact with three states: no-contact, continuous and impact/penalty state. This enables faster integration times, since the penalty is present only during the impact. When the contact is lost (no-contact) the stiffness matrix is classical (without penalty) and when fixed the contact DOF is fixed. The contact states in addition with the event-driven integration scheme can be seen on case of a clamped beam with a varying contact and a harmonic force on the free end in Fig. 5.1.

Note, that the contact states influence the accompanying reduced-models and also have an influence on the definition of integration events. The three reduced models can be computed in advance and therefore do not influence the integration process. Also the events need to be defined in reduced space. The constraint force in Event 1 (see Fig. 5.1) is derived from Eq. (5.4):

$$\mathbf{g}_b = \mathbf{M}_{b\phi}\,\ddot{\boldsymbol{\eta}}_i + \mathbf{M}_{bb}\,\ddot{\mathbf{u}}_b + \mathbf{K}_{bb}\,\mathbf{u}_b - \tilde{\mathbf{f}}_b \tag{5.6}$$

and further simplified if boundary displacements and accelerations are zero:

$$\mathbf{g}_b = \mathbf{M}_{b\phi}\,\ddot{\boldsymbol{\eta}}_i - \tilde{\mathbf{f}}_b \tag{5.7}$$

Other events (2–7, see Fig. 5.1) are defined classically.
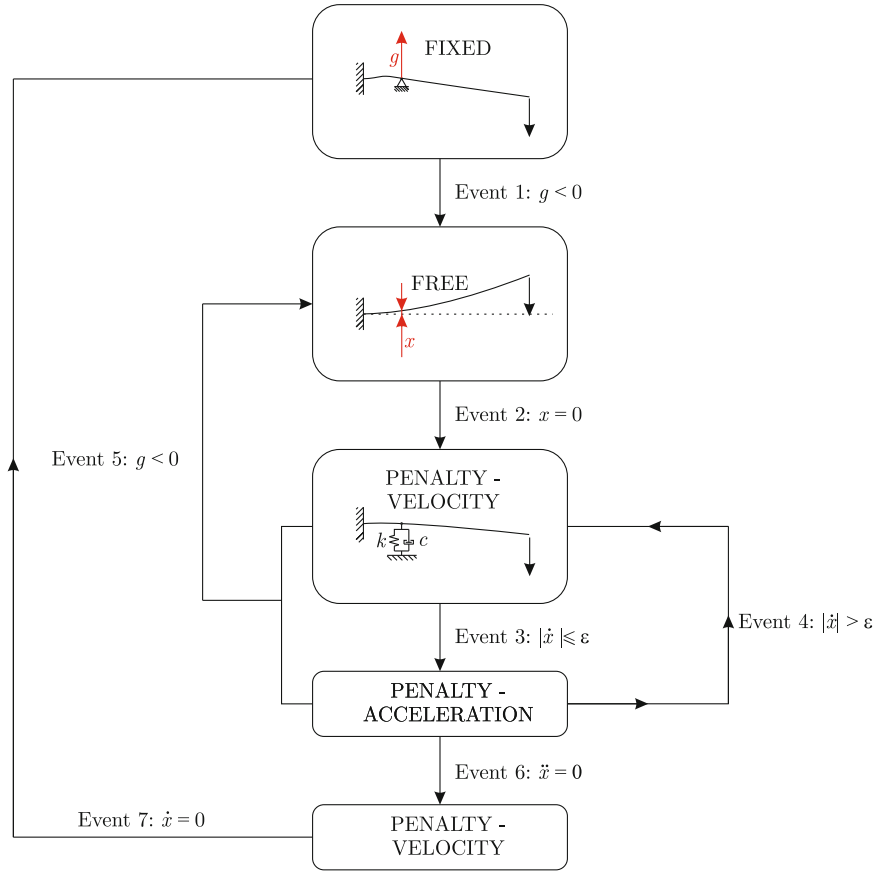
Fig. 5.1 Contact states and integration events on a clamped beam

In addition to events, also new initial conditions need to be defined in order to define transition among the three reduced states. The transition between two reduced spaces (e.g. no-contact and continuous) is done by equalizing the physical coordinates (Eq. 5.3) and since the boundary conditions are already in the physical space, the new initial conditions can be obtained:

$$\boldsymbol{\eta}_{i,free} = \boldsymbol{\Phi}_{i,free}^{+}(\boldsymbol{\Phi}_{i,fixed}\,\boldsymbol{\eta}_{i,fixed} + \boldsymbol{\Psi}_{c,fixed}\,\mathbf{u}_b - \boldsymbol{\Psi}_{c,free}\,\mathbf{u}_b). \tag{5.8}$$

Equation (5.8) can be further simplified, due to the orthogonal properties of the fixed-interface modes ($\boldsymbol{\Phi}_{i,free}^{+}\boldsymbol{\Phi}_{i,fixed} = \mathbf{I}$):

$$\boldsymbol{\eta}_{i,free} = \boldsymbol{\eta}_{i,fixed} + \boldsymbol{\Phi}_{i,free}^{+}\,(\boldsymbol{\Psi}_{c,fixed} - \boldsymbol{\Psi}_{c,free})\,\mathbf{u}_b \tag{5.9}$$

Note, that the above equation is derived for the no-contact and continuous reduced models, but the same conclusion is valid also for other combinations with the impact/penalty model.

5.4 Conclusions

A new method for modelling the dynamic response of systems with contacts is proposed. The Craig-Bampton model-reduction technique is used to reduce the number of DoF and therefore enable faster and more efficient computations of the system response. Moreover, the reduced model is upgraded with a contact formulation consisting of three main states: no-contact, continuous and impact/penalty state. This enables faster computation times than pure penalty method, since the continuous contact is modelled without the additional penalty stiffness. The use of the method is showcased on a clamped beam structure with a varying contact and a harmonic force on the free end.

References

1. Pfeiffer, F., Glocker, C.: Multibody Dynamics with Unilateral Contacts, vol. 1996, 1st edn. Springer, Wien (1996)
2. Bampton, M.C.C., Craig, R.R., Jr.: Coupling of substructures for dynamic analyses. AIAA J. **6**(7), 1313–1319 (1968)
3. Geradin, M., Rixen, D.J.: Mechanical Vibrations: Theory and Application to Structural Dynamics, 3rd edn. Wiley, Hoboken (2015)
4. Glocker, C.: Formulation of spatial contact situations in rigid multibody systems. Comput. Methods Appl. Mech. Eng. **177**(3–4), 199–214 (1999)
5. Čepon, G., Boltežar, M.: Dynamics of a belt-drive system using a linear complementarity problem for the belt-pulley contact description. J. Sound Vib. **319**(3–5), 1019–1035 (2009)

Chapter 6
Identification Reassembly Uncertainties for a Basic Lap Joint

C.W. Schwingshackl

Abstract The modelling of the dynamic response of a structure containing joints is gradually reaching a stage where somewhat realistic results can be obtained from the analysis. Regardless of the progress in the analysis, often a validation against experimental data fails due to the poor repeatability of the experimental results. Every reassembly of a joint tends to lead to a slightly different nonlinear response, since the underlying nonlinear mechanisms at the interface, driving the nonlinear response, are very sensitive to the boundary conditions. To understand the reassembly repeatability of a lap joint, a state of the art, high fidelity, modelling approach was used to investigate which parameters lead to the largest uncertainties. Variations in the friction parameters, loss of bolt preload and inaccuracies in the surface geometry were considered. It could be shown that all these effects can influence the nonlinear response of a structure with a lap joint, with the interface geometry having the larges impact.

Keywords Lap joint • Nonlinear dynamics • Friction • Simulation • Uncertainty

6.1 Introduction

The analysis of the linear dynamic response of a component has reached a very mature state today, leading to accurate predictions of the frequency response. A much bigger challenge is the response prediction of assembled structures due to the nonlinear behaviour of its joints. The main challenge thereby is the accurate capture of the micro and macro sliding events at the contact interface, which cause the amplitude dependent damping and frequency shifts. An accurate knowledge of these values is often of great significance during the development of a new design, since an unexpected resonance frequency in the operating range can lead to problems during operation.

Good progress has been made over the last years in modelling nonlinear joints [1–4], but one of the main challenges when trying to model a real joint is the uncertainty that is attached to it. This can be caused by geometric tolerances, alignment issues, inaccurate bolt torques, uncertainty of the contact parameters, contamination of the contact interface, and many other reasons, which are very difficult to control during design, manufacture and assembly of the joint. The impact of these uncertainties is often observed during measurements, leading to poor repeatability in the response, but currently mainly ignored in the analysis. For an improved modelling approach of the jointed structure, or in the future an optimised joint design for better repeatability, the sources of these variations must be better understood.

One particular joint of interest is a bolted lap joint, which is being used for the assembly of many structures, and which will be the focus of this paper. The friction input parameters, bolt preload variations, and interface geometry will be considered as potential sources of uncertainty of a beam with a bolted lap joint (Brake Reuss Beam – BRB) [5, 6].

6.2 Nonlinear Lap Joint Response

The bolted lap joint from Fig. 6.1a will be used in this analysis to investigate the influence of the interface conditions on the nonlinear dynamic response. A detailed nonlinear model of the lap joint has been presented in the past [7], and a similar, also somewhat simplified, modelling approach will be used for this investigation.

C.W. Schwingshackl (✉)

Imperial College London, Exhibition Road, SW7 2AZ, London, UK

e-mail: c.schwingshackl@imperial.ac.uk
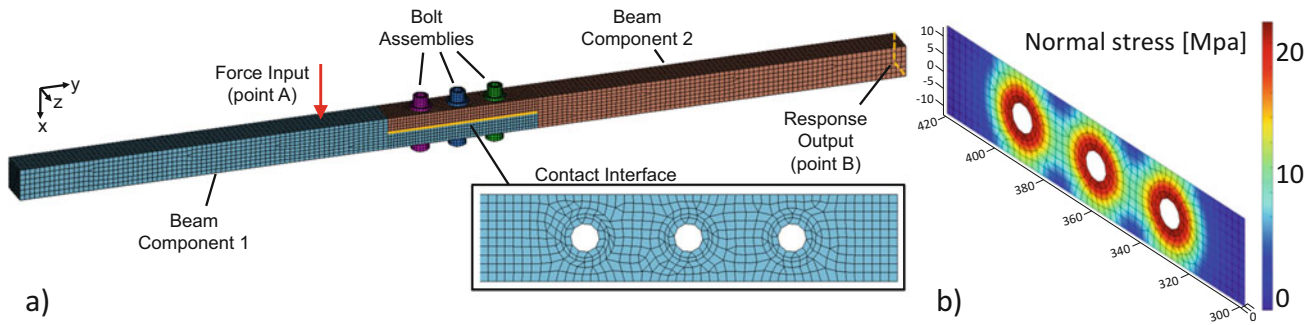
Fig. 6.1 (**a**) Finite element model of the BRB beam and (**b**) normal stress distribution for nominal bolt load
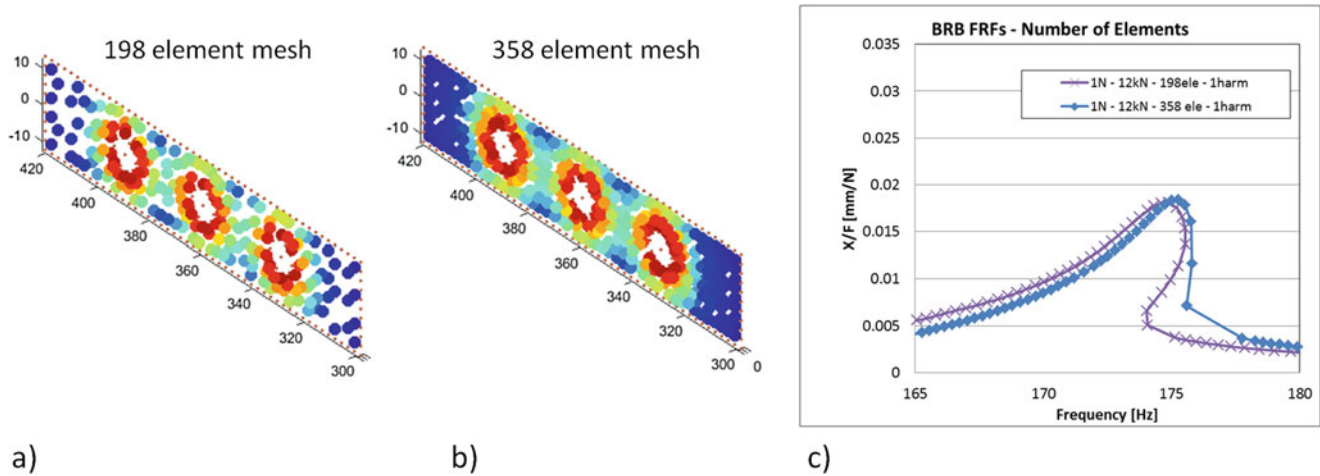
Fig. 6.2 (**a**) 198 nonlinear elements, (**b**) 358 nonlinear elements, and (**c**) FRF for two mesh densities with 1st harmonic

The joint under investigation (Brake Reusse Beam, BRB) consists of two square beams of dimensions $420 \times 30 \times 30$ mm each, that are assembled to a long beam via a flat lap joint. The joint itself has an interface dimension of 120×30 mm and contains three evenly spaced M8 bolts (see Fig. 6.1a). Initially both sides of the structure were modelled and analysed in a linear FE solver, and the results were updated and validated against experimental data. In a next step, models of the three bolts were created and added to the structure, where the bolt heads were permanently attached to the beams, whereas the bolt shafts were free to move inside their respective holes. A sliding contact interface was applied to the lap joint itself and a bolt load of 12 kN, corresponding to approx. 20 Nm torque, applied to each bolt to compute the normal load distribution at the interface. For the bolt load simulation a similar approach to [4] was used, where an equivalent thermal load was calculated and applied to the bolt shaft,

$$\Delta T = \frac{F_{bolt}}{\alpha E A_{bolt}} \tag{6.1}$$

leading to a thermal strain similar to the one expected from the mechanical strain of the torque. The normal load distribution at the interface was than calculated and the result in Fig. 6.1b shows a strong stress concentration underneath the bolts, with a very low and even distribution at the two free edges of the joint, indicating the strong influence of the pressure cones on the initial condition at the contact surface.

Based on the linear FE mesh and the normal stress distribution from Fig. 6.1, two nonlinear meshes were generated for the in house nonlinear dynamic solver FORSE [8, 9] with 198 and 358 nonlinear elements respectively (see Fig. 6.2a, b), to provide a detailed contact interface representation. Three dimensional nonlinear elements were used for the analysis to capture in plane stick and slip motion, out of plane separation and permanent gaps at the contact interface during a vibration cycle. An excitation force of 1–10 N was applied in location A and the response of the assembled beam was computed the
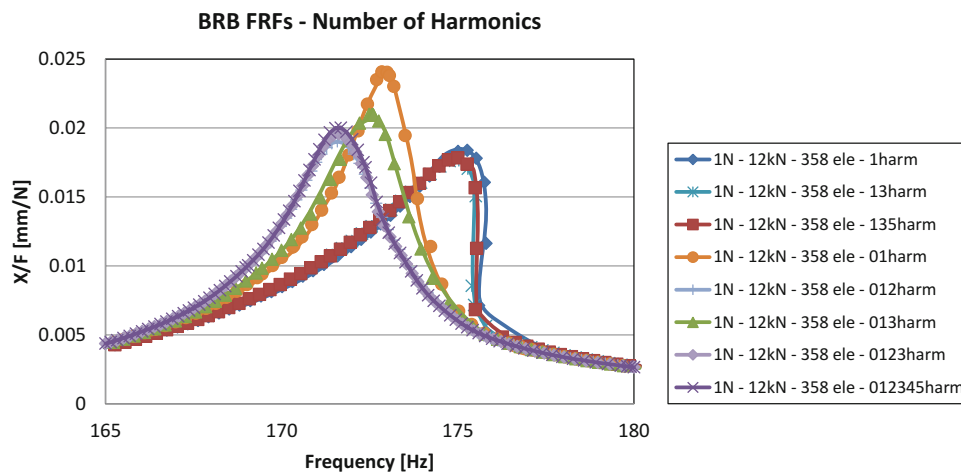
Fig. 6.3 Influence of number of harmonics on response of second bending mode

multi harmonic balance method (MHBM) for point B in Fig. 6.2a. A friction coefficient of, $\mu = 0.6$, and a tangential and normal contact stiffness, $k_t = k_n = 6kN/mm^3$, were used for the model, which led to a reasonable good agreement with previously measured data [10].

The analysis was focused on the 2nd bending mode, which had been identified as strongly nonlinear in previous tests. Initially the nonlinear frequency response function (FRF) for several model setups was calculated to ensure a reliable and converged model. A comparison of the FRFs in Fig. 6.2c between the 192 and 358 element mesh with the first harmonic included, showed a relatively similar frequency behaviour with stiffening, also the lower mesh density led to a stronger overhang, clearly not capturing the nonlinear mechanism correctly. Based on these findings the 358 element mesh was chosen for all further investigations.

In a next step the influence of the number of included harmonics was investigated (from 0–5), based on a 1 N excitation force. The harmonics are a particularly important parameter for the MHBM, since they determine the accuracy of the computation, but also significantly impact computational efficiency. Finding the right balance is therefore of uttermost importance. Figure 6.3 shows a significant sensitivity of the FRFs towards the even and uneven harmonics. The need to include the 0th harmonic was somewhat surprising, indicating the reaching of a new static equilibrium position of the flange joint during a vibration cycle, which led to a more linear response characteristic which were in good agreement with the results from the literature [10].

Based on this initial investigation it was decided to use 358 nonlinear elements at the interface, and include 0–3 harmonics in the analysis to capture the response accurately. This rather large nonlinear model required a significant amount of computational power for a converged solution and the number of computations had therefore be kept to a minimum for the following investigations.

6.3 Nominal Nonlinear Response

After identifying the best model, the nonlinear dynamic behaviour of the nominal lap joint with 12kN bolt preload was computed for 1, 10, and 100 N excitation force. The resulting FRFs in Fig. 6.4a show a significant dependence on the forcing level, indicating a strong nonlinear behaviour at the interface. A significant softening of the structure, together with a halving of the amplitude can be observed. Figure 6.4b, c show the energy dissipation and contact condition in the lap joint for the three forcing levels, where it can be seen that most of the energy is being dissipated at the transition from the outer bolt pressure cone to the very lightly loaded edges of the joint, with no apparent motion between the bolts. As the excitations levels increase the sliding zone is moving inwards and getting bigger, leading to an increased energy dissipation and a reduction in joint stiffness due to less stick. An additional dissipation zone right at the edges appears at very high response amplitudes, when the free edges are in contact during a significant amount of time during a vibration cycle.
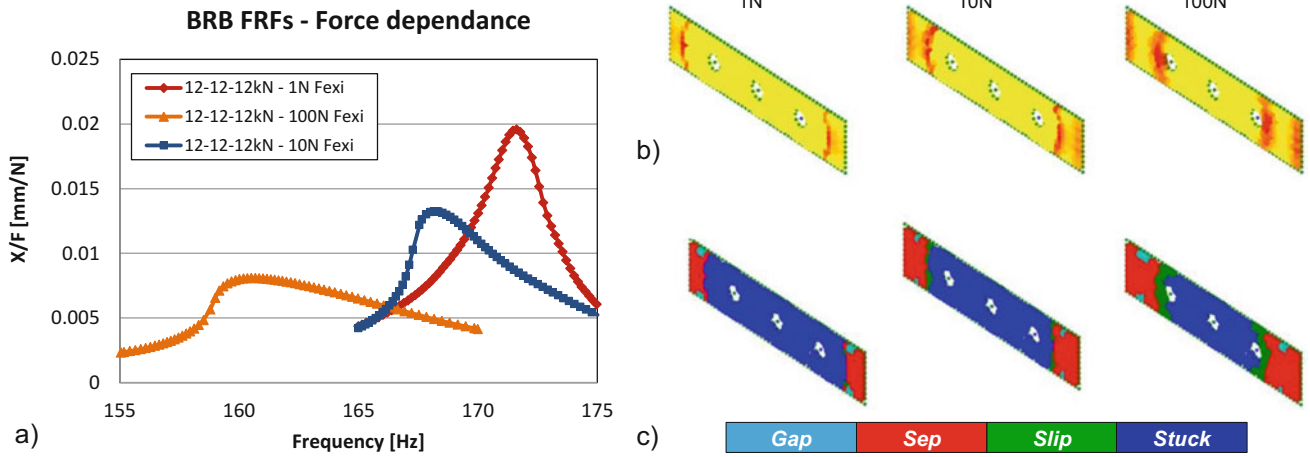
Fig. 6.4 Nominal model at 1, 10 and 100 N excitation (**a**) frequency response, (**b**) energy dissipation and (**c**) contact conditions
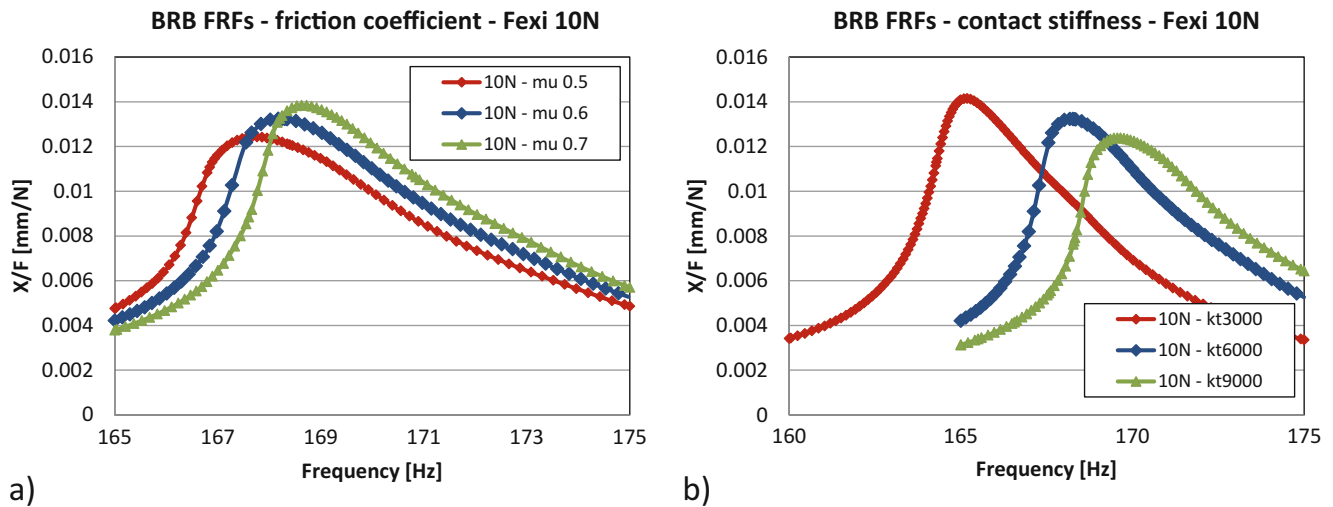
Fig. 6.5 Influence of input parameters on FRF (**a**) friction coefficient and (**b**) tangential and normal contact stiffness

6.4 Friction Input Parameters

The type and accuracy of the manufacture of the joint interface will determine the experienced contact stiffness and friction coefficient of the joint interface. Assuming that these values are strongly dependent on the interaction of the asperities on the interface, the machining process itself, but also the local orientation during assembly may play a significant role on the final friction parameters. To gain an understanding how strongly tangential and normal contact stiffness and friction coefficient influence the dynamics of the investigated lap joint, both values were varied around their nominal value.

Figure 6.5a shows the dependency of the response of the lap joint to a variation of the friction coefficient, μ, ranging from 0.5 to 0.7. The 10 N excitation test case was thereby chosen for the study, since the results from the previous section showed a strong nonlinear behaviour. A very small frequency reduction of 0.5% at the lowest friction coefficient could be observed, together with a 10% drop in amplitude due to the increased dissipation in the joint.

The tangential and normal contact stiffness, k_t and k_n, were jointly varied, from 3000-9000 N/mm^3 and the resulting FRFs can be seen in Fig. 6.5b. A frequency drop of 2.6% over the investigated range was observed, which can be attributed to the lower stiffness in the joint, coupled with an increase in amplitude of 13% due to the larger flexibility at the interface and a resulting reduction in damping.

It can be seen that the friction parameters at the interface can change the dynamic response of the lap joint, also the real variation in these parameters due to the assembly of the joint is yet unknown, and only a rough idea of their significance on the joint variability can be provided at this point.

6.5   Bolt Load

A major source of uncertainty when assembling and re-assembling a bolted joint is the applied torque in the bolt. Often a torque range will be used for that purpose, and depending on its accuracy, the contact condition in the bolt treat, and the alignment of the bolt itself, variations in the preload of the bolt can occur. In order to understand the sensitivity of the FRF to a variation in the bolt load, the nominal 12kN preload was reduced in steps down to 0 N to represent the loosening of the bolt. For each now bolt load the static FE analysis was repeated, with an adjusted temperature loading from Eq. (6.1). Two different configurations were investigated, one where the outer two bolt loads were reduced at the same time, and a second one where the central bolt of the joint was unloaded.

Figure 6.6a shows the FRFs for the loss of loading in the outer two bolts for a 1 N excitation force. A reduction of 2kN does not lead to any significant change in frequency or amplitude, but once the bolt preload is halved, more damping is present in the system. Any further loss in preload leads to an increase in damping and a loss of stiffness in the joint, until the fully unloaded case shows more than 15% frequency shift. This behaviour can be explained by a decrease of the stuck zone around the outer two bolts from Fig. 6.4b due to less loading, leading to a softening of the system and an increase in the energy dissipation due to the now larger sliding zone.

A variation of the inner bolt load (see Fig. 6.6b), has no influence on the dynamic behaviour of the beam. This indicates that the central part of the joint stays linear during a vibration at 1 N excitation force, even if the entire bolt load has been removed, suggesting that the central bolt plays no role in the dynamic response and it is redundant from a dynamics point of view.

To better understand the impact of the loss of preload on the forcing levels, the 2 kN loss cases (outer and inner bolts) were recomputed for 10 and 100 N excitation force. The results in Fig. 6.7 indicate, that at higher excitation amplitudes
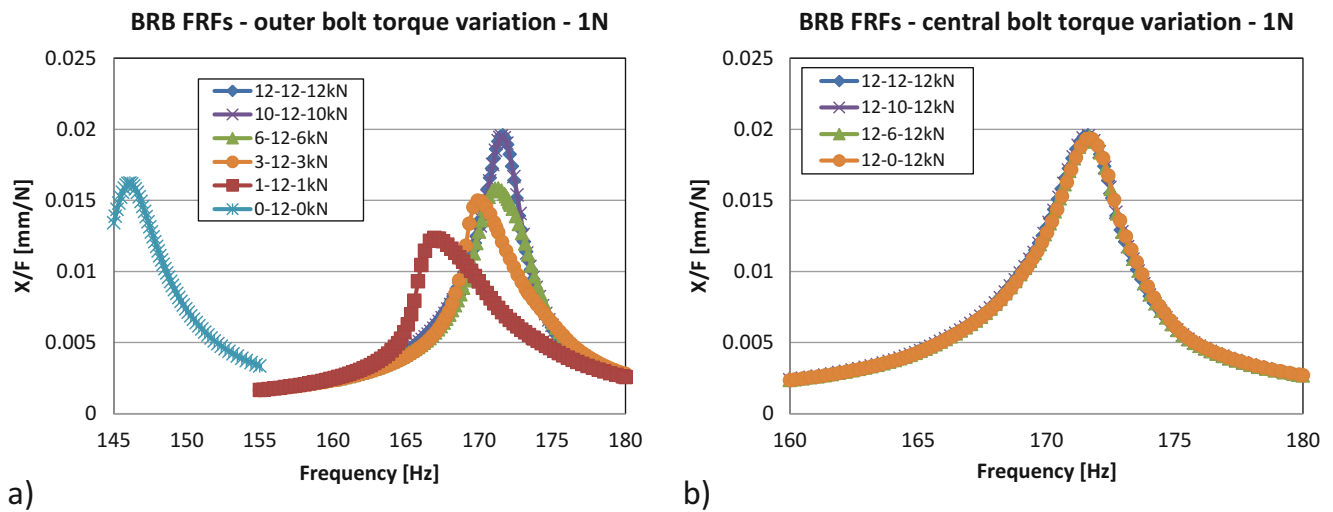

Fig. 6.6 Influence of bolt torque on the FRF (**a**) outer two bolts and (**b**) central bolt
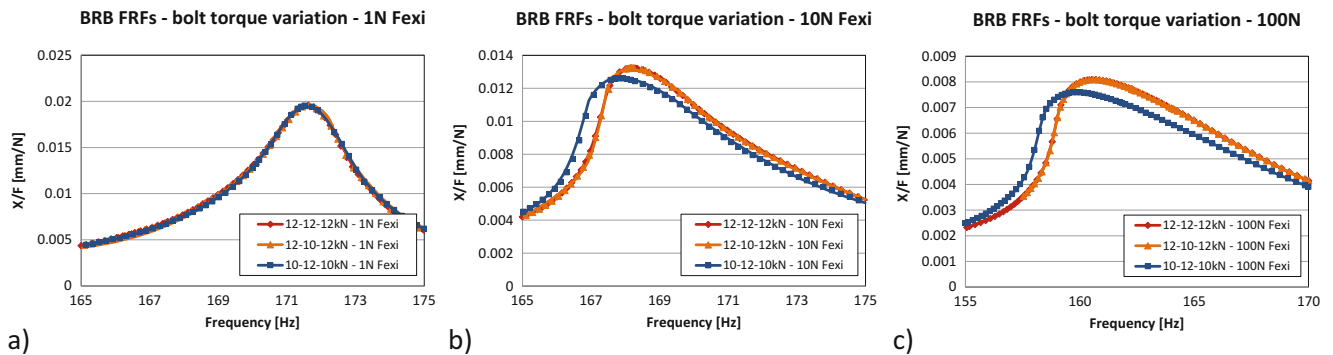
Fig. 6.7 Bolt torque sensitivity for (**a**) 1 N, (**b**) 10 N and (**c**) 100 N excitation force

(b and c) even a small loss of bolt torque on the outer two bolts leads to a little more dissipation in the joint and some minor softening, whereas the inner bolt still does not play any role and can be omitted from the design, at least from a dynamics point of view.

The effect of a variation in the bolt pre-load on the nonlinear dynamic response strongly depends on the amount of loss, the location of loss, and the excitation amplitude. The latter has thereby a relatively small effect, whereas the loss of preload close to the main dissipation area outside the outer bolts shows the larges impact.

6.6 Interface Curvature

Obtaining a perfectly flat surface at the joint interface during manufacture can be a challenging task, since the drilling of the holes and the surface finishing may lead to thermal stresses that can cause a slightly concave or convex shape, adding uncertainty to the joint response. To investigate the effect of such a geometric distortion on the FRFs, a series of artificial pressure distribution was generated. It was assumed that a concave shape would lead to more loading at the edges of the interface, and a convex shape would lead to a gap in the same location. Based on this assumption an exponential pressure distribution

$$P = ae^{-0.1x} + ae^{0.1x} \tag{6.2}$$

was selected, which resulted in an increase off pressure, or a generation of negative pressure (equivalent to a gap definition) at the free edges of the joint. The resulting pressure field, P, was then added to the existing pressure distribution, and the total loading was then rebalanced to transmit the correct total load generated by the bolts. A light change in loading ($a = \pm 0.01$) at the edges and a strong increase at ($a = \pm 0.09$) were investigated, leading to the updated concave and convex pressure fields in Fig. 6.8a–c. Note the strong negative pressure in Fig. 6.8c indicating an initial gap at the edges for the convex shape, which leads to an increased pressure underneath the bolts to balance the forces. In contrast for the concave shape an unloading of the bolt area in Fig. 6.8b can be observed.

Figure 6.9a shows the resulting FRFs for the nominal, lightly and strongly concave shape at three different excitation levels. A strong variation between the different configurations can be observed, which is not that surprising, given the nature of the underlying nonlinear mechanism. Even a slight redistribution of the pressure towards the edges leads to a frequency increase of nearly 20 Hz when compared to the nominal case. For the lightly concave case ($a = 0.01$) an increase in excitation force to 10 N activates the nonlinearity once more whereas for the strongly concave distribution only the 100 N case leads to significant slip. The convex interface shape in Fig. 6.9b for an excitation force of 10 N shows a significant softening and a loss in damping, which is particularly pronounced for the strongly convex shape.

Figure 6.10 shows the energy dissipation and contact conditions for the lightly and strongly curved concave and convex interfaces at 10 N excitation. The concave interface in Fig. 6.10a, b pushes the sliding zone away from the bolts towards the edges, thereby increasing the stuck surface area with a resulting increase in contact stiffness, and a reduction in the energy dissipation. In the extreme case of the strongly concave shape, nearly no sliding zone is left, and the FRF becomes more or less linear. In contrast the convex shape in Fig. 6.10c, d tends to force the outer edges apart, pushing the energy dissipation
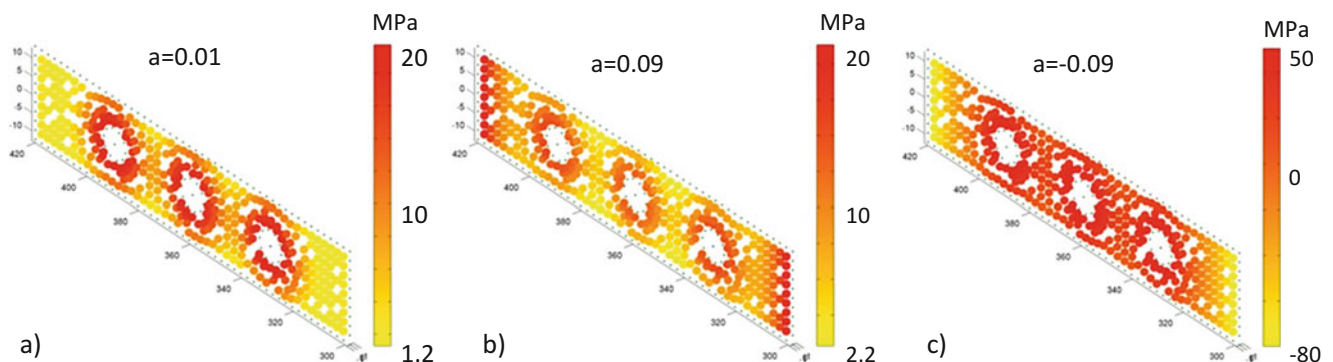
Fig. 6.8 Modified interface pressure distribution for (**a**) lightly concave, (**b**) strongly concave, and (**c**) strongly convex shape
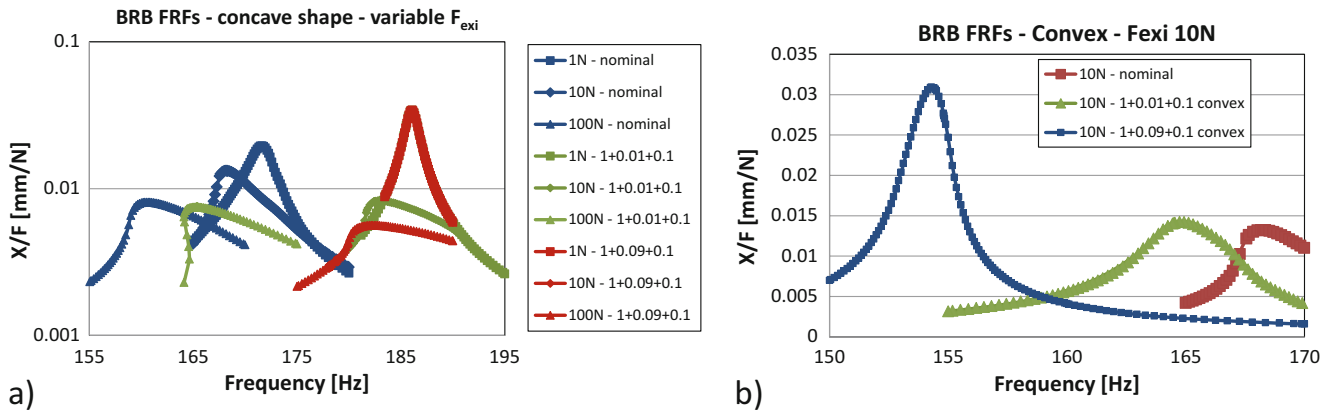
Fig. 6.9 Response characteristic for (**a**) concave interface shapes at different excitation forces and (**b**) convex shape at 10 N excitation
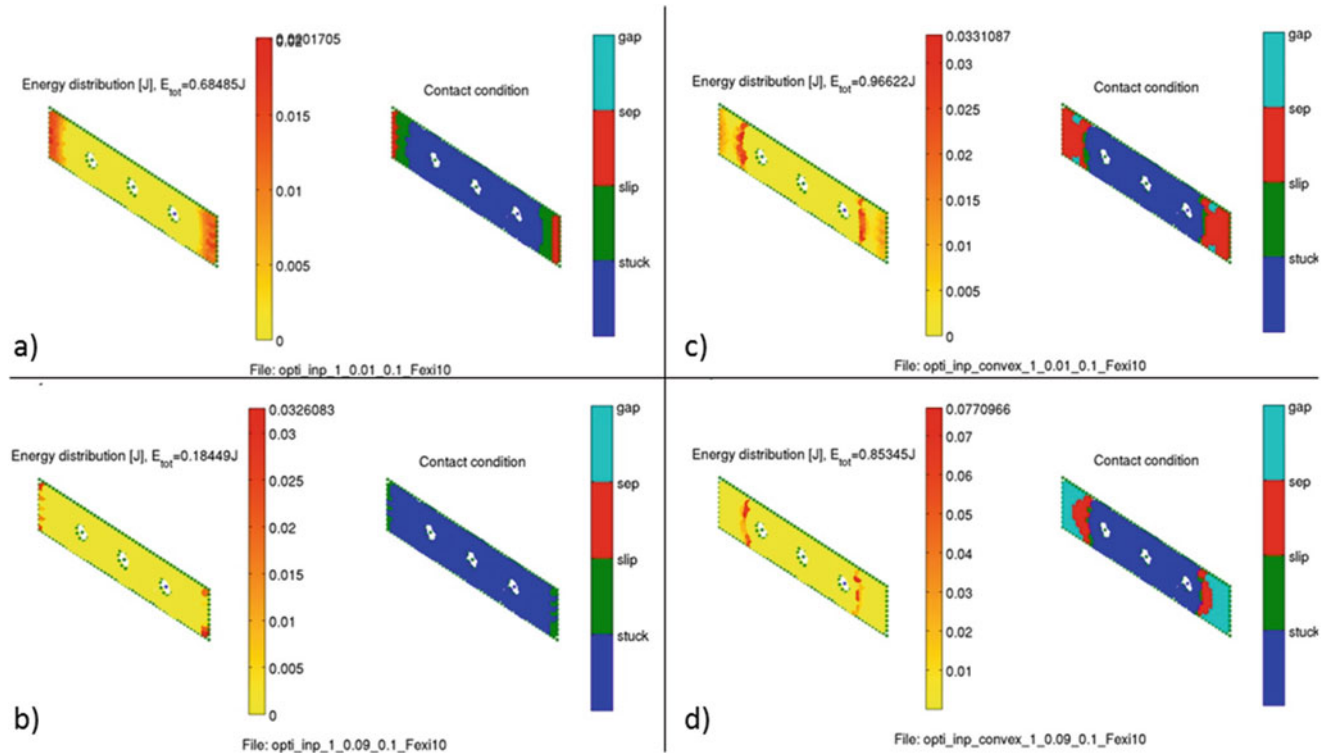
Fig. 6.10 Energy dissipation and contact condition for (**a**) light concave, (**b**) strong concave, (**c**) light convex and (**d**) strong convex pressure distribution

closer to the bolts. Since the bolt load is still sufficient to keep the contact zone underneath the bolts stuck, the result is a reduction in energy dissipation and a loss in contact stiffness, leading to the FRF behaviour in Fig. 6.9b.

6.7 Discussion

The presented results show, that the interface contact conditions, the bolt preload and the contact geometry all have an effect on the nonlinear dynamic response of the second bending mode of the beam. The nonlinear effects are localised around the free edges of the flange, with the area underneath the bolts not contributing to the nonlinear response. Any uncertainty in the dynamic response can therefore be attributed to the outer contact zones.

Changing the input parameters to simulate a slightly different alignment of the interface asperities leads to less than 5% frequency shift but can change the response amplitude by more than 10%, making them a potential source of uncertainty in the system.

A significant loss in the outer two bolt preloads would be required to reach frequency shifts similar to the friction input parameters, but even a small amount of preload loss will lead to an amplitude reduction of 25%. An increase in damping due to the joint can be considered an advantage, but it comes at the cost of a loss in static stiffness. Even the total loss of the central bolt does not affect the dynamics of the system, highlighting an overdesigned of the flange from a dynamics point of view (for the 2nd bending mode).

The largest variation on the nonlinear dynamic behaviour of the system came from a simulated change in the interface geometry. The concave shapes increased the frequency by up to 10% whereas the convex shape led to a similar frequency drop. Strong concave and convex shapes tended to reduce the damping and linearise the response since they either let to a total locking of the contact, or reduced the sliding area due to the presence of permanent gaps.

6.8 Conclusions

Understanding the potential source of uncertainty in the nonlinear response of a lap joint is very important, to decrease the variability in the response of a jointed structure. A simple lap joint with three bolts was investigated in this study, to identify the underling nonlinear mechanism and understand the sensitivity of the dynamic response to variations in the friction parameters, bolt load, and interface geometry.

It was found that all the nonlinearity during a vibration cycle originated from the area between the outer bolts and the edges of the flange, mainly caused by two sliding zones at the edge of the pressure cone and enhanced by some additional dissipation close to the edges. This nonlinear mechanism led to a significant softening and damping at higher amplitudes.

The assumed change in the friction input parameters (μ and k_t) led to a small change in the response behaviour, with the contact stiffness showing a larger effect on the frequencies. A loss of the central bolt preload had no effect on the nonlinear dynamic response, whereas a reduction of the outer bolt loads led to quite significant changes in the response. The modified interface geometry (simulated by a change in contact pressure) from a flat to a concave or convex shape had the largest impact on the frequency response, with very high levels leading to a linearisation of the system.

The lap joint response depends on all three investigated parameters, but is most sensitive to the interface geometry, which in the future may be used to optimise the response towards the requirements of the structure (linearisation, more damping, . . .).

References

1. Panning, L., Sextro, W., Popp, K.: Optimization of interblade friction damper design. In: Proceedings of ASME TURBOEXPO, pp. 1–8 (2000)
2. Szwedowicz, J., Gibert, C., Sommer, T.P., Kellerer, R.: Numerical and experimental damping assessment of a thin-walled friction damper in the rotating set-up with high pressure turbine blades. J. Eng. Gas Turb. Power. **130**(1). doi:10.1115/1.2771240
3. Schwingshackl, C.W., Petrov, E.P., Ewins, D.J.: Effects of contact interface parameters on vibration of turbine bladed disks with underplatform dampers. J. Eng. Gas Turb. Power. **134**(3), (2012) pg. 032507 1–8
4. Schwingshackl, C.W., Di Maio, D., Sever, I., Green, J.S.: Modelling and validation of the nonlinear dynamic behaviour of bolted flange joints. J. Eng. Gas Turb. Power. **135**(12), (2013) pg. 122504 1–8
5. Smith, S., Bilbao-Ludena, J.C., Catalfamo, S., Brake, M.R.W., Reuß, P., Schwingshackl, C.W.: The effects of boundary conditions, measurement techniques, and excitation type on measurements of the properties of mechanical joints. In: Proceedings of the International Modal Analysis Conference XXXIII, Orlando, FL, 2015
6. Salles, L., Swacek, C., Lacayo, R.M., Reuss, P., Brake, M.R.W., Schwingshackl, C.W.: Numerical round robin for prediction of dissipation in lap joints. In: Proceedings of the International Modal Analysis Conference XXXIII, Orlando, FL, 2015
7. Gross, J., Armand, J., Lacayo, R.M., Reuss, P., Salles, L., Schwingshackl, C.W., Brake, M.R.W., Kuether, R.J.: A numerical round robin for the prediction of the dynamics of jointed structures. In: Proceedings of the International Modal Analysis Conference XXXIV, Orlando, FL, 2016
8. Petrov, E.P., Ewins, D.J.: Generic friction models for time-domain vibration analysis of bladed disks. ASME J. Turbomach. **126**(1), 184–192 (2004)

9. Petrov, E.P., Ewins, D.J.: Analytical formulation of friction interface elements for analysis of nonlinear multiharmonic vibrations of bladed discs. ASME J. Turbomach. **125**(2), 364–371 (2003)
10. Catalfamo, S., Smith, S.A., Morlock, F., Brake, M.R.W., Reuss, P., Schwingshackl, C.W., Zhu, W.D.: Effects of experimental methods on the measurements of a nonlinear structure. In: Proceedings of the International Modal Analysis Conference XXXIV, Orlando, FL, 2016

Chapter 7
Effect of Far-Field Structure on Joint Properties

S.B. Cooper, M. Rosatello, A.T. Mathis, K. Johnson, M.R.W. Brake, Matthew S. Allen, A.A. Ferri, D.R. Roettgen, B.R. Pacini, and Randall L. Mayes

Abstract Classical structural analysis techniques have proven time and time again to be remarkably accurate for systems consisting of a single, continuous piece of material. Unfortunately, nearly all real engineering structures are assembled from multiple parts, joined by bolts, rivets, or other fasteners, and these joints introduce nonlinearities and uncertainties into systems' structural stiffness and damping. Nonlinear damping due to jointed connections in particular is critical to limiting the resonant response of a structure, yet it remains poorly understood. This work seeks to understand the degree to which joint properties are dependent on the rest of the structure. The testable hypothesis is that the boundary conditions and the far-field structure itself (i.e. distribution of the stiffness and mass) change the way in which the interface is loaded, thus altering the perceived or deduced nonlinear properties of the mechanical joint. This hypothesis is investigated using experimental impact hammer testing methods in order to understand the extent to which alteration in the boundary conditions and far-field structure change the interface properties as well as the underlying mechanics during loading. Numerical tools are also employed to investigate and complement the experimental results, focusing on two fronts: replicating the experimental results with discrete joint models, and investigating joint loading for different modes using numerical modal analysis.

Keywords Jointed structures • Nonlinear stiffness • Nonlinear damping • Hilbert transform and Impact modal test

S.B. Cooper (✉)
Department of Mechanical Engineering, University of Bristol, Bristol, UK
e-mail: sc14784@bristol.ac.uk

M. Rosatello
Laboratoire Quartz – EA 7393, SUPMECA, Saint-Ouen, France

A.T. Mathis
Department of Mechanical Engineering, University of Akron, 44325, Akron, OH, USA

K. Johnson
University of New Mexico, 87131, Albuquerque, NM, USA

Sandia National Laboratories, 87123, Albuquerque, NM, USA

M.R.W. Brake
Sandia National Laboratories, Albuquerque, NM, USA

William Marsh Rice University, Houston, TX, USA

M.S. Allen • D.R. Roettgen
Department of Engineering Physics, University of Wisconsin, Madison, WI 53706, USA

A.A. Ferri
Department of Mechanical Engineering, Georgia Tech, 30332, Atalanta, GA, USA

B.R. Pacini
Sandia National Laboratories, PO Box 5800, 87185, Albuquerque, NM, USA

R.L. Mayes
Structural Dynamics Department, Sandia National Laboratories, P.O. Box 5800 – MS0557, Albuquerque, NM 87185, USA

7.1 Introduction

Most real-world structures do not consist of a single piece of engineering material; instead, they are built-up structures containing several individual pieces constrained by mechanical connections. Despite their prevalent use, distributed contact connections such as joints, have long been difficult to characterize and model due to their nonlinear, stochastic nature. To compound matters, estimation of damping due to friction in mechanicals joints is often extremely important in high-performance applications such aerospace. As a result, many works have studied mechanical joints using analytical, numerical, and experimental methods in an effort to derive quantitative descriptions for these complex engineering systems.

Perhaps one of the most well-known works in the academic community is that of Segalman [9], where he proposes and derives a physically-based joint model using discrete arrangements of Jenkins elements, with the arrangements sometimes called Iwan elements in this context. His so-called four-parameter Iwan element is oft cited and utilized by the joints research community, as it has demonstrated the ability to qualitatively and quantitatively match certain experimental data. Roettgen et al. [8] demonstrated this for the first few modes of an automotive exhaust structure, and Allen et al. [1] developed a quasi-static approach so these types of models can be extracted more efficiently from computational models. Other reduced-order models are proposed by authors such as Quinn [7], which utilize continuum representations of both the monolithic structure and joint to derive computationally inexpensive models. Relatedly, authors have also explored the presence, or absence, of energy transfer through mode coupling, an important physical phenomenon when discussing joint characterization [4, 8]. Regardless of method or characterization technique, the literature recognizes that energy dissipation versus forcing amplitude in these systems is generally governed by a power-law, with hysteresis playing an important role.

Each of these modeling and characterization approaches has its own set of advantages and limitations; however, these works all, cumulatively focus on describing the joint itself with less regard for the surrounding, or far-field, structure. Comparatively little work has been done to assess the impact that the individual components of the built-up structure have on the nonlinear characteristics of the joint. Put another way, there is opportunity to explore the degree to which a joint's excitation, or activation, is affected by the far-field structure in a built-up system. To address that question, this work utilizes experimental methods, data-processing techniques, and numerical simulations that are current to the literature in order to characterize the nonlinear properties of nominally identical joints in structures with different far-fields.

For the experimental portion of this work, several structures with nominally identical joints and different far-field structures were excited using impact hammer testing, and the responses of those structures were identified and characterized using the aforementioned methods currently available in the literature. The basic structure of interest to this work is the Brake-Reuß Beam (BRB), and to address the effect of the far-field structure, several variations of the structure were also created with the hope of altering the response while the joint setup remained constant. These variations include an elongated BRB (LBRB) as well as a stiffness modified BRB (SBRB); details and diagrams of these structures are given in Sect. 7.2.1. This beam-structure was chosen due to the plethora of data available for comparison and its consistent use by authors in the field [2]. For the nonlinear characterization, the Hilbert transform method outlined in Kerschen's work [5] and using the smoothing process described in Roettgen et al. [8] was employed. These modal results are drastically different among the different beams, but the experimental data alone does not give an understanding as to why these modal results are so different.

To complement the experimental studies for this work, numerical methods were also employed in order to better understand the underlying physics of the system. A finite element model using discrete, physical four-parameter Iwan elements was generated and tuned to match the experimental nonlinear, modal damping and natural frequency versus amplitude that were measured from the nominal structure (the classic Brake-Reuß beam) [1]. These same physical joint parameters were then used in a model for the LBRB and the numerical modal nonlinear characterizations match remarkably well. This result implies that, despite the structural modifications, the underlying representative joint properties remain identical.

7.2 Experimental Investigation

The core of this work is the experimental investigation of three different structures with nominally identical joints. First, the design of those structures is discussed, followed by the linear then nonlinear experimental analyses. The linear experimental analysis was designed to identify the appropriate modal filter for the nonlinear characterization, and further details of the characterization method are discussed. Experimental results are shown for the first several modes of the systems, with an emphasis on the lowest three bending modes.
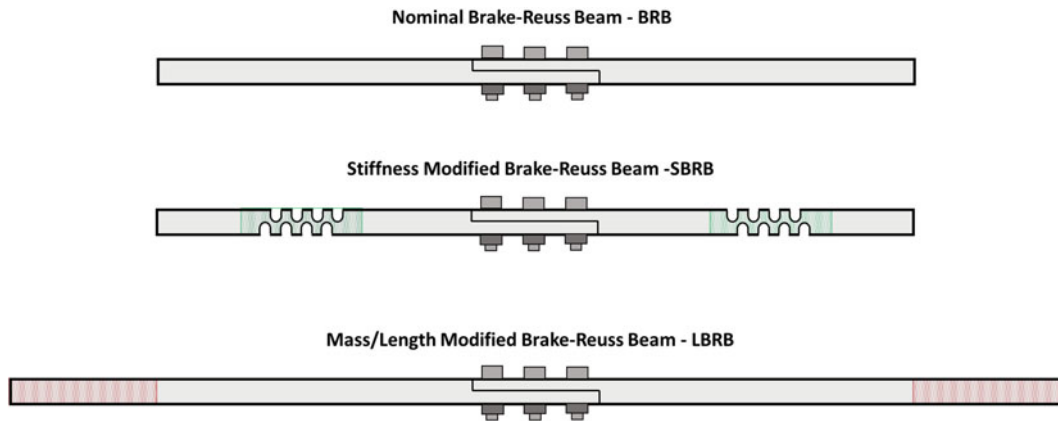
Fig. 7.1 The different beam assemblies

Table 7.1 Dimensions of tested beams

	L × H × W [mm]
BRB – nominal Brake Reus beam	720 × 25.4 × 25.4
SBRB – stiffness modified beam	720 × 25.4 × 25.4
LBRB – mass/length modified beam	1080 × 25.4 × 25.4
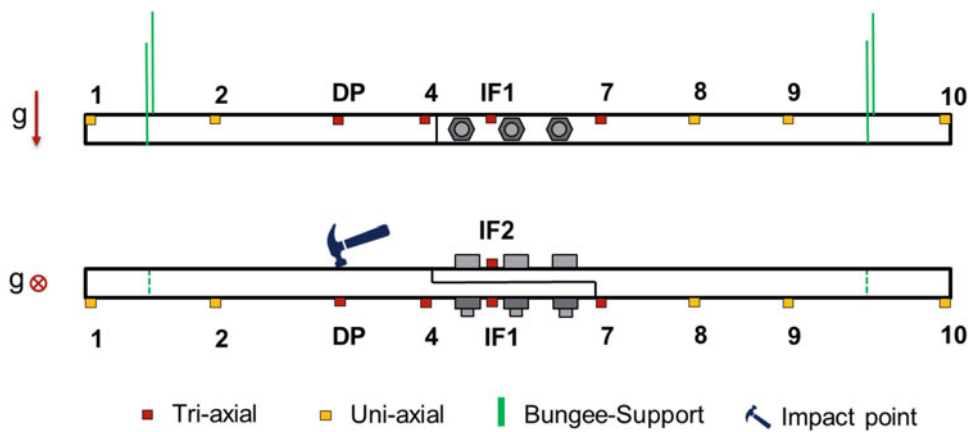
Fig. 7.2 Experimental setup

7.2.1 Experimental Setup

Three different structures were designed for this investigation in order to understand the effect of changing the geometrical properties around a mechanical joint. The first structure is known as the Brake-Reuss beam (BRB) (see [2]); it consists of two identical steel beams bolted together to form a lap-joint connection, assembled using three M8 bolts tightened to a torque of 20 Nm.

The second test structure is similar to the first lap-joint configuration, with the same bolts and torque, however each identical steel beam in this assembly has a spring shaped cut out for stiffness modification. The last test structure also consists of the same lap-joint configuration, but the length of the two parts is larger to provide mass/length modifications. Figure 7.1 shows the three tested beam assemblies configurations and Table 7.1 presents their dimensions. For simplicity, for each beam was assigned an acronym that will be used throughout this paper: BRB for the nominal Brake-Reuss Beam, LBRB for the mass/length modified beam and SBRB for the stiffness modified beam.

Figure 7.2 shows the experimental configuration for the BRB structure. The structure is supported by two bungee cords, and 10 accelerometers were distributed in a symmetrically proportional way on the beam. The chosen source of excitation is the impact hammer: this is commonly used in vibration testing, as it applies a broadband excitation signal to the test structure. The excited band spans within 0–3200 Hz to encompass as many modes as possible. The chosen impact point, or

Table 7.2 Natural frequencies and damping from linear modal analysis

	BRB		LBRB		SBRB	
MODE	f_n [Hz]	ζ (%)	f_n [Hz]	ζ (%)	f_n [Hz]	ζ (%)
1	168.3	0.24	80.5	0.17	92.1	0.12
2	584.3	0.16	291.6	0.05	194.6	0.05
3	1183.8	0.14	521.2	0.07	504.6	0.16
4	1618.3	0.20	857.9	0.19	958.9	0.09
5	1656.3	0.20	1142.9	0.11	1240.2	0.11
6	2825.9	0.15	1339.5	0.05	1623.7	0.16
7	3022.6	0.15	1583.6	0.23	2088.6	0.12
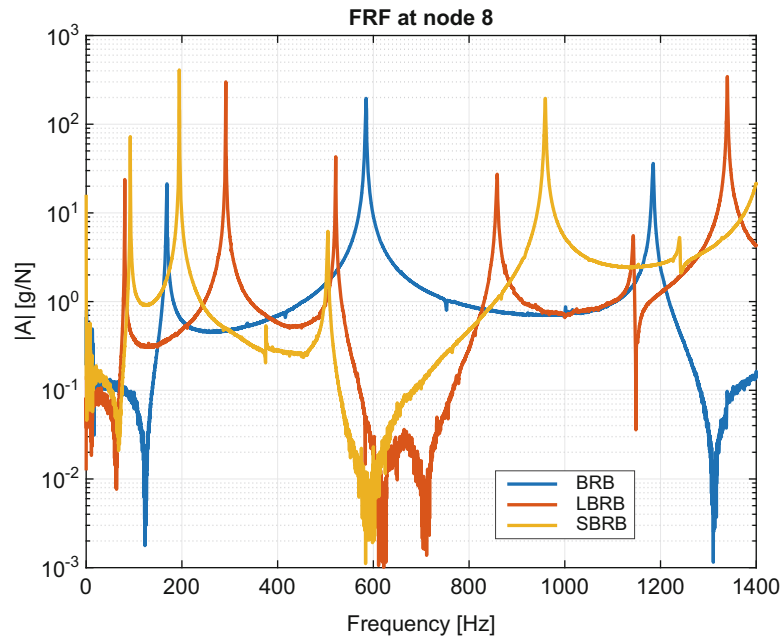
Fig. 7.3 FRF comparison at node 8

driving point (DP), is shown in Fig. 7.2. The SBRB was instrumented in the same way due to the fact that it has similar dimensions to the BRB; however because LBRB is longer than the other two, the accelerometers were attached at positions proportionally consistent with the other two systems. The data acquisition was performed using the Spectral Test module in LMS Test Lab 13.

7.2.2 Linear Experimental Analysis

In order to derive the modal filter used in the nonlinear characterization of these systems, a linear modal test was performed for all three configurations of the beam assemblies. A low level excitation test (F = 50N) was carried out for each beam. The linear natural frequencies and damping ratios were estimated from the frequency response functions (FRFs), using the frequency-domain subspace identification algorithm presented in [6]. Results are shown in Table 7.2. Figure 7.3 shows the FRFs obtained from node 8 of each beam in the range 0–1400 Hz. It is possible to observe that the responses of the three beams are very different between each other as a result of the far-field structure modifications. For example, the first bending mode of the BRB is at 168.3 Hz, for the LBRB is at 80.5 Hz, while for the SBRB is at 92.14 Hz. Furthermore, the steep resonance peaks of the FRFs indicates that the structure is lightly damped across the selected bandwidths. The authors have selected the first three bending modes for each beam assembly to be investigated further in this paper.

The mode shapes for the first three bending modes of interest are obtained from the linear modal analysis for each beam, and they are shown in Fig. 7.4. Comparing these mode shapes, it is clear that the far-field structure modifications have a large impact on the curvature of the linear modes, as expected. For all three modes, the LBRB appears to have a qualitatively similar overall shape to the original BRB. For the first mode, this can be identified more specifically by noting the generally
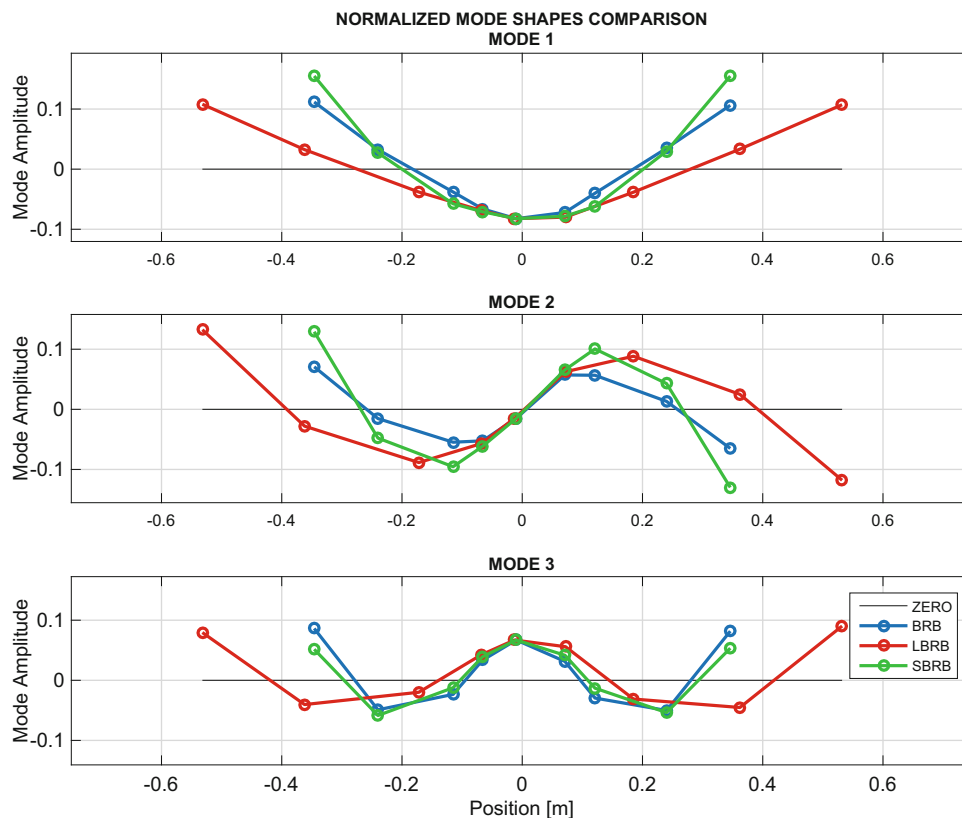
Fig. 7.4 Mode shapes for the three beams

larger radii of curvature in both the BRB and LBRB. By contrast, the SBRB mode shapes exhibit fundamental differences from the other two. Again, in the case of the first mode, the SBRB exhibits lower curvature near the joint area and higher curvature near the ends than the BRB and LBRB.

7.2.3   Nonlinear Experimental Analysis

After the linear modal analysis, the second type of investigation performed was a series of impact tests at increasing force levels in order to elicit nonlinear behavior in the different beams. Each beam was excited at the same impact point DP (see Fig. 7.2), and several impact excitation levels ranging from 50N to 750N were performed. This section details approximate nonlinear characterizations through peak-picking methods in order to illustrate the differences between the linear and nonlinear responses while Sect. 7.2.4 details a more rigorous analysis using the Hilbert Transform method.

7.2.3.1   Impact Test Characterization

Time response signals and frequency response functions (FRFs) were obtained from each test at each forcing level; Fig. 7.5a shows the time response at several excitation forces of the BRB at node 8. As an initial and simplified method to detect nonlinearities in the system, the collected FRFs at increasing impact forces were superposed and compared for each beam: Fig. 7.5b–d show the results of this process at node 8 for the first bending mode and for each beam.

The first observation that can be made is evident in Fig. 7.5a, where an absence of proportionality is noticed between the time responses at low (50N) and high (700N) excitation forces. This indicates the breakdown of superposition principle which serves as a cornerstone for linear theory. Beyond time series inspection, another meaningful method of detecting nonlinear behavior from measured data is the check for homogeneity in the frequency response functions over different excitation levels. In particular, Fig. 7.5b–d show a shift in the natural frequencies and response amplitude as the impact force increases. The characteristics observed from the extracted FRFs show that each beam assembly has a softening behavior within the
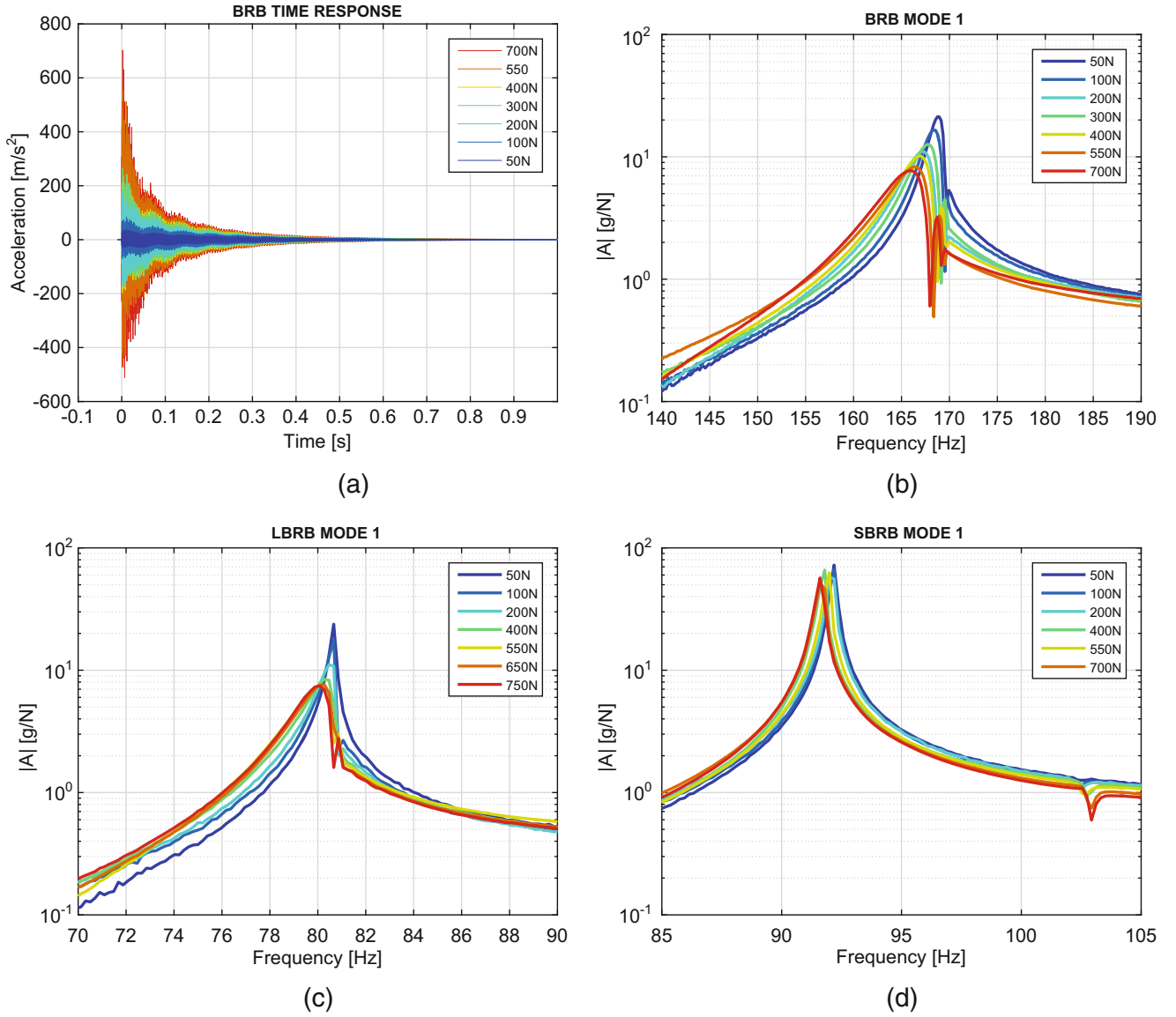
Fig. 7.5 (**a**) Time responses of the BRB at node 8 at different impact forces, and Mode 1 FRFs for (**b**) the BRB, (**c**) the LBRB, and (**d**) the SBRB

frequency range and the impact excitation levels, with the natural frequency decreasing as the impact force increases. For the first mode, for the BRB, LBRB and SBRB, frequency shifts, as estimated by the lcoation of the peak in the FRFs, between the lowest and highest impact force are respectively -2, -1.6 and -0.15%. Thus the BRB has the most nonlinear softening behaviour compared to the other beams.

7.2.3.2 Damping Shift Comparison

Since the amount of energy dissipated in the lap joint configuration depends on the amount of load it carries, it is important to measure and quantify the change in the damping and stiffness properties of the beam caused by the increase in load. In this section of the paper, the percentage shifts in natural frequency and damping ratio are used to quantify the changes in the properties of each beam. The frequency and damping shift are in a percentage form and they are obtained as,

$$f_s = \frac{|f_{min} - f_n|}{f_n} \cdot 100 \quad [\%], \qquad \zeta_s = \frac{|\zeta_{max} - \zeta_L|}{\zeta_L} \cdot 100 \quad [\%]. \tag{7.1}$$
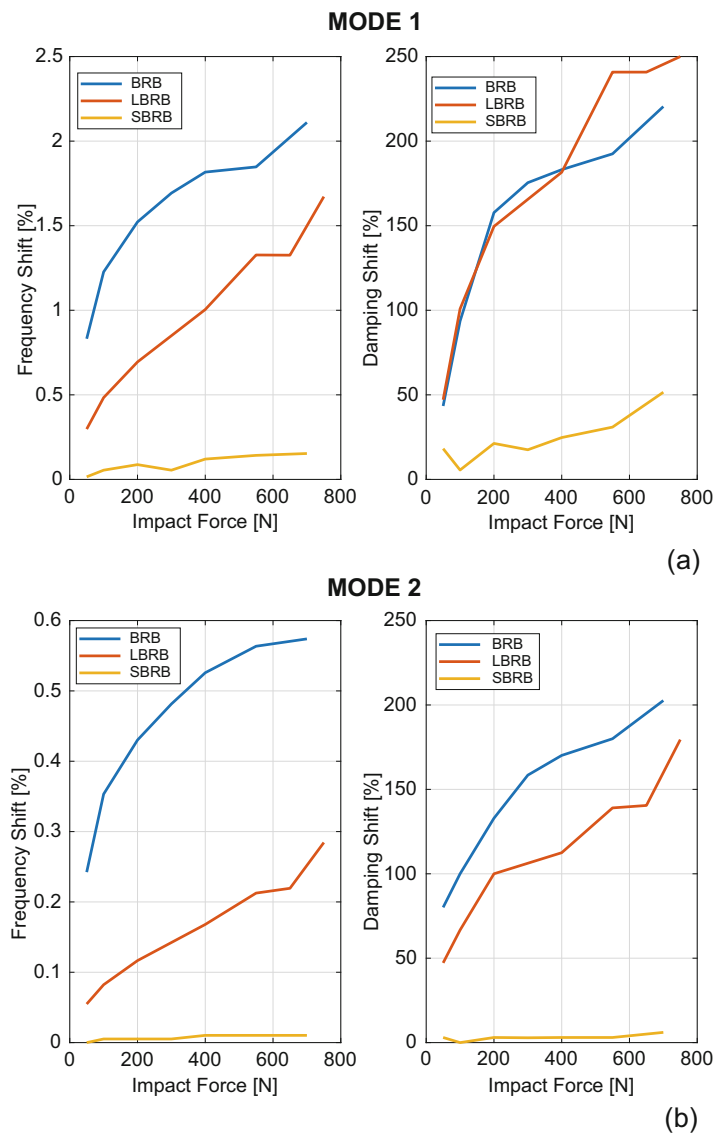
Fig. 7.6 Frequency and damping shift against impact force for Mode 1 (**a**) and Mode 2 (**b**)

The percentage frequency and damping shifts were calculated for the first three modes of each beam as the impact force changes: Fig. 7.6a, b present the frequency and damping percentage shift for all three beams against the impact force level for the first two bending modes. It can be noticed that, for the first mode, BRB shows a high shift in frequency compared to the other beams, while the LBRB shows a larger shift in the damping. Similarly, for the second mode, the shift in frequency and damping is larger for the BRB and LBRB. Turning to the SBRB, this has a very low shift in frequency and damping for the first mode and practically no shift for the second mode, as demonstrated by the constant straight line in Fig. 7.6b. From these observations it's possible to say that the BRB and LBRB structures experience the highest level of nonlinearity as a result of the increase in impact load, while the SBRB shows little or no nonlinear behavior for both modes.

In Fig. 7.7a, b, the frequency and damping shifts for the first three modes are compared against each other for the BRB and LBRB. It can be noticed that, for both beams, the frequency shift experienced by the first mode is significantly higher than the other two modes. The frequency shift for the first mode of the BRB lies between 0.8 and 2.1% while the frequency shifts for the second and third modes fall within 0.2 and 0.5%, hence the shift observed in the first mode is a factor of 4 higher than the shift observed in the other modes. A similar behavior was also observed in the LBRB configuration where the frequency shift for the first mode lies within 0.38 and 1.63%, while the shift experienced by the other modes are within 0.1 and 0.35%. Again, the first mode has a frequency shift of a factor of 4 higher than the other modes. One of the reasons for very high frequency shift observed for the first mode of both beams might be the method used to excite the beams during

BRB
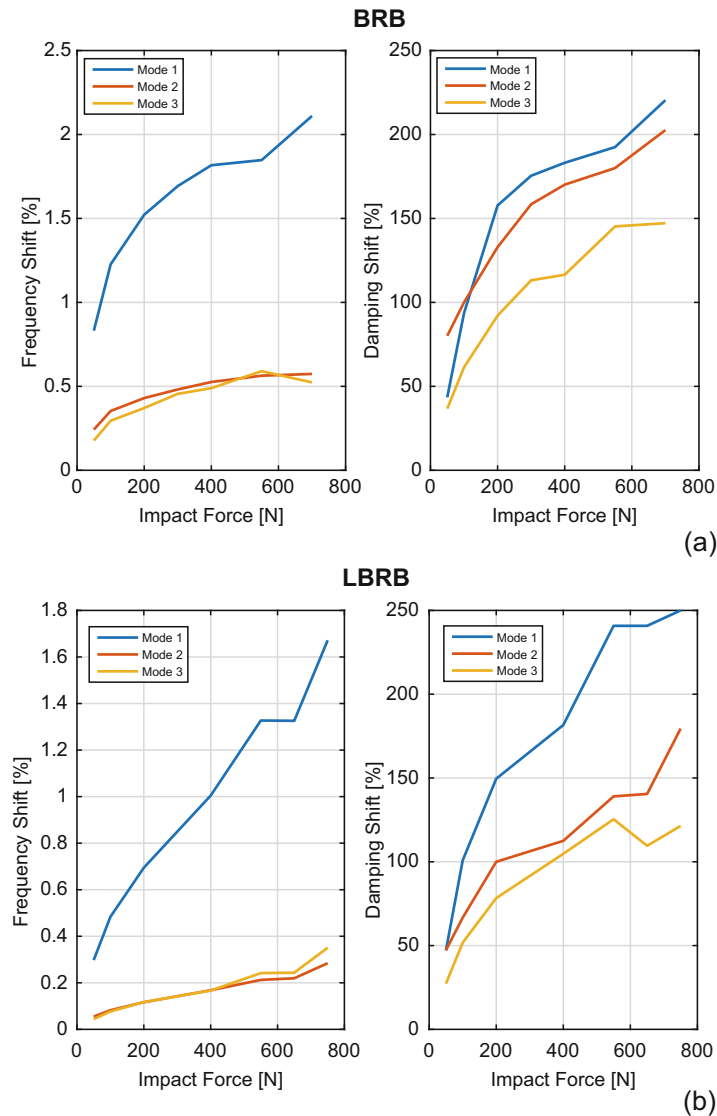
LBRB

Fig. 7.7 Frequency and damping shift against impact force for BRB (**a**) and LBRB (**b**)

the test, since the energy transferred by the impact hammer to the test structure is not always constant and it can quickly fade out without activating each mode of the structure equally. Hence the higher frequency shift observed on the first mode of each beam can be associated to this effect. However, a different behavior is observed in the damping shift for both beam configurations: in Fig. 7.7a the percentage damping shift for the first two modes are approximately within the same range, while it is slightly lower for mode three. In Fig. 7.7b, for the LBRB, it's possible to see the same behavior, only this time the damping shift is higher for the first mode, while it lies almost on the same range for the other modes. The increase in damping shift with the increase in impact force confirms the high level of nonlinear damping in both beams. The results show the typical behavior found in jointed structures, where the damping nonlinearity can be very high concurrently with a limited frequency nonlinearity.

7.2.4 Nonlinear Characterization Using Hilbert Transform

In order to develop a nonlinear characterization for each beam assembly, a three-step procedure was carried out to identify the frequency and damping behavior at several excitation levels. The first step was a homogeneity check on the FRFs at different excitation levels to detect potential nonlinearities. The second step was a transformation of measured physical
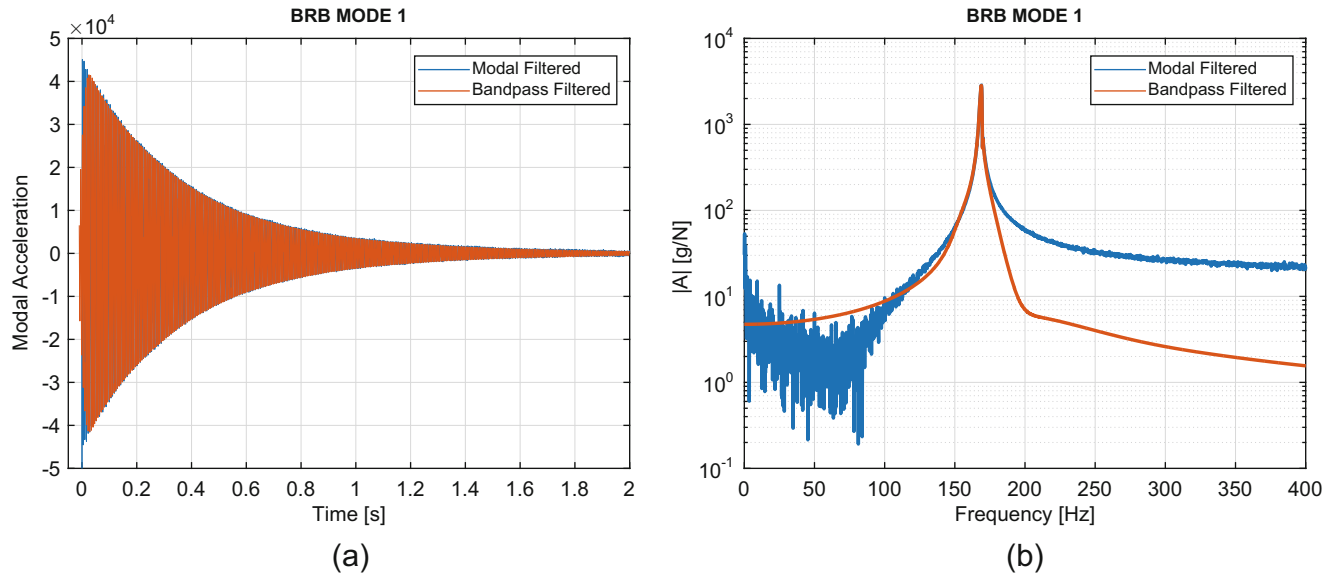
Fig. 7.8 BRB modal filtered and bandpass filtered signal comparison in (**a**) time and (**b**) frequency

data into modal coordinates, performed by applying first a modal filter and then a bandpass one, in order to isolate the contribution of a single mode. The third step consisted of the nonlinear identification and characterization of nonlinearities using the Hilbert Transform (HT). The HT method was used to deduce frequency and damping ratio trends against modal displacement amplitude (see [3–8]).

7.2.4.1 Data Filtering

Prior to the nonlinear characterization of the beams, each measured data was modally filtered, i.e. the data were transformed from physical coordinates into modal coordinates. The modal filter was performed using the physical time series data and the mode shapes matrix obtained previously from the linear modal analysis. After the application of the modal filter, a bandpass filter with an order specified between 4 and 8 was performed on each selected mode of each beam, in order to isolate a single mode in the response. An example of a transformed response after the modal and bandpass filters for the first mode of the BRB is presented in Fig. 7.8, respectively in the time (Fig. 7.8a) and frequency (Fig. 7.8b), domains. Modally filtered data was used for the BRB characterization; however, for the LBRB and the SBRB, the bandpass filter performed better, hence it was used in the characterization section.

7.2.4.2 Nonlinear Characterization

The next step in the experimental investigation was to quantify the change in natural frequency and damping with amplitude. First the Hilbert Transform was applied to the previously obtained modal acceleration data for several modes of each beam system. Then, a 4th order spline fit was applied to the Hilbert amplitude and phase over a selected time window, in order to get the instantaneous damping and frequency, respectively (see [3, 8]). The spline fit serves as a smoothing mechanism in order to estimate the instantaneous damping and frequency; however, because the Hilbert Transform is susceptible to noise at the extremes of the fit, the time window must be carefully selected. Figure 7.9 shows how well the blue filtered modal acceleration is reproduced by the green reconstructed time signal from the fitted Hilbert Transform for the first bending mode of the BRB. The modal velocity and displacement amplitudes V_{fit} and X_{fit} were calculated as,

$$V_{fit} = \frac{A_{fit}}{\omega_{d,fit}}, \qquad X_{fit} = \frac{A_{fit}}{\omega_{d,fit}^2}, \qquad (7.2)$$

where A_{fit} and $\omega_{d,fit}$ are the modal acceleration amplitude fit and the instantaneous damped natural frequency obtained from the Hilbert Transform spline fit, respectively.
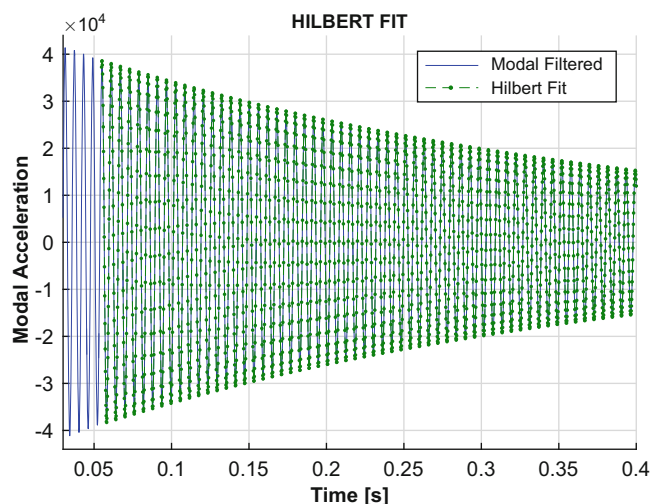
Fig. 7.9 Bandpass filtered modal acceleration and Hilbert fit – BRB Mode 1

Figure 7.10 shows the instantaneous frequency and damping curves against modal displacement amplitude X_{fit} for the first bending mode of the three beams. All three beams show the same softening behavior, with higher impact forces generating higher frequency shifts. The damping behavior exhibited by all three beams shows a power-law relationship, which is dependent on the excitation amplitude. The same analysis was repeated for the second and third modes, for which the damping curves showed the same increasing trend. For mode 3, the Hilbert transform only produced useful results over a range of small amplitudes; however a similar power-law relationship was observed. It is important to point out the fact that the impact point DP is very close to a node of the third mode, especially for the SBRB. As a result of this, the third mode may not have been properly excited and results for this specific mode may be inaccurate.

Comparing the results from the three beams, it is possible to say that the BRB and LBRB graphs show smooth curves and consistent trends at several impact forces, while for the SBRB, the curves are noisier and scattered. This can be due to the fact that, compared to the BRB and LBRB, SBRB shows smaller frequency and damping shifts and to the previously cited Hilbert Transform flaws. A summary of the observed nonlinearities for the three structures is given in Table 7.3; f_n and ζ_L are, respectively, the linear natural frequency and linear damping ratio measured from the flat parts of the frequency-amplitude and damping-amplitude plots, while $f_{n,min}$ and ζ_{max} are the minimum frequency and maximum damping ratio measured from the same plots at the highest impact force.

Further, comparing the damping curves for all three beams directly leads to some interesting conclusions regarding the effect of the far-field structure on the response. Figure 7.11 plots the damping curves for each of the three beams at all forcing levels for the first two bending modes, i.e. all of the nonlinear damping characterizations for the BRB are shown in blue, LBRB in red, SBRB in green. The key observation from these figures is that the three beams, each with a different far-field structure, have very different modal responses. In particular, while the BRB and LBRB exhibit the typical power-law nonlinearity that is consistent with literature, the SBRB shows a roughly linear response. While directly comparing the modal responses for these beams is useful and illuminating, one must keep in mind that the mode shapes for each of these beams are markedly different, as illustrated in Fig. 7.4. At first, this may seem to be an unfair comparison; however, the dependence of the modal response on the mode shape is explored later in the numerical section of this paper in order to draw meaningful conclusions regarding the root-cause of the experimental observations show here.

7.3 Numerical Investigation

From the experimental findings of this work, it is clear that different far-field structures elicit vastly different modal responses; however, this observation alone does not directly confirm or deny the hypothesis that altering the far-field structure changes the way in which the joint is excited or activated. In order to firmly and rigorously arrive at a scientific conclusion, one must "close the loop" by returning to the physical domain and identify a root cause for the experimental observation. The numerical study for this project does just that through validation of the experimental findings.
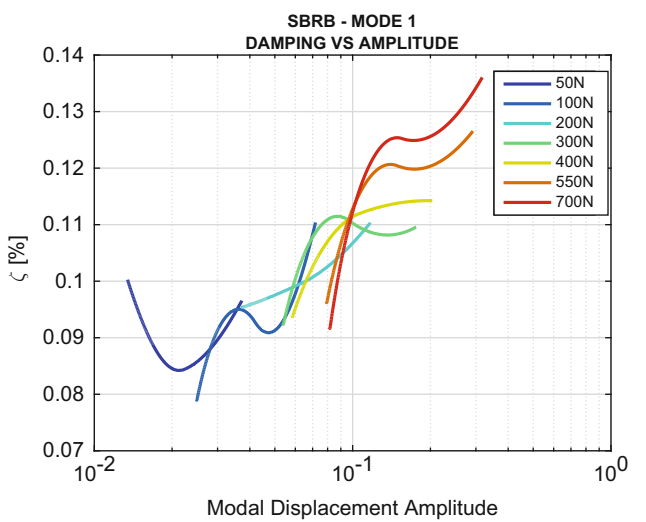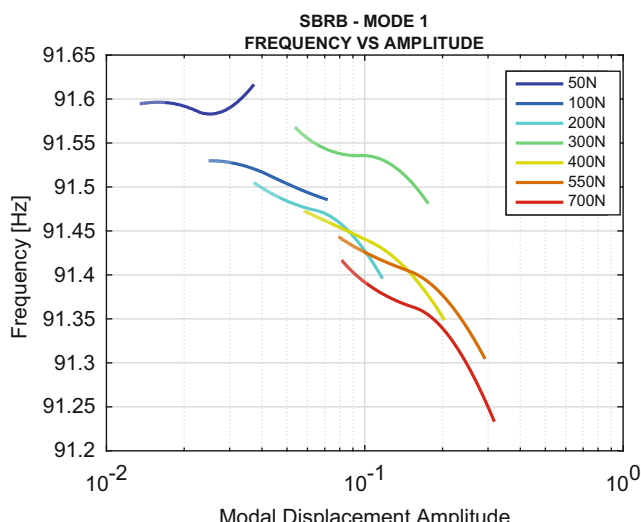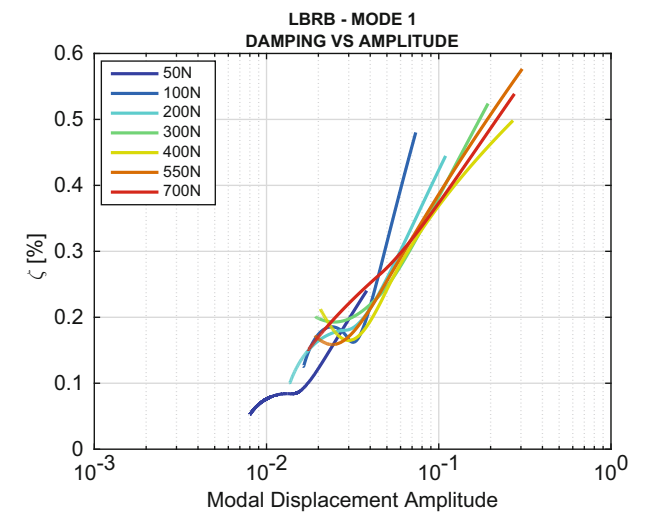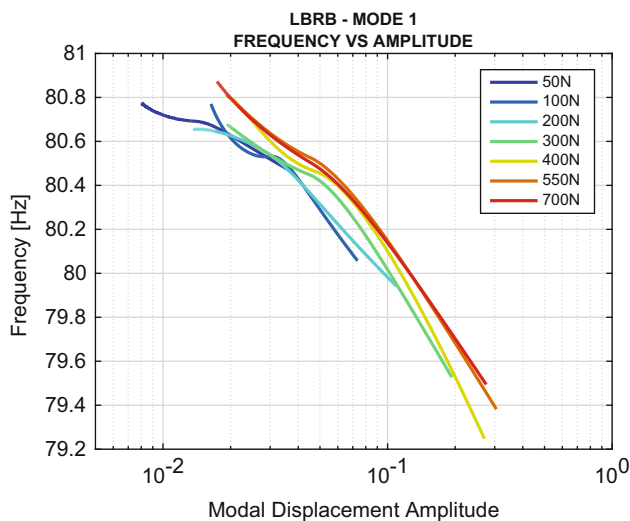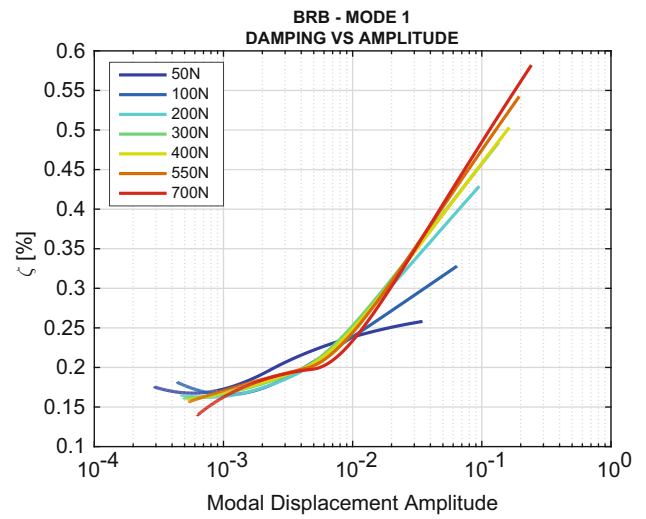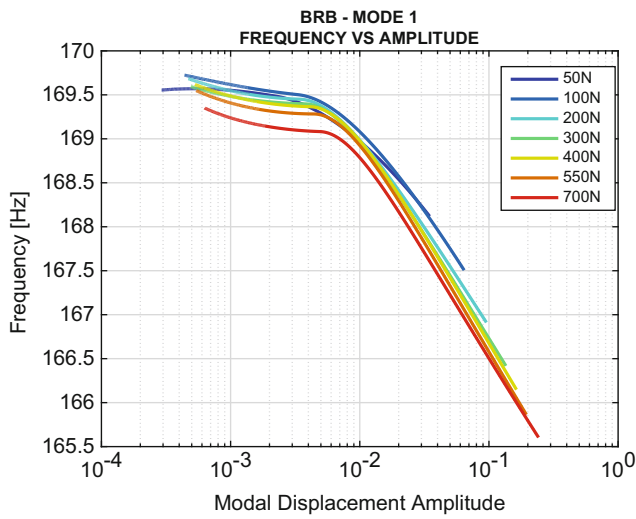
Fig. 7.10 Frequency and damping against modal displacement amplitude for BRB (**a–b**), LBRB (**c–d**), and SBRB (**e–f**)

Table 7.3 Measures of nonlinearities

	MODE	f_n[Hz]	$f_{n,min}$ [Hz]	ζ_L (%)	ζ_{max} (%)
BRB	1	169, 4	165, 6	0, 17	0, 58
	2	585, 7	582, 05	0, 08	0, 23
	3	1185, 5	1178, 2	0, 08	0, 22
LBRB	1	80, 7	79, 4	0, 12	0, 46
	2	291, 7	290, 9	0, 04	0, 11
	3	521, 5	519, 8	0, 06	0, 16
SBRB	1	91, 5	91, 3	0, 10	0, 15
	2	194, 3	194, 3	0, 03	0, 04
	3	496, 1	494, 7	0, 20	0, 44
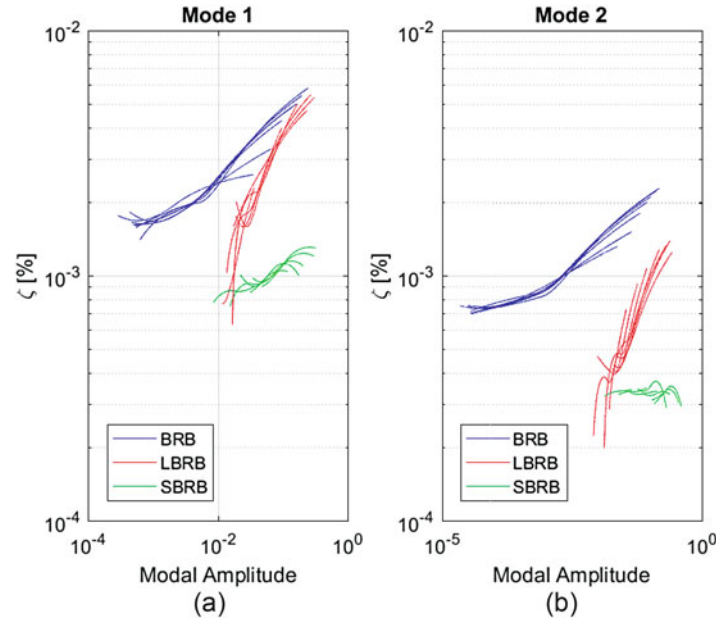
Fig. 7.11 Comparison of the damping ratios as functions of response amplitude for all three beams across all force levels tested for both (**a**) Mode 1 and (**b**) Mode 2

7.3.1 Nonlinear Amplitude Dependent Properties from Quasi-static Finite Element

In this numerical study, discrete, physical four-parameter Iwan elements were implemented into finite element models. It was found that a single set of physical Iwan model parameters can be implemented into two of the different beam structures to match experimental, modal findings. This result lends credibility to the underlying assumption that the joints in the structures are nominally similar, as they can be physically represented by the same set of modeling parameters.

7.3.1.1 Modeling Procedure

To begin, solid finite element model was created in a finite element program, and this model was extracted as a Craig-Bampton reduced-order model into MATLAB. In the finite element program, the two beams were modeled separately and connected with weak springs; Fig. 7.12 shows and example of the mesh used for the beams. Then, in MATLAB, stiffness elements were added between the spidered-joints between the beams; four-parameter Iwan elements were also added along the length of the beam to the five spider patches. Figure 7.13 illustrates the symmetric arrangement of these spider elements.

The parameters of these elements were fine-tuned to match the amplitude dependent information using standard Brake-Reuss beam information provided by the experimental results for the first two modes. The parameters for the four-parameter Iwan models are given in Table 7.4. To do this, rather than computing the dynamic response of the FEM to an impulsive load, a quasi-static loading was applied in the shape of the structure to the FEM model. The loadings were applied at various
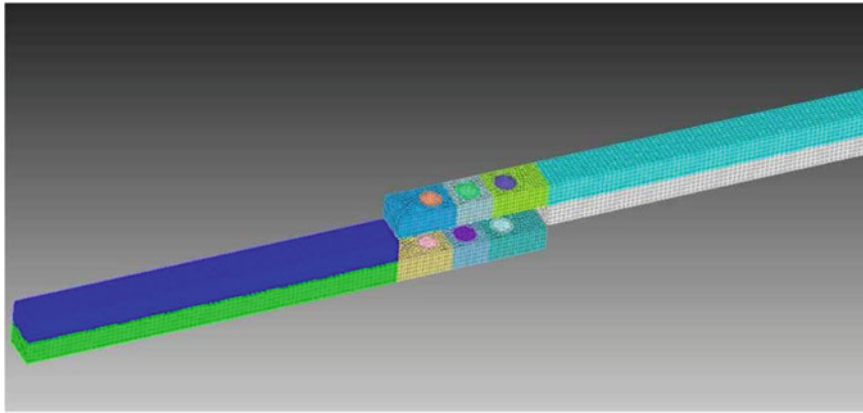
Fig. 7.12 Finite element model with discrete, physical Iwan elements
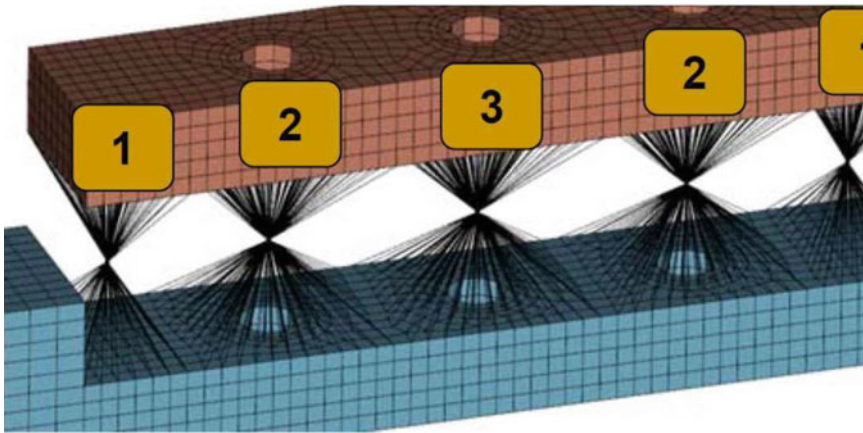
Fig. 7.13 Distribution of spider elements

Table 7.4 Tuned Iwan parameters for quasi-static FEM

Joint ID	F_s	K_t	χ	β
1	35,000	1.5e5	−0.60	0.25
2	35,000	2.2e5	−0.90	0.35
3	1750	2.2e5	−0.15	0.05

amplitudes in order to generate the expected amplitude-dependent curves. Next, the same tuned physical parameters were applied to a model of the LBRB. Using the same quasi-static loading technique based on its mode shapes, modal data for the LBRB model was also recovered.

7.3.1.2   Comparison of Numerical and Experimental Results

Comparisons between the experimental and tuned numerical modal results for the BRB are given in Fig. 7.14. The tuned physical parameters are remarkably effective at capturing the modal responses for the first two modes. Then, using those same identified physical parameters, the comparison of the experimental and numerical results for the LBRB is presented in Fig. 7.15. Without any retuning, the numerical model is still able to recover the experimentally-derived modal results. This result heavily suggests that the joints for these systems are nominally identical, and that it is indeed the far-field structure that is responsible for changing the modal responses for these systems. This work thus serves to validate the experimental findings. Put another way, these data show that the joint model's parameters were not significantly influenced by the far-field structure; however, because the total dynamics of the system are, figuratively, the sum of the joint, that evidently behaves the
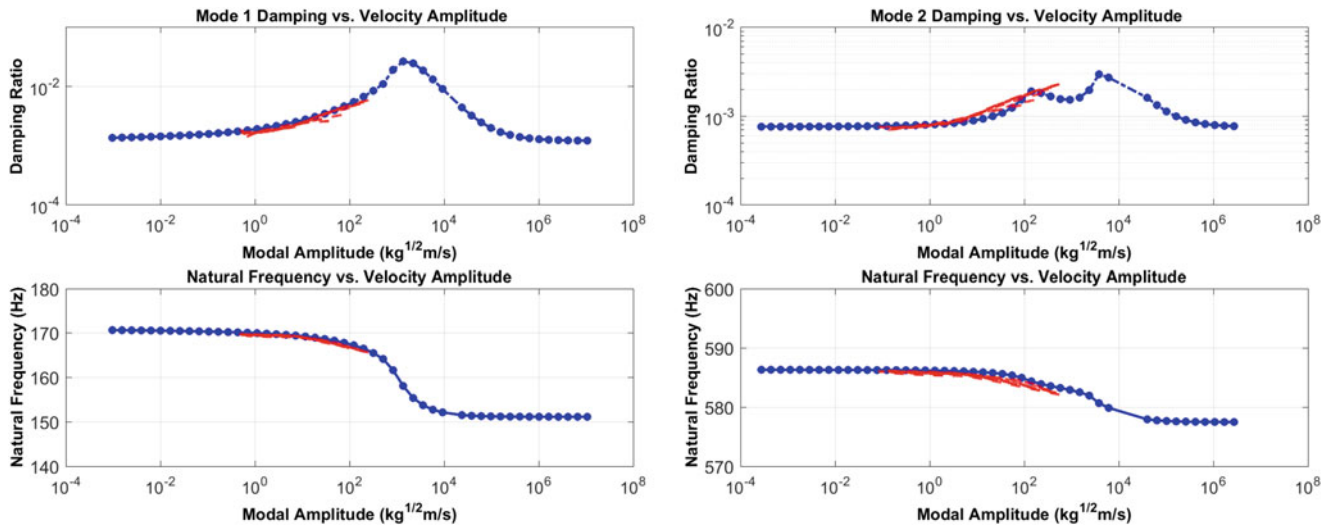
Fig. 7.14 Comparison of numerical and experimental frequency damping curves for the BRB
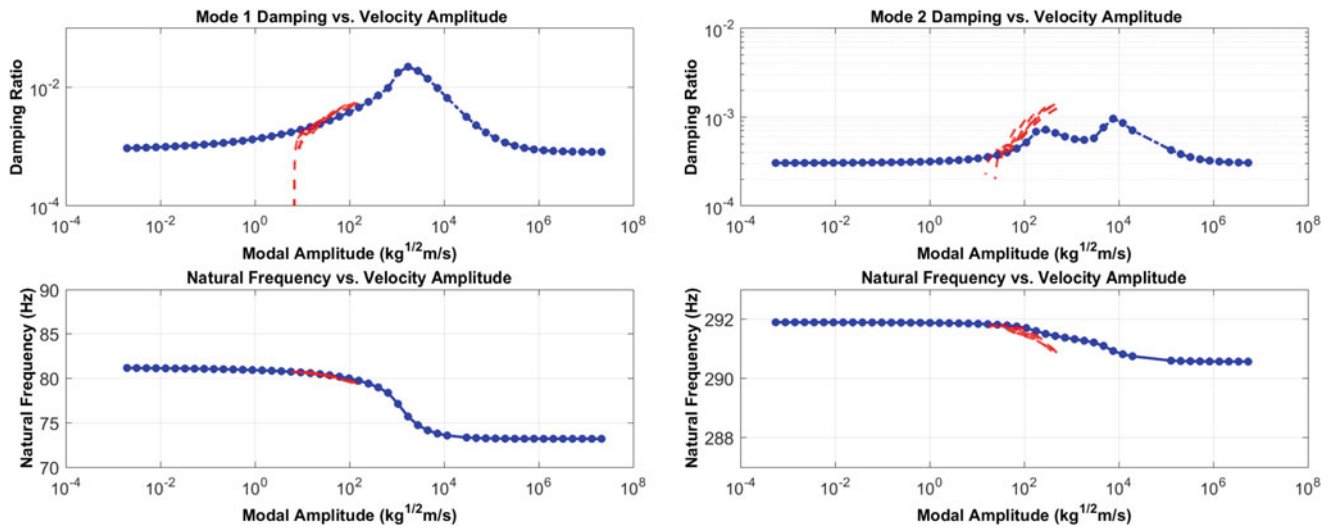
Fig. 7.15 Comparison of numerical and experimental frequency damping curves for the LBRB

same regardless of the far-field structure, and the linear dynamics of the surrounding structure, the modal responses observed experimentally exhibit different characteristics.

7.4 Conclusions

While this work comprises a multitude of techniques, approaches and ideas, it ultimately reduces to a single result. First, it was experimentally observed that the far-field structures of the considered Brake-Reuß beams had significant effects on the modal nonlinear stiffness and damping characteristics of each beam. Then, it was numerically shown that identical physical joint properties can be implemented into the different beam structures to match these experimental modal results without retuning, illustrating that the physical joint properties of these systems are nominally identical. Naturally then, one way to think of each of these systems is the sum of two parts, the nonlinear dynamics of the joint and the linear dynamics of the far-field structure. The ramifications of these results are that physical models of joints can be accurately constructed; however, the parameters must be deduced in the context of the surrounding structure. Thus, to characterize a joint, the *Surrogate System Hypothesis* is proposed:

The Surrogate System Hypothesis states that a surrogate structure, which is easy to model and machine, that contains the same joint as the system of interest can be used to deduce the properties of the joint. These properties, once accounting for the properties of the surrogate structure, can then be substituted directly into the system of interest as a spatially discrete joint model (as opposed to a modal model).

From the modal perspective, relocating the same joint to a new system necessitates the development of a new set of modal joint parameters. In this work, the quasi-static approach in [1] was used to do this. As is done in linear modal substructuring or structural modification, one must recognize that changes to any part of the structure will change the effective modal parameters, and for the nonlinear system, this results in a change to the damping versus amplitude and frequency versus amplitude curves.

Reference

1. Allen, M.S., Lacayo, R.M., Brake, M.R.: Quasi-static modal analysis based on implicit condensation for structures with nonlinear joints. In: The 2016 Leuven Conference on Noise and Vibration Engineering (2016)
2. Breake, M.R., Reuss, P., Segalman, D.J., Gaul, L.: Variability and repeatability of jointed structures with frictional interfaces. In: Allen, M., Mayes, R.L., Rixen, D.J. (eds.) Dynamics of Coupled Structures: Proceedings of the 32nd IMAC, a Conference 2014, Orlando, vol. 1, pp. 245–252. Springer (2014)
3. Deaner, B.J., Allen, M.S., Starr, M.J., Segalman, D.J., Sumali, H.: Application of viscous and Iwan modal damping models to experimental measurements from bolted structures. ASME J. Vib. Acoust. **137**, 021012 (2015)
4. Do, N., Ferri, A.A.: Energy transfer and dissipation in a three-degree-of-freedom system with stribeck friction. In: Proceedings of IMECE 2005, Orlando (2005)
5. Kerschen, G., Worden, K., Vakakis, A.F., Golinval, J.: Past, present and future of nonlinear system identification in structural dynamics. Mech. Syst. Signal Process. **20**(3), 505–592 (2005)
6. Peeters, B., Van der Auweraer, H., Guillaume, P., Leuridan, J.: The polymax frequency-domain method: a new standard for modal parameter estimation? Shock. Vib. **11**, 395–410 (2004)
7. Quinn, D.D.: Modal analysis of jointed structures. J. Sound Vib. **331**(1), 81–93 (2012)
8. Roettgen, D.R., Allen, M.S.: Nonlinear characterization of a bolted, industrial structure using a modal framework. Mech. Syst. Signal Process. **84**(Part B), 152–170 (2017)
9. Segalman, D.J.: A four-parameter Iwan model for lap-type joints. J. Appl. Mech. 72, 752–760 (2005)

Chapter 8
Real-Time Hybrid Model Testing of Moored Floating Structures Using Nonlinear Finite Element Simulations

Stefan A. Vilsen, Thomas Sauder, and Asgeir J. Sørensen

Abstract The paper proposes an application of real-time hybrid model testing (abbreviated ReaTHM testing) for the study of moored offshore structures. The structure under study is a moored axisymmetric floater with various bilge configurations, whose hydrodynamic properties are of interest. The system is partitioned into a physical substructure, consisting of a scaled model of the floater, and a numerical substructure, consisting of 12 mooring lines. All mooring lines are described by a nonlinear finite element model, to capture important phenomena such as geometric stiffness and drag-induced damping. The paper describes the substructuring strategy, the architecture of the test setup, and provides details regarding its components, namely the sensors, kinematic observer, predictor, numerical model, control/allocation system, and actuators. Results from qualification tests in calm water are presented, the main sources of time delays (which are compensated for) are identified, and the presence of jitter induced by Newton-Raphson iterations is discussed.

Keywords Real-time hybrid model testing • Marine hydrodynamics • Finite element method • Real-time dynamic substructuring • Real-time hybrid simulations

8.1 Real-Time Hybrid Model Testing in Marine Hydrodynamics

During the past decade, various research communities have been using real-time hybrid testing on problems that could be solved by an *online* coupling of a numerical model with a physical experimental setup. Let us take the field of earthquake engineering as an example. On the one hand, the characteristics of typical shaking tables facilities are insufficient to accommodate some structures of interest, as tall buildings or bridges. On the other hand, the focus of the studies is often on the deformations of local energy-absorbing components, with a highly nonlinear and rate-dependent behavior. As a consequence, several studies have been conducted [1, 2], in which part of the structure (including the component of interest) has been modeled physically on a shaking table, while the remaining part has been simulated in real-time using a linear dynamic finite element model. During the emulated seismic event, the numerical and experimental *substructures* interact through sensors, measuring reaction loads from the structure, and powerful hydraulic actuators, prescribing displacements at given locations of the structure. This interaction happens *in real-time* to ensure a correct behavior of the rate-dependent elements. The present paper does not intend to provide a thorough review of the vast literature in this field but an overview of the recent projects in the NEES network [1] can be a useful starting point for the reader. Real-time hybrid testing has also been used for component testing in other fields, such as automotive [3], naval [4] and aeronautic engineering [5]. Furthermore, in addition to being a research *method*, real-time hybrid testing has also become a research topic in itself, involving specialists in experimental mechanics, computational mechanics, mechatronics and control theory [5–8].

———————————

Authors one and two contributed equally to the present research.

S.A. Vilsen (✉) • T. Sauder
Department of Marine Technology, Centre for Autonomous Marine Operations and Systems, NTNU AMOS, Norwegian University of Science and Technology, NTNU, NO-7491, Trondheim, Norway

SINTEF Ocean, NO-7450, Trondheim, Norway
e-mail: stefan.vilsen@sintef.no; thomas.sauder@ntnu.no

A.J. Sørensen
Department of Marine Technology, Centre for Autonomous Marine Operations and Systems, NTNU AMOS, Norwegian University of Science and Technology, NTNU, NO-7491, Trondheim, Norway
e-mail: asgeir.sorensen@ntnu.no

Designing marine structures, such as oil production platforms, fish farms, offshore wind turbines, requires in many cases to perform model-scale testing for verification purposes. This is mainly due to complex hydrodynamic phenomena near the free surface such as higher-order wave loads, hydroelasticity, slamming loads, viscous loads on slender structures as nets or risers, and wave-current interaction. Efficient simulations based on potential theory are not able to tackle some of these phenomena, and a full resolution of the flow details using Navier-Stokes equation is not feasible yet in an engineering context.

The denomination *real-time hybrid model testing* is chosen as an extension to *classical* hydrodynamic model testing, and to emphasize that tests are performed at model scale, and in real-time due to the rate dependency of hydrodynamic phenomena. The acronym *ReaTHM testing*[1] is used in the following.

One limitation of model testing, and one motivation to develop ReaTHM testing for the study of marine structures arises from conflicting scaling laws. This aspect is important in particular for offshore wind turbines, and has been developed in [9]. Another motivation is the limitation of existing research infrastructures addressing very different spatial ranges and resolution. Indeed, when offshore oil platforms anchored in ultra deep water (as 2000–3000 m water depth) are to be studied at a reasonable scale, existing ocean basins suffer from a limited water depth, limited horizontal dimensions and limited current generation capabilities along the water column. Alternative strategies to classical testing have been suggested that rely on an arguably work-intensive post-processing phase [10]. As in the earthquake engineering application described previously, ReaTHM testing could be applied by separating the studied system into a physical and a numerical substructure. The physical substructure would include the floating structure, and thus the complex hydrodynamic loading near the free-surface, while the numerical substructure would represent the mooring lines and riser systems extending to the seafloor, for which efficient high-fidelity models exist, [11, 12].

The objective of the present work was to develop and integrate the components required to perform such a test. The physical part of the setup was an axisymmetric floating structure with various bilge configurations, whose hydrodynamic properties are of interest. The numerical substructure consisted of a set of 12 mooring lines ensuring station-keeping of the floater. Mooring loads were evaluated in real-time from a nonlinear finite element (FE) model, based on Newton-Raphson iterations, and applied on the floater. The main scientific contribution of the present work is (1) the development of a ReaTHM testing framework for marine hydrodynamic problems involving slender marine structures and nonlinear FE analyses, and (2) the demonstration of its feasibility even in quite demanding test conditions (small scale, little physical damping).

The paper is organized as follows. Section 8.2 describes the emulated system and numerical and physical substructures. Section 8.3 constitutes the main part of the article: it presents the architecture of the test setup, and describes each of its components: sensor system, observers, predictor, controller, allocation procedure, and the actuation system. Section 8.4 presents the results of the first qualification steps, consisting here in static and free decay tests. Comments are made regarding time delays in the control loop, and jitter induced by the nonlinear iterations, before concluding in Sect. 8.5.

8.2 Emulated and Substructed Systems

The emulated system i.e. the system to be studied before substructuring is performed, was a circular buoy moored with 12 identical mooring lines (see Fig. 8.1). The floater had a radius of 43.2 m in full-scale, a draft of 14.4 m and a mass of 86,500 metric tonnes. Three geometric variations of the bottom corner of the cylinder were studied, as seen in Fig. 8.2. The baseline case was a cylinder with sharp corners. The first variation included a protuberant step of square cross section (denoted bilge box), with a side length equal to one quarter of the draft. The second variation had rounded bottom corners, with a curvature radius equal to half the draft. The horizontal stiffness of the mooring system ranged from ca. 150–280 kN/m. As in classical model testing involving hydrodynamics, Froude scaling [13] was applied to ensure dynamic similarity of the surface waves at model scale and full-scale. A geometric scaling factor of 1:144 was used, leading to a time scaling factor of 1:12. Note that these values are significantly lower than those used in classical hydrodynamic model testing; in which the geometrical scaling factor is rarely less than 1:100 [14].

---

[1]ReaTHM® is a registered trademark of SINTEF Ocean.
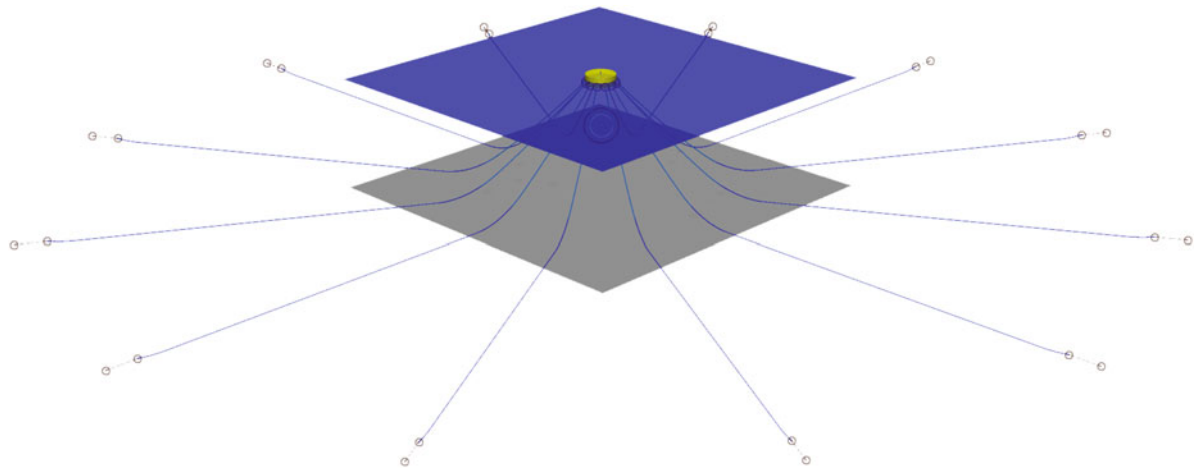
Fig. 8.1 A representation of the emulated system: an axisymmetric floating structure and 12 identical *mooring lines*
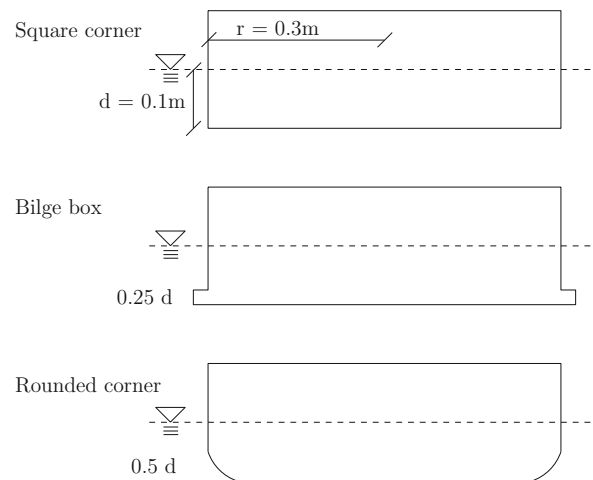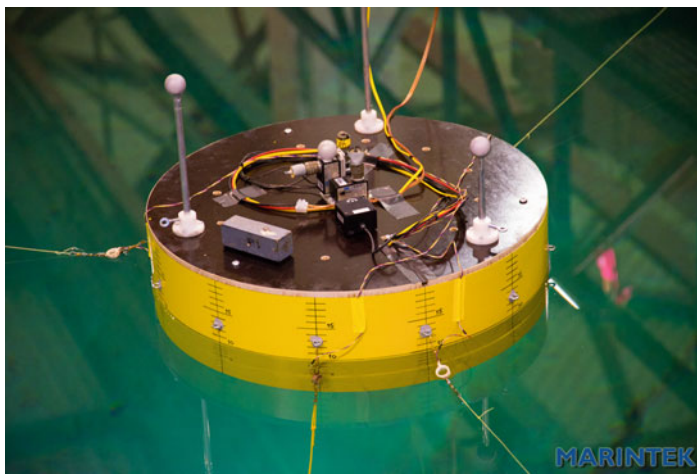
Fig. 8.2 (*Left*) Model of the axisymmetric floater in the basin. Actuation lines are visible, around the model, as well as instrumentation mounted on the top of the floater. (*Right*) Dimensions of the model, and variations in bottom geometry

8.2.1 Substructuring Strategy

When performing substructuring, dynamic and kinematic equilibrium must be ensured on the interface between the substructures [15]. Different control strategies can be applied to achieve this, such as displacement control, where a measured force is given as input to the numerical model, and a resulting displacement is actuated on to the physical model, and force/impedance control, where a measured displacement is used as input, and the calculated force is applied on the physical model through a feedback loop [3]. While displacement control is commonly used in the seismic engineering communities [16], it does not suit well with the present application. Environmental load effects on the physical model would indeed have to be handled by the numerical substructure [17]. Force control was chosen here.[2] A higher level control loop handled the kinematic equilibrium requirement, by sending the measured kinematic parameters of the physical substructure to the numerical substructure which performed load calculations. This loop ran at a frequency of 100 Hz. A lower level control loop updated the position of the actuators, based on feedback control of the measured force at the interface, at a frequency of 200 Hz.

---

[2]This ensured that the physical substructure was subjected to an applied force calculated from the numerical substructure.

8.2.2 Physical and Numerical Substructures

The physical substructure was manufactured at SINTEF Ocean at a scale of 1:144, see Fig. 8.2. It was ballasted to a model-scale weight of 28.27 kg, with a low center of gravity, to minimize the motions in roll and pitch. The instrumentation package, which will be described later on, was embedded in the model. The numerical substructure consisted of 12 identical mooring lines, radially and uniformly distributed around the floater, see Fig. 8.1. The dynamic response of the mooring system was simulated, in full-scale, using the commercial RIFLEX software [11], part of SINTEF Ocean SIMA workbench. Seventy-five beam elements were used to describe each mooring line. A Newton-Raphson iteration scheme was used to account for nonlinearities, and a classical Newmark-β scheme was used for time-integration. Important effects as a varying touchdown point and drag loads on the lines were included. RIFLEX provided the three components of the top force of each mooring line, leading to a six-component load vector at the interface between the substructures. In the present tests, only the two translational horizontal components were applied on the physical model. As the full-scale mooring model was connected in real-time to the physical model at scale 1:144, it was required to run 12 times faster than real-time. This was obtained by setting the time step in the simulating model to 0.12 s (full-scale time), and running the simulation at 100 Hz. The model ran on a conventional PC, communicating with the control system on a dedicated local network.

8.3 Architecture and Components of the ReaTHM Test Setup

The overall system architecture is outlined in Fig. 8.3.

The physical substructure was equipped with a sensor system. Three linear accelerometers measured the accelerations in the surge, sway and heave at 300 Hz. A three-component gyrometer measured the rotation rates in roll, pitch and yaw at 300 Hz. The position and attitude of the floater was evaluated at 100 Hz by an optical position measurement system.

Three actuation lines, visible in Fig. 8.2, were connected to the floater, to apply the calculated load from the numerical substructure on the physical model. Servo motors combined with a stiffness element were used to control the line tension. The applied force was measured through load cells attached between the model and the actuation lines, and filtered using a second-order Butterworth low-pass filter with a cutoff frequency of 20 Hz.

The sensor output was read by a data acquisition system (DAQ) and sent to a Sensor/Actuator interface, as well as to an external logging system (LOG). The Sensor/Actuator interface made the data from the DAQ available in real-time, and ensured the low-level control of the actuators. The external controller was running the control loop presented in Fig. 8.4, including an observer, a predictor and the communication with the numerical substructure. All parameters sent and received from the numerical substructure, as well as the actuator commands, were sent to the external logging system. The system clock for the external controller, sensor/actuator interface and the DAQ were synchronized, to ensure the traceability of data logged from different sources.

8.3.1 Kinematic Observer

The required input to the numerical substructures and feed-forward term in the controller are the position and velocity of the body. However, the sensor system mounted on the physical model measured its position/attitude, angular velocity and linear accelerations. The linear velocities could be obtained by integration of the accelerations, but would tend to drift due
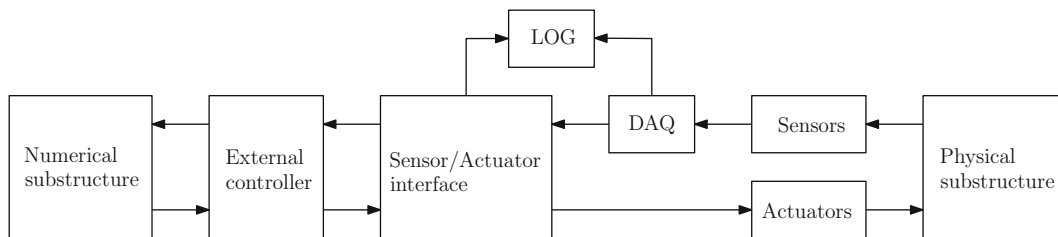
Fig. 8.3 Overall architecture of the ReaTHM test setup. The LOG block represents the external logging system, and DAQ block the data acquisition system
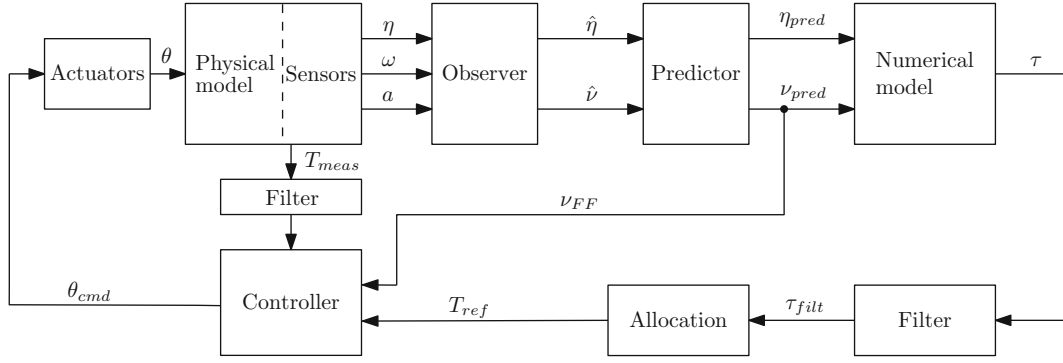
Fig. 8.4 Detailed view of the external controller. $\eta \in \mathbb{R}^6$ and $\nu \in \mathbb{R}^6$ are the position/attitude vector and the velocity vector of the body, respectively. $\omega_{b/n}^b \in \mathbb{R}^3$ is the angular velocity vector and $a_{b/n}^b \in \mathbb{R}^3$ the linear acceleration vector, both expressed in the body-fixed coordinate system. $\tau \in \mathbb{R}^2$ represents the two-component load vector, T the corresponding tension of the actuator lines, and θ represent the angles of the servomotors. Hats refer to estimated values, and FF relates to the feed-forward controller

to sensor bias. Furthermore, sensor outputs are subject to some degree of noise, which could generate errors or instability of the numerical substructure and actuation system. This led to the requirement of an observer performing state estimation, with some filtering capability. A nonlinear passive observer for integration of Inertial Measurement Units (IMU) and Global Navigation Satellite System (GNSS) data has been proposed [18]. There is a relevant similarity to the present system, since the optical position measurement system acts similarly to a GNSS, while the embedded sensor package provided output similar to an IMU. The implemented observer consisted in of the following formulation:

$$\dot{\hat{p}} = \hat{v} + K_1 \tilde{y}_1 \tag{8.1}$$

$$\dot{\hat{v}}^n = R(\Theta)[a - \hat{b}_{acc}] + g + K_2 \tilde{y}_1 \tag{8.2}$$

$$\dot{\hat{b}}_{acc} = K_3 R(\Theta)^T \tilde{y}_1 \tag{8.3}$$

$$\tilde{y}_1 = y_1 - \hat{y}_1 = p - \hat{p} \tag{8.4}$$

$$\hat{v}^b = R^T(\Theta)\hat{v}^n \tag{8.5}$$

where $\eta = [p, \Theta] \in \mathbb{R}^6$ is the position/attitude vectors of the body in the inertial frame of reference, $\nu = [v^b, \omega] \in \mathbb{R}^6$ is the body linear/angular velocity vectors, expressed in the body-fixed frame of reference. $v^n \in \mathbb{R}^3$ is the body linear velocity vector *expressed in the inertial frame*. a is the body-fixed acceleration vector, and b_{acc} the acceleration bias vector. g is the acceleration due to gravity. Superscript hat denotes estimated values. $R(\Theta)$ is the attitude-dependent rotation matrix allowing to convert body-fixed vector coordinates into coordinates expressed in the inertial frame of reference. The observer gain matrices K_1, K_2 and K_3 can be tuned such that the system error converges exponentially to zero [18].

As mentioned earlier, angular rates ω were measured by a gyrometer installed on the floater. The rates are used in the feed-forward controller, which sets requirements for accuracy of the measurements. Gyrometer measurements have a non-zero bias error, which would result in a constant feed forward error. An estimator was developed to cancel out the bias term,. The bias was estimated through derivation of the Euler angles, which are measured by the optical measurement system. The error between the derivative rates and the gyro measured rates was integrated to obtain the gyro bias, which was subtracted from the measured values. This method is only locally stable.

8.3.2 Efficient Prediction

Time delays are introduced in the control loop by calculation time, data processing and transport time, and sensor/actuator dynamics. They can be the cause of instabilities and loss of accuracy [16]. To alleviate this issue, *predicted* values of the motions were sent to the numerical substructure, instead of the observed motions: when the prediction time is exactly equal to the delay, the calculated load is applied at the time the physical substructure has actually reached the predicted position, which ensures consistency of the coupling.

The applied prediction strategy was the following. Since the dynamics of the physical substructure was assumed to be unknown, model-based prediction of the motions [16] was not chosen, and polynomial extrapolation of each quantity was used instead. A third order polynomial identification was performed using the 50 latest buffered data points, and the identified polynomial was used to extrapolate 6 data points ahead. This corresponded to time intervals of 250 and 30 ms, respectively. The delay was assumed constant, which was a motivated by the fact that the frequency-dependent actuator dynamics was not the main source of delay.

To minimize the computational burden related to identification and extrapolation, the following procedure was implemented. Let $f(x, a) = \sum_{j=0}^{n} a_j x^j$ be the polynomial used to describe a given quantity y. The first step was to evaluate $a = (a_j)_{j \in \{0,...,n\}}$. Using the m last known values of the quantity $(y_i)_{i \in \{1...m\}}$, a can be evaluated by solving the following minimization problem:

$$\min_{a \in \mathbb{R}^N} \sum_{i=1}^{m} (f(x_i, a) - y_i)^2 \tag{8.6}$$

Denoting $J(a)$ the objective function, the solution a^* is characterized by the fact that $\nabla J(a^*) = 0$. This leads to the following $n + 1$ equations

$$\forall k \in \{0, \ldots, n\}, \sum_{i=1}^{m} (f(x_i, a) - y_i) x_i^k = 0 \tag{8.7}$$

which is successively equivalent to

$$\forall k \in \{0, \ldots, n\}, \ \sum_{i=1}^{m} \left(\sum_{j=0}^{n} a_j x_i^j - y_i \right) x_i^k = 0 \tag{8.8}$$

$$\sum_{j=1}^{n} \sum_{i=1}^{m} a_j x_i^j x_i^k = \sum_{i=1}^{m} y_i x_i^k \tag{8.9}$$

which can be written as $\Lambda a = \mu$, where $\Lambda \in \mathbb{R}^{(n+1) \times (n+1)}$ and $\mu \in \mathbb{R}^{n+1}$, are given by

$$\forall (k, j) \in \{1, \ldots, n\}^2, \ \Lambda_{kj} = \sum_{i=1}^{m} x_i^{j-1} x_i^{k-1} = \sum_{i=1}^{m} x_i^{j+k-2} \tag{8.10}$$

$$\forall k \in \{1, \ldots, n\}, \qquad \mu_k = \sum_{i=1}^{m} x_i^{k-1} y_i \tag{8.11}$$

Note that Λ is symmetric, and that Λ^{-1} could be evaluated *offline*, on beforehand. Assume now that the x_i are regularly spaced, $x_i = i \Delta x$ with $\Delta x = 1$, without loss of generality. Then:

$$\forall (k, j) \in \{1, \ldots, n\}^2, \ \Lambda_{kj} = \sum_{i=1}^{m} i^{j+k-2} \tag{8.12}$$

$$\forall k \in \{1, \ldots, n\}, \ \mu_k = \sum_{i=1}^{m} i^{k-1} y_i \tag{8.13}$$

At each time step, μ_t and $a_t = \Lambda^{-1} \mu_t$ were evaluated by using the m last available values of y. The predicted value of y, p samples ahead, was given by $\hat{y}_t = f(m + p, a_t) = \sum_{j=0}^{n} a_{j_t} (m + p)^j$. This can be written as $\hat{y}_t = a_t^\top \xi$, where $\xi = (1, m + p, (m + p)^2, \ldots, (m + p)^n)^\top$ could be evaluated on beforehand. This method is arguably simplistic, due to the assumptions of constant delay, constant prediction horizon, and regularly spaced sample points, but it allowed to reduce the number of operations to be performed online to a matrix multiplication and an inner product (Fig. 8.5).

8.3.3 Force Allocation

As mentioned earlier, the global load vector τ to be applied on the physical substructure was obtained by summation of the contribution from each (numerical) mooring line top force vector. Given that only the horizontal forces, and possibly the yaw moment, were considered in the present case, $\tau \in \mathbb{R}^3$. This load was to be applied through n_l actuators lines connected to the buoy with $2\pi/n_l$ radians angular spacing. Here $n_l = 3$.
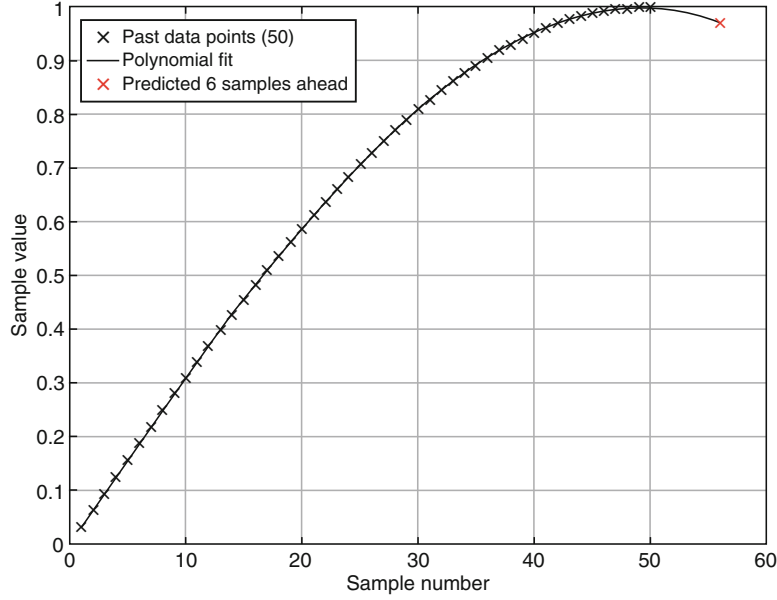
Fig. 8.5 Polynomial least square fit using 50 data points, and predictions 6 samples ahead

A simple and efficient allocation procedure was developed, which is detailed in the following. A pretensioning T_0 of the lines was applied to ensure that no lines became slack, which could generate a loss of controllability and snatch loads. Let $f_i = (T_0 + T_i)u_i$ be the force vector applied on the buoy from the ith line. $u_i \in \mathbb{R}^3$ is the unit vector $\frac{l_i}{||l_i||}$ where $l_i = H_i G_i$ is the vector spanning from the actuator position H_i to the attachment point on the buoy G_i. Let T_0 and T be vectors of dimension n_l containing the pretension and the additional tension of each line. The sum $T_0 + T$ will be referred to as the total tension. In the following derivation, we assume that $\eta = [N, E, \psi]^\top \in \mathbb{R}^3$, where N and E are the North and East position of the body, respectively, and ψ its yaw angle. In two dimensions, the rotation matrix from the body-fixed frame to the earth-fixed inertial frame is reduced to the following expression:

$$R(\eta) = \begin{pmatrix} \cos\psi & -\sin\psi \\ \sin\psi & \cos\psi \end{pmatrix} \tag{8.14}$$

The allocation problem consists first in defining a configuration matrix $A(\eta)$, and finding T so that

$$\tau = A(\eta)(T_0 + T) \tag{8.15}$$

We will derive expressions for l_i, $||l_i||$, and u_i, and of the configuration matrix $A(\eta)$. Denoting R_i the distance to the actuator, we start with $l_i = p_{G_i/\{n\}} - p_{H_i/\{n\}} = p_{G_i/\{n\}} - (p_{B/\{n\}} + R_b^n(\eta)p_{H_i/\{b\}})$, where

$$p_{G_i/\{n\}} = \begin{pmatrix} R_i \cos\frac{2(i-1)\pi}{n_l} \\ R_i \sin\frac{2(i-1)\pi}{n_l} \end{pmatrix} \tag{8.16}$$

$$p_{B/\{n\}} = \begin{pmatrix} N \\ E \end{pmatrix} \tag{8.17}$$

and

$$p_{H_i/\{b\}} = \begin{pmatrix} r\cos\frac{2(i-1)\pi}{n_l} \\ r\sin\frac{2(i-1)\pi}{n_l} \end{pmatrix} \tag{8.18}$$

This gives, using trigonometric identities,

$$l_i = \begin{pmatrix} (R_i - r) \cos \frac{2(i-1)\pi}{n_l} - N + 2r \sin \frac{\psi}{2} \sin \left(\frac{\psi}{2} + \frac{2(i-1)\pi}{n_l} \right) \\ (R_i - r) \sin \frac{2(i-1)\pi}{n_l} - E + 2r \sin \frac{\psi}{2} \cos \left(\frac{\psi}{2} + \frac{2(i-1)\pi}{n_l} \right) \end{pmatrix} \tag{8.19}$$

Defining

$$\Delta_{N_i} = (R_i - r) \cos \frac{2(i-1)\pi}{n_l} - N$$

$$\Delta_{E_i} = (R_i - r) \sin \frac{2(i-1)\pi}{n_l} - E$$

$$\Delta_i = \sqrt{\left(\Delta_{N_i}^2 + \Delta_{E_i}^2 \right)}$$

It is found from (8.19) that

$$||l_i||^2 = \Delta_i^2 + 4r^2 \sin^2 \frac{\psi}{2} + 4r \sin \frac{\psi}{2} \Delta_i \left(\sin \left(\frac{\psi}{2} + \frac{2(i-1)\pi}{2} \right) \frac{\Delta_{N_i}}{\Delta_i} - \cos \left(\frac{\psi}{2} + \frac{2(i-1)\pi}{2} \right) \frac{\Delta_{E_i}}{\Delta_i} \right)$$

Let α_i be such that $\cos \alpha_i = \Delta_{N_i}/\Delta_i$ and $\sin \alpha_i = \Delta_{E_i}/\Delta_i$, we obtain the following expression:

$$||l_i||^2 = \Delta_i^2 + 4r \sin^2 \frac{\psi}{2} \left(r + \Delta_i \sin \left(\frac{\psi}{2} + \frac{2(i-1)\pi}{2} \right) - \alpha_i \right) \tag{8.20}$$

Expressions for the vector l_i and its norm, being derived, the unit vector $u_i = (u_{i,1}, u_{i,2}) = l_i/||l_i||$ can be evaluated. The force vector from line i is given by $f_i = (T_{0_i} + T_i)u_i$. The total load (expressed in $\{n\}$) on the buoy is then obtained by

$$\tau = \left(\sum_{i=1}^{n_l} f_{i_1}, \sum_{i=1}^{n_l} f_{i_2}, \sum_{i=1}^{n_l} (BH_{i/\{n\}} \times f_i) \cdot b_3 \right)^\top$$

with

$$BH_{i/\{n\}} = R_b^n(\psi) \begin{pmatrix} r \cos \frac{2(i-1)\pi}{n_l} \\ r \sin \frac{2(i-1)\pi}{n_l} \end{pmatrix} = \begin{pmatrix} r \cos \left(\psi + \frac{2(i-1)\pi}{n_l} \right) \\ r \sin \left(\psi + \frac{2(i-1)\pi}{n_l} \right) \end{pmatrix}$$

Defining $m_i = r \left(\cos \left(\psi + \frac{2(i-1)\pi}{n_l} \right) u_{i,2} - \sin \left(\psi + \frac{2(i-1)\pi}{n_l} \right) u_{i,1} \right)$, we can express the configuration matrix as

$$A(\eta) = \begin{pmatrix} u_{1,1}(\eta) & \dots & u_{n_l,1}(\eta) \\ u_{1,2}(\eta) & \dots & u_{n_l,2}(\eta) \\ m_1(\eta) & \dots & m_{n_l}(\eta) \end{pmatrix} \tag{8.21}$$

If $A(\eta)$ has full rank, a tension vector $T \in \mathbb{R}^3$ can be found from (8.15), leading to the desired τ. However, it is clear that when $\eta = (0, 0, 0)^\top$, for instance, no moment can be exerted on the buoy, whatever the line tension combination. This translates mathematically by the fact that the third row of A is $(0,0,0)$, reducing the rank of A to 2. The origin is not the only position for which moment allocation cannot be achieved. Since we only wish to apply two force components, and no moment, we can define $A_r \in \mathbb{R}^{2 \times 3}$ consisting of the two first rows of A. We obtain T using the pseudo-inverse of A_r, which leads to a minimum $|T|^2$ satisfying equation (8.22).

$$T = A_r^\dagger (\tau - AT_0) \tag{8.22}$$
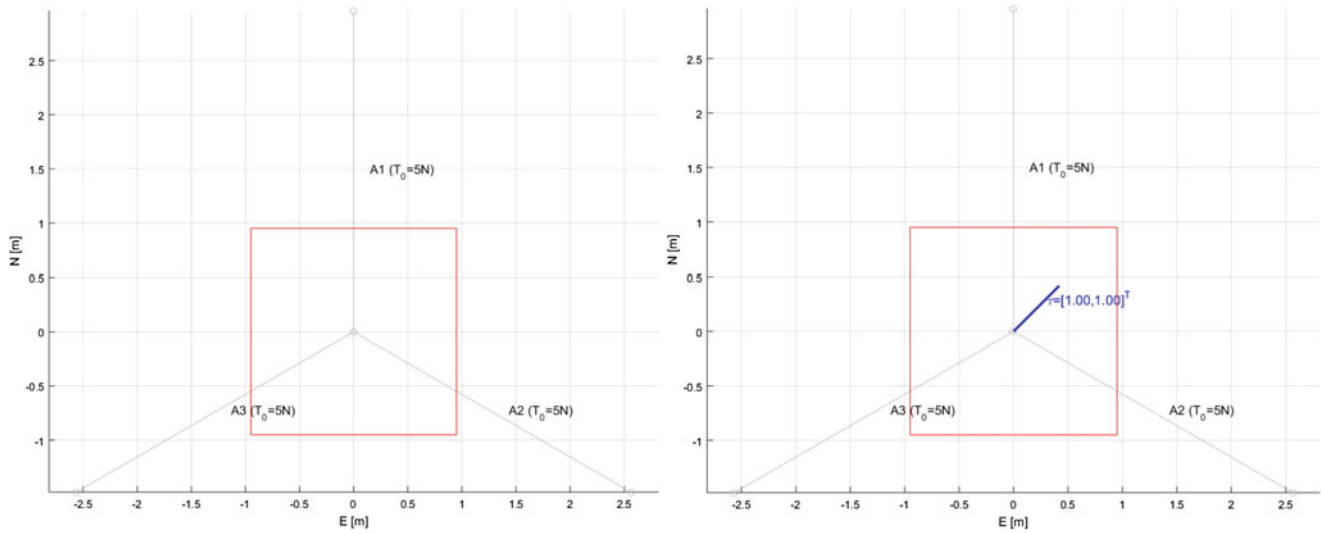
Fig. 8.6 Actuator lines (in *grey*) and studied zone of excursion (in *red*). The desired applied net force equal to zero on the *left*, and to [1,1]N on the *right*
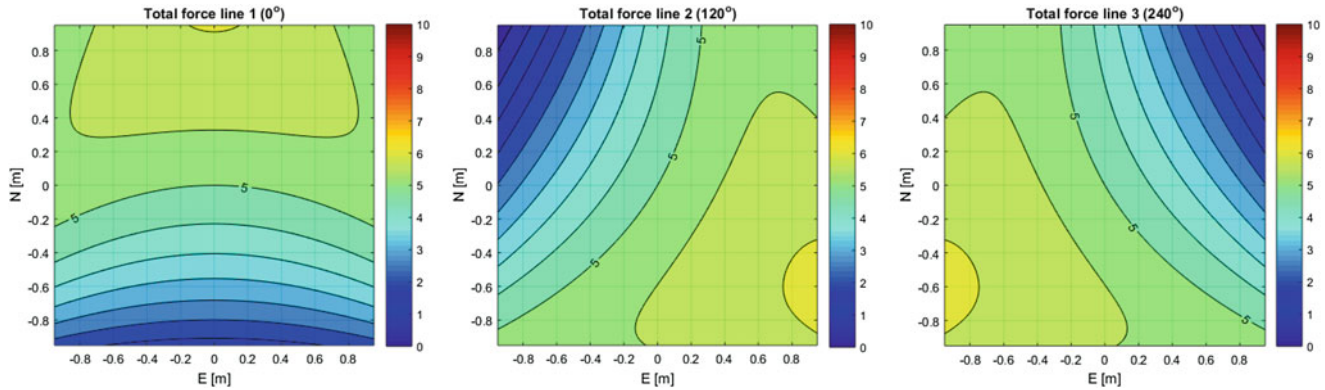
Fig. 8.7 Result of the allocation algorithm: commanded line tension for each actuator as a function of the floaters position. The desired applied net force is equal to zero

The following example illustrates the allocation procedure. Figure 8.6 to the left shows the setup when three actuators are located 2.9 m radially away from the origin. The radius of the floater r is 0.3 m. The pretension is set to 5N. We let the buoy's position evolve in an excursion zone symbolized by the red square. The yaw angle of the buoy ψ is assumed to be zero. The objective is, first, to find tension values, leading to a *zero* net horizontal force on the buoy. In Fig. 8.7, the total line tension (the sum of the pretension T_0 and of T) is represented for each line as a function of the horizontal position of the buoy in the excursion zone. At the origin, we see that only the pretension of 5N is applied. When the buoy moves towards G_1 (first actuator), the tension from line 1 increases, while the tension from lines 2 and 3 decreases, to compensate for the fact that their projection along the North axis is increased by the displacement. The right-hand side of Figs. 8.6 and 8.8 show similar results when the net force to be applied is non-zero: the symmetric patterns observed in the previous allocation plots are not present anymore.

8.3.4 Force Controller

For each actuation line, the control objective was (1) to perform dynamic tracking of the tension obtained from the allocation procedure, and (2) to reject the disturbances induced by the motions of the floater. A conventional feedback controller, coupled to a motion feed-forward controller, was used for this purpose. For each line, the feedback controller integrated the tension error to output a motor angle command. Only an integral term was used in the present tests, since the proportional
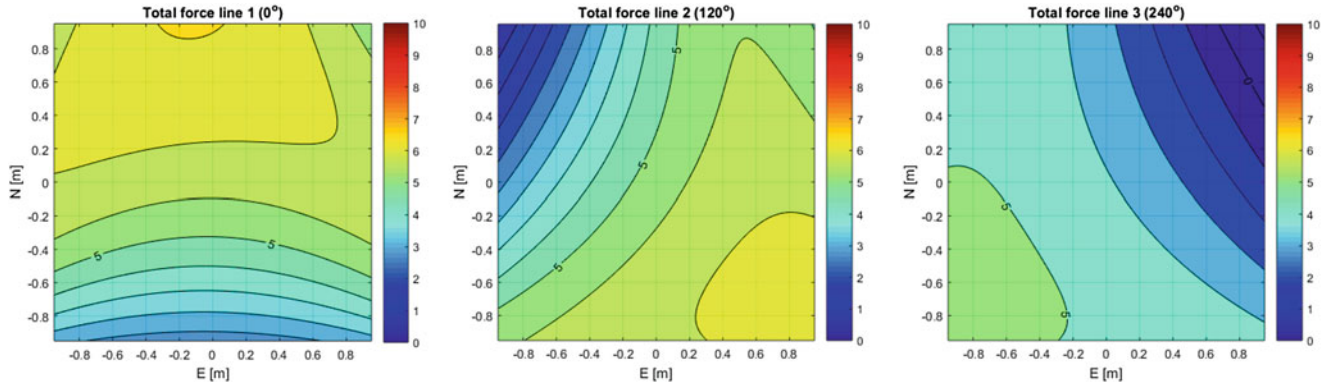
Fig. 8.8 Result of the allocation algorithm when the desired applied net force is equal to [1,1]N

and derivative terms interacted with the eigenfrequencies of actuation system and caused instabilities. The feed-forward controller was designed to perform disturbance rejection and to minimize the workload on the feedback controller. The velocity of the physical substructure was estimated by the observer, and an elongation velocity of each actuation line $\dot{\delta}$ was evaluated. The feed forward controller commanded the motor angle to follow the motion of the floater.

$$\theta_{FF}(t) = r_w \int_0^t \dot{\delta}(t')dt' \tag{8.23}$$

where r_w is the radius of the pulley mounted on the motor. This minimized the spurious forces induced directly by the floater motion, and left only the reference load from the numerical substructure to be applied by the feedback controller.

In addition to the integral and feed forward controllers, located in the external controller, and calculating a desired motor angle for each actuator, an additional low-level controller was involved. It consisted of a local PD controller, located inside each actuator, regulating the motor angle based on an internal motor angle encoder/register, and on the desired values.

8.4 Test Results

The ReaTHM test setup described in the previous section was implemented in a basin at MARINTEK. Two different numerical substructures were used: the full nonlinear finite element model described above denoted FEM, and a simple linear isotropic restoring force, denoted LIR. The FEM was expected to result in a varying, so-called geometric stiffness, and to introduce damping, induced by (numerical) drag forces on the mooring lines. The LIR was not supposed to introduce any damping which would allow to studying in detail the hydrodynamic damping properties of the physical substructure with the appendages depicted in Fig. 8.2.

8.4.1 Static Tests

Static pull-out tests were performed to validate the ability to apply a correct static force response from the numerical substructure. The model was gradually displaced from the equilibrium position, by steps of approximately 25% of the floater radius. The stiffness of the FEM and LIR were nearly equal near the equilibrium position, and equal to 280 kN/m in the present example. The stiffness of the FEM model was expected to increase with the increasing distance from equilibrium. Results from the pull-out test are shown in Fig. 8.9. The measured force response is plotted against the target values, obtained in offline simulation. In both the linear LIR and the nonlinear FEM case, the applied force corresponds well with the target values, and the nonlinearity induced by the geometrical stiffness in FEM is clearly observed.
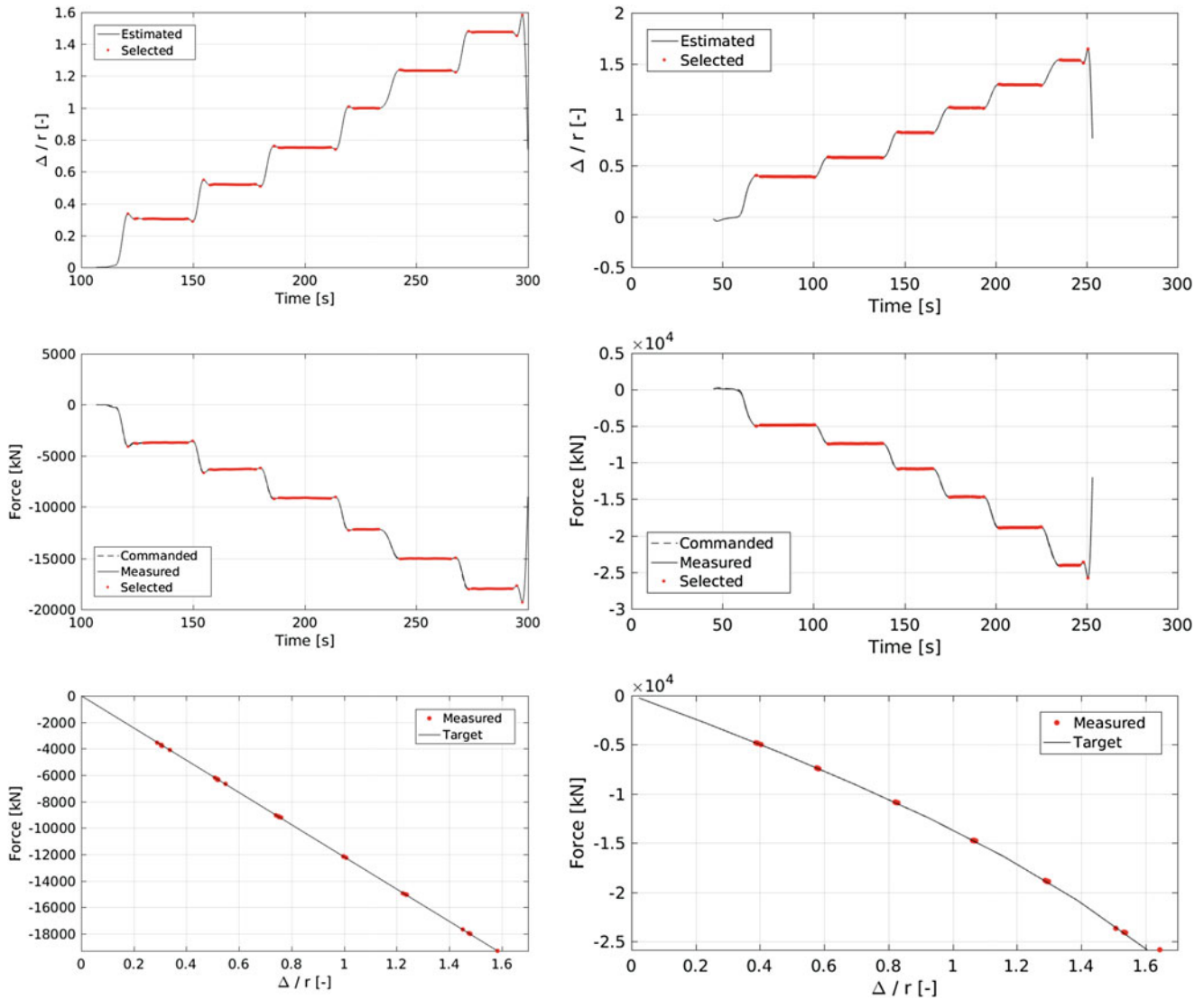
Fig. 8.9 Pull-out test results. LIR on the *left hand side*, and FEM on the *right hand side*. The time series of the floater displacement and mooring restoring force are presented in the first and second rows, respectively. The *red points* selected for drawing the displacement/restoring characteristic (third row)

8.4.2 Dynamic Test

The dynamic response of the system was investigated by performing free-decay tests: the model position is first prescribed to a position away from the equilibrium position and then released. As mentioned earlier, when the LIR was used, the only damping source should be hydrodynamic damping from the physical substructure. This damping comes mainly from two phenomena: flow separation and skin friction. The latter source was expected to be relatively small for all bilge configurations, while the former was expected to be significantly smaller for the "rounded corner" bilge configuration than for the two other appendages. This behavior is confirmed by the results presented in Fig. 8.10. It has also been found that the hydrodynamic added mass evaluated from these decay tests was in line with previous experience. Furthermore, when comparing Figs. 8.10 and 8.11, it can be seen that the damping level significantly increased when the nonlinear FEM model is used as a numerical substructure, illustrating how drag-induced loads from the mooring system influence the motions of the physical substructure. These results are merely of a qualitative nature, but are consistent with the expected behavior of the emulated system. A quantitative analysis of the results will be the object of a future publication.
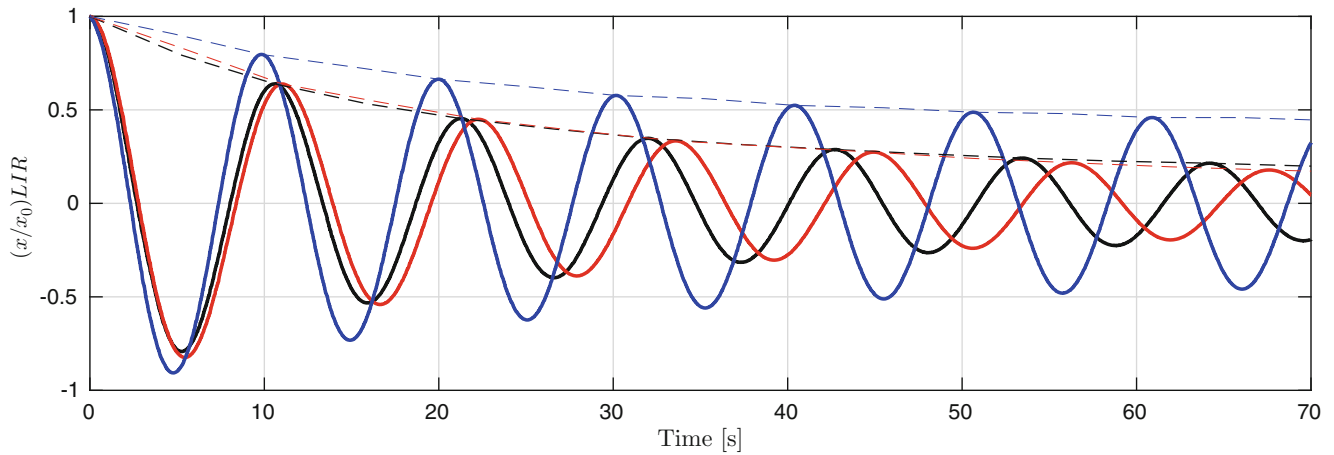
Fig. 8.10 Decay test with the LIR numerical substructure (Linear Isotropic Restoring). Baseline configuration in *black*, bilge box configuration in *red*, and rounded corner configuration in *blue*. The two former exhibit a similar level of damping, which is in turn significantly larger than the for the rounded corner configuration
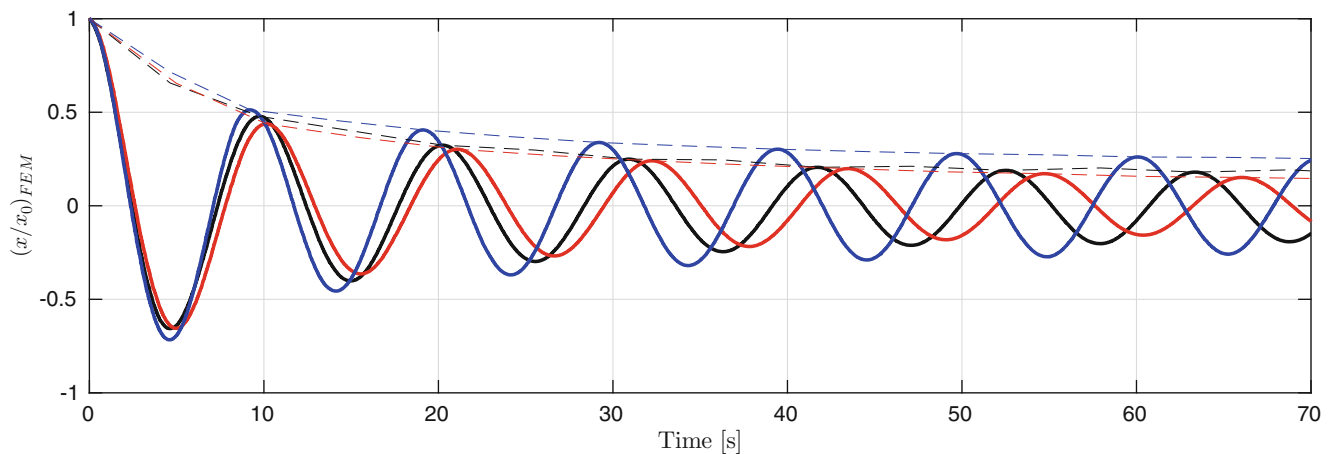
Fig. 8.11 Decay test with the FEM numerical model. *Color code* is the same as in Fig. 8.10

8.4.3 Time Delays and Jitter

Identification of time delays is a central aspect to ensure consistency of the dynamic equilibrium of the system, and avoid instabilities and losses of accuracy. A delay analysis was performed by cross-correlation of a reference signal, logged at each block in Fig. 8.3. A sensor reading was used as a reference signal. A 20 ms delay was identified from the DAQ, through the numerical model, and back to the Sensor/Actuator interface. The Sensor/Actuator interface sends then the commanded motor angle to the LOG and to the actuators. The measured motor angle was returned and logged. The delay between the commanded and measured motor angle consists of a constant delay induced by the communication forth and back, and a frequency dependent delay induced by the motor dynamics. Earlier studies with the motor type [19], showed a 3 ms delay while following a 75 Hz sine wave of 4° amplitude. The significant frequencies in the present system being all well below 1 Hz, the delay induced by actuator *dynamics* was considered constant. The motor command delay was measured to approximately 10 ms, giving a total delay of 30 ms, which was the value used in the predictor. As discussed in e.g. [9] deviations from the predicted value and the real value of the time delay would translate into an artificial damping or excitation force. This was indeed observed in the present setup when hydrodynamic damping on the physical substructure became insignificant (rounded corners, and very low motion amplitudes).

Dynamic testing with a high velocity of the floater results in a large change of the mooring line configuration, leading to an increased number of Newton-Raphson iterations per time step. If the simulation does not complete on time, this introduces jitter, i.e. deviation from the time delays evaluated above. This can be seen in Fig. 8.12. In the presented case, even though jitter occurs during the simulation, the accumulated delay after 700 s of simulation is less than 300 ms,
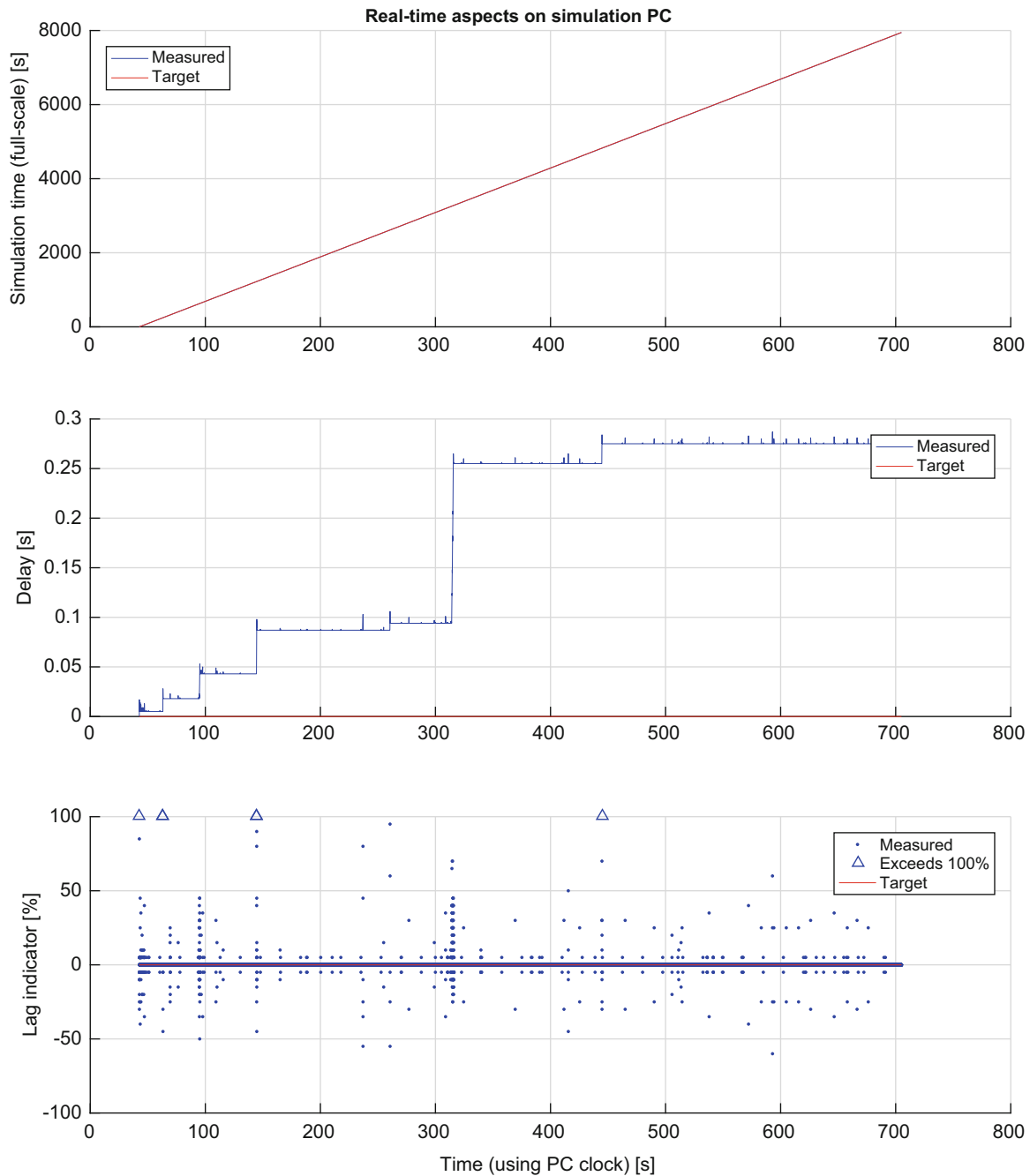
Fig. 8.12 *Top*: Time stamp of the FEM simulation in full-scale. The target value should flow 12 times faster than the wall-clock time. *Middle*: Delay between the effective and target simulation time. *Bottom*: Ration between the time used to simulate one time step and the target duration (10 ms)

which may be acceptable if there is no constraint of synchronizing time-dependent *external* loads, as wave loads, in the numerical and physical substructures. However, in some cases, when the numerical model did not manage to complete the iterations procedure over several time steps, peaks were observed in the output force.[3] They were due to artificially high accelerations input to the numerical model: the physical substructure had time to move several steps ahead, while the

---

[3]It is seen that the ReaTHM setup manages to catch up minor deviation to the target time. However, jitter induced by a large number of Newton-Raphson iterations causes the delay between target and measured simulation time to accumulate. See middle Figure.

numerical substructure was assuming that the received positions were for the *next* time step. To avoid these unphysical force jumps from influencing the physical model, the calculated force was low-pass filtered before being sent to the force allocation.

8.5   Conclusion

This paper presented an application of real-time hybrid model testing for the study of marine structures. The physical substructure was the model-scale version of a floating offshore structure, while the numerical substructure consisted of 12 identical mooring lines ensuring stationkeeping of the structure. A commercial nonlinear finite element program (RIFLEX) was used to evaluate the loads induced by the mooring system, which were applied in real-time on the physical substructure. Froude scaling, with a geometric scale factor of 1:144, was selected, leading to the requirement for the ReaTHM test setup to run 12 times faster than real-time. The control system developed to achieve this goal is described in details in the paper. The system performance was first evaluated through so-called pull-out tests and free-decay tests, during which the expected effects of the geometric stiffness and the drag-induced damping from the (numerical) mooring lines were indeed observed. Identification and quantification of time delays was then performed, and the occurrence of jitter due to nonlinear Newton-Raphson iterations was commented. Ongoing work focuses on the behavior of the present ReaTHM test setup when surface waves, representing higher frequency excitation, are present, and on defining criteria for ensuring an acceptable level accuracy for such a test.

References

 1. Shao, X., Griffith, C.: An overview of hybrid simulation implementations in nees projects. Eng. Struct. **56**, 1439–1451 (2013)
 2. Dion, C., Bouaanani, N., Tremblay, R., Lamarche, C.: Real-time dynamic substructuring testing of a bridge equipped with friction-based seismic isolators. J. Bridg. Eng. **17**, 4–14 (2012)
 3. Plummer, A.R.: Model-in-the-loop testing. Proc. Inst. Mech. Eng. I. J. Syst. Control Eng. **220**(3), 183–199 (2006)
 4. Botelho, R.M., Christenson, R.E.: Mathematical framework for real-time hybrid substructuring of marine structural systems. In: Dynamics of Civil Structures, Volume 4. Proceedings of the 32nd IMAC, A Conference on Structural Dynamics (2014)
 5. Wallace, M.I., Wagg, D.J., Nield, S.A., Bunniss, P., Lieven, N.A.J., Crewe, A.J.: Testing coupled rotor blade-lag damper vibration dynamics using real-time dynamic substructuring. J. Sound Vib. **305**(3–5), 734–754 (2007)
 6. Bursi, O.S., Wang, Z., Wu, B.: Monilithic and partitioned time integration methods for real-time heterogeneous simulations. Comput. Mech. **52**, 99–119 (2013)
 7. Drazin, P.L., Govindjee, S., Mosalam, K.M.: Hybrid simulation theory for continuous beams. J. Eng. Mech. **141**(7), 04015005 (2015)
 8. Wallace, M.I., Sieber, J., Neild, S.A.,Wagg, D.J., Krauskopf, B.: Stability analysis of real-time dynamic substructuring using delay differential equation models. Earthq. Eng. Struct. Dyn. **34**, 1817–1832 (2004)
 9. Sauder, T., Chabaud, V., Thys, M., Bachynski, E., Saether, L.: Real-time hybrid model testing of a braceless semi-submersible wind turbine. Part 1: the hybrid approach. In: Proceedings of the ASME 2016 35th International Conference on Ocean, Offshore and Arctic Engineering (2016)
10. Baarholm, R., Fylling, I., Stansberg, C.T., Oritsland, O.: Model testing of ultra-deepwater floater systems: truncation and software verification methodology. In: Proceedings of the ASME 2006 25th International Conference on Offshore Mechanics and Arctic Engineering (2013)
11. MARINTEK: RIFLEX 4.8.0 user manual, MARINTEK (2016)
12. Cao, Y., Tahchiev, G.: A study on an active hybrid decomposed mooring system for model testing in ocean basin for offshore platforms. In: Proceedings of the ASME 2013 32nd International Conference on Ocean, Offshore and Arctic Engineering OMAE2013 (2013)
13. Faltinsen, O.M.: Sea Loads on Ships and Offshore Structures. No. 0521458706. Cambridge University Press, Cambridge (1990)
14. Stansberg, C.T., Ormberg, H., Oritsland, O.: Challenges in deep water experiments: hybrid approach. J. Offshore Mech. Arct. Eng. **124**, 90–96 (2002)
15. De Klerk, D., Rixen, D.J., Voormeeren, S.N.: General framework for dynamic substructuring: history, review, and classification of techniques. AIAA J. **46**(5), 1169-1181 (2008)
16. Carrion, J.E., Spencer, B.F.: Model-based strategies for real-time hybrid testing, NSEL report series, report no. NSEL-006 (2007)
17. Kurfess, T.R.: Robotics and Automation Handbook. No. 0-8493-1804-1. CRC Press LLC, Boca Raton (2005)
18. Fossen, T.I.: Handbook of Marine Craft Hydrodynamics and Motion Control. No. 9781119991496. Wiley, Chichester (2011)
19. Chabaud, V., Steen, S., Skjente, R.: Real-time hybrid testing for marine structures: challenges and strategies. In: Proceedings of the ASME 2013 32nd International Conference on Ocean, Offshore and Arctic Engineering (2013)

Chapter 9
DIC Measurement of the Kinematics of a Friction Damper for Turbine Applications

L. Pesaresi, M. Stender, V. Ruffini, and C.W. Schwingshackl

Abstract High cycle fatigue (HCF) caused by large resonant stresses is a common cause for turbine blades failure. Passive damping systems, such as friction dampers are often used by aero-engine manufacturers to reduce the resonant stresses and mitigate the risk of HCF. The presence of friction dampers makes the dynamics of the system highly nonlinear, due to the complex stick-slip and separation phenomena taking place at the contact interface. Due to this nonlinear behaviour, an accurate understanding of the operating deflection shapes is needed for an accurate stress prediction.

In this study, digital image correlation (DIC) in combination with a high speed camera is used to provide insights into the kinematics of the damper in a recently developed test rig. The in-phase and out-of-phase first bending modes of the blades were investigated leading to a full field measurement of the global ODS of the blades, and the local motion of the damper against its platforms. A significant change in the blades operational deflection shape could be observed due to the damper, and the sliding and rolling motion of the damper during a vibration cycle was accurately visualised.

Keywords DIC measurement • Underplatform damper • Friction joint • Nonlinear dynamics • Stick-slip

9.1 Introduction

One of the most common causes of failure for turbine blades is high-cycle fatigue caused by large resonant stresses [1]. Passive damping systems, based on friction energy dissipation, are often used as an effective means to reduce these large resonant stresses. Various sources of friction dissipation were used in the past for turbine blades, with the most common relying on underplatform dampers [2]. The underplatform damper is a metal device which is located between the platforms of two adjacent blades, and it is loaded by the centrifugal force during operation. The presence of the damper shifts the resonance frequencies of the bladed disk upward, and also provides the energy dissipation to reduce the vibration amplitude of the blades [3, 4]. The dynamic behaviour of a bladed disk with a friction damper is strongly nonlinear due to the friction forces at the interfaces, and some difficulties arise to reliably predict the dynamic response. For this reason, simplified experimental set-ups are often used to reproduce the fundamental dynamics of the problem without the uncertainties of an engine test. One of the most common set-ups is a double blade configuration with a single damper between the two blades where the centrifugal load is simulated via loaded wires [3, 5–7]. The latest test rig of this kind, able to mimic the main dynamic characteristics of a real high-pressure turbine (HPT) blade, was developed at Imperial College London [8, 9] (see Fig. 9.1).

It is well known that the nonlinear dynamic response of bladed disk assemblies is highly dependent on the motion of the damper and its contact states (stick-slip-separation). In [7, 9] a laser set-up was used to track the motion of distinct points on the edge of the damper, giving a low resolution insight into the kinematics of the damper associated with the different vibration modes. In this study, a more advanced set-up based on a high speed camera together with digital image correlation (DIC) will be used to obtain a more complete and detailed picture of the kinematics of the blades and damper, as well as to identify the stick-slip and separation phases experienced at the contact interface.

L. Pesaresi (✉) • V. Ruffini
Department of Mechanical Engineering, Imperial College London, Exhibition road, SW72AZ, London, UK
e-mail: luca.pesaresi12@imperial.ac.uk

C.W. Schwingshackl
Imperial College London, Exhibition Road, SW7 2AZ, London, UK

M. Stender
Hamburg University of Technology, 21073, Hamburg, Germany
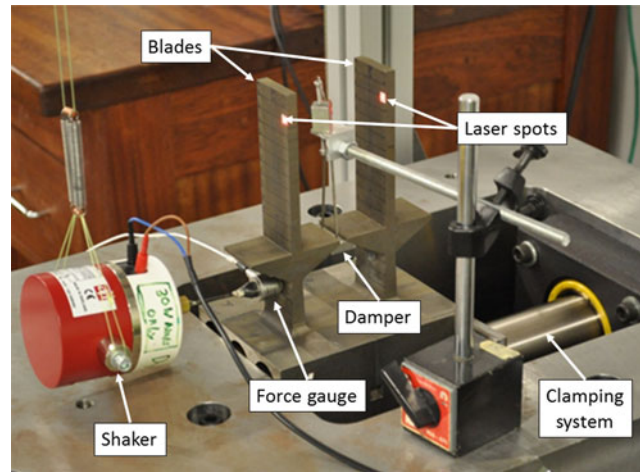
Fig. 9.1 UPD rig lab set-up

9.2 Underplatform Damper Test Rig

The underplatform damper (UPD) test rig is an experimental set up that allows the investigation of the effect of UPDs on blade like structures. A detailed discussion of the rig can be found in [9], and only a short discussion will be presented here for completeness. A static rig design was chosen to create a simplified experimental set up. The assembly of the rig can be seen in Fig. 9.1. Two pseudo beam-like blades are fixed to a common base, simulating a rigid disk, and are clamped via a hydraulic cylinder to a large inertia block. The damper is a wedge type, [3], which has a triangular cross section with a characteristic angle. Unlike a real high pressure turbine blade (HPT), the aerofoil is replaced by a straight rectangular cross-section beam, but still maintaining vibration modes similar to a real blade. The centrifugal load is simulated via a pulley system with calibrated masses, and the excitation is provided by an electrodynamic shaker attached near the root of the blade. Two single point laser Doppler vibrometers are used to measure the dynamic response of both blades at the tip.

9.3 Nonlinear Measurements

The nonlinear measurements focussed on the first flexural mode (1F), as it normally leads to the highest alternating stresses near the blade root. Two modes were investigated, the 1F out of phase mode of the blades (OOP) and the 1F in phase mode of the blades (IP). A stepped sine test was used for the excitation, where the level of shaker force was kept constant throughout the sweep. The excitation level was varied over a large range, from 0.01 N, where the response of the system was almost linear, to 17 N (shaker limit) where a strong nonlinearity was observed. The pulling load of the damper was kept constant at a high level (960 N) to ensure a good conformity at the contact interface. The evolution of the OOP and IP modes at various excitation levels can be observed in Fig. 9.2a, b.

The OOP mode (see Fig. 9.2a) shows a clear amplitude reduction, even present at lower excitation levels, and a slight frequency shift of about 2 Hz. This behaviour seems to indicate that the contact is experiencing "microslip", as this slight frequency shift is normally caused by the progressive evolution of the contact interface from a fully stuck contact to a full slip condition. The IP mode, which was measured from high to low frequencies seems to be dominated by a significant FRF softening, characterised by the left-leaning and jumping response (see Fig. 9.2b). A possible explanation could be based on the tendency of the damper to roll in the IP mode [3, 7], which can reduce the damper-platform contact area at higher amplitudes, leading to a softer system. The dynamic behaviour of the IP and OOP modes varies quite strongly, and a good understanding of the blade and damper motion is needed.
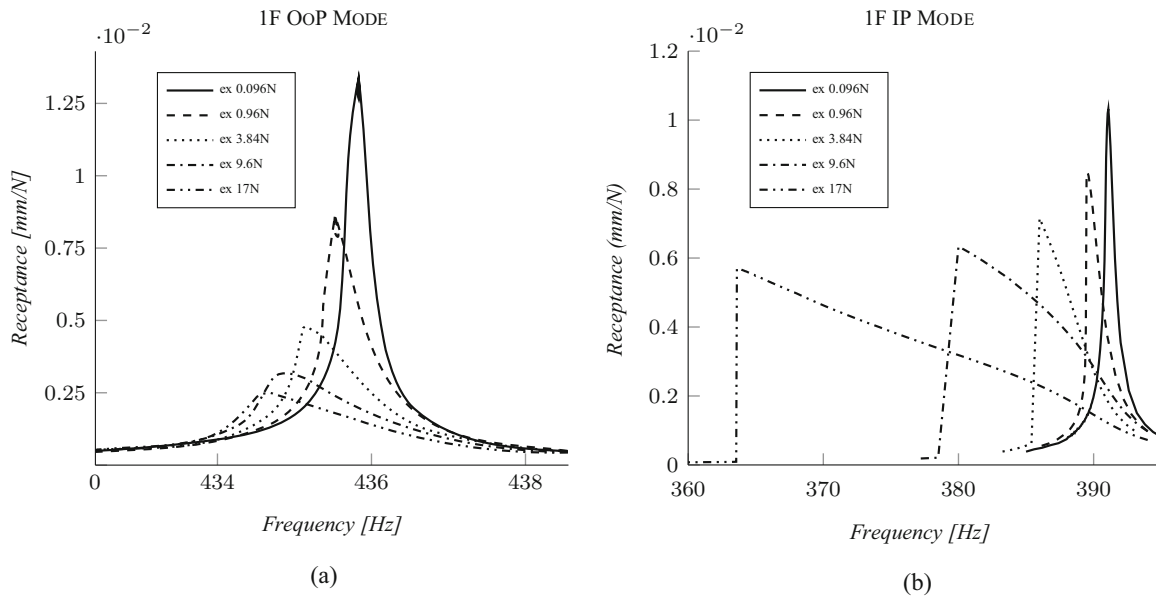
Fig. 9.2 Experimental FRFs at various excitation forces and constant damper load (960 N), (**a**) OOP mode, (**b**) IP mode

9.4 DIC Visualization of the UPD Test Rig

To investigate the motion of the damper and the blades during a nonlinear response of the system, a high speed camera set-up in combination with DIC analysis was used. The camera is a Photron Mini UX100 and is capable of 4000 fps at the full frame resolution (1280×1024 pixels). Two different Nikon lenses were used, a standard photographic Nikon DX SWM VR 18–55 mm to capture the whole blade and a Nikkor Micro SWM VR ED IF 105 mm lens which was used for a close up of the damper. The camera was aligned along an axis perpendicular to the lateral plane of the damper rig, as shown in Fig. 9.3, to allow a clear 2D view of the bending modes of the blades and the damper. Two LED spotlights were used to illuminate the structure and allow a higher camera shutter speed, thus avoiding the risk of blurred images.

Digital image correlation was used to analyse the recorded images and extract the displacement field for the damper and blades. DIC is a powerful tool as it allows the post-processing of the results of a contactless fullfield measurement system (high-speed camera) with a high spatial and temporal resolution. For this study, an open source Matlab-based code developed at the Georgia Institute of Technology, Ncorr, was used where the main components and concepts are described by Blaber et al. [10].

9.4.1 Operational Deflection Shape

The first application of the DIC was to investigate the change in the ODS caused by the presence of the damper. The presence of the damper stiffens the FRF of the blades significantly leading to a frequency shift from 269 to 392 Hz for the IP mode, and 435 Hz for the OOP mode. It is likely that such a fundamental change in frequency is associated with a different ODS which may lead to a different distribution of cyclic stresses, and therefore impact the expected life of the blades. The high-speed camera was adjusted to frame one of the two blades, and two spotlights directed towards the upper and lower part of the blade were used to have a uniform distribution of light (see Fig. 9.4).

After initial trials, a white and black random pattern was applied to the surface of the blade, as it significantly improves the signal to noise ratio of the DIC. The procedure used for the test was the following: (i) the frequency range of the mode of interest was identified, (ii) a stepped sine test was performed with a constant shaker excitation, (iii) at resonance a short video was recorded, and finally (iv) The DIC was then performed, and the average displacement for cross sections of the blade at increasing distances from the root was extracted. Three tests around the first bending mode were carried out, a low shaker level (0.5 N) test without the damper, a 17 N (shaker limit) test with the damper for the 1F IP and 1F OOP mode.
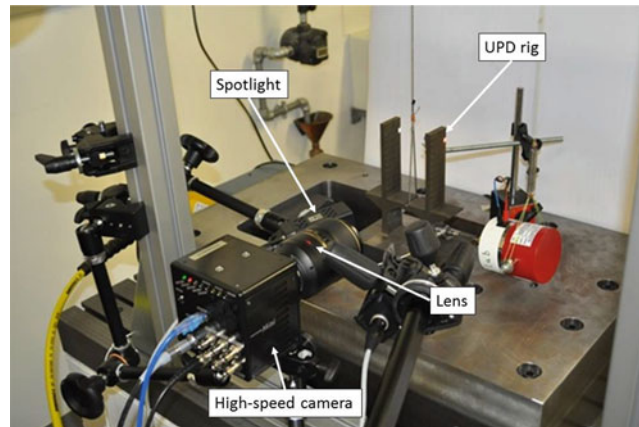
Fig. 9.3 High-speed camera set up applied to the UPD rig
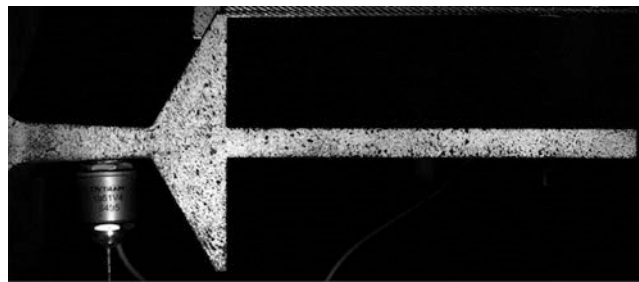
Fig. 9.4 High-speed camera view of the blade

When the damper was in place, the response level was much lower due to the added damping, leading to difficulties in the DIC post-processing at excitation amplitudes below 17N. The ODS results for the three tests and for different recorded frames are shown in Fig. 9.5. A change in shape for the 1F mode is evident when the damper is present, as the damper tends to couple the adjacent platforms and increases the curvature of the mode near the platforms. The IP mode is still very similar to the linear case without a damper but the OOP mode is very different (see Fig. 9.5d). The lower part of the blade is not deformed at all, and the blades tend to behave as a shorter beam. In this latter case, the peak stress is not expected near the blade root but higher up at the platform level, leading to a very different HCF scenario. These results show a great sensitivity of the DIC with regards to relatively small motions, since even the very small displacement close to the root (in the order of $10 \, \mu$m) could be resolved. It should be said that the accuracy of the DIC may not be as accurate as that of an accelerometer or an LDV, but its relatively quick set-up and its provision of the full ODS in a single measurement clearly makes it a very interesting tool to investigate the nonlinear dynamic behaviour.

9.4.2 Damper Kinematics

The second application of the DIC was to investigate the kinematics of the damper associated with the different modes, to better understand the underlying nonlinear mechanism that drives the nonlinear response. The levels of displacement experienced by the damper are much lower than those of the blades, and for this reason the high-speed camera set-up was modified: a macro Nikkor lens was used to reduce the field of view to the damper, platforms and relative contact interface only (see Fig. 9.6a).

Once more a movie at 4000 fps and at full HD resolution was taken to capture the damper motion. A more detailed DIC analysis was then performed, with a grid of several tracking points in the region of the damper and the two platforms. A post-processing tool was developed in order to extract for each tracking point the absolute displacement against a reference image, which is then represented by a arrow. The displacement quiver plot obtained from the DIC analysis for the OOP and IP mode are shown in Fig. 9.7. The two frames shown for each mode are chosen near the maximum and minimum of the vibration amplitude. In the OOP mode (Fig. 9.7a, b), the damper has a pure vertical translation following the platform
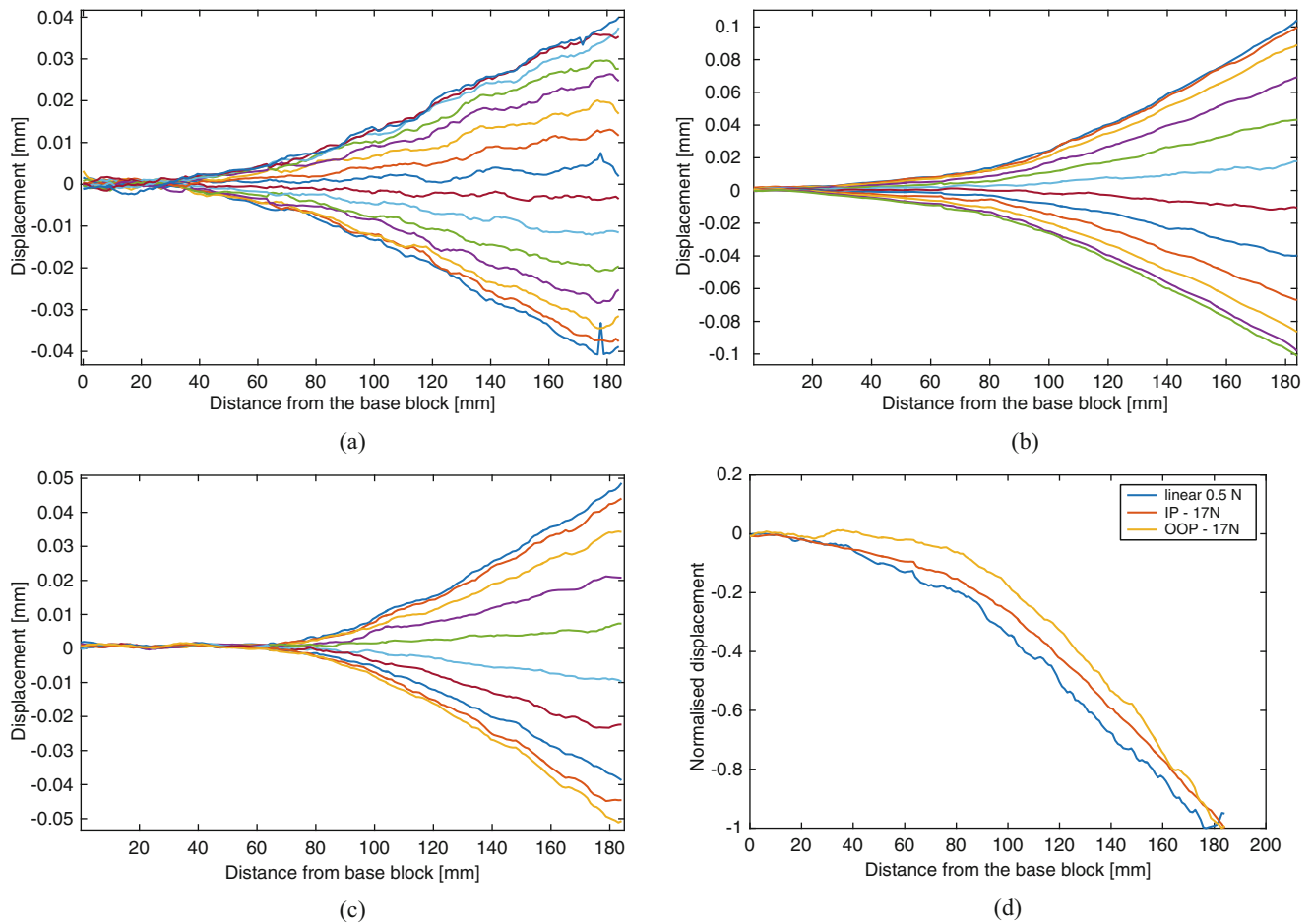
Fig. 9.5 DIC visualization of the blades ODS for different configurations: (**a**) linear without damper 0.5 N excitation, (**b**) with damper IP mode 17 N excitation, (**c**) with damper OOP mode 17 N excitation, (**d**) comparison of configurations normalised to relative max
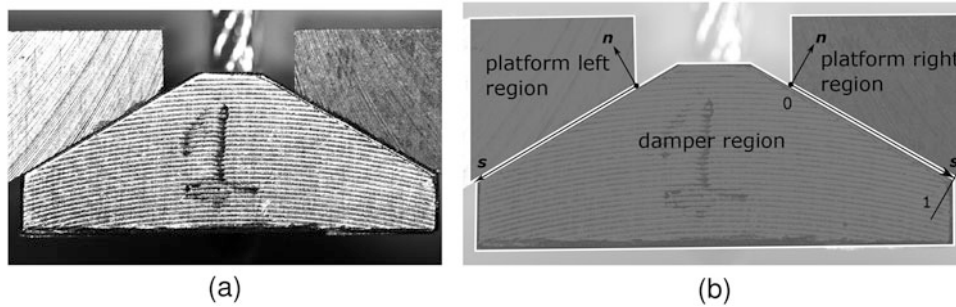
Fig. 9.6 (**a**) Camera view of the damper, (**b**) local coordinate system defined at the contact interface

motion. At the same time, the platforms tend to move to the sides, away from the centre of the frame when the damper is shifting up, and tend to move to the centre of the frame when the damper is shifting down. In Fig. 9.7c, d, which show the IP mode, the platforms exhibit an opposite vertical motion. As a consequence, following the platforms, the damper is subject to a counter clockwise rotation when the blades are moving to the right (Fig. 9.7c) leading to a horizontal translation. It is likely that this rotation leads to a change of the contact area at the interface, which can explain the strong softening of the FRF observed in the IP mode.
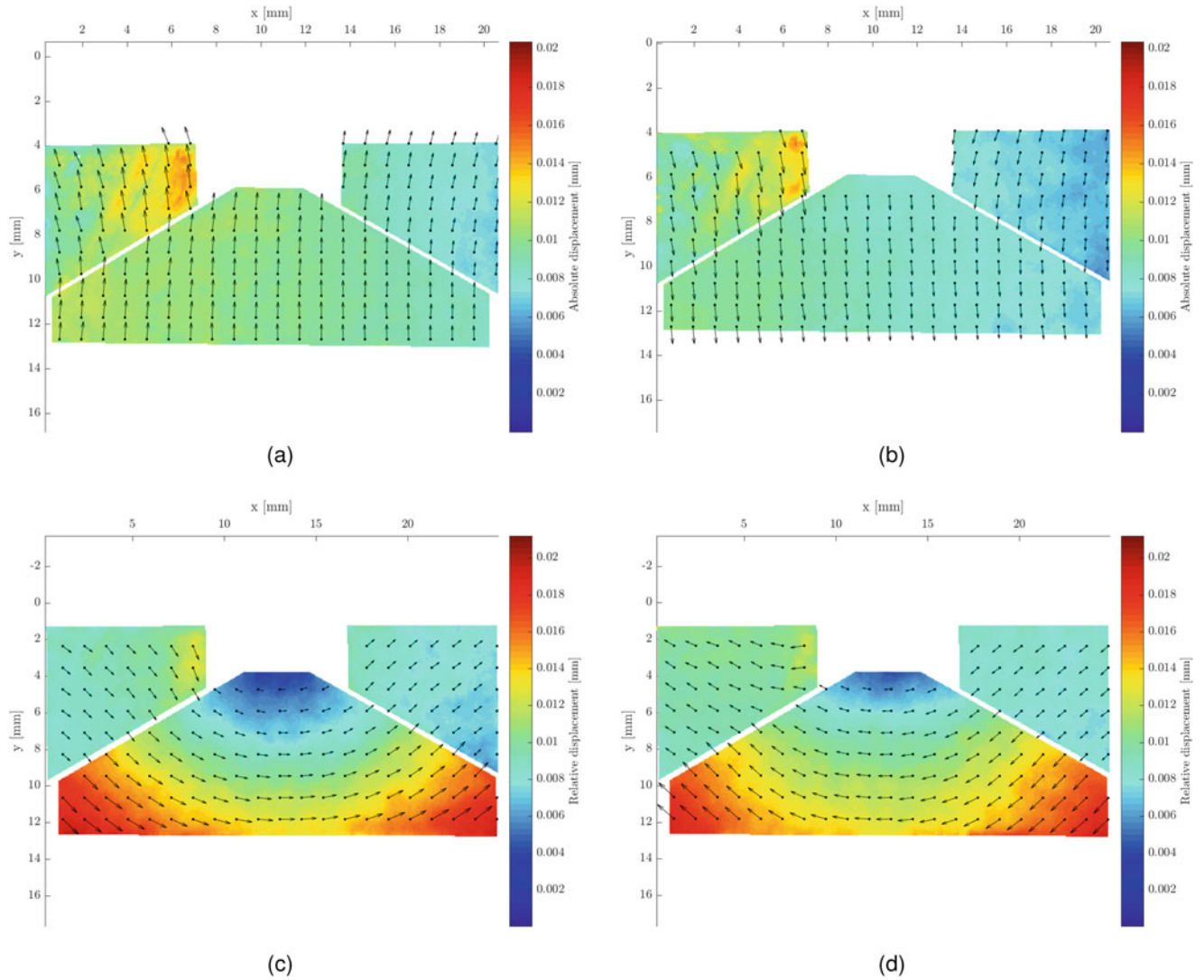
Fig. 9.7 DIC visualization of the kinematics of the damper: (**a**) first frame OOP mode, (**b**) second frame OOP mode, (**c**) first frame IP mode, (**d**) second frame IP mode

9.4.3 Damper Stick-Slip

To get a better understanding of the friction phenomena which are driving the nonlinear behaviour of the rig, a DIC analysis was performed at the contact interface. A post-processing tool was developed to calculate the relative contact motion at the interface, and evaluate the potential areas of slip, microslip or separation. A contact line was defined for the right and left interface (see Fig. 9.6b), and the tracking points in the vicinity of the contact line were divided into two groups, depending on whether they belonged to the damper or the platform. A local coordinate system was then defined in order to decompose the local displacement into normal and tangential components at the interface. To analyse the relative damper-platform displacement, it was necessary to unload the damper to 120 N since it was not possible to have a good signal to noise ratio with the 960 N preload used earlier, even at the highest excitation level (17 N).

Figures 9.8 and 9.9 show subsequent frames of the normal ($\perp$) and tangential ($\parallel$) displacement for both damper and platform, allowing a direct comparison between the two in order to detect stick-slip and separation phases. In particular, when the two lines are not overlapped, a separation is expected for the normal displacement plots, and a slip phase is expected for the tangential displacement plots. Looking at the OOP mode (see Fig. 9.8), it seems that the platform-damper interface is always in contact even if a slight separation could be observed in Fig. 9.8e, f near the bottom edge. In this mode a strong energy dissipation is expected, looking at the large macroslip observed in Fig. 9.8c–e where the damper is slipping
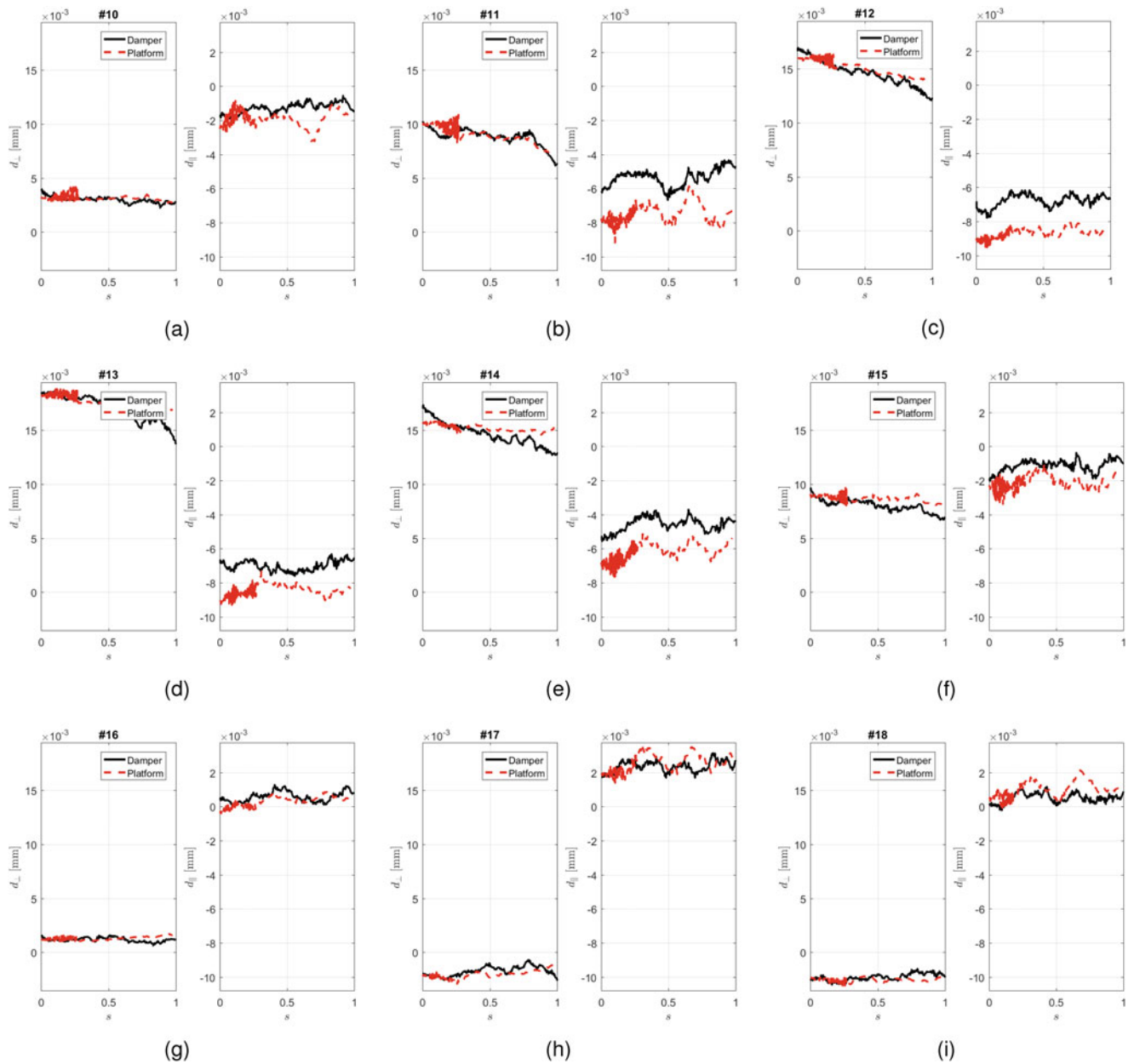
Fig. 9.8 DIC visualization of subsequent frames of the right contact displacement for both damper and platform, OOP mode

and in contact at the same time. This strong energy dissipation was supported by the nonlinear measurements in Fig. 9.2a where a higher damper load was used there. With regards to the IP mode (Fig. 9.9), a partial loss of contact can be observed for most of the frames captured indicated by the difference in displacement in the normal direction. In particular, Fig. 9.9h, i show that only a small part close to the upper edge is in contact, whereas the lower part experiences a separation of more than 10 microns. This strong separation explains the softening of the FRFs observed in the blades response at high excitation levels (see Fig. 9.2b). Only a small tangential relative displacement is visible in Fig. 9.9b, d, h which is much less dominant than for the OOP mode. This small tangential displacement ties up with the nonlinear measurements (see Fig. 9.2b), where high excitation levels did not lead to significant amplitude reduction in the response of the IP mode.
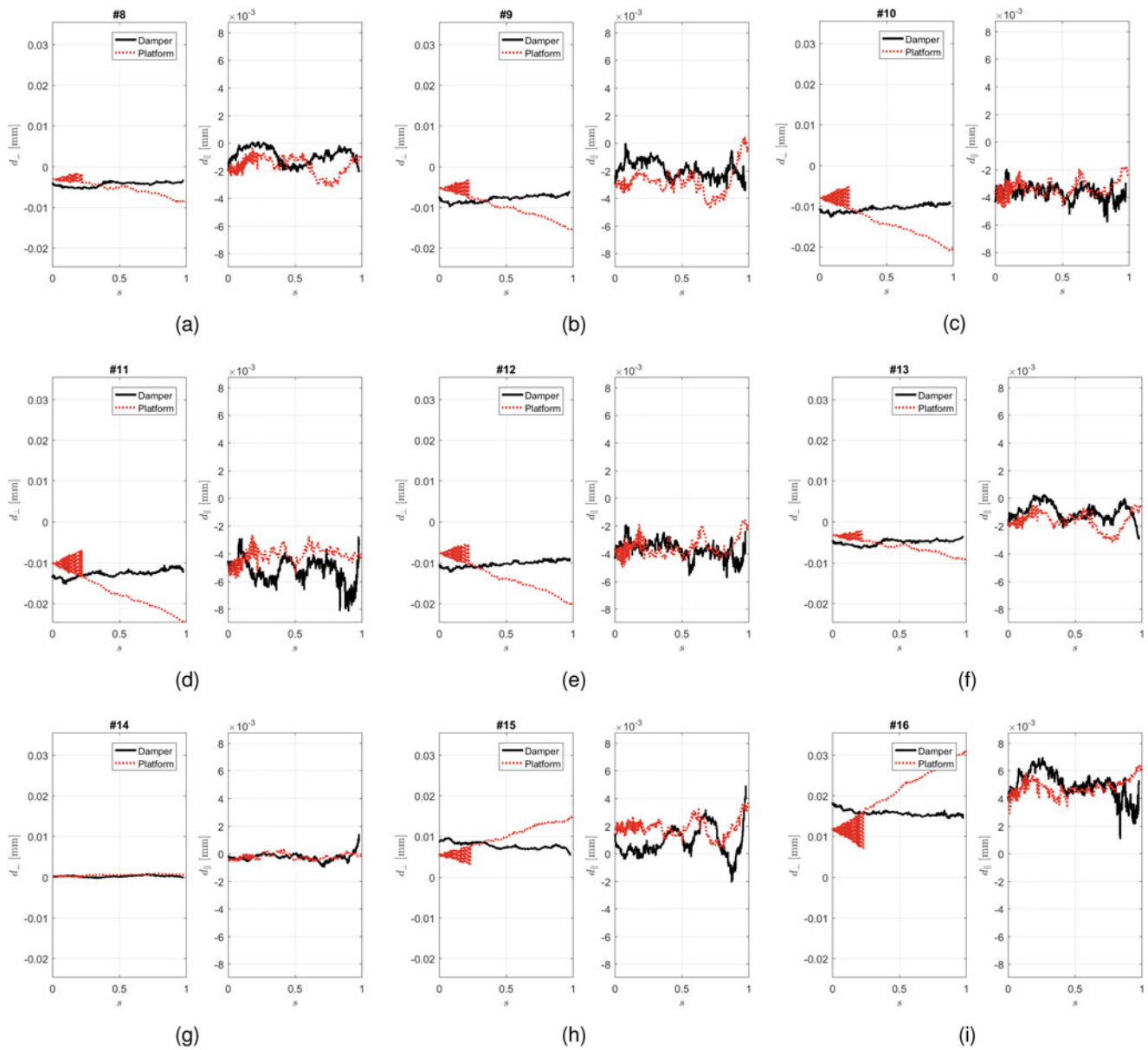
Fig. 9.9 DIC visualization of subsequent frames of the left contact displacement for both damper and platform, IP mode

9.5 Conclusions

In this study, a high-speed camera set-up in combination with a DIC analysis was applied to a recently developed underplatform damper test rig to obtain a more detailed understanding of the global and local motion of the system. The nonlinear response for the first flexural in-phase (IP) and out-of-phase (OOP) mode were measured, highlighting that at high amplitudes there was significant energy dissipation for the OOP mode and a strong softening with jumps for the IP mode.

An initial DIC analysis was focused on measuring the ODS of the two blades to gain an understanding of the change in the blade motion caused by the presence of the damper. The IP mode only showed a small change in the ODS, but the OOP was significantly altered with much less motion close to the root, and a strong curvature near the damper location, indicating a strong restraint from the damper.

Focusing the DIC analysis on the damper itself highlighted a pure damper translation for the OOP mode and a rotation for the IP mode. Zooming in even further on the contact interface, and tracking its motion during a vibration cycle, it was

possible to identify the different phases of stick-slip and separation which occurred in the μm range. The most evident aspects observed were a strong separation for large part of the contact area in the IP mode, and macroslip in the OOP mode.

The high speed camera in combination with DIC post-processing proved to be a powerful tool to understand more closely the local mechanisms which are responsible for the nonlinear dynamics of turbine blades constrained by friction dampers. Therefore, DIC methods offer great opportunities for the validation of numerical simulation results as complete displacement fields can be obtained, and are a welcome extension in the tool set to investigate the nonlinear behaviour of joints.

References

1. Cowles, B.A.: High cycle fatigue in aircraft gas turbine – an industry prospective. Int. J. Fract. **80**, 147–163 (1996)
2. Griffin, J.H.: A review of friction damping of turbine blade vibration. Int. J. Turbo Jet Engines **7**, 297–307 (1990)
3. Sanliturk, K.Y., Ewins, D.J., Stanbridge, A.B.: Underplatform dampers for turbine blades: theoretical modeling, analysis, and comparison with experimental data. J. Eng. Gas Turbines Power **123**(4), 919 (2001)
4. Sanliturk, K.Y., Ewins, D.J., Elliott, R., Green, J.S.: Friction damper optimization: simulation of rainbow tests. J. Eng. Gas Turbines Power **123**(4), 930 (2001)
5. Panning, L., Sextro, W., Popp, K.: Optimization of interblade friction damper design. In: Proceedings of ASME TURBOEXPO, pp. 1–8 (2000)
6. Pfeiffer, F., Hajek, M.: Stick-slip motion of turbine blade dampers. Philos. Trans. R. Soc. Lond. A **338**, 503–517 (1992)
7. Firrone, C.M.: Measurement of the kinematics of two underplatform dampers with different geometry and comparison with numerical simulation. J. Sound Vib. **323**(1–2), 313–333 (2009)
8. Pesaresi, L., Salles, L., Elliot, R., Jones, A., Green, J.S., Schwingshackl, C.W.: Numerical and experimental investigation of an underplatform damper test rig. Appl. Mech. Mater. **849**(1–12), 10 (2016)
9. Pesaresi, L., Salles, L., Jones, A., Green, J., Schwingshackl, C.: Modelling the nonlinear behaviour of an underplatform damper test rig for turbine applications. Mech. Syst. Signal Process. **85**, 662–679 (2017)
10. Blaber, J., Adair, B., Antoniou, A.: Ncorr: open-source 2D digital image correlation Matlab software. Exp. Mech. **55**(6), 1105–1122 (2015)

Chapter 10
A Simultaneous Iterative Scheme for the Craig-Bampton Reduction Based Substructuring

Jie Cui, Jianwei Xing, Xing Wang, Yunjie Wang, Shijie Zhu, and Gangtie Zheng

Abstract A simultaneous iterative procedure for the fixed-interface component modal synthesis (CMS) method is developed in this paper toward fast calculating the modal parameters and ROM of a large-scale and/or complicated structure. Different from existing iterative fixed-interface CMS methods, in the proposed iterative scheme, an eigenvalue independent matrix, whose columns' projections in the exact reduced space are the global eigenvectors of interest, is chosen as the iterative term and then used as a Ritz basis to generate reduced system matrices. Consequently, all the required modes can be solved simultaneously and a ROM can be derived after one round of iterations. For reference, an implementation is given together with computational considerations. Compared with other methods for solving modal parameters and/or model order reduction, the proposed method has such merits as high computational efficiency, especially for reanalysis tasks and parallel programming. A numerical example is provided to illustrate and validate the proposed method.

Keywords Component modal synthesis • Substructure • Simultaneous iterative procedure • Model order reduction • Craig-Bampton method

10.1 Introduction

Efficiently calculating high precision modal parameters and/or reduce-order models (ROMs) of large-scale and/or complicated structures, for instance the civil and aerospace engineering structures [1–4], are receiving more attentions in the optimal design, model modification and updating tasks [5–7]. Among the existing solution techniques, component modal synthesis (CMS) [8, 9] is a well-known method addressing such problems. By analyzing a global structure at its component level, the CMS method can significantly reduce the computational cost of an analysis process, especially for reanalysis problems and parallel computing, and thus can be attractive to the engineers.

Historically, the CMS method was firstly developed by Hurty in the 1960s [10, 11], where the dynamic properties of components are approximated via their lower modes. Then, extra mode bases, specifically the static constrained modes and residual flexible modes, corresponding to the well-known "fixed-interface" [12] and "free-interface" [13] CMS methods respectively, were added to the original low-order modal basis for truncation compensation. In practice, the fixed-interface CMS method, or the Craig-Bampton (C-B) method, is more popular and widely used due to its simplicity and robustness, especially for obtaining the ROM, and thus will be focused in this paper. Developments in decades for improving the performance of C-B type methods can be summarized with reference to the method for truncation compensation, specifically the approximation based [14] and iterated [15] method. Besides, the C-B method can be generalized to the automated multilevel substructuring (AMLS) method [16] by applying modal truncation on the junction parts between components and generalizing the concept of component partitioning. Notice that the C-B method has a close relationship with the dynamic condensation (DC) based substructuring method [17, 18], since both of them assemble the components in the primal form. Based on this relationship, ideas of these two kinds of methods can be compared and unitized reciprocally. For example,

J. Cui • Y. Wang • S. Zhu • G. Zheng (✉)
School of Aerospace Engineering, Tsinghua University, 100084, Beijing, China
e-mail: j-cui12@mails.tsinghua.edu.cn; gtzheng@mail.tsinghua.edu.cn

J. Xing
Beijing Institute of Space Launch Technology, 100076, Beijing, China

X. Wang
Department of Mechanical Engineering, University of Bristol, BS8 1TR, Bristol, UK

both Qiu's iterative C-B (ICB) method [15] and Friswell's iterated improved reduced system (IIRS) method [19] solve the nonlinear reduced eigen-equaiton iteratively; Kim and Lee [20] employed the O'Callahan's idea [21] to improve the classic C-B method.

Nevertheless, for the case that high precision modal parameters and ROMs are required, all the existing C-B type methods have their own shortcomings and thus may not be the most appropriate choice. For the approximated methods, truncation errors exist in the final results and thus more component modes should be kept for highly accurate results. However, the computational cost of solving component level eigen-problems, which usually cost the most of the CPU time in a CMS method, will be heavily increased correspondingly and the order of the ROM will be higher as well [22, 23]. For the iterative methods, the precision of modes has to be improved one by one and a linear ROM is not available as a result of the eigenvalue dependent reduced mass matrix, which can largely increase the computational burden when the global dynamic properties are of interest in a relatively wider frequency band. In general, it may still be necessary to improve the C-B type CMS method for enhancing the efficiency.

In this paper, a new iteration scheme with complete theoretical frameworks is developed for the C-B type CMS method, which employs the idea of Friswell for improving the IIRS method [30] and can be treated as an extension of the previous simultaneous iterative procedure for the free-interface CMS approach [23]. In this iteration scheme, an eigenvalue independent matrix, whose column projections in the exact reduced space are the interested global eigenvectors, is chosen as the iterative term and then used as a Ritz basis to generate the reduced system matrices. Therefore, all the interested modes can be solved simultaneously and a linear ROM can be derived after one round of iterations. Furthermore, an expansion formula of the iterative term is developed based on the series expansion of the component receptance matrices. Consequently, by decomposing the components' constrained stiffness matrices during the initializing, only the forward and back substitution processes are needed to update the iterative term in each iteration step. Then, an implementation is given for reference together with some computational considerations. Finally, a simple numerical example is presented to illustrate the method and validate its precision and convergence.

The remainder of this paper is organized as follows: Sect. 10.2 defines the problem of C-B reduction, briefly reviews the conventional iterated C-B method and presents the proposed method together with implementation issues. Section 10.3 presents a numerical example to briefly illustrate and validate the proposed method. Finally, conclusions and future works are summarized in Sect. 10.4.

10.2 The Simultaneous Iterated C-B Substructuring

10.2.1 Primal Assembly and C-B Reduction

In this paper, the scope is limited to the eigen-problem of a $\bar{N}$-DoFs global structure consisting of n components, where the over-bar indicates that the term below is associated with the global structure. The mass and stiffness matrices of the jth ($j = 1, 2, \ldots, n$) component with $N^{(j)}$ DoFs are denoted by $\mathbf{M}^{(j)}$ and $\mathbf{K}^{(j)}$, respectively. In addition, the system matrices of the components can be partitioned with respect to the interior and boundary DoFs as[1]

$$\mathbf{K}^{(j)} \triangleq \begin{bmatrix} \mathbf{K}_i^{(j)} & \mathbf{K}_c^{(j)} \\ \left(\mathbf{K}_c^{(j)}\right)^{\mathrm{T}} & \mathbf{K}_b^{(j)} \end{bmatrix}, \mathbf{M}^{(j)} \triangleq \begin{bmatrix} \mathbf{M}_i^{(j)} & \mathbf{M}_c^{(j)} \\ \left(\mathbf{M}_c^{(j)}\right)^{\mathrm{T}} & \mathbf{M}_b^{(j)} \end{bmatrix} \tag{10.1}$$

where the subscripts "i","c" and "d" indicate the interior, coupling and boundary DoFs, respectively. Then, the primly assembled eigen-equations of the global structure can be expressed as

$$\left(\bar{\mathbf{K}} - \bar{\lambda}_k \bar{\mathbf{M}}\right) \bar{\boldsymbol{\phi}}_k = \mathbf{0} \tag{10.2}$$

for $k = 1, 2, \ldots, \bar{N}$, where

---

[1]Throughout this paper, matrices, column vectors, variables and functions and scripts are denoted by bold, bold and italic, italic and roman letters, respectively.

$$\bar{\mathbf{K}} \triangleq \begin{bmatrix} \bar{\mathbf{K}}_{\mathrm{i}} & \bar{\mathbf{K}}_{\mathrm{c}} \\ (\bar{\mathbf{K}}_{\mathrm{c}})^{\mathrm{T}} & \bar{\mathbf{K}}_{\mathrm{b}} \end{bmatrix}, \bar{\mathbf{M}} \triangleq \begin{bmatrix} \bar{\mathbf{M}}_{\mathrm{i}} & \bar{\mathbf{M}}_{\mathrm{c}} \\ (\bar{\mathbf{M}}_{\mathrm{c}})^{\mathrm{T}} & \bar{\mathbf{M}}_{\mathrm{b}} \end{bmatrix}$$

$$\bar{\mathbf{K}}_{\mathrm{i}} \triangleq \mathrm{diag}\left(\mathbf{K}_{\mathrm{i}}^{(1)}, \mathbf{K}_{\mathrm{i}}^{(2)}, \cdots, \mathbf{K}_{\mathrm{i}}^{(n)}\right), \bar{\mathbf{M}}_{\mathrm{i}} \triangleq \mathrm{diag}\left(\mathbf{M}_{\mathrm{i}}^{(1)}, \mathbf{M}_{\mathrm{i}}^{(2)}, \cdots, \mathbf{M}_{\mathrm{i}}^{(n)}\right)$$

$$\bar{\mathbf{K}}_{\mathrm{c}} \triangleq \left[(\mathbf{K}_{\mathrm{c}}^{(1)}\mathbf{L}_{\mathrm{b}}^{(1)})^{\mathrm{T}}, (\mathbf{K}_{\mathrm{c}}^{(2)}\mathbf{L}_{\mathrm{b}}^{(2)})^{\mathrm{T}}, \cdots, (\mathbf{K}_{\mathrm{c}}^{(n)}\mathbf{L}_{\mathrm{b}}^{(n)})^{\mathrm{T}} \right]^{\mathrm{T}}, \bar{\mathbf{M}}_{\mathrm{c}} \triangleq \left[(\mathbf{M}_{\mathrm{c}}^{(1)}\mathbf{L}_{\mathrm{b}}^{(1)})^{\mathrm{T}}, (\mathbf{M}_{\mathrm{c}}^{(2)}\mathbf{L}_{\mathrm{b}}^{(2)})^{\mathrm{T}}, \cdots, (\mathbf{M}_{\mathrm{c}}^{(n)}\mathbf{L}_{\mathrm{b}}^{(n)})^{\mathrm{T}} \right]^{\mathrm{T}} \qquad (10.3)$$

$$\bar{\mathbf{K}}_{\mathrm{b}} \triangleq \sum_{j=1}^{n} (\mathbf{L}_{\mathrm{b}}^{(j)})^{\mathrm{T}}\mathbf{K}_{\mathrm{b}}^{(j)}\mathbf{L}_{\mathrm{b}}^{(j)}, \bar{\mathbf{M}}_{\mathrm{b}} \triangleq \sum_{j=1}^{n} (\mathbf{L}_{\mathrm{b}}^{(j)})^{\mathrm{T}}\mathbf{M}_{\mathrm{b}}^{(j)}\mathbf{L}_{\mathrm{b}}^{(j)}$$

$$\bar{\boldsymbol{\phi}}_k \triangleq \left[\bar{\boldsymbol{\phi}}_{\mathrm{i},k}^{\mathrm{T}}, \bar{\boldsymbol{\phi}}_{\mathrm{b},k}^{\mathrm{T}} \right]^{\mathrm{T}}, \bar{\boldsymbol{\phi}}_{\mathrm{i},k} \triangleq \left[(\bar{\boldsymbol{\phi}}_{\mathrm{i},k}^{(1)})^{\mathrm{T}}, (\bar{\boldsymbol{\phi}}_{\mathrm{i},k}^{(2)})^{\mathrm{T}}, \cdots, (\bar{\boldsymbol{\phi}}_{\mathrm{i},k}^{(n)})^{\mathrm{T}} \right]^{\mathrm{T}}$$

Here, $\mathbf{L}_{\mathrm{b}}^{(j)}$ is a Boolean localization matrix relating assembled boundary DoFs to the jth component's boundary DoFs [9].

To reduce the eigen-problem defined by equation (10.2), one can express $\bar{\boldsymbol{\phi}}_{\mathrm{i},k}$ in terms of $\bar{\boldsymbol{\phi}}_{\mathrm{b},k}$ by

$$\bar{\boldsymbol{\phi}}_{\mathrm{i},k} = \underline{\mathbf{T}}_{\mathrm{ib},k}\bar{\boldsymbol{\phi}}_{\mathrm{b},k} \qquad (10.4)$$

where

$$\underline{\mathbf{T}}_{\mathrm{ib},k} \triangleq (\bar{\mathbf{K}}_{\mathrm{i}} - \bar{\lambda}_k\bar{\mathbf{M}}_{\mathrm{i}})^{-1} (\bar{\mathbf{K}}_{\mathrm{c}} - \bar{\lambda}_k\bar{\mathbf{M}}_{\mathrm{c}}) = \bar{\mathbf{K}}_{\mathrm{i}}^{-1}\bar{\mathbf{K}}_{\mathrm{c}} + \bar{\lambda}_k\bar{\mathbf{K}}_{\mathrm{i}}^{-1} (\bar{\mathbf{M}}_{\mathrm{i}}\underline{\mathbf{T}}_{\mathrm{ib},k} - \bar{\mathbf{M}}_{\mathrm{c}}) \qquad (10.5)$$

represents the transmissibility of interior DoFs to boundary DoFs at $\bar{\lambda}_k$ and the underline together with the index k indicates the term depends on the global eigenvalue $\bar{\lambda}_k$. A ROM and lower global eigen-pairs can be obtained by solving $\underline{\mathbf{T}}_{\mathrm{ib},k}$ exactly via a DC based method, in which an iterative solution scheme is usually required as $\underline{\mathbf{T}}_{\mathrm{ib},k}$ is eigenvalue dependent.

Notice that the transformation in equation (10.4) can be expressed in an alternative way as

$$\bar{\boldsymbol{\phi}}_{\mathrm{i},k} = \underline{\mathbf{T}}_{\mathrm{ib},k}\bar{\boldsymbol{\phi}}_{\mathrm{b},k} = \bar{\mathbf{K}}_{\mathrm{i}}^{-1}\bar{\mathbf{K}}_{\mathrm{c}}\bar{\boldsymbol{\phi}}_{\mathrm{b},k} + \bar{\lambda}_k\bar{\mathbf{K}}_{\mathrm{i}}^{-1} (\bar{\mathbf{M}}_{\mathrm{i}}\underline{\mathbf{T}}_{\mathrm{ib},k} - \bar{\mathbf{M}}_{\mathrm{c}}) \bar{\boldsymbol{\phi}}_{\mathrm{b},k} \triangleq \bar{\mathbf{K}}_{\mathrm{i}}^{-1}\bar{\mathbf{K}}_{\mathrm{c}}\bar{\boldsymbol{\phi}}_{\mathrm{b},k} + \boldsymbol{q}_k \qquad (10.6)$$

The corresponding reduced eigen-equation is

$$\begin{bmatrix} \mathbf{k}_{\mathrm{i}} - \bar{\lambda}_k\mathbf{m}_{\mathrm{i}} & -\bar{\lambda}_k\mathbf{m}_{\mathrm{c}} \\ -\bar{\lambda}_k\mathbf{m}_{\mathrm{c}}^{\mathrm{T}} & \mathbf{k}_{\mathrm{b}} - \bar{\lambda}_k\mathbf{m}_{\mathrm{b}} \end{bmatrix} \begin{Bmatrix} \boldsymbol{q}_k \\ \bar{\boldsymbol{\phi}}_{\mathrm{b},k} \end{Bmatrix} = \begin{Bmatrix} \mathbf{0} \\ \mathbf{0} \end{Bmatrix} \qquad (10.7)$$

with

$$\mathbf{k}_{\mathrm{i}} \triangleq \bar{\mathbf{K}}_{\mathrm{i}}, \mathbf{m}_{\mathrm{i}} \triangleq \bar{\mathbf{M}}_{\mathrm{i}}$$

$$\mathbf{k}_{\mathrm{b}} \triangleq \bar{\mathbf{K}}_{\mathrm{b}} - \bar{\mathbf{K}}_{\mathrm{c}}^{\mathrm{T}}\bar{\mathbf{K}}_{\mathrm{i}}^{-1}\bar{\mathbf{K}}_{\mathrm{c}}, \mathbf{m}_{\mathrm{c}} \triangleq \bar{\mathbf{M}}_{\mathrm{c}} - \bar{\mathbf{M}}_{\mathrm{i}}^{\mathrm{T}}\bar{\mathbf{K}}_{\mathrm{i}}^{-1}\bar{\mathbf{K}}_{\mathrm{c}} \qquad (10.8)$$

$$\mathbf{m}_{\mathrm{b}} \triangleq \bar{\mathbf{M}}_{\mathrm{b}} - \bar{\mathbf{M}}_{\mathrm{c}}^{\mathrm{T}}\bar{\mathbf{K}}_{\mathrm{i}}^{-1}\bar{\mathbf{K}}_{\mathrm{c}} - \bar{\mathbf{K}}_{\mathrm{c}}^{\mathrm{T}}\bar{\mathbf{K}}_{\mathrm{i}}^{-1}\bar{\mathbf{M}}_{\mathrm{c}} + \bar{\mathbf{K}}_{\mathrm{c}}^{\mathrm{T}}\bar{\mathbf{K}}_{\mathrm{i}}^{-1}\bar{\mathbf{M}}_{\mathrm{c}}^{\mathrm{T}}\bar{\mathbf{K}}_{\mathrm{i}}^{-1}\bar{\mathbf{K}}_{\mathrm{c}}$$

From equations (10.7) and (10.3), we know that this transformation make $\bar{\mathbf{K}}$ block diagonal via Gaussian elimination and thus the reduced model in equation (10.7) is exact. Nevertheless, compared with the ROM from the transformation of equation (10.4), the size is largely increased, although the reduced eigen-equation is linear.

To solve this problem, the contributions of the high-order term, i.e. $\boldsymbol{q}_k$, can be considered in a certain frequency band. In the C-B method, this certain frequency band is usually the lower interested frequency band, i.e., assuming

$$\boldsymbol{q}_k = \boldsymbol{\Phi}_{\mathrm{L}}\boldsymbol{\psi}_k + \boldsymbol{\Phi}_{\mathrm{H}}\boldsymbol{\eta}_k \approx \boldsymbol{\Phi}_{\mathrm{L}}\boldsymbol{\psi}_k \qquad (10.9)$$

where $\boldsymbol{\psi}_k$ and $\boldsymbol{\eta}_k$ are the coordinate vectors of $\boldsymbol{q}_k$ in the space spanned by $\boldsymbol{\Phi}_{\mathrm{L}}$ and $\boldsymbol{\Phi}_{\mathrm{H}}$, respectively; $(\boldsymbol{\Phi}_{\mathrm{L}}, \boldsymbol{\Lambda}_{\mathrm{L}})$ and $(\boldsymbol{\Phi}_{\mathrm{H}}, \boldsymbol{\Lambda}_{\mathrm{H}})$ are the lower and higher eigen-pair matrices of the matrix pencil $(\bar{\mathbf{K}}_{\mathrm{i}}, \bar{\mathbf{M}}_{\mathrm{i}})$ with mass-orthogonality; the subscripts "L" and "H" indicate those terms belong to the low-order (kept) and high-order (omitted) modes group, respectively. With the consideration of equations (10.6) and (10.9), the reduced system matrices of the C-B method are

$$\mathbf{K}_{\text{CB}} \triangleq \mathbf{T}_{\text{CB}}^{\text{T}} \bar{\mathbf{K}} \mathbf{T}_{\text{CB}}, \mathbf{M}_{\text{CB}} \triangleq \mathbf{T}_{\text{CB}}^{\text{T}} \bar{\mathbf{M}} \mathbf{T}_{\text{CB}} \tag{10.10}$$

with

$$\begin{Bmatrix} \bar{\boldsymbol{\phi}}_{\text{i},k} \\ \bar{\boldsymbol{\phi}}_{\text{b},k} \end{Bmatrix} = \begin{bmatrix} \boldsymbol{\Phi}_{\text{L}} & \bar{\mathbf{K}}_{\text{i}}^{-1}\bar{\mathbf{K}}_{\text{c}} \\ \mathbf{0} & \mathbf{I}_{\text{b}} \end{bmatrix} \begin{Bmatrix} \boldsymbol{\psi}_k \\ \bar{\boldsymbol{\phi}}_{\text{b},k} \end{Bmatrix} \triangleq \mathbf{T}_{\text{CB}} \boldsymbol{p}_{\text{CB},k} \tag{10.11}$$

Specifically, in equation (10.11), $k = 1, 2, \ldots, n_{\text{CB}}$, where n_{CB} is the dimension of system $(\mathbf{K}_{\text{CB}}, \mathbf{M}_{\text{CB}})$ (or the number of elements of the generalized coordinate vector $\boldsymbol{p}_{\text{CB},k}$) and the subscript "CB" denotes the C-B method. For simplicity, k varies from 1 to n_{CB}, and j varies from 1 to n in the followings of this paper without particular specifications.

In general, the C-B method has a close relationship with the DC method. Instead of compensating the truncation effect $\bar{\lambda}_k \bar{\mathbf{K}}_{\text{i}}^{-1} (\bar{\mathbf{M}}_{\text{i}} \underline{\mathbf{T}}_{\text{ib},k} - \bar{\mathbf{M}}_{\text{c}}) \bar{\boldsymbol{\phi}}_{\text{b},k}$ approximately or iteratively, an additional basis, the components' constrained modes, is employed for compensation. This can lead to a simpler but more reliable criterion for the selection of generalized coordinates since all the approximations are included via the modal truncation in equation (10.9), which can be controlled by adjusting the truncation frequency of the component constrained modes. This criterion can be attractive to the engineers, since an appropriate choice of master DoFs, which largely decides both the precision and convergence of DC methods, may not be easy to find for a large-scale and/or complicated structure. The trade-offs of the C-B method mainly lie in the increment of the size of the final ROM, which will increase the computational burden and may become a serious problem as the precision requirement become stringent, since much more constrained component modes have to be included in such case. The iterative method developed by Qiu could be a solution, which will be reviewed in the next subsection.

10.2.2 Exact Reduced Eigen-Equation of C-B Methods

The exact reduced eigen-equation of the C-B method can be started by omitting the approximation in equation (10.9), i.e. let $\boldsymbol{q}_k = \boldsymbol{\Phi}_{\text{L}} \boldsymbol{\psi}_k + \boldsymbol{\Phi}_{\text{H}} \boldsymbol{\eta}_k$. Substituting this transformation into equation (10.7) yields

$$\begin{bmatrix} \boldsymbol{\Lambda}_{\text{L}} - \bar{\lambda}_k \mathbf{I}_{\text{L}} & \mathbf{0} & -\bar{\lambda}_k \boldsymbol{\Phi}_{\text{L}}^{\text{T}} \mathbf{m}_{\text{c}} \\ \mathbf{0} & \boldsymbol{\Lambda}_{\text{H}} - \bar{\lambda}_k \mathbf{I}_{\text{H}} & -\bar{\lambda}_k \boldsymbol{\Phi}_{\text{H}}^{\text{T}} \mathbf{m}_{\text{c}} \\ -\bar{\lambda}_k \mathbf{m}_{\text{c}}^{\text{T}} \boldsymbol{\Phi}_{\text{L}} & -\bar{\lambda}_k \mathbf{m}_{\text{c}}^{\text{T}} \boldsymbol{\Phi}_{\text{H}} & \mathbf{k}_{\text{b}} - \bar{\lambda}_k \mathbf{m}_{\text{b}} \end{bmatrix} \begin{Bmatrix} \boldsymbol{\psi}_k \\ \boldsymbol{\eta}_k \\ \bar{\boldsymbol{\phi}}_{\text{b},k} \end{Bmatrix} = \begin{Bmatrix} \mathbf{0} \\ \mathbf{0} \\ \mathbf{0} \end{Bmatrix} \tag{10.12}$$

From the second line of equation (10.12), one can have

$$\boldsymbol{\eta}_k = (\boldsymbol{\Lambda}_{\text{H}} - \bar{\lambda}_k \mathbf{I}_{\text{H}})^{-1} \boldsymbol{\Phi}_{\text{H}}^{\text{T}} \mathbf{m}_c \bar{\boldsymbol{\phi}}_{\text{b},k} \tag{10.13}$$

Substituting equation (10.13) back into equation (10.12) gives

$$\begin{bmatrix} \boldsymbol{\Lambda}_{\text{L}} - \bar{\lambda}_k \mathbf{I}_{\text{L}} & -\bar{\lambda}_k \boldsymbol{\Phi}_{\text{L}}^{\text{T}} \mathbf{m}_{\text{c}} \\ -\bar{\lambda}_k \mathbf{m}_{\text{c}}^{\text{T}} \boldsymbol{\Phi}_{\text{L}} & \mathbf{k}_{\text{b}} - \bar{\lambda}_k \mathbf{m}_{\text{b}} - \bar{\lambda}_k^2 \mathbf{m}_{\text{c}}^{\text{T}} \underline{\mathbf{X}}_k \mathbf{m}_{\text{c}} \end{bmatrix} \begin{Bmatrix} \boldsymbol{\psi}_k \\ \bar{\boldsymbol{\phi}}_{\text{b},k} \end{Bmatrix} = \begin{Bmatrix} \mathbf{0} \\ \mathbf{0} \end{Bmatrix} \tag{10.14}$$

where

$$\underline{\mathbf{X}}_k \triangleq \boldsymbol{\Phi}_{\text{H}} (\boldsymbol{\Lambda}_{\text{H}} - \bar{\lambda}_k \mathbf{I}_{\text{H}})^{-1} \boldsymbol{\Phi}_{\text{H}}^{\text{T}} \tag{10.15}$$

represents the transmissibility of truncated constrained component modes at $\bar{\lambda}_k$. Besides, the exact transformation matrix of equation (10.14) is

$$\underline{\mathbf{T}}_k \triangleq \mathbf{T}_{\text{CB}} + \bar{\lambda}_k \begin{bmatrix} \mathbf{0} & \underline{\mathbf{X}}_k \mathbf{m}_{\text{c}} \\ \mathbf{0} & \mathbf{0} \end{bmatrix} \triangleq \mathbf{T}_{\text{CB}} + \underline{\mathbf{t}}_k \tag{10.16}$$

from equations (10.6), (10.9) and (10.13). Therefore, the global eigenvectors $\bar{\boldsymbol{\phi}}_k$ can be recovered from the reduced eigenpairs $(\bar{\lambda}_k, \boldsymbol{\psi}_k)$ by

$$\bar{\boldsymbol{\phi}}_k = \underline{\mathbf{T}}_k \left\{ \begin{matrix} \boldsymbol{\psi}_k \\ \bar{\boldsymbol{\phi}}_{\mathrm{b},k} \end{matrix} \right\} \triangleq \underline{\mathbf{T}}_k \boldsymbol{p}_k \tag{10.17}$$

Equation (10.14) is an exact reduced eigen-equation of the C-B substructuring method. Notice that equation (10.14) is nonlinear as it contains an eigenvalue dependent term $\underline{\mathbf{X}}_k$, and thus an iterative procedure is required if the exact solutions are required for a general large-scale and/or complicated structure. Here, for reference and comparison, we briefly list the solution procedure derived by Qiu.

Firstly, rewrite equation (10.14) as

$$\left[\mathbf{K}_{\mathrm{CB}} - \bar{\lambda}_k \left(\mathbf{M}_{\mathrm{CB}} + \bar{\lambda}_k \begin{bmatrix} \mathbf{0} & \mathbf{0} \\ \mathbf{0} & \mathbf{m}_{\mathrm{c}}^{\mathrm{T}} \underline{\mathbf{X}}_k \mathbf{m}_{\mathrm{c}} \end{bmatrix} \right) \right] \boldsymbol{p}_k = \mathbf{0} \tag{10.18}$$

Then, the reduced eigen-pairs can be solved iteratively by evaluating

$$\underline{\mathbf{X}}_k^{[i]} \triangleq \boldsymbol{\Phi}_{\mathrm{H}} \left(\boldsymbol{\Lambda}_{\mathrm{H}} - \bar{\lambda}_k^{[i]} \mathbf{I}_{\mathrm{H}} \right)^{-1} \boldsymbol{\Phi}_{\mathrm{H}}^{\mathrm{T}} \tag{10.19}$$

and solving the eigen-problem

$$\mathbf{K}_{\mathrm{CB}} \boldsymbol{p}_k^{[i]} = \bar{\lambda}_k^{[i]} \left(\mathbf{M}_{\mathrm{CB}} + \bar{\lambda}_k^{[i-1]} \begin{bmatrix} \mathbf{0} & \mathbf{0} \\ \mathbf{0} & \mathbf{m}_{\mathrm{c}}^{\mathrm{T}} \underline{\mathbf{X}}_k^{[i-1]} \mathbf{m}_{\mathrm{c}} \end{bmatrix} \right) \boldsymbol{p}_k^{[i]} \tag{10.20}$$

for $i = 1, 2, \ldots$ with $\bar{\lambda}_k^{[0]} \triangleq 0$. Assuming that the kth reduced eigen-pair converges after the ith iteration, the kth global eigenvector can be recovered by

$$\bar{\boldsymbol{\phi}}_k^{[i]} = \left(\mathbf{T}_{\mathrm{CB}} + \bar{\lambda}_k^{[i]} \begin{bmatrix} \mathbf{0} & \underline{\mathbf{X}}_k^{[i]} \mathbf{m}_{\mathrm{c}} \\ \mathbf{0} & \mathbf{0} \end{bmatrix} \right) \boldsymbol{p}_k^{[i]} \tag{10.21}$$

In this approach, the iterative process also has to be performed mode by mode as $\underline{\mathbf{X}}_k^{[i]}$ varies from mode to mode. Therefore, the computational efficiency could be raised if the precision of all the interested modes can be simultaneously improved in a single round of iterations. From this point of view, a new iterative procedure will be developed in the following subsection.

10.2.3   Procedure of Simultaneous Iterative Method

The simultaneous iterative procedure, developed in Ref. [23] for solving exact reduced eigen-equation Equation of the free-interface CMS method, will be applied to the C-B method, i.e. the solution of equation (10.14) in this subsection. In general, the simultaneous iterative procedure is based on the fact that the exact reduced eigen-equation (10.14) is eigenvalue dependent as a result of its corresponding eigenvalue dependent transformation matrix $\underline{\mathbf{T}}_k$, defined in equation (10.16), and only "$\underline{\mathbf{T}}_k \boldsymbol{p}_k$", a n_{CB}-dimensional vector, instead of the $\bar{N} \times n_{\mathrm{CB}}$ matrix "$\underline{\mathbf{T}}_k$", is indispensable to recover the kth global eigenvector. Therefore, the new iterative scheme can be started by using an eigenvalue independent matrix, denoted by $\mathbf{T}_{\mathrm{S}}$, as a transformation matrix (reduction basis) to construct the space spanned by all the reduced eigen-pairs $(\bar{\lambda}_k, \boldsymbol{p}_k)$. Here, the subscript "S" denotes the simultaneous iterative procedure. Specifically, $\mathbf{T}_{\mathrm{S}}$ can be defined as follows.

Lemma 1. *There exists an eigenvalue independent matrix $\mathbf{T}_{\mathrm{S}}$ of size $\bar{N}$-by-n_{CB} such that*

$$\mathbf{T}_{\mathrm{S}} \boldsymbol{p}_k = \underline{\mathbf{T}}_k \boldsymbol{p}_k \tag{10.22}$$

Specifically, $\mathbf{T}_{\mathrm{S}}$ can be defined by

$$\mathbf{T}_{\mathrm{S}} \triangleq \begin{bmatrix} \underline{\mathbf{T}}_1 \boldsymbol{p}_1 & \underline{\mathbf{T}}_2 \boldsymbol{p}_2 & \ldots & \underline{\mathbf{T}}_{n_{\mathrm{CB}}} \boldsymbol{P}_{n_{\mathrm{CB}}} \end{bmatrix} \mathbf{P}_{\mathrm{S}}^{-1} \tag{10.23}$$

In equation (10.23), $\mathbf{P}_\mathrm{S} \triangleq \left[\boldsymbol{p}_1 \, \boldsymbol{p}_2 \ldots \boldsymbol{p}_{n_\mathrm{CB}} \right]$ *is a matrix form of the exact reduced eigenvectors and the corresponding eigenvalue matrix is* $\boldsymbol{\Lambda}_\mathrm{S} \triangleq \mathrm{diag}\left(\bar{\lambda}_1, \bar{\lambda}_2, \ldots, \bar{\lambda}_{n_\mathrm{CB}}\right)$.

Proof. Notice that all the exact reduced eigenvectors can construct a basis for the $\mathbb{R}^{n_\mathrm{CB}}$ space in a fixed-interface CMS method, i.e. $\mathbf{P}$ is invertible and thus $\mathbf{T}_\mathrm{S}$ exists. $\qquad\square$

Lemma 2. $\mathbf{P}_\mathrm{S}$ *and* $\boldsymbol{\Lambda}_\mathrm{S}$ *can satisfy*

$$\mathbf{K}_\mathrm{S}\mathbf{P}_\mathrm{S} = \mathbf{M}_\mathrm{S}\mathbf{P}_\mathrm{S}\boldsymbol{\Lambda}_\mathrm{S} \tag{10.24}$$

where

$$\mathbf{K}_\mathrm{S} \triangleq \mathbf{T}_\mathrm{S}^\mathrm{T}\bar{\mathbf{K}}\mathbf{T}_\mathrm{S}, \ \mathbf{M}_\mathrm{S} \triangleq \mathbf{T}_\mathrm{S}^\mathrm{T}\bar{\mathbf{M}}\mathbf{T}_\mathrm{S} \tag{10.25}$$

are the reduced stiffness and mass matrices corresponding to $\mathbf{T}_\mathrm{S}$.

Proof. Firstly, one can have the followings according to equations (10.8), (10.11), (10.15) and (10.16).

$$\mathbf{T}_\mathrm{CB}^\mathrm{T}\bar{\mathbf{K}}\underline{\mathbf{t}}_k = \bar{\lambda}_k \begin{bmatrix} \mathbf{0} & \boldsymbol{\Phi}_\mathrm{L}\bar{\mathbf{K}}_\mathrm{i}\underline{\mathbf{X}}_k\mathbf{m}_\mathrm{c} \\ \mathbf{0} & \mathbf{0} \end{bmatrix} = \mathbf{0}, \mathbf{T}_\mathrm{CB}^\mathrm{T}\bar{\mathbf{M}}\underline{\mathbf{t}}_k = \bar{\lambda}_k \begin{bmatrix} \mathbf{0} & \mathbf{0} \\ \mathbf{0} & \mathbf{m}_\mathrm{c}^\mathrm{T}\underline{\mathbf{X}}_k\mathbf{m}_\mathrm{c} \end{bmatrix}$$

$$\underline{\mathbf{t}}_r^\mathrm{T}\bar{\mathbf{K}}\underline{\mathbf{t}}_k = \bar{\lambda}_k^2 \begin{bmatrix} \mathbf{0} & \mathbf{0} \\ \mathbf{0} & \mathbf{m}_\mathrm{c}^\mathrm{T}\underline{\mathbf{X}}_r\bar{\mathbf{K}}_\mathrm{i}\underline{\mathbf{X}}_k\mathbf{m}_\mathrm{c} \end{bmatrix}, \underline{\mathbf{t}}_r^\mathrm{T}\bar{\mathbf{M}}\underline{\mathbf{t}}_k = \bar{\lambda}_k^2 \begin{bmatrix} \mathbf{0} & \mathbf{0} \\ \mathbf{0} & \mathbf{m}_\mathrm{c}^\mathrm{T}\underline{\mathbf{X}}_r\bar{\mathbf{M}}_\mathrm{i}\underline{\mathbf{X}}_k\mathbf{m}_\mathrm{c} \end{bmatrix} \tag{10.26}$$

for $r = 1, 2, \ldots, n_\mathrm{CB}$. Then, one can have

$$\begin{aligned}
&\underline{\mathbf{T}}_r^\mathrm{T}\bar{\mathbf{K}}\underline{\mathbf{T}}_k - \bar{\lambda}_k\underline{\mathbf{T}}_r^\mathrm{T}\bar{\mathbf{M}}\underline{\mathbf{T}}_k \\
&= \mathbf{K}_\mathrm{CB} - \bar{\lambda}_k\mathbf{M}_\mathrm{CB} - \bar{\lambda}_k^2 \begin{bmatrix} \mathbf{0} & \mathbf{0} \\ \mathbf{0} & 2\mathbf{m}_\mathrm{c}^\mathrm{T}\underline{\mathbf{X}}_k\mathbf{m}_\mathrm{c} - \mathbf{m}_\mathrm{c}^\mathrm{T}\underline{\mathbf{X}}_r\left(\bar{\mathbf{K}}_\mathrm{i} - \bar{\lambda}_k\bar{\mathbf{M}}_\mathrm{i}\right)\underline{\mathbf{X}}_k\mathbf{m}_\mathrm{c} \end{bmatrix} \\
&= \mathbf{K}_\mathrm{CB} - \bar{\lambda}_k\left(\mathbf{M}_\mathrm{CB} + \bar{\lambda}_k \begin{bmatrix} \mathbf{0} & \mathbf{0} \\ \mathbf{0} & \mathbf{m}_\mathrm{c}^\mathrm{T}\underline{\mathbf{X}}_k\mathbf{m}_\mathrm{c} \end{bmatrix}\right)
\end{aligned} \tag{10.27}$$

for $r = 1, 2, \ldots, n_\mathrm{CB}$. Therefore, with equations (10.18), (10.22), (10.25) and (10.27), one can have

$$\begin{aligned}
\boldsymbol{p}_r^\mathrm{T}\left(\mathbf{K}_\mathrm{S} - \bar{\lambda}_k\mathbf{M}_\mathrm{S}\right)\boldsymbol{p}_k &= \boldsymbol{p}_r^\mathrm{T}\mathbf{T}_\mathrm{S}^\mathrm{T}\left(\bar{\mathbf{K}} - \bar{\lambda}_k\bar{\mathbf{M}}\right)\mathbf{T}_\mathrm{S}\boldsymbol{p}_k \\
&= \boldsymbol{p}_r^\mathrm{T}\underline{\mathbf{T}}_r^\mathrm{T}\left(\bar{\mathbf{K}} - \bar{\lambda}_k\bar{\mathbf{M}}\right)\underline{\mathbf{T}}_k\boldsymbol{p}_k \\
&= \boldsymbol{p}_r^\mathrm{T}\left[\mathbf{K}_\mathrm{CB} - \bar{\lambda}_k\left(\mathbf{M}_\mathrm{CB} + \bar{\lambda}_k \begin{bmatrix} \mathbf{0} & \mathbf{0} \\ \mathbf{0} & \mathbf{m}_\mathrm{c}^\mathrm{T}\underline{\mathbf{X}}_k\mathbf{m}_\mathrm{c} \end{bmatrix}\right)\right]\boldsymbol{p}_k \\
&= 0
\end{aligned} \tag{10.28}$$

for $r = 1, 2, \ldots, n_\mathrm{KC}$, i.e. $\mathbf{P}_\mathrm{S}^\mathrm{T}\left(\mathbf{K}_\mathrm{S} - \bar{\lambda}_k\mathbf{M}_\mathrm{S}\right)\boldsymbol{p}_k = \mathbf{0}$. This can lead to $\left(\mathbf{K}_\mathrm{S} - \bar{\lambda}_k\mathbf{M}_\mathrm{S}\right)\boldsymbol{p}_k = \mathbf{0}$ as $\mathbf{P}_\mathrm{S}$ is a basis. $\qquad\square$

Remark 1. In Qiu's iterative method, solving equation (10.20) leads to n_CB vectors in total for a certain mode order k, but $(n_\mathrm{CB} - 1)$ of them are non-eigenvectors except for the one associated with $\bar{\lambda}_k$. In contrast, the proposed method only uses the eigenvectors to construct the reduced system, as shown by Lemma 2.

Nevertheless, equation (10.23) does not provide an efficient way of calculating $\mathbf{T}_\mathrm{S}$ in practice. Therefore, an iteration formula of $\mathbf{T}_\mathrm{S}$ will be developed, started by the identity equation of $\mathbf{T}_\mathrm{S}$ as follow.

Lemma 3. *The term* $\mathbf{T}_\mathrm{S}$ *can satisfy*

$$\mathbf{T}_\mathrm{S} = \mathbf{T}_\mathrm{CB} + \mathbf{S}_0\bar{\mathbf{M}}\mathbf{T}_\mathrm{S}\mathbf{M}_\mathrm{S}^{-1}\mathbf{K}_\mathrm{S} \tag{10.29}$$

where

$$\mathbf{F} \triangleq \boldsymbol{\Phi}_{\mathrm{H}} \boldsymbol{\Lambda}_{\mathrm{H}}^{-1} \boldsymbol{\Phi}_{\mathrm{H}}^{\mathrm{T}}$$

$$\mathbf{S}_0 \triangleq \begin{bmatrix} \mathbf{F} & \mathbf{0} \\ \mathbf{0} & \mathbf{0} \end{bmatrix} \qquad (10.30)$$

are the residual flexibility of the constraint components and projector of the simultaneous iterative procedure, respectively.

Proof. Notice that $\mathbf{F}$ can be expanded as

$$\underline{\mathbf{X}}_k = \mathbf{F} + \bar{\lambda}_k \mathbf{F} \bar{\mathbf{M}} \underline{\mathbf{X}}_k \qquad (10.31)$$

and thus one has

$$
\begin{aligned}
\underline{\mathbf{T}}_k &= \mathbf{T}_{\mathrm{CB}} + \bar{\lambda}_k \begin{bmatrix} \mathbf{0} & \left(\mathbf{F} + \bar{\lambda}_k \mathbf{F} \bar{\mathbf{M}} \underline{\mathbf{X}}_k \right) \mathbf{m}_{\mathrm{c}} \\ \mathbf{0} & \mathbf{0} \end{bmatrix} \\
&= \mathbf{T}_{\mathrm{CB}} + \bar{\lambda}_k \begin{bmatrix} \mathbf{0} & \mathbf{F} \mathbf{m}_{\mathrm{c}} \\ \mathbf{0} & \mathbf{0} \end{bmatrix} + \bar{\lambda}_k \mathbf{S}_0 \bar{\mathbf{M}} \underline{\mathbf{t}}_k \\
&= \mathbf{T}_{\mathrm{CB}} + \bar{\lambda}_k \mathbf{S}_0 \bar{\mathbf{M}} \left(\mathbf{T}_{\mathrm{CB}} + \underline{\mathbf{t}}_k \right) \\
&= \mathbf{T}_{\mathrm{CB}} + \bar{\lambda}_k \mathbf{S}_0 \bar{\mathbf{M}} \underline{\mathbf{T}}_k
\end{aligned} \qquad (10.32)
$$

with equations (10.16), (10.30) and (10.31) and the following relationship

$$\mathbf{S}_0 \bar{\mathbf{M}} \mathbf{T}_{\mathrm{CB}} = \begin{bmatrix} \mathbf{F} \bar{\mathbf{M}}_{\mathrm{i}} & \mathbf{F} \bar{\mathbf{M}}_{\mathrm{c}} \\ \mathbf{0} & \mathbf{0} \end{bmatrix} \begin{bmatrix} \boldsymbol{\Phi}_{\mathrm{L}} & \bar{\mathbf{K}}_{\mathrm{i}}^{-1} \bar{\mathbf{K}}_{\mathrm{c}} \\ \mathbf{0} & \mathbf{I}_{\mathrm{b}} \end{bmatrix} = \begin{bmatrix} \mathbf{0} & \mathbf{F} \mathbf{m}_{\mathrm{c}} \\ \mathbf{0} & \mathbf{0} \end{bmatrix} \qquad (10.33)$$

Then, with equation (10.23), post-multiplying both sides of equation (10.32) by $\boldsymbol{p}_k$ yields

$$\mathbf{T}_{\mathrm{S}} \boldsymbol{p}_k = \underline{\mathbf{T}}_k \boldsymbol{p}_k = \mathbf{T}_{\mathrm{CB}} \boldsymbol{p}_k + \bar{\lambda}_k \mathbf{S}_0 \bar{\mathbf{M}} \underline{\mathbf{T}}_k \boldsymbol{p}_k = \mathbf{T}_{\mathrm{CB}} \boldsymbol{p}_k + \bar{\lambda}_k \mathbf{S}_0 \bar{\mathbf{M}} \mathbf{T}_{\mathrm{S}} \boldsymbol{p}_k \qquad (10.34)$$

The matrix form of equation (10.34) is "$\mathbf{T}_{\mathrm{S}} \mathbf{P}_{\mathrm{S}} = \mathbf{T}_{\mathrm{CB}} \mathbf{P}_{\mathrm{S}} + \mathbf{S}_0 \bar{\mathbf{M}} \mathbf{T}_{\mathrm{S}} \mathbf{P}_{\mathrm{S}} \boldsymbol{\Lambda}_{\mathrm{S}}$", which is equivalent to

$$\mathbf{T}_{\mathrm{S}} \mathbf{P}_{\mathrm{S}} = \mathbf{T}_{\mathrm{CB}} \mathbf{P}_{\mathrm{S}} + \mathbf{S}_0 \bar{\mathbf{M}} \mathbf{T}_{\mathrm{S}} \mathbf{M}_{\mathrm{S}}^{-1} \mathbf{K}_{\mathrm{S}} \mathbf{P}_{\mathrm{S}} \qquad (10.35)$$

with the relationship "$\mathbf{P}_{\mathrm{S}} \boldsymbol{\Lambda}_{\mathrm{S}} = \mathbf{M}_{\mathrm{S}}^{-1} \mathbf{K}_{\mathrm{S}} \mathbf{P}_{\mathrm{S}}$" from equation (10.24). As $\mathbf{P}_{\mathrm{S}}$ is a basis of the reduced modal space, equation (10.35) is equivalent to equation (10.29). □

Finally, an algorithm of the simultaneous iterative procedure based C-B (SCB) method can be developed according to Lemmas 1, 2, and 3, as shown in Algorithm 1. Specifically, the maximum interested global eigenvalue is $\bar{\lambda}_{\max}$ and the precision requirement is *Tol*.

For Algorithm 1, some lines should be commented as follow.

(1a) The partitioning concept is not limited to the conventional substructuring method, that in other methods such as the (a) AMLS or (b) balanced domain decomposition methods can also considered and are clearly compatible with the proposed method since both of them belong to the primal domain decomposition method [24].

(1b) For a general large-scale structure, an algebraic generalized eigenvalue problem solver [25], especially the iterative projection based method such as the subspace iteration method [26] or Lanczos [27] method, is preferred to solve $\left(\mathbf{K}^{(j)}, \mathbf{M}^{(j)} \right)$ for the component modal parameters. Besides, the value of factor θ_{ev} can be selected from 1 to 1.5 according to the experience of the previous CMS approaches [23].

(2a) As the matrices $\mathbf{F}$, $\bar{\mathbf{K}}_{\mathrm{i}}$, $\bar{\mathbf{M}}$ and $\boldsymbol{\Phi}_{\mathrm{L}}$ are block diagonal with respect to the component modal coordinates, some matrices in the algorithm should be derived by calculating their blocks independently at the component level first and then assembling the blocks for the whole matrices. Specifically, they are $\mathbf{S}_0$, $\mathbf{T}_{\mathrm{CB}}$ in Line (2) and $\mathbf{T}_{\mathrm{S}}^{[i]}$, $\mathbf{K}_{\mathrm{S}}^{[i]}$, $\mathbf{M}_{\mathrm{S}}^{[i]}$ in Line (4).

Algorithm 1 Simultaneous iterative C-B method

————————*Preparing*————————

(1)   (a) *Partition* $(\bar{\mathbf{K}}, \bar{\mathbf{M}})$ into components $(\mathbf{K}^{(j)}, \mathbf{M}^{(j)})$ according to the problem and then (b) *solve* the components' lower eigen-pairs under the condition "max $\{\mathrm{diag}(\boldsymbol{\Lambda}_{\mathrm{L}})\} = \theta_{\mathrm{ev}} \times \bar{\lambda}_{\mathrm{max}}$".

(2)   *Calculate* (a) $\mathbf{F} = \boldsymbol{\Phi}_{\mathrm{H}} \boldsymbol{\Lambda}_{\mathrm{H}}^{-1} \boldsymbol{\Phi}_{\mathrm{H}}^{\mathrm{T}}$ and (b) $(\bar{\mathbf{K}}_{\mathrm{i}})^{-1} \bar{\mathbf{K}}_{\mathrm{c}}^{(j)}$ to construct $\mathbf{S}_0$ and $\mathbf{T}_{\mathrm{CB}}$, respectively.

————————*Initializing*————————

(3)   (a) *Start* with $\mathbf{T}_{\mathrm{S}}^{[1]} = \mathbf{T}_{\mathrm{CB}}$ and $\left(\mathbf{K}_{\mathrm{S}}^{[1]}, \mathbf{M}_{\mathrm{S}}^{[1]}\right) = (\mathbf{K}_{\mathrm{CB}}, \mathbf{M}_{\mathrm{CB}})$, then (b) *solve* $\left(\mathbf{K}_{\mathrm{S}}^{[1]}, \mathbf{M}_{\mathrm{S}}^{[1]}\right)$ for $\bar{\lambda}_k^{[1]}$, consequently, a truncation order l_{S} can be decided from $\left\{\bar{\lambda}_1^{[1]}, \bar{\lambda}_2^{[1]}, \ldots, \bar{\lambda}_{n_{\mathrm{CB}}}^{[1]}\right\}$ and $\bar{\lambda}_{\mathrm{max}}$.

————————*Iterating*————————

do while $i \geq 2$

(4)   *Calculate* (a) $\mathbf{T}_{\mathrm{S}}^{[i]} = \mathbf{T}_{\mathrm{CB}} + \mathbf{S}_0 \bar{\mathbf{M}} \mathbf{T}_{\mathrm{S}}^{[i-1]} \left(\mathbf{M}_{\mathrm{S}}^{[i-1]}\right)^{-1} \mathbf{K}_{\mathrm{S}}^{[i-1]}$ and (b) $\mathbf{K}_{\mathrm{S}}^{[i]} = \left(\mathbf{T}_{\mathrm{S}}^{[i]}\right)^{\mathrm{T}} \bar{\mathbf{K}} \mathbf{T}_{\mathrm{S}}^{[i]}$, $\mathbf{M}_{\mathrm{S}}^{[i]} = \left(\mathbf{T}_{\mathrm{S}}^{[i]}\right)^{\mathrm{T}} \bar{\mathbf{M}} \mathbf{T}_{\mathrm{S}}^{[i]}$.

(5)   *Solve* $\left(\mathbf{K}_{\mathrm{S}}^{[i]}, \mathbf{M}_{\mathrm{S}}^{[i]}\right)$ for $\lambda_k^{[i]}$.

(6)   **if** $\left|\lambda_k^{[i]} - \lambda_k^{[i-1]}\right| / \left|\lambda_k^{[i]}\right| \leq Tol$ for $k = 1, 2, \ldots, l_{\mathrm{S}}$, **then** set $\bar{\lambda}_k = \lambda_k^{[i]}$ and **stop do**.
          else set $i = i + 1$.
          end if
        end do

————————*Solving eigenvectors*————————

(7)   *Solve* $\boldsymbol{p}_k^{[i]}$ from $\mathbf{K}_{\mathrm{S}}^{[i]} \boldsymbol{p}_k^{[i]} = \lambda_k^{[i]} \mathbf{M}_{\mathrm{S}}^{[i]} \boldsymbol{p}_k^{[i]}$ for $k = 1, 2, \ldots, l_{\mathrm{S}}$.

(8)   *Calculate* $\bar{\boldsymbol{\phi}}_k = \mathbf{T}_{\mathrm{S}}^{[i]} \boldsymbol{p}_k^{[i]}$ for $k = 1, 2, \ldots, l_{\mathrm{S}}$.

(2a) The matrix $\mathbf{F}$ should be calculated alternatively by

$$
\begin{aligned}
\mathbf{F} &\triangleq \mathrm{diag}\left(\mathbf{F}^{(1)}, \mathbf{F}^{(2)}, \cdots, \mathbf{F}^{(n)}\right) \\
&= \mathrm{diag}\left(\boldsymbol{\Phi}_{\mathrm{H}}^{(1)}(\boldsymbol{\Lambda}_{\mathrm{H}}^{(1)})^{-1}(\boldsymbol{\Phi}_{\mathrm{H}}^{(1)})^{\mathrm{T}}, \boldsymbol{\Phi}_{\mathrm{H}}^{(2)}(\boldsymbol{\Lambda}_{\mathrm{H}}^{(2)})^{-1}(\boldsymbol{\Phi}_{\mathrm{H}}^{(2)})^{\mathrm{T}}, \cdots, \boldsymbol{\Phi}_{\mathrm{H}}^{(n)}(\boldsymbol{\Lambda}_{\mathrm{H}}^{(n)})^{-1}(\boldsymbol{\Phi}_{\mathrm{H}}^{(n)})^{\mathrm{T}}\right) \\
&= \mathrm{diag}\left((\mathbf{K}_{\mathrm{i}}^{(1)})^{-1} - \boldsymbol{\Phi}_{\mathrm{L}}^{(1)}(\boldsymbol{\Lambda}_{\mathrm{L}}^{(1)})^{-1}(\boldsymbol{\Phi}_{\mathrm{L}}^{(1)})^{\mathrm{T}}, (\mathbf{K}_{\mathrm{i}}^{(2)})^{-1} - \boldsymbol{\Phi}_{\mathrm{L}}^{(2)}(\boldsymbol{\Lambda}_{\mathrm{L}}^{(2)})^{-1}(\boldsymbol{\Phi}_{\mathrm{L}}^{(2)})^{\mathrm{T}}, \cdots, (\mathbf{K}_{\mathrm{i}}^{(n)})^{-1} - \boldsymbol{\Phi}_{\mathrm{L}}^{(n)}(\boldsymbol{\Lambda}_{\mathrm{L}}^{(n)})^{-1}(\boldsymbol{\Phi}_{\mathrm{L}}^{(n)})^{\mathrm{T}}\right)
\end{aligned}
\tag{10.36}
$$

instead of by definition, which needs to obtain all the higher component constraint modes. Here, $\left(\boldsymbol{\Phi}_{\mathrm{L}}^{(j)}, \boldsymbol{\Lambda}_{\mathrm{L}}^{(j)}\right)$ and $\left(\boldsymbol{\Phi}_{\mathrm{H}}^{(j)}, \boldsymbol{\Lambda}_{\mathrm{H}}^{(j)}\right)$ are the lower and higher constraint modes of the *j*th component, respectively.

(2a) The inverse of $\mathbf{K}_{\mathrm{i}}^{(j)}$ is not explicitly required, instead, $\mathbf{K}_{\mathrm{i}}^{(j)}$ should be factorized first before Line (2) such that its sparseness can be made use of. Consequently, the following processes such as Lines (2b) and (4a) can be realized by performing a forward and backward substitution only. For real modes, as $\mathbf{K}_{\mathrm{i}}^{(j)}$ is symmetric, an LDLT decomposition is preferred to the LU decomposition. Specifically, the supernodal Cholesky decomposition based packages can be considered, which are proved to be effective for large matrices [28]. Furthermore, re-ordering techniques such as those provided by METIS [29] should be used before the decomposition to minimize the half-bandwidths of the factor matrices, which are usually much larger than those of $\mathbf{K}_{\mathrm{i}}^{(j)}$ due to the non-zero fill-ins.

(6) For convergence check, the criterion may not be unique. For instance, the relative mode error or an residual vector based error estimator can be considered as well [26]. Studies on the most appropriate stopping criterion are not contained in this paper and will be conducted in future works.

For the proposed iterative procedure, based on the above derivations, the following issues should be raised.

10.2.3.1   Issue 1: Comparisons with Qiu's Conventional Iterative C-B Method

As all the terms being iterated, i.e. $\mathbf{T}_{\mathrm{S}}^{[i]}$, $\mathbf{K}_{\mathrm{S}}^{[i]}$ and $\mathbf{M}_{\mathrm{S}}^{[i]}$ do not vary from mode to mode, all the interested modes can be obtained in one round of iterations following the proposed method. Apparently, this is different from Qiu's iterative procedure [15] and can be mathematically explained as the ICB method is intended to find each diagonal term of $\boldsymbol{\Lambda}_{\mathrm{S}}$ while the proposed method is intended to find $(\mathbf{K}_{\mathrm{S}}, \mathbf{M}_{\mathrm{S}})$ instead, which is $(\boldsymbol{\Lambda}_{\mathrm{S}}, \mathrm{diag}(\mathbf{I}_{\mathrm{L}}, \mathbf{I}_{\mathrm{b}}))$ in the basis $\mathbf{P}_{\mathrm{S}}$.

Besides, in the proposed method, the reduced system matrices are consistent with the modal transformation matrix. This is also different from the ICB method. Actually, the modal transformation of the proposed method, i.e. equation (10.25) performs as a Ritz reduction, and thus the convergence rate of the proposed method can be increased.

Notice that the derivations for development from ICB to SCB, i.e. Lemmas 1, 2, and 3, are very similar to those for the development [30] of the iterated reduced system method, which are usually called the "*p*-mode" approach in DC methods [30–32], due to the relationship between the C-B method and the DC method. Their differences lie in the choice of generalized coordinates. More specifically, the proposed method chooses the modal coordinates of retained component constraint modes in addition to the physical coordinates of boundary DoFs. In this way, the initial error can be controlled via the choice of retained modes instead of the selection of master physical DoFs.

10.2.3.2   Issue 2: Comparisons with Approximated Fixed-Interface CMS Methods

Clearly, the first iteration of the proposed method is the C-B method, a widely applied fixed-interface CMS method. This means the precision of the initial guess, which is critical for an iterative procedure from the numerical point of view, can be promised by choosing the retained component constraint modes appropriately under a frequency domain criterion, e.g. Line (1b) of Algorithm 1. Besides, for the second iteration, one can have

$$\mathbf{T}_{\mathrm{S}}^{[2]} = \mathbf{T}_{\mathrm{CB}} + \mathbf{S}_0 \bar{\mathbf{M}} \mathbf{T}_{\mathrm{S}}^{[1]} \left(\mathbf{M}_{\mathrm{S}}^{[1]} \right)^{-1} \mathbf{K}_{\mathrm{S}}^{[1]} = \mathbf{T}_{\mathrm{CB}} + \begin{bmatrix} \mathbf{0} & \mathbf{Fm}_{\mathrm{c}} \\ \mathbf{0} & \mathbf{0} \end{bmatrix} \mathbf{M}_{\mathrm{CB}}^{-1} \mathbf{K}_{\mathrm{CB}} \triangleq \mathbf{T}_{\mathrm{r}} \qquad (10.37)$$

with equation (10.33) and Lines (3a), (4a) of Algorithm 1. Notice that $\mathbf{T}_{\mathrm{r}}$ is the modal transformation of the enhanced C-B method [20], where the approaches of O'Callahan for the improvement of Guyan method are applied to the C-B method. Compared with these approximation based methods, the SCB method could be a better choice when high precision eigen-solutions are of interest, since the truncation effects are compensated via solving $\underline{\mathbf{X}}_k$ iteratively instead of being reduced via synthesising more lower component modes, which may largely increase the size of the ROM.

10.2.3.3   Issue 3: Consistency and Convergence of the Proposed Method

The consistency can be promised by the equivalence between the reduced eigen-equation of the proposed method and the exact reduced eigen-equation of the C-B method, i.e. Lemma 2. Besides, it can be proved in a similar way to that of the simultaneous iterative free-interface CMS method [23].

The convergence of the simultaneous iterative procedure can be explained by the convergence of the series in equation (10.31) and the properties of the Rayleigh-Ritz quotient. A more rigorous explanation can be refer to the convergence verification of the simultaneous iterative free-interface CMS method [23] or the iterated DC methods [30–32], since the iterative updating formulas of all these model reduction methods, e.g. Line (4a) of Algorithm 1, have the same mathematical form as that of the improved IIRS method developed by Friswell et al. [30]. A mathematical proof of the convergence for this kind of iteration methods is not available at hand and deserves further studies.

10.2.3.4   Issue 4: A Shortcoming of the Proposed Method

From equations (10.16) and (10.23), all the boundary DoFs should be retained in $\boldsymbol{p}_k$, and thus the column size of the iterative term and the size of ROM may be much larger than the number of interested global modes, which may include extra computational burdens. This is an important problem for the primal substructuring based reduction techniques. A solution may lie in the reduction of boundary DoFs through modal truncation, as has been done in the AMLS method, where the boundaries shared by components are also treated as substructures. The trade-offs lie in the sacrificing of precision of initial guess. Nevertheless, this error can be compensated by evaluating it precisely and then reducing it iteratively, as has been done in Sects. 10.2.2 and 10.2.3 of this paper. Details of this improvement will be conducted in further works.

10.3 Numerical Examples

In this section, a free-free beam model is employed as a numerical example for illustrating the method. As shown in Fig. 10.1, the beam is made of aluminum, with a length of 1.8 m, a cross-sectional area of 1.0×10^{-6} m^2, and a moment of inertia of 4.17×10^{-10} m^4. It is equally discretized into 40 beam elements in total and then evenly divided into four components. Each component has 22 DoFs and its maximum eigenvalue is 2.99×10^{11} rad^2/s^2. For simplicity, the operations in this section are conducted in MATLAB2014a [33].

To examine the precision of the proposed approach, the interested frequency range of the beam is set to (0, 680) Hz (corresponding to the first 11 modes and $\bar{\lambda}_{11} = 1.82 \times 10^7$ rad^2/s^2). For reference, the global modal parameters solved by the built function "eig" [34] are employed as the exact values. The configurations of the proposed method are set as: (a) the precision requirement is 1×10^{-6}; (b) the first 3 constrained modes of components 1 & 4, and the first 2 constrained modes of components 2 & 3 are kept, where $\lambda_3^{(1)} = \lambda_3^{(4)} = 2.16 \times 10^7$ rad^2/s^2 and $\lambda_2^{(2)} = \lambda_2^{(3)} = 2.23 \times 10^7$ rad^2/s^2. The relative errors of the first 9 elastic eigen-pairs solved by the proposed method are listed in Table 10.1. Here, the error of the kth global eigenvector is calculated with the Modal Assurance Criterion (MAC) by equation (10.38).

$$\text{Error of } \bar{\phi}_{\text{CMS},k} \overset{\text{def}}{=} 1 - \frac{\left(\bar{\phi}_k^{\text{T}} \bar{\phi}_{\text{CMS},k}\right)^2}{\left(\bar{\phi}_k^{\text{T}} \bar{\phi}_k\right)\left(\bar{\phi}_{\text{CMS},k}^{\text{T}} \bar{\phi}_{\text{CMS},k}\right)} \tag{10.38}$$

where the subscript "CMS" indicates the results given by a CMS method. In particular, results in the columns "Init" and "1st" are the modal parameters from the C-B and enhance C-B method, respectively.

It can be known from Table 10.1 that the eigenvalues of the first 9 elastic modes approach the exact values as the number of iterations increases. The "lower" modes converge faster than the "higher" modes because the truncation errors of the "higher" modes are larger in the initial step and the approximate convergence rate $\bar{\lambda}_k/\bar{\lambda}_{11}$ approaches unity as k increases. In the meantime, the errors of the eigenvectors are reduced to a negligible level after convergence. Compared with the (enhanced) C-B method, the precision of all the modal parameters is significantly improved. The above results indicate that high precision modal parameters can be obtained with the proposed method.

To further study the convergence, the relative errors of the eigenvalues whose modal frequencies are larger than the truncation frequency are plotted in Fig. 10.2 with respect to the number of iterations. As shown in Fig. 10.2, for all the five modes, the proposed method still converges, although the convergence rate is much slower than the lower modes. Here, $\bar{\lambda}_{16} = 1.14 \times 10^8$ rad^2/s^2, which is five times of $\bar{\lambda}_{\text{max}}$. This again validates the consistency and convergence of the proposed method.
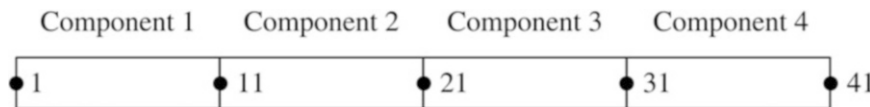

Fig. 10.1 The free-free beam and its components

Table 10.1 Relative errors of the proposed method for the beam model

Mode order	Exact value (rad^2/s^2)	Eigenvalues				Eigenvectors	
		Init	1st	2nd	3rd	Init	Final
3	1.03×10^4	5.52×10^{-6}	7.57×10^{-11}	7.57×10^{-11}	7.34×10^{-11}	1.78×10^{-8}	0
4	7.86×10^4	6.33×10^{-5}	2.22×10^{-11}	2.85×10^{-11}	2.87×10^{-11}	7.92×10^{-7}	4.44×10^{-16}
5	3.04×10^5	2.36×10^{-4}	2.68×10^{-10}	7.91×10^{-12}	2.01×10^{-12}	6.20×10^{-6}	2.44×10^{-14}
6	8.39×10^5	1.79×10^{-4}	1.86×10^{-9}	9.83×10^{-11}	4.15×10^{-11}	1.09×10^{-5}	6.73×10^{-13}
7	1.90×10^6	5.23×10^{-4}	8.96×10^{-9}	1.06×10^{-10}	3.33×10^{-11}	2.52×10^{-5}	7.26×10^{-13}
8	3.76×10^6	2.75×10^{-3}	6.73×10^{-7}	2.55×10^{-8}	1.06×10^{-8}	3.25×10^{-4}	4.31×10^{-10}
9	6.78×10^6	1.50×10^{-2}	1.88×10^{-5}	1.64×10^{-7}	1.86×10^{-8}	2.92×10^{-3}	7.84×10^{-10}
10	1.14×10^7	6.01×10^{-3}	1.57×10^{-5}	9.98×10^{-7}	4.14×10^{-7}	2.13×10^{-3}	3.10×10^{-8}
11	1.82×10^7	4.62×10^{-2}	2.17×10^{-4}	5.03×10^{-6}	5.67×10^{-7}	1.23×10^{-2}	3.58×10^{-8}
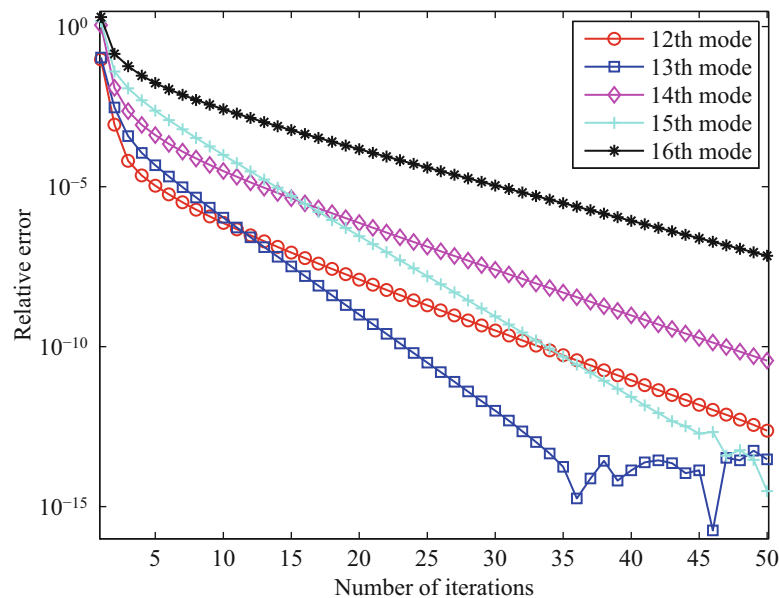
Fig. 10.2 Convergence of the proposed iterative method for modes over the truncation frequency

10.4 Conclusions

A simultaneous iterative procedure for the fixed-interface CMS method is developed in this paper toward fast calculating the modal parameters and ROM of a large-scale and/or complicated structure. In the proposed iteration scheme, an eigenvalue independent matrix, whose column projections in the exact reduced space are the interested global eigenvectors, is chosen as the iterative term and then used as a Ritz basis to generate the reduced system matrices. Consequently, all the interested modes can be solved simultaneously and a linear ROM can be derived after one round of iterations. Complete theoretical frameworks of the proposed method, including the existence of iterative term, consistency of the ROM and an identity formula of the iterative term, are presented with mathematical proof. For reference, an implementation is given together with some computational considerations. The numerical example shows that the proposed method can be converged and effective.

In future works, the convergence of the proposed iterative scheme and its generalization for the C-B type methods with interface reduction will be studied. Besides, the upper bound of precision of the ROM of the proposed method will be verified.

References

1. Duan, Y.F., Xu, Y.L., Fei, Q.G., Wong, K.Y., Chan, K.W.Y., Ni, Y.Q.: Full 3D finite element model for criticality analysis of Tsing Ma Bridge. In: International Conference on Bridge Engineering, HongKong (2006). CD-Rom
2. Ni, Y.Q., Xia, Y., Liao, W.Y., Ko, J.M.: Technology innovation in developing the structural health monitoring system for Guangzhou new TV tower. Struct. Control Health Monit. **16**(1), 73–98 (2009)
3. Wei, F., Liang, L., Zheng, G.T.: Parametric study for dynamics of spacecraft with local nonlinearities. AIAA J **48**(8), 1700–1707 (2010)
4. Liu, M.H., Zheng, G.T.: Component synthesis method for transient response of nonproportionally damped structures. AIAA J **48**(11), 2556–2563 (2010)
5. Masson, G., Brik, B.A., Cogan, S., Bouhaddi, N.: Component mode synthesis (CMS) based on an enriched Ritz approach for efficient structural optimization. J. Sound Vib. **296**(4–5), 845–860 (2006)
6. Mottershead, J.E., Friswell, M.I.: Model updating in structural dynamics: a survey. J. Sound Vib. **167**(2), 347–375 (1993)
7. Voormeeren, S., Rixen, D.: Updating component reduction bases of static and vibration modes using preconditioned iterative techniques. Comput. Methods Appl. Mech. Eng. **253**(1), 39–59 (2013)
8. Craig, R.R., Hale, A.: Review of time-domain and frequency domain component mode synthesis methods. Int. J. Anal. Exp. Modal Anal. **2**(2), 59–72 (1987)

9. de Klerk, D., Rixen, D.J., Voormeeren, S.N.: General framework for dynamic substructuring: history, review, and classification of techniques. AIAA J. **46**(5), 1169–1181 (2008)
10. Hurty, W.C.: Vibrations of structural systems by component mode synthesis. J. Eng. Mech. Am. Soc. Civ. Eng. **86**(4), 51–69 (1960)
11. Hurty, W.C.: Dynamic analysis of structural systems using component modes. AIAA J. **3**(4), 678–685 (1965)
12. Craig, R.R., Bampton, M.C.C.: Coupling of substructures for dynamic analysis. AIAA J. **6**(7), 1313–1319 (1968)
13. MacNeal, R.H.: Hybrid method of component mode synthesis. Comput. Struct. **1**(4), 581–601 (1971)
14. Suarez, L.E., Singh, M.P.: Improved fixed interface method for modal synthesis. AIAA J. **30**(12), 2952–2958 (1992)
15. Qiu, J.B., Ying, Z.G., Williams, F.W.: Exact modal synthesis techniques using residual constraint modes. Int. J. Numer. Methods Eng. **40**(13), 2475–2492 (1997)
16. Bennighof, J.K., Kim, C.K.: An adaptive multi-level substructuring method for efficient modeling of complex structures. In: Proceedings of the AIAA 33rd SDM Conference, Dallas, pp. 1631–1639 (1992)
17. Kim, H., Cho, M.: Improvement of reduction method combined with subdomain scheme in large-scale problem. Int. J. Numer. Methods Eng. **70**(2), 206–251 (2007)
18. Liu, Z.S., Wu, Z.G.: Iterative-order-reduction substructuring method for dynamic condensation of finite element models. AIAA J. **49**(1), 87–96 (2001)
19. Friswll, M.I., Garvey, S.D., Penny, J.E.T.: Model reduction using dynamic and iterated IRS techniques. J. Sound Vib. **186**, 311–323 (1995)
20. Kim, J.G., Lee, P.S.: An enhanced Craig-Bampton method. Int. J. Numer. Methods Eng. **103**, 79–93 (2015)
21. O'Callahan J. A procedure for an improved reduced system (IRS) model. In: Proceeding the 7th International Modal Analysis Conference, Bethel, pp. 17–21 (1989)
22. Weng, S., Xia, Y., Xu, Y.L., Zhu, H.P.: An iterative substructuring approach to the calculation of eigensolution and eigensensitivity. J. Sound Vib. **330**(14), 3368–3380 (2011)
23. Cui, J., Guan, X., Zheng, G.T.: A simultaneous iterative procedure for the Kron's component modal synthesis approach. Int. J. Numer. Methods Eng. **105**(13), 990–1013 (2016)
24. Gosselet, P., Rey, C.: Non-overlapping domain decomposition methods in structural mechanics. Arch. Comput. Meth. Eng. **13**(4), 515–572 (2006)
25. Bai, Z., Demmel, J., Dongarra, J., Ruhe, A., van der Vorst, H.: Templates for the Solution of Algebraic Eigenvalue Problems: A Practical Guide. SIAM: Philadelphia (2000)
26. Bathe, K.J., Wilson, E.L.: Numerical Methods in Finite Element Analysis. Prentice-Hall, Engle Cliffs (1989)
27. Lanczos, C.: An iteration method for the solution of the eigenvalue problem of linear differential and intergral opertators. J. Res. Natl. Bur. Stand. **45**, 255–282 (1950)
28. Chen, Y.Q., Davis, T.A., Hager, W.W., Rajamanickam, S.: Algorithm 887: CHOLMOD, supernodal sparse Cholesky factorization and update/downdate. ACM Trans. Math. Softw. **35**(3), 1–14 (2008)
29. Mao, Y.D., Morris, R., Kaashoek, F.: Optimizing MapReduce for multicore architectures. Technical report MIT-CSAIL-TR-2010–020, MIT (2010)
30. Friswell, M.I., Garvey, S.D., Penny, J.E.T.: The Convergence of the iterated IRS method. J. Sound Vib. **211**(1), 123–132 (1998)
31. Xia, Y., Lin, R.M.: A new iterative order reduction (IOR) method for eigensolutions of large structures. Int. J. Numer. Methods Eng. **59**(1), 153–172 (2004)
32. Xia, Y., Lin, R.M.: Improvement on the iterated IRS method for structural eigensolutions. J. Sound Vib. **270**(4–5), 713–727 (2004)
33. MATLAB Mathematics Release 2014a. The Mathworks, Inc., Natick (2014)
34. Lehoucq, R.B., Sorensen, D.C., Yang, C.: ARPACK Users Guide: Solution of Large-Scale Eigenvalue Problems with Implicitly Restarted Arnoldi Methods. SIAM, Philadelphia (1998)

Chapter 11
Using Blocked Force Data for Vibro-Acoustic Prediction and Simulation

A.T. Moorhouse, A.S. Elliott, and J.W.R. Meggitt

Abstract The context of the paper is the need across many industries for prediction and simulation of vibro-acoustic response of assembled structures. One of the main areas of difficulty is to know the excitation forces. The blocked force method allows vibration sources to be characterised independently using conventional measurements similar to those used in Transfer Path Analysis (TPA). A major advantage is that the blocked force data remains valid when for example the same vibration source is attached to different receiver structures. It is shown how measured blocked forces can be validated using an 'on board validation' procedure. Progress in the standardisation of the blocked force method is also described. The question is then considered of how this blocked force data can be fed into vibro-acoustic models to provide realistic excitation and response prediction. It is shown that a substucturing step is needed in which the passive properties of the source and receiver structures are combined. Examples are presented to demonstrate that this substructuring step can be a source of significant error and ways of minimising the errors are discussed.

Keywords Blocked force • Source characterisation • Transfer path analysis • Vibro-acoustic simulation • Excitation forces

11.1 Introduction

The context of the paper is the need across many industries for prediction and simulation of vibro-acoustic response of assembled structures. The lack of data to describe excitation by active components is arguably one of the biggest limitations of numerical models in vibro-acoustics; models typically produce unscaled responses due to arbitrary unit force excitation. In this paper we consider how experimental blocked force data can be combined with measured or modelled FRF data so as to allow prediction of vibro-acoustic response in an assembly.

11.2 Contact Forces and Blocked Forces

Consider a source substructure installed on a receiver structure (see Fig. 11.1). The source substructure is excited by internal forces when operational. The effect of the source on the receiver can be represented simply in terms of the contact forces at the interface, as in Fig. 11.1b. This free body diagram approach is so well known that it hardly needs any justification. Less well known is the second equivalent system, shown in Fig. 11.1c. Here the passive assembly of source and receiver is excited at the interface by a set of forces which reproduce the identical response field in the receiver. It turns out that these forces are equal to the blocked forces of the source, i.e. the forces which the operational source would exert on a perfectly rigid receiver [1, 2]. Thus, the response field in the receiver can be represented in two equivalent forms:

$$\mathbf{a_R} = \mathbf{A_R}\mathbf{f} = \mathbf{A_C}\bar{\mathbf{f}}$$

where $\mathbf{a_R}$ is the vector of the response field in the receiver, $\mathbf{A_R}$, $\mathbf{A_C}$ are the receiver FRF and coupled FRF of the assembly and $\mathbf{f}$, $\bar{\mathbf{f}}$ are the force and blocked force vector respectively. The first form on the rhs of Eq. 1 corresponds to Fig. 11.1b and

A.T. Moorhouse (✉) • A.S. Elliott • J.W.R. Meggitt
Acoustics Research Centre, University of Salford, Salford, M5 4WT, UK
e-mail: a.t.moorhouse@salford.ac.uk
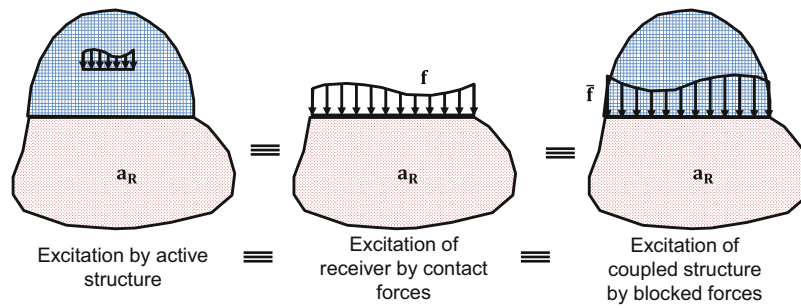
Fig. 11.1 (**a**) Operating source on receiver (**b**) free body diagram of receiver (**c**) equivalent blocked force excitation

the second form to Fig. 11.1c. The major potential advantage of the second formulation is that, whereas the contact forces applied by a source are a function of the receiver and therefore vary from one installation to the next, the blocked forces on the other hand are theoretically an invariant property of the source and can therefore be transferred from one installation to another, for example from a test bench to a real installation. Eq. 1 provides the theoretical basis for obtaining the blocked forces by inverse methods as will be described in the following section.

11.3   Blocked Forces in Transfer Path Analysis

The first form of eq. 1a is the basis for the classical form of transfer path analysis (TPA). A two-stage measurement method is employed: in the operational stage, the receiver responses are measured, normally using accelerometers close to the source-receiver interface; in the passive stage the FRFs are measured, typically using a hammer or shaker. Note that in order to obtain contact forces, the source and receiver substructures must be physically separated so as to allow $\mathbf{Y_R}$ to be measured. With knowledge of the FRFs and the response field, one can obtain an estimate of the contact forces by inverting Eq. 1b. Knowing the contact forces, a forward calculation can be carried out to predict the response at a point of interest, such as a driver's ear, using $\mathbf{a_p} = \mathbf{H_{pf}f}$ where $\mathbf{a_p}$ is the response and $\mathbf{H_{pf}}$ the FRF connecting these points with the source-receiver interface. The contributions of the individual forces in $\mathbf{f}$ to $\mathbf{a_p}$ provide a rank-ordering which is useful for diagnosis and redesign.

One can perform a 'blocked force TPA' (also known as component TPA [3] or in situ TPA [4]) by following the same steps as for a classical TPA but with the sole difference that the source and receiver substructures are not separated prior to FRF measurement. Leaving the assembly intact may sometimes provide practical advantages - it saves time and avoids any need to remove and replace accelerometers which can be a cause of inconsistency and errors. In other situations it may be disadvantageous, for instance if removing the source allows better access to measurement points. However, aside from practical details, blocked forces have a major advantage over contact forces in that the data remains valid when the source is transferred to a new receiver. Blocked force data can therefore potentially provide realistic excitation data for vibro-acoustic simulations in a new assembly.

Before going on to consider a simulation example, we note that considerable care is required to avoid potentially large errors during inversion. This topic is too large to be covered here except for two remarks. First, it is the authors' experience that many problems are caused by poor quality or erroneous input data and that the overriding consideration is therefore to obtain the best quality measurement data possible. Secondly, we would highlight the advantages of cross checking the blocked forces (or contact forces) using an 'on board validation' step. The latter is achieved by predicting the response at a spare receiver location (not used in the inverse calculation) and comparing with the directly measured value. This is not a fool proof independent validation but is likely to show up inversion errors which are the main source of poor results.

11.4   Blocked Forces in Simulation

As mentioned above, the use of blocked forces, rather than contact forces, potentially opens up important possibilities for prediction and simulation of sound and vibration. However, the application of blocked force data in prediction is not necessarily straightforward. Consider that the response in a new receiver is given by:

$$\mathbf{a_{R,new}} = \mathbf{A_{C,new}}\,\bar{\mathbf{f}}$$

where $\mathbf{a_{R,new}}$ is the response to be predicted and $\mathbf{A_{R,new}}$ is the coupled FRF of the new assembly. Irrespective of whether the assembly FRF is to be obtained from measured or modelled data, a substructuring step is required to calculate $\mathbf{A_{C,new}}$.the challenges of which are well known e.g. [5]. The only situation in which substructuring can be avoided is when the assembly already exists so that $\mathbf{A_{C,new}}$ can be measured directly. However, if this is the case then it is unlikely that prediction will be required since the receiver response could be measured directly.

We now go on to describe a case study of predicted vibration response using blocked force data. The case study presented here concerns the construction of a 'virtual assembly' whereby a four footed electric pump is resiliently mounted to a Perspex receiver plate. This study is a realistic but relatively simple example in that the resilient couplings allow degrees of freedom other than the vertical to be neglected.

The construction of the virtual assembly first required the determination of the coupled assembly's FRF matrix. This was achieved through a sub-structuring procedure whereby FRFs of each sub-structure were determined by measurement and they were then coupled computationally. Source and receiver sub-structures were characterised by their free FRF, whilst the resilient coupling elements where characterised via an in-situ approach [6]. It should be noted that whilst characterising the receiver sub-structure an additional remote measurement position was included to so as to provide an on board validation.

Having acquired the assembly's FRF matrix, the blocked force of the source sub-structure was determined whilst installed on a different resiliently mounted assembly. These blocked forces were subsequently injected into the initial assembly's sub-structured mobility matrix and a prediction made for the remote receiver position.

For comparative purposes the same assembly was physically constructed. Shown in Fig. 11.2 are the narrow band velocity spectra for the virtual assembly (i.e. blocked forces injected into a sub-structured mobility matrix) and the physical assembly. It can be seen that a reasonable prediction is achieved across the majority of the frequency range. Noticeable errors can be observed at low and high frequencies. These are believed to be due to neglected co-ordinate DoFs (i.e. rotational), and noisy resilient element data, respectively. Regardless of these errors, the agreement in the prediction clearly demonstrates the potential of the blocked forces as a source characterisation for use in vibro-acoustic simulation.
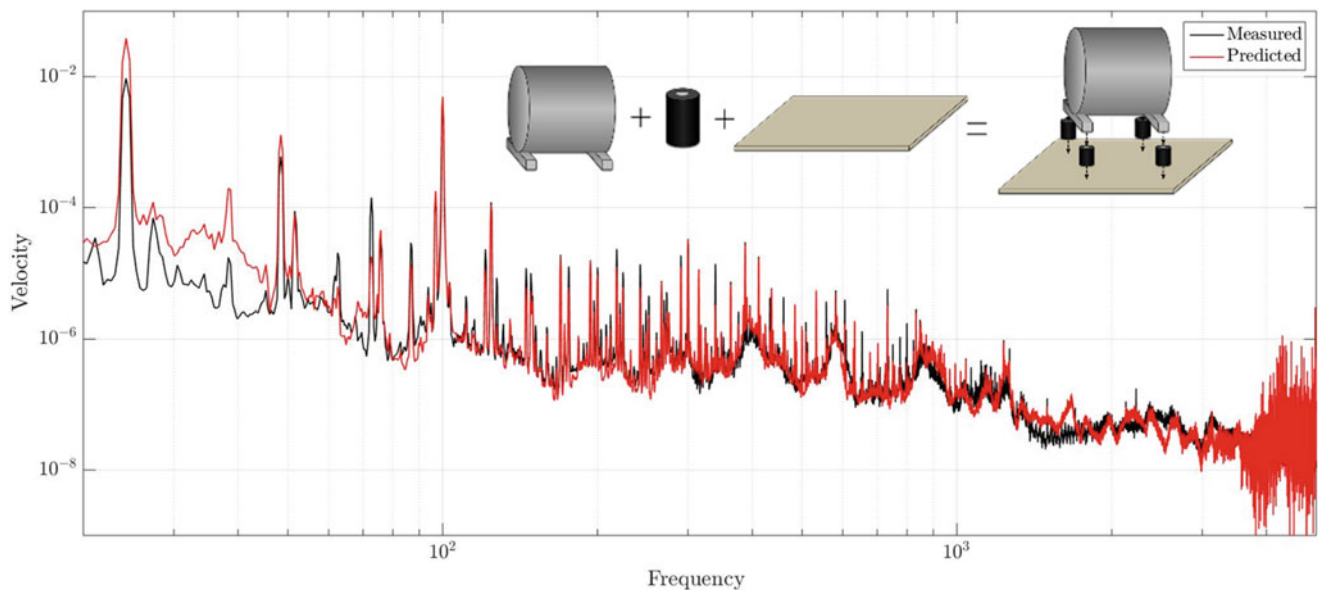
Fig. 11.2 Predicted response of the assembly obtained from blocked forces and substructured FRFs compared with measurement

11.5 Conclusions

It has been argued that blocked forces have a major potential advantage over contact forces in that the data is transferrable and can therefore be used for prediction of sound and vibration in addition to its use in TPA. Reliable solution of the inverse problem represents a difficulty, but there is an increasing number of case studies to demonstrate that, with adequate care, good results can be obtained [7]. An additional difficulty for prediction is that a substructuring step is required and this fact has so far not been widely addressed in the literature. The somewhat simplified but realistic example presented here of a pump on resilient isolators has shown good results but there is much work to do before blocked forces achieve their full potential.

References

1. Bobrovnitskii, Y.I.: A theorem on the representation of the field of forced vibrations of a composite elastic system. Acoust. Phys. **47**(5), 507–510 (2001)
2. Moorhouse, A.T., Elliott, A.S., Evans, T.A.: In situ measurement of the blocked force of structure-borne sound sources. J. Sound Vib. **325**(4), 679–685 (2009)
3. van der Seijs, M.V., de Klerk, D., Rixen, D.J.: General framework for transfer path analysis: history, theory and classification of techniques. Mech. Syst. Signal Process. **68**, 217–244 (2016)
4. Elliott, A.S., Moorhouse, A.T., Huntley, T., Tate, S.: In-situ source path contribution analysis of structure borne road noise. J. Sound Vib. **332**(24), 6276–6295 (2013)
5. Klerk, D.D., Rixen, D.J., Voormeeren, S.N.: General framework for dynamic substructuring: history, review and classification of techniques. AIAA J. **46**(5), 1169–1181 (2008)
6. Meggitt, J.W.R., Elliott, A.S., Moorhouse, A.T., Lai, H.K.: In situ determination of dynamic stiffness for resilient elements. Proc. Inst. Mech. Eng. C J. Mech. Eng. Sci. **230**(6), 986–993 (2016)
7. Lennström, D., Olsson, M., Wullens, F., Nykänen, A.: Validation of the blocked force method for various boundary conditions for automotive source characterization. Appl. Acoust. **102**, 108–119 (2016)

Chapter 12
CMS with Large Contact Patches

P. Coffin, A.R. Brink, M.T. Merewether, and N.K. Crane

Abstract Component Mode Synthesis (CMS) and specifically Craig-Bampton Reductions (CBRs) are popular methods for constructing reduced-complexity models of substructures for structural dynamics modeling. When the interfaces between these substructures are of limited complexity, such as a discrete set of bolts, these approaches work well, providing compact and portable models. With large interfaces relative to the volume, such as contact patches, these approaches become less convenient. Interfaces are generally represented as a series of nodes that do not retain element face (interface) topology that may be critical to using more advanced contact algorithms or providing for contact between substructures. The interface may also lead to sufficient model complexity that each reduced model should be decomposed into multiple domains when included in system level models. In this work we outline the construction of a CBR where interface topology is retained so that models with CBR-CBR contact can be constructed and demonstrated with a set of example problems. We also investigate simple approaches to decomposing the CBR into multiple domains for parallel computing and their relative efficiency.

Keywords CMS • CBR • Craig-Bampton reduction • Contact • Finite element analysis

12.1 Introduction

The Finite Element Method (FEM) is commonly used to model and analyze the vibration of mechanical structures [1]. To reduce the computational complexity and cost of performing mechanical vibration analyses, reduced order models of system components are often constructed using Component Mode Synethesis (CMS). CMS, introduced by [2] and [3], simplifies the component's complete FE model into one that is a function of a smaller set of Degrees Of Freedom (DOFs). Review of traditional CMS techniques are provided by [4] and [5].

CMS techniques, particularly the method described in [3] and [6] (Craig-Bampton Reduction), decompose the model into degrees of freedom (DOFs) associated with motion on the interface (constraint modes) and the degrees of freedom associated with motion internal to a component (fixed-interface modes). Using modal analysis, a small set of internal, fixed-interface modes are used to represent important component structural dynamics. If the number of interface connections is also small, as when components are connected by a few bolted joints, a compact model can be constructed with CMS.

A component interface that contains many FE faces or nodes yields a less compact model using the typical Craig-Bampton Reduction (CBR) since each of the DOFs are retained and are directly coupled to every other DOF on the interface. An approach to alleviate this problem is given by [7], where a subset of characteristic modes on the interface replaces the typical constraint modes.

In this work we are interested in the use of CMS models where there is a large interface (relative to the volume) that may be in contact with other components. This use case poses two challenges: one, to accurately represent contact a detailed representation of the interface must be retained along with its topology for modeling by existing contact algorithms; two, for a typical CBR, this large number of interface DOFs (constraint modes) yields a large model that is completely coupled (dense) amongst those interface DOFs, which may become too large to represent on one processor.

We present numerical examples of CBR behavior when considering contact, enabled by retaining interface topology in Sect. 12.2.2. We also present preliminary efforts and results of decomposing a component with a large interface into multiple domains. The component is decomposed using typical FE domain decomposition tools and then a CBR is performed on each decomposed domain, resulting in a set of coupled CBRs. We will discuss the benefits and pitfalls of this approach in Sect. 12.3.4. In Sect. 12.3 we study the behavior of these approaches with a selection of numeric examples.

P. Coffin • A.R. Brink (✉) • M.T. Merewether • N.K. Crane
Sandia National Laboratories, Albuquerque, NM, USA
e-mail: arbrink@sandia.gov

This work was completed using a combination of Matlab scripts and preprocessing utilities along with the Sierra Mechanics [8, 9] FE codes and SEACAS domain decomposition tools from Sandia National Labs.

12.2 Method

12.2.1 Craig-Bampton Reduction Overview

In this work we utilize the CBR as our CMS technique. The CBR operates on the undamped FE model of a given component:

$$\mathbf{M}^\alpha \ddot{\mathbf{u}}^\alpha + \mathbf{K}^\alpha \mathbf{u}^\alpha = \mathbf{f}^\alpha, \tag{12.1}$$

where $\mathbf{u}^\alpha$ are the DOFs associated with the component, $\ddot{\mathbf{u}}^\alpha$ the second-order time derivatives of the displacement DOFs (acceleration), $\mathbf{f}^\alpha$ the external forces at nodes, $\mathbf{M}^\alpha$ the mass matrix and $\mathbf{K}^\alpha$ the stiffness matrix.

The DOFs in the complete (α) component model are broken into two groups: DOFs that lie on the interface of the component, constraint DOFs (c) and DOFs that lie interior (I) to the component. The decomposed linear system is represented as:

$$\begin{bmatrix} \mathbf{M}_{II} & \mathbf{M}_{IC} \\ \mathbf{M}_{CI} & \mathbf{M}_{CC} \end{bmatrix} \begin{Bmatrix} \ddot{\mathbf{u}}_I \\ \ddot{\mathbf{u}}_C \end{Bmatrix} + \begin{bmatrix} \mathbf{K}_{II} & \mathbf{K}_{IC} \\ \mathbf{K}_{CI} & \mathbf{K}_{CC} \end{bmatrix} \begin{Bmatrix} \mathbf{u}_I \\ \mathbf{u}_C \end{Bmatrix} = \begin{Bmatrix} \mathbf{f}_I \\ \mathbf{f}_C \end{Bmatrix}. \tag{12.2}$$

The CBR transforms the complete system of both constraint (c) and interior (I) DOFs into a system of the constraint DOFs (c) and a set corresponding to interior structural mode shapes (k):

$$\begin{bmatrix} \mathbf{M}_{kk} & \mathbf{M}_{kc} \\ \mathbf{M}_{ck} & \mathbf{M}_{cc} \end{bmatrix} \begin{Bmatrix} \ddot{\mathbf{u}}_k \\ \ddot{\mathbf{u}}_c \end{Bmatrix} + \begin{bmatrix} \mathbf{K}_{kk} & \mathbf{K}_{kc} \\ \mathbf{K}_{ck} & \mathbf{K}_{cc} \end{bmatrix} \begin{Bmatrix} \mathbf{u}_k \\ \mathbf{u}_c \end{Bmatrix} = \begin{Bmatrix} \mathbf{f}_k \\ \mathbf{f}_c \end{Bmatrix}. \tag{12.3}$$

Note that the CBR results in system matrices that have the following form:

$$\begin{aligned}
\mathbf{M}_{kk} &= I_{kk} \quad \text{(diagonal)} \\
\mathbf{M}_{kc} &= \mathbf{M}_{ck}^T \quad \text{(dense)} \\
\mathbf{M}_{CC} &= - \quad \text{(dense)} \\
\mathbf{K}_{kk} &= \Lambda_{kk} \quad \text{(diagonal)} \\
\mathbf{K}_{kc} &= \mathbf{K}_{ck}^T \quad = \mathbf{0} \\
\mathbf{K}_{CC} &= - \quad \text{(dense)}.
\end{aligned} \tag{12.4}$$

Due to the form of these matrices, the computational complexity of the reduced model quickly becomes driven by the interface when more than a few element faces or points lie on the interface. That is:

$$N_k \gg N_C, \tag{12.5}$$

the number of interface DOFs is greater than the number of fixed interface DOFs. For large interfaces this means either controlling this growth in complexity via a method such as characteristic constraint or being able to decompose the component or submodel.

In this work, the Sierra/Structural Dynamics (SD) code is used to compute the CBR for a given component. Analysis of the system model, often involving contact between components, is performed in Sierra/Solid Mechanics (SM) using an explicit time solver. In the Sierra mechanics codes, CBRs are represented in the construct of a superelement. A superelement is simply a generic linear element where the nodes, DOFs, and element matrices are defined in input file. This information is read into the code, nodes and DOFs are correlated between the superelement and the rest of the existing mesh and the superelement matrices are used to compute the element response.

12.2.2 General Contact

In the Sierra/SM code, contact is either defined between a set of nodes and a set of element faces or between two sets of element faces. Considering a superelement, contact can only be defined between the nodes on the superelement and faces in the rest of the FE mesh. One key limitation of this is that superelements can not be in contact with each other, as superelements do not retain topology information about their interfaces.

The most convenient solution to this problem would be to augment the file defining the superelement with information about the interface topology. This information could be passed along to the typical contact algorithms within the finite element code and little further effort would be necessary. Due to the complexity of code changes necessary for this approach, an alternative approach is used to demonstrate superelement-superelement contact here.

In this work we demonstrate contact with superelements by introducing fictitious shell elements at the superelement interface. This is a relatively simple intermediate step completed by a Matlab script. The original FE mesh of the component that is subject to the CBR contains both a nodeset and sideset that define the interface (constraint) nodes for the CBR. The sideset provides topology information about the nodes that make up the element faces that is then directly used to add blocks of shell elements to the FE mesh that the CBR is later be included in.

12.2.3 Decomposition

A simple approach to reducing CMS complexity for components with large interfaces is to use traditional FEA domain decomposition tools. We propose decomposing a component into n-domains and constructing a CMS reduction of that domain. In each decomposed domain, the CMS interface is a union of the original component interface on that domain and the interface between the decomposed domain and its neighbors. Figure 12.1 depicts this process, in which the outer surface of the component represents both CBR interface nodes and contact surface. For the purpose of contact, fictitious shell elements will be located here. The shell elements and CBR interface share nodes and DOFs so constraints tieing them are unnecessary. The internal component interfaces resulting from decomposition are additional CBR interface nodes. These interface nodes are shared between decomposed domain CBRs and naturally provide the connection between them.

To study the expected complexity of these decompositions we compute the number of DOFs associated with decomposing a cube. We assume the cube has a structured mesh, with consistent sizing in all directions and an even number of elements along each edge. We compute resulting decompositions based on cutting the cube N_{cuts} times in each direction. The number of total domains then is:

$$N_{Domain} = (N_{cuts} + 1)^3 , \tag{12.6}$$

where the total number of DOFs $N_{Dofs,Total}$ is:

$$N_{Dofs,Total} = (N_{EPL} + 1)^3 , \tag{12.7}$$

where N_{EPL} is the number of elements per line (or edge). The number of nodes per edge N_{PL} in the decomposed domain is:

$$N_{PL} = \left(\frac{N_{EPL}}{N_{cuts} + 1} + 1 \right) . \tag{12.8}$$

The number of interface DOFs per domain (assuming 3 DOFs per node) is:

$$N_{IfaceDofsPerDom} = 3 \left(6N_{PL}^2 - 12N_{PL} + 8 \right) . \tag{12.9}$$

This means that the approximate number of interface DOFs per domain ($N_{IFDofsPerDom}$) is:

$$N_{IFDofsPerDom} \approx 18 \frac{N_{EPS}^2}{N_{DOM}^{2/3}} . \tag{12.10}$$
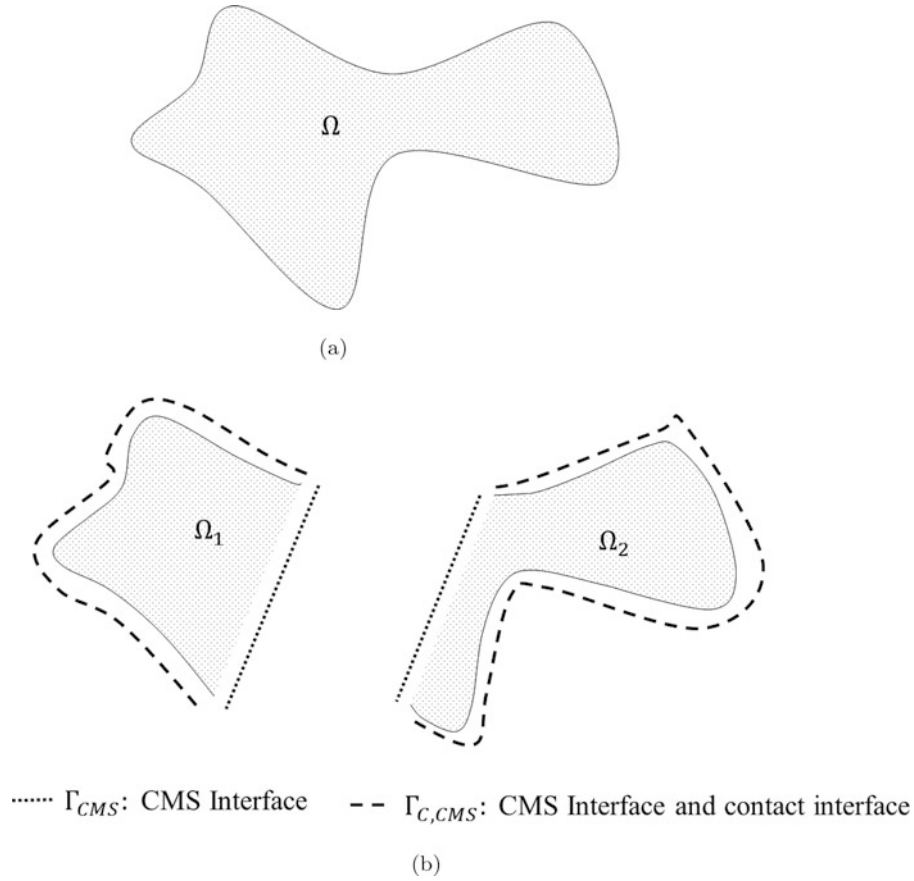
Fig. 12.1 Decomposition approach creating multiple CBRs within original component. Here the outer surface of the component will be in contact with other components, the decomposed component domains are linked via their contiguous nodes and DOFs. (a) Original component domain. (b) Decomposed domains CBR interfaces

In terms of total component DOFs this is:

$$N_{IFDofsPerDom} \approx 18 \left(\frac{N_{Dofs,Total}}{N_{DOM}} \right)^{2/3}. \tag{12.11}$$

The total number of interface DOFs in all domains ($N_{IFDofsTot}$) is therefore:

$$N_{IFDofsTot} \approx 18 N_{Dofs,Total}^{2/3} N_{DOM}^{1/3}. \tag{12.12}$$

Assuming that for large interfaces, the total number of nonzero matrix entries (in either the mass or stiffness matrix) is dominated by the interface-interface terms (N_{IFDOF}^2), the number of nonzero entries per domain ($N_{NNZPerDom}$) is:

$$N_{NNZPerDom} \approx 36 \left(\frac{N_{Dofs,Total}}{N_{DOM}} \right)^{4/3}. \tag{12.13}$$

The total across all domains is then:

$$N_{NNZTot} \approx 36 \left(\frac{N_{Dofs,Total}^4}{N_{DOM}} \right)^{1/3}. \tag{12.14}$$

This can be compared with a regular FE mesh compressed of 8-node hexahedral elements where the number of nonzero entries would be bound as:

$$N_{FE,NNZCube} < N_{EPL}^3 N_{DOFPerElem}^2, \tag{12.15}$$

where N_{EPL} is the number of element edges per line and $N_{DOFPerElem}$ is the number of DOFs per element (8 Nodes x 3 Dimensions = 24). We can again consider a decomposition with N_{cuts} slices in each dimensions so that the number of nonzero entries on a given domain is:

$$N_{FE,NNZPerDomain} < \frac{N_{Dofs,Total}}{N_{Domain}} N_{DOFPerElem}^2. \tag{12.16}$$

The total nonzero entries across all domains is:

$$N_{FE,NNZTotal} < N_{Dofs,Total} N_{DOFPerElem}^2. \tag{12.17}$$

These estimates show that the number of nonzero matrix entries may scale better in the original FE mesh than in the CMS model. This reinforces that a traditional CBR is a poor choice for domains with large interfaces. Decomposition is not effective at reducing the CMS models' complexity below that of the original FE model. In this work we constrain ourselves to a traditional CBR as it retains the DOFs of the original element faces that will be used by contact algorithms. The results of this section indicate that more work is necessary to enable the use of more advanced interface models (such as characteristic constraint modes) while modeling contact.

12.3 Numerical Examples

In this section we study the behavior of CBRs in contact using three examples and the effectiveness of decomposition with another example. First, the mechanical impact of two identical blocks where the influence of CBR interface is demonstrated. The second example is the impact of two blocks with dissimilar stiffness and density in which the shape of one block is varied to show the impact of curvature. In the third example a single CBR has a sharp traction load applied to one of its faces, further clarifying the influences of CBR interface definition observed in the first example. The gains in computational cost via decomposition are demonstrated in the last numerical example.

12.3.1 CBR-CBR Contact: Identical Blocks

We first demonstrate contact between superelements, particularly CBRs, with the problem depicted in Fig. 12.2.

Throughout the numerical examples in this work we depict the motion of the two blocks via plots of position over time, demonstrated in Fig. 12.3. In these examples, the *x*-axis is the axial direction, the primary direction of motion. In examples
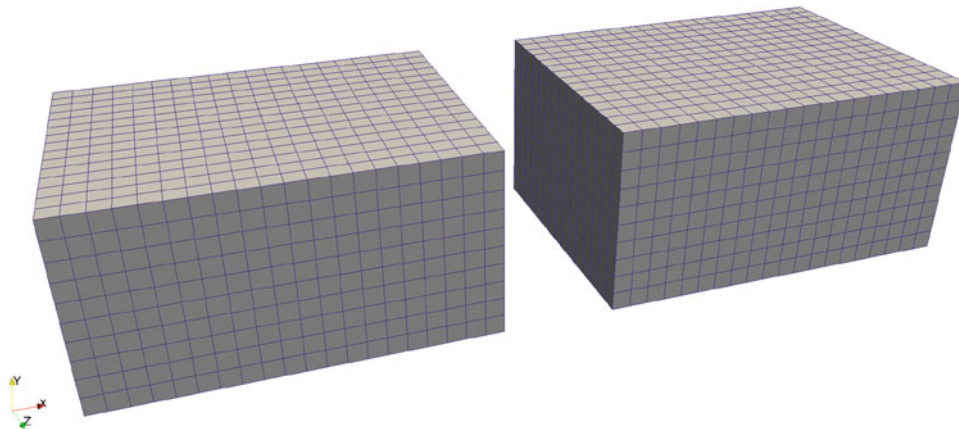
Fig. 12.2 Test problem for CBR-CBR contact, two blocks. Right-most block initially at rest, left-most block initially in motion with a velocity of 3810 m/s to the *right*
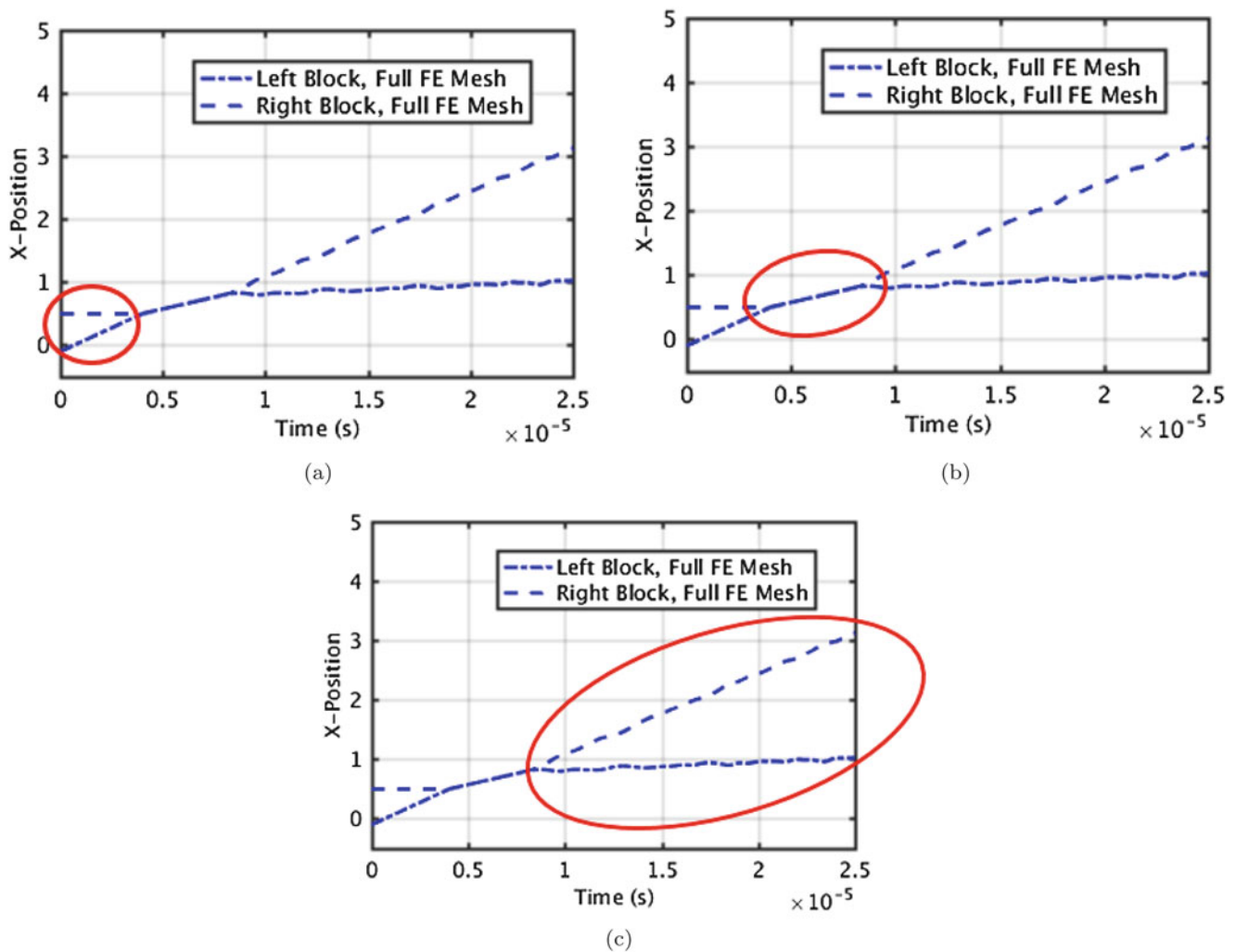
Fig. 12.3 Plotted left and right face positions over time during test problem of Fig. 12.2. These are the right-most face of the left block and the left-most face of the right block, respectively. (**a**) Time before block contact. (**b**) Block contact. (**c**) Block separation

with only bricks (first and third examples), we plot the average *x*-position of the brick faces that come into contact. In the second example, the average position of each entire block is plotted (Table 12.1).

In Fig. 12.3 there are three clear segments of time during the simulation: Fig. 12.3a is the time before the blocks impact, Fig. 12.3b is the time during which the two blocks are in close contact and finally Fig. 12.3c shows the time after the blocks have separated and are traveling away from each other.

An important consideration for any CBR is the proper choice of the set of nodes and element faces to define as the CBR interface. In a typical reduction the connections are known and are the obvious choice for the interface definition. When considering contact, a large area is generally necessary. In our example there are a few logical options for defining the CBR interface, these are shown in Fig. 12.4. Figure 12.4a represents the most compact interface, the face of the brick that contacts the other brick (the right-most face on the left brick and the left-most face on the right brick). A more general interface is to include both the left and right faces as in Fig. 12.4b, such that both blocks are identical. The most conservative choice, allowing for completely general contact between the brick and other components, is shown in Fig. 12.4c, the entire outer face of the brick.

As shown in Fig. 12.5, the choice of interface for the CBR has a significant influence on the dynamics of the CBR. Here the total number of DOFs (interface + internal) for the CBR is held constant with varying interface. The total number of DOFs is chosen to be a large percentage of the original FE mesh's, retaining much of its dynamics. In Fig. 12.5 the dark blue curves are the results from a regular FE mesh, that is no CBR on either brick. It is clear from the green curves that if only the contacting interfaces Fig. 12.4a are defined, the resulting dynamics are drastically different than with the original FE mesh.

Table 12.1 Problem details for block-block impact (Fig. 12.2)

Parameter	Value
Left block dimensions (m)	[0.0508,0.0254,0.0381]
Right block dimensions (m)	[0.0508,0.0254,0.0381]
Left block initial position (center of body, m)	[−0.0279,0,0]
Right block initial position (center of body, m)	[0.0381,0,0]
Number of elements per block	3000
Total number of DOFs in each CBR (constraint + internal)	4406
Elastic modulus (Pa)	5.17×10^{12}
Poisson ratio	0.3
Density (kg/cu. meter)	7836
Left block initial velocity (m/sec)	[3810,0,0]
Right block initial velocity (m/sec)	[0,0,0]

(a)   (b)   (c)
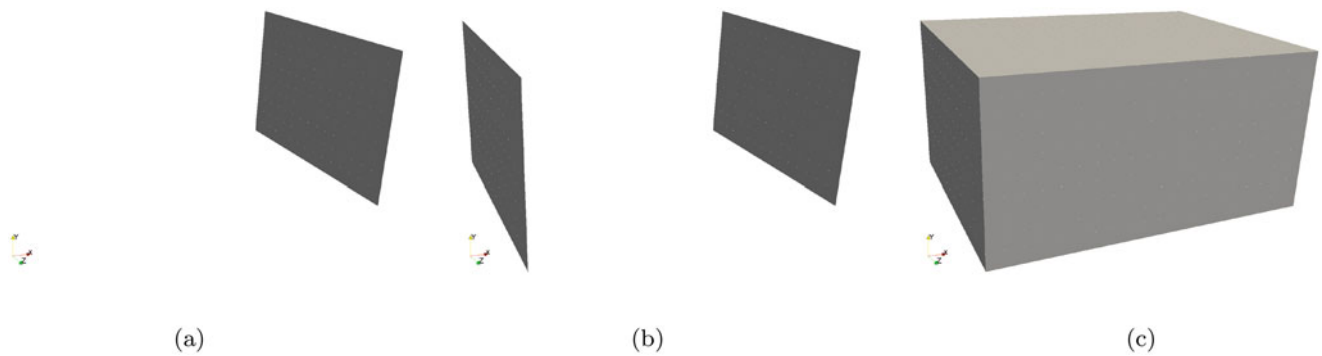
Fig. 12.4 Choices of surface for CBR interface definition when constructing CBR for test contact problem. (**a**) Only surface expected to be in contact. (**b**) Both front and back surfaces of block. (**c**) Entire outer surface of block
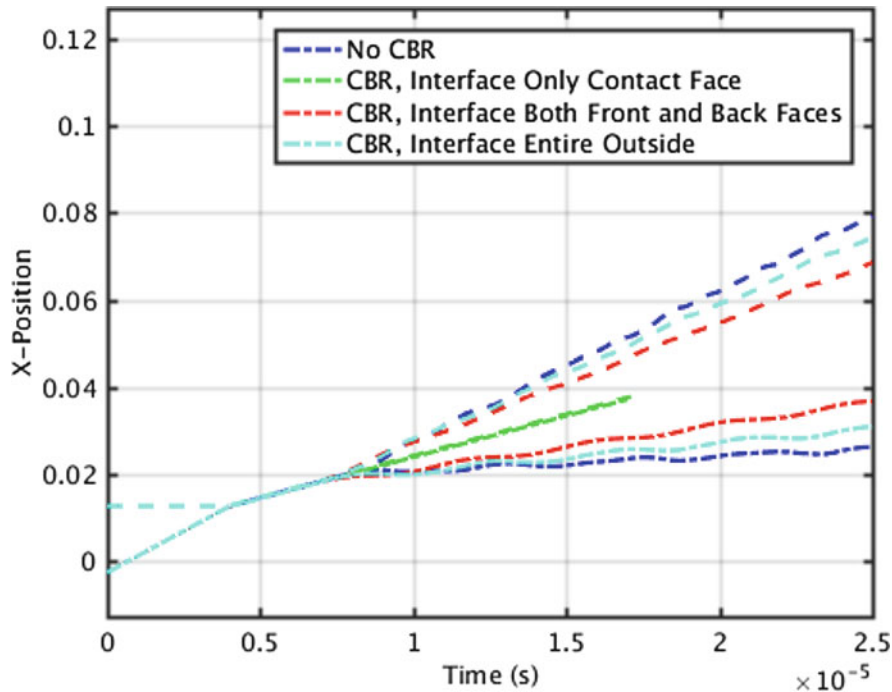
Fig. 12.5 Comparison of motion resulting from the choice of interface region when defining CBR. Here the total number of DOFs in the CBR remains constant, one fewer than the total number of DOFs in the original FE Mesh
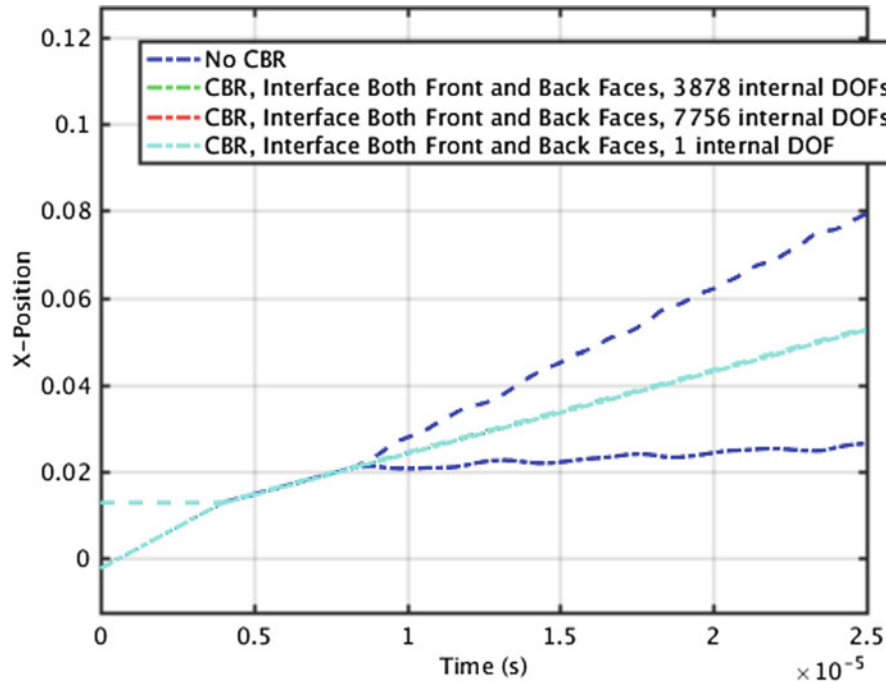
Fig. 12.6 Comparison of motion resulting from varying the number of fixed interface modes retained in the CBR. The differences are small, all curves for the CBR result lieing on top of each other visually

They behave as if there is no elasticity in the contact, the two faces coming into contact and never separating, continuing along together. As more interface is defined (Fig. 12.4b, c), the dynamics more closely match the traditional FE mesh result.

The influence of the number of fixed interface (internal) modes retained is shown in Fig. 12.6. We see here that the number of modes retained has little influence on the solution, all of the curves lieing on top of each other. This indicates that the behavior in this example is driven by constraint (interface) DOFs and modes.

The differences in these contact results are likely due to the dissimilar nature of the basis functions and construction that are used for the constraint and component modes. The internal, component modes are the dynamic modes with the entire interface fixed. Each interface mode is the result of a static analysis with unit displacement applied to that particular interface DOF, while all other interface DOFs are fixed to zero. That is, the behavior due to interface DOFs are the result of a static condensation, while the component DOFs represent a dynamic construction.

A simple example of inaccuracies is to consider the steady state solution to a 1D bar element under constant acceleration. In this example, one of the two nodes is considered interface (u_1). This means that the constraint mode would be: $u_1 = u_2 = 1$, and the component mode would be: $u_1 = 0$, $u_2 = -1$. Assuming a constant acceleration and steady-state solution:

$$\ddot{\mathbf{u}}_k = \mathbf{K}_{kk}^{-1} \, \mathbf{K}_{kc} \, \mathbf{u}_c, \tag{12.18}$$

and considering Eq. 12.4, it is clear that for a unit acceleration at the interface, there is no response in the rest of the component. This does not reflect the response that would be expected for an acceleration only applied at the interface.

12.3.2 CBR-CBR Contact: Dissimilar Blocks

Here we study the relative response between the traditional FE mesh and CBR models of two different impactor geometries. Figure 12.7a shows the first geometry, a sphere. Figure 12.7b shows the second geometry, a brick, similar to that of the first example. Both geometries are impacting a larger, more stiff and more dense brick, simulating a relatively solid body. The complete problem details are outlined in Table 12.2.

Figure 12.8 depicts the differences in CBR behavior resulting from varying impactor geometry. Qualitatively in this example, the response of the CBR of the sphere and of the brick match the full FE mesh behavior similarly. The number
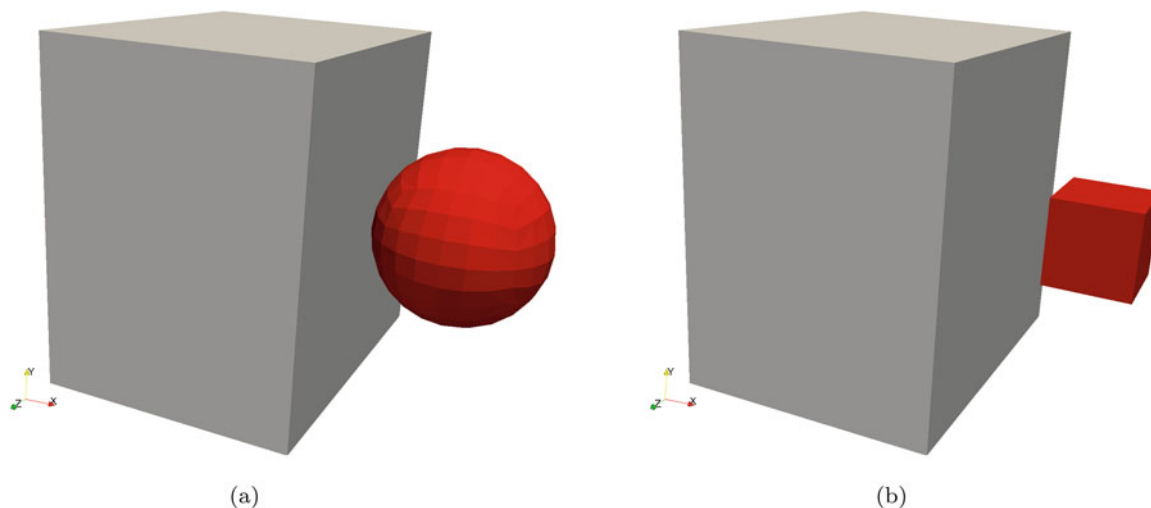
Fig. 12.7 Depiction of block geometries for comparison of CBR contact response with flat vs. curved surfaces. (**a**) Sphere impacting stiff, dense brick. (**b**) Brick impacting stiff, dense brick

Table 12.2 Problem details for dissimilar block-block impact (Fig. 12.7)

Parameter	Value
Left block dimensions (m)	[0.0762,0.1016,0.1016]
Right block dimensions (m)	[0.0254,0.0254,0.0254]
Left block initial position (center of body, m)	[−0.0279,0,0]
Right block initial position (center of body, m)	[0.0381,0,0]
Number of elements per block, left	6000
Number of elements per block, right (sphere, brick)	864 , 1000
Number of internal modes	200
Number of constraint DOFs (sphere, brick)	654 , 1806
Elastic modulus, left block (Pa)	5.17×10^{14}
Elastic modulus, right block (Pa)	5.17×10^{12}
Poisson ratio	0.3
Density, left block (kg/cu. m)	7.836×10^4
Density, right block (kg/cu. m)	7.836×10^3
Left block initial velocity (m/sec)	[0,0,0]
Right block initial velocity (m/sec)	[3810,0,0]

of internal modes retained for the CBR was held constant. Due to the geometry to the two bodies, this means that the brick (Fig. 12.8b) had nearly three times the total number of DOFs as the sphere (Fig. 12.8a).

12.3.3 CBR with Force Load

To more carefully study the influence of the interface definition on CBR behavior we load a single CBR with a sharp load. This load is designed to be short in duration to excite higher frequency behavior as one may expect contact to also do. The problem details are found in Table 12.3. Here the load is applied to the nodes of the center-most two element faces on one of the brick faces. To allow the CBR to retain the most information, the total number of DOFs associated with each CBR remains constant. This number is nearly the same as the total number of DOFs associated with the full FE mesh. Due to solver limitations we retain 1 fewer DOF in the CBR representation than in the full FE mesh. We study this problem both using the Sierra/SM and Sierra/SD codes.

In Fig. 12.9 a comparison of the average position of the loaded face is shown, highlighting differences between the results produced by Sierra/SM using an explicit time solver and the original FE model in Sierra/SD (where the CBR was created). In
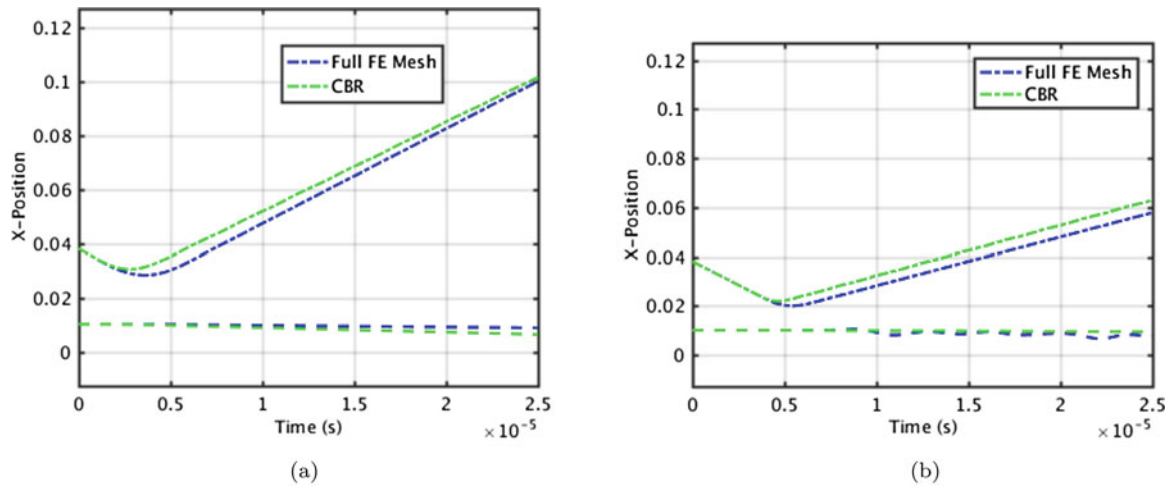
Fig. 12.8 Comparison of motion between traditional FE mesh and CBR model with a soft object impacting a stiff, dense brick. (**a**) Sphere impacting stiff, dense brick. (**b**) Brick impacting stiff, dense brick

Table 12.3 Problem details for brick with force load

Parameter	Value
Brick dimensions (m)	[0.0508,0.0254,0.0381]
Number of elements per block	3000
Total number of DOFs in each CBR (constraint + internal)	1781
Elastic modulus (Pa)	5.17×10^{12}
Poisson ratio	0.3
Density (kg/cu. m)	7836
Load location	center-most two element faces on x-max face
Load direction	$[-1, 0, 0]$
Load function	linear interpolation
Interpolation time values	$[0, 3 \times 10^{-7}, 6 \times 10^{-7}]$
Interpolation load values	$[0, 6.90 \times 10^8, 0]$
Fictitious shell elastic modulus (Pa) [Large, Small]	$[6.9 \times 10^3, 6.9 \times 10^{-5}]$
Fictitious shell density (kg/cu. m) [Large, Small]	$[0.11, 1.1 \times 10^{-5}]$
Fictitious shell thickness (m) [Thin, Thick]	$[2.5 \times 10^{-10}, 2.5 \times 10^{-4}]$

this figure all of the Sierra/SM explicit runs lie on top of each other (visually), regardless of the incorporation of the fictitious shell elements or their parameters, indicating that the fictitious shell elements have little influence. This also indicates that for a simple load, the interface definition is unimportant. Future study of the contact algorithms used by Sierra/SM is necessary to understand how the CBR construction may be leading to the differences observed in Sect. 12.3.1.

To verify the CBR for this problem, we show Fig. 12.10, which shows that in Sierra/SD the full FE mesh behaves identically to the CBRs within visual tolerances. In this comparison we show the Sierra/SD solution with no fictitious shell elements since they were shown to be not influential in Fig. 12.9. This was also confirmed for Sierra/SD results not shown here. The time-step is varied to ensure that does not impact the solution, also shown in Fig. 12.10.

As a final step we show Fig. 12.11 to observe the influence of time step on the Sierra/SM solution. Time step does not appear to significantly influence the observed behavior. Here the time step is a multiple of the smallest element critical time step; this multiple is identified in the legend of Fig. 12.11. Additionally, in this Figure the full FE mesh is run in Sierra/SM explicit. In this case the default 8-node hexahedral element formulation in Sierra/SD and Sierra/SM is different, Sierra/SM using a fully integrated bubble function element while Sierra/SM uses an underintegrated element with hourglass control. The author was unable to run the CBR in Sierra/SM using an implicit time solver due to convergence issues. The observed strain in the full FE mesh observed in Sierra/SM was < 0.5%.
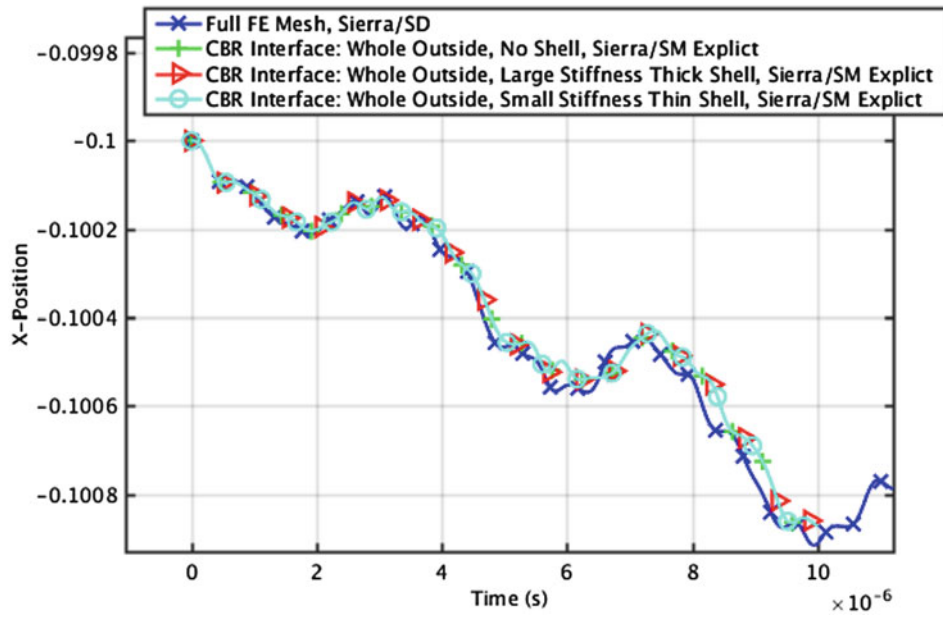
Fig. 12.9 Comparison of motion between traditional FE mesh and CBR models with pressure load applied to two element faces. Here showing differences between Sierra/SM explicit solution and original Sierra/SD solution
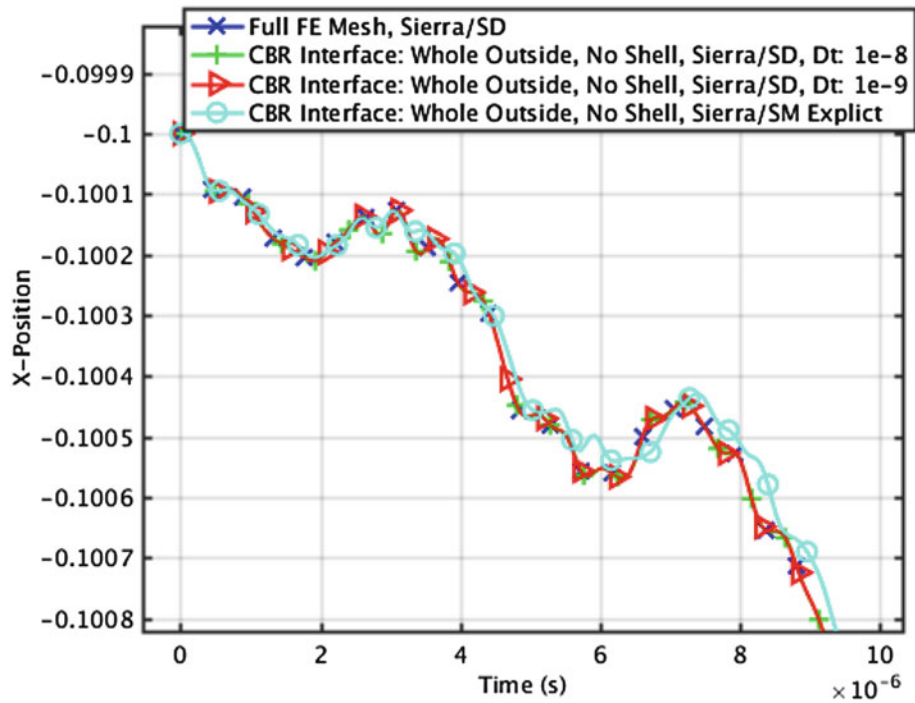
Fig. 12.10 Comparison of motion between traditional FE Mesh and CBR models with pressure load applied to two element faces. Here showing the similarities between Sierra/SD solution with CBRs and with the original FE mesh
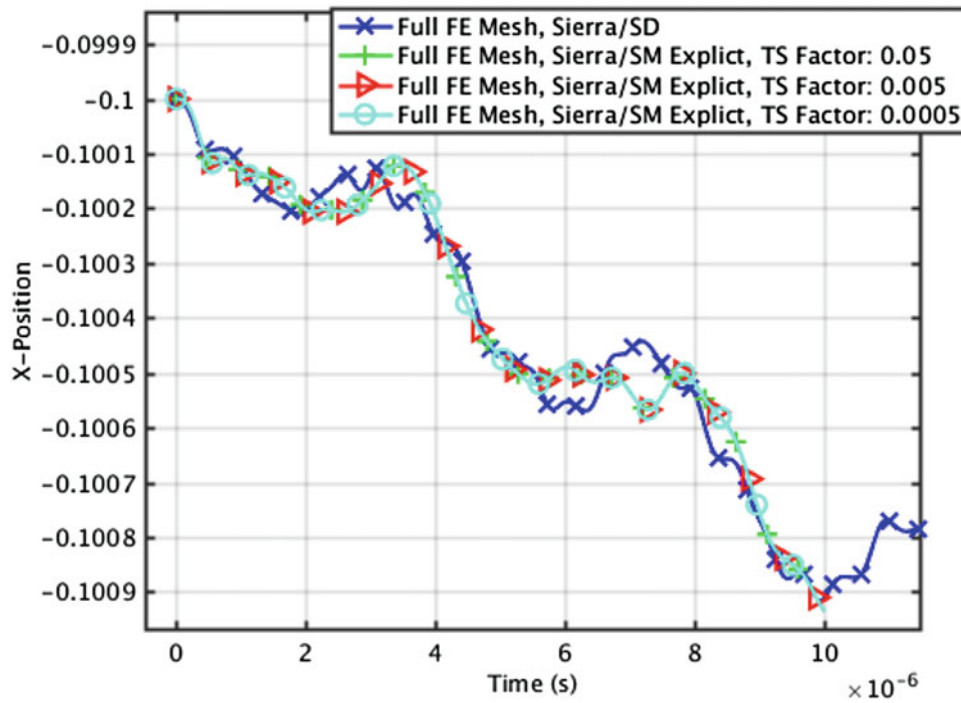
Fig. 12.11 Comparison of motion between traditional FE Mesh and CBR models with pressure load applied to two element faces. Here showing the differences between the Sierra/SD and Sierra/SM solutions using the full mesh. The impact of time step is also shown here

Table 12.4 Problem details for timing test

Parameter	Value
Block dimensions (m)	$[1.91 \times 10^{-2}, 1.91 \times 10^{-2}, 1.91 \times 10^{-2}]$
Total number of internal modes retained in each CBR	50
Elastic modulus (Pa)	5.17×10^{12}
Poisson ratio	0.3
Density (kg/cu. m)	7.836×10^3

12.3.4 Decomposition Performance

The decomposition approach is implemented with a series of scripts combined with both the Sierra/SD and SM FE codes. We test the gains in computational time (wall clock) for this decomposition approach by varying the mesh refinement of a brick and the number of decomposition domains. The test problem is a cube with all displacements fixed on one face and a constant force applied to the opposite face in a direction normal to the face. More detailed problem parameters are described in Table 12.4. Spot checking showed that displacements for varying decompositions were identical within the solver precision.

The impact on computation time while using an explict solver is shown in Fig. 12.12, more domains requiring more computational time. In order to handle these mass matrices in an explicit code, a solve of the assembled mass matrices for all coupled CBRs is required. In the current implementation, this requires a serial solve of the assembled CBR mass matrices of the entire decomposed component. This negates any other gains in computational efficiency from this decomposition approach. A parallel linear solve for this step would be more ideal, but still relatively expensive.

This decomposition approach for CMS holds more promise in the context of an implicit time solve as the non-diagonal mass matrices on each domain yield no such additional computational costs. Figure 12.12b shows the timing results using an implicit time solver. Here the timing results are more promising, showing that with more decomposition domains, the total computational cost decreases.
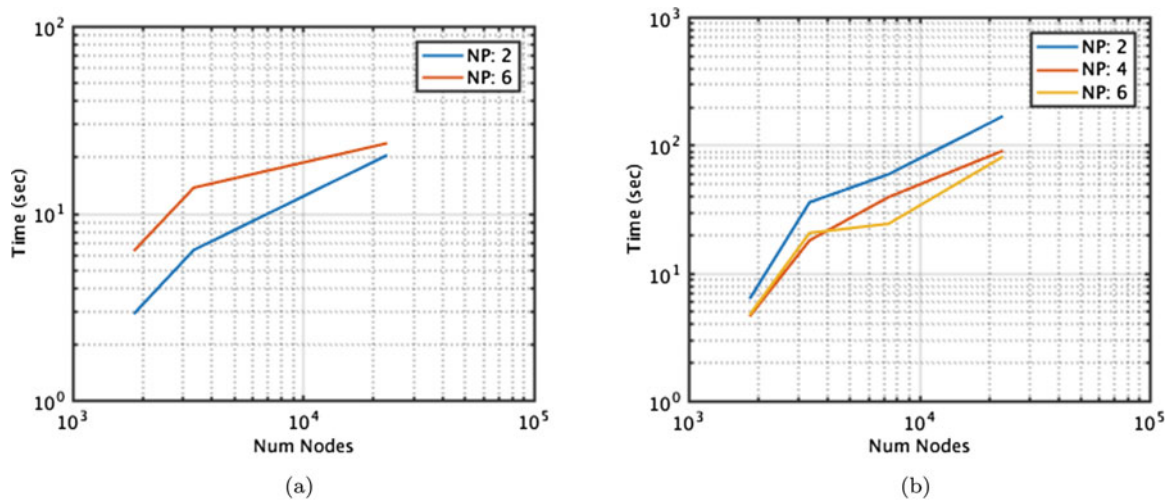
Fig. 12.12 Comparison of computational cost with decomposition on different numbers of processors (NP) and for different time solvers. (**a**) Explicit time solver. (**b**) Implicit time solver

12.4   Conclusions

We have demonstrated that contact can be incorporated into CMS methods using fictitious elements utilizing standard finite element contact algorithms and that components with large interfaces can be decomposed into multiple CBRs with a savings in number of DOFs per CBR. Demonstration of CBR-CBR contact also showed that the behavior is strongly dependent on the interface nodes of the CBR. Further testing with no contact showed that these interface dependent differences were only observed with contact. Small differences between the original FE mesh or CBR solution in Sierra/SD and those in Sierra/SM were still observed.

Decomposing a component with a large interface into multiple CBRs was shown to hold promise for situations where memory is limited but not be a good solution to speed up explicit solutions. The requirement of assembling and solving the coupled mass matrices in an explicit method negates the possible impact of this approach. FE analyses using an implicit time solver may find this decomposition beneficial as was demonstrated in testing. A simple estimation of nonzero matrix entries associated with the decomposed CBR indicate that this approach does not offer any significant advantage over retaining the original FE mesh, and may be worse. At a fundamental level, CBRs with complex interfaces present a significant challenge to incorporate in a computationally efficient manner in an explicit FE method. Approaches combining more advanced interface models (such as characteristic constraint modes) with the modeling of contact appear to be necessary to achieve the reduced complexity desired of CMS methods.

References

1. Inman, D.J., Singh, R.C.: Engineering Vibration, vol. 3. Prentice Hall, Upper Saddle River (2001)
2. Hurty, W.C.: Dynamic analysis of structural systems using component modes. AIAA J. **3**(4), 678–685 (1965)
3. Bampton, M.C., Craig, R.R., Jr.: Coupling of substructures for dynamic analyses. AIAA J. **6**(7), 1313–1319 (1968)
4. Hintz, R.M.: Analytical methods in component modal synthesis. AIAA J. **13**(8), 1007–1016 (1975)
5. Craig, R.R., Jr.: A review of time-domain and frequency-domain component mode synthesis method. In: Proceedings of the Joint Mechanics Conference, Albuquerque, 24–26 June 1985 (A86-26876 11-39). American Society of Mechanical Engineers, New York (1985)
6. Craig, R.R., Jr.: Structural Dynamics: An Introduction to Computer Methods. Society for Experimental Mechanics, Inc, Bethel (1995). 527
7. Castanier, M.P., Tan, Y.-C., Pierre, C.: Characteristic constraint modes for component mode synthesis: AIAA J. **39**(6), 1182–1187 (2001)
8. Reese, G.M., et al.: Sierra structural dynamics theory manual. Technical report, Sandia National Laboratories (SNL-NM), Albuquerque (2015)
9. Team, S.S.M.: Sierra/solid mechanics 4.22 user's guide. SAND2011-7597, Sandia National Laboratories (2011)

Chapter 13
In Situ Measurements of Contact Pressure for Jointed Interfaces During Dynamic Loading Experiments

M.R.W. Brake, J.G. Stark, S.A. Smith, D.P.T. Lancereau, T.W. Jerome, and T. Dossogne

Abstract One of the greatest challenges for developing and validating models for the dynamics of jointed interfaces is measuring and characterizing the contact pressure within a joint. Previous approaches have focused on static measurements, typically taken separately from the dynamic testing of a jointed system. In this research, an electrical contact pressure measurement system is used to measure the contact pressures within a jointed interface during dynamic testing of the jointed system. These experiments invalidate a previously held modeling assumption: that the static pressure distribution is representative of the contact pressure during service of a jointed interface. In fact, for the measurements reported, the extent and magnitude of contact pressures dramatically change across the interface during sinusoidal excitation of the jointed system with more than a quarter of the interface oscillating between being in and out of contact during each period of excitation. While preliminary and scoping in nature, these experiments corroborate recent numerical studies that predict that the contact pressures across an interface significantly change over time as a function of the applied loading. The ramifications of these results are that the energy dissipation mechanisms within a jointed interface significantly evolve over time, resulting in more energy being dissipated in the interface away from the bolts than previously anticipated. This, in turn, necessitates a new constitutive modeling approach for reduced order modeling representations of joints in which the local kinematics are not regularized (such as in traditional Iwan models) and the normal contact forces are directly modeled and allowed to vary with load (contrary to most of the current modeling approaches).

Keywords Joint mechanics • Bolted joints • Interfacial mechanics • Frictional dissipation • Wave propagation • Dynamic contact

13.1 Introduction

The modeling and prediction of the response of jointed structures is a challenging engineering problem for multiple reasons. First, the frictional interactions within the interface of a jointed structure are not well understood: Coulomb friction breaks down when used to describe the frictional energy dissipation and is unable to capture both macroslip and microslip effects within the same model [3, 17]. Further, the frictional characteristics of a jointed structure change over time as wear is accumulated [1, 11–15].

M.R.W. Brake (✉)
Sandia National Laboratories, Albuquerque, NM, USA

William Marsh Rice University, Houston, TX, USA
e-mail: brake@rice.edu

J.G. Stark
Sensor Products Inc., Madison, NJ, USA

S.A. Smith
University of Maryland, Baltimore County, 1000 Hilltop Circle, 21250, Baltimore, MD, USA

Sandia National Laboratories, PO Box 5800, 87185, Albuquerque, NM, USA

D.P.T. Lancereau
Cranfield University, SN6 8LA, Shrivenham, Swindon, UK

T.W. Jerome
Graduate Program in Acoustics, The Pennsylvania State University, State College, 16801, PA, USA

Sandia National Laboratories, PO Box 5800, 87185, Albuquerque, NM, USA

T. Dossogne
University of Liège, 9, Allée de la Découverte B52/3, 4000, Liège, Belgium

Second, the extent and evolution of the contact patch during dynamic excitation is unknown. Recent numerical studies have highlighted that the contact patch dynamically evolves over a period of excitation [5]. Complicating matters, though, is that the contact patch is unable to be directly measured during use as it is internal to a system. Methods to infer what may be occurring internal to the joint, by their very nature, change what the response will be (not unlike the observer effect in quantum physics [9]). Nonetheless, any information regarding how the contact patch evolves during dynamic excitation would be able to provide crucial insights to modeling. Allowing the contact patch to evolve in a dynamic model yields a much higher degree of agreement with experimental measurements [10].

This research seeks to develop new insights into the evolution of the contact patch by measuring the contact pressure within the interface in real time during dynamic excitation. While the measurement method (a polymer contact film inserted between the two mating surfaces) changes the response of the system, it is expected that meaningful insights can be developed from these results in order to improve the dynamic modeling and prediction of jointed structures. In what follows, Sect. 13.2 details the experimental setup, and the measurements are detailed in Sect. 13.3. Lastly, the ramifications of these results are discussed in Sect. 13.4.

13.2 Experimental Setup

To study the evolution of the contact pressure in the interface of a jointed system, the benchmark system of the Brake-Reuß beam is used [2–4, 18]. The Brake-Reuß beam (Fig. 13.1) consists of two stainless steel beams joined via a three bolt lap joint. While the system is straightforward to manufacture, the nonlinearity introduced by the lap joint yields a highly nonlinear response.

The system is setup similar to Fig. 13.2. The Brake-Reuß beam is suspended via two bungee cords connected to fishing lines to approximate free-free boundary conditions. An electromagnetic shaker is attached via stinger to the beam on one side of the interface. A force transducer and accelerometer at the stinger attachment location are used to control the shaker. In the following experiments, the shaker is operated in an amplitude control mode.

Pressure films developed by Sensor Products Inc that are 1 in by 1 in with 256 sensors (on a 16 by 16 grid) are used to measure the contact pressure in the interface in real time during the dynamic excitation of the system. In the following experiments, data is acquired at a rate of 488 Hz. In order to accommodate the pressure films, the interface configuration is modified from Fig. 13.2. The limitations of the pressure film used restrict the experiments to only 500 Psi in the interface. Thus, in order to not permanently damage the pressure film, the bolts are only tightened to 2 Nm. Additionally, only two bolts are used, with the pressure film centered about the third bolt hole (i.e. the bolt closest to the shaker location). Further, to relieve stresses in the pressure film, shims made from a similar material are inserted into the interface around the other two bolt holes such that there is an equally thick layer of material across the entire interface. While this changes the nature of the contact mechanics within the interface, the results from the following experiments are expected to still yield meaningful insights into how the contact pressure within the interface evolves during dynamic excitation.
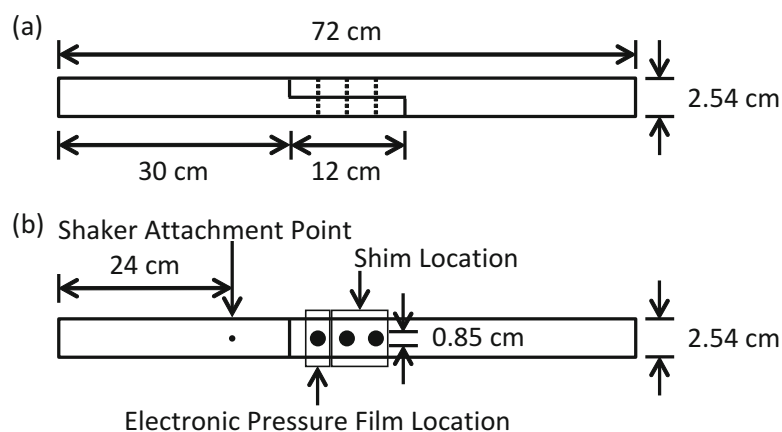
Fig. 13.1 The geometry of the Brake-Reuß beam for (**a**) top view and (**b**) side view. Note that the shaker acts in the direction orthogonal to the interface surface in view (a)
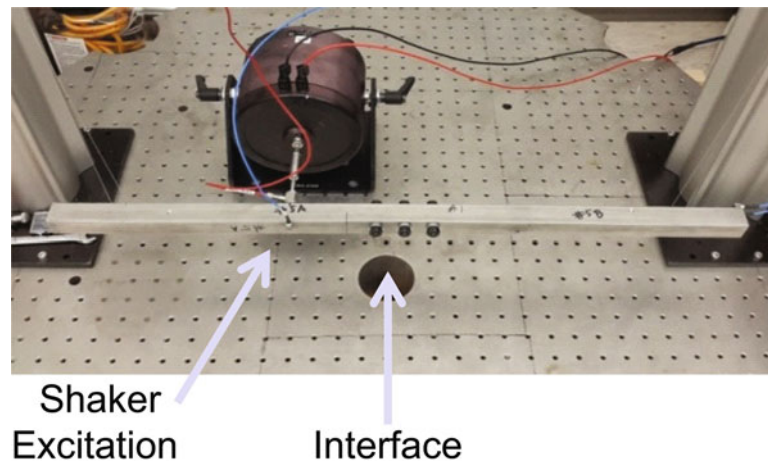
Fig. 13.2 The typical experimental setup for the Brake-Reuß beam

For each experiment, the shaker is used to excite the Brake-Reuß beam over a narrow band of frequencies centered about the first natural frequency in order to study the transition through resonance. Real time measurements of the contact pressure in the interface were recorded, and are presented in Sect. 13.3.

In what follows, several caveats are important to keep in mind:

– The bolt torques are 2.0 Nm, compared to the nominal 20 Nm.
– Only two bolts are used to connect the interface.
– The interface contains a polymeric material, which changes the contact from metal on metal to metal on polymeric on metal.

13.3   Results and Discussion

As an initial inspection of the system, an experiment is conducted in which the excitation frequency is swept from 100–160 Hz at a rate of 1 Hz/s with the shaker amplitude set to 4 N. The primary resonance of the system (including the pressure film) is located near 124 Hz. As the excitation sweeps through resonance (near 30 s), a significant change is observable in the contact area (Fig. 13.3). The contact area transitions from being a nearly constant value of 0.3 in^2 to varying between 0.05 and 0.35 in^2. After resonance has passed, the contact area returns to the nearly constant value of 0.3 in^2.

The contact force for the studied portion of the interface is calculated by summing the contact pressures over the interface and multiplying by the area of each pressure sensor $(1/16 \text{ in})^2$. The contact forces are observed to vary significantly about resonance. Below resonance, the contact force in the left quarter of the interface is observed to be constant at approximately 60 lbs. Near resonance, however, the contact force varies between 2 and 70 lbs. At frequencies above resonance, the contact force returns to a constant value (though increasing slightly with frequency) of approximately 62 lbs (Fig. 13.4).

To understand the evolution of the contact pressure during resonance, a second set of experiments were conducted in which the excitation frequency was swept from 123–125 Hz at a rate of 0.05 Hz/s. Three different excitation amplitudes were used: 1, 2, and 3 N (denoted as low, medium, and high in what follows).

As before, a significant variation in the contact area is observed in the measurements for all three excitation amplitudes (Fig. 13.5 for low, Fig. 13.6 for medium, and Fig. 13.7 for high). As the excitation amplitude is increased from low to high, the maximum contact area changes from 0.3 to 0.7 in^2 at resonance (approximately 15 s), with a minimum contact area of 0 in^2 in all cases .

Likewise, the peak contact forces (Fig. 13.8 for low, Fig. 13.9 for medium, and Fig. 13.10 for high) are observed to vary from 50 lbs for the low excitation force to 84 lbs for the high excitation force. Both before and after the forced excitation, the contact forces are measured as approximately 18 lbs. Thus, significant variations are observed in the specific conditions of the contact interface during dynamic excitation near resonance, and the contact area is significantly different than the static measurement of the contact area.
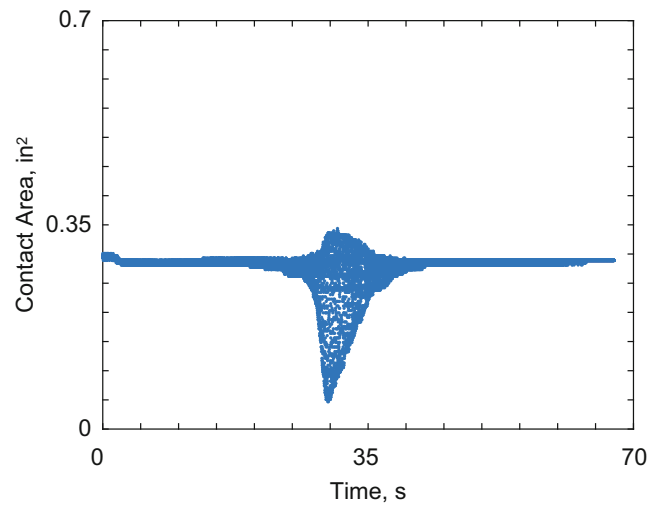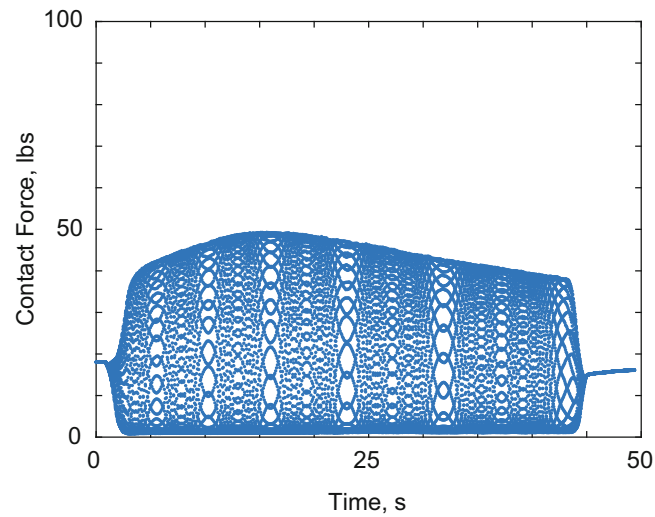
Fig. 13.3 Contact area as a function of time over the left quarter of the interface for the 100–160 Hz sweep
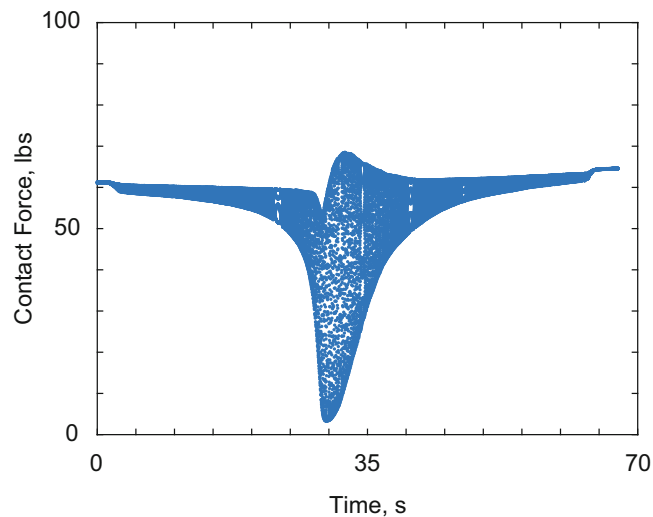
Fig. 13.4 Contact force as a function of time over the left quarter of the interface for the 100–160 Hz sweep

To further visualize the evolution of the contact interface during dynamic excitation near resonance, Figs. 13.11, 13.12, and 13.13 (for the low, medium, and high excitations respectively), show the two-dimensional contact pressure maps at four different phases during a period of excitation. The coordinate system is setup such that the left hand side of the plots are the edge of the contact pressure film closest to the middle bolt hole, and the right hand side is the edge of the contact pressure film closest to the shaker. The contact pressure (and correspondingly contact area) is observed to be zero at one point in time for all three excitation amplitudes (Figs. 13.11a, 13.12a, and 13.13a). As the phase increases, the interface is observed to come into contact around the unused bolt hole (as evident by the dark circular region in Fig. 13.13d). Due to the asymmetric loading of the interface (as a result of the particular experimental setup), the lower corner of the contact pressure film never is fully engaged. For both the low (Fig. 13.11) and medium (Fig. 13.12) excitation amplitudes, the interfacial contact is never observed to fully encircle the bolt hole.

13.4 Discussion and Conclusions

As has previously been observed in numerical studies [5], this research experimentally confirms that the contact patch evolves during dynamic excitation. While several caveats exist, the extent of the contact patch in the present research is observed to change by over an inch (note that the contact pressure sensor is only one inch in width). For larger bolt torques, of course,
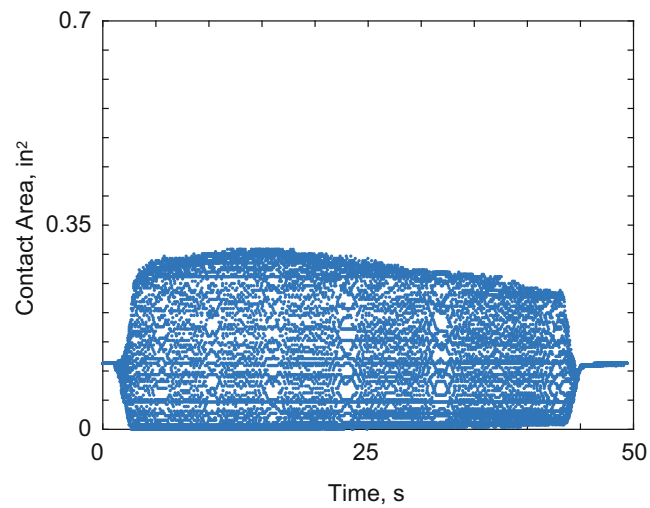
Fig. 13.5 Contact area as a function of time over the left quarter of the interface for the 123–125 Hz sweep at a low excitation amplitude
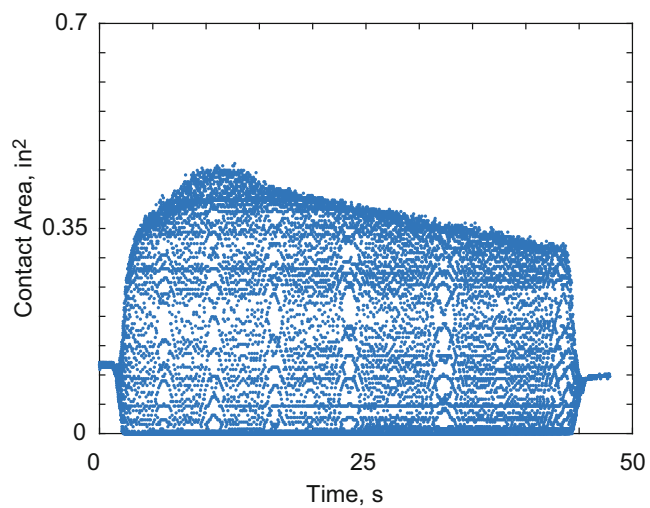
Fig. 13.6 Contact area as a function of time over the left quarter of the interface for the 123–125 Hz sweep at a medium excitation amplitude
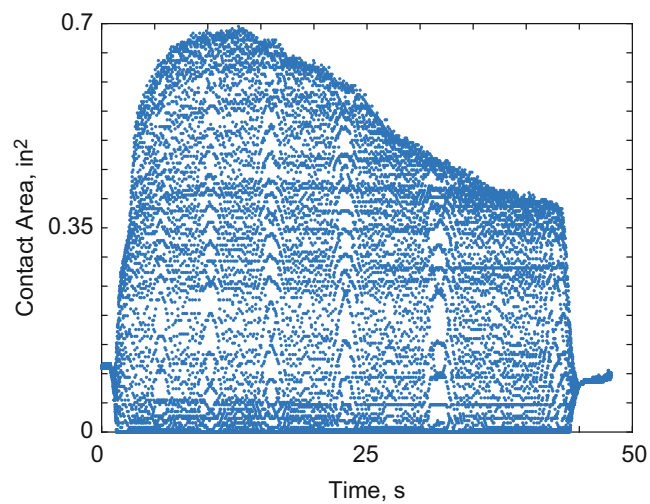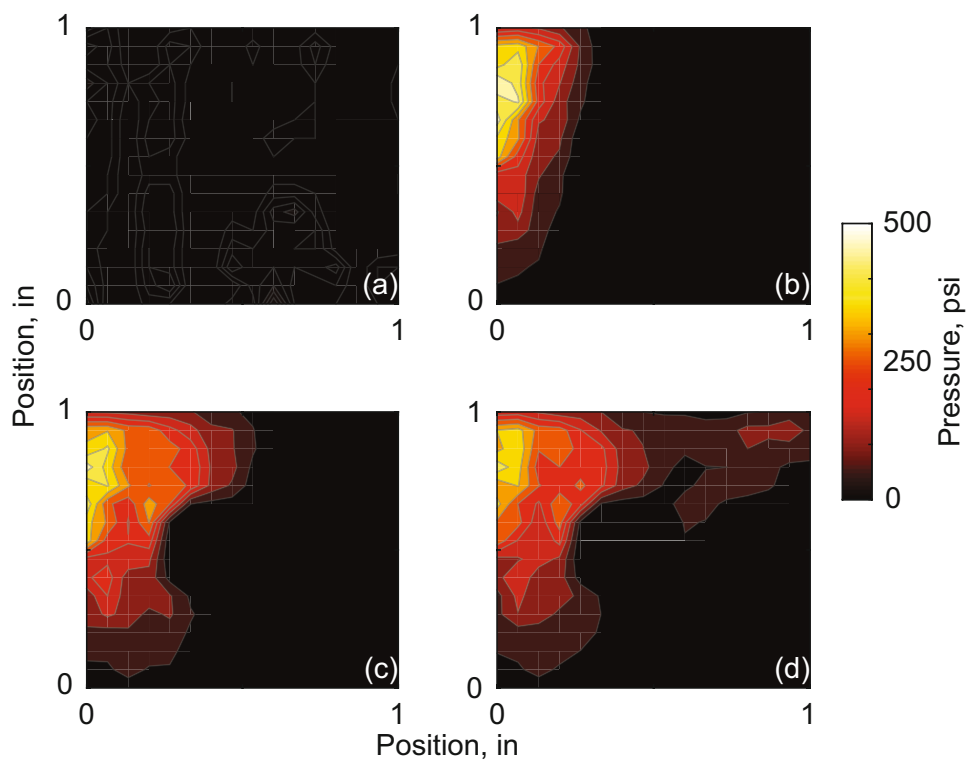

Fig. 13.7 Contact area as a function of time over the left quarter of the interface for the 123–125 Hz sweep at a high excitation amplitude

Fig. 13.8 Contact force as a function of time over the left quarter of the interface for the 123–125 Hz sweep at a low excitation amplitude
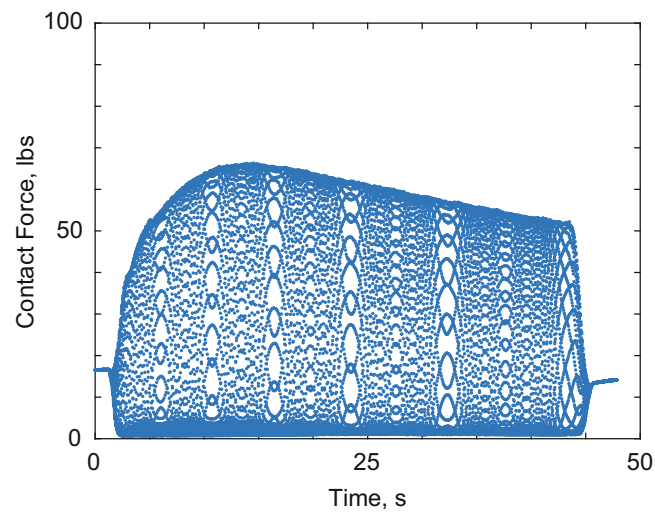
Fig. 13.9 Contact force as a function of time over the left quarter of the interface for the 123–125 Hz sweep at a medium excitation amplitude

the magnitude of the contact area change is expected to decrease; nonetheless, this series of experiments shows that the interface cannot be assumed to be static during dynamic excitation as had been previously assumed. Instead, models of jointed structures must be able to capture the evolution of the contact patch during dynamic excitation. Further, as the energy dissipated in an interface is dominated by the regions away from the bolts where contact pressure is lowest [6–8], it may be imperative to model the extent of these regions accurately.

When coupled with the findings of the numerical study of [10], in which it was shown that better agreement between experiments and models could be achieved by allowing the contact patch to evolve during dynamic excitation, there is, perhaps, a significant and far-reaching ramification: interface models must be improved to capture the local kinematics of contact. This conclusion is somewhat contrary to one of the main approaches for modeling jointed structures, namely the typical manner in which Iwan elements are employed [3, 16, 17]. Typically, Iwan elements are used to represent an entire interface, which necessitates that the local kinematics of an interface be regularized to a single (or a small number of) contact patches. This regularization, though, has the potential to go too far and neglect effects such as the evolution of the contact patch during excitation. The advantage of this modeling approach is a significant reduction in the number of degrees of freedom used to represent the interface of a jointed structure. Other methods that are able to incorporate the evolution of the contact patch require orders of magnitude more degrees of freedom in the contact patch than the Iwan modeling approach [10].
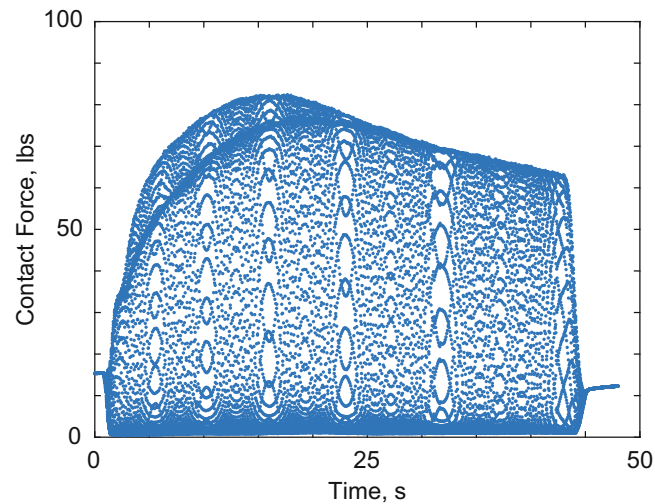
Fig. 13.10 Contact force as a function of time over the left quarter of the interface for the 123–125 Hz sweep at a high excitation amplitude
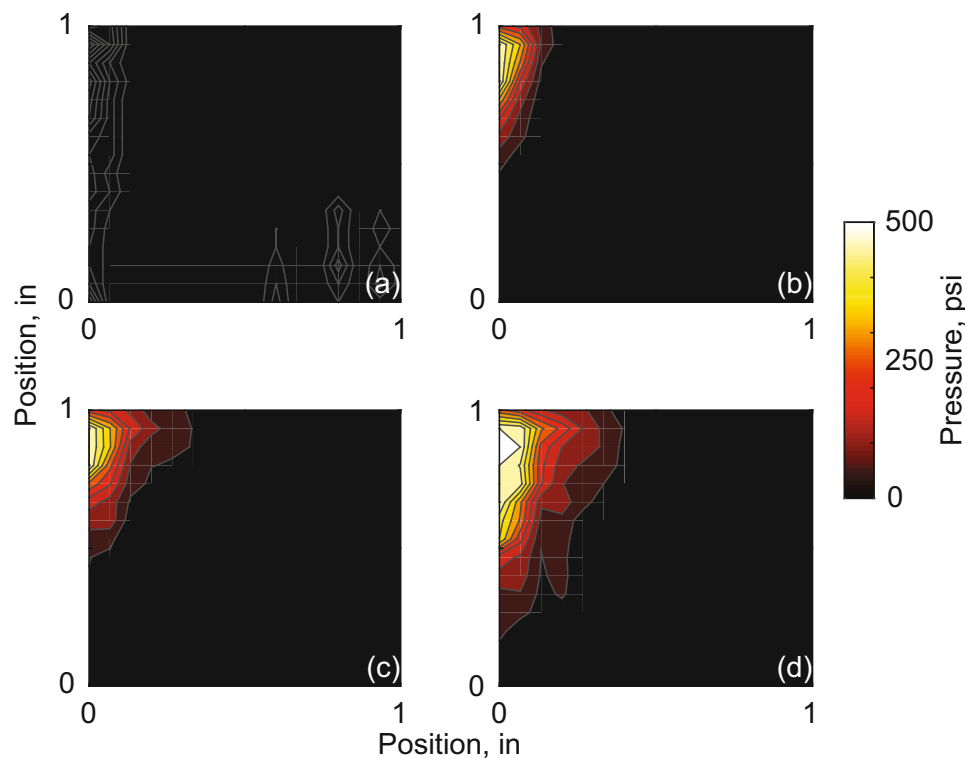
Fig. 13.11 Contact pressure at four different phases during an excitation of 124 Hz at a low excitation amplitude

Future work, therefore, must further study the importance of capturing the local kinematics in modeling jointed structures. If it is further confirmed that the modeling of the local kinematics are essential for *predicting* the response of a jointed structure, then a compromise is needed between the different numerical approaches – one where the local kinematics are able to be preserved while reducing the total number of degrees of freedom necessary to represent them accurately. One potential avenue may be to use multiple contact patches defined over an interface (such as in [10], but perhaps to a greater extent) over which both an Iwan model is defined for the tangential forces and a normal contact model is defined (unlike in [10]) to capture the local kinematics. A second potential avenue may require a fundamentally different approach from Iwan elements altogether, which requires novel constitutive modeling insights.
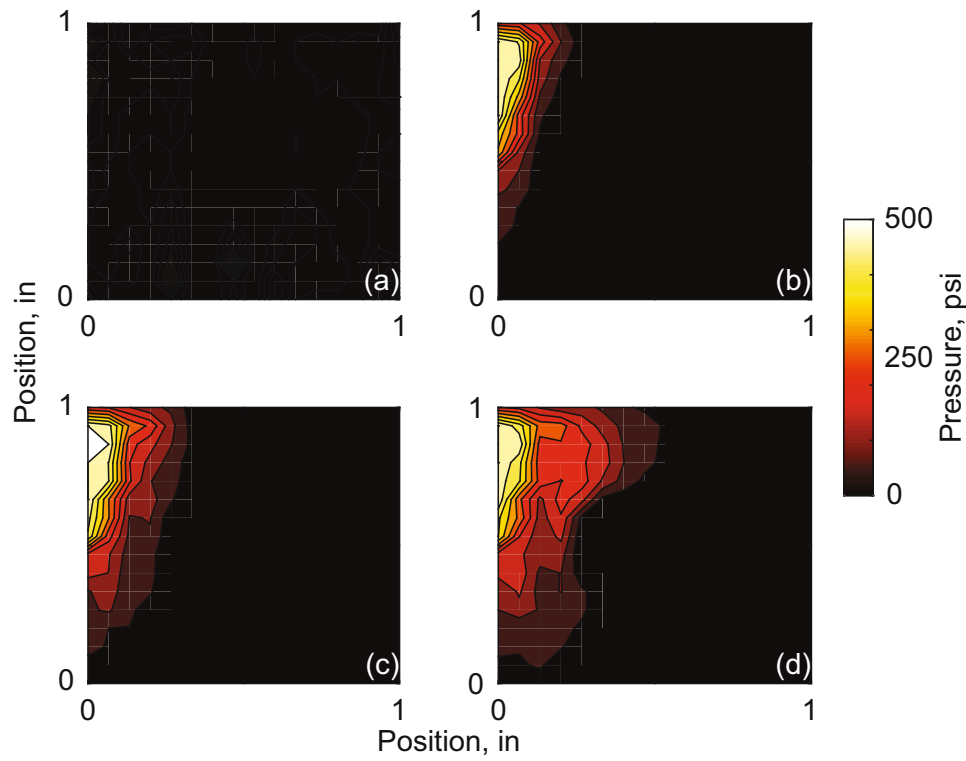
Fig. 13.12 Contact pressure at four different phases during an excitation of 124 Hz at a medium excitation amplitude

Fig. 13.13 Contact pressure at four different phases during an excitation of 124 Hz at a high excitation amplitude

References

1. Bode, K., Ostermeyer, G.P.: A comprehensive approach for the simulation of heat and heat-induced phenomena in friction materials. Wear **311**, 47–56 (2014)
2. Brake, M.R., et al: Variability and repeatability of jointed structures with frictional interfaces. In: 32nd International Modal Analysis Conference (IMAC XXXII), Orlando (2014)
3. Brake, M.R.W. (ed.): The Mechanics of Jointed Structures. Springer, New York, USA (2017)
4. Catalfamo, S., et al.: Effects of experimental methods on the measurement of a nonlinear system. In: 34th International Modal Analysis Conference (IMAC XXXIV), Orlando (2016)
5. Flicek, R.C., et al.: Stress waves propagating through jointed connections. In: 34th International Modal Analysis Conference (IMAC XXXIV), Orlando (2016)
6. Goyder, H.G.D., Ind, P., Brown, D.: Measurement of damping due to bolted joints. In: ASME International Design Engineering Technical Conferences IDETC/CIE, Portland (2013)
7. Goyder, H.G.D., Ind, P., Brown, D.: Measurement of damping in a chain of bolted joints. In: ASME International Design Engineering Technical Conferences IDETC/CIE, Buffalo (2014)
8. Goyder, H.G.D., Ind, P., Brown, D.: Damping in a composite beam with a joined interface. In: ASME International Design Engineering Technical Conferences IDETC/CIE, Boston (2015)
9. Heisenberg, W.: Physics and Philosophy: The Revolution in Modern Science. George Allen and Unwin LTD, London (1959)
10. Lacayo, R.M., et al.: A numerical round robin to predict the dynamics of an experimentally-measured brake-reuss beam. In: 35th International Modal Analysis Conference (IMAC XXXV), Garden Grove (2017)
11. Müller, M., Ostermeyer, G.P.: A cellular automation model to describe the three-dimensional friction and wear mechanism of brake systems. Wear **263**, 1175–1188 (2007)
12. Müller, M., Ostermeyer, G.P.: Cellular automata method for macroscopic surface and friction dynamics in brake systems. Tribol. Int. **40**, 942–952 (2007)
13. Mulvihill, D.M., et al.: Investigation of non-coulomb friction behaviour in reciprocating sliding. Wear **271**, 802–816 (2011)
14. Ostermeyer, G.P., Müller, M.: Dynamic interaction of friction and surface topography in brake systems. Tribol. Int. **39**, 370–380 (2006)
15. Schwingshackl, C.W., Petrov, E.P., Ewins, D.J.: Measured and estimated friction interface parameters in a nonlinear dynamic analysis. Mech. Syst. Signal Process. **28**, 574–584 (2012)
16. Segalman, D.J.: A four-parameter Iwan model for lap-type joints. ASME J. Appl. Mech. **72**, 752–760 (2005)
17. Segalman, D.J., et al.: Handbook on Dynamics of Jointed Structures. Technical report SAND2009-4164. Sandia National Laboratories, Albuquerque (2009)
18. Smith, S.A., et al.: The effects of boundary conditions, measurement techniques, and excitation type on measurements of the properties of mechanical joints. In: 33rd International Modal Analysis Conference (IMAC XXXIV), Orlando (2015)

Chapter 14
Dual Craig-Bampton Method with Reduction of Interface Coordinates

Fabian M. Gruber, Tim L. Bürchner, and Daniel Jean Rixen

Abstract Dynamic substructuring techniques divide large models into substructures whereby each substructure is reduced and then assembled into a reduced model of low order which approximates the behaviour of the original model. Thereby the boundary degrees of freedom (degrees of freedom shared with adjacent substructures) are kept and only the internal degrees of freedom of each substructure are reduced to a small number of generalized coordinates.

If the interfaces between the substructures are large or if many substructures are used, the number of interface degrees of freedom is high. In that case the boundary degrees of freedom form a large subset of the generalized coordinates of the reduced substructures, which often is not necessary for the accurate description of the overall dynamics, but is present just for the interface assembly. To overcome this drawback and get a reduced model of low order, the interface degrees of freedom have to be reduced as well.

In this contribution, the reduction of interface coordinates for the dual Craig-Bampton method is demonstrated. The dual Craig-Bampton method employs free-interface vibration modes together with attachment modes to build the reduction bases of the substructures and assembles the substructures using interface forces (dual assembly). Considering the interface problem, a static reduction (Guyan reduction) of the interface coordinates is derived to obtain interface modes for the approximation of the interface degrees of freedom. Further, a reduction of interface coordinates using interface normal modes is demonstrated. The approximation accuracy of the different interface reduction approaches is evaluated. Focus will be directed to the influence on the negative eigenvalues of the reduced system which are intrinsic to the dual Craig-Bampton method. The proposed approach will be illustrated on examples where interface modes can be visualized in order to analyze their influence on the approximation quality of the reduced system.

Keywords Dynamic substructuring • Component mode synthesis • Dual Craig-Bampton method • Free interface method • Interface reduction • Interface modes

14.1 Introduction

The increasing performance of modern computers makes it possible to solve very large linear systems of millions of degrees of freedom (DOFs) very fast. Nevertheless, since the refinement of finite element models is increasing faster than the computing capabilities, dynamic substructuring still remains an essential tool for analyzing dynamical systems in an efficient manner. Building reduced models of submodels of a structure enables sharing models between design groups. Moreover the reduction of the DOFs of substructures is also important for building reduced order models for optimization and control. If a single component of a system is changed, only that component needs to be reanalyzed and the system can be analyzed at low additional cost. Thus dynamic substructuring offers a flexible and efficient approach to dynamic analysis [1, 2, 4, 6, 8, 9, 12, 13].

Dynamic substructuring techniques can be classified in two categories depending on the underlying modes which are used [1]. The term mode can refer to all kind of structural shape vectors. The first class consists of methods using fixed interface vibration modes and interface constraint modes to represent the substructure dynamics. The method commonly used is the Craig-Bampton method [2] which assembles the substructures in a primal way using interface displacements in order to enforce interface compatibility. The second class consists of methods using free interface vibration modes and

F.M. Gruber (✉) • T.L. Bürchner
Chair of Applied Mechanics, Faculty of Mechanical Engineering, Technical University of Munich, Boltzmannstr. 15, 85748, Garching, Germany
e-mail: fabian.gruber@tum.de; tim.buerchner@tum.de

D.J. Rixen
Technical University of Munich, Boltzmannstraße 15, D-85748, Garching, Germany
e-mail: rixen@tum.de

attachment modes. Representatives of that class are MacNeal's method [8] and Rubin's method [12] using a primal assembly process as well. In contrast to the aforementioned methods, the dual Craig-Bampton method (DCBM) [9] uses also free interface vibration modes and attachment modes, but assembles the substructures in a dual way using interface forces. As a consequence, the DCBM enforces only weak interface compatibility between the substructures, thereby avoiding interface locking problems as sometimes experienced in the primal assembly approaches. Furthermore, the DCBM leads to simpler reduced matrices compared to other free interface methods and the reduced matrices are sparse, similar to the classical Craig-Bampton matrices [9].

   All methods divide the large model of a dynamical system into substructures, each substructure is reduced and then assembled into a reduced model of low order which approximate the behavior of the original large model. During this process the DOFs of each substructure are divided into internal DOFs (not shared with any adjacent substructure) and boundary DOFs (shared with adjacent substructures and therefore forming the interface degrees of freedom of the model). Most substructuring methods keep all boundary DOFs and the process only reduces the internal DOFs of each substructure to a small number of generalized coordinates.

   As long as the number of interface DOFs is low these substructuring methods result in reduced models of low order that approximates the dynamic behavior of the original model with excellent accuracy. But if the interfaces are large or if many substructures are used the number of interface DOFs is high. In that case the boundary DOFs constitute a significant part of the generalized coordinates of the reduced substructures, which often are not necessary for the description of the overall dynamics, but merely enables convenient assembly of the substructures. To overcome this drawback and get a reduced model of low order, the interface degrees of freedom have to be reduced as well. For many substructuring methods, e.g. the Craig-Bampton method (1968), different approaches for the reduction of the interface coordinates were proposed [3]. Thereby commonly the interface problem is considered and the interface DOFs are represented by a reduced number of interface modes and corresponding generalized interface coordinates. In this contribution we intend to demonstrate the reduction of interface coordinates for the dual Craig-Bampton method [9] which enables the reduction of interface coordinates significantly without deteriorating the approximation accuracy in the low frequency range.

   In Sect. 14.2, the original formulation and an alternative formulation of the dual Craig-Bampton method are presented and are compared. Following this, a static reduction (Guyan reduction) and a modal reduction of the interface coordinates are derived in Sect. 14.3. The properties of these interface reduction methods will be illustrated subsequently in detail in Sect. 14.4 using a two-dimensional solid plane stress problem. Subsection 14.4.3 tries to give some interpretation of the interface modes using a simple example. Finally we conclude with some general remarks in Sect. 14.5 and give an outlook on further research.

14.2   Governing Equations

Consider a finite element model of a global domain Ω. This domain Ω is divided into N non-overlapping substructures called $\Omega^{(s)}$ such that every node belongs to exactly one substructure except for the nodes on the interface boundaries. The linear/linearized equation of motion of one substructure s is written as

$$M^{(s)}\ddot{u}^{(s)} + K^{(s)}u^{(s)} = f^{(s)} + g^{(s)}, \quad s = 1, \ldots, N \tag{14.1}$$

where the superscript (s) is the label of the particular substructure. $M^{(s)}$, $K^{(s)}$ and $u^{(s)}$ are the mass matrix, the stiffness matrix and the displacement vector of the substructure, respectively. $f^{(s)}$ is the external force vector and $g^{(s)}$ is the vector of reaction forces on the substructure due to its connection to adjacent substructures at its boundary DOFs $u_b^{(s)}$. The local displacements vector $u^{(s)}$ of each substructure is divided in local internal DOFs $u_i^{(s)}$ and boundary DOFs $u_b^{(s)}$.

   One way to enforce the interface compatibility between the different substructures is to consider the interface connecting forces $g^{(s)}$ as unknowns. These forces must be determined to satisfy the interface compatibility condition (displacement equality) and the local equation of motion of the substructures:

$$\sum_{s=1}^{N} B^{(s)}u^{(s)} = 0 \tag{14.2}$$

$$M^{(s)}\ddot{u}^{(s)} + K^{(s)}u^{(s)} + B^{(s)^T}\lambda = f^{(s)} \tag{14.3}$$

$B^{(s)}$ is a signed Boolean matrix (constraint matrix) acting on the substructure DOFs $u^{(s)}$. $B^{(s)^T}\lambda$ is representing the interconnecting forces between substructures which is corresponding to the negative interface reaction force vector $g^{(s)}$

in Eq. (14.1) meaning

$$g^{(s)} = -B^{(s)^T} \lambda, \tag{14.4}$$

and λ is the vector of all Lagrange multipliers acting on the interfaces which are the additional unknowns.

Using the block-diagonal matrices

$$M = \begin{bmatrix} M^{(1)} & & 0 \\ & \ddots & \\ 0 & & M^{(N)} \end{bmatrix}, \quad K = \begin{bmatrix} K^{(1)} & & 0 \\ & \ddots & \\ 0 & & K^{(N)} \end{bmatrix}, \tag{14.5}$$

the corresponding partitioned vectors and Boolean matrix

$$u = \begin{bmatrix} u^{(1)} \\ \vdots \\ u^{(N)} \end{bmatrix}, \quad f = \begin{bmatrix} f^{(1)} \\ \vdots \\ f^{(N)} \end{bmatrix}, \quad B = \begin{bmatrix} B^{(1)} \cdots B^{(N)} \end{bmatrix}, \tag{14.6}$$

the substructure Eqs. (14.2) and (14.3) can be assembled as

$$M_{dual} \begin{bmatrix} \ddot{u} \\ \ddot{\lambda} \end{bmatrix} + K_{dual} \begin{bmatrix} u \\ \lambda \end{bmatrix} = \begin{bmatrix} M & 0 \\ 0 & 0 \end{bmatrix} \begin{bmatrix} \ddot{u} \\ \ddot{\lambda} \end{bmatrix} + \begin{bmatrix} K & B^T \\ B & 0 \end{bmatrix} \begin{bmatrix} u \\ \lambda \end{bmatrix} = \begin{bmatrix} f \\ 0 \end{bmatrix} = f_{dual}. \tag{14.7}$$

In this hybrid formulation the Lagrange multipliers λ enforce the interface compatibility constraints and can be identified as interface forces [9].

14.2.1   Original Formulation of the Dual Craig-Bampton Method (DCBM)

Considering the equation of motion (14.3) of substructure s, every substructure can be seen as being excited by the interface connection forces and the external forces [9]. This indicates that the displacements of each substructure $u^{(s)}$ can be expressed in terms of local static solutions $u_{stat}^{(s)}$ and in terms of eigenmodes associated to the entire substructure matrices $K^{(s)}$ and $M^{(s)}$:

$$u^{(s)} = u_{stat}^{(s)} + \sum_{j=1}^{n^{(s)}-r^{(s)}} \theta_j^{(s)} \eta_j^{(s)} \qquad \text{with} \qquad u_{stat}^{(s)} = -K^{(s)^+} B^{(s)^T} \lambda + \sum_{j=1}^{r^{(s)}} R_j^{(s)} \alpha_j^{(s)}. \tag{14.8}$$

$n^{(s)}$ is the dimension of the local substructure problem and $K^{(s)^+}$ is equal to the inverse of $K^{(s)}$ if there are enough boundary conditions to prevent the substructure from floating when its interface with adjacent substructures is free [9]. If a substructure is floating, the generalized inverse $K^{(s)^+}$ has to be used. $R^{(s)}$ is the matrix containing the $r^{(s)}$ rigid body modes as columns which are mass orthonormalized. The vector $\alpha^{(s)}$ contains the amplitudes $\alpha_j^{(s)}$ of the rigid body modes $R^{(s)}$. The flexibility matrix $G^{(s)}$ in inertia-relief format is computed from any generalized inverse $K^{(s)^+}$ by projecting out the rigid body modes $R^{(s)}$ using the inertia-relief projection matrix $P^{(s)}$ which is defined as [4, 5]

$$P^{(s)} = I^{(s)} - M^{(s)} R^{(s)} R^{(s)^T} \tag{14.9}$$

and therefore

$$G^{(s)} = P^{(s)^T} K^{(s)^+} P^{(s)}. \tag{14.10}$$

The vector $\eta^{(s)}$ contains the amplitudes $\eta_j^{(s)}$ of the local eigenmodes $\theta_j^{(s)}$ being eigensolutions of the generalized eigenproblem

$$K^{(s)}\theta_j^{(s)} = \omega_j^{(s)^2} M^{(s)}\theta_j^{(s)}. \tag{14.11}$$

These free interface normal modes $\theta_j^{(s)}$ are also mass orthonormalized. An approximation is obtained by retaining only the first free interface normal modes $\theta_j^{(s)}$ corresponding to the $n_\theta^{(s)}$ lowest eigenvalues $\omega_j^{(s)^2}$. Calling $\Theta^{(s)}$ the matrix containing these eigenmodes, the approximation of the displacements $u^{(s)}$ of the substructure is given by

$$u^{(s)} \approx -G^{(s)}B^{(s)^T}\lambda + R^{(s)}\alpha^{(s)} + \Theta^{(s)}\eta^{(s)}. \tag{14.12}$$

$\Theta^{(s)}$ is satisfying

$$\Theta^{(s)^T}K^{(s)}\Theta^{(s)} = \Omega^{(s)^2} = \mathrm{diag}(\omega_j^{(s)^2}) \qquad \text{and} \qquad \Theta^{(s)^T}M^{(s)}\Theta^{(s)} = I \tag{14.13}$$

with $\Omega^{(s)}$ being a diagonal matrix containing the remaining $n_\theta^{(s)}$ eigenvalues $\omega_j^{(s)}$. Since a part of the subspace spanned by $\Theta^{(s)}$ is already included in $G^{(s)}$ the residual flexibility matrix $G_r^{(s)}$ can be used instead of the flexibility matrix $G^{(s)}$, which is defined by

$$G_r^{(s)} = \sum_{j=n_\theta^{(s)}+1}^{n^{(s)}-r^{(s)}} \frac{\theta_j^{(s)}\theta_j^{(s)^T}}{\omega_j^{(s)^2}} = G^{(s)} - \sum_{j=1}^{n_\theta^{(s)}} \frac{\theta_j^{(s)}\theta_j^{(s)^T}}{\omega_j^{(s)^2}}. \tag{14.14}$$

Note that, by construction $G_r^{(s)} = G_r^{(s)^T}$, which is computed using the second equality in Eq. (14.14). For further properties of $G_r^{(s)}$ see [9, 10]. As a result the approximation of one substructure writes

$$u^{(s)} \approx -G_r^{(s)}B^{(s)^T}\lambda + R^{(s)}\alpha^{(s)} + \Theta^{(s)}\eta^{(s)} = \begin{bmatrix} R^{(s)} & \Theta^{(s)} & -G_r^{(s)}B^{(s)^T} \end{bmatrix} \begin{bmatrix} \alpha^{(s)} \\ \eta^{(s)} \\ \lambda \end{bmatrix}. \tag{14.15}$$

Assembling all substructures N in a dual fashion according to Eq. (14.7) by keeping the interface forces λ as unknowns, the entire structure can consequently be approximated by

$$\begin{bmatrix} u \\ \lambda \end{bmatrix} \approx \begin{bmatrix} R^{(1)} & \Theta^{(1)} & & 0 & 0 & -G_r^{(1)}B^{(1)^T} \\ & & \ddots & \ddots & & \vdots \\ 0 & 0 & & R^{(N)} & \Theta^{(N)} & -G_r^{(N)}B^{(N)^T} \\ 0 & 0 & & 0 & 0 & I \end{bmatrix} \begin{bmatrix} \alpha^{(1)} \\ \eta^{(1)} \\ \vdots \\ \alpha^{(N)} \\ \eta^{(N)} \\ \lambda \end{bmatrix} = \underbrace{\begin{bmatrix} R & \Theta & -G_rB^T \\ 0 & 0 & I \end{bmatrix}}_{T_{DCB}} \begin{bmatrix} \alpha \\ \eta \\ \lambda \end{bmatrix}. \tag{14.16}$$

The approximation of the dynamic equations of the dual assembled system (14.7) is

$$M_{DCB} \begin{bmatrix} \ddot{\alpha} \\ \ddot{\eta} \\ \ddot{\lambda} \end{bmatrix} + K_{DCB} \begin{bmatrix} \alpha \\ \eta \\ \lambda \end{bmatrix} = f_{DCB} \tag{14.17}$$

with

$$M_{DCB} = T_{DCB}^T \begin{bmatrix} M & 0 \\ 0 & 0 \end{bmatrix} T_{DCB} = \begin{bmatrix} I & 0 & 0 \\ 0 & I & 0 \\ 0 & 0 & M_r \end{bmatrix}, \quad M_r = BG_rMG_rB^T = \sum_{s=1}^{N} B^{(s)}G_r^{(s)}M^{(s)}G_r^{(s)}B^{(s)^T}, \tag{14.18}$$

$$K_{DCB} = T_{DCB}^T \begin{bmatrix} K & B^T \\ B & 0 \end{bmatrix} T_{DCB} = \begin{bmatrix} 0 & 0 & R^T B^T \\ 0 & \Omega^2 & \Theta^T B^T \\ BR & B\Theta & -F_r \end{bmatrix}, \quad F_r = BG_r B^T = \sum_{s=1}^{N} B^{(s)} G_r^{(s)} B^{(s)^T}, \tag{14.19}$$

$$f_{DCB} = T_{DCB}^T \begin{bmatrix} f \\ 0 \end{bmatrix}. \tag{14.20}$$

The DCBM reduced system has the final size $n_{DCB} = n_{rig} + \sum_{s=1}^{N} n_{\theta}^{(s)} + n_{\lambda}$ with n_{rig} being the number of rigid body modes of all substructures, $n_{\theta}^{(s)}$ the number of free interface normal modes of substructure s and n_{λ} the number of Lagrange multipliers [9].

14.2.2   Alternative Formulation of the Dual Craig-Bampton Method

The original formulation of the DCBM [9] (see Sect. 14.2.1) uses residual attachment modes which are the columns of the residual flexibility matrix $G_r^{(s)}$ and the reduced matrices in Eqs. (14.18) and (14.19) are resulting [11]. The coupling between residual attachment modes and free interface normal modes is contained in the reduced stiffness matrix K_{DCB}. In the following an alternative formulation of the dual Craig-Bampton method [11] is recalled using attachment modes which are columns of the flexibility matrix $G^{(s)}$, instead of residual attachment modes. This shifts the coupling between attachment modes and free interface normal modes to the reduced mass matrix which is beneficial for the computation of interface modes used afterwards for the reduction the interface coordinates. Assembling all substructures N which are approximated by Eq. (14.12) instead of Eq. (14.15), the entire structure can consequently be approximated by

$$\begin{bmatrix} u \\ \lambda \end{bmatrix} \approx \begin{bmatrix} R^{(1)} & \Theta^{(1)} & & 0 & 0 & -G^{(1)}B^{(1)^T} \\ & \ddots & \ddots & & & \vdots \\ 0 & 0 & & R^{(N)} & \Theta^{(N)} & -G^{(N)}B^{(N)^T} \\ 0 & 0 & & 0 & 0 & I \end{bmatrix} \begin{bmatrix} \alpha^{(1)} \\ \eta^{(1)} \\ \vdots \\ \alpha^{(N)} \\ \eta^{(N)} \\ \lambda \end{bmatrix} = \underbrace{\begin{bmatrix} R & \Theta & -GB^T \\ 0 & 0 & I \end{bmatrix}}_{\bar{T}_{DCB}} \begin{bmatrix} \alpha \\ \eta \\ \lambda \end{bmatrix}. \tag{14.21}$$

The approximation of the dynamic equations of the dual assembled system (14.7) corresponding to the alternative formulation of the DCBM is

$$\bar{M}_{DCB} \begin{bmatrix} \ddot{\alpha} \\ \ddot{\eta} \\ \ddot{\lambda} \end{bmatrix} + \bar{K}_{DCB} \begin{bmatrix} \alpha \\ \eta \\ \lambda \end{bmatrix} = \bar{f}_{DCB} \tag{14.22}$$

with

$$\bar{M}_{DCB} = \bar{T}_{DCB}^T \begin{bmatrix} M & 0 \\ 0 & 0 \end{bmatrix} \bar{T}_{DCB} = \begin{bmatrix} I & 0 & 0 \\ 0 & I & -\Omega^{-2}\Theta^T B^T \\ 0 & -B\Theta\Omega^{-2} & \bar{M}_r \end{bmatrix}, \tag{14.23}$$

$$\bar{M}_r = BGMGB^T = \sum_{s=1}^{N} B^{(s)} G^{(s)} M^{(s)} G^{(s)} B^{(s)^T}, \tag{14.24}$$

$$\bar{K}_{DCB} = \bar{T}_{DCB}^T \begin{bmatrix} K & B^T \\ B & 0 \end{bmatrix} \bar{T}_{DCB} = \begin{bmatrix} 0 & 0 & R^T B^T \\ 0 & \Omega^2 & 0 \\ BR & 0 & -\bar{F}_r \end{bmatrix}, \quad \bar{F}_r = BGB^T = \sum_{s=1}^{N} B^{(s)} G^{(s)} B^{(s)^T}, \tag{14.25}$$

$$\bar{f}_{DCB} = \begin{bmatrix} f \\ 0 \end{bmatrix}. \tag{14.26}$$

The final size of the reduced system using the alternative formulation of the DCBM is obviously the same as for the original formulation.

14.2.3 Comparison of the Two Formulations of the Dual Craig-Bampton Method

Equation (14.27) repeats the reduced equations of motion obtained by applying the original formulation of the DCBM [9] and Eq. (14.28) the reduced equations of motion obtained by applying the alternative formulation of the DCBM [11]:

$$
\begin{bmatrix} I & 0 & 0 \\ 0 & I & 0 \\ 0 & 0 & M_r \end{bmatrix} \begin{bmatrix} \ddot{\alpha} \\ \ddot{\eta} \\ \ddot{\lambda} \end{bmatrix} + \begin{bmatrix} 0 & 0 & R^T B^T \\ 0 & \Omega^2 & \Theta^T B^T \\ BR & B\Theta & -F_r \end{bmatrix} \begin{bmatrix} \alpha \\ \eta \\ \lambda \end{bmatrix} = T_{DCB}^T \begin{bmatrix} f \\ 0 \end{bmatrix} \tag{14.27}
$$

$$
\begin{bmatrix} I & 0 & 0 \\ 0 & I & -\Omega^{-2}\Theta^T B^T \\ 0 & -B\Theta\Omega^{-2} & \bar{M}_r \end{bmatrix} \begin{bmatrix} \ddot{\alpha} \\ \ddot{\eta} \\ \ddot{\lambda} \end{bmatrix} + \begin{bmatrix} 0 & 0 & R^T B^T \\ 0 & \Omega^2 & 0 \\ BR & 0 & -\bar{F}_r \end{bmatrix} \begin{bmatrix} \alpha \\ \eta \\ \lambda \end{bmatrix} = \bar{T}_{DCB}^T \begin{bmatrix} f \\ 0 \end{bmatrix} \tag{14.28}
$$

The reduced matrices of Eqs. (14.27) and (14.28) of the two formulations are different but it should be noted that the reduction basis and the dual assembly procedure is the same for both formulations [11]. Therefore both formulations are mathematically equivalent and will give the same results. Using residual attachment modes, the coupling between these modes and the free interface normal modes appears in the stiffness matrix. As opposed to this, using attachment modes the coupling between the attachment modes and the free interface modes appears in the mass matrix.

One important fact used later for the interface reduction is that the subpart of the reduced matrices of the alternative formulation

$$
\begin{bmatrix} I & 0 \\ 0 & \bar{M}_r \end{bmatrix} \begin{bmatrix} \ddot{\alpha} \\ \ddot{\lambda} \end{bmatrix} + \begin{bmatrix} 0 & R^T B^T \\ BR & -\bar{F}_r \end{bmatrix} \begin{bmatrix} \alpha \\ \lambda \end{bmatrix} = \begin{bmatrix} R^T f \\ -BGf \end{bmatrix}, \tag{14.29}
$$

which corresponds to the rigid body modes and the attachment modes, does not change when the number of free interface normal modes retained in the reduction basis $n_\theta = \sum_{s=1}^{N} n_\theta^{(s)}$ is changed. This is due to the flexibility matrix G, which is implicitly included in $\bar{M}_r$ and $\bar{F}_r$, being independent on the number of free interface normal modes n_θ retained in the reduction basis. That is not the case for the original formulation of the DCBM (see Sect. 14.2.1) since the subspace spanned by the free interface normal modes Θ according to Eq. (14.14) is projected out of the flexibility matrix G to obtain the residual flexibility matrix G_r. This makes G_r dependent on Θ and therefore G_r is changing if Θ is changed. Consequently F_r and M_r are also changing in that case since F_r and M_r depend again on G_r as can be seen in Eqs. (14.18) and (14.19).

14.3 Reduction of Interface Coordinates

Using the DCBM (it does not matter which formulation) the number of Lagrange multipliers n_λ and also the number rigid body modes n_{rig} remains constant during the reduction process. The size of the interface problem $n_{int} = n_\lambda + n_{rig}$ is not affected by the DCBM reduction. If the number of substructures increases the size of the corresponding interface problem increases, so that for a large number of substructures the reduced system can still have a significant number of DOFs. For the Craig-Bampton method [2] different reduction methods were proposed in [3], namely "Modal reduction of junction coordinates", "Guyan reduction of junction coordinates" and "Ritz reduction of junction coordinates" (which is the most general case including the first two techniques as special cases). These techniques consist in representing the interface DOFs in terms of a reduced number of modes with corresponding generalized interface mode coordinates. In order to reduce the interface problem of the DCBM we want to demonstrate a Guyan reduction and a modal reduction of the interface coordinates of the DCBM in the following.

Therefore we consider the interface problem for the DCBM which is obtained by static condensation (no free vibration modes are included in the reduction basis) of the dual assembled problem (14.7). The static reduction

$$
\begin{bmatrix} u \\ \lambda \end{bmatrix} \approx \underbrace{\begin{bmatrix} R & -GB^T \\ 0 & I \end{bmatrix}}_{T_{stat}} \begin{bmatrix} \alpha \\ \lambda \end{bmatrix}, \tag{14.30}
$$

which is obtain by deleting the column corresponding to Θ in $\bar{T}_{DCB}$ of Eq. (14.21) resulting in the static reduction matrix T_{stat} gives the interface problem

$$\begin{bmatrix} I & 0 \\ 0 & \bar{M}_r \end{bmatrix} \begin{bmatrix} \ddot{\alpha} \\ \ddot{\lambda} \end{bmatrix} + \begin{bmatrix} 0 & R^T B^T \\ BR & -\bar{F}_r \end{bmatrix} \begin{bmatrix} \alpha \\ \lambda \end{bmatrix} = \begin{bmatrix} R^T f \\ -BGf \end{bmatrix} \tag{14.31}$$

with the mass matrix M_{int} and stiffness matrix K_{int} of the interface problem:

$$M_{int} = T_{stat}^T \begin{bmatrix} M & 0 \\ 0 & 0 \end{bmatrix} T_{stat} = \begin{bmatrix} I & 0 \\ 0 & \bar{M}_r \end{bmatrix}, \qquad K_{int} = T_{stat}^T \begin{bmatrix} K & B^T \\ B & 0 \end{bmatrix} T_{stat} = \begin{bmatrix} 0 & R^T B^T \\ BR & -\bar{F}_r \end{bmatrix} \tag{14.32}$$

Note that is does no matter if either the original formulation of the DCBM or the alternative formulation of the DCBM is used to obtain this static problem since when no vibration modes are kept the (residual) flexibility matrices $G_r = G$ are equal [11].

14.3.1 Guyan Reduction of Interface Coordinates

Analogously to the Craig-Bampton method with Guyan reduction of interface coordinates [3], now the Lagrange multipliers λ are divided in kept λ_k and approximated λ_a DOFs. The rigid body modes α are kept in any case. By reordering Eq. (14.31), the partitioned interface problem for free vibration writes

$$\begin{bmatrix} M_{int,\alpha\alpha} & 0 & 0 \\ 0 & M_{int,\lambda_k\lambda_k} & M_{int,\lambda_k\lambda_a} \\ 0 & M_{int,\lambda_a\lambda_k} & M_{int,\lambda_a\lambda_a} \end{bmatrix} \begin{bmatrix} \ddot{\alpha} \\ \ddot{\lambda}_k \\ \ddot{\lambda}_a \end{bmatrix} + \begin{bmatrix} 0 & K_{int,\alpha\lambda_k} & K_{int,\alpha\lambda_a} \\ K_{int,\lambda_k\alpha} & K_{int,\lambda_k\lambda_k} & K_{int,\lambda_k\lambda_a} \\ K_{int,\lambda_a\alpha} & K_{int,\lambda_a\lambda_k} & K_{int,\lambda_a\lambda_a} \end{bmatrix} \begin{bmatrix} \alpha \\ \lambda_k \\ \lambda_a \end{bmatrix} = \begin{bmatrix} 0 \\ 0 \\ 0 \end{bmatrix}. \tag{14.33}$$

Solving the third row of the static problem (14.33)

$$K_{int,\lambda_a\alpha}\alpha + K_{int,\lambda_a\lambda_k}\lambda_k + K_{int,\lambda_a\lambda_a}\lambda_a = 0, \tag{14.34}$$

the approximated DOFs λ_a are obtained by

$$\lambda_a = -K_{int,\lambda_a\lambda_a}^{-1}K_{int,\lambda_a\alpha}\alpha - K_{int,\lambda_a\lambda_a}^{-1}K_{int,\lambda_a\lambda_k}\lambda_k = \Psi_{ak,\alpha}\alpha + \Psi_{ak,\lambda}\lambda_k. \tag{14.35}$$

This leads to the Guyan interface reduction matrix $T_{DCB,Guyan}$

$$\begin{bmatrix} \alpha \\ \eta \\ \lambda_k \\ \lambda_a \end{bmatrix} \approx \underbrace{\begin{bmatrix} I & 0 & 0 \\ 0 & I & 0 \\ 0 & 0 & I \\ \Psi_{ak,\alpha} & 0 & \Psi_{ak,\lambda} \end{bmatrix}}_{T_{DCB,Guyan}} \begin{bmatrix} \alpha \\ \eta \\ \lambda_k \end{bmatrix}. \tag{14.36}$$

The dynamic equation with Guyan reduction of interface coordinates writes

$$M_{DCB,Guyan}\ddot{u}_{DCB,Guyan} + K_{DCB,Guyan}u_{DCB,Guyan} = f_{DCB,Guyan} \tag{14.37}$$

with

$$M_{DCB,Guyan} = T_{DCB,Guyan}^T \bar{M}_{DCB} T_{DCB,Guyan} = T_{DCB,Guyan}^T \bar{T}_{DCB}^T M_{dual} \bar{T}_{DCB} T_{DCB,Guyan}, \tag{14.38}$$

$$K_{DCB,Guyan} = T_{DCB,Guyan}^T \bar{K}_{DCB} T_{DCB,Guyan} = T_{DCB,Guyan}^T \bar{T}_{DCB}^T K_{dual} \bar{T}_{DCB} T_{DCB,Guyan}, \tag{14.39}$$

$$\boldsymbol{u}_{DCB,Guyan} = \begin{bmatrix} \boldsymbol{\alpha} \\ \boldsymbol{\eta} \\ \boldsymbol{\lambda}_k \end{bmatrix}, \qquad \boldsymbol{f}_{DCB,Guyan} = \boldsymbol{T}_{DCB,Guyan}^T \bar{\boldsymbol{f}}_{DCB} = \boldsymbol{T}_{DCB,Guyan}^T \bar{\boldsymbol{T}}_{DCB}^T \boldsymbol{f}_{dual} \,. \tag{14.40}$$

A criterion for the choice of the kept Lagrange multipliers $\boldsymbol{\lambda}_k$ is the quotient κ_{jj}/M_{jj} of the diagonal entries of the stiffness and mass matrix [3] with the coordinates having smaller κ_{jj}/M_{jj} values being kept. This ensures keeping all rigid body modes, as stated before, since their corresponding quotient would be zero. The final size of a DCBM reduced system with Guyan interface reduction is $n_{DCB,Guyan} = n_{rig} + \sum_{s=1}^{N} n_\theta^{(s)} + n_{\lambda_k}$, with n_{rig} being the number of rigid body modes of all substructures, $n_\theta^{(s)}$ the number of free interface normal modes of substructure s and n_{λ_k} the number of kept Lagrange multipliers.

14.3.2 Modal Reduction of Interface Coordinates

An approach for the modal reduction of interface coordinates of the DCBM was first given in [11]. As for the Guyan interface reduction (Sect. 14.3.1) the starting point for the following derivation is the statically condensed dual problem (14.31) which is equivalent to a DCBM reduction with no free interface vibration modes included in the reduction basis. The DCBM interface modes $\boldsymbol{x}_{int,j}$ are eigensolutions of that statically condensed dual interface problem

$$\boldsymbol{K}_{int}\boldsymbol{x}_{int,j} = \mu_k^2 \boldsymbol{M}_{int}\boldsymbol{x}_{int,j} \qquad \Leftrightarrow \qquad \begin{bmatrix} \boldsymbol{0} & \boldsymbol{R}^T\boldsymbol{B}^T \\ \boldsymbol{B}\boldsymbol{R} & -\bar{\boldsymbol{F}}_{res} \end{bmatrix} \begin{bmatrix} \boldsymbol{x}_{\alpha,j} \\ \boldsymbol{x}_{\lambda,j} \end{bmatrix} = \mu_j^2 \begin{bmatrix} \boldsymbol{I} & \boldsymbol{0} \\ \boldsymbol{0} & \bar{\boldsymbol{M}}_{res} \end{bmatrix} \begin{bmatrix} \boldsymbol{x}_{\alpha,j} \\ \boldsymbol{x}_{\lambda,j} \end{bmatrix}. \tag{14.41}$$

These interface modes $\boldsymbol{x}_{int,j}$ are mass orthonormalized and an approximation of the interface coordinates is obtained by retaining only the first interface modes $\boldsymbol{x}_{int,j}$ corresponding to the n_x lowest eigenvalues μ_j^2. Calling

$$\boldsymbol{X}_{int} = \begin{bmatrix} \boldsymbol{X}_\alpha \\ \boldsymbol{X}_\lambda \end{bmatrix} \tag{14.42}$$

the matrix containing these n_x interface modes, the approximation of the interface DOFs is given by

$$\begin{bmatrix} \boldsymbol{\alpha} \\ \boldsymbol{\lambda} \end{bmatrix} \approx \boldsymbol{X}_{int}\tilde{\boldsymbol{\lambda}} = \begin{bmatrix} \boldsymbol{X}_\alpha \\ \boldsymbol{X}_\lambda \end{bmatrix} \tilde{\boldsymbol{\lambda}} \tag{14.43}$$

which leads to the modal interface reduction matrix $\boldsymbol{T}_{DCB,modal}$

$$\begin{bmatrix} \boldsymbol{\alpha} \\ \boldsymbol{\eta} \\ \boldsymbol{\lambda} \end{bmatrix} \approx \underbrace{\begin{bmatrix} \boldsymbol{0} & \boldsymbol{X}_\alpha \\ \boldsymbol{I} & \boldsymbol{0} \\ \boldsymbol{0} & \boldsymbol{X}_\lambda \end{bmatrix}}_{\boldsymbol{T}_{DCB,modal}} \begin{bmatrix} \boldsymbol{\eta} \\ \tilde{\boldsymbol{\lambda}} \end{bmatrix}. \tag{14.44}$$

$\boldsymbol{X}_{int}$ is satisfying

$$\boldsymbol{X}_{int}\boldsymbol{K}_{int}\boldsymbol{X}_{int} = \boldsymbol{\mu}^2 = \mathrm{diag}(\mu_j^2) \qquad \text{and} \qquad \boldsymbol{X}_{int}\boldsymbol{M}_{int}\boldsymbol{X}_{int} = \boldsymbol{I} \tag{14.45}$$

with $\boldsymbol{\mu}^2$ being a diagonal matrix containing the remaining n_x eigenvalues μ_j^2. The vector $\tilde{\boldsymbol{\lambda}}$ contains the amplitudes $\tilde{\lambda}_j$ of the retained interface modes $\boldsymbol{x}_{int,j}$ and the modal parameters $\boldsymbol{\eta}$ are not affected by the approximation (14.44). Applying the reduction (14.44) to the DCBM reduced system (14.22), the dynamic equation with modal reduction of interface coordinates writes

$$\boldsymbol{M}_{DCB,modal}\ddot{\boldsymbol{u}}_{DCB,modal} + \boldsymbol{K}_{DCB,modal}\boldsymbol{u}_{DCB,modal} = \boldsymbol{T}_{DCB,modal}^T \bar{\boldsymbol{f}}_{DCB} \tag{14.46}$$

with

$$\boldsymbol{M}_{DCB,modal} = \boldsymbol{T}_{DCB,modal}^T \bar{\boldsymbol{M}}_{DCB} \boldsymbol{T}_{DCB,modal} = \boldsymbol{T}_{DCB,modal}^T \bar{\boldsymbol{T}}_{DCB}^T \boldsymbol{M}_{dual} \bar{\boldsymbol{T}}_{DCB} \boldsymbol{T}_{DCB,modal} \ , \tag{14.47}$$

$$\boldsymbol{K}_{DCB,modal} = \boldsymbol{T}_{DCB,modal}^T \bar{\boldsymbol{K}}_{DCB} \boldsymbol{T}_{DCB,modal} = \boldsymbol{T}_{DCB,modal}^T \bar{\boldsymbol{T}}_{DCB}^T \boldsymbol{K}_{dual} \bar{\boldsymbol{T}}_{DCB} \boldsymbol{T}_{DCB,modal} \ , \tag{14.48}$$

$$\boldsymbol{u}_{DCB,modal} = \begin{bmatrix} \boldsymbol{\eta} \\ \tilde{\boldsymbol{\lambda}} \end{bmatrix}, \qquad \boldsymbol{f}_{DCB,modal} = \boldsymbol{T}_{DCB,modal}^T \bar{\boldsymbol{f}}_{DCB} = \boldsymbol{T}_{DCB,modal}^T \bar{\boldsymbol{T}}_{DCB}^T \boldsymbol{f}_{dual} \ . \tag{14.49}$$

Eq. (14.46) can be written as

$$\begin{bmatrix} \boldsymbol{I} & -\boldsymbol{\Omega}^{-2}\boldsymbol{\Theta}^T\boldsymbol{B}^T X_\lambda \\ -X_\lambda^T \boldsymbol{B}\boldsymbol{\Theta}\boldsymbol{\Omega}^{-2} & \boldsymbol{I} \end{bmatrix} \begin{bmatrix} \ddot{\boldsymbol{\eta}} \\ \ddot{\tilde{\boldsymbol{\lambda}}} \end{bmatrix} + \begin{bmatrix} \boldsymbol{\Omega}^2 & \boldsymbol{0} \\ \boldsymbol{0} & \boldsymbol{\mu}^2 \end{bmatrix} \begin{bmatrix} \boldsymbol{\eta} \\ \tilde{\boldsymbol{\lambda}} \end{bmatrix} = \boldsymbol{T}_{DCB,modal}^T \bar{\boldsymbol{T}}_{DCB}^T \boldsymbol{f}_{dual} \tag{14.50}$$

which shows the relation between generalized modal parameters of the substructures $\boldsymbol{\eta}$ and the generalized interface parameters $\tilde{\boldsymbol{\lambda}}$. The physical displacement $\boldsymbol{u}$ of the original system can be reconstructed by the simple back transformation

$$\begin{bmatrix} \boldsymbol{u} \\ \boldsymbol{\lambda} \end{bmatrix} = \bar{\boldsymbol{T}}_{DCB} \boldsymbol{T}_{DCB,modal} \begin{bmatrix} \boldsymbol{\eta} \\ \tilde{\boldsymbol{\lambda}} \end{bmatrix} = \begin{bmatrix} \boldsymbol{\Theta} & (RX_\alpha - GB^T X_\lambda) \\ \boldsymbol{0} & X_\lambda \end{bmatrix} \begin{bmatrix} \boldsymbol{\eta} \\ \tilde{\boldsymbol{\lambda}} \end{bmatrix} \tag{14.51}$$

The size of the DCBM reduced system with modal interface reduction is $n_{DCB,modal} = \sum_{s=1}^{N} n_\theta^{(s)} + n_x$. If, as described before, the alternative formulation of the DCBM using attachment modes is applied the dual interface modes do not change no matter how many free interface vibration modes are included in the reduction basis. The corresponding eigenvalue problem (14.41) does not change and therefore the interface reduction can be conducted first and afterwards the reduction basis can be enriched by an arbitrary number of free interface vibration modes without affecting Eq. (14.41).

14.4   Numerical Example of Two-Dimensional Solid

In order to demonstrate the approximation accuracy of the DCBM with interface reduction, as described in Sect. 14.3, the problem of a two dimensional rectangle decomposed in 12 substructures as illustrated in Fig. 14.1 is considered [7]. Each substructure is discretized by 16×9 bilinear four-noded elements (plane stress) and the structure is clamped on the left side in both directions. This gives 4020 DOFs in the displacement vector $\boldsymbol{u}$ and $n_\lambda = 436$ Lagrange multipliers resulting in a total number of $n_{total} = 4456$ DOFs of Eq. (14.7). The objective is to approximate the lowest eigenfrequencies ω of the full structure with the DCBM and with the DCBM with additional interface reduction. Using 8 free interface normal modes per substructure (not including potential rigid body modes) the relative error
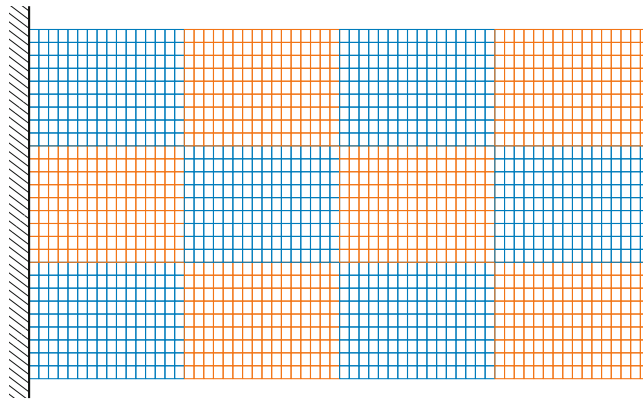
Fig. 14.1 Two dimensional solid problem decomposed in 12 substructures. Each substructure is discretized by 16×9 bilinear four-noded elements (plane stress) and the structure is clamped on the left side in both directions [7]
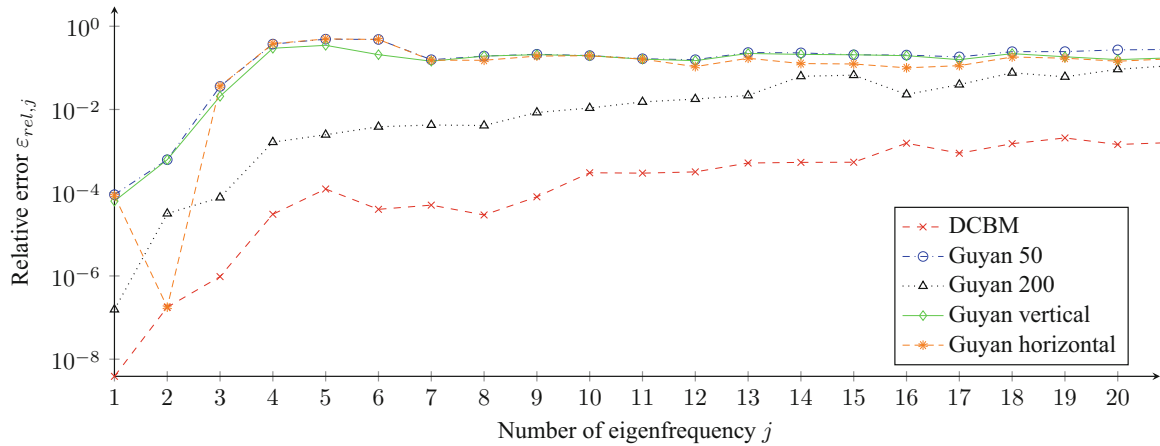
Fig. 14.2 Relative error of DCBM and DCBM with Guyan interface reduction

Table 14.1 Excerpt of eigenvalues after DCBM reduction without interface reduction. The first negative eigenvalue is the 82nd value

j	Eigenvalue
80	2.303
81	2.324
82	−2.360
83	−2.361
84	2.398

$$\varepsilon_{rel,j} = \frac{|\omega_{red,j} - \omega_{full,j}|}{\omega_{full,j}} \tag{14.52}$$

of eigenfrequency j depicted in Fig. 14.2 is resulting (graph denoted by "DCBM") with $\omega_{red,j}$ being the j-th eigenfrequency of the reduced system and $\omega_{full,j}$ being the j-th eigenfrequency of the full (non-reduced) system, which is computed additionally. The eigenfrequencies are ordered by ascending values. In this example the DCBM reduces the total number of $n_{total} = 4456$ DOFs to $n_{DCB} = n_{rig} + n_\theta + n_\lambda = 27 + 96 + 436 = 559$ DOFs (which is a reduction of around 88% of the number of degrees of freedom). But this makes also the necessity of an interface reduction obvious since in this example the number of Lagrange multipliers $n_\lambda = 436$, which has a significant contribution to the number of DOFs of the DCBM reduced system, remains unchanged. The number of Lagrange multipliers $n_\lambda = 436$ still make around 78% of the degrees of freedom of the DCBM reduced system. This makes an interface reduction absolutely essential which is demonstrated in the following by way of example. Note that the first negative eigenvalue is the 82nd in the case of DCBM without interface reduction as illustrated in Table 14.1.

14.4.1 Guyan Reduction of Interface Coordinates

To illustrate the DCBM with Guyan interface reduction we reduce the number of rigid body modes and Lagrange multipliers of $n_{rig} + n_\lambda = 27 + 436 = 463$ to $n_{kept} = 200$ kept DOFs. As criterion for the choice of the kept DOFs the quotient K_{ii}/M_{ii} of the diagonal entries of the stiffness and mass matrix is used. Giving zero for rigid body modes all these modes are kept. The size of the reduced system is now $n_{Guyan} = 96 + 200 = 296$ and the corresponding graph showing the relative error of this reduction in Fig. 14.2 is denoted by "Guyan 200". The reduced system has a number of negative eigenvalues equal to the number of kept Lagrange multipliers $n_{\lambda,k} = 173$. The approximation accuracy of the eigenvalues compared to the DCBM without interface reduction is decreased by a factor around 100. The first negative eigenvalue of the system with Guyan interface reduction is the 117th eigenvalue, as shown in Table 14.2. Compared to the DCBM without interface reduction (82nd eigenvalue is the first negative, see Table 14.1), negative eigenvalues occur now in the a higher frequency spectrum which can have some advantages. Note that the computational effort of the Guyan reduction is very small compared to a modal interface reduction since no additional eigenvalue problem has to be solved.

Table 14.2 Excerpt of eigenvalues after DCBM reduction with Guyan interface reduction ($n_{int} = 200$ interface modes kept). The first negative eigenvalue is the 117rd value

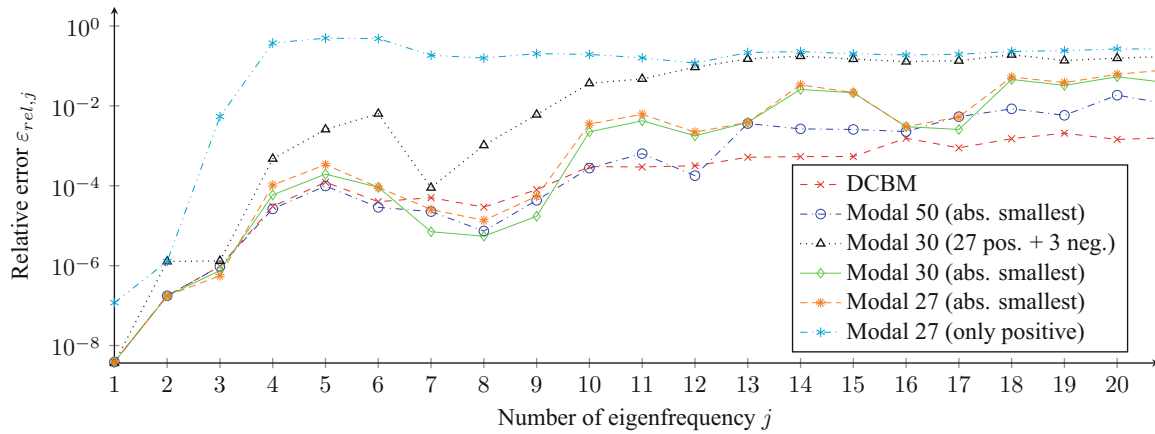| j	Eigenvalue
115	2.341
116	2.395
117	−2.427
118	2.563
119	2.617
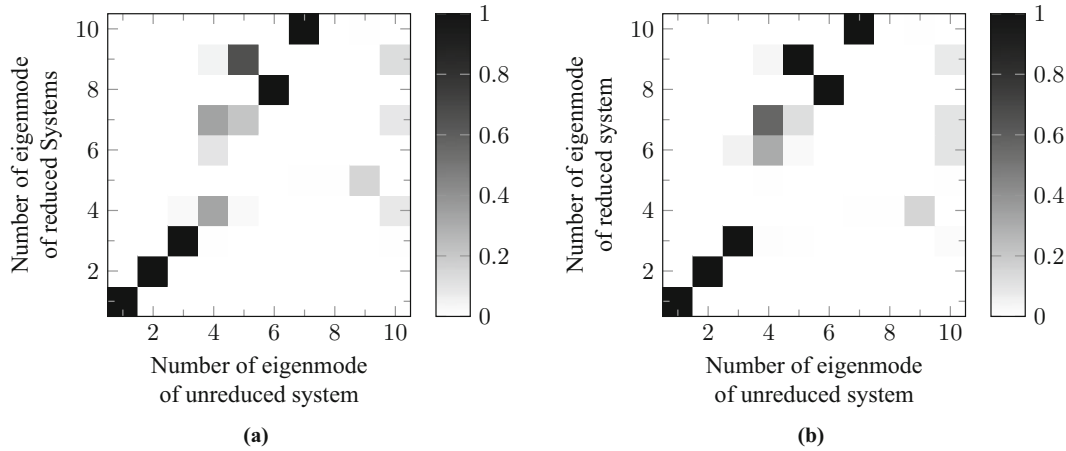
Fig. 14.3 MAC for DCBM reduced system with Guyan interface reduction. (**a**) DCBM with Guyan interface reduction (vertical DOFs kept). (**b**) DCBM with Guyan interface reduction (horizontal DOFs kept)

If the number of rigid body modes an Lagrange multipliers is reduced to only $n_{Guyan} = 50$ DOFs, the results become considerably worse which is shown by the graph "Guyan 50" in Fig. 14.2. Already the 4th eigenfrequency has an error greater than 10% which is an amount not acceptable in practical applications.

Analogous to Guyan interface reduction for the Craig-Bampton method [3], in which the displacement DOFs of the interface can be divided into horizontal and vertical DOFs, the Lagrange multipliers can divided in the same way. In the following a Guyan interface reduction is performed the one time keeping rigid body modes and vertical Lagrange multipliers and the other times keeping rigid body modes and horizontal Lagrange multipliers as reduced interface DOFs. The results for both computations are shown in Fig. 14.2 and denoted by "Guyan vertical" and "Guyan horizontal", respectively. Except the 2nd eigenfrequency the two graphs are almost parallel. Figure 14.3a, b show the MAC (modal assurance criterion) values of the two Guyan interface reductions when comparing the modes of the unreduced system to the modes of the DCBM reduced system with Guyan interface reduction, respectively. Both figures are hardly different and therefore, compared to the Guyan interface reduction for the Craig-Bampton method [3], it can not be concluded anymore that retaining vertical interface DOFs improves the approximation of eigenmodes with mainly vertical direction of movement or that retaining horizontal interface DOFs improves the approximation of eigenmodes with mainly horizontal direction of movement significantly. This effect is only visible for the 2nd eigenmode which is the 1st longitudinal mode and is represented by the horizontal Lagrange multipliers with high accuracy. The reason is that rigid body modes are retained for DCBM with Guyan reduction in any case. The rigid body modes have contributions in vertical and horizontal direction such that eigenmodes with displacements in both directions can be approximated in a certain accuracy range even if only Lagrange multipliers in one direction are kept. Nevertheless the approximation accuracy is poor for both cases considering the relative errors in Fig. 14.2 and the correlations of the MAC values in Fig. 14.3.

14.4.2 Modal Reduction of Interface Coordinates

For the demonstration of the DCBM with modal reduction of interface coordinates again the system depicted in Fig. 14.1 is considered. As described at the beginning of Sect. 14.4, the DCBM reduction gives a reduced system with $n_{DCB} = n_{rig} + n_\theta + n_\lambda = 27 + 96 + 436 = 559$ remaining DOFs for this example. $n_\theta = 12 \cdot 8 = 96$ is the number of kept free interface normal modes of all twelve substructures, $n_{rig} = 9 \cdot 3 = 27$ the number of rigid body modes of all (free floating) substructures and $n_\lambda = 436$ the number of Lagrange multipliers. Therefore the system has 123 positive and 436 negative

Fig. 14.4 Relative error of DCBM and DCBM with modal interface reduction

Table 14.3 First eigenvalues of dual interface problem

j	Eigenvalue
1	0.0009
2	0.0097
3	0.0132
4	−0.0228
5	−0.0234
6	−0.0264
7	0.0647
8	0.0917
9	0.0933
10	0.0991

eigenvalues corresponding to the kept free interface normal modes (including the rigid body modes) and the Lagrange multipliers, respectively [6]. The relative error of the eigenfrequencies of the reduced system in the low frequency range using 8 free interface normal modes per substructure are depicted in Fig. 14.4 (graph is denoted by "DCBM") and will be used as reference for the modal interface reduction with different numbers of kept interface modes in the following [6].

#### 14.4.2.1 Modal Interface Reduction with 50 Interface Modes

Now the rigid body modes and the Lagrange multipliers are reduced to $n_{int} = 50$ interface DOFs resulting in a reduced system of size $n_{DCB,Modal} = 146$. Table 14.3 illustrates that already in the low frequency range interface modes with corresponding negative eigenvalues occur. As criterion for the choice of the kept interface modes, the lowest absolute eigenvalue is used. The interface problem has 27 interface modes with positive eigenvalues corresponding to the number of rigid body modes and 436 interface modes with negative eigenvalues corresponding to the number of Lagrange multipliers, respectively. Among the $n_{int} = 50$ kept interface modes with lowest absolute eigenvalues are 26 interface modes with positive eigenvalues and 24 interface modes with negative eigenvalues. Keeping 24 interface modes with negative eigenvalues, the reduced system has 24 negative eigenvalues as well. The graph denoted by "Modal 50" in Fig. 14.4 depicts the relative errors of the lowest eigenfrequencies of this interface reduction.

The relative error of the first four eigenfrequencies is approximated as good as for the DCBM without interface reduction (graph "DCBM"). Surprisingly, the relative errors with interface reduction of the subsequent eigenfrequencies are lower up to the 10th eigenfrequency. A few values are thus approximated better with interface reduction than without interface reduction. This is not intuitive since errors are expected to be lower when no interface reduction is carried out. However since the DCBM is reducing a problem written in primal and dual variables the convergence is not guaranteed to be monotonic [11]. It is also noteworthy that the negative eigenvalues after modal interface reduction take the greatest absolute values of all eigenvalues. That means, if the eigenvalues are sorted by absolute values, the negative values are at the upper end of the spectrum. All 122 positive eigenvalues have smaller absolute values than the 24 negative eigenvalues. Against that, the first negative eigenvalue is the 82nd in the case of applying the DCBM without interface reduction. As the case here, it is often advantageous negative

Table 14.4 Excerpt of eigenvalues after DCBM reduction with modal interface reduction ($n_{int} = 50$ interface modes kept). The first negative eigenvalue is the 123rd value

j	Eigenvalue
120	3.238
121	3.412
122	3.535
123	-4.923
124	-5.989

Fig. 14.5 MAC for dual interface modes
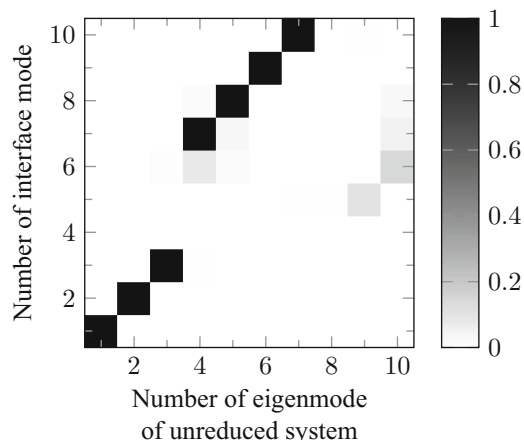
eigenvalues only appearing in the higher frequency range. Tables 14.1 and 14.4 show excerpts from the eigenvalue spectrum in which the first negative eigenvalues appear. Since eigenmodes with negative eigenvalues are non-physical and, for instance, can lead to problems during time integration, it is obvious to prefer interface modes with positive eigenvalues and not only take the absolute values of the eigenvalues as criterion for the choice of the kept interface modes.

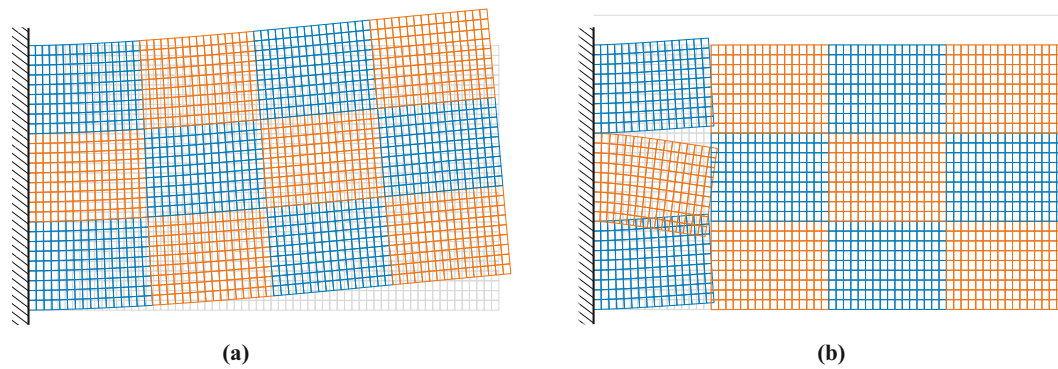#### 14.4.2.2   Modal Interface Reduction with 30 Interface Modes

Keeping $n_{int} = 50$ interface modes corresponding to the eigenvalues with smallest absolute values in the previous example (Sect. 14.4.2.1) led to 24 interface modes with negative eigenvalues and 26 with positive eigenvalues. If we were taken now all 27 interface modes with positive eigenvalues and fill up with 23 interface modes with negative eigenvalues with smallest absolute value (keeping the number of interface modes $n_{int} = 50$ constant) the basis for the interface modes would only change by one mode.

Therefore we consider now the case only keeping the $n_{int} = 30$ interface modes for the modal interface reduction. On the one hand we keep the interface modes with smallest absolute values leading to kept interface modes corresponding to 17 positive and 13 negative eigenvalues. On the other hand we keep all 27 interface modes with positive eigenvalues and fill up with only 3 interface modes with negative eigenvalues to obtain a interface reduction basis of dimension $n_{int} = 30$. Figure 14.4 depicts the relative errors of the lowest 20 eigenfrequencies for the two cases denoted by "Modal 30 (27 pos. + 3 neg.)" and "Modal 30 (abs. smallest)", respectively.

The approximation of the eigenfrequencies is much better for the interface modes corresponding to the smallest absolute values (graph "Modal 30 (abs. smallest)" in Fig. 14.4). For the first three eigenfrequencies the relative errors are comparable to the error of the DCBM without interface reduction. Starting from the 4th eigenfrequency the modal interface reduction with the interface modes corresponding to the 30 smallest absolute values is around one order better than the reduction keeping all interface modes corresponding to positive eigenvalues in the reduction basis.

It can be concluded that for the most accurate approximation of the eigenfrequencies of the system applying modal interface reduction, the interface modes corresponding to negative eigenvalues have significant contributions. The interface modes corresponding to negative eigenvalues are necessary for the most accurate calculation of the eigenfrequencies. It is recommended to keep the interface modes for the modal interface reduction with corresponding smallest absolute eigenvalues which is not intuitive.

Figure 14.5 shows the MAC numbers for the first 10 global eigenmodes of the unreduced system and the first 10 dual interface modes. Figure 14.6 shows the first and fourth dual interface mode of the system. The interface mode corresponding to a negative eigenvalues in Fig. 14.6b shows large interface incompatibility which makes it for the time being difficult to imagine that this mode improves the approximation accuracy.

Fig. 14.6 Dual interface modes of wo dimensional solid problem decomposed in 12 substructures (see Fig. 14.1). (**a**) First interface mode. (**b**) Fourth interface mode

Fig. 14.7 MAC for DCBM reduced system with modal interface reduction ($n_{int} = 27$ interface modes with positive eigenvalues kept)
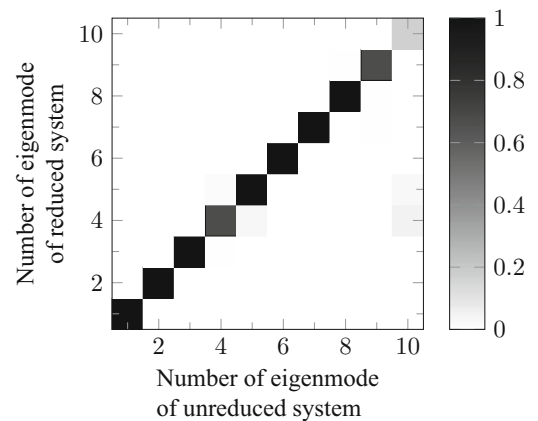
The dual interface modes with negative eigenvalues (number 4, 5 and 6) do not have any correlation to the first eigenmodes of the unreduced system. All other interface modes correlate strongly to eigenmodes of the unreduced system. Nevertheless the graphs in Fig. 14.4 indicate clearly that the interface modes corresponding to negative eigenvalues improve the approximation accuracy while keeping the final size of the reduced system constant.

14.4.2.3 Modal Interface Reduction with 27 Interface Modes

Since in many applications, for example time integration, negative eigenvalues cause major problems, now a modal interface reduction is investigated which uses only all the 27 interface modes with positive eigenvalues. Therefore the reduced system does not have an negative eigenvalues anymore. In this example the system is reduced to size $n_{DCB,Modal} = 96 + 27 = 123$. For comparison a second interface reduction is conducted which keeps 27 interface modes corresponding to the eigenvalues with smallest absolute values. The graphs "Modal 27 (only positive)" and "Modal 27 (abs. smallest)" in Fig. 14.4 show the relative errors for these two computations.

The approximation accuracy for the interface reduction with interface modes corresponding to only positive eigenvalues is acceptable for the first 3 eigenfrequencies. From the 4th eigenfrequency the relative error is already over 10% which is a very poor approximation. In contrast to this, the accuracy of modal interface reduction with interface modes corresponding to the smallest absolute eigenvalues is significantly better for all of the first 20 eigenfrequencies. This emphasizes the positive effect of the interface modes corresponding to negative eigenvalues on the approximation accuracy of the lowest eigenfrequencies of the system.

Considering the MAC numbers for the first 10 global eigenmodes of the unreduced system and the first 10 eigenmodes of the reduced system with interface reduction using only the interface modes corresponding to the 27 positive eigenvalues in Fig. 14.7, it is noteworthy that the MAC number is greater than 0.8 up to the 8th eigenvalue. This shows that the eigenmodes of the reduced system are approximating the eigenmodes of the unreduced system very good although the eigenfrequencies of these modes show large errors (more than 10%) starting with the 4th eigenfrequency (see Fig. 14.4). It can be concluded that keeping the interface modes corresponding to positive eigenvalues results in a good approximation of the eigenmodes of the unreduced system but the corresponding eigenfrequencies are not approximated so well.

14.4.3   Interpretation of Dual Interface Normal Modes

In this section all computations refer to the system depicted in Fig. 14.8 which is a simplification of the system in Fig. 14.1 and is used now for the sake of simplicity. This gives 660 DOFs in the displacement vector u and $n_\lambda = 20$ Lagrange multipliers resulting in a total size of the dual assembled system of 680. The shapes of the eigenmodes of the unreduced system of Fig. 14.8 corresponding to the 8 lowest eigenfrequencies are shown in Fig. 14.9. The 1st eigenmode represents the 1st bending mode with vibration node at the clamped end. The 2nd eigenmode corresponds to the 1st longitudinal mode having the vibration node also at the clamped end. The 3rd, 4th, 6th, 7th and 8th eigenmode represents the 2nd, 3rd, 4th, 5th and 6th bending mode, respectively, while the 5th eigenmode represents the 2nd longitudinal mode.

For the time being the system is reduced by the DCBM using 8 free interface normal modes per substructure and additionally 3 rigid body modes for the right substructure which is free floating. The original system of size $n_{total} = 680$ is reduced by the DCBM to $n_{DCB} = n_\theta + n_{rig} + n_\lambda = 39$ remaining DOFs with the number of free interface normal modes $n_\theta = 2 \cdot 8 = 16$, the number of rigid body modes $n_{rig} = 3$ and the number of Lagrange multipliers $n_\lambda = 20$. This reduced system is the starting point for the analysis of the modal interface reduction of the DCBM. In the following the number of kept free interface modes is varied systematically to gain insight into the interface reduction method.

First of all we want to consider the first 5 dual interface modes corresponding to the smallest absolute eigenvalues in Fig. 14.10. There are 23 interface modes in total. Three of them have positive corresponding eigenvalues (according to the number of the rigid body modes) and 20 of them have negative eigenvalues (according to the number of Lagrange


Fig. 14.8 Two dimensional solid problem decomposed in two substructures

(a)

(b)

(c)

(d)

(e)

(f)

(g)

(h)
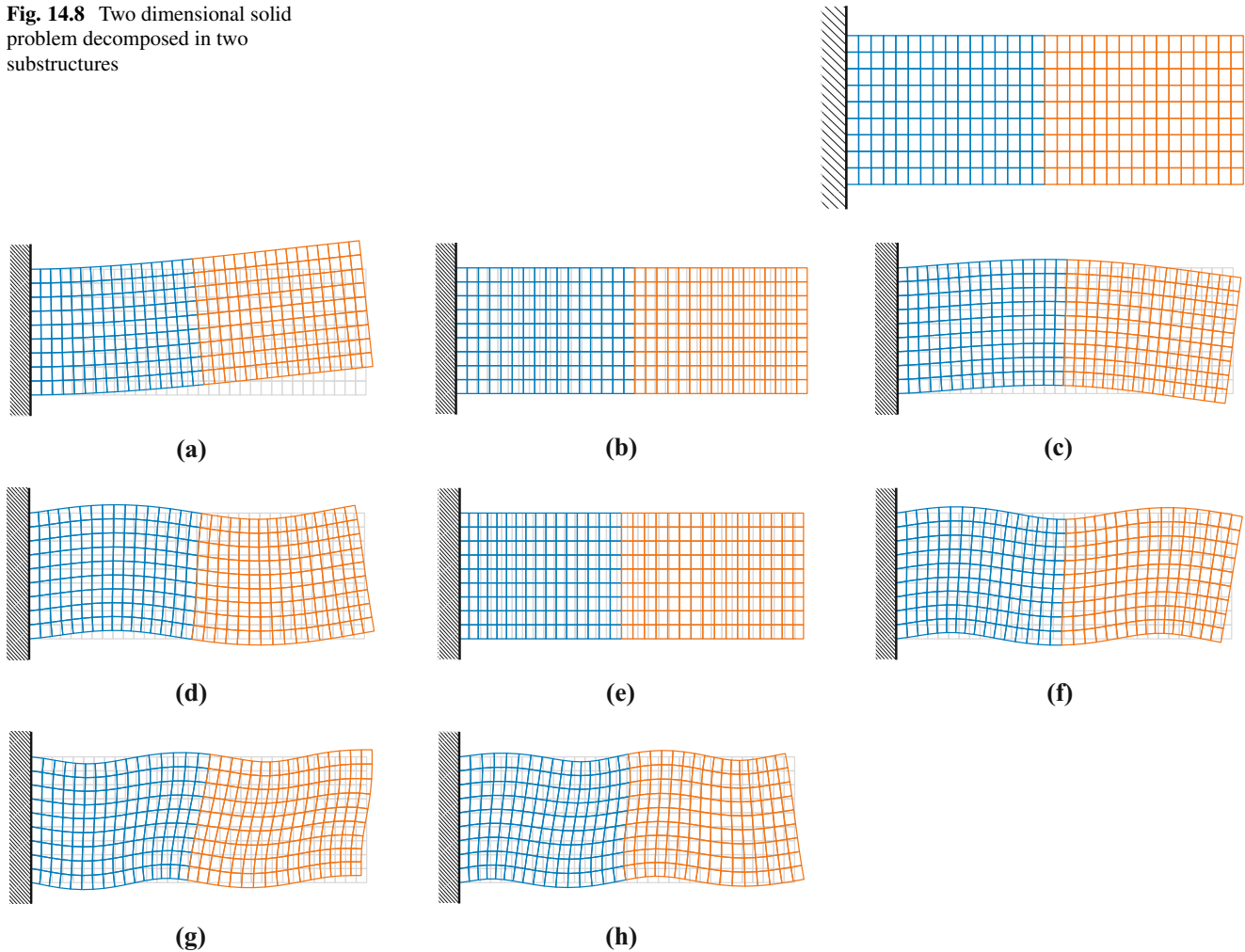
Fig. 14.9 First eight eigenmodes of the system depicted in Fig. 14.8 (without any reduction). (**a**) 1. eigenmode: $\omega^2 = 0.0019$. (**b**) 2. eigenmode: $\omega^2 = 0.0386$. (**c**) 3. eigenmode: $\omega^2 = 0.0398$. (**d**) 4. eigenmode: $\omega^2 = 0.1911$. (**e**) 5. eigenmode: $\omega^2 = 0.3476$. (**f**) 6. eigenmode: $\omega^2 = 0.4409$. (**g**) 7. eigenmode: $\omega^2 = 0.7229$. (**h**) 8. eigenmode: $\omega^2 = 0.8441$
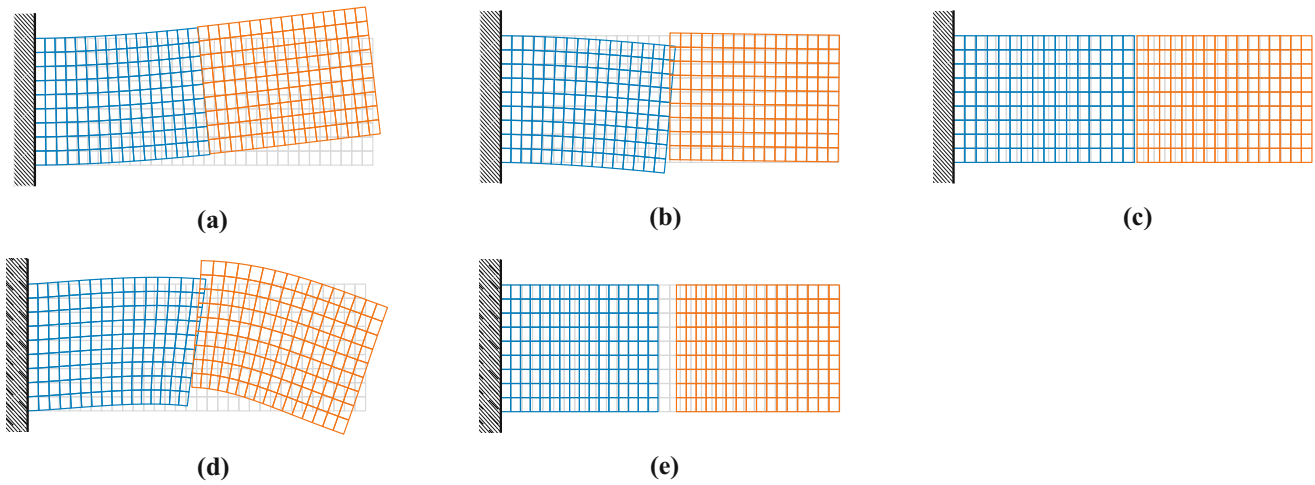
Fig. 14.10 First five dual interface modes. (**a**) 1. interface mode: $\omega^2 = 0.0019$. (**b**) 2. interface mode: $\omega^2 = -0.0298$. (**c**) 3. interface mode: $\omega^2 = 0.0400$. (**d**) 4. interface mode: $\omega^2 = 0.0565$. (**e**) 5. interface mode: $\omega^2 = -0.2744$
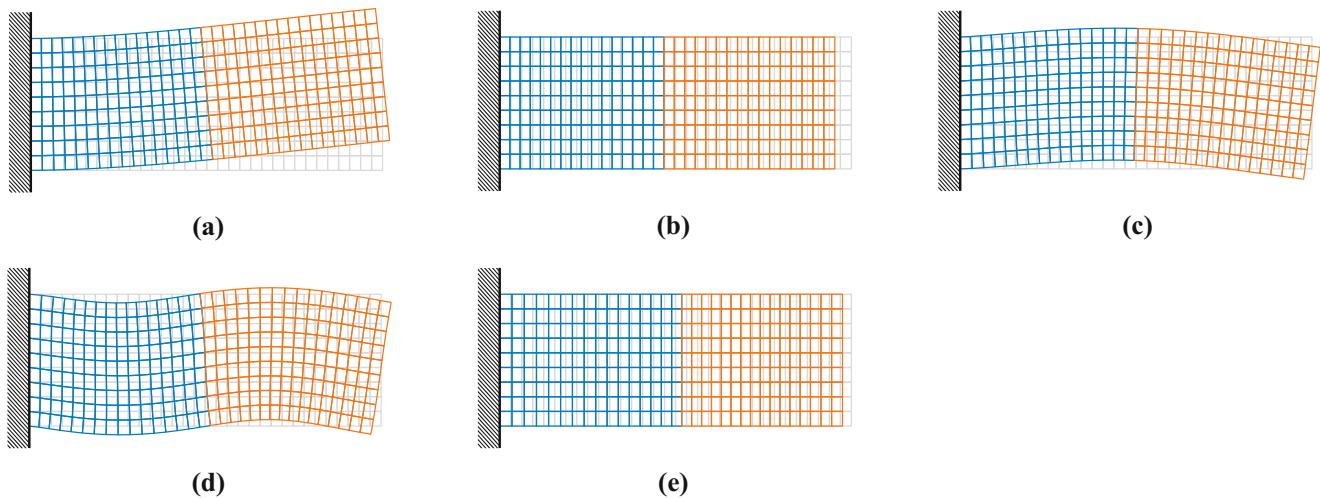
Fig. 14.11 First five eigenmodes after DCBM ($n_\theta^{(1)} = n_\theta^{(2)} = 8$) without interface reduction. (**a**) 1. eigenmode: $\omega_{DCB}^2 = 0.0019$. (**b**) 2. eigenmode: $\omega_{DCB}^2 = 0.0386$. (**c**) 3. eigenmode: $\omega_{DCB}^2 = 0.0398$. (**d**) 4. eigenmode: $\omega_{DCB}^2 = 0.1912$. (**d**) 5. eigenmode: $\omega_{DCB}^2 = 0.3479$

multipliers). The 3 interface modes corresponding to the positive eigenvalues seem to be physically meaningful since the 1st and 4th mode in Fig. 14.10 look like the first 2 bending modes of the unreduced system in Fig. 14.1 and the 3rd interface modes looks similar to the 1st longitudinal mode of the unreduced system. Because of the high interface incompatibilities of the interface modes corresponding to negative eigenvalues no comparable equivalent can be found for these modes.

14.4.3.1 Dual Craig-Bampton Reduction Without Interface Reduction

First of all, the system of Fig. 14.8 is reduced by the DCBM using 8 free interface normal modes per substructure from $n_{total} = 680$ DOFs to $n_{DCB} = 39$ DOFs. The shapes of the eigenmodes corresponding to the 5 smallest absolute eigenvalues of the reduced system are shown in Fig. 14.11. The first eigenmodes of the reduced system (Fig. 14.11) show a high correlation to the eigenmodes of the unreduced system (Fig. 14.8) which is also confirmed by the MAC values of the first 10 eigenmodes in Fig. 14.14a. The relative error of the eigenfrequencies of the reduced system in the low frequency range using 8 free interface normal modes per substructure without interface reduction are depicted in Fig. 14.12 (graph is denoted by "DCBM") and will be used as reference for the modal interface reduction in the following.
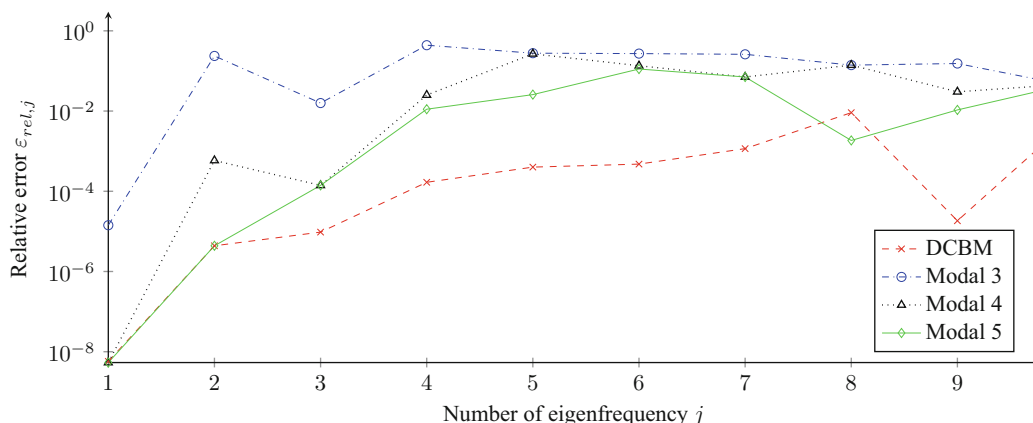
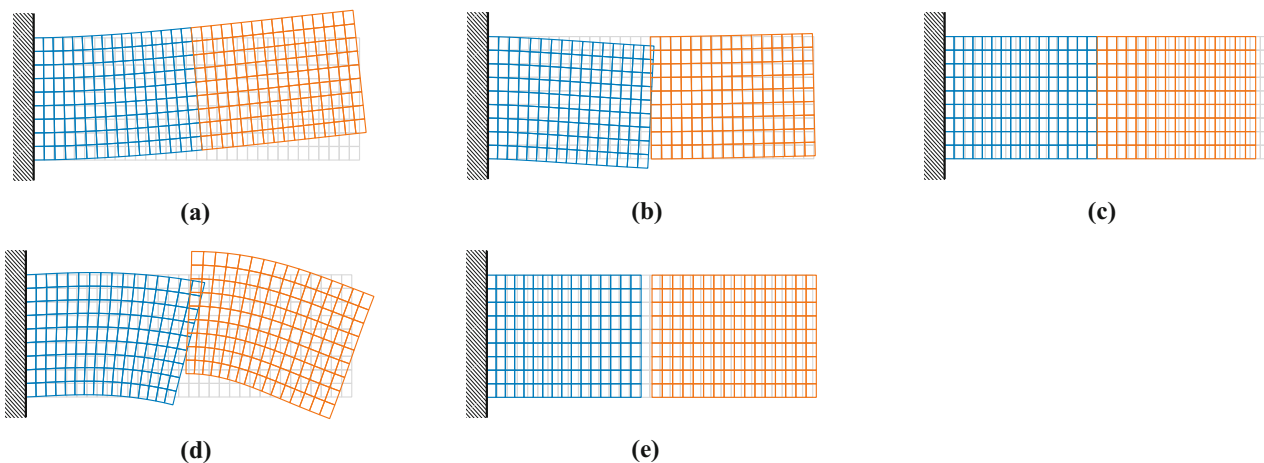**Fig. 14.12** Relative error of DCBM and DCBM with modal interface reduction with 3, 4 or 5 kept interface modes

Fig. 14.13 First five eigenmodes after DCBM ($n_\theta^{(1)} = n_\theta^{(2)} = 8$) with modal interface reduction ($n_{int} = 3$ interface modes kept). (**a**) 1. eigenmode: $\omega_{DCB,mod}^2 = 0.0019$. (**b**) 2. eigenmode: $\omega_{DCB,mod}^2 = 0.0225$. (**c**) 3. eigenmode: $\omega_{DCB,mod}^2 = 0.0385$. (**d**) 4. eigenmode: $\omega_{DCB,mod}^2 = 0.0603$. (**e**) 5. eigenmode: $\omega_{DCB,mod}^2 = 0.1816$

14.4.3.2 Modal Interface Reduction with Three Interface Modes Corresponding to the Three Positive Eigenvalues

For the investigation of the modal interface reduction exclusively the 3 interface modes corresponding to positive eigenvalues are used first. This leads to a reduced system without negative eigenvalues. The graph "Modal 3" in Fig. 14.12 shows the relative errors of the eigenfrequencies with this interface reduction. Only the first eigenfrequency is approximated with acceptable accuracy. From the second eigenfrequency the relative errors are at least 10% which is unacceptable at the first glance.

Considering the shapes of the eigenmodes of the reduced system in Fig. 14.13 and the MAC values in Fig. 14.14b leads to the insight that the graph in Fig. 14.12 has to be looked at differently. Figure 14.13a shows that there is a high correlation between the 1st bending mode of the reduced system (Fig. 14.13a) and the 1st bending mode of the unreduced system (Fig. 14.9a). Moreover the 3rd eigenmodes of the reduced system (Fig. 14.13c) correlates highly with the 2nd eigenmode of the unreduced system (Fig. 14.9b), which is also confirmed by a MAC value near 1 as shown in Fig. 14.14b.

In addition the relative error between the corresponding eigenvalues of these two modes is very low. Though a mode with high interface incompatibility shows up at 2nd position after the interface reduction (see Fig. 14.13b) which looks similar to the interface mode corresponding to the negative eigenvalue with smallest absolute value as shown in Fig. 14.10b. Hence eigenfrequencies of modes, which do not correlate, are compared in the calculation of the relative errors according to Eq. (14.52). As shown in Fig. 14.14b there is no high correlation between the first 10 eigenmodes of the reduced and the unreduced system. The interface incompatibilities of the 4th and 5th eigenmodes are also very high (Fig. 14.13d, e). Therefore we want demonstrate the effect adding more interface modes for this example in the following.
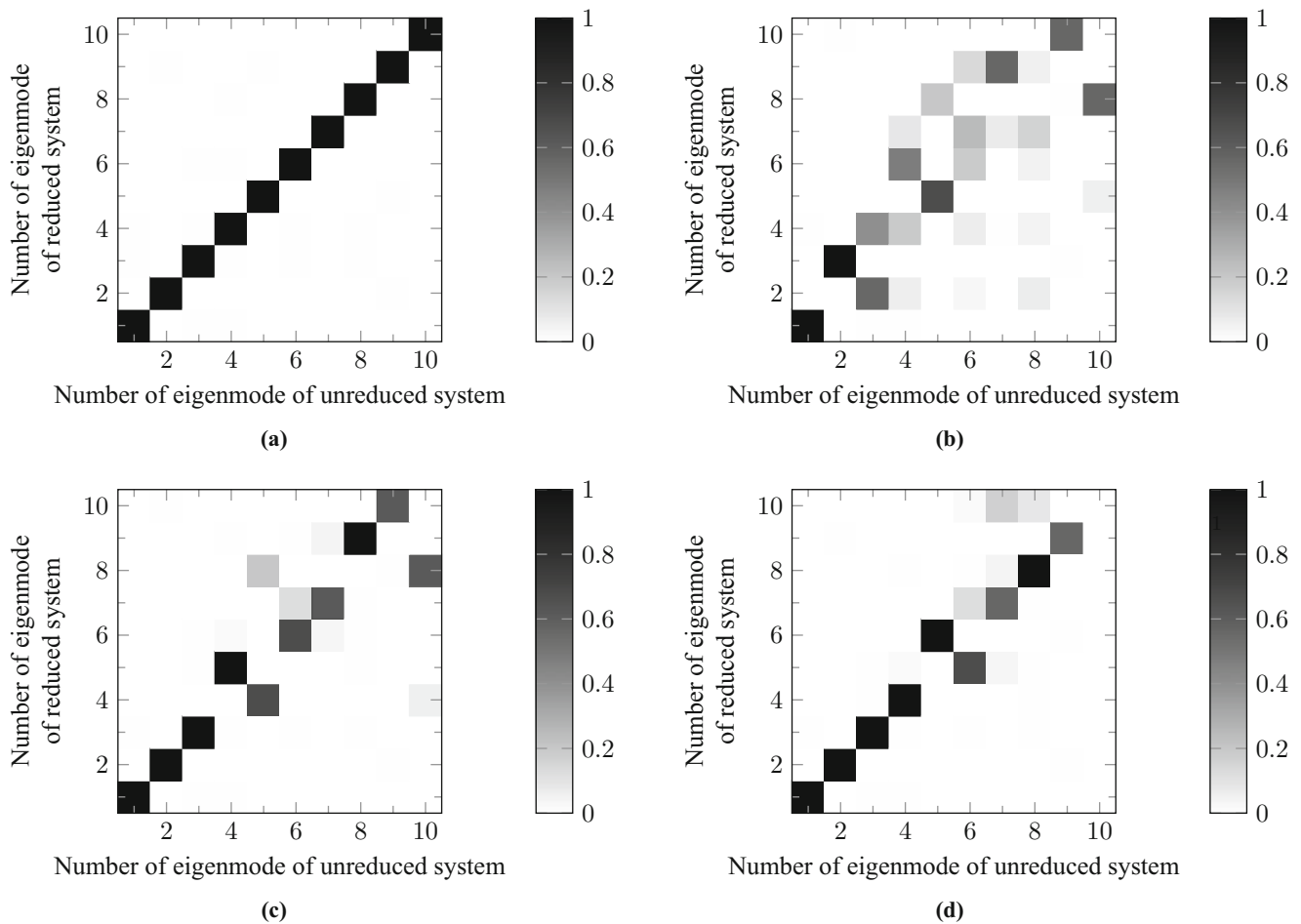
Fig. 14.14 MAC for DCBM reduced system with and without modal interface reduction. (**a**) DCBM. (**b**) DCBM with $n_{int} = 3$ kept interface modes. (**c**) DCBM with $n_{int} = 4$ kept interface modes. (**d**) DCBM with $n_{int} = 5$ kept interface modes

14.4.3.3 Modal Interface Reduction with Three Interface Modes Corresponding to the Three Positive Eigenvalues Plus One Additional Interface Mode Corresponding to the Negative Eigenvalue with Smallest Absolute Value

For further investigation a modal interface reduction is conducted again, but the interface mode corresponding to the negative eigenvalues with smallest absolute values (mode shape shown in Fig. 14.10b) is added to the 3 interface modes corresponding to the positive eigenvalues as demonstrated in Sect. 14.4.3.2. The graph "Modal 4" in Fig. 14.12 shows the relative errors of the first 10 eigenfrequencies with this interface reduction. Including the 2nd interface mode enhances the approximation significantly, especially the relative errors of the first 4 eigenfrequencies are improved noticeably. Figure 14.15 depicts the mode shapes corresponding to the 8 lowest eigenvalues of the reduced system and the MAC values of the first 10 eigenmodes between the unreduced and reduced system are shown in Fig. 14.14c. Figure 14.15a–c demonstrate that the first 3 eigenmodes of the unreduced system are represented very accurate by the reduced system with 4 kept interface modes. This is confirmed by MAC values near 1 in Fig. 14.14c. Moreover the eigenvalue errors for these modes are very small and only very low interface incompatibilities can be seen.

The 2nd (incompatible) eigenmode of the previous section (Fig. 14.13b) seems to be compensated by including the interface mode corresponding to the smallest negative eigenvalue (Fig. 14.10b) in such a way that the first 3 eigenmodes show up in the right order now. Moreover the MAC values in Fig. 14.14c illustrate that the 5th eigenmode of the reduced system (Fig. 14.13e) correlates to the 4th eigenmode of the unreduced system (Fig. 14.9d). The difference between the corresponding eigenvalues is also very small.

But one mode with high interface incompatibility shows up at 4th position in Fig. 14.15. This modes seems to correlate to the 5th eigenmode, which is the 2nd longitudinal mode, of the unreduced system as indicated by the corresponding MAC
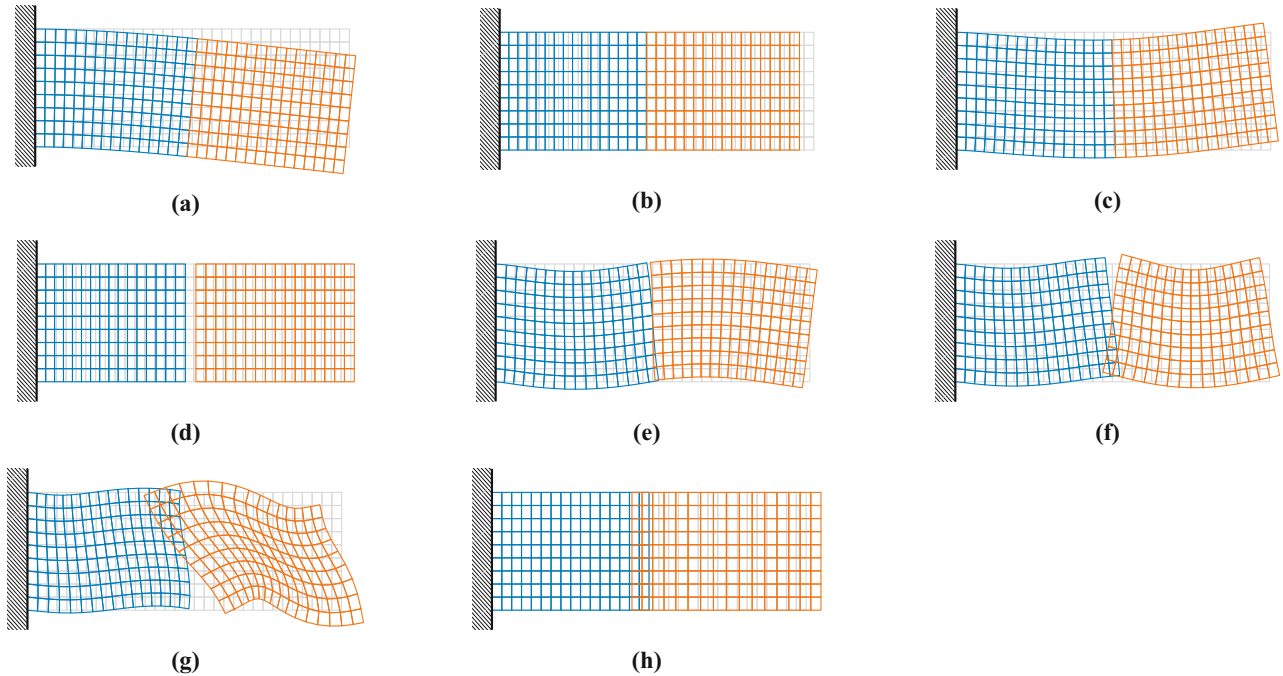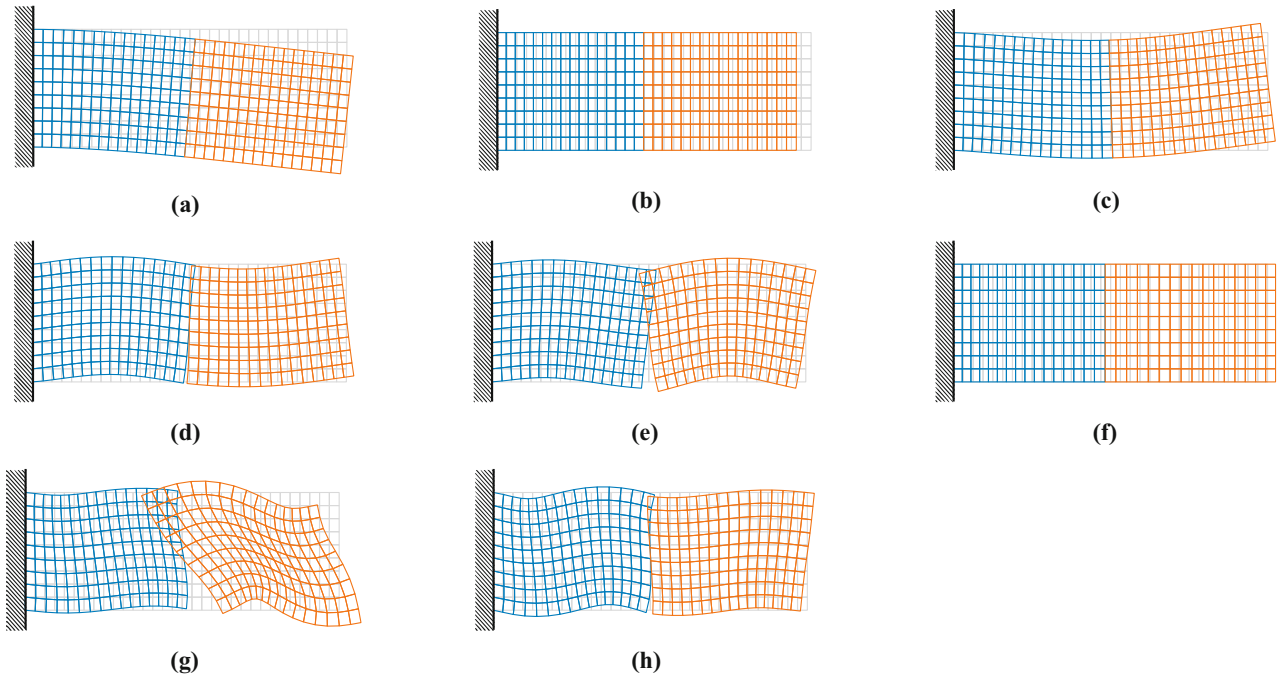
Fig. 14.15 First eight eigenmodes after DCBM ($n_\theta^{(1)} = n_\theta^{(2)} = 8$) with modal interface reduction ($n_{int} = 4$ interface modes kept). (**a**) 1. eigenmode: $\omega_{DCB,mod}^2 = 0.0019$. (**b**) 2. eigenmode: $\omega_{DCB,mod}^2 = 0.0385$. (**c**) 3. eigenmode: $\omega_{DCB,mod}^2 = 0.0398$. (**d**) 4. eigenmode: $\omega_{DCB,mod}^2 = 0.1816$. (**e**) 5. eigenmode: $\omega_{DCB,mod}^2 = 0.1869$. (**f**) 6. eigenmode: $\omega_{DCB,mod}^2 = 0.3300$. (**g**) 7. eigenmode: $\omega_{DCB,mod}^2 = 0.6243$. (**h**) 8. eigenmode: $\omega_{DCB,mod}^2 = 0.6247$

value in Fig. 14.14c. The 6th and 7th mode of the reduced system correlate to the respective modes of the unreduced system according to the MAC values but there are high incompatibilities in the mode shapes depicted in Fig. 14.15f, g.

To sum up, it can be concluded that including the interface modes corresponding to negative eigenvalues improves the approximation accuracy significantly which will be refined in the subsequent section. Especially the first 3 bending modes of the system can be represented much better in this example and also the interface incompatibilities are reduced significantly. That is not the case without including this additional interface mode.

14.4.3.4 Modal Interface Reduction with Three Interface Modes Corresponding to the Three Positive Eigenvalues Plus Two Additional Interface Mode Corresponding to the Two Negative Eigenvalues with Smallest Absolute Values

Finally one more additional interface mode corresponding to a negative eigenvalue is added to the reduction basis. This interface mode has also strong interface incompatibilities as depicted in Fig. 14.10e. In total 5 interface modes are used now whereby 3 of them have positive eigenvalues and the other 2 have negative eigenvalues (see Fig. 14.10a–e). The graph "Modal 5" in Fig. 14.12 shows the relative errors of the first 10 eigenfrequencies with this interface reduction. Again the approximation accuracy is improved significantly compared to the interface reduction without the additional interface mode as illustrated by the graph "Modal 4" in Fig. 14.12. The 2nd eigenfrequency is as accurate as without interface reduction and the relative error of the eigenfrequencies is below 1% up to the 5th eigenfrequency. Figure 14.16 shows the shapes of the first 8 eigenmodes corresponding to the lowest eigenvalues of the reduced system. Figure 14.16a–d illustrate that the first 4 eigenmodes correspond to the first 4 eigenmodes of the unreduced system (see also Fig. 14.9a-d) which is confirmed by the MAC values in Fig. 14.14d. Moreover the eigenfrequency of the 1st longitudinal mode (2nd eigenmode) is approximated much better by including the 5th interface modes as can be seen in Fig. 14.12. Furthermore including this 5th interface modes, the 4th eigenmode of the previous section, which shows large interface incompatibilities (Fig. 14.15d), is compensated by this mode and hence disappears or is shifted to higher frequencies. The 3rd bending mode (Fig. 14.16d) is also on the right position now.

Fig. 14.16 First eight eigenmodes after DCBM ($n_\theta^{(1)} = n_\theta^{(2)} = 8$) with modal interface reduction ($n_{int} = 5$ interface modes kept). (**a**) 1. eigenmode: $\omega_{DCB,mod}^2 = 0.0019$. (**b**) 2. eigenmode: $\omega_{DCB,mod}^2 = 0.0386$. (**c**) 3. eigenmode: $\omega_{DCB,mod}^2 = 0.0398$. (**d**) 4. eigenmode: $\omega_{DCB,mod}^2 = 0.1869$. (**e**) 5. eigenmode: $\omega_{DCB,mod}^2 = 0.3300$. (**f**) 6. eigenmode: $\omega_{DCB,mod}^2 = 0.3479$. (**g**) 7. eigenmode: $\omega_{DCB,mod}^2 = 0.6243$. (**h**) (8) eigenmode: $\omega_{DCB,mod}^2 = 0.8472$

Considering the 5th interface mode (Fig. 14.10e) it is obvious that this mode only influences longitudinal modes. This explains the improvement of the eigenfrequency of the 1st longitudinal mode as can be seen in Fig. 14.12 when adding this interface mode.

The MAC values in Fig. 14.14d show a high correlation between the 6th eigenmode of the reduced system and the 5th eigenmode of the unreduced system. This mode corresponds to the 2nd longitudinal mode which is represented very good now since the interface incompatibilities are compensated by the additional interface mode. However an eigenmode with high interface incompatibility is on the 5th position now (Fig. 14.16e) which seems to have a certain correlation to the 6th eigenmode of the unreduced system as can be seen in the MAC plot in Fig. 14.14d. According to the MAC values the 7th, 8th and 9th eigenmode of the reduced system corresponds to the 7th, 8th and 9th eigenmode of the unreduced system, respectively. This is obvious for the 8th eigenmode when comparing the mode shapes in Figs. 14.9h and 14.16h and the corresponding eigenvalues are also approximated accurately. High interface incompatibilities are observable for the 5th and 7th eigenmode in Fig. 14.16e, g which have also high relative eigenvalue errors compared to the other values in the low spectrum.

14.5 Conclusions

In this paper two interface reduction techniques for the dual Craig-Bampton method (DCBM) were presented. The modal interface reduction outperforms the static (Guyan) interface reduction when keeping the same number of interface modes but having additional costs since another eigenvalue problem has to be solved. Solving the static condensed interface problem and using the obtained interface normal modes as reduction basis can decrease the number of interface degrees of freedom significantly without deteriorating the approximation accuracy of the eigenfrequencies in the low frequency range. This was shown in an example reducing the remaining 559 degrees of freedom without interface reduction by a subsequent modal interface reduction to 146 degrees of freedom without changing the approximation accuracy of the 20 lowest eigenfrequencies.

Since the number of interface modes corresponding to negative eigenvalues is equal to the number of Lagrange multipliers, the kept interface modes for the reduction have to be chosen with care. It is possible to keep only the interface modes corresponding to positive eigenvalues which has the pleasant side effect that the resulting reduced system does not have any negative eigenvalues anymore which is unavoidable for the DCBM without interface reduction. This could be beneficial in order to avoid possible instabilities occurring when time integrating DCBM reduced systems. Nevertheless keeping only interface modes corresponding to positive eigenvalues decreases the approximation accuracy of the eigenvalues significantly and the corresponding eigenmodes appearing in the low frequency spectrum with high interface incompatibilities do not have any correlation to the eigenmode shapes of the unreduced system. A comprehensible example was used to show that including interface modes corresponding to negative eigenvalues shifts these eigenmodes with high interface incompatibilities out of the low frequency range and therefore improves the approximation accuracy of the eigenvalues. It is recommended to keep interface modes corresponding to negative eigenvalues if the eigenvalues of a system have to be approximated. In future research we plan to study the effect of the interface reduction in the DCBM on the time integration of the reduced system.

References

1. Craig, R.R.: Coupling of substructures for dynamic analyses: an overview. In: Proceedings of AIAA/ASME/ASCE/AHS/ASC Structures, Structural Dynamics, and Materials Conference and Exhibit, Atlanta, pp. 1573–1584 (2000)
2. Craig, R.R., Bampton, M.C.C.: Coupling of substructure for dynamic analyses. AIAA J. **6**(7), 1313–1319 (1968)
3. Craig, R.R., Chang, C.-J.: Substructure coupling for dynamic analysis and testing. Technical report (1977)
4. Craig, R.R., Kurdila, A.J.: Fundamentals of Structural Dynamics. Wiley (2006) ISBN:0471430447
5. Géradin, M., Rixen, D.J.: Mechanical Vibrations: Theory and Application to Structural Dynamics. Wiley (2014) ISBN:1118900197
6. Gruber, F.M., Rixen, D.J.: Evaluation of substructure reduction techniques with fixed and free interfaces. Strojniški vestnik J. Mech. Eng. **62**(7–8), 452–462 (2016). doi: 10.5545/svjme.2016.3735, ISSN:00392480
7. Gruber, F.M., Rutzmoser, J.B., Rixen, D.J.: Comparison between primal and dual Craig-Bampton substructure reduction techniques. In: Moltezar M., Slavic, J., Wiercigroch, M. (eds.) Proceedings of the 11th International Conference on Engineering Vibration, Ljubljana pp. 1245–1254 (2015)
8. MacNeal, R.H.: A hybrid method of component mode synthesis. Comput. Struct. **1**(4), 581–601 (1971). doi: 10.1016/00457949(71)900319, ISSN:00457949
9. Rixen, D.J.: A dual Craig-Bampton method for dynamic substructuring. J. Comput. Appl. Math. **168**(1–2), 383–391 (2004). doi: 10.1016/j.cam.2003.12.014, ISSN:03770427
10. Rixen, D.J.: Dual Craig-Bampton with enrichment to avoid spurious modes. In: Proceedings of IMAC-XXVII (2009)
11. Rixen, D.J.: Interface reduction in the dual Craig-Bampton method based on dual interface modes. In: Proulx, T. (ed.) Linking Models and Experiments, Volume 2: Proceedings of the 29th IMAC, A Conference on Structural Dynamics, 2011, pp. 311–328. Springer, New York (2011). doi: 10.1007/97814419-93052_22, ISBN: 978-1-4419-9305-2
12. Rubin, S.: Improved component-mode representation for structural dynamic analysis. AIAA J **13**(8), 995–1006 (1975). doi: 10.2514/3.60497, ISSN:0001-1452
13. Voormeeren, S.N., Valk, P.L.C. van der, Rixen, D.J.: Generalized methodology for assembly and reduction of component models for dynamic substructuring. AIAA J. **49**(5), 1010–1020 (2011). doi: 10.2514/1.J050724, ISSN:0001-1452

Chapter 15
Substructuring of a Nonlinear Beam Using a Modal Iwan Framework, Part I: Nonlinear Modal Model Identification

Daniel Roettgen, Matthew S. Allen, Daniel Kammer, and Randall L. Mayes

Abstract This work uses a method whereby weak nonlinearity in a substructure, as typically arises due to microslip in bolted interfaces, can be captured and modeled on a mode-by-mode basis. The method relies on the fact that the modes of a weakly nonlinear structure tend to remain uncoupled so long as their natural frequencies are distinct and higher harmonics generated by the nonlinearity do not produce significant response in other modes. A single degree-of-freedom (DOF) system with an Iwan joint, which is known as a modal Iwan model, effectively captures the way in which the stiffness and damping depend on amplitude for each mode. This work presents the experiments used to generate these modal Iwan models. In a companion paper this model is assembled to another component using dynamic substructuring techniques to estimate the amplitude dependent frequency and damping of the full assembly.

Keywords Experimental Nonlinear Detection • Nonlinear Modeling • Modal Iwan Models

15.1   Introduction

Experimental-analytical substructuring allows one to predict the dynamic response of an assembly by coupling substructures derived from experiments with substructures represented by finite element models. There are numerous applications of experimental-analytical substructuring, but in particular this is useful when one has a subcomponent of a system that is difficult to model. When using subcomponents to predict the response of an assembly there are often many joints in the structure; either contained within a given subcomponent or in between two of them. Such joints are known to be a significant source of nonlinear damping in built up assemblies. Capturing these nonlinear joint dynamics in an experimental subcomponent model is one way to account for these dynamics when predicating responses for the full assembly. This work outlines methods used for testing structures with weakly nonlinear joints by using a recently proposed framework that models the structure as a collection of uncoupled, weakly nonlinear (in the case of micro-slip) oscillators. These nonlinear modal-like models are used in a companion paper, " Substructuring of a nonlinear beam using modal Iwan framework, Part II: Nonlinear Modal Substructuring" [1] in order to complete substructuring predictions. This paper addresses the detection, identification, and verification of these models on subcomponent structures.

The nonlinear models in this paper build on the efforts of Segalman, and his colleagues at Sandia National Laboratories, who pursued a multi-year project in which models for mechanical joints were derived and calibrated to match experimental force-dissipation measurements [2, 3]. They showed that one can determine the parameters for each joint in a structure and employ nonlinear time integration to compute the response including the effects of the joints. More recently, Segalman proposed to model each mode of a structure as independent but with an Iwan joint in parallel with the modal stiffness to capture the nonlinear damping (and to a lesser extent nonlinear stiffness) of the joint [4]. Using this method one can identify amplitude dependant modal stiffness and damping for each mode. Allen and Deaner extended Segalman's work by adding a

D. Roettgen (✉) • M.S. Allen • D. Kammer
Department of Engineering Physics, University of Wisconsin, Madison, WI 53706, USA
e-mail: droettgen@wisc.edu; msallen@engr.wisc.edu; kammer@engr.wisc.edu

R.L. Mayes
Structural Dynamics Department, Sandia National Laboratories, P.O. Box 5800 – MS0557, Albuquerque, NM 87185, USA
e-mail: rlmayes@sandia.gov

viscous damper in parallel with the Iwan element to account for the linear material damping that dominates for each mode at very small amplitudes [5] and began to more thoroughly explore the extent to which this modal approximation is accurate for real structures with several joints [6]. The approach used here is similar to that which was first used by Deaner to characterize a beam with a bolted joint. However, this work presents an updated means of interpreting the dissipation in the modal Iwan model that allows one to more clearly see how the damping ratio changes with response amplitude [7], while still allowing power-law behavior to be identified. In industry, modeling nonlinearities is often avoided by testing the structure at single amplitude, with the expectation that the resulting linearized model will be relevant in the environment of interest or the worst case environment. However, even though the idea is generally sound, when nonlinearities are ignored it is likely that the resulting model will be inaccurate because each mode may activate the nonlinearity at a different amplitude.

The paper is organized as follows. Section 15.2 outlines the theory behind the toolbox used for detection and identification of nonlinear modal models. Section 15.3 contains details about the test specimen, the Brake-Reuss Beam (BRB), and experimental set-up information. In Section 15.4 these techniques are validated by generating nonlinear modal models for the Brake-Reuss Beam system using modal Iwan models. A simulation of these models is then compared to that of the true structure. Section 15.5 concludes the paper and discusses some future work in this research area. This work continues in Part II [1] where these modal models are used in a dynamic substructuring prediction.

15.2 Nonlinear Modal Models

This section contains an overview of our latest process for experimental detection and characterization of nonlinear modal behavior. Figure 15.1 shows the steps of the processes we go through to detect, characterize and verify these nonlinear modal models. The goal is to highlight each step of the process and give insight into the different tools used when looking for nonlinear modal behavior in an experimental system. A more rigorous explanation to many of these tools is contained in [7].
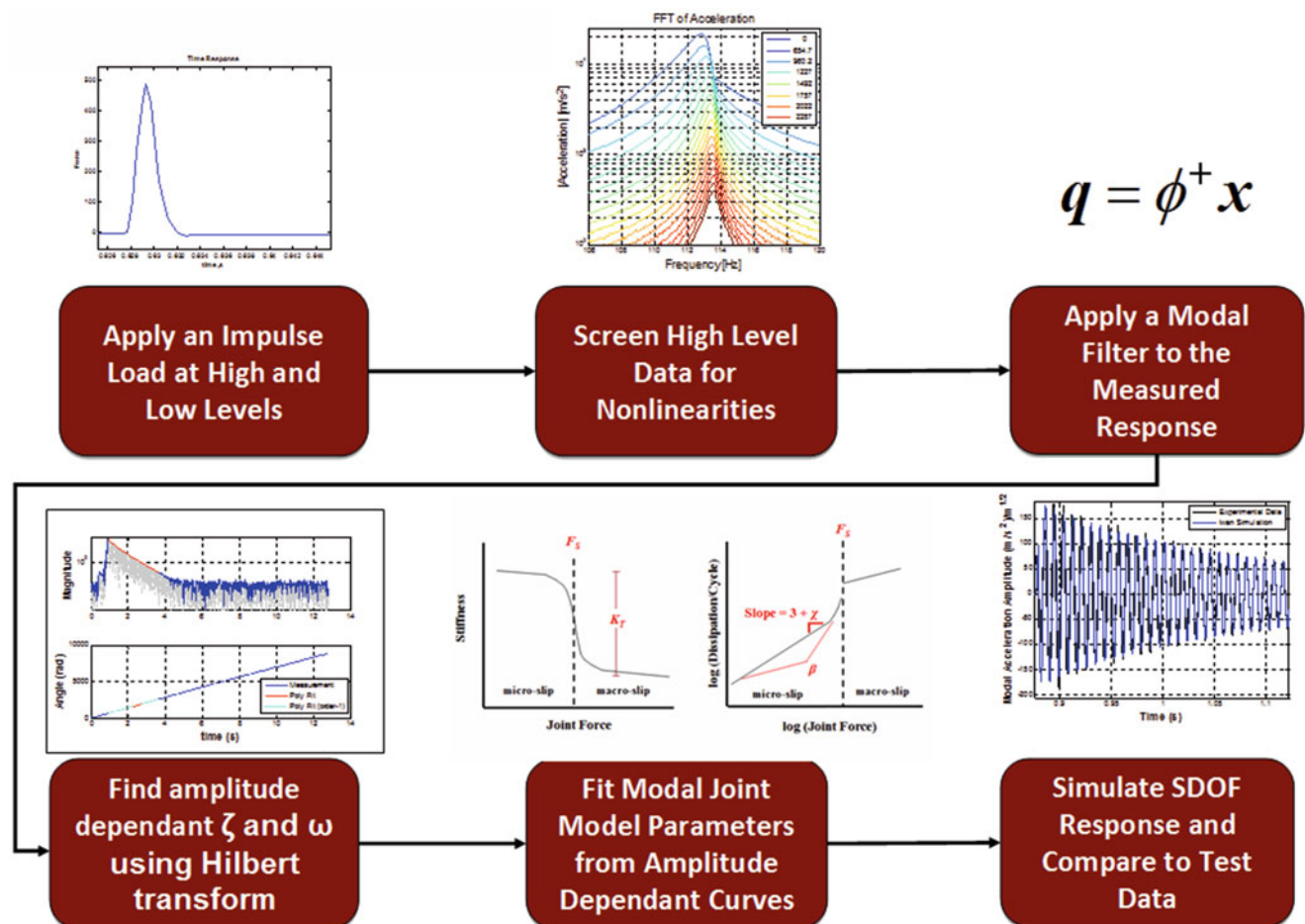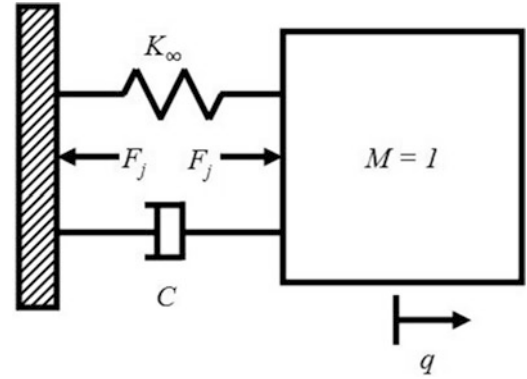

Fig. 15.1 Nonlinear modal behavior workflow

Fig. 15.2 Schematic of SDOF
model used for each modal
degree of freedom

The fundamental equation or motion for a structure can be written as:

$$\mathbf{M}\ddot{x} + \mathbf{C}\dot{x} + \mathbf{K}x + F_j(x, \theta) = F \tag{15.1}$$

where $\mathbf{M}$, $\mathbf{C}$, and $\mathbf{K}$ represent the linear mass, damping and stiffness matrices, F is the excitation force and F_j is a nonlinear force due to the joints in the structure. Each mode is assumed to be independent and its mode shape is assumed to remain the same as in the low-level linear system. These assumptions remain valid as long as the jointed structure remains weakly nonlinear and the modes remain uncoupled and are not closely spaced. [7, 8]

To begin identifying the nonlinear modal models contained in F_j, the structure is excited with an impulsive load at high and low force levels. The low force level measurement is used to find linear modal parameters as is the common practice in industrial applications. Next, the high load level data is used to screen each mode for nonlinear behavior.

Often in weakly nonlinear structures very small frequency shifts are observed but, large changes in damping are seen as amplitude increases. These differences are apparent when once compares the modal parameters extracted from a high forcing level impact test with those from a low forcing level. Additionally, comparing the frequency response function of the measured signals can provide insight as to how the response of the system changes at high and low amplitudes. All measurements are related to one modal response, thus the following equation can be solved in a least squares sense to obtain the modal amplitude from the acceleration measurements,

$$\boldsymbol{\varphi}_r \ddot{q}_r(t) = \ddot{x}(t) \tag{15.2}$$

where $\boldsymbol{\varphi}_r$ is the rth mass-normalized mode vector, $\ddot{q}_r(t)$ is the corresponding modal response and $\ddot{x}(t)$ is a vector of accelerations that were measured during a single-impact hammer test. This method allows multiple hammer strikes to be compared even from different driving point locations.

Each mode can now be represented as a single degree-of-freedom (SDOF) system as shown in Fig. 15.2. This SDOF system contains a modal mass which is tied to ground with a linear spring and damper. Also, a nonlinear element representing the joint force is also connected to this mass which can be used to describe the nonlinear behavior of this modal response. This nonlinear element could take many forms but for this work a 4-parameter Iwan element is used to represent this nonlinear joint force.

The original equation of motion can now be written in modal coordinates as shown in Eq. (15.3).

$$\mathbf{I}\ddot{q} + \left[\diagdown(2\zeta_0\omega_0)_{\diagdown} \right]\dot{q} + \left[\diagdown(\omega_0{}^2)_{\diagdown} \right]q + \{F_j\} = \boldsymbol{\phi}^T F \tag{15.3}$$

The next step in the process is to quantify the change in frequency and damping with amplitude. This is accomplished using the Hilbert transform algorithm as detailed in [5, 9]. This approach fits the modal response, $q(t)$, to the following analytic functional form:

$$\ddot{q}(t) = e^{\psi_r(t) + i\psi_i(t)} \tag{15.4}$$

where $\psi_r(t)$ and $\psi_i(t)$ are a series of splines in time and are, respectively, the real and imaginary parts of the time varying response model. The damped natural frequency can be related to the phase of the analytic signal as was discussed in [5]. Obtaining the damping ratio is covered in detail [7] but relates to both the amplitude and phase of the analytic signal. Based

on the derivations mentioned the modal parameters can be obtained as shown in Eq. (15.5). In addition to describing the nonlinear characteristics of the mode, these parameters also allow for the conversion of modal acceleration to modal velocity and displacement.

$$\omega_d(t) \triangleq \frac{d\psi_i}{dt} \qquad -\zeta\omega_n(t) \triangleq \frac{d\psi_r}{dt} \qquad (15.5)$$

Recall, each mode will be modeled with a single degree of freedom system with a spring, damper, and nonlinear joint force which is modeled as a 4-Parameter Iwan model. This joint force can be written in the following form,

$$F_j(t) = \int_0^\infty \rho(\phi) \left[u(t) - x\left(t, \phi\right) \right] d\phi \qquad (15.6)$$

where F_j is the force in the joint, u is joint displacement, ρ is a kernel that characterizes the joint and x is a continuum of state variables that evolve as

$$\dot{x}(t, \phi) = \begin{cases} \dot{u} & \text{if } \|u - x(t, \phi)\| \\ & \text{and } \dot{u}(u - x(t, \phi)) > 0 \\ 0 & \text{otherwise} \end{cases} \qquad (15.7)$$

The form of the kernel, $\rho(\phi)$, is discussed in detail in [3] and can be defined by four parameters, $[F_s, K_T, \chi, \beta]$, where F_s is the joint force required to begin macro-slip, K_T is the stiffness in the joint, χ is related to the exponent in the power-law relationship between damping and amplitude in the micro-slip regime and β defines the shape of the dissipation curve near the transition from micro to macro-slip. This kernel was designed to reproduce the power-law damping that has been observed in experiments. When this joint model is used in a modal framework, these four parameters define the nonlinear characteristics of each mode in the system and can be obtained from experimental measurements as outlined in [5, 7].

15.3 Experimental System: Brake-Reuss Beam System

This process was applied to a bolted structure consisting of two half beams with a lap joint containing three individual bolts. This beam is known as the Brake-Reuss beam (BRB) system first researched by Brake and Reuss in [10]. The bolts in this assembly were tightened to the recommended 20 ft.-lb. torque [11]. This system has been studied by several groups at the Nonlinear Mechanics and Dynamics (NOMAD) institute hosted by Sandia National Labs in the past [12, 13]. The beam studied here consists of beam halves 1A and 1B from the 2015 NOMAD institute (Fig. 15.3).
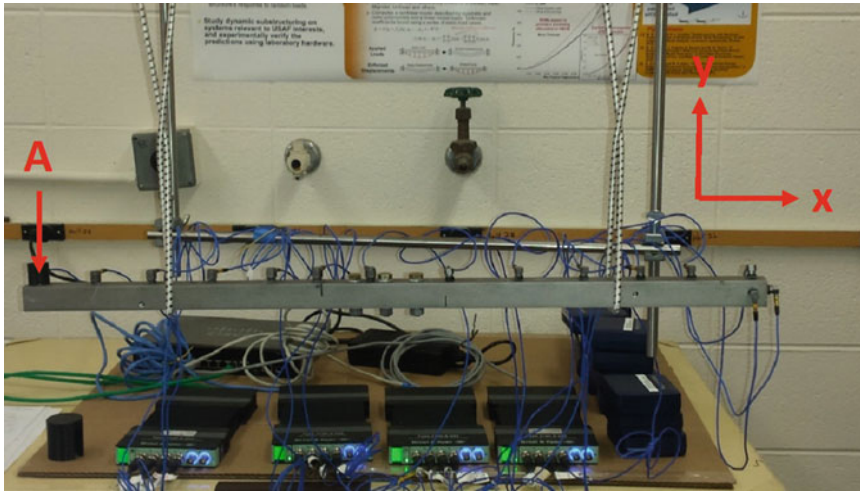
Fig. 15.3 Photograph of Brake-Reuss beam system experimental set-up
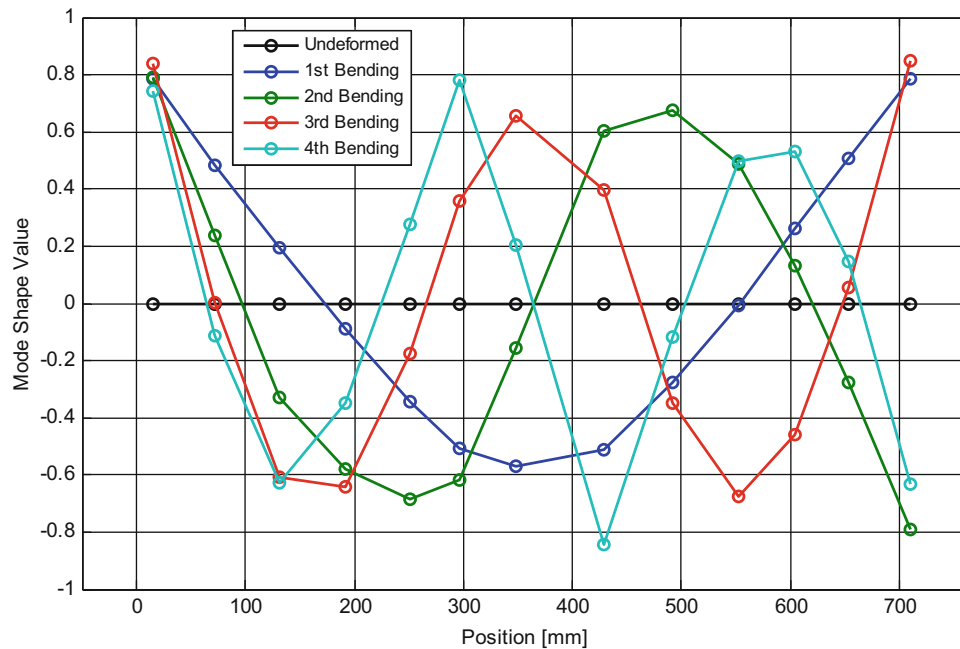
Fig. 15.4 Bending mode shapes of Brake-Reuss beam structure

Table 15.1 Linear (low amplitude) modal parameters

Elastic mode index	Natural frequency [Hz]	Damping ratio	Deflection type
1	172.70	0.00095	1st Bending
2	583.26	0.00143	2nd Bending
3	1179.99	0.00376	3rd Bending
4	1645.43	0.00814	4th Bending

The primary modes of interest in this study are the bending modes in the xy-plane as defined in Fig. 15.4. Based on previous experiments [12] the frequency range of interest was 0–2000 Hz, where the first few bending modes could be readily obtained. The system was instrumented with 15 low sensitivity (5 mV/g) accelerometers, 13 of these sensors are in the primary direction of interest with 2 off-axis sensors for troubleshooting. Using low level hammer hits on the accelerometer at point A, the modal parameters of the first four bending modes were extracted from the test specimen. Figure 15.4 shows these bending modes for the measurement points in the y-direction.

Table 15.1 contains a list of the natural frequencies and damping ratios extracted for each of the modes using the Algorithm of Mode Isolation (AMI), a linear modal parameter identification algorithm that is detailed in [14]. With linear modes defined, the next step is to screen these modes for nonlinear behavior and identify candidate nonlinear modal models.

15.4 Nonlinear Modal Behavior: Detection and Model Identification

15.4.1 Nonlinear Model Behavior: Detection

With a linear model for the first four bending modes established, the structure was ready to be tested at higher impact levels in order to screen for nonlinearity. The assembly was probed by hitting the beam several times at varying load levels and at several drive points to deduce whether any modes might behave nonlinearly. By comparing the frequency response function for each of these hits we can see how the response of the first mode changes as force level is increased, see Fig. 15.5. In a truly linear system all of these curves would overlay as the amplitude of the force and response would be linearly scaled. Due to the nonlinearities in the Brake-Reuss Beam assembly, increasing the impulsive force results in a slight decrease in the resonant frequency and an increase in the modal damping observed by the decreasing FRF amplitude. These changes are similar to what has been observed in the past when a nonlinear modal model was well suited to fit the response [7].
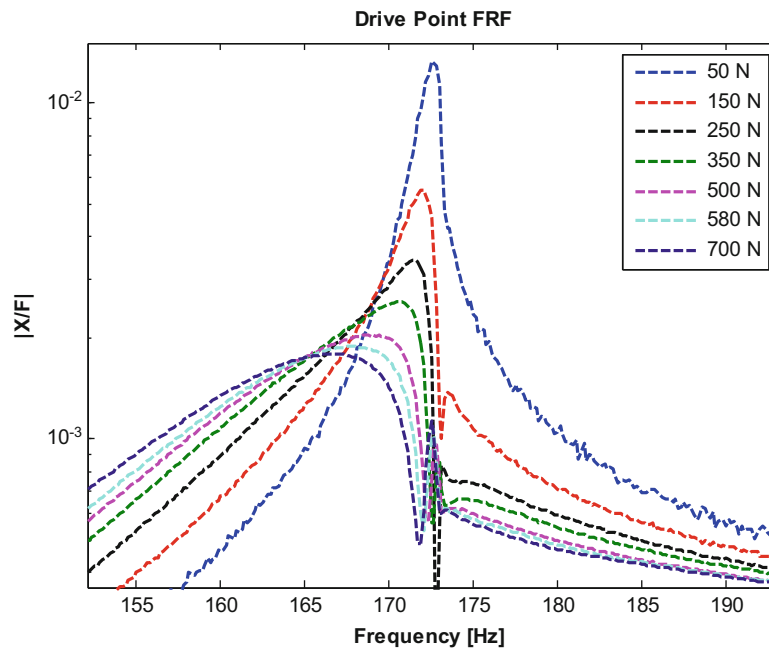
Fig. 15.5 First bending mode multi-level frequency response function

Table 15.2 Summary of results for Brake-Reuss Beam system NA = not applicable (linear mode).

Elastic mode	Natural frequency [Hz]	% Shift in peak frequency	Linear damping ratio[a]	Maximum damping ratio[a]	% Shift in damping
1	172.70	−3.81%	0.00095	0.01060	+1015%
2	583.26	−1.28%	0.00143	0.00625	+337%
3	1179.99	NA	0.00376	NA	NA
4	1645.43	NA	0.00814	NA	NA

[a]Damping Ratios obtained from Half Power Bandwidth of highest and lowest force level strikes.

While this frequency shift shows that the stiffness nonlinearity is quite small, this mode exhibited much more significant nonlinearity in damping. A similar analysis was performed on the second elastic mode, which also revealed a measurable shift in the natural frequency of over the same range of input force. The third and forth elastic modes showed smaller traces of nonlinearity so it was decided to create nonlinear modal models for the first two bending modes and use linear models for the third and fourth bending modes. A summary of the observed frequency and damping nonlinearities is shown in Table 15.2. The trends from this table are used solely to screen modes and make sure the results of the fit models are reasonable.

Now that the first two modes have been identified as nonlinear, their corresponding amplitude dependent stiffness and damping need to be obtained. A spatial filter is first applied to each of the measured data sets in order to isolate each mode as in Eq. (15.2). This results in a SDOF response for each mode for each test run completed. The fast Fourier transform of these spatially filtered signals is shown in the Fig. 15.6. It is important to properly filter the signals into single harmonic, any contamination from closely spaced modes can cause major distortions when the stiffness and damping are fit versus amplitude.

Next, the Hilbert transform is used to obtain an expression in the form of Eq. (15.4) for each single degree of freedom response. In order to achieve a higher quality fit of frequency and damping, a band-pass filter is applied to the modally filtered signal to ensure the signal is a single harmonic. Then a mirroring algorithm is used to mirror the time signal back in time directly after the impulse is applied. This mirroring makes the change in amplitude less abrupt and reduces the end effects in the Hilbert transform. Figure 15.7 shows this mirrored signal for the 1st bending mode. The magnified plots show that the signal has smoothly varying amplitude and hence will be well describe by the SDOF model.

The envelope and phase of this mirrored signal was then fit to a spline with 30 knots as shown in Fig. 15.8. The top portion of the subplot shows a fit of the Hilbert envelope and the middle portion shows a fit of the unwrapped phase. Finally the bottom plot shows how well the Hilbert signal recreated the original spatially filtered response.

Using the relationships from Eq. (15.5), the fit envelope and phase can be related to the damping and stiffness of the signal. Plotting the damping and stiffness versus amplitude yields a relationship from which nonlinear modal model parameters can
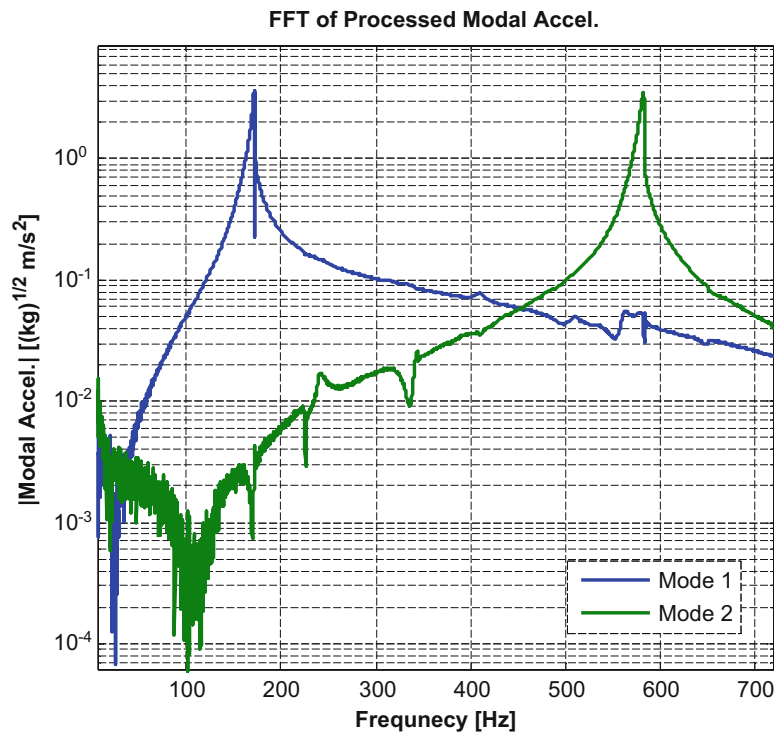
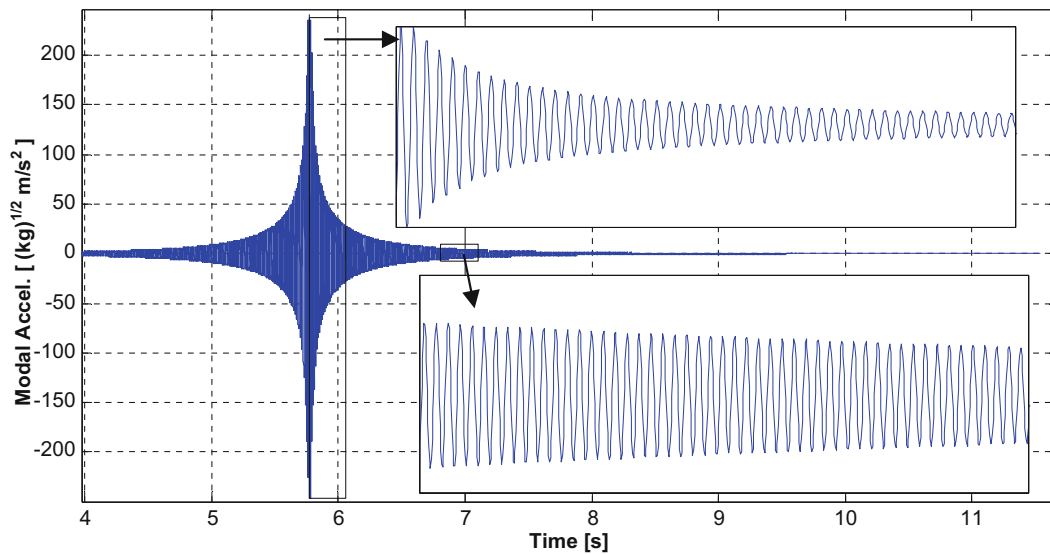**Fig. 15.6** FFT of spatially filtered signals

Fig. 15.7 Mirrored signal of 1st bending mode modal acceleration

be extracted. Figures 15.9 and 15.10 show an example of this process for the 1st bending mode of the system where the damped natural frequency and damping ratio are plotted versus time and amplitude, respectively.

Note that later in time (lower in amplitude) a frequency is seen near 172.7 Hertz which is the linear frequency from modal testing in Table 15.1. Early in the time signal (when the modal amplitude is high) the frequency gets as low as 169 Hz, or about a 2% shift in frequency, close to what was observed by testing at multiple forcing levels as shown in Fig. 15.5. Similar comparisons can be seen in the linear damping ratio which matches the measurement present in Table 15.1. The nonlinear damping ratio reaches levels much higher than observed in the simple FRF screening process, most likely due to the half-power bandwidth assumption being used on a nonlinear data set.
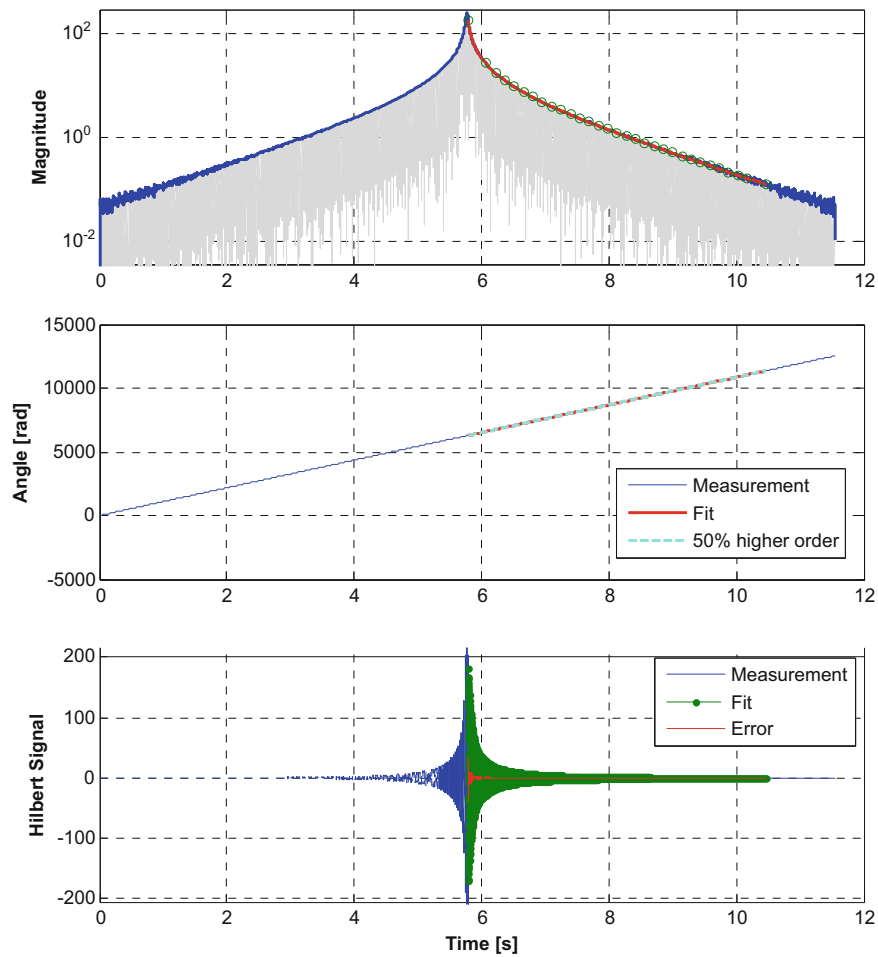
Fig. 15.8 Hilbert fit for 1st bending mode: Hilbert Envelop (*top*), Hilbert Phase (*middle*), Reconstructed Signal (*bottom*)
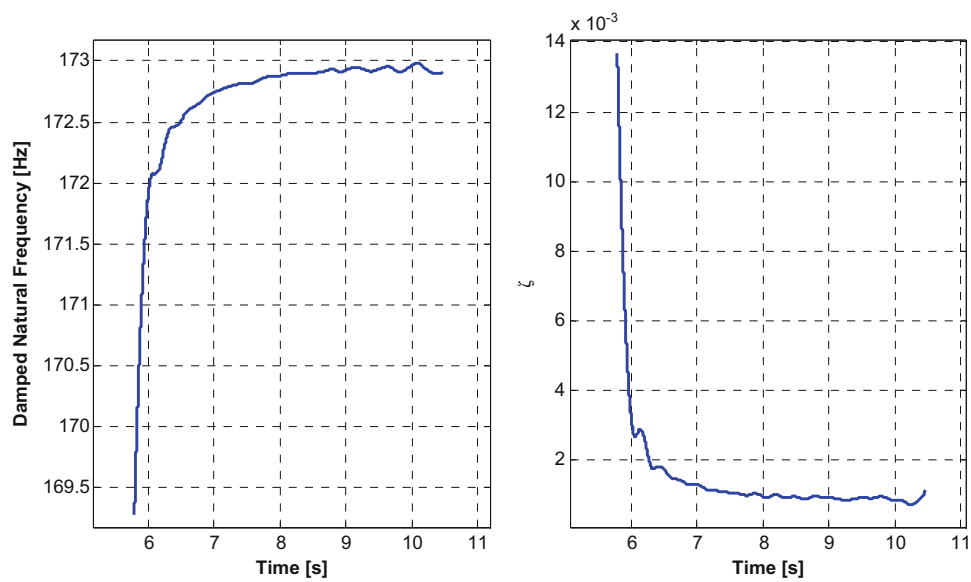
Fig. 15.9 Hilbert fit for 1st bending stiffness and damping mode in time
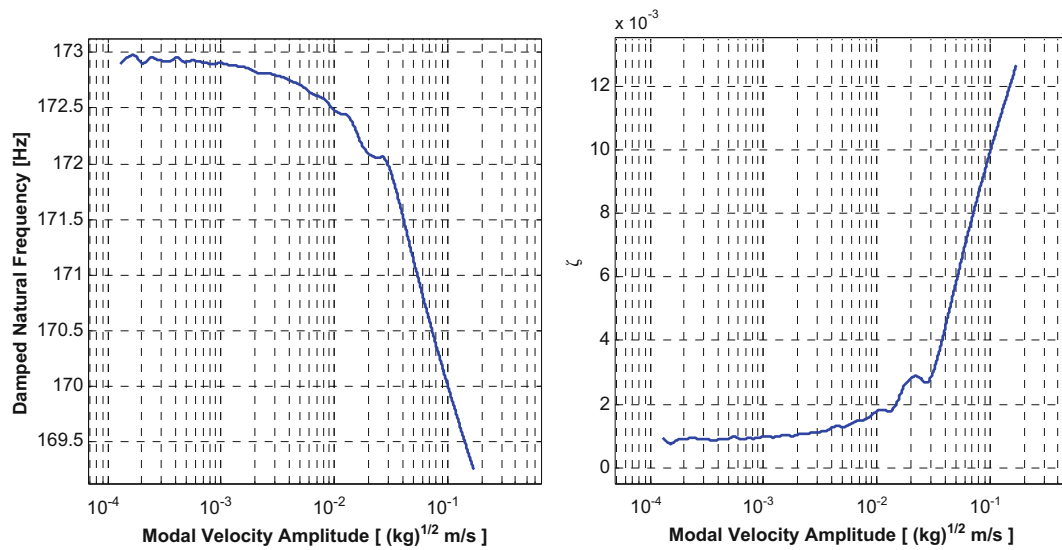
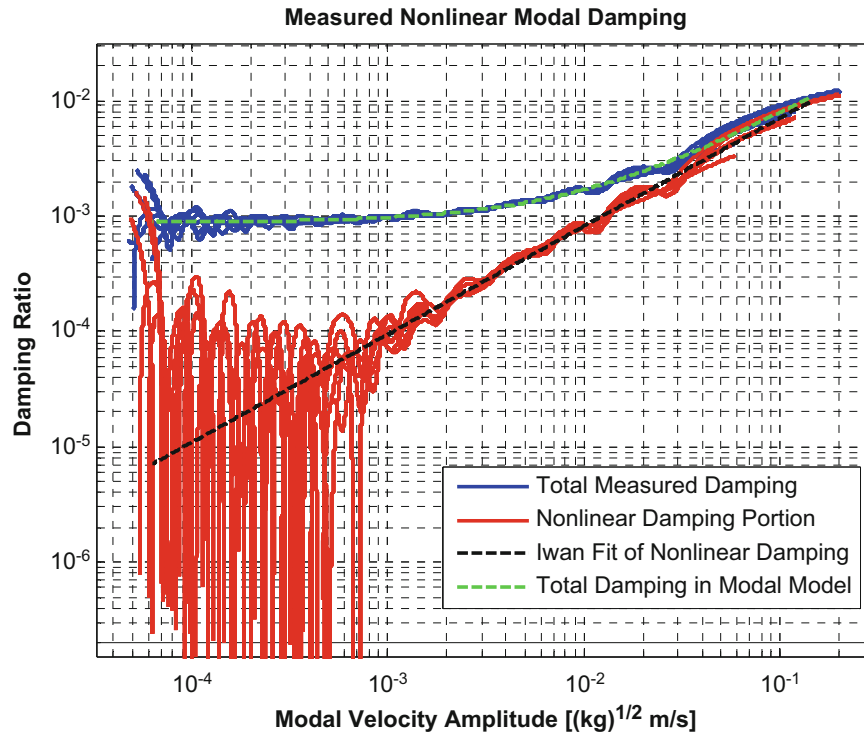**Fig. 15.10** Amplitude dependant stiffness and damping curves

Fig. 15.11 Measured modal damping for mode 1

15.4.2 Nonlinear Model Behavior: Model Identification

The results shown in Figs. 15.9 and 15.10 were extracted from only one of the excitation amplitudes at which tests were performed. The spectra at various load levels are shown in Fig. 15.5. To ensure that the modes were adequately uncoupled, testing was also conducted from differing drive point locations. For each impact test a pair of stiffness and damping curves were generated. This ensemble of damped natural frequency and damping ratio curves for each nonlinear mode can be overlaid to see how repeatable these amplitude dependent measurements are. These overlaid curves were used to extract modal Iwan model parameters as shown in Fig. 15.11.

The modal Iwan model is defined by four parameters, $[F_s, K_T, \chi, \beta]$. To fit the dissipation parameter, χ, of the Iwan modal model these amplitude dependant damping curves were fit in a least squares sense. In this figure the total modal damping in the mode, extracted by the Hilbert transform, is given by the blue curves. Next, the linear contribution was removed from these curves revealing the nonlinear part of the damping in red (i.e. the part that is not linear and viscous). At low amplitudes this can be very noisy but at higher amplitudes a distinct trend is clear on this log-log scale. χ is then fit to this distinct high amplitude potion of the nonlinear damping curve by setting the slope of this curve equal to $\chi + 1$. This Iwan fit is shown in black. Finally to ensure the total modal damping is well simulated the linear portion of the damping is added back to the Iwan fit to obtain the total modal damping, shown in green.

The other modal Iwan parameters are more ambiguous but were selected based off of engineering judgment and previous testing history. There was no obvious evidence of macro-slip in the experimental test; therefore, the slip force can be assumed to be greater than any of the excitations applied experimentally.

$$F_S \geq \varphi_{dp} F \tag{15.8}$$

The joint stiffness, K_T, is dependent on the frequency shift observed once the structure is in macro-slip, and because macro-slip wasn't achieved in these tests this parameter can't be readily estimated. This beam was previously tested by Bonney et al. [12] and their tests included higher amplitude impacts where the macroslip frequency for the first mode was observed to be 130 Hz. This was used to estimate K_T using :

$$K_T = K_0 - K_\infty = \omega_0^2 - \left(\omega_0 - \omega_{shift}\right)^2 \tag{15.9}$$

In principle, the parameter β can be found from the y-intercept of the dissipation versus amplitude curve, but in this case this would not be reliable since F_s and K_T are not known precisely. Instead β was assumed to be zero (corresponding to a case where the power law term in the Iwan model is much larger than the macro-slip term) and then varied to see whether the results were sensitive to that assumption.

These concepts were used to estimate starting values for the parameters and then they were varied until the frequency and damping versus amplitude curves of the modal Iwan model (found by integrating the SDOF equation of motion with the Newmark algorithm [15]) matched what was measured experimentally. Table 15.3 shows the final parameters that were used in order to model the first and second elastic modes.

The accuracy of these final parameters was initially checked by simulating a SDOF modal response to a singe impact for each nonlinear mode and comparing the results to the corresponding measured modal filtered signal. Figure 15.12 shows this comparison in the time domain for the first bending mode. Here, one can observe that in both early and late time the modal model closely matches the measured data.

These responses can be further compared via their amplitude dependent stiffness and damping curves of each signal. These curves were extracted from the simulated response using the Hilbert transform as described previously. Figures 15.13 and 15.14 show the comparison between the measured and simulated response for the simulated loading case. The model obtains good correlation throughout the amplitude range of interest. A similar process was followed for the second bending mode leading to another nonlinear modal model. All of these figures show an excellent agreement between the model and measured data. Therefore the modal Iwan model with parameters from Table 15.3 sufficiently captures the nonlinear characteristics of the first two elastic modes.

With nonlinear modal models for the first two bending modes, the fidelity of the multi-modal model can now be assessed. The responses of four elastic modes were simulated due to modal forces corresponding to a 180 N impulsive force at drive point location A from Fig. 15.3. Each mode was integrated separately with the first two elastic modes using the nonlinear modal model in as in Eq. (15.3). Once each single degree of freedom calculation was complete, the linear mode shape matrix was used to transform these results back into physical space. Figure 15.15 shows the simulated nonlinear and measured drive point acceleration responses. Note, a simulation was also conducted using a purely linear modal model using the parameters from Table 15.1. Here one can observe that the standard linear model over predicts the amplitude of response for a large majority of the ring down.

Table 15.3 Iwan model parameters Brake-Reuss Beam System

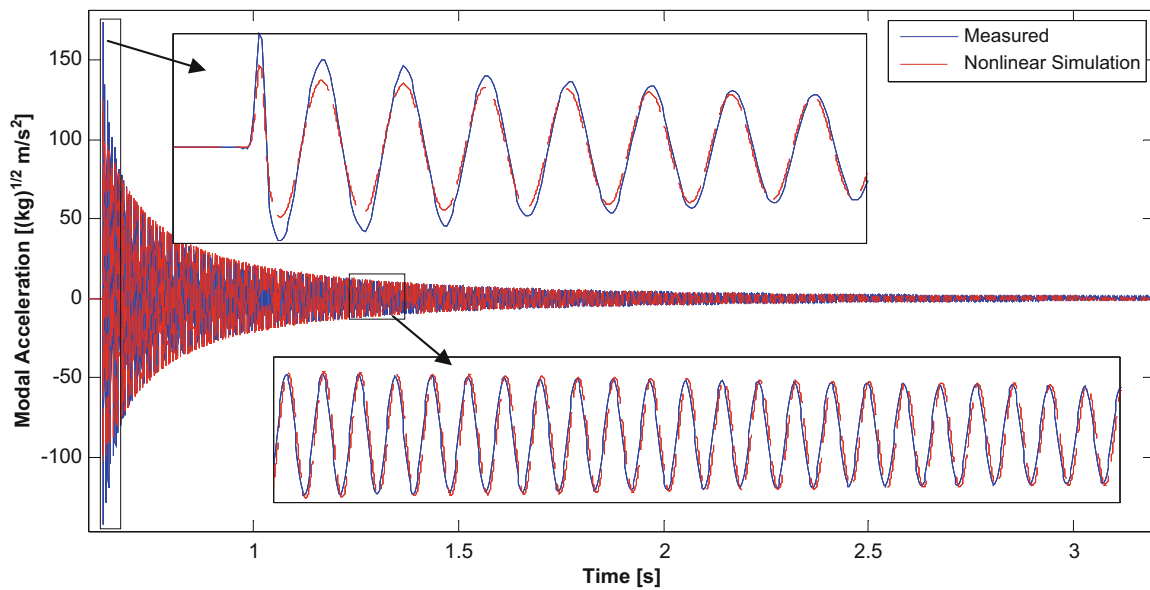| Parameter	Simulation case 1st mode	Simulation case 2nd mode
F_s	137.72	152.14
K_T	484680	2668200
β	0.26159	0.29688
χ	−0.049947	−0.41637

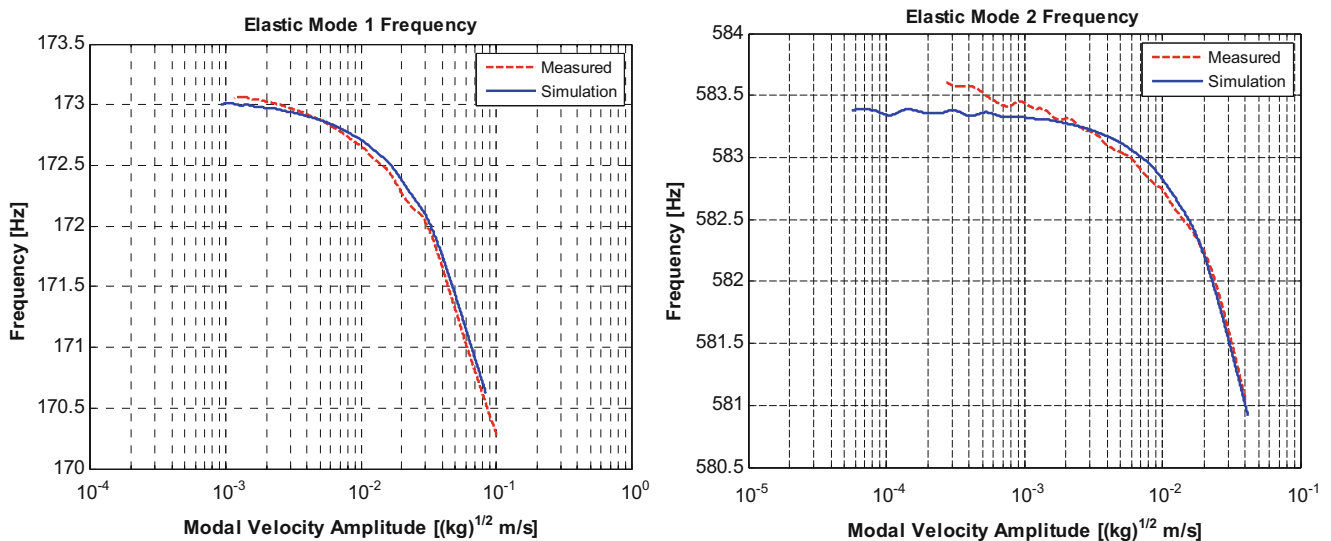**Fig. 15.12** Modal acceleration - 1st elastic mode

Fig. 15.13 Measured and simulated modal frequency for elastic modes 1 and 2

In Fig. 15.16 one can again observe the transient response due to an impulsive load but the linear model has been removed for visual clarity. The amplitude matches fairly well in low and high amplitudes and the frequency is only off slightly later in the decay. This validates the assumption earlier that the nonlinearity in the third and fourth bending modes was sufficiently small.

Figure 15.17 shows the FFT of the modal acceleration for the simulated response. Enhanced views in Fig. 15.18 show how well the nonlinear prediction matches the true measurement. As expected based on a viewing of the time history, a linear model over predicts the amplitude by under predicting amplitude.

15.5   Conclusions

This work explored the applicability of a modal Iwan model for a Brake-Reuss Beam assembly. Experimental results were initially screened by examining the frequency response functions in order to determine which modes needed to be treated as nonlinear. Mirrored time history data was used with the Hilbert transform to estimate the amplitude dependent stiffness
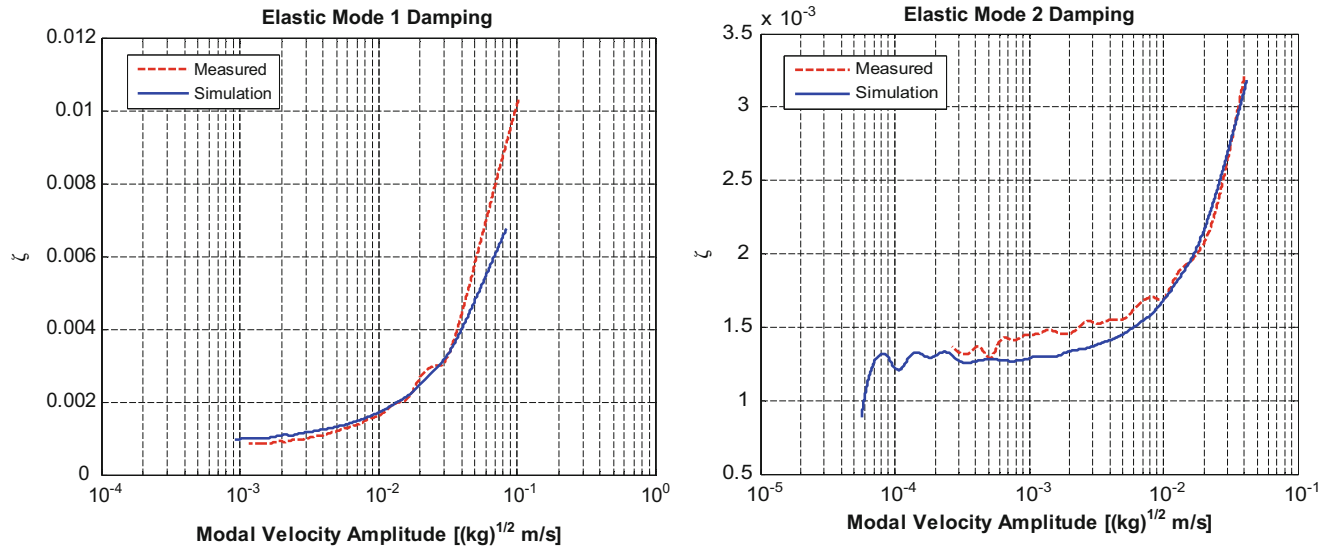
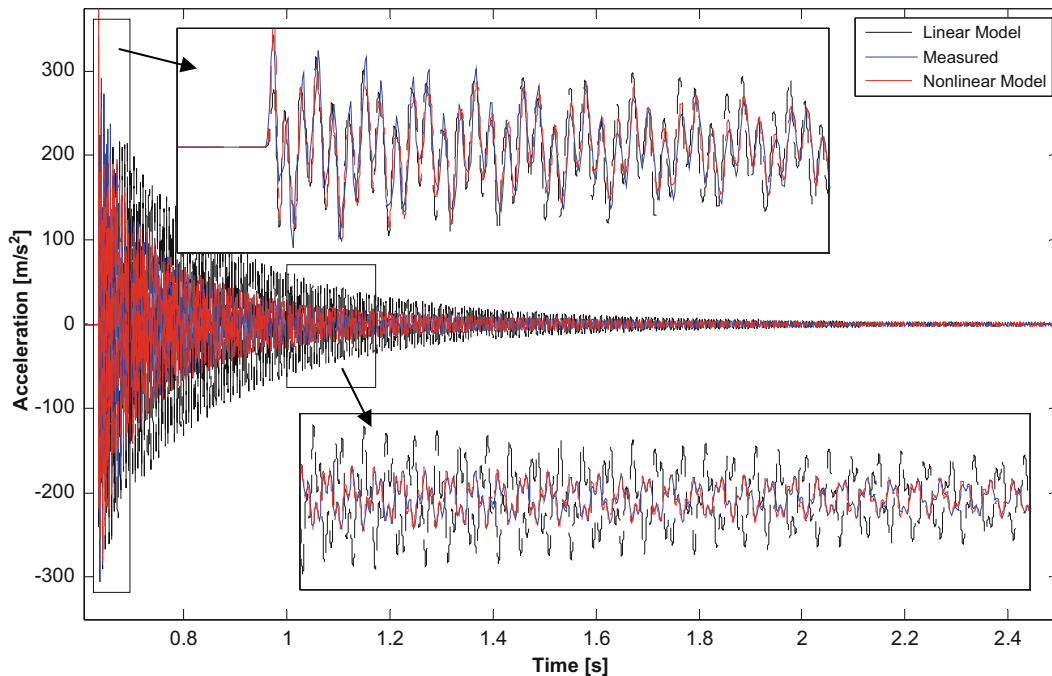**Fig. 15.14** Measured and simulated modal damping for elastic modes 1 and 2

Fig. 15.15 Drive point acceleration with the linear model

and damping behavior of each mode. Modal Iwan parameters were extracted for these nonlinear bending modes using a combination of engineering judgment, previous testing experience, and amplitude dependent stiffness and damping curves. This type of model is only accurate if the modes of the system to be reasonably spaced and remain dynamically uncoupled. Each simulated nonlinear modal model response correlated with the modally filtered measured signal well.

A nonlinear pseudo-modal model consisting of six modes was then created. This model contained two rigid modes, two nonlinear modes, and two linear modes. A simulation was conducted in which the response of this nonlinear multi-mode model was compared to measured data in the physical domain. By just treating the first two elastic modes as nonlinear, the measured response of the system was well matched and showed great improvement over a standard linear model. By just treating the first two elastic modes as nonlinear modal models the response of the system was well represented, showing great improvement over a standard linear model.
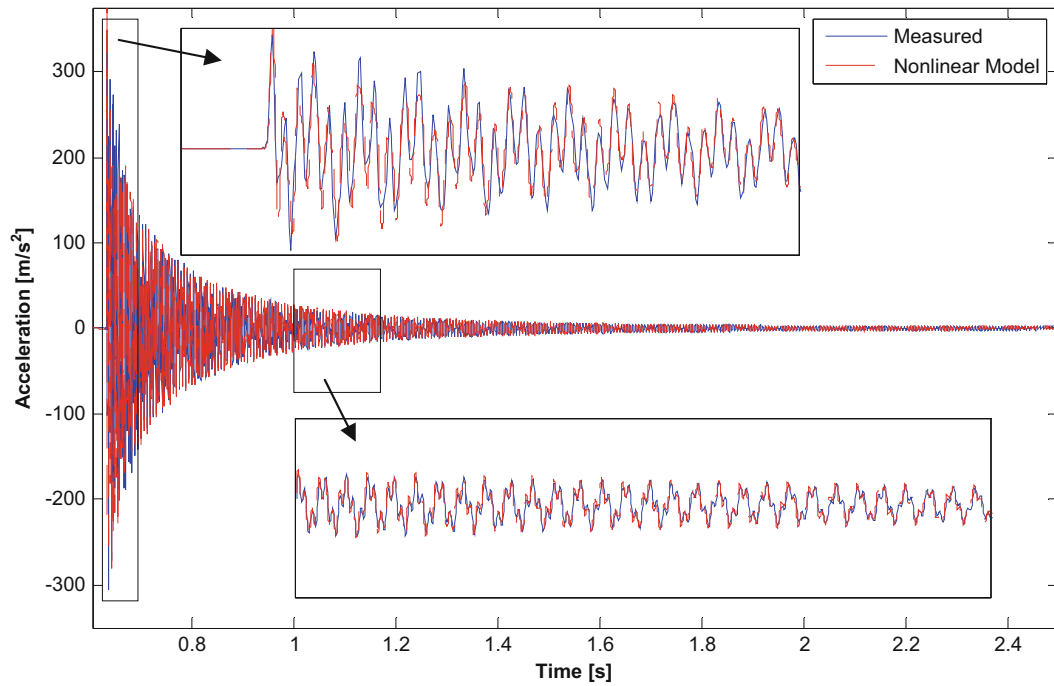
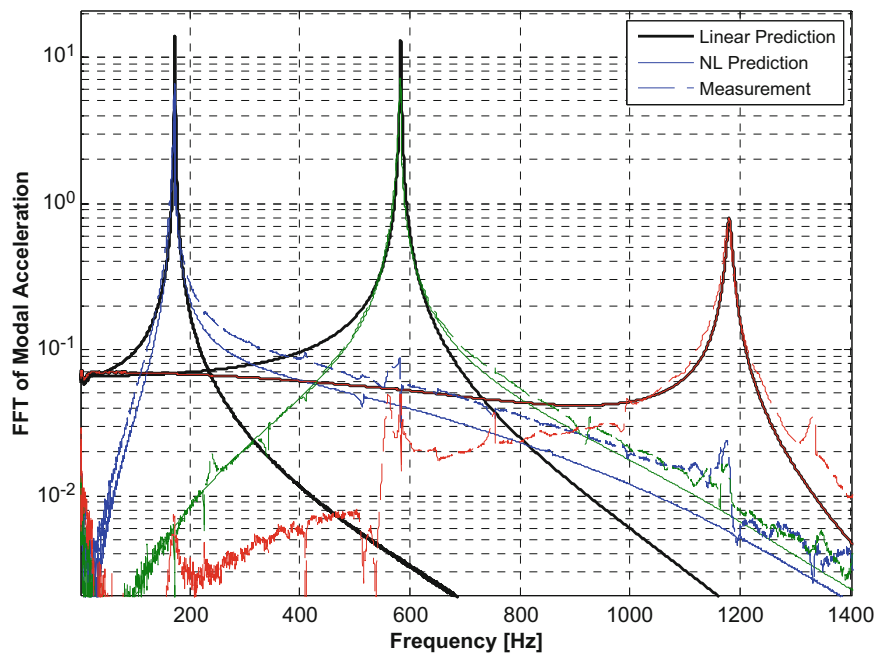**Fig. 15.16** Drive point acceleration

Fig. 15.17 FFT of modal acceleration

As mentioned previously, this is one subcomponent of an assembly that we desire to study. This model is clearly superior to the standard linear model at representing this subcomponent and is therefore expected to produce a more accurate substructuring prediction. Part II [1] of this paper will explore the results of utilizing these nonlinear modal models in a component mode synthesis dynamic substructuring framework. Thus far the modes of the system have remained uncoupled. Substructuring will only succeed if the modal model is still valid even after a subcomponent is removed and added to another structure.
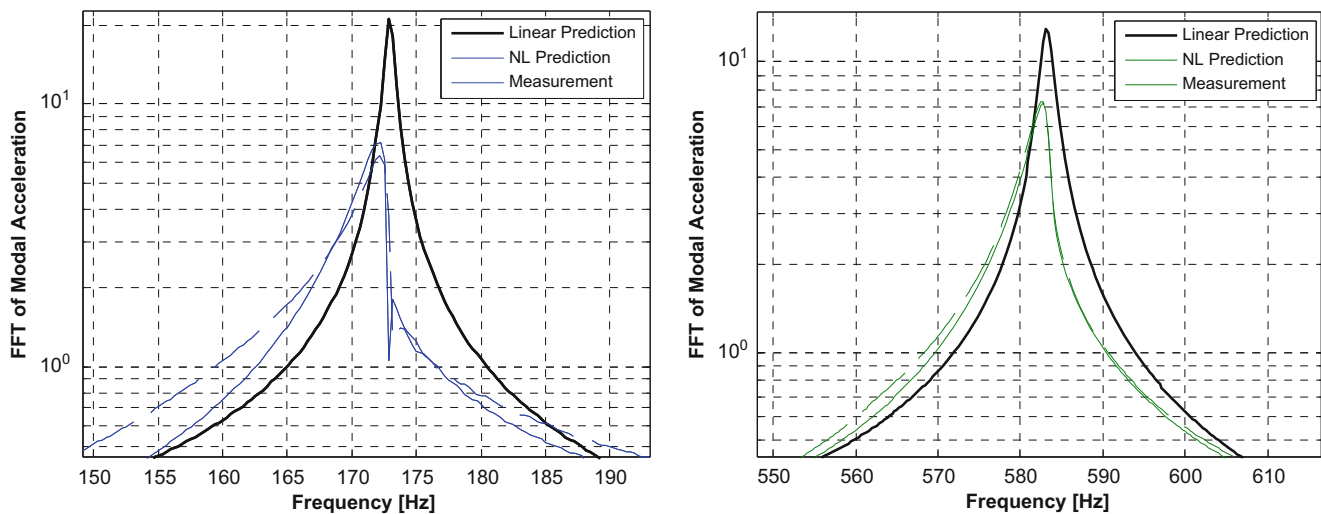
Fig. 15.18 FFT of Modal acceleration enhanced view of elastic modes 1 (*left*) and 2 (*right*)

References

1. Roettgen, D.R., et al.: Substructuring of a nonlinear beam using modal Iwan framework, part II: nonlinear modal substructuring. Presented at the international modal analysis conference XXXV, Garden Grove, 2017
2. Segalman, D.J.: An Initial Overview of Iwan Modelling for Mechanical Joints. Sandia National Laboritories, Albuquerque, SAND2001–0811 (2001)
3. Segalman, D.J.: A four-parameter Iwan model for lap-type joints. J. Appl. Mech. **72**, 752–760 (2005)
4. Segalman, D.J.: A Modal Approach to Modeling Spatially Distributed Vibration Energy Dissipation. Sandia National Laboratories, Albuquerque/Livermore, SAND2010–4763 (2010)
5. Deaner, B., Allen, M.S., Starr, M.J., Segalman, D.J., Sumali, H.: Application of viscous and Iwan modal damping models to experimental measurements from bolted structures. ASME J. Vib. Acoust.**137**, (2015)
6. Lacayo, R., et al.: A numerical study on the limitations of modal Iwan models for impulsive excitations. J. Sound Vib. **390**, 118 (2016)
7. Roettgen, D.R., Allen, M.S.: Nonlinear characterization of a bolted, industrial structure using a modal framework. Mech. Syst. Signal Process. **84**, 152 (2016)
8. Eriten, M., et al.: Nonlinear system identification of frictional effects in a beam with a bolted joint connection. Mech. Syst. Signal Process. **39**, 245–264 (2013)
9. Sracic, M.W., et al.: Identifying the modal properties of nonlinear structures using measured free response time histories from a scanning laser Doppler vibrometer. Presented at the 30th International Modal Analysis Conference, Jacksonville, 2012
10. Brake M. R.W., et al.: Variability and repeatability of jointed structures with frictional interfaces. Presented at the International Modal Analysis Conference, Orlando, 2014
11. Oberg, E.: Machinery's Handbook, 29th edn. Industrial Press, New York (2012)
12. Bonney, M. S., et al.: Experimental determination of frictional interface models. Presented at the international modal analysis conference XXXIV, Orlando, 2016
13. Catalfamo, S., et al.: Effects of experimental methods on the measurements of a nonlinear structure. Presented at the international modal analysis conference XXXIV, Orlando, 2016
14. Allen, M.S., Ginsberg, J.H.: A global, single-input-multi-output (SIMO) implementation of the algorithm of mode isolation and applications to analytical and experimental data. Mech. Syst. Signal Process. **20**, 1090–1111 (2006)
15. Cook, R.D., et al.: Concepts and Applications of Finite Element Analysis, 4th edn. Wiley, New York (2002)

Chapter 16
Substructuring of a Nonlinear Beam Using a Modal Iwan Framework, Part II: Nonlinear Modal Substructuring

Daniel Roettgen, Matthew S. Allen, Daniel Kammer, and Randall L. Mayes

Abstract In a companion paper (Roettgen, D.R., et al.: Substructuring of a nonlinear beam using modal Iwan framework, Part 1: nonlinear modal model identification. Presented at the international modal analysis conference XXXV, Garden Grove, 2017), "Substructuring of a nonlinear beam using modal Iwan framework, Part I: Nonlinear Modal Model Identification", nonlinear modal models are constructed for an experimental substructure that represent the dynamics using a set of uncoupled weakly nonlinear modes. This assumes that the linear modes of the structure remain uncoupled so that the nonlinearity can be described in a mode by mode fashion. These nonlinear modal models can be used to simulate the response of the experimental system. This paper demonstrates the use of these models to represent a substructure in an experimental-analytical substructuring prediction. The authors utilize the transmission simulator method on the experimentally derived models to generate predictions of a modified Brake-Reuss Beam system. The substructuring predictions are then compared to a truth test data set to validate the method. To further understand the limitations of the method and its sensitivity to measurement noise, the modal substructuring approach is also simulated on a finite element model of the beam that contains three discrete nonlinear elements to represent the joint.

Keywords Experimental Nonlinear Substructuring • Modal Iwan Models • Transmission Simulator Method

16.1 Introduction

Experimental-analytical substructuring allows one to predict the dynamic response of an assembly by coupling substructures derived from experiments with substructures represented by finite element models. There are numerous applications of experimental-analytical substructuring, but in particular this is useful when one part of a system is difficult to model. When building a structure from several subcomponents, there are often many joints involved, either contained within one subcomponent or between them. Such joints are known to be a significant source of nonlinear damping in built-up assemblies, and their stiffness is difficult to predict when modeling. One way to account for these dynamics when predicting responses for the full assembly is to use an experimental subcomponent model. However, few methods have been proposed to identify and utilize nonlinear subcomponent models in substructuring.

In Part I the authors outlined a method used for testing and identifying weakly nonlinear structures that can be modeled as a collection of uncoupled, weakly nonlinear (in the case of micro-slip) oscillators. This work builds on that using the identified nonlinear modal models to describe subcomponents in an experimental-analytical dynamic substructuring prediction. A more in depth study of these modal models is contained in [1]. Experimental identification of nonlinear modal models has also been explored previously on an industrial system in [2] using 4-parameter modal Iwan models. More, recently the Iwan modal models have been compared with polynomial models in [3, 4].

D. Roettgen (✉) • M.S. Allen • D. Kammer
Department of Engineering Physics, University of Wisconsin, Madison, WI 53706, USA
e-mail: droettgen@wisc.edu; msallen@engr.wisc.edu; kammer@engr.wisc.edu

R.L. Mayes
Structural Dynamics Department, Sandia National Laboratories, P.O. Box 5800 – MS0557, Albuquerque, NM 87185, USA
e-mail: rlmayes@sandia.gov

There are several methods of experimental-analytical substructuring. In [5] deKlerk and Rixen discuss many methods and their history. The synthesis procedures in these techniques apply to both linear and nonlinear systems. In the work described herein, the transmission simulator method was used to generate dynamic substructuring predictions. This method uses an experimental system that includes a fixture (or transmission simulator) as one subcomponent. This fixture is meant to simulate the boundary conditions of the subcomponent of interest in the next level assembly. The rationale behind the transmission simulator method can be found in [6–8]. One main advantage of this method is its ability to capture the stiffness and damping between the substructures because the same joint is used between the transmission simulator and the structure of interest as that in the full assembly. Here this is especially important because it allows one to capture the nonlinearity generated by the joint in a single experimental substructure, using the transmission simulator to excite the joint dynamics. This means that one can capture the nonlinearities in the system on the subcomponent level, then assemble the substructure models to see how those nonlinear forces affect the fully assembled structure.

A few methods have been explored for completing synthesis with nonlinear components. In [9] Kalaycioglu and Ozguven discuss component mode synthesis with nonlinear structural modifications. More recently, Krack explored using component mode synthesis with nonlinear normal modes in [10]. This work focuses on weakly nonlinear structures where the modes remain uncoupled in microslip amplitude ranges. This is the first attempt to use these nonlinear modal models in a synthesis approach using the transmission simulator method and weakly nonlinear modes. This is a continuation based on the approach presented by the authors in [11].

Substructuring methods are not yet commonly used in industry, but in most applications practitioners seek to create finite element models of the structure of interest, possibly including nonlinearities, and to update the model to reproduce the available experimental measurements. This alternative is also briefly explored here by modeling the Brake-Reuss Beam with a discrete Iwan joint to represent the area around each bolt. The parameters of these models are then updated to best match test data. This also provides a model that can be used to simulate modal substructuring on the Brake-Reuss Beam. In a companion paper [12] this same approach is used to predict the response of the Brake-Reuss Beam after modifying part of the structure away from the joint.

This paper is organized as follows. Sect. 16.2 outlines the theory behind dynamic substructuring when using these nonlinear modal models. Sect. 16.3 contains an overview of the substructuring problem being investigated as well as detailed descriptions of each substructure. In Sect. 16.4 these substructuring techniques are employed on both a FEM assembly and experimental-analytical assembly of the Brake-Reuss Beam. Section 16.5 concludes the paper and discusses some future work in this research area.

16.2 Nonlinear Modal Substructuring Using the Transmission Simulator Method

This section begins with a discussion on traditional linear dynamic substructuring, then the nonlinear forces are implemented into the problem as described later. Traditional substructuring is explained well in [13] and [5], but an overview is provided here for convenience. For a general linear system, each substructure can be written as

$$\mathbf{M}_C \ddot{\mathbf{x}}_C + \mathbf{C}_C \dot{\mathbf{x}}_C + \mathbf{K}_C \mathbf{x}_C = \mathbf{F}_C \tag{16.1}$$

where, $\mathbf{M}_C$, $\mathbf{C}_C$, and $\mathbf{K}_C$ are the mass, damping and stiffness matrices of substructure C. This work implements modal substructuring so this equation of motion is now cast into modal space by using the modal transformation where the physical displacements, $\mathbf{x}_C$, on substructure C are related to the mode shapes and modal coordinates, $\mathbf{q}_C$, of the substructure. This transformation is completed by using the linear mode shape matrix, $\boldsymbol{\phi}_C$.

$$\mathbf{x}_C = \boldsymbol{\phi}_C \mathbf{q}_C \tag{16.2}$$

After making this substitution and premultiplying by the transposed mode shape matrix the equations of motion for the substructure leads to the modal equations of motion presented in Eq. (16.3).

$$\mathbf{I}_C \ddot{\mathbf{q}}_C + \left[\diagdown (2\zeta_C \omega_{n,C}) \diagdown \right] \dot{\mathbf{q}}_C + \left[\diagdown (\omega_{n,C}^2) \diagdown \right] \mathbf{q}_C = \boldsymbol{\phi}_C{}^T \mathbf{F}_C \tag{16.3}$$

The transmission simulator method begins by writing the modal equations of motion for each substructure in block diagonal form as shown in Eq. (16.4). Note that as shown, substructure C and B are positive and substructure A is negative

in the block diagonal; this is the common transmission simulator scenario where one is adding two substructures together and removing the effects of the transmission simulator from the system.

$$
\begin{bmatrix} \mathbf{I}_C & 0 & 0 \\ 0 & \mathbf{I}_B & 0 \\ 0 & 0 & -\mathbf{I}_A \end{bmatrix} \begin{Bmatrix} \ddot{\mathbf{q}}_C \\ \ddot{\mathbf{q}}_B \\ \ddot{\mathbf{q}}_A \end{Bmatrix} + \begin{bmatrix} \diagdown(2\zeta_C\omega_{n,C})\diagdown & 0 & 0 \\ 0 & \diagdown(2\zeta_B\omega_{n,B})\diagdown & 0 \\ 0 & 0 & \diagdown(-2\zeta_A\omega_{n,A})\diagdown \end{bmatrix} \begin{Bmatrix} \dot{\mathbf{q}}_C \\ \dot{\mathbf{q}}_B \\ \dot{\mathbf{q}}_A \end{Bmatrix}
$$
$$
+ \begin{bmatrix} \diagdown(\omega_{n,C}^2)\diagdown & 0 & 0 \\ 0 & \diagdown(\omega_{n,B}^2)\diagdown & 0 \\ 0 & 0 & \diagdown(-\omega_{n,A}^2)\diagdown \end{bmatrix} \begin{Bmatrix} \mathbf{q}_C \\ \mathbf{q}_B \\ \mathbf{q}_A \end{Bmatrix} = \begin{Bmatrix} \boldsymbol{\phi}_C{}^T\mathbf{F}_C \\ \boldsymbol{\phi}_B{}^T\mathbf{F}_B \\ \boldsymbol{\phi}_A{}^T\mathbf{F}_A \end{Bmatrix}
\tag{16.4}
$$

Note that each substructure in the equations above is uncoupled from the other components. Additionally, each mode of each substructure is uncoupled from the other modes. In order to complete dynamic substructuring we must enforce constraints between the individual substructures which can be written as follows.

$$
\mathbf{B} \begin{bmatrix} \mathbf{x}_C \\ \mathbf{x}_B \\ \mathbf{x}_A \end{bmatrix} = 0
\tag{16.5}
$$

These constraints tie physical degrees of freedom on different substructures to enforce displacement compatibility at the interface between substructures. Here, $\mathbf{B}$, is a Boolean matrix that defines this compatibility. These constraints can be cast into the modal domain as shown in Eq. (16.6).

$$
\mathbf{B} \begin{bmatrix} \boldsymbol{\phi}_C & 0 & 0 \\ 0 & \boldsymbol{\phi}_B & 0 \\ 0 & 0 & \boldsymbol{\phi}_A \end{bmatrix} \begin{bmatrix} \mathbf{q}_C \\ \mathbf{q}_B \\ \mathbf{q}_A \end{bmatrix} = 0
\tag{16.6}
$$

Then a new set of coordinates, $\boldsymbol{\eta}$, are defined that can take on any values without violating the constraints. This is accomplished by finding a transformation matrix, $\mathbf{L}$, that resides in the nullspace of $\overline{\mathbf{B}}$.

$$
\mathbf{q} = \mathbf{L}\boldsymbol{\eta}
\tag{16.7}
$$

$$
\mathbf{B} \begin{bmatrix} \boldsymbol{\phi}_C & 0 & 0 \\ 0 & \boldsymbol{\phi}_B & 0 \\ 0 & 0 & \boldsymbol{\phi}_A \end{bmatrix} \mathbf{L} \begin{bmatrix} \boldsymbol{\eta}_C \\ \boldsymbol{\eta}_B \\ \boldsymbol{\eta}_A \end{bmatrix} = \overline{\mathbf{B}}\mathbf{L} \begin{bmatrix} \boldsymbol{\eta}_C \\ \boldsymbol{\eta}_B \\ \boldsymbol{\eta}_A \end{bmatrix} = 0
\tag{16.8}
$$

$$
\mathbf{L} = null\left(\overline{\mathbf{B}}\right)
\tag{16.9}
$$

This transformation matrix can now be applied to the modal equations of motion, Eq. (16.4), to synthesize the system.

$$
\overline{\mathbf{M}}\ddot{\boldsymbol{\eta}} + \overline{\mathbf{C}}\dot{\boldsymbol{\eta}} + \overline{\mathbf{K}}\boldsymbol{\eta} = \mathbf{L}^T \begin{Bmatrix} \boldsymbol{\phi}_C{}^T\mathbf{F}_C \\ \boldsymbol{\phi}_B{}^T\mathbf{F}_B \\ \boldsymbol{\phi}_A{}^T\mathbf{F}_A \end{Bmatrix}
\tag{16.10}
$$

In Part I, the authors explored representing a single substructure as a combination of linear and weakly nonlinear modes. Thus the equations of motion for such a substructure could be written as:

$$
\mathbf{I}_C\ddot{\mathbf{q}}_C + \left[\diagdown(2\zeta_C\omega_{n,C})\diagdown\right]\dot{\mathbf{q}}_C + \left[\diagdown(\omega_{n,C}^2)\diagdown\right]\mathbf{q}_C + \{\mathbf{F}_{NL,C}\} = \boldsymbol{\phi}_C{}^T\mathbf{F}_C
$$
$$
\{\mathbf{F}_{NL,C}\}^T = [F_{NL,1,C}(q_{1,C}) \quad F_{NL,2,C}(q_{2,C}) \quad \cdots]^T
\tag{16.11}
$$

where, $F_{NL,n,C}(q_{n,C})$, is an force describing the joint nonlinearity of the nth mode based on the state of that modes amplitude. This could take many forms but in this work this force is represented by a 4-parameter modal Iwan model. Each mode of the subcomponent is still treated as uncoupled; thus the authors assume the mode shapes do not change with increased force level

and that the modes of the system remain uncoupled. This limits this methodology to substructuring with weakly nonlinear substructures. As first proposed in [11], these joint forcing terms can be added to the synthesized equations through the same transformation matrix.

$$\overline{\mathbf{M}}\ddot{\boldsymbol{\eta}} + \overline{\mathbf{C}}\dot{\boldsymbol{\eta}} + \overline{\mathbf{K}}\boldsymbol{\eta} + \mathbf{L}^T \begin{Bmatrix} \mathbf{F}_{NL,C} \\ \mathbf{F}_{NL,B} \\ \mathbf{F}_{NL,A} \end{Bmatrix} = \mathbf{L}^T \begin{Bmatrix} \boldsymbol{\phi}_C{}^T\mathbf{F}_C \\ \boldsymbol{\phi}_B{}^T\mathbf{F}_B \\ \boldsymbol{\phi}_A{}^T\mathbf{F}_A \end{Bmatrix} \qquad (16.12)$$

Also note that the nonlinear forces themselves depend on the substructure DOF $\mathbf{q}_C$, $\mathbf{q}_B$ and$\mathbf{q}_A$, which are related to $\boldsymbol{\eta}$ via eq. (16.7). In Part I [1], each modal DOF remained uncoupled and hence the response of the substructure could be found by integrating each SDOF modal equation of motion independent of the others. However, when assembling the substructures these nonlinear forces are spread to all DOF via $\mathbf{L}^T$ and thus the modal DOF are no longer uncoupled in the assembled system. In [11] the authors detail specifically how to implement these with the use of a 4-parameter Iwan modal model in a Newmark integration algorithm, so that is not repeated here. In the next section, the authors define each substructure studied in this work, the Brake-Reuss Beam.

16.3 Substructure Identification

With dynamic substructuring theory in place, this section will discuss the individual substructures of interest for this study. The system of interest for this study is the Brake-Reuss Beam which is a pair of metallic half-beams bolted at the center with a lap joint. Figure 16.1 shows the Brake-Reuss Beam in an experimental set-up.

Figure 16.2 shows the three substructures and the built-up, modified structure. Substructure C is the standard Brake-Reuss Beam that is represented by: (1) an experimental model, detailed in [1], (2) a FEM model discussed in Sect. 16.3.2 of this work. Substructure A will be the transmission simulator for these predictions and is simply the right half of the Brake-Reuss Beam system. This substructure is modeled using a finite element model, detailed in Sect. 16.3.3. Substructure B is a design modification, a half beam with a mass attached to the end. Finally, the assembly of interest is the modified Brake-Reuss Beam represented by substructure D.

The goal is to predict the dynamics of a modified Brake-Reuss Beam (substructure D) in which the right beam (substructure A) is replaced with a modified structure (substructure B). This simulates an industrial application where a design modification is made to one part of the assembly such that its dynamics are changed considerably. This task was completed following two parallel paths where substructure C is embodied using two different methods. The first path
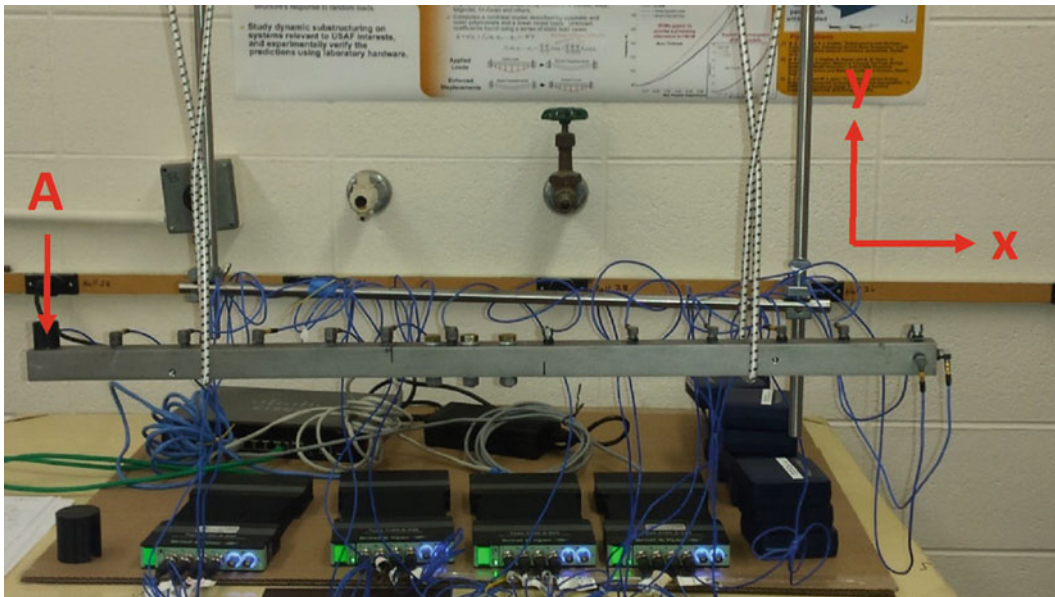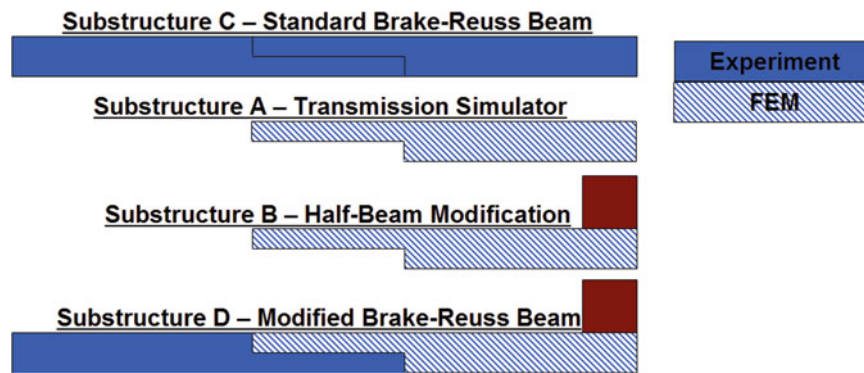

Fig. 16.1 Brake-Reuss Beam experimental set-up

Fig. 16.2 Substructure overview

Table 16.1 Substructure designation

	FEM substructuring	Experimental-analytical substructuring
Substructure C:Standard BRB	FEM	Experiment
Substructure A:Transmission Simulator	FEM	FEM
Substructure B:Half-Beam Modification	FEM	FEM
Substructure D: Comparison for Prediction	Full Simulation	Truth Test

Table 16.2 System C experimental parameters [1]

Modal index	Natural frequency [Hz]	Damping ratio	Linear or nonlinear	F_s	K_T	β	χ
1	172.70	0.00095	Nonlinear	137.7	484,680	0.2616	−0.04995
2	583.26	0.00143	Nonlinear	152.1	2,668,200	0.2969	−0.4164
3	1180.10	0.00376	Linear	–	–	–	–
4	1645.40	0.00814	Linear	–	–	–	–

utilized a FEM of the substructure where three discrete nonlinear Iwan joints were included between the two substructures to represent the bolts. The four parameters describing each Iwan joint were updated to match experimental response measurements. The second is a combined experimental-analytical substructure where the nonlinear modal model from Part I [1] is employed. Both paths will attempt to utilize their respective substructure models in order to predict the response of a modified Brake-Reuss Beam, substructure D.

Table 16.1 shows the source of each substructure for the two substructuring paths. When completing substructuring with the FEM model, the response prediction will be compared to a response generated from a full FEM simulation. For the experimental-analytical substructuring, the predicted response will be compared to the measured response from a truth test. The following subsections will provide the identification for each substructure used in these predictions.

16.3.1   Experimental Substructure C: Standard Brake-Reuss Beam

Substructure C is the standard Brake-Reuss Beam which was studied in detail in Part I [1], but a brief summary is contained here. The Brake-Reuss Beam was instrumented with 15 low sensitivity (5 mV/g) accelerometers as shown in Fig. 16.1. A low level modal test was used in order to determine the linear parameters of the system as listed in Table 16.2. High level impact testing was used to fit nonlinear modal models for the first and second elastic modes of the substructure. As detailed in Part I, only the first two elastic modes of the system were found to behave nonlinearly and thus were modeled with 4-parameter Iwan modal models (i.e. an Iwan joint in parallel with the modal stiffness and damping, as shown in Fig. 16.3). The experimentally extracted Iwan parameters are repeated Table 16.2 for convenience.

Each mode of the system is uncoupled from all others, so each can be represented as a single degree of freedom oscillator as shown in Fig. 16.3. Fj is an instantaneous force in the Iwan Joint which can be found as described by Segalman in [14].

Fig. 16.3 Schematic of SDOF
model used for each modal
degree of freedom
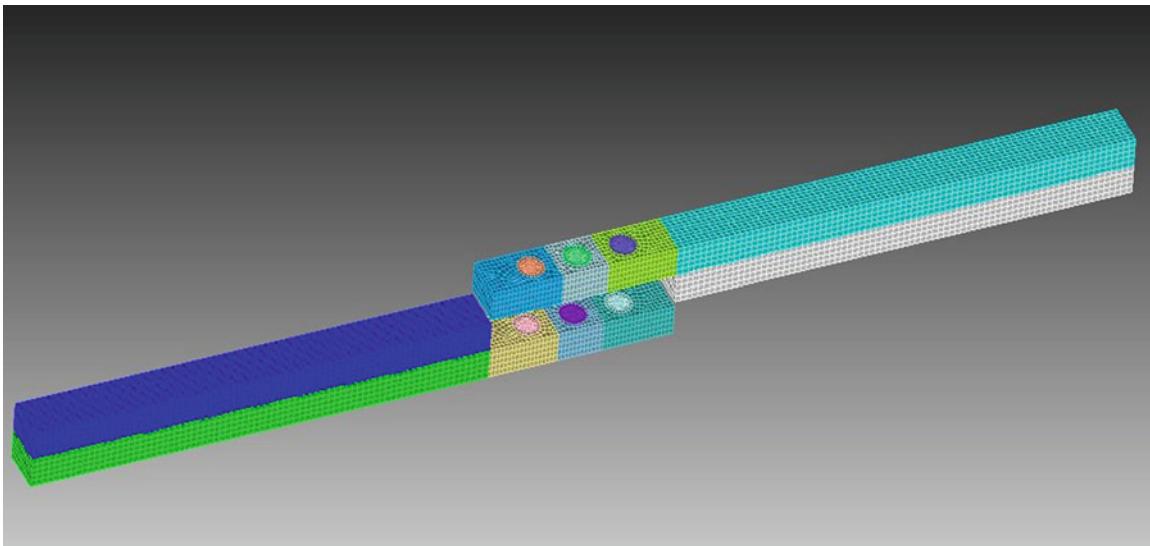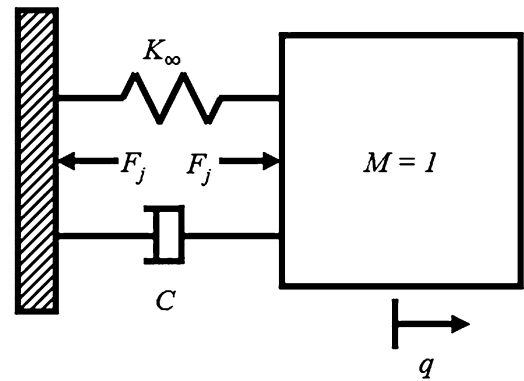
**Fig. 16.4** Finite element mesh for Brake-Reuss Beam substructure C

These Iwan parameters were obtained by fitting amplitude dependent stiffness and damping curves from several high level impact tests. The same high level testing data was used to calibrate the next substructure, the numerical FEM model of substructure C.

16.3.2 Numerical Substructure C: Standard Brake-Reuss Beam

A finite element model of substructure C was also developed. This allowed the authors to determine how accurate modal substructuring could be when experimental error is removed from the predictions. A solid mesh was made of the Brake-Reuss Beam system using 22,000 elements, as shown in Fig. 16.4. The half beams of the system were modeled and meshed separately at this stage.

In order to connect the two half beams, the joint surfaces were connected to a virtual node using averaging rigid bar elements (i.e. RBE3 in Nastran). These spider-like connections are shown in Fig. 16.5. At these virtual nodes, a set of linear springs and an Iwan joint in the axial direction was added to the system in order to couple the two beams.

A Craig-Bampton (CB) model was extracted from the FEM program. This model was derived from the model used by Gross, Lacayo, et al. in [15]. The CB model contained 30 fixed interface modes and the three virtual nodes at interface locations with 6 degrees of freedom each. After the CB model was extracted, linear springs were added between the two beams except in the axial direction. At each of the three virtual nodes, the DOFs in the axial direction were instead coupled using a 4-parameter Iwan model. The parameters of these discrete Iwan elements will later be updated to match experimental measurements from the assembled Brake-Reuss Beam. Note that, although one could connect each pair of the nodes at the joint surface with a nonlinear element, this would be contrary to the idea of using an Iwan element, which internally contains a parallel array of slider elements that are tuned to represent the stiffness and damping of an entire joint.
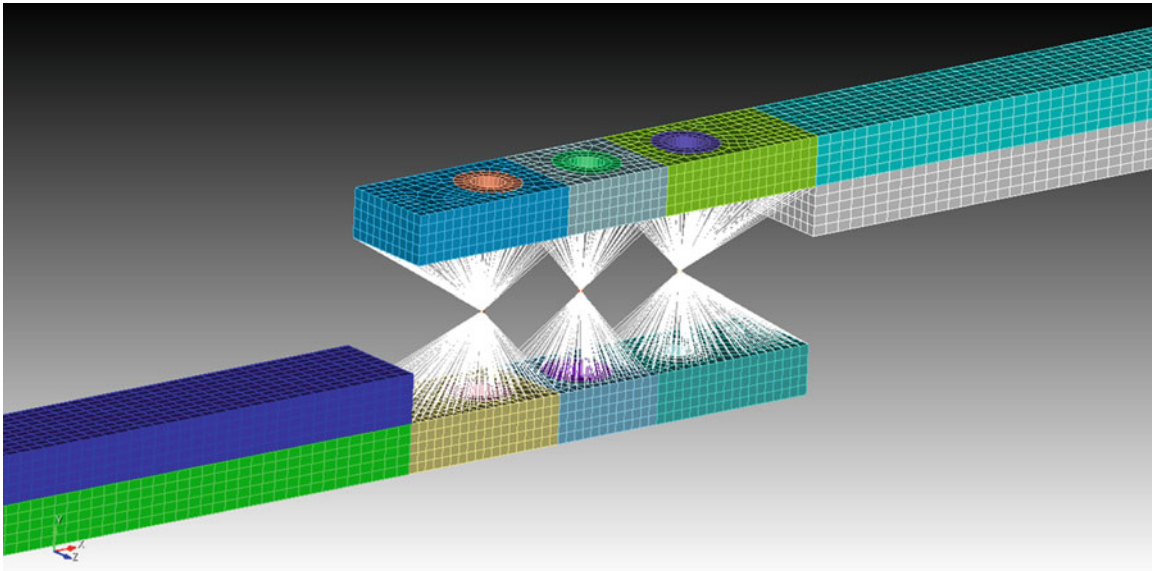
Fig. 16.5 Finite element joint surface spider-patch

Table 16.3 System C experimental parameters

Modal index	Experimental natural frequency [Hz]	FEM natural frequency [Hz]	Frequency % Error	MAC
1	172.70	172.09	−0.35%	0.9994
2	583.26	578.53	−0.81%	0.9975
3	1180.10	1195.20	1.28%	0.9962
4	1645.40	1616.10	−1.78%	0.9897

The two beams were assembled as described above with the Iwan elements represented by springs with the low amplitude stiffness, $\mathbf{K}_0$, and the eigen value problem was solved to obtain the natural frequencies and mode shapes, see Table 16.3. Also included in Table 16.3 are the MAC values between the FEM and experimental mode shapes. The model matches very well with frequency errors under 2% and MAC values above .98 for all the modes of interest. Figure 16.6 shows a comparison for the first two elastic modes between the FEM model and the experimentally extracted mode shapes.

In [16] Allen, Lacayo and Brake presented an adaptation of the quasi-static algorithm of [17] that statically loads a structure in the shape of a mode to excite one mode of interest. The study in [16] showed that this algorithm accurately estimates the behavior of each mode of a typical structure in a small fraction of the time required to perform a dynamic simulation. The authors made use of this algorithm to calibrate the parameters of the three discrete Iwan joints of the assembled Craig-Bampton model by matching the amplitude dependent natural frequency and damping curves for the first two elastic modes extracted from the FEM with the corresponding curves extracted from the measured impact data as outlined in Part I [1]. Figure 16.7 shows the results of this quasi-static simulation for the first elastic mode of substructure C.

After manual trial and error, the Iwan parameters for the three discrete joints were found and are given in Table 16.4.

In order to simulate experimental modal substructuring for this model, simulated experimental measurements were needed from which a SDOF nonlinear model could be estimated for each mode. For convenience, the quasi-static solutions (such as that shown in Fig. 16.7 for Mode 1) were fit to a 4-parameter <u>modal</u> Iwan model for each mode. Recall that in Part I [1], only the first two elastic modes in the experimental system were observed to exhibit measurable nonlinearity. However, when a structure contains even one nonlinear element, all bending modes can end up exhibiting some traces of nonlinearity. Such was the case here, so a nonlinear modal model was fit to each of the four bending modes. Table 16.5 contains the parameters for the four elastic modes of the numerical version of substructure C. These four nonlinear elastic modes in combination with 2 rigid modes comprise the numerical model of the system.

It is interesting to consider why the experimental model did not show similar evidence of nonlinearity in the 3rd and 4th bending modes. One possible explanation is that perhaps the force level applied during the experiments was not adequate to excite the nonlinearity in the 3rd and 4th bending modes. Conversely, it could be that the discrete Iwan elements used here are not a perfect model for the actual beam. This numerical substructure is only used to prove out nonlinear substructuring techniques. As such, it was necessary to tune the Iwan parameters to get realistic amplitude dependant results, but not perfectly match the experimental results.
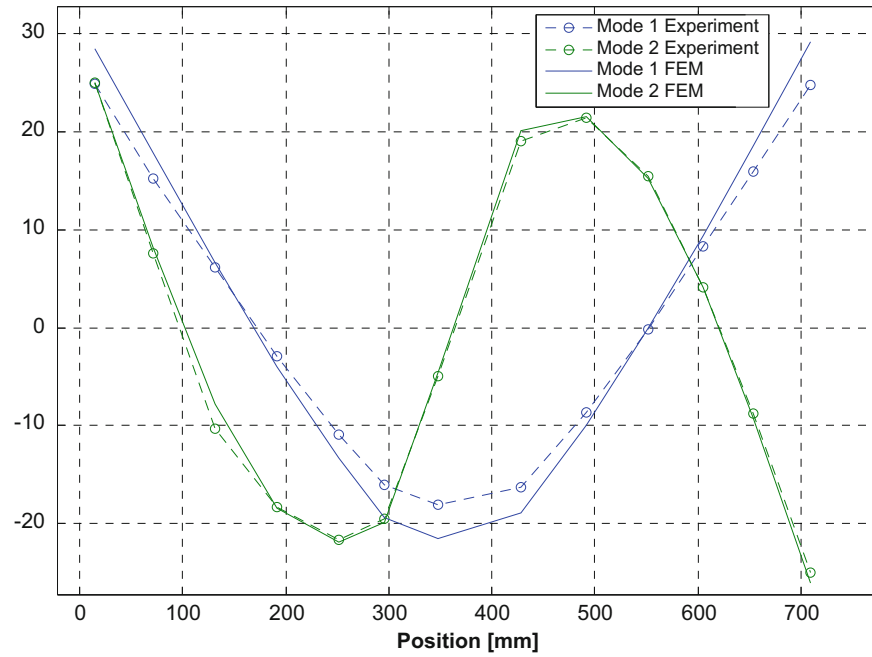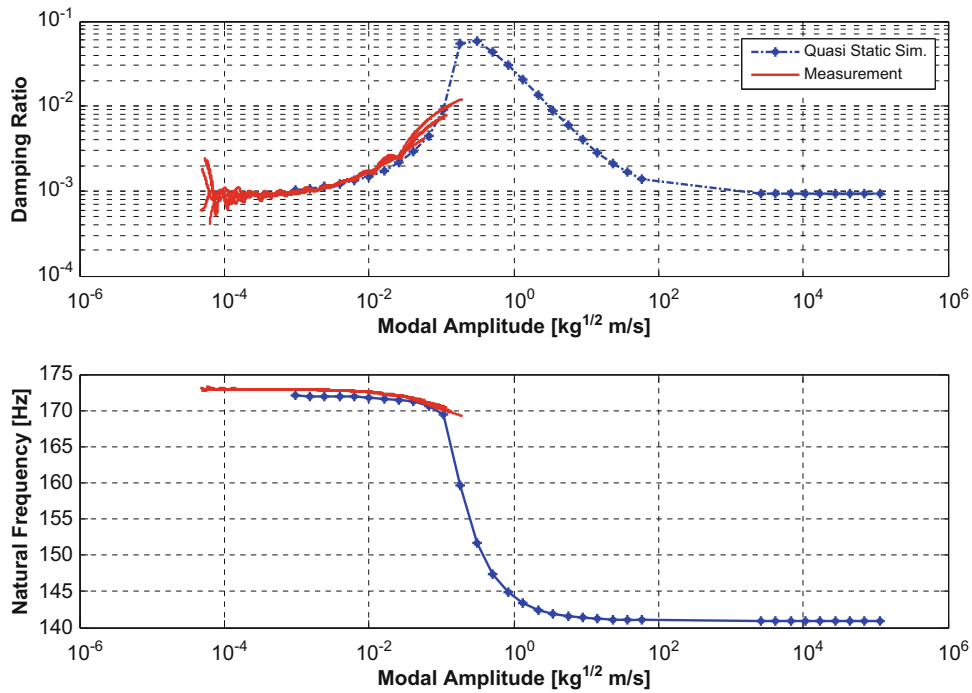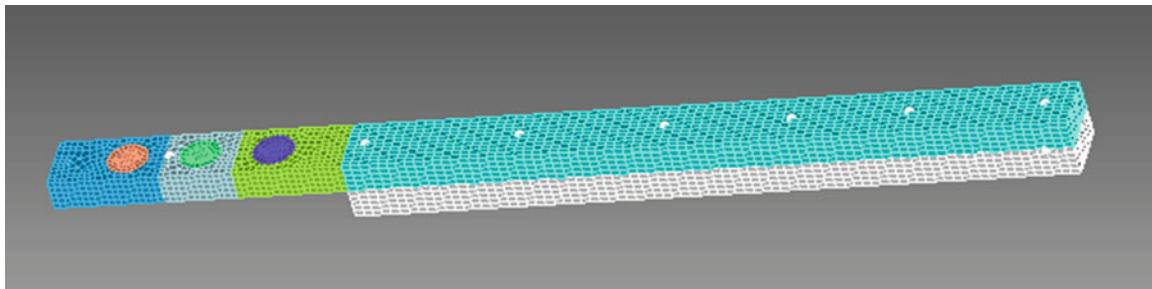
Fig. 16.6 FEM and experimental mode shapes

Fig. 16.7 Quasi-Static results for amplitude dependent damping and frequency

Table 16.4 System C Discrete
Iwan parameters

Joint #	F_s	K_T	β	χ
1	25	2,200,000	−.3500	0.0500
2	10	1,840,000	−.9000	0.0500
3	25	2,200,000	−.3500	0.0500

Table 16.5   Substructure C numerical FEM parameters

Modal index	Natural frequency [Hz]	Damping ratio	Linear or nonlinear	F_s	K_T	β	χ
1	171.26	0.0010	Nonlinear	30.50	385,920	4.25	–0.13546
2	578.28	0.0010	Nonlinear	250.01	927,330	1.25	–0.72461
3	1195.20	0.0010	Nonlinear	3297.4	9,322,300	0.25	–0.25792
4	1616.10	0.0010	Nonlinear	39,000	77,249,000	0.25	–0.69576

Fig. 16.8   FEM and experimental mode shapes

Table 16.6   Modified system frequency shifts

Modal index	Substructure A [Hz]	Substructure B [Hz]	% Change	Substructure C (Linear FEM) [Hz]	Substructure D (Linear FEM) [Hz]	% Change
1	623.37	539.12	–13.52%	171.26	151.83	–11.35%
2	1438.72	1134.38	–21.15%	578.28	578.28	–10.85%
3	3033.48	2295.71	–24.32%	1195.20	1195.20	–15.71%
4	4562.07	3930.13	–13.85%	1616.10	1616.10	–6.04%

### 16.3.3   Substructure A and B: Standard and Half-Beam Modification

The transmission simulator and half-beam modification were modeled in a finite element program. The first is a simple half-beam from the Brake-Reuss Beam system. This substructure will act as the transmission simulator, so modal constraints will be used to couple the negative copy of this substructure to the measured transmission simulator at all measurement points. Thus its effects will be removed from the assembly during the substructuring process. Figure 16.8 shows the finite element mesh for the transmission simulator. The nodes shown in white depicted on Fig. 16.8 the are the measurement points.

Recall from Fig. 16.2 that the transmission simulator will be replaced with the half-beam modification in the assembly of interest. In order to verify that substructures A and B are sufficiently different so that the substructuring problem is not trivial, their natural frequencies were compared and the results are shown in Table 16.6. Each natural frequency shifts by at least 13% (more than 100 times the width of the peak in the FRF), so the change is judged to be adequate to provide an interesting case study. A 0.75 kg mass was attached to the end of the beam to sufficiently shift the frequencies of the first few bending modes of the system. Material damping of 0.1% was used for each mode in the standard and modified transmission simulator.

Figure 16.9 displays the FEM mesh of the half-beam modification. The added mass was connected to the beam using high stiffness springs between each pair of adjoining nodes.

16.4   Nonlinear Modal Substructuring Results

Next, the transmission simulator equations, Eqs. (16.11) and (16.12) were used to generate predictions of the modified assembly (substructure D). First, predictions were constructed using the numerical model and compared to the full FEM simulation, as detailed in Sect. 16.4.1. With the numerical model it is simple to test different scenarios such as sensor placement and the number of modes retained in each substructure. This also gives an indication of how well this method can work in the absence of experimental noise. The process was repeated using the experimental-analytical substructuring approach in Sect.16.4.2. These experimental-analytical predictions are compared directly to measured test data to assess their quality.
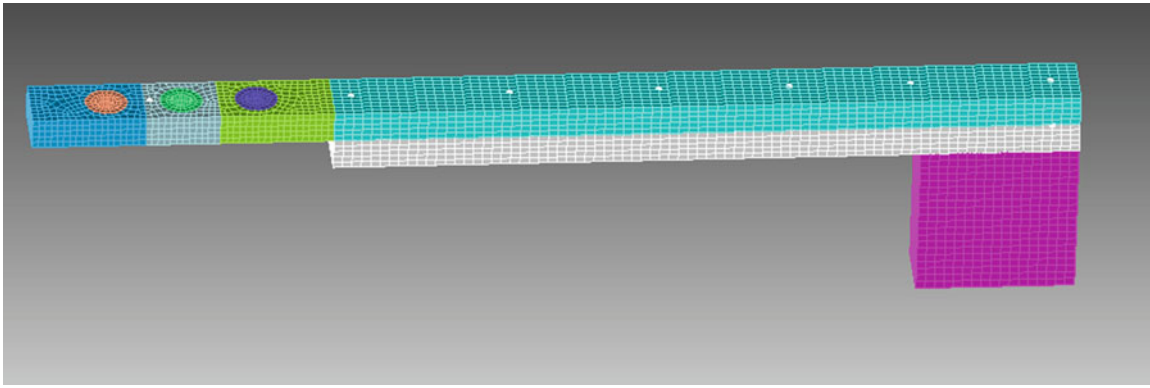
Fig. 16.9 FEM and experimental mode shapes
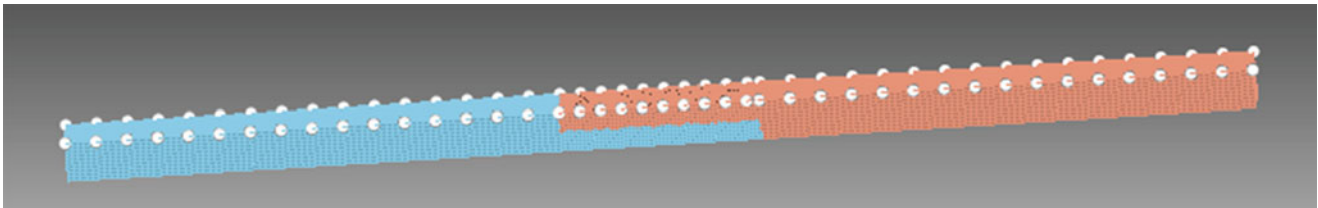
Fig. 16.10 FEM with expanded sensor selection

Table 16.7 Numerical linear substructuring predictions

Elastic mode #	Full FEM frequency [Hz]	Substr. prediction frequency [Hz]	% Error
1	151.83	148.57	–2.39%
2	515.55	515.37	–1.00%
3	1007.37	1037.12	1.72%
4	1518.52	1519.61	0.72%

16.4.1 Numerical Substructuring Results

With the numerical model of Substructure C, it was possible to use as many nodes as desired in the simulation. The authors selected a reduced set to best simulate an experiment where finite instrumentation pieces may limit sensor locations. In order to evaluate modal convergence for each substructure, this large sensor set was used. This provides high quality mode shapes even for higher order bending modes. Figure 16.10 shows an expanded set of degrees of freedom used in the numerical substructuring.

A study was completed to determine how many modes of each substructure were needed for a high-quality, linear prediction. Table 16.7 shows the linear frequencies that this substructuring model predicts for the first four elastic modes. For this case, 6 modes (2 rigid and 4 elastic) were used in each of substructures C and B; while only 4 modes (2 rigid and 2 elastic) were used for the transmission simulator. The frequencies are reasonably accurate, suggesting that modal truncation will not be too severe if at least four elastic modes can be measured.

The number of modes in each substructure was varied to understand how sensitive the results were to the particular modes used for each substructure. Table 16.8 shows several of the combinations evaluated. Here, Case #1 is case that was just discussed. A few important observations may be made. Cases #4 and #7 show that the error increases significantly if the 4th mode of A it not included. Cases #9–#11 can be compared to Case #3 and we can see that additional modes in substructure C do not improve the quality of the prediction. The configuration from Case #3 was chosen to evaluate the nonlinear substructuring. This includes 6 modes in substructure C and B, but only 4 modes in the transmission simulator, substructure A.

Now that the number of modes to be retained in each substructure have been determined, the nonlinear forces can be added to the assembled equations of motion and a Newmark integrator can be used to predict the nonlinear response to 20 N impulsive loading at the center of the modified assembly (substructure D). The response was then decomposed into the contribution of each mode using a linear modal filter. A truth FEM was constructed using the same CB model of Substructure

Table 16.8 Mode convergence study

Case	# Modes in C	# Modes in A	# Modes in B	RMS Frequency % Error
1	6	6	6	0.911%
2	6	5	6	0.930%
3	6	4	6	0.798%
4	6	3	6	5.261%
5	6	5	5	0.813%
6	6	4	4	0.749%
7	6	3	3	4.682%
8	6	2	2	5.702%
9	7	4	6	0.798%
10	8	4	6	0.798%
11	9	4	6	0.797%
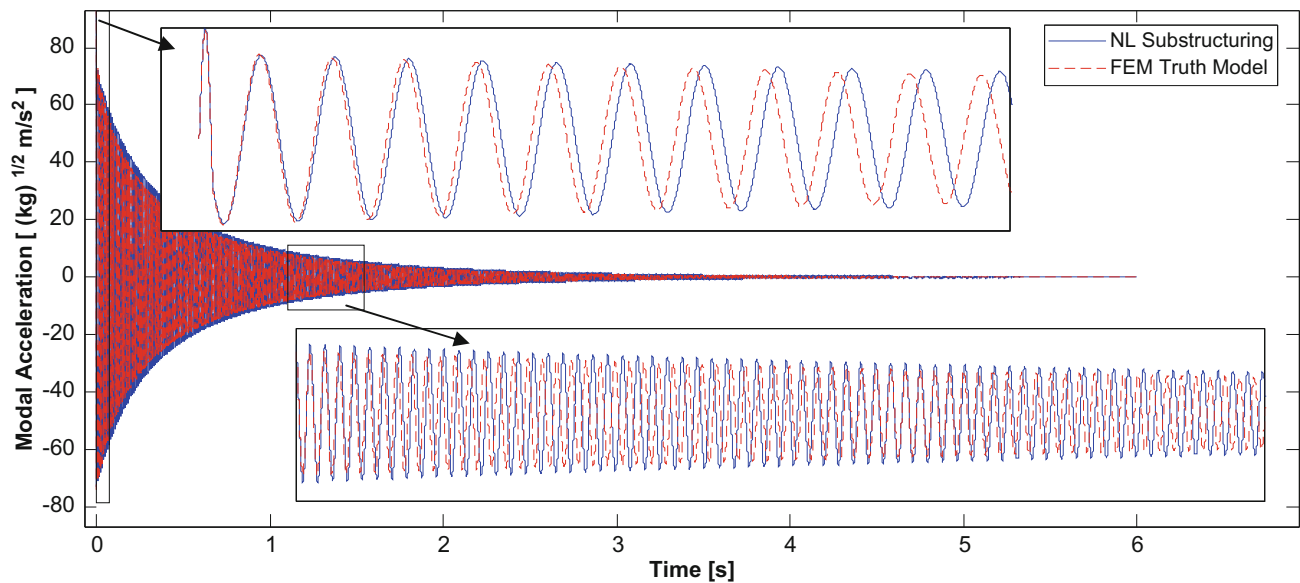
Fig. 16.11 1st Elastic mode: modal acceleration time history (Numerical Substructuring)

C with the transmission simulator, A, replaced with the half-beam modification, B. Note that the parameters of the three discrete Iwan joints were not altered when A was replaced with B as the discrete joint properties were believed to be unaffected by the modifications seen in B. The time histories for the first and second elastic modes are shown in Figs. 16.11 and 16.12. Both modes match the full truth FEM simulation remarkably well with the first elastic mode fitting slightly better than the second. The frequency for both modes is off slightly, but this is to be expected considering the frequency error present in Table 16.7.

These signals can be compared in the frequency domain as well by applying an FFT to the time history, as shown in Fig. 16.13. Here, the peaks between the nonlinear substructuring prediction and the full FEM solutions correlate well. A small nonlinear distortion is visible in both the substructuring prediction and the truth model and the only major source of error is due to a frequency shift in the linear substructuring prediction.

Additionally, the response predicted by substructuring can be compared to the full finite element simulation by way of the amplitude dependent natural frequency and damping ratio extracted from the time histories, as shown in Fig. 16.14. The frequency is normalized to the linear natural frequency to make the trends visually comparable despite the difference in the linear natural frequencies. Both the frequency and damping correlate well between the prediction and the FEM simulation for the 1st elastic mode.

The comparison was not so straightforward with the second mode. Figure 16.15 shows the amplitude dependent results for this mode. At higher amplitudes the curves have similar trends but at lower amplitudes the Hilbert algorithm apparently fails to accurately capture the frequency and damping. However, because the time signals and FFTs compared very well in Figs. 16.12 and 16.13 we suspect that this is simply an anomaly of the Hilbert algorithm.
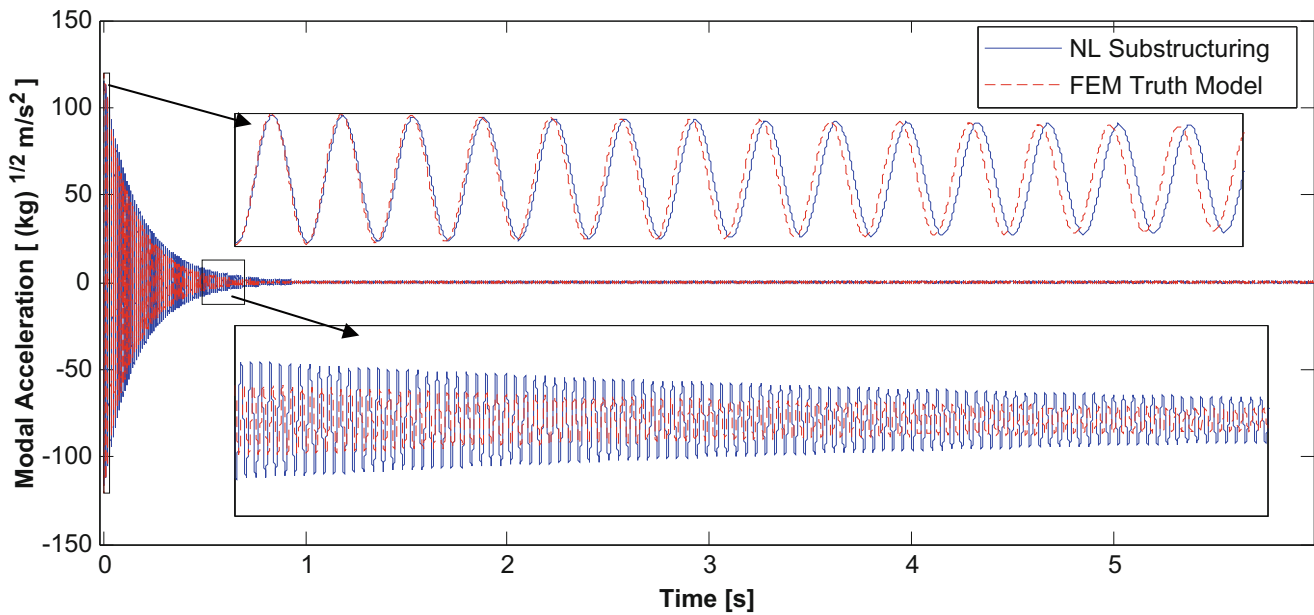
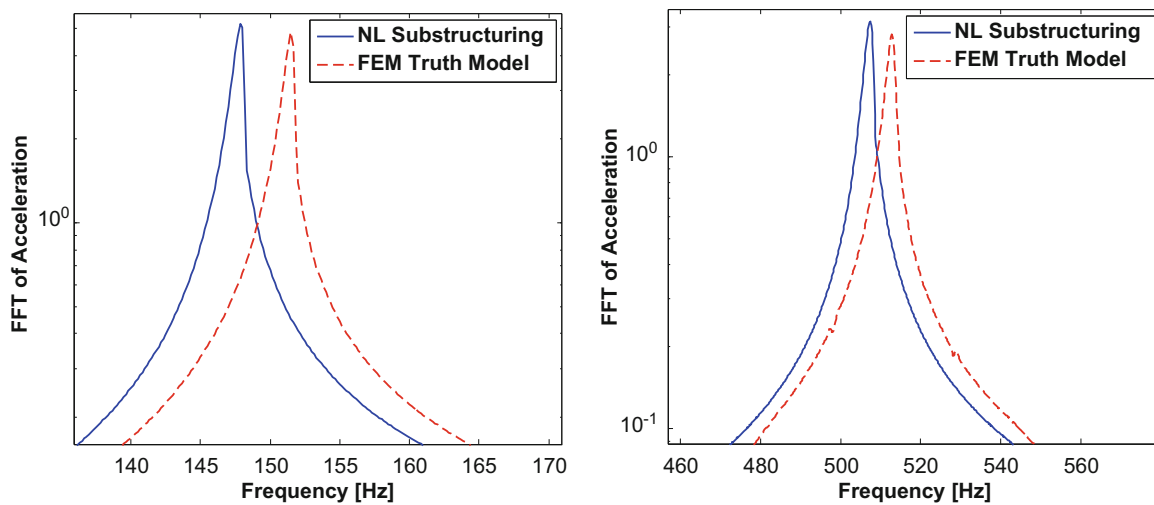**Fig. 16.12** 2nd Elastic mode: modal acceleration time history (Numerical Substructuring)

Fig. 16.13 FFT of modal acceleration for 1st (*right*) and 2nd (*left*) elastic modes

Overall, the nonlinear numerical substructuring prediction seemed to be a good estimate of the FEM solution. The simulation model suggests that nonlinear modal substructuring will work given an appropriate number of modes.

16.4.2 *Experimental-Analytical Substructuring Results*

To begin the experimental-analytical substructuring process the linear substructuring prediction is first completed. To do this the nonlinear forces for each mode were replaced with linear springs corresponding to the completely stuck state ($\mathbf{K}_0$). For this example, 6 modes each were retained for substructures C and B, with only 4 modes in substructure A. The predictions of the modal parameters of the first four elastic modes are compared with those from the truth test in Table 16.9. This captures how well a <u>linear</u> substructuring prediction did compared to a <u>linear</u> (low level) truth test!

In Table 16.9 the frequency errors are small. It is important to remember how much a mode changes due to the nonlinearity in the system. It is common to see frequency shifts around the 1–5% range due to high level impact testing. Thus, it may be
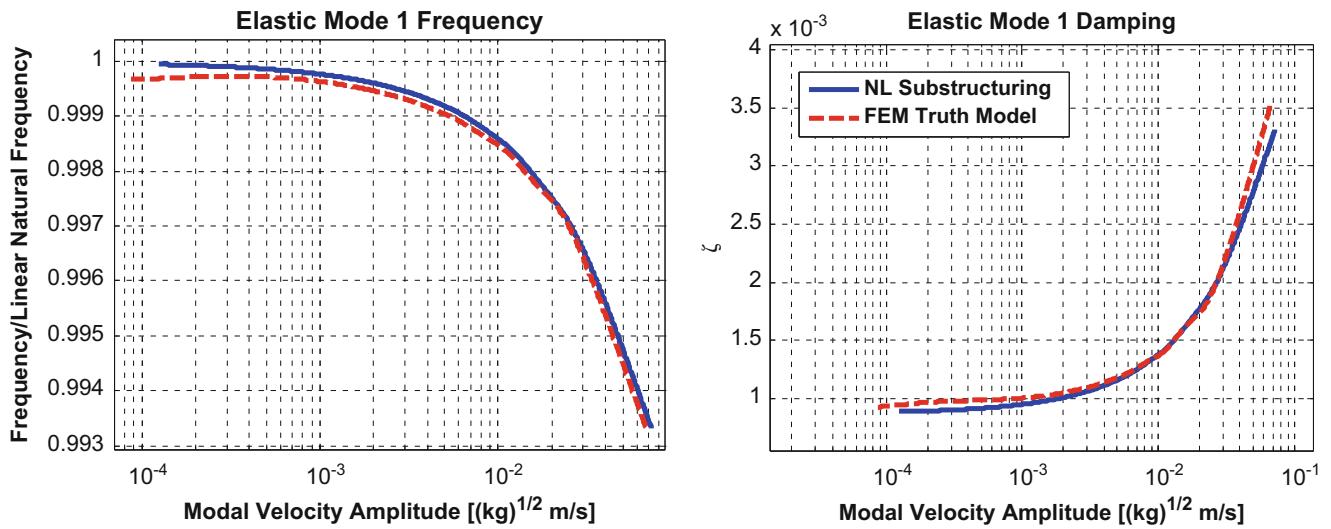
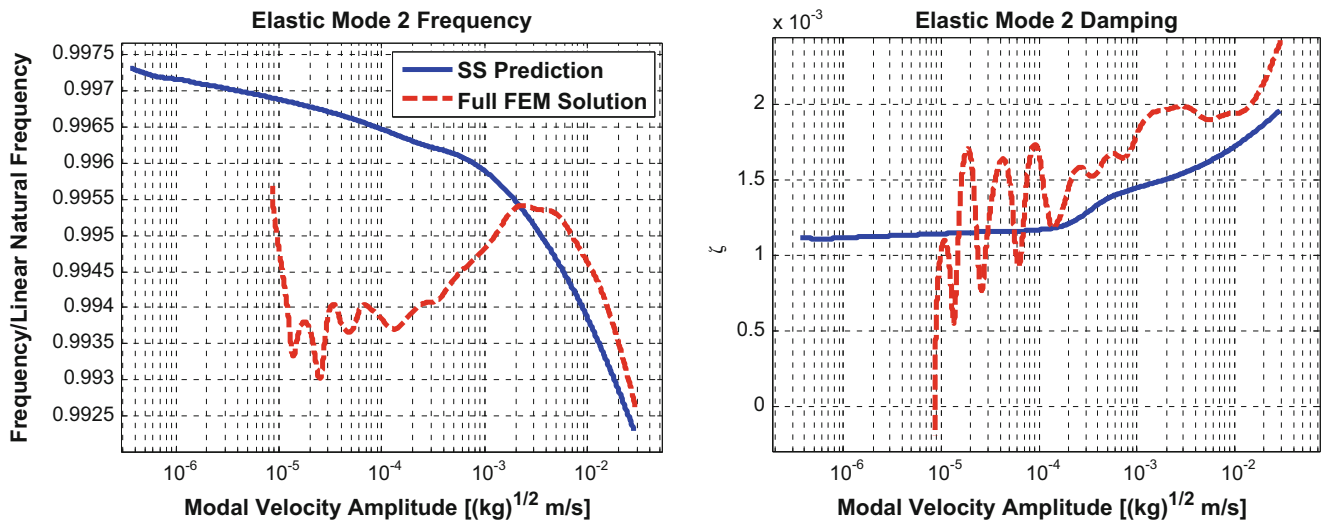**Fig. 16.14** Amplitude dependent frequency and damping - 1st elastic mode

Fig. 16.15 Amplitude dependent frequency and damping - 2nd elastic mode

Table 16.9 Experimental-analytical <u>linear</u> substructuring predictions

Mode #	Linear truth test frequency [Hz]	Substr. prediction frequency [Hz]	% Error	Truth ζ	Substr. prediction ζ	% Error	MAC
1	150.80	153.13	1.54%	0.00194	0.00186	–3.98%	0.999
2	513.69	515.69	0.39%	0.00174	0.00141	–18.84%	0.991
3	994.68	983.23	–1.15%	0.00321	0.00339	5.72%	0.980
4	1507.53	1515.92	0.56%	0.00458	0.00668	45.99%	0.962

difficult to evaluate the effectiveness of the nonlinear modal models to capture the nonlinear stiffness. In contrast, damping errors in Table 16.9 are larger. Damping often changes by larger factors often being amplified by 200–400%. Although we have significant error in predicting damping, the error is small relative to how much the damping changes with amplitude. This change with amplitude is what we hope to represent with our nonlinear model.

The MAC values show that the modes correlate between the truth test and the substructured predictions very well. Figure 16.16 shows the modes shapes of the first two elastic modes. For each of these modes the prediction matches the experiment very well. Here, predicted modes are shown using the stuck ($\mathbf{K}_0$) case for the linear substructure and also the case when the
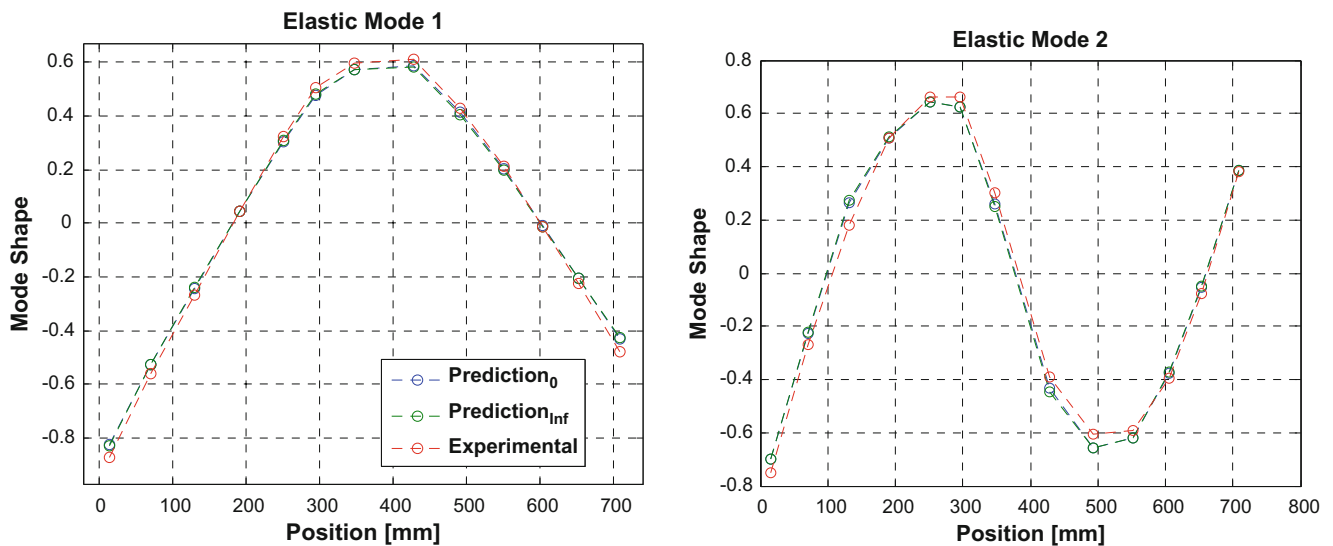
Fig. 16.16 Predicted mode shapes

joints are replace with springs corresponding to the fully slipped ($\mathbf{K}_\infty$) case. The mode shapes do not change in a measurable way between these two cases, revealing that the modes are apparently preserved at higher forcing levels even though the modal stiffness and damping have changed!

Now that the linear substructuring prediction quality is understood, the nonlinear forces can be added to the assembled equations of motion and a Newmark integrator can be used to predict the nonlinear response to 500 N impulsive loading at the end of the beam. Figure 16.17 compares the results of this response simulation in the frequency domain. The "Linear Measured" curve is a driving point FRF measurement for a low level test case, aiming to capture a linear driving point response. Another curve has been added to this plot which is the drive point frequency response function due to a 500 N impulsive load on the end of the beam. The difference between these two curves (green and red) are what the nonlinear modal models desire to replicate. The "Linear Substructuring Prediction" black curve is a curve fit of the modal parameters found from the linear substructuring process. Therefore, the shift between the green and black curves illustrates the error in the linear substructuring predictions.

When the nonlinear forces were added to the substructuring by using a Newmark integrator to solve Eq. (16.12) the impact of the nonlinear modal models became clear. The blue curve represents this nonlinear substructuring prediction. As mentioned previously, comparing the red and green curves highlights the change in the response due to the nonlinearity in the mode. Likewise comparing the blue and black curves highlights a similar change exists in the substructured predictions. The frequency of the nonlinear resonant peak is still off by the 1.17% frequency error from Table 16.9 but the lean of the peak and damping levels are much closer to the measured result. This is remarkable as the nonlinear models were fit at a substructure level, yet the predictions at the assembled level seem to represent the measured nonlinearity accurately!

In Fig. 16.18 the time history of the modal acceleration for the first mode of the modified Brake-Reuss Beam (substructure D) is shown. Here one can observe that early in time the linear model, the nonlinear prediction and the measured data match fairly well. However, the linear model has too little damping and so it overestimates the amplitude of the signal by a factor of approximately 5 late in the time history. In contrast, the nonlinear prediction tracks the measured, modally filtered result very well.

Figure 16.19 shows these amplitude dependent properties of the first and second bending modes obtained using the Hilbert Transform as shown in [1]. In the damping curve for the first bending mode, at an amplitude of about (0.040 $kg^{1/2}$ m/s), the response from the substructuring prediction starts to diverge and under predict the damping when compared to the measured data. This could be due to an error in how the modal Iwan Models were fit for substructure C, but similar effects at high amplitudes have been observed in works by Lacayo et al. [18] so it was suspected this may be due to important modal coupling at high amplitude levels.
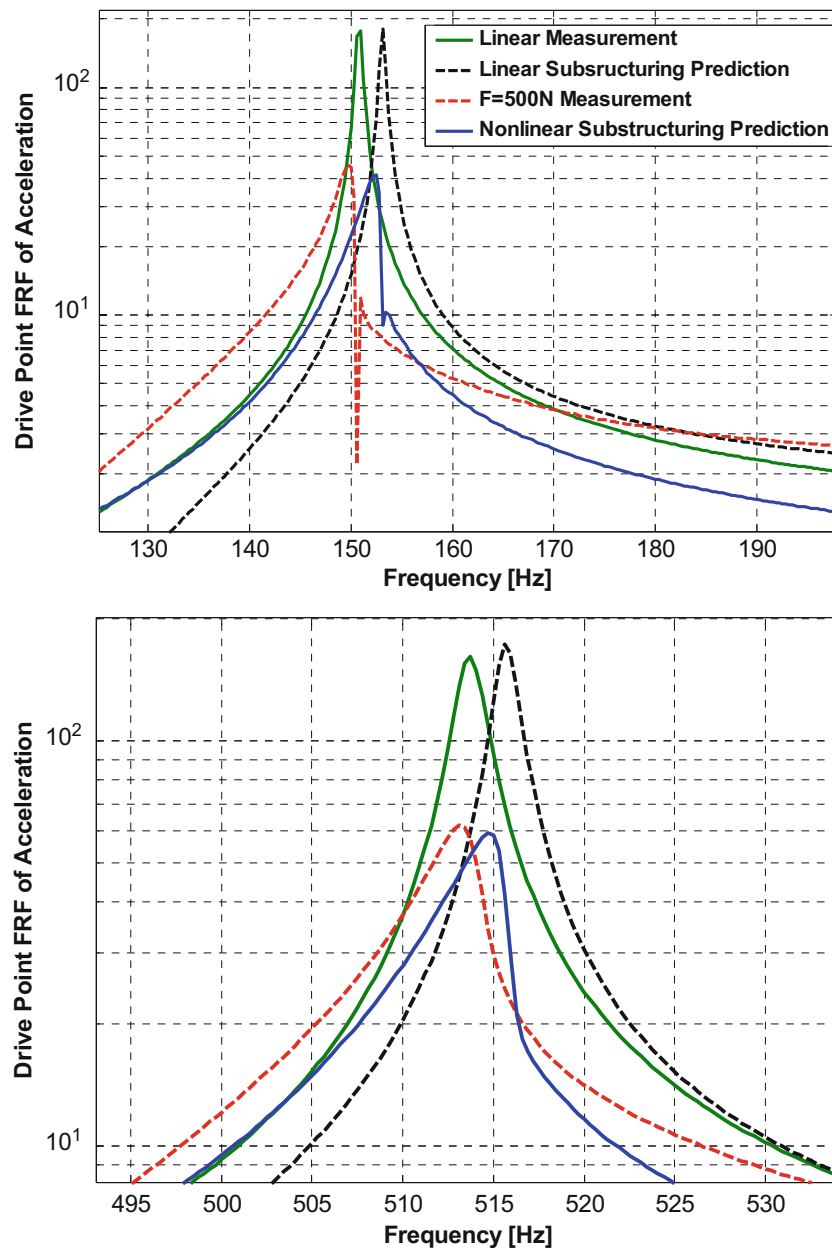
Fig. 16.17 Frequency domain comparison: 1st Bending (*Top*) 2nd Bending (*Bottom*)

Recall from Part I that these models were fit in a least squares sense over several different impulsive loading cases. These loading cases in general were much smaller than the 500 Newtons being tested here. Higher level hits on a substructure level may have led to a model that appropriately fits the damping in a larger range. Another possibility is that the system is reaching the onset of macroslip, and previous studies have shown that nonlinear modal models are accurate only until the onset of macroslip [18]. Therefore if one of the joints is in macro slip, this could lead to erroneous results. Note, for mode 2 the damping seems to match the measured value in the micoslip region and that the offset in the low level damping region is mainly due to inaccuracy in the prediction of the linear damping ratio for this mode.

Using the linear mode shape matrix, the prediction of the modal coordinate response can be transformed into the physical domain and compared to the measured response. Figure 16.20 shows the drive point acceleration obtained using linear substructuring, the nonlinear substructuring prediction and the measured result. As was the case with the individual modes, all three models correlate well very early in time, but the linear model contains insufficient damping and becomes inaccurate later in time. The nonlinear prediction has the correct amplitude over all of the time window.
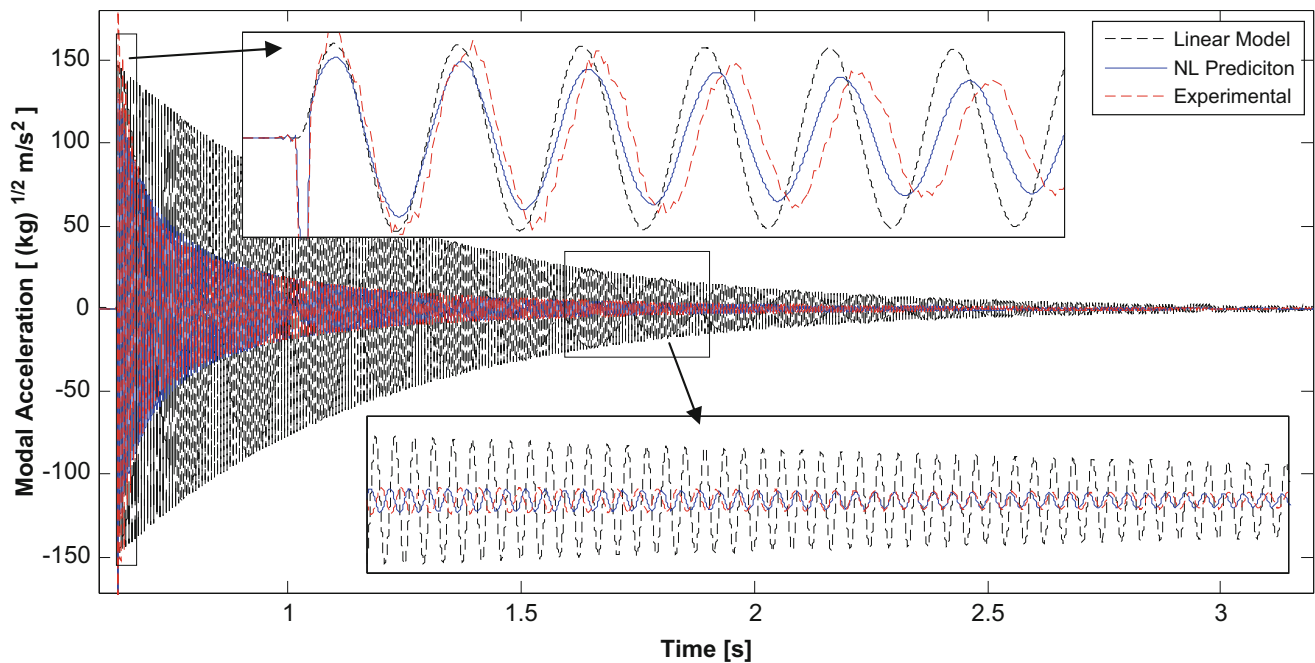
Fig. 16.18 1st Elastic mode: modal acceleration time history

Figure 16.21 removes the linear model from the plot to provide a clearer comparison between the measurement and the nonlinear substructuring prediction. Early in time the nonlinear prediction does a great job capturing the motion of the measured system. Later in time, the shape and amplitude of the curve matches very well with a slight phase shift, due to the frequency error present in the linear substructuring predictions.

16.5   Conclusions

This work utilized uncoupled nonlinear modal models to represent a substructure in a dynamic substructuring problem. These individual components were coupled using the transmission simulator method in order to generate a nonlinear model for the assembly. It is interesting to note that, even though each mode in the original substructure is modeled by an uncoupled, nonlinear single-degree-of-freedom system, the substructuring process spreads the nonlinearity into every mode of the assembled system. As a result, a Newmark integration routine was used to simulate its response to various impulsive loads and thus to compare the amplitude dependent frequency and damping predicted by the model with that measured on a truth model. Each mode of the simulation model and the truth model again behaved as a nonlinear (uncoupled) single-degree-of-freedom system.

Experimental-analytical substructuring predictions were very promising. Linear frequency errors were low (less than 2%) but damping errors were larger (under 50%). The nonlinearity due to the bolted joint caused the damping to change by factors of 6–8; therefore, even though there were relatively large errors in the linear damping ratio predicted by substructuring the effects of the damping nonlinearity were still captured with reasonable accuracy. The nonlinear substructuring results were quite favorable and showed that the substructuring process is quite effective for this system, whose nonlinearity is dominated by micro-slip. The accuracy of the substructured prediction appears to be tied to the accuracy of the modal model used to describe the nonlinear behavior of the structure subcomponents. At high enough amplitudes the authors suspect a significant amount of modal coupling begins to occur, which reveals the main limitation of this methodology.
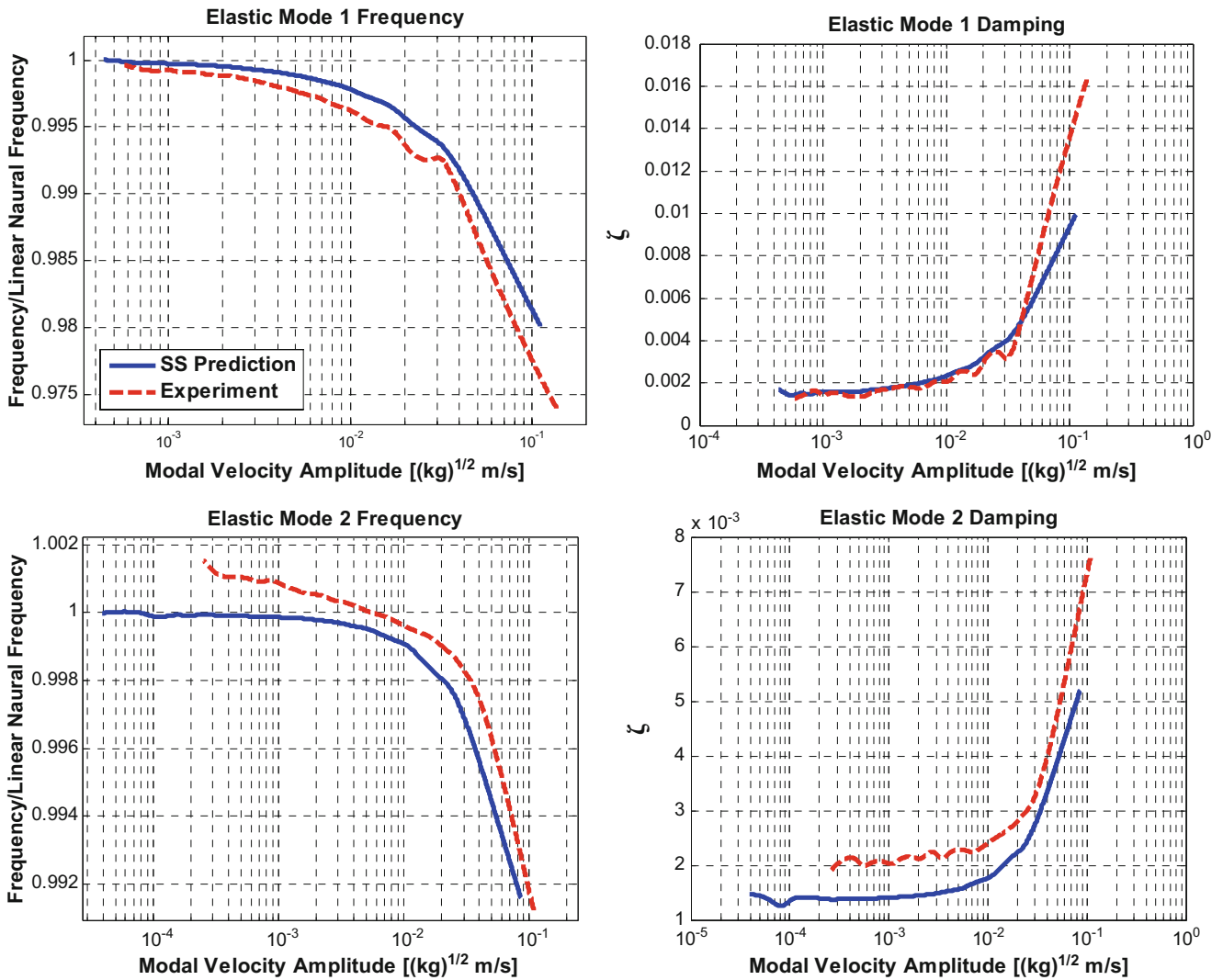
Fig. 16.19 1st and 2nd elastic mode: amplitude dependent stiffness and damping

A FEM model of the beam substructure was also generated for this study. The beam model was updated to linear experimental measurements. Then discrete Iwan parameters were fit to best simulate the nonlinear behavior that was observed in test. This model was used to evaluate the number of sensors needed and their locations as well as to explore the effect of the number of modes retained for each subcomponent. A response prediction based on substructuring with FEM subcomponents was compared to a simulated response from a truth FEM model created by replacing Substructure A with B in the original FEM model. The substructuring predictions from the numerical substructuring suggest that in the absence of experimental noise this nonlinear modal substructuring approach is a quite accurate. In [12] it was tested whether far-field effects and changes on a structure away from the joint change the discrete joint parameters. There the authors used a similar FEM model of the Brake-Reuss Beam. Discrete parameters were fit to match the unmodified system. The FEM was then modified to adjust the far-field structure and these FEM results were compared to test. The results demonstrated (once again when the joints are confined to the microslip regime) that the far-field changes did not significantly change the discrete Iwan parameters that best describe the joints.
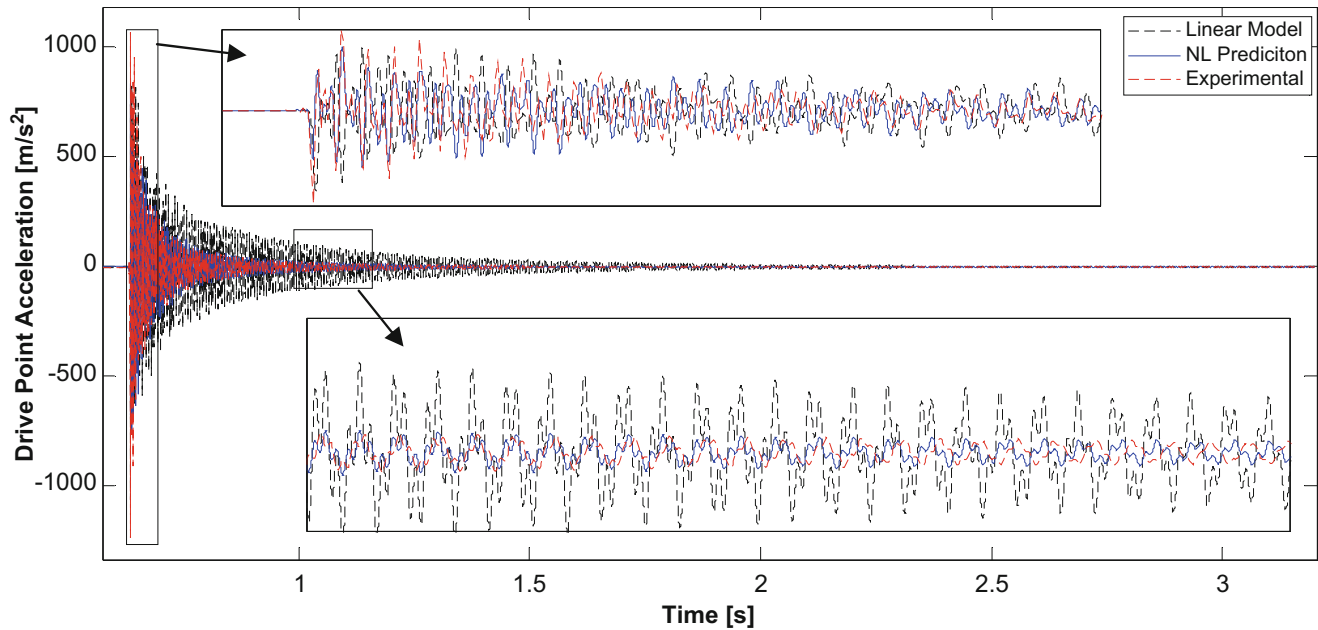
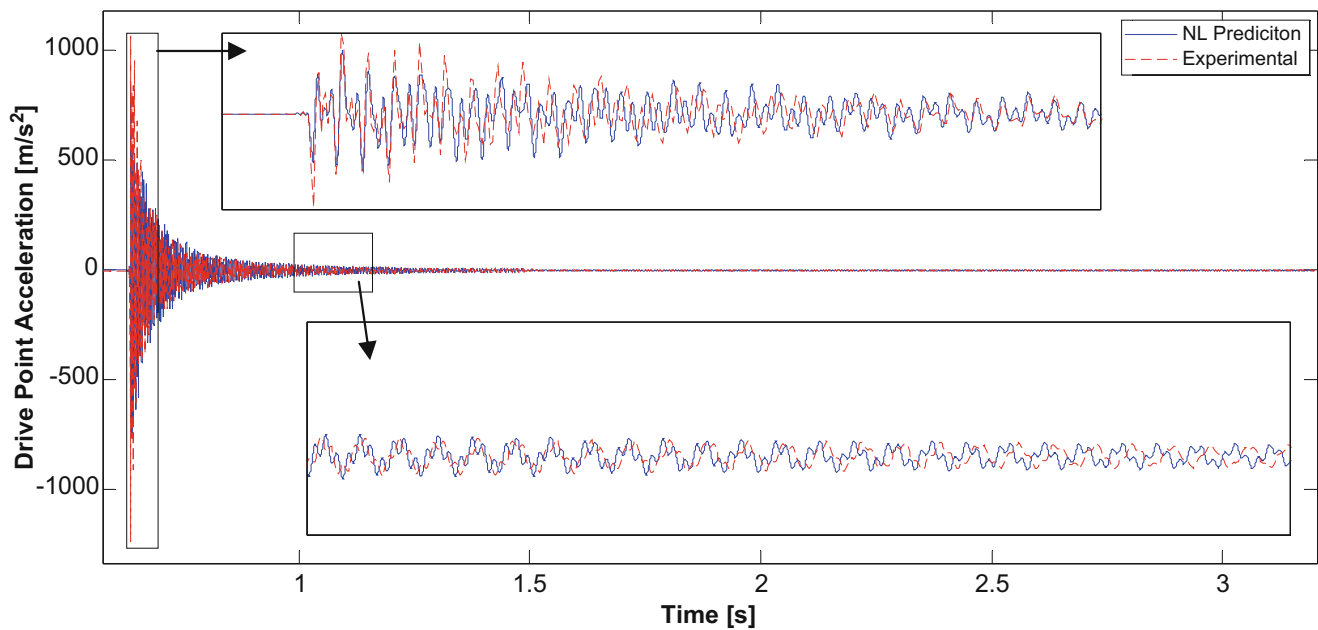**Fig. 16.20** Drive point acceleration for 500 N impulsive load with linear model

Fig. 16.21 Drive point acceleration for 500 N impulsive load

References

1. Roettgen, D.R., et al.: Substructuring of a nonlinear beam using modal Iwan framework, Part 1: nonlinear modal model identification. Presented at the international modal analysis conference XXXV, Garden Grove, 2017
2. Roettgen, D.R., Allen, M.S.: Nonlinear characterization of a bolted, industrial structure using a modal framework. Mech. Syst. Signal Process. **84**, 152 (2016)
3. Carne T.G., et al.: Force reconstruction using a sum of weighted accelerations technique. Presented at the 10th international modal analysis conference (IMAC X), San Diego, 1992
4. Mayes R.L., et al.: A modal model to simulate typical structural dynamic nonlinearity. Presented at the international modal analysis conference XXXIV, Orlando, 2016

5. de Klerk, D., et al.: General framework for dynamic substructuring: history, review, and classification of techniques. AIAA J. **46**, 1169–1181 (2008)
6. Allen, M.S., et al.: Experimental modal substructuring to couple and uncouple substructures with flexible fixtures and multi-point connections. J. Sound Vib. **329**, 4891–4906 (2010)
7. Mayes, R.L., et al.: Correcting indefinite mass matrices due to substructure uncoupling. J. Sound Vib. **332**, 5856–5866 (2013)
8. Allen, M.S., et al.: Metrics for diagnosing negative mass and stiffness when uncoupling experimental and analytical substructures. J. Sound Vib. **331**, 5435–5448 (2012)
9. Kalaycioglu, T., Ozguven, H.N.: Harmonic response of large engineering structures with nonlinear modifications. Presented at the EURODYN, Leuven, 2011
10. Krack, M., et al.: A method for nonlinear modal analysis and synthesis: application to harmonically forced and self-excited mechanical systems. J. Sound Vib. **332**, 6798–6814 (2013)
11. Allen M.S., et al.: Experimental modal substructuring with nonlinear modal Iwan models to capture nonlinear subcomponent damping. Presented at the international modal analysis conference XXXIV, Orlando, 2016
12. Cooper, S., et al.: Effect of far-field structure on joint properties. Presented at the international modal analysis conference XXXV, Garden Grove, 2016
13. Ginsberg, J.H.: Mechanical and Structural Vibrations, 1st edn. Wiley, New York (2001)
14. Segalman, D.J.: A four-parameter Iwan model for lap-type joints. J. Appl. Mech. **72**, 752–760 (2005)
15. Gross, J., et al.: A numerical round robin for the prediction of the dynamics of jointed structures. Presented at the international modal analysis conference XXXIV, Orlando, 2016
16. Lacayo, R., et al.: Quasi-static modal analysis based on implicit condensation for structures with nonlinear joints. Presented at the international conference on noise and vibration engineering, Leuven, 2016
17. Festjens, H., et al.: Nonlinear model order reduction of jointed structures for dynamic analysis. J. Sound Vib. **333**, 2100–2113 (2014)
18. Lacayo, R., et al.: A numerical study on the limitations of modal Iwan models for impulsive excitations. J. Sound Vib. **390**, 118 (2016)

Chapter 17
Dynamic Decoupling of Nonlinear Systems

Taner Kalaycıoğlu and H. Nevzat Özgüven

Abstract Structural decoupling problem has been well investigated for three decades and led to several decoupling methods. In spite of the inherent nonlinearities in a structural system in various forms all decoupling studies are for linear systems. In this study, decoupling problem for nonlinear systems is addressed for the first time and a method is proposed for calculating the frequency response functions of a substructure decoupled from a coupled nonlinear structure where nonlinearity can be modelled as a single nonlinear element. The method proposed is validated through simulated case studies.

Keywords Nonlinear decoupling • Nonlinear uncoupling • Nonlinear inverse substructuring • Nonlinear subsystem identification • Nonlinear substructure decoupling

17.1 Introduction

Since engineering structures are generally designed as an assembly of several components, considerable effort has been devoted to structural decoupling of linear systems, some of those worth mentioning is listed in references [1–3]. However, the problem where system to be decoupled includes a nonlinear element such as clearance, friction and nonlinear stiffness remains untouched. In this paper, a method is developed for the decoupling problem of nonlinear systems. The method is tested on simple lumped parameter systems by using simulated experimental data.

17.2 Theory

The uncoupling problem is studied as three separate problems, depending on the location of the nonlinear element in the coupled system: The nonlinearity can be either in the unknown subsystem or in the known subsystem, or it can connect two subsystems. The method proposed for the solution of this problem is mainly based on the application of the following techniques:

- The controlled displacement amplitude testing technique Additional Comment #4 for nonlinear systems.
- The decoupling technique proposed by D'Ambrogio et al. [1] for linear systems.
- The parametric modal identification technique proposed by Arslan et al. [4] for nonlinear systems.

The method proposed is applicable to systems where the nonlinearity can be modelled as a single nonlinear element. It is also assumed that the location of this nonlinear element is known.

T. Kalaycıoğlu (✉) • H.N. Özgüven
Department of Mechanical Engineering, Middle East Technical University, 06800, Ankara, Turkey
e-mail: tkalayci@aselsan.com.tr; ozguven@metu.edu.tr

T. Kalaycıoğlu
MGEO Business Sector, ASELSAN Inc., 06750, Ankara, Turkey

17.2.1 Nonlinearity in the Unknown Subsystem

In this case, it is assumed that known subsystem is linear whereas unknown subsystem is nonlinear and the location of the nonlinear element is known. Firstly, the complete FRF matrix of the known subsystem for the coordinates we are interested in is obtained by using the known system parameters. Then, various different sets of linear FRFs of the coupled system for the coordinates we are interested in are obtained by keeping the amplitude of the relative harmonic displacement between the end coordinates of the nonlinear element constant at a different value for each set of FRFs. Note that, depending on the location of the nonlinearity, the number of coordinates at which FRFs should be measured in the coupled system can be reduced. Using available FRFs, sets of linear FRF curves for the unknown subsystem can be obtained by applying the decoupling formulation proposed by D'Ambrogio et al. [1] for linear systems, each set corresponding to a different response level. Then, by applying the modal identification technique developed by Richardson and Formenti [5], a set of modal parameters will be obtained from each FRF curve. As the identified modal parameters vary with the response amplitude, they can be expressed as a function of the amplitude of the relative harmonic displacement between the end coordinates of the nonlinear element [4]. Then, the FRFs of the unknown subsystem can be calculated at different response levels by using the modal parameter variations obtained.

17.2.2 Nonlinearity in the Known Subsystem

In this case, it is assumed that known subsystem is nonlinear whereas unknown subsystem is linear. Nonlinear element may be located at any place in the known subsystem. Firstly, the point and transfer FRFs of the coupled system as well as of the known subsystem at coordinates that belong to the known subsystem should be obtained by keeping the amplitude of the relative harmonic displacement between the end coordinates of the nonlinear element at a specific value throughout the desired frequency range. FRFs of the known system will be calculated whereas those of the coupled system should be measured by making controlled displacement amplitude testing. This will yield a set of linear FRF curves for the coupled system, as well as for the known subsystem. Note that the nonlinearity matrices, first introduced by Tanrıkulu et al. [6] and then used in many applications, added to the dynamic stiffness matrices of the coupled system and the known subsystem will have the same values at each frequency throughout the desired frequency range. Hence, the existence of nonlinearity will be the same as adding a linear stiffness matrix to the known part of the system, and thus the problem will be reduced into decoupling of linear systems. Consequently, the FRFs of the unknown subsystem at its coupling DOFs can be calculated using the FRFs of the known and coupled systems obtained above by applying the decoupling formulation proposed by D'Ambrogio et al. [1].

17.2.3 Nonlinearity in the Connection of Two Subsystems

When the nonlinear element connects two subsystems, the problem can be reduced into the one of those defined in sect. 17.2.1 or sect. 17.2.2, depending on the availability of the properties of the nonlinear element. If the parameters of the nonlinear connection element are not known, it should be taken as a part of the unknown subsystem with a massless node at the other end, which is rigidly connected to the connection node of the known subsystem. A similar approach has been followed by the authors in [7]. Thus, the system will be reduced into the system considered in sect. 17.2.1. In case where the parameters of the nonlinear element are known, the system can be reduced into the system considered in sect. 17.2.2 in the same vein.

17.3 Simulated Case Studies

In this section, applications of the proposed decoupling method to a lumped parameter system are presented in order to demonstrate the validity and the efficiency of the method developed.

17.3.1 Decoupling of a Lumped Parameter Nonlinear System: Nonlinearity at the Unknown Subsystem

In this case study, decoupling of a 2 DOF nonlinear subsystem from a 3 DOF lumped parameter system is demonstrated by applying the decoupling method proposed. The nonlinear element is assumed to be a grounded cubic stiffness connected to the coupling DOF of the unknown subsystem. Firstly, the complete FRF matrix (for the DOFs we are interested in) of the known subsystem are theoretically obtained from the known subsystem parameters. Secondly, we need to obtain point and transfer FRFs of the coupled system at coordinates that belong to the known subsystem experimentally through a controlled displacement amplitude test in the frequency range of interest for different constant harmonic displacement amplitudes of the second DOF of the coupled system. These values are theoretically obtained, but in order to include the effect of experimental errors, they are polluted by adding a complex random number. Then the decoupling formulation proposed by D'Ambrogio et al. [1] for linear systems is applied for each 20 different sets of point and transfer FRF curves of the coupled subsystem at coordinates that belong to the known subsystem in order to obtain the point FRF of the unknown subsystem at its coupling DOF. The results are given in Fig. 17.1.

Note in Fig. 17.1 that, each FRF curve shows linear behavior, as it is obtained for a constant harmonic displacement amplitude of the nonlinear element. Firstly, the variation of modal parameters with respect to the amplitude of the relative harmonic displacement between the end coordinates of the nonlinear element is obtained by first fitting FRF curves to the calculated FRF values and then identifying modal parameters for each FRF curve by applying linear modal identification. Then, harmonic response of the unknown subsystem at its coupling DOF is calculated for a harmonic excitation of magnitude 1 N applied at the same point, by employing the approach proposed by Arslan et al. [4] and using the modal parameters calculated above (as a function of response amplitude). The same calculation is also performed through the application of the Harmonic Balance Method (HBM) by using the actual data for the unknown subsystem. These results are compared in Fig. 17.2. An excellent agreement of two response curves for both forward and backward sweeps in the whole frequency range demonstrates the validity of the method proposed.
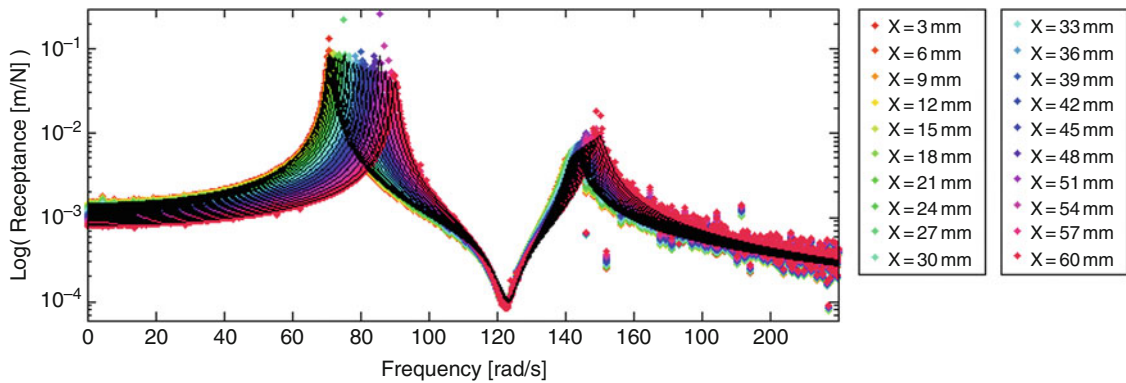

Fig. 17.1 Point FRFs of the unknown subsystem at its coupling DOF (*colored points*) and fitted FRF curves (—, *black*)
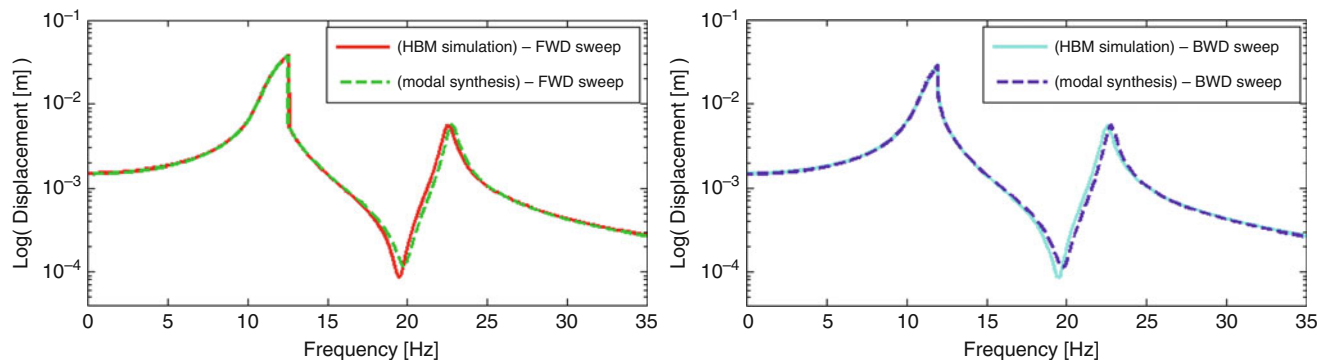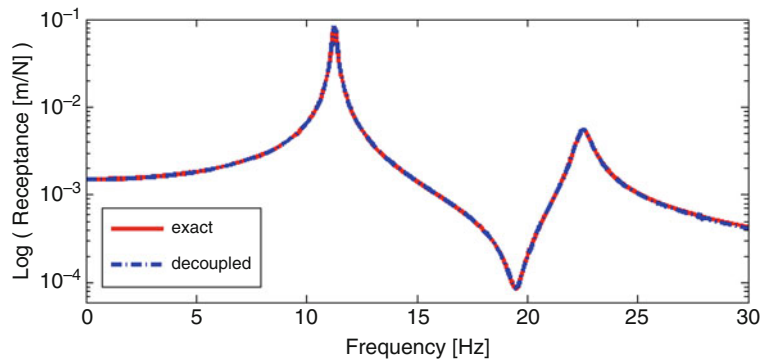

Fig. 17.2 Forward (FWD) and backward (BWD) frequency sweep responses of the unknown subsystem at its coupling DOF

Fig. 17.3 Exact and decoupled point receptances of the unknown subsystem at its coupling DOF

17.3.2 Decoupling of a Lumped Parameter Nonlinear System: Nonlinearity at the Known Subsystem

In this case study, decoupling of a 2 DOF linear subsystem from a 3 DOF lumped parameter nonlinear system is demonstrated by applying the decoupling method proposed. The nonlinear element is again assumed to be a grounded cubic stiffness connected to the internal DOF of the known subsystem. Then, the exact point and transfer FRFs of the coupled system and the known subsystem at coordinates that belong to the known subsystem are calculated by keeping the amplitude of the relative harmonic displacement between end coordinates of the cubic nonlinearity at a specific constant value (20 mm for both systems). In order to include the effect of noise in real testing, a complex random perturbation is added to the calculated FRFs. Finally, the decoupling formulation proposed by D'Ambrogio et al. [1] for linear systems is applied to obtain the point receptance of the unknown subsystem at its coupling DOF by using the FRF curves fitted to the point and transfer receptances of the coupled system obtained through simulated experiment, and receptances of the known subsystem. The results are given in Fig. 17.3.

Fig. 17.3 shows that the FRF obtained using the decoupling method proposed almost the same as the exact FRF. Then it can be concluded that the decoupling method developed yields very good results for the case where the nonlinearity is in the known subsystem.

17.4 Discussion and Conclusions

Although there are some accuracy problems, the dynamic decoupling problem of linear structures is well addressed in literature. However, there has been almost no effort to tackle the dynamic decoupling problem of nonlinear structures. This paper presents the first attempt to solve this problem by suggesting a method that can be applied when the nonlinearity can be modelled as a single element. It is also assumed in this method that the location of nonlinearity is known. The approach proposed can be applied for all possible cases as far as the location of the nonlinear element is concerned, i.e. nonlinearity can be either in the known or unknown subsystem, or it can be at the connection. The method proposed is validated through simulated case studies.

References

1. D'Ambrogio, W., Fregolent, A.: The role of interface DOFs in decoupling of substructures based on the dual domain decomposition. Mech. Syst. Signal Process. **24**(7), 2035–2048 (2010)
2. Batista, F.C., Maia, N.M.M.: Uncoupling techniques for the dynamic characterization of sub-structures. Proceedings of the 29th international modal analysis conference. Jacksonville, USA (2011)
3. Voormeeren, S.N., Rixen, D.J.: A family of substructure decoupling techniques based on a dual assembly approach. Mech. Syst. Signal Process. **27**, 379–396 (2012)
4. Arslan, Ö., Aykan, M., Özgüven, H.N.: Parametric identification of structural nonlinearities from measured frequency response data. Mech. Syst. Signal Process. **25**(4), 1112–1125 (2011)

5. Richardson, M.N., Formenti, D.L. Parameter estimation from frequency response measurements using rational fraction polynomials. Proceedings of the 1st international modal analysis conference. Orlando, USA (1982)
6. Tanrıkulu, Ö., Kuran, B., Özgüven, H.N., İmregün, M.: Forced harmonic response analysis of non-linear structures using describing functions. AIAA J. **31**(7), 1313–1320 (1993)
7. Kalaycıoğlu, T., Özgüven, H.N.: Nonlinear structural modification and nonlinear coupling. Mech. Syst. Signal Process. **46**(2), 289–306 (2014)

Chapter 18
Nonlinear Substructuring Using Fixed Interface Nonlinear Normal Modes

Marco Falco, Morteza Karamooz Mahdiabadi, and Daniel Jean Rixen

Abstract This study introduces a nonlinear dynamic substructuring (NDS) method assembling a truncated number of nonlinear normal modes (NNMs). A generic nonlinear structure is first divided into substructures and each substructure is reduced by taking a truncated number of fixed interface NNMs in addition to the proposed nonlinear constraint modes at each energy level. Using this basis a reduced quasi linear model of the substructures is computed at each energy level. Then the assembly of the quasi linear substructures using the Component Mode Synthesis (CMS) method yields the NNMs of the whole structure. The proposed method can be considered as an extension of the Craig-Bampton (CB) method for nonlinear structures. In order to evaluate the performance of the proposed nonlinear Craig-Bampton (NCB) approach, it is applied on a numerical example and the substructuring results are validated.

Keywords Craig-Bampton • Fixed interface modes • Nonlinear constraint modes • Nonlinear normal modes • Nonlinear substructuring

18.1 Introduction

Dynamic substructuring approach (DS) is a powerful tool in the design stage of structures, as it allows engineers to decrease computational costs during the design and optimization procedure. In this methodology, starting from study and analysis of smaller subcomponents of a large structure, the dynamic response of the whole structure is obtained by assembling these subcomponents. Furthermore, investigation of the local dynamics of a large structure makes the optimization process of its small substructures more efficient. DS has been well developed for structures with linear behavior during the past decades (e.g. see [1–5]). Among them, Craig and Bampton [6] developed a very well-known and easy modal substructuring method. They reduced each substructure using a truncated fixed interface modes in addition to the static deformation of the internal Degrees of Freedom (DOFs) imposing a unit displacement to each boundary DOF while the other boundary DOFs are fixed. Furthermore, MacNeal [2], Rubin [3], Craig and Chang [4] and Rixen [5] developed substructuring methods based on free interface modes of the system.

By development of high-tech productions in recent years with lightweight materials as well as strong thermal or electrical interactions with mechanical structures, they can no longer be considered as linear elements. Ewin and Ferreira [7] considered a nonlinear dynamic substructuring (NDS) approach in frequency domain by defining nonlinear receptances of substructures based on harmonic balance and then coupling the underlying receptances. Keuther and Allen [8] developed an NDS for geometrical nonlinear finite element models (FEM). They built the reduced order models of the substructures by taking a linear Craig-Bampton basis in addition to quadratic and cubic terms due to geometric nonlinearities with unknown coefficients. Then these unknown coefficients are identified applying a set of static forces to the FEM and computing the corresponding displacements in a non-intrusive manner, and the substructures are coupled using CMS method. Nonlinear normal modes (NNMs) are used in this work as a convergence gauge to check the accuracy of the reduced order model with substructuring. The concept of NNMs was first introduced by Rosenberg [9, 10] who defined them as synchronous and periodic oscillations of a nonlinear structure. In other words NNMs are considered as an extension of linear normal modes

M. Falco (✉)
Politecnico di Torino, Corso duca degli Abruzzi 24, 10129, Torino, Italy
e-mail: s220184@studenti.polito.it; marco.nisu92@gmail.com

M. Karamooz Mahdiabadi • D.J. Rixen
Technical University of Munich, Boltzmannstraße 15, D-85748, Garching, Germany
e-mail: m.karamooz@tum.de; rixen@tum.de

(LNMs) for nonlinear structures. A different definition of NNMs was proposed by Shaw and Pierre [11]. They introduced an NNM as a geometrical invariant manifold in phase space.

NNMs have been already used in some substructuring works in the literature, e.g. referring to Rosenborg's NNM definition, Allen et al.[12] proposed a substructuring method in which at discrete energy levels the free interface NNMs of substructures are coupled for the prediction of the NNMs of the complete structure. The definition given by Shaw and Pierre was used in the method proposed by Apiwattanalunggarn at al. [13]. In this method every substructure is reduced to a single-DOF structure, taking one fixed interface NNM as the master mode, while the others are slave modes. For coupling the substructures, linear constraint modes were used. However this method was found to be computationally costly when applied to complex structures.

In this study, inspired by the procedure of free-interface energy level method proposed by Allen [12], a new technique is introduced. The fixed interface NNMs of each substructure are computed within an energy range of interest and discrete energy levels are chosen as reference steps. At each of these energy levels a quasi-linear model for all the substructures is obtained using the truncated set of fixed interface NNMs in companion with a set of nonlinear constraint modes. The reduced quasi-linear subsystems obtained are then coupled in order to reassemble the complete structure. In this method NNMs are also used to validate the assembled structure with the truth model. As the energy increases the behaviour of the NNMs of the complete structure is predicted through the coupling of the substructures' NNMs. The technique is applied on a simple nonlinear structure, to evaluate the efficiency of the proposed method.

Next section gives an outline of the theory with the presentation of Quasi linear models, the revision of theory of the linear Craig Bampton and the explanation of the new non-linear Craig-Bampton technique. In Sect. 18.3 the method is applied on a numerical example. Finally in Sect. 18.4 the conclusions are presented.

18.2 Theory

18.2.1 Quasi-linear Model

The equations of motions for a nonlinear substructure can be written as:

$$M\ddot{x} + Kx + f_{nl}(x) = g \tag{18.1}$$

The system can be expressed in matrix form, considering the internal DOFs, x_i, and the boundary DOFs, x_b.

$$\begin{bmatrix} M_{ii} & M_{ib} \\ M_{bi} & M_{bb} \end{bmatrix} \begin{bmatrix} \ddot{x}_i \\ \ddot{x}_b \end{bmatrix} + \begin{bmatrix} K_{ii} & K_{ib} \\ K_{bi} & K_{bb} \end{bmatrix} \begin{bmatrix} x_i \\ x_b \end{bmatrix} + \begin{bmatrix} f_{nl,i} \\ f_{nl,b} \end{bmatrix} = \begin{bmatrix} 0 \\ g(t) \end{bmatrix} \tag{18.2}$$

where M and K are the mass and stiffness matrices and f_{nl} contains the nonlinear term, depending only on displacements, as damping is neglected. g(t) is the reaction force between substructures. This n-DOF system has at least n NNMs that are considered as periodic solution for the equations (18.1). Nonlinear normal modes are used to describe the dynamics of each susbtructure in the considered energy range and also to assemble the substructures. The NNM definition used here is the one proposed by Rosenberg [9], namely, it is a periodic and synchronous motion in a vibrating system. The shooting and Pseudo-Arclength continuation methods [14] are employed to compute NNMs, putting the phase condition (initial velocities) equal to zero.

For the tth energy-dependent NNM of a substructure, at energy level E_s, it is possible to define a vector $x_{NNM,t}(0, E_s)$ of initial conditions. This is also the maximum displacements vector and is used for creating the quasi-linear model at the energy level E_s.

$$\Phi_{QL,t}(E_s) = \frac{x_{NNM,t}(0, E_s)}{\sqrt{x_{NNM,t}^T(0, E_s) [M] x_{NNM,t}(0, E_s)}} \tag{18.3}$$

In this way the quasi-linear mode shape, represented by $\Phi_{QL,t}(E_s)$, of the tth NNM at the energy level E_s is created. The corresponding frequency $\omega_{NNM,t}(E_s)$ of this QL model is simply the tth NNM frequency at the same energy level. The relation between the displacement vector and the modal shape vector, at E_s, can be expressed using a scaling factor $k_{t,s}$ as:

$$x_{NNM,t}(0, E_s) = \Phi_{QL,t}(E_s) k_{t,s} \tag{18.4}$$

Eigenfrequencies and mode shapes, in a nonlinear structure, are energy-dependent, therefore a different quasi-linear model can be defined at each energy level. The modal parameters of one substructure taken at a determined energy level (E_s) are expressed as

$$\Phi_{QL}(E_s) = \begin{bmatrix} \Phi_{QL,1}(E_s) & \Phi_{QL,2}(E_s) & \ldots & \Phi_{QL,p}(E_s) \end{bmatrix} \tag{18.5}$$

$$\Pi_{QL}(E_s) = \mathrm{diag} \begin{bmatrix} \omega_{NNM,1}(E_s)^2 & \omega_{NNM,2}(E_s)^2 & \ldots & \omega_{NNM,p}(E_s)^2 \end{bmatrix} \tag{18.6}$$

where each substructure has a truncated set of NNMs, thus p denotes the number of NNMs retained in each substructure model and $\omega_{NNM,i}(E_s)$ is the frequency of NNM number i at energy level E_s. Using the matrices of equations (18.5) and (18.6), the equations of motion of one substructure at the energy level E_s can be written as

$$[I]\{\ddot{q}_{QL}\} + [\Pi_{QL}(E_s)]\{q_{QL}\} = 0 \tag{18.7}$$

where I is the identity matrix and q_{QL} is the new set of generalized DOFs obtained through the modal transformation:

$$\{x(t)\} \simeq [\Phi_{QL}(E_s)]\{q_{QL}\} \tag{18.8}$$

These QL models have been used by Allen et al. [12] starting from free interface NNMs, whereas the method proposed in Sect. 18.2.3 uses fixed interface modes.

18.2.2   The Linear Craig-Bampton

The linear Craig-Bampton method uses a reduction basis made of reduced *fixed-interface modes* and *constraint modes* [6]. Fixed-interface modes are computed fixing the boundary DOFs of a substructure, while constraint modes are obtained imposing a unit displacement to each boundary DOF at a time. Neglecting the inertia forces, the internal DOFs are projected onto the boundary DOFs. Splitting the generalized set of DOFs into boundary DOFs u_b and internal DOFs u_i, the differential equation are written as

$$\begin{bmatrix} M_{bb} & M_{bi} \\ M_{ib} & M_{ii} \end{bmatrix} \begin{bmatrix} \ddot{u}_b \\ \ddot{u}_i \end{bmatrix} + \begin{bmatrix} K_{bb} & K_{bi} \\ K_{ib} & K_{ii} \end{bmatrix} \begin{bmatrix} u_b \\ u_i \end{bmatrix} = \begin{bmatrix} g_b \\ 0 \end{bmatrix} \tag{18.9}$$

where g_b is the reaction force from the neighboring substructures. The internal DOFs are now expressed in terms of constraint modes (Ψ_c) and fixed-interface vibration modes (Φ_i)

$$u_i = \Psi_c u_b + \Phi_i \eta_i \tag{18.10}$$

where η_i is a reduced set of modal coordinates. Then the reduction basis in matrix form is written as

$$\begin{bmatrix} u_b \\ u_i \end{bmatrix} = \begin{bmatrix} u_b \\ \Psi_c u_b + \Phi_i \eta_i \end{bmatrix} = \begin{bmatrix} I & 0 \\ \Psi_c & \Phi_i \end{bmatrix} \begin{bmatrix} u_b \\ \eta_i \end{bmatrix} = R_{CB} \begin{bmatrix} u_b \\ \eta_i \end{bmatrix} \tag{18.11}$$

Substituting (18.11) into (18.9) and premultiplying (18.9) by R_{CB}^T gives the reduced mass and stiffness matrices as:

$$\tilde{M} = R_{CB}^T M R_{CB}$$

$$\tilde{K} = R_{CB}^T K R_{CB}$$

where $\tilde{K}$ is a diagonal matrix and $\tilde{M}$ is an identity matrix in the part that corresponds to the internal DOFs.

$$\tilde{K} = \begin{bmatrix} \tilde{K}_{bb} & 0 \\ 0 & \Omega_i^2 \end{bmatrix}$$

$$\tilde{K}_{bb} = K_{bb} - K_{bi}K_{ii}^{-1}K_{ib}$$

$$\tilde{M} = \begin{bmatrix} \tilde{M}_{bb} & \tilde{M}_{bi} \\ \tilde{M}_{ib} & I \end{bmatrix}$$

$$\tilde{M}_{bb} = M_{bb} - M_{bi}K_{ii}^{-1}M_{ib} - K_{bi}K_{ii}^{-1}M_{ib} + K_{bi}K_{ii}^{-1}M_{ii}K_{ii}^{-1}K_{ib}$$

$$\tilde{M}_{ib} = \Phi_m^T(M_{ib} - M_{ii}K_{ii}^{-1}K_{ib}) = \tilde{M}_{bi}^T$$

Finally the reduced matrices are coupled using the component mode synthesis method.

Since the Craig-Bampton method is easy to implement, it is widely used in the literature for reduction of linear structures.

18.2.3 Energy Levels Method Using a Nonlinear Craig Bampton Basis

Following the procedure introduced in [12] a new reduction basis is used for nonlinear substructuring, in other words the possibility of coupling directly NNMs at the substructure level in order to predict the NNMs of the assembled structure, is investigated. Reducing a system using only free interface modes, may not include the effect of higher modes, thus to include at least the static contribution of these modes, the motion of the system at energy level E_s need to be respresented by a more complete basis.

Therefore the new technique proposed here uses a different reduction basis, which can be interpreted as a nonlinear extension of the Craig-Bampton basis. The quasi-linear reduced models for every substructure at different energy levels are constructed using fixed interface NNMs and nonlinear constraint modes (NCMs).

The whole procedure is presented in the following steps, applied on a structure, divided into two substructures α and β.

18.2.3.1 I: Compute Fixed Interface NNMs

A truncated set of fixed interface NNMs are computed for both substructures, putting the initial conditions corresponding to the boundary DOFs equal to zero. To do so, the shooting function in companion with pseudo-arclength approach is used as explained in [14]. Moreover m discrete energy levels are chosen within the global energy range, creating vector E

$$E = \begin{bmatrix} E_1 & E_2 & \dots & E_m \end{bmatrix} \tag{18.12}$$

where E_s, $s = 1, 2, \dots, m$ are the energy levels at which substructures are assembled.

18.2.3.2 II: Create the Reduction Basis at the Energy Level s

The energy for substructures α and β at level E_s is defined as:

$$E_s^\alpha = E_s^\beta = E_s \tag{18.13}$$

The frequency ω_s and the initial displacement vector $x_{NNM,s}$ are here obtained having the computed fixed-interface NNMs at the corresponding level (in case the exact energy level is not present in the data of an NNM computed before, it should be interpolated). The quasi linear vectors $\Phi_{QL,s}$ and the scaling factor $k_{t,s}$ are then computed using equations (18.3) and (18.4), respectively. Afterwards the reduction basis at energy level s is formed.

$$T_{NCB,s} = \begin{bmatrix} \Phi_{fix}(E_s) & \Psi_{nl}(E_s) \\ 0 & I \end{bmatrix} \tag{18.14}$$

where I is the identity matrix, and $\Phi_{fix}(E_s)$ is the matrix corresponding to equation (18.5), whose columns are the quasi linear vectors $\Phi_{QL,s}$ and $\Psi_{nl}(E_s)$ are the nonlinear constraint modes (NCMs). In order to calculate the NCMs taking the first line of equation (18.2) and neglecting the inertia forces gives:

$$K_{ii}x_i + K_{ib}x_b + f_{nl,i} = 0 \tag{18.15}$$

Then the nonlinear constraint modes are introduced as

$$\Psi_{nl,s} = -\left(K_{ii} + \left.\frac{\partial f_{nl,i}}{\partial u_i}\right|_{u_i=x_{NNM,s}}\right)^{-1}\left(K_{ib} + \left.\frac{\partial f_{nl,i}}{\partial u_b}\right|_{u_b=1}\right) \tag{18.16}$$

The nonlinear terms $\left.\frac{\partial f_{nl,i}}{\partial u_i}\right|_{u_i=x_{NNM,s}}$ and $\left.\frac{\partial f_{nl,i}}{\partial u_b}\right|_{u_b=1}$ are the Jacobian matrices of the nonlinear vector f_{nl}, and they take the tangent stiffnesses due to nonlinearities into account. The linearization point $x_{NNM,s}$ for the nth DOF is taken from the corresponding initial condition on the nth NNM.

Once the reduction matrix is created the quasi linear model is defined as follows

$$M_{QL,s} = T_{NCB,s}^T M \, T_{NCB,s} \tag{18.17}$$

$$K_r = T_{NCB,s}^T K \, T_{NCB,s} = \begin{bmatrix} K_{ii,r} & K_{ib,r} \\ K_{bi,r} & K_{bb,r} \end{bmatrix} \tag{18.18}$$

where $M_{QL,s}$ is the reduced mass matrix at energy level E_s. In order to obtain the quasi linear stiffness matrix $K_{QL,s}$, it is necessary to substitute the diagonal elements of the submatrix $K_{ii,r}$ with the quadratic values of the frequencies (ω^2) obtained at step II from the fixed interface NNMs and expressed as in equation (18.6). This substitution is due to the fact that the orthogonality condition does not apply for NNMs.

$$\Phi_{fix}^T K_{ii} \Phi_{fix} \neq \text{diag}(\omega_{1,s}^2, \omega_{2,s}^2, \ldots, \omega_{m,s}^2) \tag{18.19}$$

18.2.3.3   III: Couple the Reduced Substructures at Energy Level s

In order to assemble the system, QL mass and stiffness matrices of the substructures at the energy level E_s are put in a block diagonal form as

$$\begin{bmatrix} M_{QL,s}^{(\alpha)} & 0 \\ 0 & M_{QL,s}^{(\beta)} \end{bmatrix} \begin{Bmatrix} \ddot{q}_{QL}^{(\alpha)} \\ \ddot{q}_{QL}^{(\beta)} \end{Bmatrix} + \begin{bmatrix} K_{QL,s}^{(\alpha)} & 0 \\ 0 & K_{QL,s}^{(\beta)} \end{bmatrix} \begin{Bmatrix} q_{QL}^{(\alpha)} \\ q_{QL}^{(\beta)} \end{Bmatrix} = \begin{bmatrix} T_{NCB,s}^{(\alpha)} & 0 \\ 0 & T_{NCB,s}^{(\beta)} \end{bmatrix}^T \begin{Bmatrix} g(t)^{(\alpha)} \\ g(t)^{(\beta)} \end{Bmatrix} \tag{18.20}$$

where the vectors $g(t)^{(\alpha)}$ and $g(t)^{(\beta)}$ are the reaction forces due to the interactions of the two substructures. The compatibility condition can be expressed as:

$$[B]\begin{Bmatrix} x_s^{(\alpha)} \\ x_s^{(\beta)} \end{Bmatrix} = [B]\begin{bmatrix} T_{NCB,s}^{(\alpha)} & 0 \\ 0 & T_{NCB,s}^{(\beta)} \end{bmatrix}\begin{Bmatrix} q_{QL}^{(\alpha)} \\ q_{QL}^{(\beta)} \end{Bmatrix} = [B_{mod}]\begin{Bmatrix} q_{QL}^{(\alpha)} \\ q_{QL}^{(\beta)} \end{Bmatrix} = \{0\} \tag{18.21}$$

where B is the signed Boolean matrix defining the connecting DOFs, while B_{mod} expressed the compatibility in modal coordinates and is no longer Boolean. In order to create a unique set of DOFs, L_{mod} is built as the null space of B_{mod}.

$$L_{mod} = null(B_{mod}) \tag{18.22}$$

$$\begin{Bmatrix} q_{QL}^{(\alpha)} \\ q_{QL}^{(\beta)} \end{Bmatrix} = [L_{mod}]\{q_u\} \tag{18.23}$$

Where q_u represents the unique set of DOFs of the assembled system.

Substituting (18.23) into (18.20) and pre-multiplying (18.20) by L_{mod}^T, the equations of motion for the coupled system are obtained.

$$[\bar{M}_s]\{\ddot{q}_u\} + [\bar{K}_s]\{q_u\} = \{0\}$$

(18.24)

where

$$[\bar{M}_s] = [L_{mod}]^T \begin{bmatrix} M_{QL,s}^{(\alpha)} & 0 \\ 0 & M_{QL,s}^{(\beta)} \end{bmatrix} [L_{mod}]$$

(18.25)

$$[\bar{K}_s] = [L_{mod}]^T \begin{bmatrix} K_{QL,s}^{(\alpha)} & 0 \\ 0 & K_{QL,s}^{(\beta)} \end{bmatrix} [L_{mod}]$$

(18.26)

The eigenfrequency $\bar{\omega}_{n,s}$ and the eigenvector $\bar{\varphi}_{n,s}$ of (18.24) express the nth frequency and the nth QL vector of the whole system at energy level E_s. In other words they represent the nth NNM of the assembled substructure at energy level s.

18.2.3.4   IV: Convergence Check

The energy of the assembled system should be the same as the summation of the energies of the two substructures defined in step II. To evaluate this, first a global scaling factor for the nth NNM of the assembled structure at energy level E_s is computed as:

$$\bar{k}_{n,s} = \left[[L_{mod}]\{\bar{\varphi}_{n,s}\}\right]^+ \left\{ \begin{Bmatrix} k_s^{(\alpha)} \end{Bmatrix} \\ \begin{Bmatrix} k_s^{(\beta)} \end{Bmatrix} \right\}$$

(18.27)

where $()^+$ is the pseudo-inverse of a non-square matrix, $\{k_s^{(\alpha)}\}$ is a $n_\alpha \times 1$ vector and $\{k_s^{(\beta)}\}$ is a $n_\beta \times 1$ vector, with n_α and n_β that are respectively the number of DOFs of substructures α and β. These two vectors contain the scaling factors for each quasi linear mode, computed at energy level E_s. This global scaling factor allows the transformation from modal to physical coordinates:

$$\begin{Bmatrix} x_s^{(\alpha)} \\ x_s^{(\beta)} \end{Bmatrix} = \begin{bmatrix} T_{NCB,s}^{(\alpha)} & 0 \\ 0 & T_{NCB,s}^{(\beta)} \end{bmatrix} [L_{mod}]\{\bar{\varphi}_{n,s}\}\bar{k}_{n,s}$$

(18.28)

From the displacements the energies of substructures $\bar{E}_s^\alpha$ and $\bar{E}_s^\beta$ are directly obtained.

The iterative algorithm compares the energy of every subcomponent in the nth NNM to the energy at which the quasi linear models were defined at step II (E_s^α and E_s^β). The error is measured as

$$\frac{\left\| \begin{Bmatrix} E_s^\alpha \\ E_s^\beta \end{Bmatrix} - \begin{Bmatrix} \bar{E}_s^\alpha \\ \bar{E}_s^\beta \end{Bmatrix} \right\|_2}{\left\| \begin{Bmatrix} \bar{E}_s^\alpha \\ \bar{E}_s^\beta \end{Bmatrix} \right\|_2} < \varepsilon$$

(18.29)

where $\|\ \|_2$ is the 2-norm of the vector. The algorithm converges if the error is under the tolerance ε.

18.2.3.5 IVa: Convergence Achieved

If the convergence is achieved it is possible to obtain a point of the nth NNM for the coupled system, through frequency $\bar{\omega}_n$ and the total energy,

$$E_s^{total} = \bar{E}_s^{(\alpha)} + \bar{E}_s^{(\beta)}$$

A new solution is found setting $s = s + 1$.

18.2.3.6 IVb: Convergence not Achieved

If the tolerance is not satisfied, update the quasi linear model based on the energy in each subcomponent. The energy is changed as follows:

$$\begin{Bmatrix} E_{i,s}^{(\alpha)} \\ E_{i,s}^{(\beta)} \end{Bmatrix} = \lambda \begin{Bmatrix} \bar{E}_{i,s}^{(\alpha)} \\ \bar{E}_{i,s}^{(\beta)} \end{Bmatrix} + (1 - \lambda) \begin{Bmatrix} E_{i,s}^{(\alpha)} \\ E_{i,s}^{(\beta)} \end{Bmatrix} \tag{18.30}$$

where λ is a weighting factor between 0 and 1. With this new energy levels (for each substructure) a new iteration, i, should be implemented. The procedure is then repeated from step II until convergence is met. If the updated energy reaches the maximum energy level in E, terminate the solution of the nth assembly mode and initiate the next mode, $n = n + 1$.

18.3 Numerical Results

In order to validate the proposed method, a 4-DOFs nonlinear mass-spring system is taken into account. The system is divided into a 2-DOFs substructure, α, and a 3-DOFs substructure, β, as shown in Fig. 18.1. Both subsystems α and β have one nonlinear spring, $k_{nl,1}$ and $k_{nl,2}$, respectively, and are coupled through one connecting DOF. The properties of the system are:

- masses: $m_1 = 1.5\,\text{kg}$, $m_2 = 0.5\,\text{kg}$, $m_3 = 0.5\,\text{kg}$ $m_4 = 1\,\text{kg}$, $m_5 = 5\,\text{kg}$;
- linear springs: $k_1 = 3\,\text{N/m}$, $k_2 = 1\,\text{N/m}$, $k_3 = 1\,\text{N/m}$ $k_4 = 1.7\,\text{N/m}$, $k_5 = 5\,\text{N/m}$;
- nonlinear springs: $k_{nl,1} = 0.001\,\text{N/m}^3$, $k_{nl,2} = 0.0001\,\text{N/m}^3$;
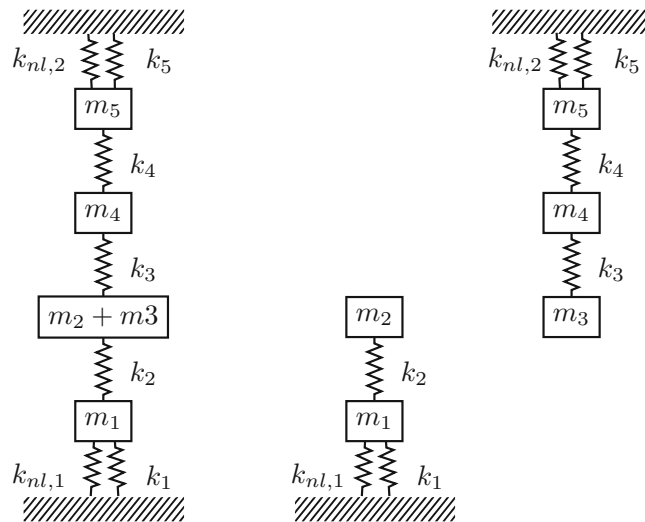
Fig. 18.1 From *left* to *right*: complete structure, substructure α and substructure β
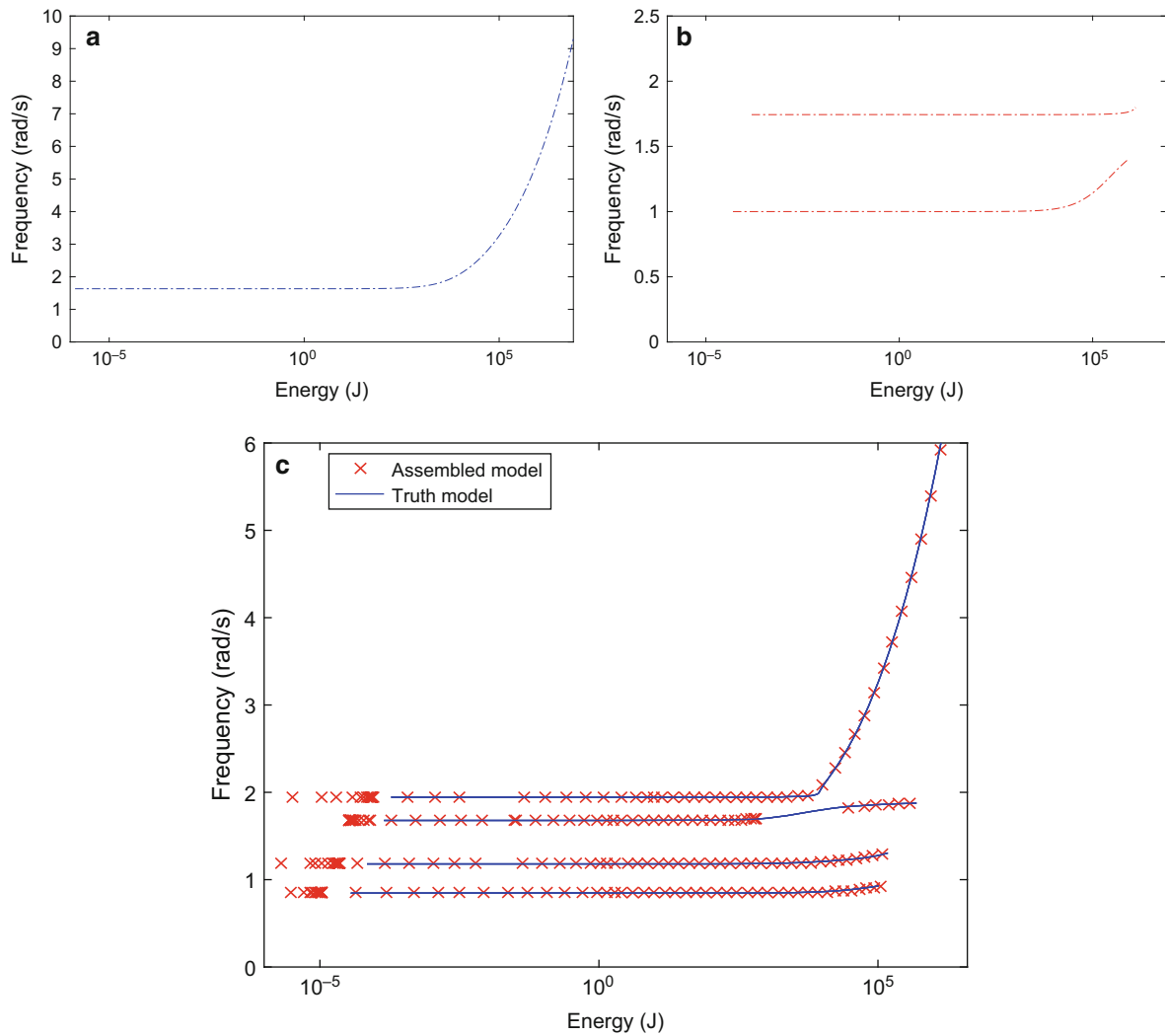
Fig. 18.2 NNM of structure α (**a**), NNM of substructure β (**b**) and the overlap of the original and the assembled NNMs of the complete structure (**c**)

Figure 18.2a shows the fixed-interface NNM of substructure α, while the two fixed-interface NNMs of substructure β are presented in Fig. 18.2b. Using the analysis developed in Sect. 18.2.3, the two substructures are coupled at each energy level employing the fixed-interface modes (one for α and two for β) in addition to the nonlinear constraint modes (one for each substructure), which results in the four NNMs of the assembled structure. In Fig. 18.2c the assembled NNMs with the NCB method are plotted. In order to evaluate the efficiency of the assembled NNMs, the NNMs of the complete model (Fig. 18.1) are also shown in Fig. 18.2c. As it can be seen in this figure, the assembled NNMs fit very well the original ones, covering a wide energy range (from 10^{-5} to 10^5 J). In the third assembled NNM, where the behavior changes from linear to nonlinear, the energy range of the assembly doesn't converge to the summation of the energies of the two substructures. The lack of points in this region can be due to this problem. Finally, it should be mentioned that the parameter λ (in equation (18.30)) for estimation of the new energy level in convergence iteration is chosen $\lambda = 0.3$ in this example. This parameter is related to the number of points computed at each NNM. Smaller values for λ lead to more points on NNM branch, in contrast, computational time is increased, and vice versa.

18.4   Conclusions

This work studies a nonlinear dynamic substructuring approach using nonlinear normal modes. A nonlinear structure is divided into substructures and a reduced Quasi-Linear (QL) model for each substructure at each energy level is constructed. The QL model is developed using a truncated set of fixed-interface NNMs in companion with selected nonlinear constraint modes. The nonlinear constraint modes are used in this study to compensate the effect of the NNM truncation in the QL model of each subtructure. In fact this method can be considered as an extension of the Craig-Bampton method for nonlinear structures. The proposed method is implemented on a numerical example and the achieved NNMs of the assembly are very well matching with the ones of the truth model in the studied energy range, giving hope that the method could be applied to large structures.

References

1. Prezmienecki, J.S.: Matrix structural analysis of substructures. AIAA J. **1**(1), 138–147 (1963)
2. MacNeal, R.H.: A hybrid method of component mode synthesis. In: Computers & Structures, vol. I, pp. 581–601. Pergamon Press, New York (1971)
3. Rubin, S.: Improved component-mode representation for structural dynamic analysis. AIAA J. **13**(8), 995–1006 (1975)
4. Chang, C., Craig, R.R.: On the use of attachement modes in substructure coupling for dynamics analysis. In: 18th Structures, Structural Dynamics and Material Conference, San Diego, 21–23 Mar, pp. 89–99. AIAA/ASME
5. Rixen, D.J.: A dual Craig-Bampton method for dynamic substructuring. J. Comput. Appl. Math. **168**, 383–391 (2004)
6. Bampton, M.C.C., Craig, R.R., Jr.: Coupling of substructures for dynamic analyses. AIAA J. **6**(7), 1313–1319 (1968)
7. Ewins, D.J., Ferreira, J.V.: Nonlinear receptance coupling approach based on describing functions. In: Proceedings of SPIE – the International Society for Optical Engineering, pp. 1034–1040 (1996)
8. Allen, M.S., Keuther, R.J.: Craig-Bampton substructuring for geometrically nonlinear subcomponents. In: 32nd IMAC, A Conference and Exposition on Structural Dynamics, Orlando. Conference Proceedings of the Society for Experimental Mechanics, pp. 167–178 (2014)
9. Rosenberg, R.M.: Normal modes of nonlinear dual-mode systems. J. Appl. Mech. **27**, 263–268 (1960)
10. Rosenberg, R.M.: The normal modes of nonlinear n-degree.of-freedom systems. J. Appl. Mech. **30**(1), 7–14 (1962)
11. Shaw, S., Pierre, C.: Non-linear normal modes and invariant manifold. J. Sound Vib. **150**(1), 170–173 (1991)
12. Allen, M.S., Keuther, R.J.: Nonlinear modal substructuring of systems with geometric nonlinearities. In: 54th AIAA/ASME/ASCE/AHS/ASC Structures, Structural Dynamics and Materials Conference, Boston, 8–11 Apr 2013
13. Apiwattanalunggarn, P.: Model reduction of nonlinear structural system using nonlinear normal modes and component mode synthesis. Ph.D. thesis, Michigan State University (2003)
14. Kerschen, G., Golinval, J.-C., Peeters, M., Vigu, R., Serandour, G.: Nonlinear normal modes, Part II: towards a practical computation using numerical continuation techniques. Mech. Syst. Signal Process. **23**(1), 195–216 (2009)

Chapter 19
Dynamic Substructuring of Geometrically Nonlinear Finite Element Models Using Residual Flexibility Modes

Morteza Karamooz Mahdiabadi, Erhard Buchmann, Duo Xu, Andreas Bartl, and Daniel Jean Rixen

Abstract A nonlinear dynamic substructuring approach using Residual Flexibility method for geometrically nonlinear structures is investigated. In order to reduce the model order of a geometrically nonlinear structure, the closed form equations of motion for the substructures are classically required. However, in industrial applications these equations are often not available, because the model of interest is constructed in a commercial finite element software package. As a result, a non-intrusive reduction method is applied. To do so, the Rubin method which contains Residual Flexibility effect is used as a linear basis and the nonlinear terms with unknown coefficients – due to geometric nonlinearity – are added to them. These nonlinear stiffness coefficients of the reduced substructure are calculated using the Implicit Condensation and Expansion Method (ICE). Then, the nonlinear reduced substructures are assembled using Component Mode Synthesis (CMS). The performance of the free-interface method of Rubin as a linear basis for nonlinear substructuring is examined by implementing the proposed methods on an academic example developed in a commercial finite element software. The accuracy of the reduced order model is assessed by comparing the Nonlinear Normal Modes (NNMs) of the reduced order model with the ones of the original model before reduction.

Keywords Nonlinear substructuring • Residual flexibility modes • Model reduction • Geometric nonlinearity • Nonlinear normal modes

19.1 Introduction

In the design procedure of dynamic structures, engineers often deal with large finite element models (FEMs) containing an enormous number of Degrees of Freedom (DOFs). On the other hand, they have to solve dynamic responses of the structure (such as eigenfrequency and eigenmodes, transient or harmonic response, etc.) many times (e.g. in optimization procedures), which leads to inadmissible computational time. In order to reduce these costs and simultaneously take the advantage of FEMs with very accurate and fine meshes, component model reduction methods are proposed. These methods are based on the idea that the motion of a system is written in terms of a superposition of the modes, and afterwards a truncated set of these modes are taken to approximate the response of the system. Model reduction techniques can be applied on a monolithic structure [4] as well as on components (substructures) of a structure, which are assembled then through substructuring techniques to build the full reduced model [1, 12, 19]. In the later case, one should also take the static deformation caused by connecting forces (or displacements) into account. These reduction methods are also called Component Mode Synthesis (CMS) [6].

While the linear reduction techniques are already well established in application, methods in nonlinear framework are actively under consideration. One of the typical kinds of nonlinearities that many lightweight structures face, is geometric nonlinearity, caused by large deflections in the structures. Nonlinear model reduction techniques for monolithic structures are basically classified into direct and indirect methods. In the former one, a closed form equations of motion is required in order to construct the nonlinear reduced order model (NLROM). Whereas, in the later, the NLROM is developed without requiring to deal with the nonlinear tensors of the FEM. In other words, giving a series of input forces (displacements) to an FE Modeling package and getting the requested output displacements (forces), the NLROM is built, without knowing the details of nonlinear terms in the primary FEM [13]. Therefore, the indirect methods (also known as non-intrusive methods) seem to be more efficient in case the structures are developed in commercial finite element (FE) packages (which is the case for most of the industrial applications), since there is no need to build the nonlinear FE tensors of the full structure [3, 5, 16].

M. Karamooz Mahdiabadi (✉) • E. Buchmann • D. Xu • A. Bartl • D.J. Rixen
Technical University of Munich, Boltzmannstraße 15, D-85748, Garching, Germany
e-mail: m.karamooz@tum.de

215

Furthermore, it is very cumbersome to reduce a nonlinear FEM containing a fine mesh with millions of DOFs at once. Alternatively, nonlinear substructuring methods are proposed in order to deal with such models [21–23]. Kuether et al. [10] developed a nonlinear substructuring approach, in which they first reduced each substructure by means of a non-intrusive method. They took two different linear basis in the procedure of indirect reduction of each substructure, namely, free interface modes and Craig-Bampton modes. Furthermore, they checked the accuracy of their NLROMs using Nonlinear Normal Modes (NNMs).

Convergence validation of NLROMs with NNMs facilitates the path of nonlinear model reduction, as time integration of the whole nonlinear structure is no more required [11].

In this paper efficient dynamic substructuring of geometrically nonlinear FEMs is investigated. A set of truncated free interface modes in companion with residual flexibility modes (instead of free interface, solely used in [9]) are taken as a linear basis for each nonlinear substructure to increase the accuracy of NLROMs. Employing this linear basis, the substructures are reduced using an indirect method with input forces (which is also known as Implicit Condensation and Expantion (ICE)). In order to compute the nonlinear coefficients for the NLROMs with ICE, a commercial FE package (Abaqus$^{\circledR}$) is used in this study. Afterwards, the NLROM substructures are coupled using primal assembly. NNMs are employed for the sake of validation of the reduced order model with the primary structure. In order to evaluate the performance of the studied method, a nonlinear FEM is developed in the FE package, divided into two substructures and the proposed method is implemented on it.

19.2 Indirect Nonlinear Model Reduction with Load Input

This section explains briefly the indirect NLROM with applied loads procedure (or ICE method) [3, 5]. Consider a structure (or substructure) with geometrical nonlinearity effect consists of n DOFs. The governing equations of motion (EOMs) in matrix form can be written as

$$M\ddot{u}(t) + Ku(t) + f_{nl}(u(t)) = f(t) \tag{19.1}$$

where M and K are the mass and linear stiffness matrices, respectively. The nonlinear restoring force vector is denoted by $f_{nl}(u(t))$, representing the geometric nonlinear effects caused by large deformations in the system, and $f(t)$ is the external forces applied on the structure (If the EOMs are written for a substructure, $f(t)$ also includes connecting forces imposed by neighboring substructures). In order to reduce the nonlinear FEM, first a proper linear reduced model for the FEM should be constructed. Therefore, the displacement of the system, $u(t)$, is approximated as superposition of a truncated number of modes

$$u(t) = T_{red}\,\eta(t) \tag{19.2}$$

Here, $\eta(t)$ is the reduced generalized coordinate vector, and T_{red} is the transformation matrix, resulting in the reduced number of DOFs in the system. For an elastic FEM with quadratic strain-displacement relation, the nonlinear restoring force due to geometric nonlinearity can be written as a function of quadratic and cubic terms including all combinations of the modal coordinates [2]. Consequently, the NLROM for the investigated structure with EOMs (19.1) is formed as

$$\hat{M}\ddot{\eta} + \hat{K}\eta + \sum_{i=1}^{m}\sum_{j=i}^{m}\alpha(i,j)\eta_i\eta_j + \sum_{i=1}^{m}\sum_{j=i}^{m}\sum_{k=j}^{m}\beta(i,j,k)\eta_i\eta_j\eta_k = T_{red}^T F_c \tag{19.3}$$

where, $\alpha_r(i,j)$ and $\beta_r(i,j,k)$ are the unknown coefficients of the quadratic and cubic terms formed from multiplication of ith and jth or ith, jth and kth modal DOFs, respectively. The number of DOFs of the reduced model is denoted by m. The linear reduced mass and stiffness matrices are denoted by $\hat{M}$ and $\hat{K}$ and are obtained as follows

$$\begin{aligned} \hat{M} &= T_{red}^T M T_{red} \\ \hat{K} &= T_{red}^T K T_{red} \end{aligned} \tag{19.4}$$

In order to compute the unknown coefficient tensors corresponding to the quadratic and cubic terms, a set of static forces are applied on the system (through the FE package) to calculate the corresponding displacements. The static forces are defined using a combination of one, two or three scaling factors as

$$F_c = K(T_{red_k}\eta_k + T_{red_l}\eta_l + T_{red_m}\eta_m) \tag{19.5}$$

here, η_k, η_l and η_m are the scaling factors corresponding to the kth, lth and mth reduced modal coordinates, respectively. The subscripts k, l and m refer to the kth, lth and mth columns of the transformation matrix T_{red}, correspondingly. Gordon et al. [3] introduced these scaling factors to be the forces needed to reach a maximum displacement in the linear system as

$$\eta_q = \frac{w_{q,\text{max}}}{T_{red_{q,\text{max}}}}\omega_q^2 \tag{19.6}$$

where ω_q and $T_{red_{q,\text{max}}}$ are the qth eigenfrequency of the reduced linear system and the maximum translational component in the corresponding mode (column) of the reduction basis. The desired maximum displacement in physical domain is denoted by $w_{q,\text{max}}$. Gordon et al. [3] discussed different criteria to choose the value of $w_{q,\text{max}}$. In this study, this value is chosen to be in the order of the structure's thickness. After importing the defined forces, F_c, as static loads in the FE package (i.e. Abaqus® in this work), the corresponding displacements, u_c, can be computed. These displacements are then transformed into the modal coordinate, η_c, as

$$(T_{red}^T M T_{red})^{-1} T_{red}^T M u_c = \eta_c \tag{19.7}$$

Now, applying several static forces to the FE package and solving for the corresponding displacements, an overdetermined problem should be solved to estimate the unknown stiffness coefficients. Therefore, the following static equation for the rth modal coordinate becomes:

$$\sum_{i=1}^{m}\sum_{j=i}^{m}\alpha_r(i,j)\eta_i\eta_j + \sum_{i=1}^{m}\sum_{j=i}^{m}\sum_{k=j}^{m}\beta_r(i,j,k)\eta_i\eta_j\eta_k = T_{red}^T F_c - \hat{K}_{rq}\eta_q \tag{19.8}$$

Afterwards, the reduced EOMs are reformulated in the form proposed by [14]

$$\hat{M}\ddot{\eta} + \hat{K}\eta + \frac{1}{2}N_1(\eta)\,\eta + \frac{1}{3}N_2(\eta)\,\eta = T_{red}^T f(t) \tag{19.9}$$

where $N_1(\eta)$ and $N_2(\eta)$ are Jacobian matrices constructed from quadratic and cubic terms, respectively.

19.3 Component Mode Synthesis with Residual Flexibility Modes

19.3.1 Rubin Reduction Basis

Consider the equations of motion for the undamped substructure, s, with n DOFs as

$$M^{(s)}\ddot{u}(t)^{(s)} + K^{(s)}u(t)^{(s)} = f(t)^{(s)} + g(t)^{(s)} \tag{19.10}$$

where, $M^{(s)}$ and $K^{(s)}$ are mass and stiffness matrices of the substructure. The acceleration and displacement vectors are shown by $\ddot{u}(t)^{(s)}$, and $u(t)^{(s)}$, respectively. The external force vector applied on the substructure is denoted by $f(t)^{(s)}$ and $g(t)^{(s)}$ is the interface force vector imposed by neighboring substructures.

An efficient way for model reduction of structures with substructuring is approximating the motion of each substructure as a truncated number of free interface modes in addition to a static deformation caused by connecting forces from neighboring substructures [12, 17, 19].

$$u^{(s)} \approx u_{static}^{(s)} + \sum_{i=1}^{k-r}\phi_{free,i}^{(s)}\,\eta_{free,i}^{(s)} \tag{19.11}$$

Here, $\phi_{free,i}^{(s)}$ is the ith vibration mode when the interface DOFs are left free, and $\eta_{free,i}^{(s)}$ is the corresponding modal coordinate. The total number of modes kept in the substructure and number of Rigid Body (RB) modes are represented with k and r, correspondingly. Equation (19.10) implies that if RB modes exist in the system, they should be included in the static deformation $u_{static}^{(s)}$. Therefore, in order to represent the static deformation of the substructure s caused by neighboring substructures, $u_{static}^{(s)}$ is introduced as follows

$$u_{static}^{(s)} = \Psi_{RFA}^{(s)} g^{(s)} + \Phi_{RB}^{(s)} \eta_{RB}^{(s)} \tag{19.12}$$

where $\Phi_{RB}^{(s)}$ and $\Psi_{RFA}^{(s)}$ are matrices including RB and Residual Flexibility Attachment (RFA) modes, respectively. The generalized coordinate vector corresponding to RFA modes is denoted by $\eta_{RB}^{(s)}$.

In order to obtain Residual Flexibility Attachment modes, first the attachment modes are defined as the displacement vector caused by applying a unit force at an interface DOF, u_b. Therefore, the columns of the flexibility matrix $G^{(s)}$ containing the attachment modes are obtained as

$$G^{(s)} = (K^{(s)})^+ \tag{19.13}$$

The superscript $+$ is the generalized inverse (or pseudo-inverse) operation, implying the fact that if the substructure has RB modes, the stiffness matrix $K^{(s)}$ is singular. Afterwards, the RFA modes are defined as

$$\Phi_{RFA}^{(s)} = (G^{(s)} - \sum_{j=1}^{r-m} \frac{\phi_{free,j}^{(s)} \phi_{free,j}^{(s)^T}}{\omega_j^2}) B^{(s)} \tag{19.14}$$

where $B^{(s)}$ is the signed Boolean matrix, specifying interface DOFs of the substructure s. The RFA modes are the static deflection of the deleted modes (which are truncated in the substructure) due to the unit force at each interface DOF. Now, having the RFA modes, $\Psi_{RFA}^{(s)}$, the Eq. (19.12) is substituted into (19.11) giving the approximation for displacement vector $u^{(s)}$

$$u^{(s)} \approx \Psi_{RFA}^{(s)} g^{(s)} + \Phi_{RB}^{(s)} \eta_{RB}^{(s)} + \Phi_{free}^{(s)} \eta_{free}^{(s)} \tag{19.15}$$

In order to provide the assembly of substructures with interface DOFs, Eq. (19.15) is pre-multiplied by $B^{(s)^T}$ and solved for the interface forces $g^{(s)}$:

$$u_b^{(s)} = B^{(s)} u^{(s)} = B^{(s)} (\Psi_{RFA}^{(s)} g^{(s)} + \Phi_{RB}^{(s)} \eta_{RB}^{(s)} + \Phi_{free}^{(s)} \eta_{free}^{(s)}) = \Psi_{RFA,b}^{(s)} g^{(s)} + \Phi_{RB,b}^{(s)} \eta_{RB}^{(s)} + \Phi_{free,b}^{(s)} \eta_{free}^{(s)} \tag{19.16}$$

$$g^{(s)} = \Psi_{RFA,b}^{+}{}^{(s)} (u_b^{(s)} - \Phi_{RB,b}^{(s)} \eta_{RB}^{(s)} - \Phi_{free,b}^{(s)} \eta_{free}^{(s)}) \tag{19.17}$$

where the subscript b for matrices denote they are pre-multiplied by $B^{(s)^T}$, and therefore, the part of the matrices corresponding the interface DOFs are included. The next step is to substitute (19.17) in (19.15) and one can obtain the final reduction basis for the internal DOFs, $u_i^{(s)}$ as [19, 20]

$$u_i^{(s)} = \Psi_{RFA,i}^{(s)} \Psi_{RFA,b}^{+}{}^{(s)} u_b^{(s)} + (\Phi_{RB,i}^{(s)} - \Psi_{RFA,i}^{(s)} \Psi_{RFA,b}^{+}{}^{(s)} \Phi_{RB,b}^{(s)}) \eta_{RB}^{(s)} +$$
$$(\Phi_{free,i}^{(s)} - \Psi_{RFA,i}^{(s)} \Psi_{RFA,b}^{+}{}^{(s)} \Phi_{free,b}^{(s)}) \eta_{free}^{(s)} \tag{19.18}$$

The reduction basis can also be written in the following matrix form

$$u^{(s)} = \begin{bmatrix} u_i^{(s)} \\ u_b^{(s)} \end{bmatrix} = T_{red} \begin{bmatrix} \eta_{free}^{(s)} \\ \eta_{RB}^{(s)} \\ u_b^{(s)} \end{bmatrix} \tag{19.19}$$

where T_{red} is the (Rubin) reduction basis by taking the Residual Flexibility modes into account and is obtained as

$$T_{red} = \begin{bmatrix} \Phi_{free,i}^{(s)} - \Psi_{RFA,i}^{(s)} \Psi_{RFA,b}^{+}{}^{(s)} \Phi_{free,b}^{(s)} & \Phi_{RB,i}^{(s)} - \Psi_{RFA,i}^{(s)} \Psi_{RFA,b}^{+}{}^{(s)} \Phi_{RB,b}^{(s)} & \Psi_{RFA,i}^{(s)} \Psi_{RFA,b}^{+}{}^{(s)} \\ 0 & 0 & I \end{bmatrix} \qquad (19.20)$$

Finally, in order to compute the reduced mass and stiffness matrices, $\hat{M}^{(s)}$ and $\hat{K}^{(s)}$, the obtained reduced basis (19.20) should be substituted in the expressions of Eq. (19.4).

19.3.2 Primal Assembly

The final step to achieve the whole NLROM, is to assemble the NLROMs of all substructures. The assembly of substructures can be performed using either interface displacements or forces. If the substructures are coupled by satisfying first the compatibility boundary conditions the assembly is called *primal*. In contrast, if the equilibrium boundary conditions are imposed to the assembly procedure first, and the compatibility is satisfied alongside the EOMs, the assembly is called *dual* [8]. This study only considers the primal assembly, which is also called Component Modes Synthesis (CMS). Considering the assembly problem of two reduced nonlinear substructures s_1 and s_2, the EOMs of the substructures in a block diagonal form is written as

$$\begin{bmatrix} \hat{M}^{(s_1)} & 0 \\ 0 & \hat{M}^{(s_2)} \end{bmatrix} \begin{Bmatrix} \eta^{(s_1)} \\ \eta^{(s_2)} \end{Bmatrix} + \begin{bmatrix} \hat{K}^{(s_1)} & 0 \\ 0 & \hat{K}^{(s_2)} \end{bmatrix} \begin{Bmatrix} \eta^{(s_1)} \\ \eta^{(s_2)} \end{Bmatrix} + \frac{1}{2} \begin{bmatrix} N_1^{(s_1)}(\eta^{(s_1)}) & 0 \\ 0 & N_1^{(s_2)}(\eta^{(s_2)}) \end{bmatrix} \begin{Bmatrix} \eta^{(s_1)} \\ \eta^{(s_2)} \end{Bmatrix} +$$

$$\cdots \frac{1}{3} \begin{bmatrix} N_2^{(s_1)}(\eta^{(s_1)}) & 0 \\ 0 & N_2^{(s_2)}(\eta^{(s_2)}) \end{bmatrix} \begin{Bmatrix} \eta^{(s_1)} \\ \eta^{(s_2)} \end{Bmatrix} = \begin{Bmatrix} T^{(s_1)^T} \{f(t)^{(s_1)} + g^{(s_1)}\} \\ T^{(s_2)^T} \{f(t)^{(s_2)} + g^{(s_2)}\} \end{Bmatrix} \qquad (19.21)$$

then the compatibility condition is expressed by

$$B\eta = 0 \qquad (19.22)$$

where B is the signed Boolean matrix, specifying the corresponding connecting DOFs (for conforming meshes) for all substructures. The equilibrium boundary condition is then defined as

$$L^T g = 0 \qquad (19.23)$$

Here, L is the Boolean localization matrix which puts the Substructures' local DOFs into the global fashion of DOFs

$$\eta = L\eta_c \qquad (19.24)$$

The subscript c denotes the coupled global set of DOFs. It is shown in [8] that the localization matrix L is the null space of the B matrix. In other words

$$\begin{aligned} BL &= 0 \\ L^T B^T &= 0 \end{aligned} \qquad (19.25)$$

Substituting Eq. (19.24) into (19.22), the compatibility condition is satisfied first

$$BL\eta_c = 0 \qquad (19.26)$$

Finally, substituting Eq. (19.24) into (19.21) and pre-multiplying (19.21) by L^T lead to the assembled EOMs as

$$L^T \begin{bmatrix} \hat{M}^{(s_1)} & 0 \\ 0 & \hat{M}^{(s_2)} \end{bmatrix} L \ddot{\eta}_c + L^T \begin{bmatrix} \hat{K}^{(s_1)} & 0 \\ 0 & \hat{K}^{(s_2)} \end{bmatrix} L \eta_c + \frac{1}{2} L^T \begin{bmatrix} N_1^{(s_1)}(\eta^{(s_1)}) & 0 \\ 0 & N_1^{(s_2)}(\eta^{(s_2)}) \end{bmatrix} L \eta_c +$$

$$\dots \frac{1}{3} L^T \begin{bmatrix} N_2^{(s_1)}(\eta^{(s_1)}) & 0 \\ 0 & N_2^{(s_2)}(\eta^{(s_2)}) \end{bmatrix} L \eta_c = L^T \left\{ \begin{matrix} T^{(s_1)^T} \left\{ f(t)^{(s_1)} + g^{(s_1)} \right\} \\ T^{(s_2)^T} \left\{ f(t)^{(s_2)} + g^{(s_2)} \right\} \end{matrix} \right\} \quad (19.27)$$

19.4 Validation

The accuracy of the NLROM depends strongly on the modes included in the reduction basis as well as the external load applied to the model when one is performing ICE. Therefore, they have to be chosen very carefully. Since there's no concrete standard about how these factors can be properly chosen so far, a validation of the NLROM model is necessary. The common procedure to validate NLROMs, is to compare the time integration of a certain DOFs of them to a given load with the ones of the full model. This method brings two obvious shortcomings. On the one hand, the computational cost can be prohibitively expensive when implementing it on models with many DOFs. On the other hand, it only validates the model at one or few load levels or response amplitudes.

Instead, Kuether et al. used Norlinear Normal Modes (NNMs) to validate NLROM in [11]. NNMs provide an insight into how the system responds to different load scenarios and can capture a wide range of response amplitudes experienced by the structure, which makes it the ideal metric for the validation of the NLROM. NNMs were first defined by Rosenberg in [18] as a periodic motion of the system, in which all DOFs reach the equilibrium position at the same time. The definition was further extended by Kerschen et al. in [7] as *not necessarily synchronous periodic responses*. Although orthogonality and modal superposition are no longer applicable for NNMs, they show other unique properties compared to the linear normal modes, such as modal interactions, bifurcation, and frequency-energy dependency.

Kerschen proposed to compute NNMs with numerical continuation methods in [15]. In order to find the periodic motion of the system, a shooting function is defined to indicate the difference between the system motion at $t = 0$ and $t = T$. The free response of the nonlinear system to a prescribed initial condition is only then periodic, when the shooting function is smaller than a given tolerance. In this way, the boundary value problem is transferred into initial value problem that can be solved with a shooting method. The branch of an NNM is followed with the pseudo-arclength algorithm proposed by Peeters et al. [15]. Prediction and correction steps are used to find the periodic solution, where Jacobian matrices are employed in prediction and correction steps and play a huge roll in computational efficiency.

The further development of this method by Kuether et al. in [11] not only improved the efficiency, more importantly, they also made it feasible to compute the NNMs of models built in commercial FE package. The Applied Modal Force method (AMF) defines the initial displacement as the nonlinear static response of the system to a prescribed external force, which is a weighted truncated subset of linear modes shapes. The weighting factors, termed as modal force amplitude, are to be determined with pseudo-arclength continuation. The individual variables are thus reduced from n to the number of truncated weighting factors m. In this way, the computational burden caused by Jacobian matrices, is largely reduced. Only one mode is used to define the initial displacement at first. The contribution of rest modes is monitored, while the energy in the system rises and corresponding modes will be activated if necessary.

In this work, the NNMs of the full order model were computed with AMF, while those of the reduced model with the method described in [15]. Due to its frequency-energy dependence, the NNMs are represented in Frequency-Energy Plot (FEP) as in [7], where the fundamental frequency of the periodic motions is plotted on the vertical axis, and the total energy in the system, including kinetic and potential energy, is plotted on the horizontal axis. Each point on an NNM curve corresponds to a periodic solution of the equation of motion.

19.5 Numerical Example

In order to evaluate the performance of the proposed method on a geometrically nonlinear structure, the two simply supported beams (also shown in Fig. 19.1) – the same as the ones studied in [10] – are investigated. Table 19.1 shows the parameters used to build the model of the substructures in Abaqus®.

The NLROMs of the substructures one and two are developed using the ICE method explained in Sect. 19.2. In order to have a more accurate linear reduction basis (compare to the free interface modes used in [9]), the method of Rubin [19] is employed. Namely, a set of truncated free interface modes in addition to the Residual Flexibility Attachment modes are taken for each substructure to span the effect of the connecting forces imposed by neighboring structures. The number of free interface modes kept for substructures one and two are 3 (out of 119 modes) and 2 (out of 80 modes), respectively.

Furthermore, the developed NLROMs of the substructures are coupled using the primal CMS assembly approach (Sect. 19.3.2) and the NNMs of the assembled structure is computed with Shooting and Pseudo-Arclength Continuation approaches developed in [15]. For the sake of efficient validation of the achieved NLROM, the NNMs of the whole geometrical nonlinear structure are also computed with the AMF method of Kuethers et al. [11]. The first computed NNM for NLROM as well as the corresponding one for the full beam is shown in Fig. 19.2. As it can be seen in this figure, until a certain energy range, the NNM computed from the NLROM converges well to the one of the full model. However, for higher energies, the difference between the two curves becomes more obvious. This can be due to the fact that quite a few number of modes (5 out of 199) are taken into account to develop the NLROM. The NNMs comparison of the NLROM with the full model for higher modes (NNMs 2, 3 and 4) is shown in Fig. 19.3 In this study, the NNMs of higher modes are only compared for one of the branches (the subbranches of the NLROM are not plotted). As it is shown in Fig. 19.3 the NNMs of the NLROM match to the ones of full model which expresses the proper performance of the proposed method.
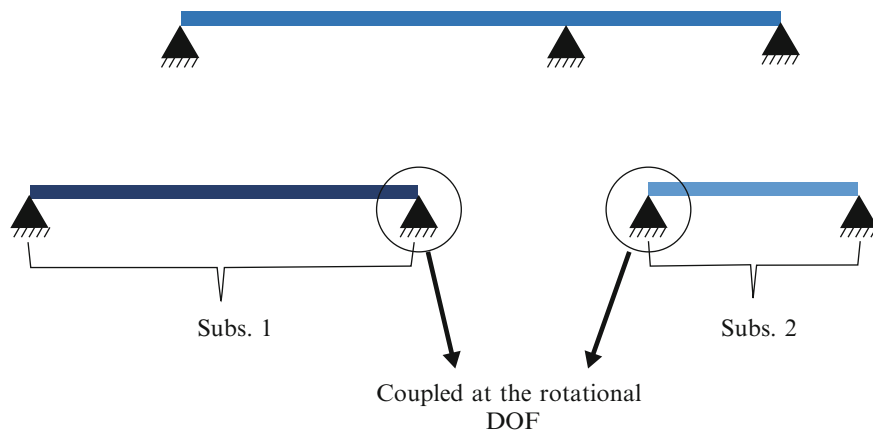
Fig. 19.1 Two simply supported beams coupled at the rotational DOF

Table 19.1 Properties of investigated model

		Substructure 1	Substructure 2
Geometry	Length	229 mm	152 mm
	Width	12.7 mm	12.7 mm
	Heigth	0.787 mm	0.787 mm
Material	Mass density	7870 kg/m³	7870 kg/m³
	Young's modulus	204.8 GPa	204.8 GPa
	Poisson's ratio	0.28	0.28
Discretization	Element-type	Euler-Bernoulli ABAQUS B31	Euler-Bernoulli ABAQUS B31
	Number of elements	40	27
	Number of degrees of freedom	119	80
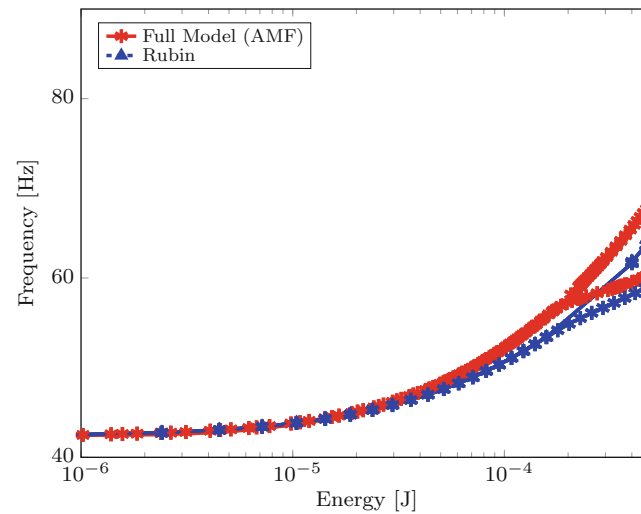
Fig. 19.2 Comparison of the first NNMs. The *red circle curve* is the full model NNM calculated with AMF, the *blue triangle* is the NNM of the NLROM with five modes (up to 500 Hz)
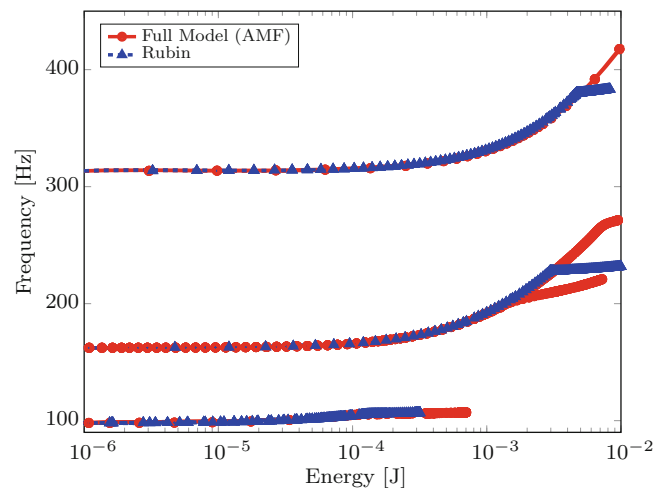
Fig. 19.3 Comparison of the second to forth NNM. The *red circles curve* are the full model NNMs calculated with AMF, the *blue triangles* are the NNMs of the NLROM with five modes (up to 500 Hz)

19.6   Conclusion

This work studies model reduction and substructuring of geometrically nonlinear finite element models proposing the Rubin reduction basis. Namely, a set of truncated free interface modes in addition to residual flexibility attachment modes are taken as a linear basis for each substructure. Nonlinear coefficients of the reduced order model due to large deflections are compute employing the non-intrusive method of Implicit Condensation and Expansion, which is efficient in case the nonlinear finite element model (FEM) is only available in a commercial FE package. Furthermore, the nonlinear reduced order substructures are assembled using Component Mode Synthesis. For the sake of validation of the nonlinear reduced order model developed with the aforementioned approach, the nonlinear normal modes (NNMs) of the primal structure and the reduced model are compared. In fact using NNMs as a convergence check let us avoid expensive time integration of the whole nonlinear structure for validation. Finally, the procedure is implemented on a geometrically nonlinear FEM divided into two substructures. Taking just 2.5% of the linear modes (5 modes out of 199 modes), the NNMs resulted from substructuring converged to the NNMs of the whole model, expressing the efficiency of the proposed method.

References

1. Craig, R.-R., Bampton, M.C.C.: Coupling of substructures for dynamics analyses. AIAA J. **6**(7), 1313 (1968). doi:10.2514/3.4741, ISSN:0001-1452

2. de Borst, R., Crisfield, M., Remmers, J., Verhoosel, C.: Non-Linear Finite Element Analysis of Solids and Structures, 2nd edn. (2012). doi:10.1002/9781118375938

3. Gordon, R.W., Hollkamp, J.J.: Reduced-order models for acoustic response prediction. Technical report. Air Force Research Laboratory AFRL-RB-WP-TR-2011-3040, pp. 1–224 (2011)

4. Guyan, R.J.: Reduction of stiffness and mass matrices. AIAA J. **3**(2), 380–380 (1965). doi:10.2514/3.2874

5. Hollkamp, J.J., Gordon, R.W.: Reduced-order models for nonlinear response prediction: implicit condensation and expansion. J. Sound Vib. **318**(4–5), 1139–1153 (2008). doi:10.1016/j.jsv.2008.04.035

6. Hurty, W.: Vibrations of structural systems by component mode synthesis. J. Eng. Mech. Div. **86**(4), 51–70 (1960). ISSN:0044-7951

7. Kerschen, G., Peeters, M., Golinval, J.-C., Vakakis, A.F.: Nonlinear normal modes, Part I: a useful framework for the structural dynamicist. Mech. Syst. Signal Process. **23**(1), 170–194 (2009)

8. Klerk, D.D., Rixen, D.J., Voormeeren, S.N.: General framework for dynamic substructuring: history, review and classification of techniques. AIAA J. **46**(5), 1169–1181 (2008). doi:10.2514/1.33274, ISSN:0001-1452

9. Kuether, R.J.: Nonlinear modal substructuring of geometrically nonlinear finite element models. Ph.D. thesis, Wisconsin-Madison, p. 181 (2014)

10. Kuether, R.J., Allen, M.S., Hollkamp, J.J.: Modal substructuring of geometrically nonlinear finite-element models. AIAA J. **54**(2), 1–12 (2015). doi:10.2514/1.J054036, ISSN:0001-1452

11. Kuether, R.J., Deaner, B.J., Hollkamp, J.J., Allen, M.S.: Evaluation of geometrically nonlinear reduced-order models with nonlinear normal modes. AIAA J. **53**(11), 3273–3285 (2015). doi:10.2514/1.J053838, ISSN:0001-1452

12. MacNeal, R.H.: A hybrid method of component mode synthesis. Comput. Struct. **1**(4), 581–601 (1971). doi:10.1016/0045-7949(71)90031-9

13. Mignolet, M.P., Przekop, A., Rizzi, S.A., Spottswood, S.M.: A review of indirect/non-intrusive reduced order modeling of nonlinear geometric structures. J. Sound Vib. **332**(10), 2437–2460 (2013). doi:10.1016/j.jsv.2012.10.017, ISSN:10958568

14. Nash, M.: Nonlinear structure dynamics by finite element modal synthesis. Ph.D. thesis, Imperial College London (1977)

15. Peeters, M., Viguié, R., Sérandour, G., Kerschen, G., Golinval, J.-C.: Nonlinear normal modes, Part II: toward a practical computation using numerical continuation techniques. Mech. Syst. Signal Process. **23**(1), 195–216 (2009)

16. Perez, R., Wang, X.Q., Mignolet, M.P.: Nonintrusive structural dynamic reduced order modeling for large deformations: enhancements for complex structures. J. Comput. Nonlinear Dyn. **9**, 031008 (2014). doi:10.1115/1.4026155, ISSN:1555-1415

17. Rixen, D.J.: A dual Craig-Bampton method for dynamic substructuring. J. Comput. Appl. Math. **168**(1–2), 383–391 (2004). doi:10.1016/j.cam.2003.12.014

18. Rosenberg, R.M.: Normal modes of nonlinear dual-mode systems. J. Appl. Mech. **27**(2), 263–268 (1960)

19. Rubin, S.: Improved component-mode representation for structural dynamic analysis. AIAA J. **13**(8), 995–1006 (1975). doi:10.2514/3.60497, ISSN:0001-1452

20. van der Valk, P.L.C.: Model reduction and interface modeling in dynamic substructuring. Master's thesis, Delft University of Technology, p. 177 (2010)

21. Wenneker, F., Tiso, P.: A substructuring method for geometrically nonlinear structures. In: Allen, M., Mayes, R., Rixen, D. (eds.) Dynamics of Coupled Structures, Volume 1: Proceedings of the 32nd IMAC, A Conference and Exposition on Structural Dynamics, 2014, pp. 157–165. Springer International Publishing, Cham (2014). doi:10.1007/978-3-319-04501-6_14

22. Wu, L., Tiso, P.: Nonlinear model order reduction for flexible multibody dynamics: a modal derivatives approach. Multibody Syst. Dyn. **36**(4), 405–425 (2016). doi:10.1007/s11044-015-9476-5

23. Wu, L., Tiso, P., Keulen, F.V.: A modal derivatives enhanced Craig-Bampton method for geometrically nonlinear structural dynamics. In: Proceedings of ISMA 2016 – International Conference on Noise and Vibration Engineering, Leuven, pp. 3615–3524 (2016)

Chapter 20
Optimal Transformation of Frequency Response Functions on Interface Deformation Modes

M. Häußler and Daniel Jean Rixen

Abstract Frequency based dynamic substructuring (FBS) allows to predict the dynamic behavior of a complex system where neither building a physical prototype of the assembled system, nor possessing a detailed numerical model of all substructures is required. A task that frequently arises in engineering practice when developing a product containing many supplier parts. However, in the experimental realm, modeling the interface connection between two substructures is not as straightforward as in numerical analysis. The consideration of rotational degrees of freedom (rdof) on the interface seems to be crucial for accurate results, but no common procedure has been established yet. By projecting measured sensor data on *interface deformation modes* (IDMs) it is possible to consider rdof as well as filtering out uncorrelated measurement noise. The transformation of a measured frequency response function (FRF) matrix on some generalized IDMs has recently been derived by directly using Moore-Penrose pseudoinverses. The transformation process can also be seen as a minimization procedure, e.g. as simple least squares for the displacements and a convex optimization for the forces.

This contribution derives the pseudoinverses starting from this minimization point of view, where the engineer is free to choose the quantity to be minimized. From this interpretation, some suggestions for including more engineering judgment in the transformation are made (either gained during testing practice, from measurement variances or mechanical energy minimization principles). We also show that the coupling of transformed FRF matrices effectively corresponds to a weakening of the interface compatibility conditions.

Thereby, we hope to give some insight in the meaning of the weighting matrices involved in the transformation, and provide a framework for deriving improved coupling methods in the future.

Keywords Experimental dynamic substructuring • Virtual point transformation • Optimal projection • Interface weakening

Nomenclature:

$\mathbf{u}, \mathbf{f}$	measured displacements/forces	$\mathbf{T}$	transformation matrix
$\mathbf{q}, \mathbf{m}$	generalized displacements/forces	$\boldsymbol{\Sigma}$	covariance matrix
$\mathbf{Y}, \mathbf{Z}$	admittance/impedance matrix	$_I\mathbf{e}$	unit vector measured in coord. system I
$\mathbf{B}$	signed Boolean matrix	$\tilde{\mathbf{f}}_2$	equivalent interface forces
$\boldsymbol{\lambda}$	Lagrange multiplier vector	$(\star)^A$	quantity pertaining to substructure A
$\mathbf{R}$	interface deformation mode matrix	$(\star)^{A\|B}$	uncoupled block notation of A and B
$\mathbf{W}$	weighting matrix	$(\star)^{AB}$	coupled quantity of A and B
$\boldsymbol{\mu}$	residual in displacement transformation	$(\star)_1$	pertaining to set of dofs 1
$\Phi(\star)$	cost function	$(\star)_{u/f}$	pertaining to disp./force transformation

M. Häußler (✉)

Faculty of Mechanical Engineering, Institute of Applied Mechanics, Technische Universität München, Boltzmannstr. 15, 85748, Garching, Germany
e-mail: michael.haeussler@tum.de

D.J. Rixen
Technical University of Munich, Boltzmannstraße 15, D-85748, Garching, Germany
e-mail: rixen@tum.de

| DS | dynamic substructuring | FBS | frequency based substructuring |
FRF	frequency response function	IDM	interface deformation mode
VPT	virtual point transformation	SEREP	system equvalent reduction and expansion
EMPC	equivalent multiple point connection	dof	degree of freedom
CMS	component mode synthesis	rdof	rotational degree of freedom

20.1 Introduction

Dynamic Substructuring (DS) has become a well accepted method that provides a framework for numerically assembling subcomponents, developed by different design teams, and predict the dynamic behavior of the complete product. Variants for coupling in different domains (e.g. the physical-, modal-, frequency -domain, etc.) can be derived straight forward [1] and can equivalently be used for decoupling of structures [2, 3]. The frequency based substructuring (FBS) method was first published by Jetmundsen [4] and is well suited for experimental dynamics (although similar methods where proposed earlier [5]). However, the definition of the interface coupling in experimental DS remains challenging. On the one hand the measured degrees of freedom (dofs) on either side of the interface are often non-matching due to practical instrumentation problems (see substructure A and B in Fig. 20.1). They can thus not be coupled by simply enforcing equality in each dof, as in numerical analysis.

Another problem involves measuring and exciting rotational degrees of freedom (rdof) on the interface. Sensors that can actually measure rdof have been discussed for a long time and can even be found in textbooks [6, p. 166ff] and [7, p. 197ff]. However, rotational acceleration sensors are still exotic and not commonly available. Nevertheless, including rdof in the coupling process has been shown to be crucial for accurate results [8, 9].

Therefore, different methods have been developed to implicitly measure and include rotations in the coupling. A large class of methods tries to infer the rotational motion on the interface by using global vibration modes of the substructures to be coupled. They are thus closely related to the component mode synthesis (CMS) techniques, well known from numerical modeling [10]. The '*system equivalent reduction and expansion*' (SEREP) procedure [11] is an elegant way to infer full motion data of the structure (including rdof) by measuring with translational sensors only at a few measurement points. An application to experimental DS can be found in [12]. An advantage of these techniques is that the mode identification processes has a 'smoothing effect' on the frequency response functions that are being coupled, thus avoiding many of the numerical instability issues that are common in FBS [13]. However, these methods have to find the global modes of the structure either by building a finite element model or performing an experimental modal analysis. In order to account for the effect of higher order modes in the frequency range of interest, one is usually extending the frequency range to include some of those higher order modes in the model and add a residual flexibility term for even higher modes [9].

For complex systems (e.g. mechatronic components in a car), the modal density might be too high for effectively performing substructuring methods based on global vibration modes and a frequency based approach is preferable. One advantage of directly using frequency response functions (FRFs) is that the measurement data already contains residual
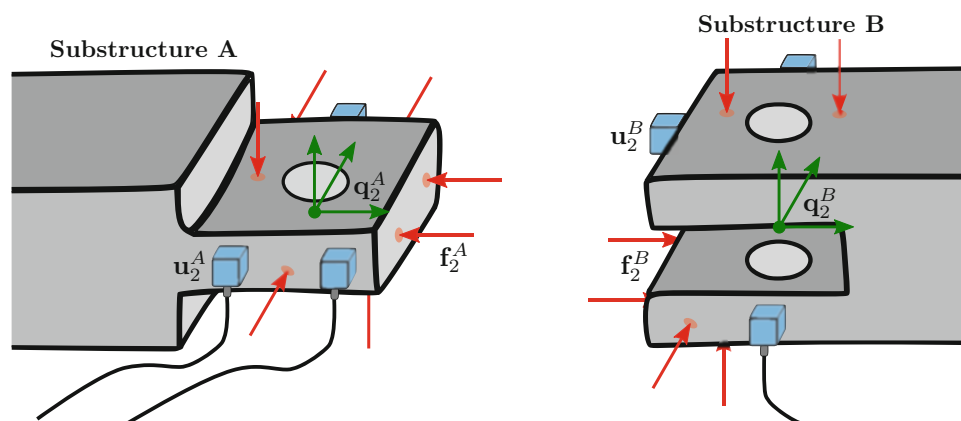
Fig. 20.1 Assembly problem in experimental dynamic substructuring. Sensors $\mathbf{u}_2$ and force inputs $\mathbf{f}_2$ on either side of the interface are non-matching

terms from higher order modes. To account for rdof implicitly some methods have used multiple connection points on the interface that are simultaneously coupled [9, 14], which has been called '*equivalent multiple point connection*' (EMPC) [8]. However, coupling too many points can result in an overdetermination of the interface coupling equations, making some of the equations almost redundant and cause numerical instabilities. Additionally the direct use of experimentally obtained data in the FRFs inherently causes numerical instabilities [13]. An interesting depiction of different methods, their problems and remedies can be found in the companion publications [2, 14], where it was found that enforcing the coupling in only a 'weak' least squares sense in many (modal) dofs, can significantly improve the substructuring results.

A recent approach that can be seen as a combination of the CMS and EMPC methods above, is using '*interface deformation modes*' (IDMs) which aren't global vibration modes but rather kinematic assumptions of the local deformation behavior directly at the interface. The IDMs can be constructed without the need of building a finite element model (which might be impossible due to the lack of information for supplier parts) or performing an experimental modal analysis (which might be infeasible due to a high modal density). However, the transformation of measured FRFs on IDMs can also provide some numerical smoothing if the transformation is overdetermined. This method has first been used in [8] with driving point FRFs and was extended in [15] to allow for different positions in sensors and force impacts, which is making it more feasible experimentally (see Fig. 20.1). In [16] the transformation matrices necessary for transforming the measured FRF matrices on generalized IDMs where derived using Moore-Penrose pseudoinverses, that allow for a different weighting of physical dofs in the transformation on the IDMs. In this contribution we will derive the transformation matrices anew from a minimization point of view and show how the weighting matrices can be utilized to further improve the transformation and coupling process. We will additionally show that the transformation of the physical dofs also has a 'weakening' effect and is enforcing the compatibility only in a 'least squares' sense.

20.2   Theory

This section gives a short review on how to couple the admittances of two substructures with matching dofs. Subsequently the transformation of measured sensor signals $\mathbf{u}_2$ on generalized IDMs $\mathbf{q}$, and the expansion of generalized forces $\mathbf{m}$ on the measured force impacts $\mathbf{f}_2$ is derived from the minimization of a cost function. This cost function can be chosen to include some optimality criterion. Concluding, the effect of coupling the transformed $\mathbf{q}$, $\mathbf{m}$ of both substructures, instead of coupling the measured quantities $\mathbf{u}_2$, $\mathbf{f}_2$ directly, is shown to act as a *weakening* of the interface compatibility conditions.

20.2.1   *Frequency Based Substructuring*

Frequency based substructuring (FBS) aims at deriving the admittance of an assembled system $\mathbf{Y}^{AB}$ from the separate admittances of two subsystems $\mathbf{Y}^A$ and $\mathbf{Y}^B$. Consider the situation depicted in Fig. 20.2. The admittances of both subsystems $\mathbf{Y}^A$ and $\mathbf{Y}^B$ are known, where their dofs are grouped into some internal dofs $((\star)_1^A$ and $(\star)_3^B)$ and some common dofs on the interface $((\star)_2^A$ and $(\star)_2^B)$. Displacements are denoted by $\mathbf{u}$, external forces in the respective dofs are denoted by $\mathbf{f}$. The admittance of the *uncoupled* substructures can be written in block diagonal form $\mathbf{Y}^{A|B}$. The following equation is the starting point for coupling $\mathbf{Y}^A$ and $\mathbf{Y}^B$, but also aims at clarifying the notation in verbose and compact form:
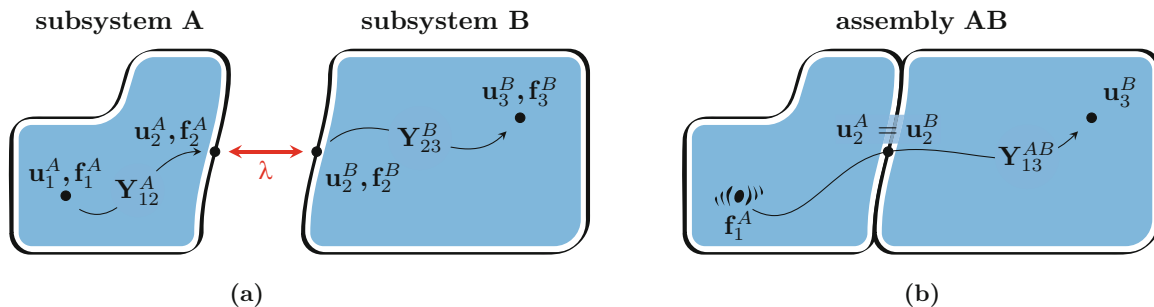
Fig. 20.2 The substructuring problem [17]. (**a**) Admittances of uncoupled subsystems A and B. (**b**) Admittance of coupled assembly AB

$$\mathbf{Y}^{A|B}\,(\mathbf{f}+\mathbf{g}) = \begin{bmatrix} \mathbf{Y}^A & \mathbf{0} \\ \mathbf{0} & \mathbf{Y}^B \end{bmatrix}\left(\begin{bmatrix} \mathbf{f}^A \\ \mathbf{f}^B \end{bmatrix} + \begin{bmatrix} \mathbf{g}^A \\ \mathbf{g}^B \end{bmatrix}\right) = \begin{bmatrix} \mathbf{Y}^A_{11} & \mathbf{Y}^A_{12} & \mathbf{0} & \mathbf{0} \\ \mathbf{Y}^A_{21} & \mathbf{Y}^A_{22} & \mathbf{0} & \mathbf{0} \\ \mathbf{0} & \mathbf{0} & \mathbf{Y}^B_{22} & \mathbf{Y}^A_{23} \\ \mathbf{0} & \mathbf{0} & \mathbf{Y}^B_{32} & \mathbf{Y}^A_{33} \end{bmatrix}\left(\begin{bmatrix} \mathbf{f}^A_1 \\ \mathbf{f}^A_2 \\ \mathbf{f}^B_2 \\ \mathbf{f}^B_3 \end{bmatrix} + \begin{bmatrix} \mathbf{0} \\ \mathbf{g}^A_2 \\ \mathbf{g}^B_2 \\ \mathbf{0} \end{bmatrix}\right) = \begin{bmatrix} \mathbf{u}^A_1 \\ \mathbf{u}^A_2 \\ \mathbf{u}^B_2 \\ \mathbf{u}^B_3 \end{bmatrix} = \mathbf{u}, \quad (20.1)$$

where $\mathbf{g}$ denotes the yet unknown reaction forces acting between the two substructures in the coupled state. When coupled, the two substrucures have to fulfill *continuity* on the interface ($\mathbf{u}^A_2 - \mathbf{u}^B_2 = \mathbf{0}$). The reaction forces $\mathbf{g}$ needed for achieving continuity fulfill *actio est reactio*, i.e. they are equal in magnitude but have opposite signs ($\mathbf{g}^A_2 = -\mathbf{g}^B_2$). They can thus be denoted by a single vector of reaction forces $\boldsymbol{\lambda}$. These conditions result in the following set of equations:

$$\mathbf{Y}^{A|B}\,(\mathbf{f} + \underbrace{\mathbf{B}^T\boldsymbol{\lambda}}_{=\mathbf{g}}) = \mathbf{u}, \quad (20.2)$$

$$\mathbf{B}\mathbf{u} = \mathbf{0} \qquad\qquad \text{where} \quad \mathbf{B} = \begin{bmatrix} \mathbf{0} & \mathbf{I} & -\mathbf{I} & \mathbf{0} \end{bmatrix}, \quad (20.3)$$

so that the reaction forces in Eq. (20.2) automatically fulfill *actio est reactio* and the statement in Eq. (20.3) enforces *continuity*. The matrix $\mathbf{B}$ is commonly called a 'signed Boolean matrix'. Inserting Eq. (20.2) in Eq. (20.3) and solving for $\boldsymbol{\lambda}$:

$$\boldsymbol{\lambda} = -\underbrace{\left(\mathbf{B}\mathbf{Y}^{A|B}\mathbf{B}^T\right)^{-1}}_{Z_{int}}\underbrace{\mathbf{B}\mathbf{Y}^{A|B}\mathbf{f}}_{\Delta\mathbf{u}_2}, \quad (20.4)$$

where the term $\Delta\mathbf{u}_2$ denotes the interface gap which would result between both structures if they where uncoupled (due to the externally applied forces $\mathbf{f}$). The term $\mathbf{Z}_{int}$ can be interpreted as the 'interface stiffness' that relates the interface gap $\Delta\mathbf{u}_2$ to the reaction forces $\boldsymbol{\lambda}$. Reinserting Eq. (20.4) in Eq. (20.2) yields the admittance matrix of the assembled system $\mathbf{Y}^{AB}$:

$$\boxed{\underbrace{\left(\mathbf{Y}^{A|B} - \mathbf{Y}^{A|B}\mathbf{B}^T\left(\mathbf{B}\mathbf{Y}^{A|B}\mathbf{B}^T\right)^{-1}\mathbf{B}\mathbf{Y}^{A|B}\right)}_{=\mathbf{Y}^{AB}}\mathbf{f} = \mathbf{u}} \quad (20.5)$$

Remark 1. Note that the assembled matrix $\mathbf{Y}^{AB}$ in Eq. (20.5) still has the same size as the unassembled block matrix $\mathbf{Y}^{A|B}$. When writing down Eq. (20.5) in the verbose form indicated in Eq. (20.1), we would notice that indeed the second and third row of $\mathbf{Y}^{AB}$ are equal, which is a direct consequence of the continuity ($\mathbf{u}^A_2 = \mathbf{u}^B_2$). Additionally we would notice that the second and third column in $\mathbf{Y}^{AB}$ are equal, meaning that the external forces on the interface $\mathbf{f}^A_2$ and $\mathbf{f}^B_2$ both have the same effect on the response of the assembled system. It is thus common practice to remove these redundant rows and columns from the final matrix $\mathbf{Y}^{AB}$, thereby (possibly) making it invertible again and treating the interface dofs as the common quantities they are:

$$\mathbf{u}^A_2 = \mathbf{u}^B_2 =: \mathbf{u}^{AB}_2 \qquad and \qquad \mathbf{f}^A_2 + \mathbf{f}^B_2 =: \mathbf{f}^{AB}_2.$$

20.2.2 Transformation of FRF Matrices

Note that we have implicitly assumed that the dofs/sensors on either side of the interface $\mathbf{u}^A_2$ and $\mathbf{u}^B_2$ are in the same geometric position and direction once the substructures are coupled. We additionally assumed that the forces $\mathbf{f}^A_2$ and $\mathbf{f}^B_2$ attack at the same positions and in the same directions, so that *actio est reactio* for the reaction forces is justified. As opposed to e.g. finite element modeling, in experimental practice this cannot always be assured (see e.g. Fig. 20.1). It is thus desirable to project the measured sensor displacements[1] $\mathbf{u}_2$ and the force inputs $\mathbf{f}_2$ on some generalized IDMs. The resulting generalized displacements $\mathbf{q}$ and generalized forces $\mathbf{m}$ are matching on either side of the interface and can thus be coupled as explained in Sect. 20.2.1. The transformation, derived in this subsection will take the following form [16]:

---

[1]Sensors are typically measuring acceleration, but for simplicity we are talking of displacements here.

$$\boxed{\mathbf{Y}_{qm} = \mathbf{T}_u \mathbf{Y}_{22} \mathbf{T}_f^T,} \tag{20.6}$$

where $\mathbf{Y}_{22}$ denotes the measured FRF matrix in the nonmatching interface dofs $\mathbf{u}_2$, $\mathbf{f}_2$ and $\mathbf{Y}_{qm}$ denotes the transformed FRF matrix in the (matching) generalized coordinates. $\mathbf{T}_u$ and $\mathbf{T}_f^T$ are the transformation matrices:

$$\mathbf{q} = \mathbf{T}_u \mathbf{u}_2; \qquad \mathbf{f}_2 = \mathbf{T}_f^T \mathbf{m}. \tag{20.7}$$

The transformation in this section will only concern the interface submatrices $\mathbf{Y}_{22}$, the transformation of the whole matrix $\mathbf{Y}^A$ or $\mathbf{Y}^B$ is straight forward (see Sect. 20.2.3). Note that the generalized IDMs can be chosen such, that also substructure models from different domains can be coupled (e.g. a finite element model coupled with an experimentally obtained model).

20.2.2.1 Displacement Modes

In the case of nonmatching sensor dofs on the interface $\mathbf{u}_2$, we can choose to represent the interface motion by some general interface deformation modes (IDMs) and the corresponding generalized coordinates $\mathbf{q}$. The number of IDMs is typically lower than the number of measured interface dofs:

$$\mathbf{u_2} \in \mathbb{C}^{n_u}, \qquad \mathbf{q} \in \mathbb{C}^p, \qquad \text{with} \quad p \le n_u.$$

Let us consider the single interface connection point depicted in Fig. 20.3. When we assume for example that the interface behaves almost rigid in the frequency range of interest we can compose the generalized coordinates of a translational part $\mathbf{q}_t^v = [q_x^v \ q_y^v \ q_z^v]^T$ and a rotational part $\mathbf{q}_\theta^v = [q_{\theta_x}^v \ q_{\theta_y}^v \ q_{\theta_z}^v]^T$. The superscript $(\star)^v$ denotes the coupling point v, of which there may be multiple on a structure. These coupling points are often called *virtual points* since they are at a geometric position where no physical sensor or input has to be [8, 15, 16]. Let us assume we want to find the displacement u_x^k measured in x-direction of sensor k (see Fig. 20.3). The relation between the motion in this single sensor channel and the generalized coordinates can easily be found, provided we know the orientation of the sensor x-axis $_I\mathbf{e}_x^k$ and the sensors distance from the virtual point $_I\mathbf{r}^k$, all measured in the global coordinate system I (as indicated by subscript $_I(\star)$).
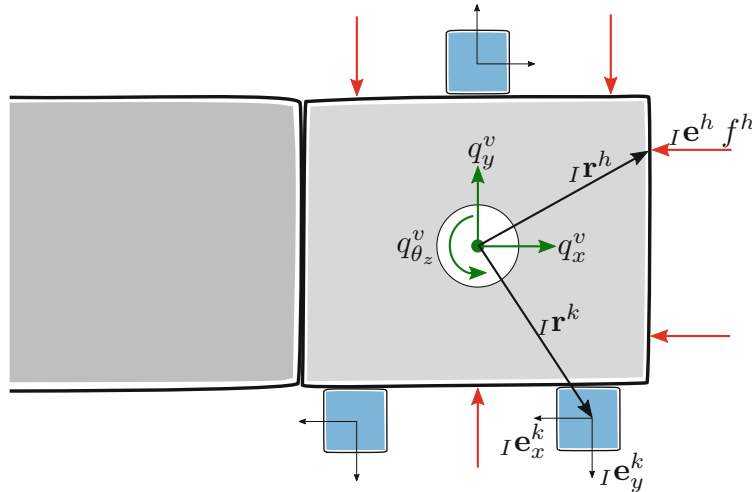
Fig. 20.3 General interface connection point. Exemplary quantities for one sensor k and one force input h

$$u_x^k = ({}_I\mathbf{e}_x^k)^T \left(\mathbf{q}_t^v + \mathbf{q}_\theta^v \times {}_I\mathbf{r}^k \right) = ({}_I\mathbf{e}_x^k)^T \begin{bmatrix} 1 & 0 & 0 & 0 & {}_Ir_z^k & -{}_Ir_y^k \\ 0 & 1 & 0 & -{}_Ir_z^k & 0 & {}_Ir_x^k \\ 0 & 0 & 1 & {}_Ir_y^k & -{}_Ir_x^k & 0 \end{bmatrix} \begin{bmatrix} q_x^v \\ q_y^v \\ q_z^v \\ q_{\theta_x}^v \\ q_{\theta_y}^v \\ q_{\theta_z}^v \end{bmatrix} = \mathbf{R}_{u_x^k}\,\mathbf{q}^v, \tag{20.8}$$

where $\mathbf{R}_{u_x^k}$ is a 1×6 matrix relating the generalized coordinates $\mathbf{q}^v$ to the displacement in channel u_x^k. The displacements in all sensor channels can be reconstructed for a given $\mathbf{q}^v$ following a similar procedure. By stacking all sensor transformation matrices for all virtual points (see [16]), we finally get:

$$\mathbf{u}_2 = \mathbf{R}_u\mathbf{q} \qquad \text{with} \quad \mathbf{R}_u \in \mathbb{R}^{n_u \times p}. \tag{20.9}$$

This can be seen as representing $\mathbf{u}_2$ by a reduced basis contained in $\mathbf{R}_u$. Note that the reduced basis $\mathbf{R}_u$ may contain arbitrary other interface deformation modes, not just the rigid modes for a *virtual point* as discussed above. One may also want to introduce some interface modes that bend the coupling area or any other modes that appear to be of special importance, e.g. after studying the operational deformation shapes of a structure. One could also approximate the motion of a continuous interface by evaluating some continuous vibration modes at the actual sensor positions and include these modes as a column in $\mathbf{R}_u$. However, the general form of (20.9), i.e. the reduction of sensor dofs will remain the same.

20.2.2.2 Displacement Transformation

In reality, the response in the sensor channels $\mathbf{u}_2$ will not behave perfectly as indicated in Eq. (20.9), meaning we can only represent a measured $\mathbf{u}_2$ with the IDMs up to a certain residual $\boldsymbol{\mu}$.

$$\mathbf{u}_2 = \mathbf{R}_u\mathbf{q} + \boldsymbol{\mu} \qquad \rightarrow \qquad \boldsymbol{\mu} = \mathbf{u}_2 - \mathbf{R}_u\mathbf{q}. \tag{20.10}$$

However, if our kinematic assumption of the interface motion, contained in $\mathbf{R}_u$, is good enough in the frequency range of interest (e.g. the rigid body assumption on a virtual point as shown above), then the residual $\boldsymbol{\mu}$ is likely to be very small and containing mostly measurement noise or other uncertainties in experimental practice. See e.g. [16] for some indicator functions that check the validity of the kinematic assumption.

Finding the $\mathbf{q}$ that best approximates the measured response $\mathbf{u}_2$ is typically a task for least squares. However we can choose the more general approach to minimize a *cost function* $\Phi(\mathbf{q})$, which is merely the error vector $\boldsymbol{\mu}$ weighted by a weighting matrix $\mathbf{W}_u$.[2] The weighting is chosen from an engineering point of view and some possible choices for $\mathbf{W}_u$ are discussed later. The function we want to minimize with the transformation, then is:

$$\Phi(\mathbf{q}) = \tfrac{1}{2}\,\boldsymbol{\mu}^T\mathbf{W}_u\boldsymbol{\mu} = (\mathbf{u}_2 - \mathbf{R}_u\mathbf{q})^T\mathbf{W}_u(\mathbf{u}_2 - \mathbf{R}_u\mathbf{q}) \tag{20.11}$$

$$= \underbrace{\mathbf{q}^T\mathbf{R}_u^T\mathbf{W}_u\mathbf{R}_u\mathbf{q}}_{quadratic} - \underbrace{2\mathbf{u}_2^T\mathbf{W}_u\mathbf{R}_u\mathbf{q}}_{linear} + \underbrace{\mathbf{u}_2^T\mathbf{W}_u\mathbf{u}_2}_{constant}.$$

If the quaratic term of this function is convex (i.e. the Hessian matrix $\mathbf{R}_u^T\mathbf{W}_u\mathbf{R}_u$ is positive definite), we can simply find the minimum of $\Phi(\mathbf{q})$ by setting its first derivative to zero:

$$\left(\frac{\partial \Phi}{\partial \mathbf{q}} \right)^T = \mathbf{R}_u^T\mathbf{W}_u\mathbf{R}_u\mathbf{q} - \mathbf{R}_u^T\mathbf{W}_u\mathbf{u}_2 \overset{!}{=} \mathbf{0}, \tag{20.12}$$

---

[2]Also frequently called *weighted least squares [18]*.

where we already assumed that $\mathbf{W}_u$ is symmetric. This means for the sought transformation matrix $\mathbf{T}_u$:

$$\mathbf{q} = \underbrace{\left(\mathbf{R}_u^T \mathbf{W}_u \mathbf{R}_u\right)^{-1} \mathbf{R}_u^T \mathbf{W}_u}_{\mathbf{T}_u} \mathbf{u}_2 \tag{20.13}$$

Where we have now found the 'optimal' solution $\mathbf{q}$ (according to the cost function (20.11)) to approximate a given $\mathbf{u}_2$ with the IDMs. This matrix is the same as the Moore Penrose pseudoinverse in [16].

Remark 2. The positive definiteness of the Hessian matrix shall get some brief attention here. In simple least squares the Hessian matrix is $\mathbf{R}_u^T \mathbf{R}_u$, which is always positive definite if the IDMs contained in $\mathbf{R}_u$ are linearly independent (i.e. we chose only such modes that can not be represented by a combination of other modes already contained in the reduced basis $\mathbf{R}_u$). Thus:

$$\mathbf{R}_u \mathbf{q} \neq \mathbf{0}; \qquad\qquad \forall \mathbf{q} \neq \mathbf{0}$$

$$\mathbf{q}^T \mathbf{R}_u^T \mathbf{R}_u \mathbf{q} =: \mathbf{x}^T \mathbf{x} > 0; \qquad\qquad \forall \mathbf{q} \neq \mathbf{0}$$

Now the same trick to show/ensure the positive definiteness of the Hessian matrix, can be applied if we choose the weighting matrix $\mathbf{W}_u$ as a symmetric positive definite matrix. Then $\mathbf{W}_u$ can be factored in its (all positive!) eigenvalues $\mathbf{\Lambda} = diag(\lambda_{ii})$ and the orthonormal eigenvectors $\mathbf{Q}$. Thus:

$$\mathbf{q}^T \mathbf{R}_u^T \mathbf{W}_u \mathbf{R}_u \mathbf{q} = \mathbf{q}^T \mathbf{R}_u^T \mathbf{Q} \mathbf{\Lambda} \mathbf{Q}^T \mathbf{R}_u \mathbf{q}$$

$$= \mathbf{q}^T \mathbf{R}_u^T \mathbf{Q} \sqrt{\mathbf{\Lambda}} \sqrt{\mathbf{\Lambda}} \mathbf{Q}^T \mathbf{R}_u \mathbf{q} \qquad =: \mathbf{x}^T \mathbf{x} > 0; \qquad \forall \mathbf{q} \neq \mathbf{0}$$

Obviously we could also add multiple weighting matrices to include different quality criteria in our transformation, e.g. $\mathbf{W}_u = \mathbf{W}_{u,1} + \mathbf{W}_{u,2}$; as long as $\mathbf{W}_{u,1}$ and $\mathbf{W}_{u,2}$ are also symmetric positive definite.

20.2.2.3   Displacement Weighting Matrices

We will now discuss some possibilities for choosing a weighting matrix $\mathbf{W}_u$ in the transformation $\mathbf{T}_u$.

Testing experience   In experimental practice it is often the case that some measurement channels are more prone to errors than others. This may be due to a loose connection with the structure, internal sensor damage or electromagnetic compatibility issues. Another example are sensors that cannot be positioned as accurately as others. The positioning and orientation of the sensors plays an important role in the quality of the transformation (see e.g. $_I\mathbf{r}^k$ and $_I\mathbf{e}_x^k$ in Eq. (20.8)). An example for this importance can be found in [19, pp. 63–65].

For one of these reasons, the experimentalist may feel that this/these specific sensor channels (let us call them s) may not be trusted as much as the other channels. Hence, minimizing their error μ_s must not be emphasized as much in the transformation. The weighting matrix $\mathbf{W}_u$ can thus be chosen as a diagonal matrix with lower weights for the untrusted sensors, e.g.:

$$\mathbf{W}_u = diag(W_{ii}) \qquad \text{with} \quad W_{ii} = 1, \qquad \text{for} \quad i \neq s \tag{20.14}$$

$$0 < W_{ii} < 1, \qquad \text{for} \quad i = s$$

Statistics   In statistics it is common to automatically give low weights to uncertain sensor channels, by using their inverse covariance matrix as weighting: $\mathbf{W}_u = \mathbf{\Sigma}_{u_2}^{-1}$. It can be shown [18, pp. 200–216] that, when choosing the inverse covariance matrix of the sensor channels as $\mathbf{W}_u$ in the transformation to $\mathbf{q}$, one is effectively minimizing all entries in the covariance matrix of the outputs $\mathbf{\Sigma}_q$.

The basic idea of this approach becomes obvious if we assume that the errors in $\mathbf{u}_2$ are uncorrelated, i.e. $\mathbf{\Sigma}_{u_2} = diag(\sigma_{ii}^2)$ is a diagonal matrix containing the squared variances in the single sensor channels. Using $\mathbf{W}_u = \mathbf{\Sigma}_{u_2}^{-1}$ is then simply putting less weight on those sensor channels with a high variance σ_{ii}.

Notice, that when transforming an FRF matrix $\mathbf{Y}_{q2} = \mathbf{T}_u \mathbf{Y}_{22}$, one is using the same transformation for each column of the matrix. We will denote the column j by $\mathbf{Y}_{22}(:, j)$. Each column j respresents the response in the sensor channels $\mathbf{u}_2$ to a unit force input in j and will have a specific error variance. Thus, we might want to transform each column j separately, using a different weighting matrix which is representing the sensor errors for *this* force input.

We will now try to come up with a transformation specifically suited to experimental dynamics, by using the same ideas as in statistics. A common quantity to indicate the reliability of a measured FRF matrix entry $Y(i, j)$ is its coherence $\gamma(i, j)$, where $0 \leq \gamma(i, j) \leq 1$. The coherence is typically low at frequencies where a force input in j is exciting only a small motion in sensor channel i, so that a large part of the measured sensor signal is due to background noise and may thus not be trusted as much. The coherence is also a standard output, being calculated by most experimental modal analysis softwares, which may facilitate implementation of a statistical criterion that is based on the coherence. A straightforward approach to transform the FRF matrix, would be to utilize the (e.g. squared) coherences of an FRF matrix column $\mathbf{Y}_{22}(:, j)$ as a diagonal weighting matrix for the transformation of *this* matrix column:

$$\mathbf{Y}_{q2}(:, j) = \underbrace{\left(\mathbf{R}_u^T \mathbf{W}_{u,j} \mathbf{R}_u\right)^{-1} \mathbf{R}_u^T \mathbf{W}_{u,j}}_{\mathbf{T}_{u,j}} \mathbf{Y}_{22}(:, j) \qquad \text{with,} \tag{20.15}$$

$$\mathbf{Y}_{22}(:, j) = \begin{bmatrix} Y_{22}(1, j) \\ Y_{22}(2, j) \\ \vdots \end{bmatrix}, \qquad \mathbf{W}_{u,j} = \begin{bmatrix} \gamma^2(1, j) & & \\ & \gamma^2(2, j) & \\ & & \ddots \end{bmatrix}. \tag{20.16}$$

Notice that the weighting matrix in this case, is changing for each measured frequency ω, since also the coherence is changing for each measured frequency. It is thereby changing the 'trusted' sensor channels depending on the frequency, since at some frequencies a specific sensor channel might be in an antiresonance with very low signal to noise ratio but be valuable in other frequency regions. This might be an advantage over using a fixed weighting matrix as in Eq. (20.14).

Energy minimization When considering the transformation error in the displacements $\boldsymbol{\mu}$, it is a natural choice to minimize the energy produced by this error, i.e.:

$$\text{Minimize:} \quad \Phi(\mathbf{q}) = \boldsymbol{\mu}^T \mathbf{Z}_{22} \boldsymbol{\mu}, \tag{20.17}$$

where $\mathbf{Z}_{22}$ denotes the impedance matrix in the interface dofs $\mathbf{u}_2$. As will be seen in Sect. 20.2.3, the coupling of two transformed FRF matrices effectively means a weakening of the interface compatibility condition, i.e. the residuals of the transformation $\boldsymbol{\mu}$ on either side of the interface are left uncoupled. A minimization as shown above would therefore ensure minimal energy transmission loss over the interface.

However there are also some practical problems associated to choosing $\mathbf{W}_u = \mathbf{Z}_{22}$. The first issue is the availability of $\mathbf{Z}_{22}$, since it would require measuring a driving point admittance in all sensor dofs on the interface, i.e. excitation forces in positions and directions equal to the sensor dofs. This may not be possible in all cases (exciting on the sensor faces directly is not recommended, see e.g. [15]). This may be overcome at the expense of building a finite element model of the interface, and thereby obtaining a symmetric $\mathbf{Z}_{22}$ in the interface dofs.

Another problem is more related to the noise pollution of the sensor signals. Typically the displacement response in those directions that are very stiff (i.e. producing a high energy) is also low. Thus, one would effectively over-emphazise those components of $\mathbf{u}_2$ in the in the transformation, that already have a lower signal to noise ratio.

20.2.2.4 Force Modes

In essence we have to make the same kinematic assumptions for representing the forces as for the displacements. The number of force inputs n_f is typically higher than the number of IDMs p. Their position must also be carefully chosen, so that all IDMs are excited [16].

$$\mathbf{f_2} \in \mathbb{C}^{n_f}, \qquad \mathbf{m} \in \mathbb{C}^p, \qquad \text{with} \quad p \leq n_f.$$

Let us consider again the example in Fig. 20.3, with a locally rigid interface on virtual point v. All input forces $\mathbf{f}_2$ will result in a generalized force $\mathbf{m}_t^v$ and a generalized moment $\mathbf{m}_\theta^v$. For one single force input f^h this can be expressed by:

$$\mathbf{m}^v = \begin{bmatrix} \mathbf{m}_t^v \\ \mathbf{m}_\theta^v \end{bmatrix} = \begin{bmatrix} {}_I\mathbf{e}^h \\ {}_I\mathbf{r}^k \times {}_I\mathbf{e}^h \end{bmatrix} f^h = \mathbf{R}_{f^h}^T f^h, \tag{20.18}$$

where $\mathbf{R}_{f^h}^T$ denotes the 6×1 matrix representing the virtual point load $\mathbf{m}^v$ resulting from a unit force input in f^h and ${}_I\mathbf{e}^h$ denotes the direction vector in which the force was applied. The virtual point loads resulting from the other force inputs can be found following a similar procedure. Putting each contribution in a column of $\mathbf{R}_f^T$, we can write

$$\mathbf{m} = \mathbf{R}_f^T \mathbf{f}_2 \qquad \text{with} \quad \mathbf{R}_f^T \in \mathbb{R}^{p \times n_f}. \tag{20.19}$$

Notice that $\mathbf{R}_f^T$ is written *transposed* since it would directly correspond to the transpose of $\mathbf{R}_u$ in Eq. (20.9) if we were measuring driving point FRFs only, i.e. if all force inputs would have a corresponding sensor channel in the same geometric position and in the same direction. However, it is a great practical advantage that different dofs can be used for force inputs and displacement outputs.

20.2.2.5 Force Transformation

In order to transform a measured FRF matrix according to Eq. (20.6) we need to find a force transformation matrix $\mathbf{T}_f^T$ that transforms a given load in the generalized forces $\mathbf{m}$, to an equivalent vector of input forces $\tilde{\mathbf{f}}_2$:

$$\tilde{\mathbf{f}}_2 = \mathbf{T}_f^T \mathbf{m}, \tag{20.20}$$

$$\text{where}: \qquad \mathbf{R}_f^T \tilde{\mathbf{f}}_2 \overset{!}{=} \mathbf{m}. \tag{20.21}$$

The problem in Eqs. (20.20) and (20.21) is fundamentally different from the displacement transformation, stated in Eq. (20.10). The requirement in Eq. (20.21) is an underdetermined problem and there are infinitely many possible solutions for $\tilde{\mathbf{f}}_2$ that fulfill this requirement. Any vector in the nullspace of $\mathbf{R}_f^T$, lets call an example vector $\tilde{\mathbf{f}}_{2,null}$, could be added to $\tilde{\mathbf{f}}_2$ to produce yet another possible solution to Eq. (20.21). For the assumption of a locally rigid interface, all $\tilde{\mathbf{f}}_{2,null}$ would be exciting only flexible modes. Figure 20.4 shows a depiction of such a possible $\tilde{\mathbf{f}}_{2,null}$.

The question for the transformation now remains: how do we find a solution $\tilde{\mathbf{f}}_2$ from those possible combinations, which is 'good' from an engineering point of view? We can state a standard convex optimization problem where we seek to minimize a scalar cost function $\Phi(\tilde{\mathbf{f}}_2)$, while the optimum solution $\tilde{\mathbf{f}}_2$ is subject to constraints $\mathbf{g}(\tilde{\mathbf{f}}_2)$:
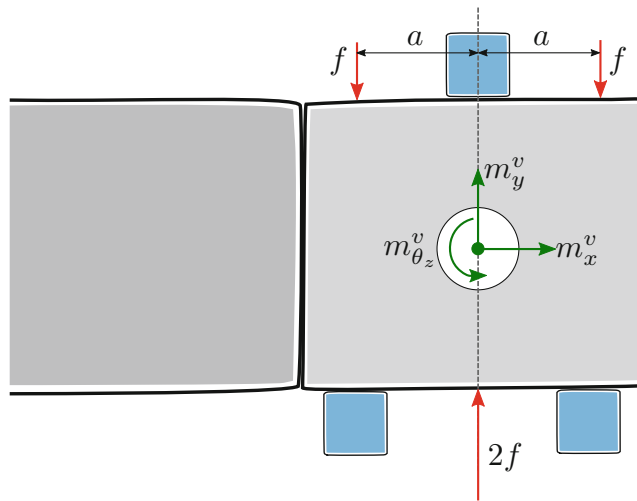
Fig. 20.4 Exemplary nullspace vector for input forces

$$\text{Minimize :} \qquad \Phi(\tilde{\mathbf{f}}_2) = \tfrac{1}{2}\,\tilde{\mathbf{f}}_2^T \mathbf{W}_f \tilde{\mathbf{f}}_2, \tag{20.22}$$

$$\text{Subject to :} \qquad \mathbf{g}(\tilde{\mathbf{f}}_2) = \mathbf{R}_f^T \tilde{\mathbf{f}}_2 - \mathbf{m} = \mathbf{0}, \tag{20.23}$$

where we made use of the force weighting matrix $\mathbf{W}_f$. Now following the same arguments as in the transformation of the displacements, we can state that $\Phi(\tilde{\mathbf{f}}_2)$ has only one global minimum, if the weighting matrix $\mathbf{W}_f$ is positive definite. We then put this together in the standard optimization formulation for finding a constrained minimum, i.e. forming the Lagrangian $\mathcal{L}(\tilde{\mathbf{f}}_2, \boldsymbol{\lambda})$ and search for its stationary point:

$$\mathcal{L}(\tilde{\mathbf{f}}_2, \boldsymbol{\lambda}) = \Phi(\tilde{\mathbf{f}}_2) + \boldsymbol{\lambda}^T \mathbf{g}(\tilde{\mathbf{f}}_2), \tag{20.24}$$

$$\left(\frac{\partial \mathcal{L}}{\partial \tilde{\mathbf{f}}_2}\right)^T = \mathbf{W}_f \tilde{\mathbf{f}}_2 + \mathbf{R}_f \boldsymbol{\lambda} \overset{!}{=} \mathbf{0}, \tag{20.25}$$

$$\left(\frac{\partial \mathcal{L}}{\partial \boldsymbol{\lambda}}\right) = \mathbf{R}_f^T \tilde{\mathbf{f}}_2 - \mathbf{m} \overset{!}{=} \mathbf{0}, \tag{20.26}$$

where Eq. (20.26) is basically enforcing the constraints. Equation (20.25) states that at the optimum the gradient of $\Phi(\tilde{\mathbf{f}}_2)$ can be expressed as a linear combination (determined by $\boldsymbol{\lambda}$) of the constraint function gradients. This effectively means that at the optimum $\tilde{\mathbf{f}}_2$ there is no 'direction' $\Delta \tilde{\mathbf{f}}_2$ that could improve the value of $\Phi(\tilde{\mathbf{f}}_2)$ without changing/violating one of the constraints in $\mathbf{g}(\tilde{\mathbf{f}}_2) = \mathbf{0}$ (see e.g. [18, p. 603ff] or any standard text on optimization).

We can then use Eq. (20.25) to solve for $\tilde{\mathbf{f}}_2 = -\mathbf{W}_f^{-1}\mathbf{R}_f\boldsymbol{\lambda}$ and insert this in Eq. (20.26) to solve for the Lagrange multipliers $\boldsymbol{\lambda}$, yielding:

$$\boldsymbol{\lambda} = -(\mathbf{R}_f^T \mathbf{W}_f^{-1} \mathbf{R}_f)^{-1} \mathbf{m}, \tag{20.27}$$

which, reinserted in Eq. (20.25), means for the 'optimal' solution $\tilde{\mathbf{f}}_2$:

$$\tilde{\mathbf{f}}_2 = \underbrace{\mathbf{W}_f^{-1}\mathbf{R}_f(\mathbf{R}_f^T \mathbf{W}_f^{-1}\mathbf{R}_f)^{-1}}_{\mathbf{T}_f^T}\mathbf{m}, \tag{20.28}$$

where we call $\mathbf{T}_f^T$ the transformation matrix for transforming a VP load $\mathbf{m}$ to an equivalent $\tilde{\mathbf{f}}_2$ in the force dofs (which we actually physically measured in $\mathbf{Y}_{22}$). Note that it is particularly easy to verify that this solution $\tilde{\mathbf{f}}_2$ satisfies the constraints Eq. (20.23). The above transformation matrix can also directly be seen as a right Moore-Penrose pseudoinverse [16].

20.2.2.6 Force Weighting Matrices

We will now explain some common choices for the force weighting matrix $\mathbf{W}_f$, which is in large parts similar to the discussion for the displacements, but differs in some details.

Testing experience In practice some impacts in the set of measurements might be trusted less than the other impacts, let us denote them with s. One reason could be that the space for applying a hammer impact was very narrow and putting in enough excitation energy was difficult or most often yielded a double impulse. For badly accessible impact positions, it is also hard to assure that the point is hit exactly in the assumed position $_l\mathbf{r}^j$ and direction $_l\mathbf{e}^j$ (see Fig. 20.3). This may result in a bad coherence for the measured column s in the FRF matrix, $\mathbf{Y}_{22}(:, s)$. Overall, many engineering reasons might yield the conclusion that the solution $\tilde{\mathbf{f}}_2$ in Eq. (20.21) should better contain less contribution of scalar forces in s and make more use of the other 'trusted' force dofs. This criterion might be included by using the following weighting matrix:

$$\mathbf{W}_f = diag(W_{ii}) \qquad \text{with} \quad W_{ii} = 1 \quad \text{for} \quad i \neq s, \tag{20.29}$$

$$W_{ii} > 1 \quad \text{for} \quad i = s.$$

This way the particular entries $\tilde{\mathbf{f}}_2(s, 1)$ are 'penalized' in the search for the minimum, since they lead to a more rapid growth of the quality measure $\Phi(\tilde{\mathbf{f}}_2)$ when compared to the other force inputs $\tilde{\mathbf{f}}_2(i, 1) \quad i \neq s$.

Statistics Similar as for the displacements, it might be desired to choose a frequency dependent optimality criterion also for the force transformation. In order to account for the statistical reliability of the FRF matrix entries we can again take the coherence $\gamma(i, j)$ as an indicator. When performing the transformation to generalized forces, $\mathbf{Y}_{2m} = \mathbf{Y}_{22}\mathbf{T}_f^T$, one is effectively transforming each row of the matrix. That means the response of a single sensor channel i to a combination of all measured force inputs $\mathbf{f}_2$ (contained in row $\mathbf{Y}_{22}(i, :)$) is transformed to the response of channel i to a combination of the virtual point loads $\mathbf{m}$ (contained in row $\mathbf{Y}_{2m}(i, :)$). Since the coherence differs for each channel i it is desirable to transform each row of the FRF matrix separately:

$$\mathbf{Y}_{2q}(i, :) = \mathbf{Y}_{22}(i, :) \underbrace{\mathbf{W}_{f,i}^{-1}\mathbf{R}_f \left(\mathbf{R}_f^T\mathbf{W}_{f,i}^{-1}\mathbf{R}_f\right)^{-1}}_{\mathbf{T}_{f,i}^T} \qquad \text{with,} \tag{20.30}$$

$$\mathbf{Y}_{22}(i, :) = \begin{bmatrix} Y_{22}(i, 1) \\ Y_{22}(i, 2) \\ \vdots \end{bmatrix}^T, \qquad \mathbf{W}_{f,i}^{-1} = \begin{bmatrix} \gamma(i, 1)^2 & & \\ & \gamma(i, 2)^2 & \\ & & \ddots \end{bmatrix}. \tag{20.31}$$

This proposed transformation would automatically prefer the 'trusted'/high coherence force inputs at each frequency over the force inputs with a low coherence. Thus the equivalent force $\tilde{\mathbf{f}}_2$ for a given generalized force $\mathbf{m}$ would contain less contribution of the 'untrusted' force inputs.

Energy minimization When minimizing a cost function $\Phi(\tilde{\mathbf{f}}_2)$, it is a natural choice to minimize the energy produced by the equivalent input forces $\tilde{\mathbf{f}}_2$, i.e.:

$$\text{Minimize :} \quad \Phi(\tilde{\mathbf{f}}_2) = \tilde{\mathbf{f}}_2^T\mathbf{Y}_{22}\tilde{\mathbf{f}}_2, \tag{20.32}$$

where $\mathbf{Y}_{22}$ denotes the admittance matrix in the interface force dofs $\tilde{\mathbf{f}}_2$.

Notice that the transformation in Eq. (20.28) requires only the inverse of the force weighting matrix. So effectively, the same practical problems associated to choosing $\mathbf{W}_f = \mathbf{Y}_{22} = \mathbf{Z}_{22}^{-1}$ as in the energy minimization for the displacements in Sect. 20.2.2.3 apply here.

20.2.3 Weakening of the Compatibility Condition

In the last section we have derived the transformation matrices necessary for transforming the intercae dofs $\mathbf{u}_2, \mathbf{f}_2$ on the generalized dofs $\mathbf{q}, \mathbf{m}$. The interface transformation of substructure A's full admittance matrix $\mathbf{Y}^A$ may thus be written as:

$$\tilde{\mathbf{Y}}^A = \begin{bmatrix} \mathbf{Y}_{11}^A & \mathbf{Y}_{1m}^A \\ \mathbf{Y}_{q1}^A & \mathbf{Y}_{qm}^A \end{bmatrix} = \begin{bmatrix} \mathbf{I} & \mathbf{0} \\ \mathbf{0} & \mathbf{T}_u^A \end{bmatrix} \begin{bmatrix} \mathbf{Y}_{11}^A & \mathbf{Y}_{12}^A \\ \mathbf{Y}_{21}^A & \mathbf{Y}_{22}^A \end{bmatrix} \begin{bmatrix} \mathbf{I} & \mathbf{0} \\ \mathbf{0} & (\mathbf{T}_f^A)^T \end{bmatrix}, \tag{20.33}$$

where $\tilde{\mathbf{Y}}^A$ denotes the transformed substructure matrix. An analogous expression would yield $\tilde{\mathbf{Y}}^B$, the transformed admittance matrix of substructure B. The two transformed matrices can directly be coupled to each other, as shown in Sect. 20.2.1, since their generalized dofs on either side of the interface are matching:

$$\tilde{\mathbf{Y}}^{AB} = \tilde{\mathbf{Y}}^{A|B} + \tilde{\mathbf{Y}}^{A|B}\mathbf{B}^T \left(\mathbf{B}\tilde{\mathbf{Y}}^{A|B}\mathbf{B}^T\right)^{-1} \mathbf{B}\tilde{\mathbf{Y}}^{A|B} \qquad \text{where} \qquad \tilde{\mathbf{Y}}^{A|B} = \begin{bmatrix} \tilde{\mathbf{Y}}^A & \mathbf{0} \\ \mathbf{0} & \tilde{\mathbf{Y}}^B \end{bmatrix}. \tag{20.34}$$

We will now show that coupling the transformed matrices of A and B corresponds to a weakening of the interface compatibility condition.

Assume we are coupling the non-transformed (i.e. measured) admittance matrices, written in block diagonal form $\mathbf{Y}^{A|B}$ as in Eq. (20.1). However, we are now enforcing the compatibility only in the direction of the generalized dofs $\mathbf{q}$ and allow only reaction forces in the generalized forces $\mathbf{m}$:

$$\mathbf{Y}^{A|B}\,(\mathbf{f}+\underbrace{\mathbf{B}_f^T\boldsymbol{\lambda}}_{=\mathbf{g}})=\mathbf{u}, \qquad\qquad \text{where}\quad \mathbf{B}_f=\begin{bmatrix}\mathbf{0}\ \mathbf{T}_f^A\ -\mathbf{T}_f^B\ \mathbf{0}\end{bmatrix}, \qquad (20.35)$$

$$\mathbf{B}_u\mathbf{u}=\mathbf{0}, \qquad\qquad \text{where}\quad \mathbf{B}_u=\begin{bmatrix}\mathbf{0}\ \mathbf{T}_u^A\ -\mathbf{T}_u^B\ \mathbf{0}\end{bmatrix}. \qquad (20.36)$$

Inserting Eq. (20.35) in Eq. (20.36) yields:

$$\boldsymbol{\lambda}=-\underbrace{\left(\mathbf{B}_u\mathbf{Y}^{A|B}\mathbf{B}_f^T\right)^{-1}}_{Z_{int}}\underbrace{\mathbf{B}_u\mathbf{Y}^{A|B}\mathbf{f}}_{\Delta\mathbf{q}} \qquad (20.37)$$

$$=-\underbrace{\left(\mathbf{Y}_{qm}^A+\mathbf{Y}_{qm}^B\right)^{-1}}_{Z_{int}}\underbrace{\begin{bmatrix}\mathbf{0}\ \mathbf{T}_u^A\ -\mathbf{T}_u^B\ \mathbf{0}\end{bmatrix}}_{=\mathbf{B}_u}\mathbf{Y}^{A|B}\mathbf{f}$$

Reinserting $\boldsymbol{\lambda}$ in Eq. (20.35) yields the 'weakly coupled' admittance $\mathbf{Y}_{weak}^{AB}$:

$$\underbrace{\left(\mathbf{Y}^{A|B}-\mathbf{Y}^{A|B}\mathbf{B}_F^T\left(\mathbf{B}_u\mathbf{Y}^{A|B}\mathbf{B}_f^T\right)^{-1}\mathbf{B}_u\mathbf{Y}^{A|B}\right)}_{\mathbf{Y}_{weak}^{AB}}\mathbf{f}=\mathbf{u}. \qquad (20.38)$$

Notice that $\mathbf{Y}_{weak}^{AB}$ has the same size as the non-transformed block matrix $\mathbf{Y}^{A|B}$. However, as opposed to $\mathbf{Y}^{AB}$ in Eq. (20.5), when writing down $\mathbf{Y}_{weak}^{AB}$ in the verbose 4×4 block matrix notation (indicated in Eq. (20.1)) we would notice that the second and third row are not identical! Meaning that the displacements $\mathbf{u}_2^B$ and $\mathbf{u}_2^A$ are not perfectly coupled, but remain uncoupled in the residuals of the transformation $\boldsymbol{\mu}$. Inserting Eq. (20.13) in Eq. (20.10), we can write for the interface residuals $\boldsymbol{\mu}$:

$$\boldsymbol{\mu}=(\mathbf{I}-\mathbf{R}_u\mathbf{T}_u)\,\mathbf{u}_2. \qquad (20.39)$$

These 'residual motions' $\boldsymbol{\mu}$ may be present on either side of the interface as a part of the real motion $\mathbf{u}_2=\mathbf{R_u}\mathbf{q}+\boldsymbol{\mu}$. However, when transforming the residual parts $\boldsymbol{\mu}$ in Eq. (20.39) on the IDMs we see that of course $\mathbf{T}_u\boldsymbol{\mu}=\mathbf{0}$. When looking at the last part of Eq. (20.37) this means that the residual motions on either side are not producing any reaction force $\boldsymbol{\lambda}$ and are thus remaining uncoupled.

This weakly coupled $\mathbf{Y}_{weak}^{AB}$ may then be transformed to the generalized dofs via:

$$\tilde{\mathbf{Y}}^{AB}=\begin{bmatrix}\mathbf{I}&\mathbf{0}&\mathbf{0}&\mathbf{0}\\\mathbf{0}&\mathbf{T}_u^A&\mathbf{0}&\mathbf{0}\\\mathbf{0}&\mathbf{0}&\mathbf{T}_u^B&\mathbf{0}\\\mathbf{0}&\mathbf{0}&\mathbf{0}&\mathbf{I}\end{bmatrix}\mathbf{Y}_{weak}^{AB}\begin{bmatrix}\mathbf{I}&\mathbf{0}&\mathbf{0}&\mathbf{0}\\\mathbf{0}&(\mathbf{T}_f^A)^T&\mathbf{0}&\mathbf{0}\\\mathbf{0}&\mathbf{0}&(\mathbf{T}_f^B)^T&\mathbf{0}\\\mathbf{0}&\mathbf{0}&\mathbf{0}&\mathbf{I}\end{bmatrix}, \qquad (20.40)$$

which can be verified to be the same matrix $\tilde{\mathbf{Y}}^{AB}$ that we would have obtained if we had directly coupled the reduced matrices (see Eq. (20.34)). This result is pointing out two important assumptions that the engineer has to make when coupling two admittances that where projected on IDMs (Eq. (20.34)):

- Substructures are left uncoupled in the directions not contained in the IDMs.
- All important motion is contained in the IDMs and thus external excitations and motions in directions not contained in the IDMs are negligible or not of special interest.

The result of Eq. (20.38) could also be used to purposely couple two substructures only in predefined directions or modes while leaving their full set of dofs in the equation.

20.3 Conclusion

In this paper we derived the weak compatibility in the coupling of transformed FRFs from a minimization point of view. The use of weighting matrices in the transformation shall be further explored in the future. We have also shown that the coupling of projected FRFs in fact corresponds to a weakening of the interface compatibility condition. The findings of past publications, such as '*that the lack of RDOF data underestimates in frequency the correct predictions [of the coupled system resonances, M.H.].*' [9], can be clearly attributed to the weakening effect on the interface compatibility when leaving out the rotational IDMs. However this weakening can also be used to purposely keep certain modes uncoupled (e.g. in structures containing relatively loose joints in certain directions). Mayes and Allen have impressively shown in [2, 14] that solving the compatibility condition in experimental substructuring only in a least squares way (called 'MCFS' in these publications), can dramatrically improve the results. This is also an encouraging result for the coupling of substructures in a 'weak' manner as in the projection developed in [8, 15, 16] and described in this contribution. One important assumption for the use of transformed matrices is that the major excitations and deformations can be adequately modeled with the IDMs. This assumption is also important for TPA methods in general [17], since there the whole complexity of a source is described via the forces applied on the interface $\mathbf{f}_2/\mathbf{m}$.

References

1. de Klerk, D., Rixen, D.J., Voormeeren, S.N.: General framework for dynamic substructuring: history review and classification of techniques. AIAA J. **46**(5), 1169–1181 (2008). doi:10.2514/1.33274, ISSN:0001-1452
2. Allen, M.S., Mayes, R.L.: Comparison of FRF and modal methods for combining experimental and analytical substructures. In: 25th International Modal Analysis Conference (IMAC XXV), Orlando (2007)
3. Voormeeren, S.N., Rixen, D.J.: A family of substructure decoupling techniques based on a dual assembly approach. In: Mechanical Systems and Signal Processing **27**(1), 379–396 (2012). doi:10.1016/j.ymssp.2011.07.028, ISSN:08883270
4. Jetmundsen, B., Bielawa, R.L., Flannelly, W.G.: Generalized frequency domain substructure synthesis. J. Am. Helicopter Soc. **33**(1), 55–64 (1988)
5. Crowley, J.R., Klosterman, A.: Direct structural modification using frequency response functions. In: Proceedings of IMAC II (1984)
6. Ewins, D.J.: Modal Testing: Theory and Practice, vol. 15. Research studies press, Letchworth (1984)
7. McConnell, K.G., Varoto, P.S.: Vibration Testing: Theory and Practice, 2nd edn. Wiley, Hoboken (2008)
8. de Klerk, D., et al.: Solving the RDoF problem in experimental dynamic substructuring. In: Proceedings of the 26th International Modal Analysis Conference IMAC (2008). ISBN:9781605600666
9. Duarte, M.L.M., Ewins, D.J.: Some insights into the importance of rotational degrees-of-freedom and residual terms in coupled structure analysis. In: Proceedings of the 13th International Modal Analysis Conference, Nashville, pp. 164–170. Society for Experimental Mechanics (1995)
10. Craig, R.R., Jr., Kurdila, A.J.: Fundamentals of Structural Dynamics. Wiley, Hoboken (2006). ISBN:978-0-471-43044-5
11. O'Callahan, J., Avitabile, P., Riemer, R.: System equivalent reduction expansion process (SEREP). In: Proceedings of the 7th International Modal Analysis Conference, vol. 1, pp. 29–37. Union College Schnectady, New York (1989)
12. Williams, A., Chipman, C., Avitabile, P.: Modal and frequency based substructuring using rotational DOF considerations. In: Proceedings of the 26th International Modal Analysis Conference, Orlando (2008)
13. Rixen, D.: How measurement inaccuracies induce spurious peaks in frequency based substructuring. In: Proceedings of the Twenty Sixth International Modal Analysis Conference, Orlando. Society for Experimental Mechanics, Bethel (2008). ISSN:21915644. http://semproceedings.com/26i/sem.org-IMAC-XXVI-Conf-s28p02-How-Measurement-Inaccuracies-Induce-Spurious-Peaks-Frequency-Based.pdf
14. Mayes, R.L., Stasiunas, E.C.: Lightly damped experimental substructures for combining with analytical substructures. In: 25th International Modal Analysis Conference (IMAC XXV), Orlando (2007)
15. van der Seijs, M., et al.: Validation of current state frequency based substructuring technology for the characterisation of steering gear–vehicle interaction. In: Mayes, R., Rixen, D., Allen, M. (eds.) Topics in Experimental Dynamic Substructuring, Volume 2: Proceedings of the 31st IMAC, A Conference on Structural Dynamics, 2013, New York, Chap. 20, pp. 253–266. Springer, New York (2014). doi:10.1007/978-1-4614-6540-9, ISBN:978-1-4614-6539-3, http://link.springer.com/10.1007/978-1-4614-6540-9
16. van der Seijs, M.V., et al.: An improved methodology for the virtual point transformation of measured frequency response functions in dynamic substructuring. In: 4th ECCOMAS Thematic Conference on Computational Methods in Structural Dynamics and Earthquake Engineering, June 2013. doi:10.13140/RG.2.1.2715.3126
17. van Der Seijs, M.V., De Klerk, D., Rixen, D.J.: General framework for transfer path analysis: history, theory and classification of techniques. In: Mechanical Systems and Signal Processing, pp. 68–69; 217–244, Feb 2016. doi:10.1016/j.ymssp.2015.08.004. ISSN:10961216. http://dx.doi.org/10.1016/j.ymssp.2015.08.004%20http://linkinghub.elsevier.com/retrieve/pii/S0888327015003647
18. Strang, G.: Computational Science and Engineering, 1st edn. Wellesley-Cambridge Press, Wellesley (2007). ISBN:9780961408817
19. van der Seijs, M.V.: Experimental dynamic substructuring, analysis and design strategies for vehicle development. Ph.D. thesis, Delft University of Technology (2016)

Chapter 21
A Recursive Coupling-Decoupling Approach to Improve Experimental Frequency Based Substructuring Results

R. Cumbo, S. Manzato, G. Coppotelli, A. Fregolent, and W. D'Ambrogio

Abstract Substructure decoupling techniques allow identifying the dynamic behavior of a substructure starting from the dynamic behavior or the assembled system and a residual subsystem. Standard approaches rely on the knowledge of all FRFs at the interface DOFs between the two substructures. However, as these typically include also rotational DOFs which are extremely difficult and most of the time impossible to measure, several techniques have been investigated to overcome these limitations. A very attractive solution consists in defining mixed or pseudo interfaces, that allow to substitute unmeasurable coupling DOFs with internal DOFs on the residual substructure. Additionally, smoothing/denoising techniques have been proposed to reduce the detrimental effect of FRF noise and inconsistencies on the decoupling results. Starting from these results, some recent analysis on the possibility of combining coupling and decoupling FBS to validate the results and compensate for inconsistencies will be presented in this paper. The proposed method relies on errors introduced in the substructuring process when assuming that the interface behaves rigidly, while it is generally known that this assumption is seldom verified. Consequently, a recursive coupling-decoupling approach will be used to improve the estimation of the dynamic response of either the residual structure (for decoupling) or the assembly (for coupling). The method, validated on analytical data, will be here analyzed on a numerical example inspired by an experimental campaign used to validate the finite element models and on which standard substructuring techniques showed some limitations. The results discussed in this paper will be then used as guidelines to apply the proposed methodologies on experimental data in the future.

Keywords Substructuring • FBS • Coupling • Decoupling • Connections

21.1 Introduction

Dynamic Substructuring (DS) is a technique allowing the componentwise analysis of a structural system. In the framework of dynamic analysis, it has some important advantages over global methods where the entire problem is handled at once [1]:

– It allows the experimental evaluation of the dynamic behavior of structures that are too large or complex to analyze as a whole (as for example an aircraft). Numerically, this holds when the number of DoFs is such that solution techniques cannot find results in a reasonable time
– By analyzing the subsystems, local dynamic behavior can be recognized more easily than when the entire system is analyzed
– DS also allows the identification of internal modifications referred to a subsystem

―――――――――――――――

R. Cumbo
Siemens Industry Software NV, Interleuvenlaan 68, 3001, Leuven, Belgium

Università degli Studi di Roma "La Sapienza", Dipartimento di Ingegneria Meccanica e Aerospaziale, Via Eudossiana 18, 00184, Rome, Italy

S. Manzato (✉)
Siemens Industry Software NV, Interleuvenlaan 68, 3001, Leuven, Belgium
e-mail: simone.manzato@siemens.com

G. Coppotelli
Università degli Studi di Roma "La Sapienza", Dipartimento di Ingegneria Meccanica e Aerospaziale, Via Eudossiana 18, 00184, Rome, Italy

A. Fregolent
Dipartimento di Ingegneria Meccanica e Aerospaziale, Università di Roma La Sapienza, Via Eudossiana 18, I 00184, Rome, Italy

W. D'Ambrogio
Dipartimento di Ingegneria Industriale e dell'Informazione e di Economia, Università dell'Aquila, Via G. Gronchi, 18, I-67100, L'Aquila, Italy

The concept of substructuring holds its roots in the field of domain decomposition and includes two main branches: decoupling and coupling [2]. Given a known assembled system RU, decoupling consists in the identification of the dynamics of the unknown structure U by decoupling R (residual substructure) from RU. Coupling, on the other hand, evaluates the dynamic behavior of an unknown RU system starting from the knowledge of the two subsystems R and U. Even if structural modification techniques are generally not considered as substructuring, the two concepts are instead almost the same [3]: one could see the coupling problem as the structural modification of R caused by the addition of subsystem U. Same considerations can be done for the decoupling: the subtraction of R is a negative modification of mass, stiffness and damping of the assembled system RU [4]. DS can be studied in three different domains: physical, modal or frequency. The latter is known as Frequency Based Substructuring (FBS) and it is the one analyzed and applied in this paper. As already explained, the DS can be applied both numerically and experimentally, or even to combine numerical and experimental substructure models. The main issues in this field, extensively reported in literature, are related to the applicability of the technique to experimental data. At first, the intrinsic formulation of the problem together with the presence of noise will result in an ill-conditioned matrix which has to be inverted in the substructuring formulation (see for instance [5, 6]). The second problem is linked to the actual measurement process: sometimes it is really difficult to compensate for the impossibility of measuring the rotational DoFs, That leads to the definition of incorrect or incomplete compatibility and equilibrium equations imposed at the interface, especially for the coupling approach [7–9].

After a brief theoretical summary of the FBS, different developed methods will be explained. They are focused on the identification of the connection errors that usually lead to wrong results in the experimental measurements. The aim of the error identification at the connection is to find an useful way to apply this information in next substructuring applications of the same system.

21.2   Framework for FBS

Considering a generic linear and time-invariant subsystem R, the equation of motion in the physical domain is:

$$Z^R(\omega) u^R(\omega) = f^R(\omega) + g^R(\omega) \tag{21.1}$$

where Z^R, u^R, f^R, g^R are respectively the dynamic stiffness matrix, the vector of DoFs, the external force vector and the vector of connecting forces with the other substructures. The same equation can be written also for the unknown substructure U. To evaluate the coupled dynamic response of the two substructures, the compatibility and the equilibrium equations at the connection points must be added to the resulting equations of motion of the two subsystems. The former condition implies:

$$u_c^R - u_c^U = 0 \tag{21.2}$$

This condition can be generally expressed as $Bu = 0$, where each row of B corresponds to a pair of matching DoFs. Note that the Eq. (21.2) is referred to a rigid connection. The equilibrium condition implies that the sum of the connecting forces across a connection for a pair of matching DoFs is zero:

$$g_c^R + g_c^U = 0 \tag{21.3}$$

For the internal DoFs of each subsystem $g = 0$ holds. For generalization, the above conditions can be expressed as $L^T g = 0$, where the matrix L is the Boolean localization matrix and it is defined as the nullspace of B. The final system of equations will be:

$$\begin{cases} Z(\omega) u(\omega) = f(\omega) + g(\omega) \\ Bu(\omega) = 0 \\ L^T g(\omega) = 0 \end{cases} \tag{21.4}$$

In which $u(\omega)$ is a vector with all components of the DoFs of R and U and $Z(\omega)$ is the following diagonal matrix:

$$Z(\omega) = \begin{bmatrix} Z^R(\omega) & 0 \\ 0 & Z^U(\omega) \end{bmatrix} \tag{21.5}$$

The system of Eq. (21.4) represents the so-called 3-field formulation. Starting from the 3-field formulation, several assembly techniques can be devised: dual, primal and hybrid assembly (see [10]). Even if all assembly techniques give the same results for $N_E = N_C$ (i.e. the number of compatibility DoFs is the same as the number of equilibrium DoFs), the dual assembly involves the least number of matrix inversions and for this reason it will be used in the following sections. In the dual assembly, the equilibrium condition $L^T g(\omega) = 0$ is satisfied by writing $g = -B^T \lambda$. Eq. (21.4) becomes:

$$\begin{cases} Z(\omega) u(\omega) + B^T \lambda = f(\omega) \\ B u(\omega) = 0 \end{cases} \tag{21.6}$$

21.2.1 FBS Coupling

Considering the two substructures, let us indicate the internal DoFs of R and U respectively with r and u and the connection DoFs with c. The algorithm proposed by Jetmundsen provides less matrix inversions, thus overcoming a big amount of numerical problems:

$$H^{RU} = \begin{bmatrix} H_{rr}^R & H_{rc}^R & 0 \\ H_{cr}^R & H_{cc}^R & 0 \\ 0 & 0 & H_{uu}^U \end{bmatrix} - \begin{bmatrix} H_{rc}^R \\ H_{cc}^R \\ -H_{uc}^U \end{bmatrix} \left[H_{cc}^R + H_{cc}^U \right]^{-1} \begin{bmatrix} H_{rc}^R \\ H_{cc}^R \\ -H_{uc}^U \end{bmatrix}^T \tag{21.7}$$

In Eq. (21.7) and in the following, the dependency of the Frequency Response Function to the frequency will be omitted for simplicity. It's worth to note that in the latter equation the connecting DoFs are assumed to belong to R. If one assumes these DoFs belonging to U, the coupled equation is modified as:

$$H^{RU}(\omega) = \begin{bmatrix} H_{rr}^R(\omega) & 0 & 0 \\ 0 & H_{cc}^U(\omega) & H_{uc}^U(\omega) \\ 0 & H_{cu}^U(\omega) & H_{uu}^U(\omega) \end{bmatrix} - \begin{bmatrix} -H_{rc}^R(\omega) \\ H_{cc}^U(\omega) \\ H_{uu}^U(\omega) \end{bmatrix} \left(H_{cc}^R(\omega) + H_{cc}^U(\omega) \right)^{-1} \begin{bmatrix} -H_{rc}^R(\omega) \\ H_{cc}^R(\omega) \\ H_{uu}^U(\omega) \end{bmatrix}^T \tag{21.8}$$

However, both Eqs. (21.7) and (21.8) will lead to the same results [11]. Using numerical data, these two equations lead to the same FRF matrix of RU. Using experimental data only, on the other hand, the FRFs referred to coupling DoFs are slightly different depending on the equation being used.

21.2.2 FBS Decoupling

The decoupling problem aims at finding the dynamic behavior of the unknown U substructure, starting from the knowledge of RU and R. In general U is influenced not only by external forces but also by connection force of R. Hence, in order to decouple, it is needed to apply to RU additional force opposing these connection forces: the effect of this calculation is thus the behavior of the substructure U without the influence of R. Starting from the dual formulation approach:

$$H^U = \left(H^{RU} - H^{RU} B_{RU}^T \left(B_{RU} H^{RU} B_{RU}^T - B_R H^R B_R^T \right)^{-1} B_{RU} H^{RU} \right) \tag{21.9}$$

Note that the above equation is valid in case of collocated interface and it is the one that we will use in this paper. If one wants to use the non-collocated interface, it's needed to define different Boolean matrices for equilibrium and compatibility conditions [10]. In order to build the Boolean matrix in the decoupling problem, the type of interface has to be chosen among those displayed in Fig. 21.1.

Experimentally, there are many difficulties in measuring the connection DoFs of the assembled structure RU. This means that it is generally not possible to use the first three types of interface displayed in Fig. 21.1. However, when using the pseudo-interface, a right choice of the internal DoFs is needed: in fact, in order to perform a good decoupling of R from RU, it is important to measure all the information about the dynamics of R in the considered range of frequency.
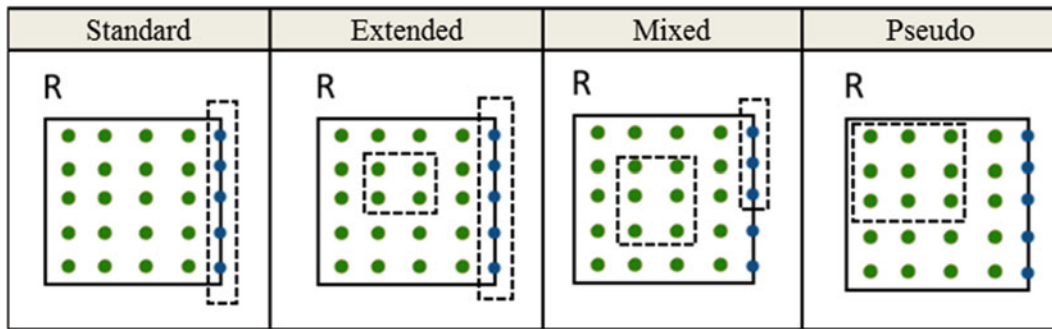
Fig. 21.1 Scheme of the different types of interface considered (*Green*: internal DoFs – *Blue*: connection DoFs)

21.3 Iterative Approaches on Dynamic Substructuring

The two iterative approaches that will be explained in this section were developed with the aim of finding the connection error resulting from DS application with experimental data. Information about identified connection error can be then used again in future DS applications on the same structures:

– During the design phase of a project, one might want to modify one of the subsystems and verify its effect on the dynamics of the assembly. A useful way of analyzing how the complete system changes is by studying it experimentally. Considering the coupling problem, one might be able to compensate for connection errors/uncertainties using a priori information. This connection compensation value was previously found by applying one of the proposed iterative approaches. In this way, the second measurement of the complete system RU is not needed anymore (Fig. 21.2).
– Another example is given in Fig. 21.3:

  • First Step: the dynamic response of each structure (R, U and RU) is known at time T_0. Starting from this, one of the iterative approaches to find the connection error can be applied to improve the quality of the coupling results
  • Second Step: after the operative life (at time $\bar{T}$), the subsystem U (i.e. the engine) is subject to dynamic modification or needs to be updated with a newer model. Assuming no changing on R, the connection error can be applied on the coupled structure in order to reliably evaluate the dynamic response based on the dynamic model of the new U.

In the following section, the proposed approaches will be explained: FCU-R (Frequency Connection Updating – Rigid) and FCU-F (Frequency Connection Updating – Flexible). The method to be applied on each specific case will depend on the assumption made to model the connection; in particular, when introducing the method, we will refere to rigid or flexible connections (depending on the compatibility condition applied) and point vs. multipoint connections, which depend on the size of the connection area.

21.3.1 FCU-R: Frequency Connection Updating – Rigid

The first discussed method is based on the application of the Predictor-Corrector (PC) Frequency Domain Updating Method ([12, 13]) on DS. The basic idea is to update the dynamic measured RU model in order to find the uncertainty in terms of mass and stiffness at the interface DoFs, such that $R + U + \Delta \in_c = RU$. It means that this procedure could represent the connection errors as a local perturbation of mass and stiffness properties ($\Delta \in_c = \Delta m$, $\Delta \in_c = \Delta k$ or a combination of them) at the same local point. Rigid connections are assumed.

For this purpose, two approaches were initially investigated:

– Correlation between the exact (measured) U and the decoupled one
– Correlation between the exact (measured) RU and the coupled one

The solution to the first problem will not be discussed here because it finds difficult experimental applications. A hard requirement for both techniques is that the physical mass and stiffness matrices are needed in order to apply the PC. Consequently, the FE model of each assembly has to be updated and so validated FE model are required. It is worth to note that, assuming there is no noise in the data, the error will only be associated to connection uncertainties. Furthermore,
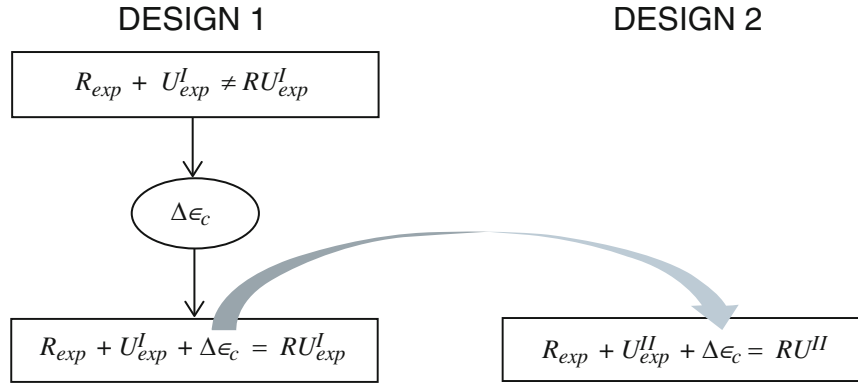
Fig. 21.2 Scheme of the use of the connection error in a design phase of a project
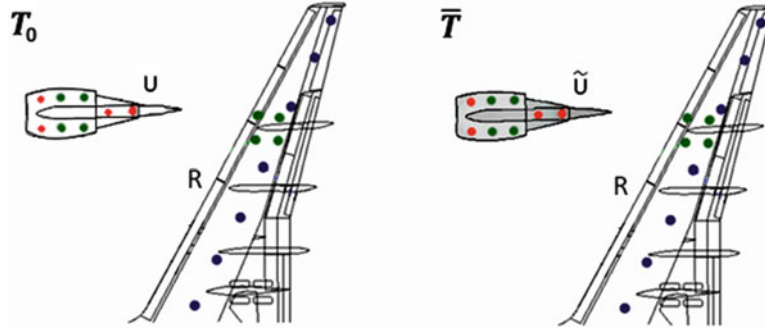
Fig. 21.3 Substructure U (engine) subject to a modification at a certain time $\overline{T}$ – Substructure R: wing

these methods are applicable only with point connections. Indeed, starting from the FE model, we locally update the FRF only at the connection points which will be subjected to the compatibility and the equilibrium equations. In case of distributed contact between the substructures, and assuming a point connection, the updating of the local properties will not allow to compensate for the lack of information. In this case one should find the minimum number of point connections which is able to represent accurately the actual contact at least in the frequency range of interest. Another problem is related to the rotational DoFs at the connection, which are typically impossible to measure experimentally. As the proposed method will not be able to compensate for them, an alternative approach is try to impose compatibility on a higher number of translation DoFs over the same contact surface. (see Sect. 4.1.).

The aim of the FCU-R method is to correlate directly the measured structure RU with the one that in the substructure decoupling algorithm can give the exact U. This can be performed in the following way:

– supposing that U and R are known experimentally, one can evaluate the coupled RU_{coup} using the solution proposed by Jetmundsen, considering that the connection DoFs belong to the substructure U (Eq. (21.8))
– coming back to the decoupling problem, we can evaluate $RU_{coup} - R$ using a pseudo-interface and the results will give us the exact dynamic behavior of U

Therefore, we can affirm that: *the coupled structure RU_{coup}, evaluated with the Jetmundsen equation* (Eq. (21.8)), *is such that if one decouples it from R imposing a pseudo-interface, the results give the exact solution U.*

The FCU-R can be demonstrated imposing the following system:

$$
\begin{bmatrix}
H_{coup}^{RU} = \begin{bmatrix} H_{rr}^{R} & H_{rc}^{R} & 0 \\ H_{cr}^{R} & H_{cc}^{R} & 0 \\ 0 & 0 & H_{uu}^{U} \end{bmatrix} - \begin{bmatrix} H_{rc}^{R} \\ H_{cc}^{R} \\ -H_{uc}^{U} \end{bmatrix} [H_{cc}^{R} + H_{cc}^{U}]^{-1} \begin{bmatrix} H_{rc}^{R} \\ H_{cc}^{R} \\ -H_{uc}^{U} \end{bmatrix}^{T} \\
H_{dec}^{U} = H^{U} = H_{RU} - \begin{bmatrix} H_{cc}^{RU,coup} \\ H_{uc}^{RU,coup} \end{bmatrix} \left(H_{cc}^{RU,coup} - H_{cc}^{R} \right)^{-1} \begin{bmatrix} H_{cc}^{RU,coup} \\ H_{uc}^{RU,coup} \end{bmatrix}^{T}
\end{bmatrix}
\tag{21.10}
$$

Then RU and RU_{coup} are correlated using the classical PC method, updating mass and stiffness parameters only on the connection measured DoFs. Note that this method can be used also in the decoupling problem: in fact if one find the connection error, then it can be applied in a second measurement on RU. Thus, decoupling R from the modified assembled structure, one will find exactly the dynamic behavior of U.

21.3.2   FCU-F: Frequency Correction Updating – Flexible

This method finds applicability in those cases where there is the possibility to measure the connection DoFs of the coupled structure on both sides: the one belonging to U as well as the one belonging to R. A typical example is that of two substructures connected by a spring with sufficient free length: in this case one can measure both connected points of the spring and the coupled structure RU will have one more measured DoF compared to the rigid interface.

FCU-F was developed starting from the concept of compliant interface studied by De Klerk [14], where, considering no damping at the connection, the compatibility equation and the Lagrange multiplier can be written respectively as:

$$Bu = \Delta u_c \tag{21.11}$$

$$\lambda = K_c \Delta u_c = Z_c \Delta u_c \tag{21.12}$$

The final modified expression for decoupling is then:

$$H^U = \left(H^{RU} - H^{RU} B_{RU}^T \left(B_{RU} H^{RU} B_{RU}^T - B_R H^R B_R^T + H_C \right)^{-1} B_{RU} H^{RU} \right) \tag{21.13}$$

with $H_c = Z_c^{-1}$. Clearly for rigid connection, $H_c H_c$ goes to zero and one can find back Eq. (21.9).

Starting from the approach developed by De Klerk, the innovation with the FCU-R is its application in Experimental Dynamic FBS, as we are going to demonstrate in Sect. 4.2 by a numerical example. Starting from the knowledge of all systems R, U and RU, the term H_c can be derived as:

$$H_C = -\left(\left(\begin{bmatrix} -H_{(r,c)c}^R \\ H_{(u,c)c}^U \end{bmatrix}^T \begin{bmatrix} -H_{(r,c)c}^R \\ H_{(u,c)c}^U \end{bmatrix} \right)^{-1} \begin{bmatrix} -H_{(r,c)c}^R \\ H_{(u,c)c}^U \end{bmatrix}^T \left(H_{ref}^{RU} - \begin{bmatrix} H^R & 0 \\ 0 & H^U \end{bmatrix} \right) \begin{bmatrix} -H_{(r,c)c}^R \\ H_{(u,c)c}^U \end{bmatrix}^T \left(\begin{bmatrix} -H_{(r,c)c}^R \\ H_{(u,c)c}^U \end{bmatrix}^T \begin{bmatrix} -H_{(r,c)c}^R \\ H_{(u,c)c}^U \end{bmatrix} \right)^{-1} \right)^{-1} - H_{cc}^U - H_{cc}^R \tag{21.14}$$

Inverting the expression of H_c, one can find a diagonal matrix K_c of dimensions $N_C \times N_C$ in which each element will represent the value of the stiffness connection relative to that interface DoF. As this represents a physical stiffness its value will be constant at each spectral line. Both numerically and experimentally (as we will explain later) the results are not really constant because of respectively numerical errors and noise problems, or a combination of both. For both cases an averaging of the results in frequency is performed:

– by first smoothing the resulting frequency-dependent elements of matrix K_c, to regularize the results and cancel the effect of numerical noise
– by calculating then the mean value across frequency for each element of the matrix

Then, an iterative process of coupling-decoupling is proposed in order to enforce the regularization of the results.

Note that in case of flexible connection, the PC updating shows a hard applicability. In fact one could find the stiffness parameters by updating the coupled rigid system and comparing the latter with the reference one (with the "spring" connection) but of course the two systems will not only show a shift in frequency but also differences in modes.

21.4   Numerical Validation

In this section, the applicability and validation of FCU-R and FCU-F on the coupling of two beams are presented. Firstly, the analyzed system is described (Fig. 21.4): the substructures (horizontal beam R and vertical beam U) are coupled at four locations, which are realized by bolts (point connections). The size of the cross section is 0.8 cm × 4 cm. Both of them are in Aluminium and the analyzed frequency range is [0–3200] Hz. In Table 21.1, the natural frequencies (bending – 'z' direction) of the validated FE model of the reference structure RU and of the coupled one are reported. Note that the latter is the result of coupling between the validated FE models of R and U. The difference between the reference and the coupled models are in the connection area. The FE model validation of the reference system (which was in fact experimentally analyzed – Fig. 21.5) led to modeling the connection points with a total of 8 spiders (4 for each substructure) around the connection
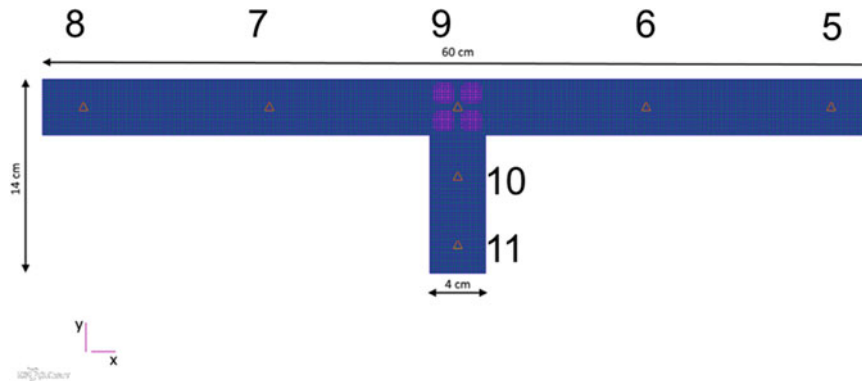
Fig. 21.4 Reference structure RU with name of the measured DoFs. Connection modeled by 8 spiders and 4 rigid connections on all DoFs

Table 21.1 Natural frequencies (bending out of plane in z direction) of the coupled and the reference model RU

Coupled Ru [Hz]	Reference RU [Hz]	Relative error [%]
107.16	112.60	4.83
311.92	312.20	0.09
565.66	591.90	4.43
854.78	915.30	6.61
1014.70	1019.00	0.42
1434.40	1499.70	4.35
1955.20	1975.90	1.05
1974.30	2023.40	2.43
2682.20	2808.00	4.48
3117.50		

Green torsion of R and bending of U, *Orange* bending of R and torsion of U, *Cyan* out-of-band mode

Fig. 21.5 Experimental setup of RU. Connection area on the right size
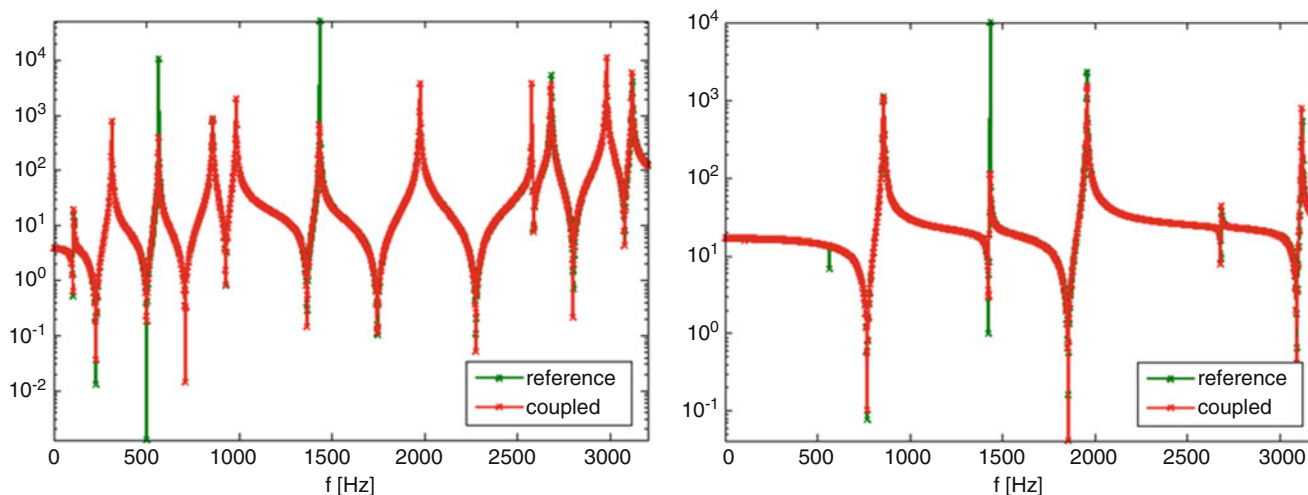
Fig. 21.6 FBS coupling, DoFs 7 (left) and 10 (right): comparison between FRFs of the reference case (8 spiders, 4 RBE all DoFs) and the simulated experimental coupling case (4 RBE 'z' DoF)

points and 4 RBEs between corresponding connection points on the two substructures. We demonstrated numerically that it is possible to obtain good results on the coupling between R and U by simply applying 4 rigid connections along translational 'z' DoFs (Fig. 21.6). Thus, by simulating the experimental coupled structure, the FE model has only 4 RBE elements. Note that it is only a simulation. In fact, experimentally, the connection area wasn't wide enough to allow measuring directly the 4 connection points with accelerometers (Fig. 21.5).

In Table 21.1, the modes showing coupling between torsion and bending are underlined. Note that these modes are very sensitive to the correct modeling of the connection: if one aims at predicting this behavior neglecting the rotational DoFs, at least all four connection points are required. A comparison between the reference model and a simulated experimental case (in which, because of the size of the interface area, one could measure only one connection point) is reported: in Figs. 21.7 and 21.8 the coupled modes and a result of the FBS coupling for this case (numerical data) are respectively shown. Because of the wrong assumptions at the connection, the coupling between the substructures leads to erroneous results.

Taking into account the reference model and the coupled one with four connections, the FCU-R and FCU-F methods will be applied and validated numerically in the following sections.

21.4.1 Application of FCU-R

In this section, we will validate the applicability of FCU-R using the system discussed in the previous paragraph. To achieve it, a first analysis was performed to find a distributed parameters error: material properties of the connection area (E_c and ρ_c) were found as a result of an optimization analysis in Siemens LMS Virtual.Lab (Fig. 21.9). It should be noted that, to increase
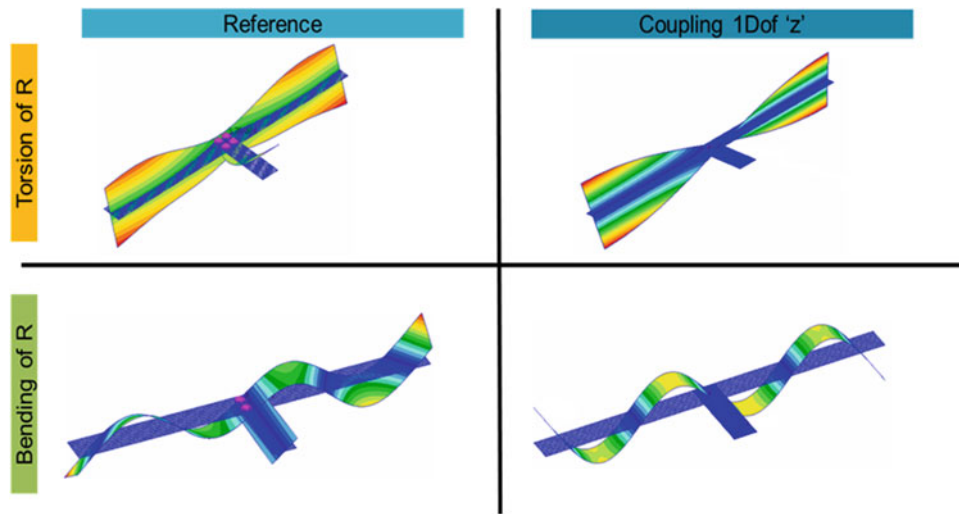
Fig. 21.7 Comparison between coupled modes of the reference case (8 spiders, 4 RBE all DoFs) and the simulated experimental coupling case (1 RBE 'z' DoF)
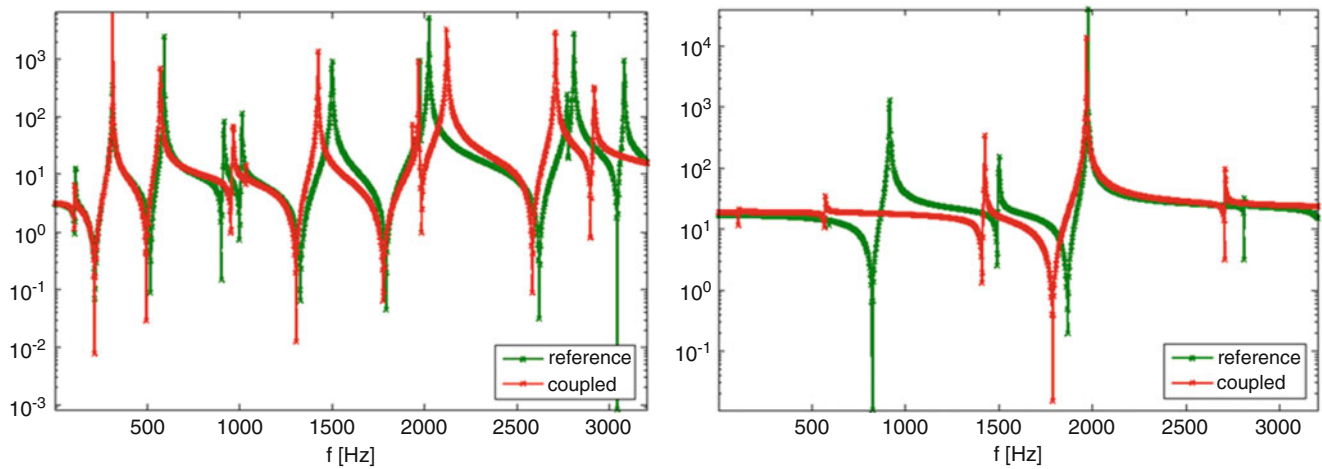
Fig. 21.8 FBS coupling, DoFs 7 (left) and 10 (right): comparison between FRFs of the reference case (8 spiders, 4 RBE all DoFs) and the simulated experimental coupling case (1 RBE 'z' DoF)
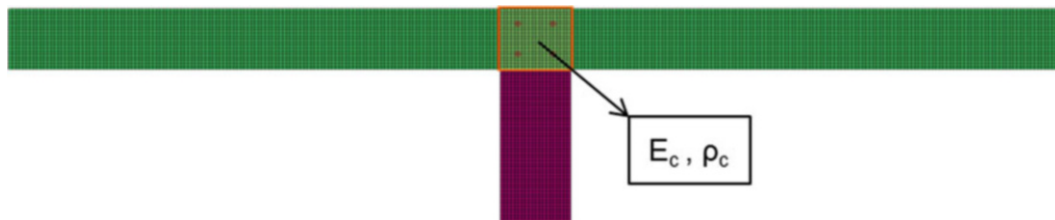
Fig. 21.9 Definition of different material properties of the connection area.

the efficiency of the calculations, a Craig-Bampton model order reduction was applied on both substructures before coupling. Although the accuracy of the reduction was verified, some small errors were still present leading to a slight decrease in the correlation with the reference coupled model shown in Table 21.1

The obtained optimal values are: $E_c = 90 GPa$ and $\rho_c = 2400 kg/m^2$. The percentage errors before and after the update are reported in Fig. 21.10. As one can note, they are reduced for all frequencies, in particular in the medium-high range where the dynamics of the connection appears.

Time T_0

	1	2	3	4	5	6	7	8	9
Original	4.83	0.09	4.43	6.61	0.42	4.35	1.05	2.43	4.48
Updated	2.07	0.01	1.88	4.03	0.09	2.34	0.24	1.06	2.56
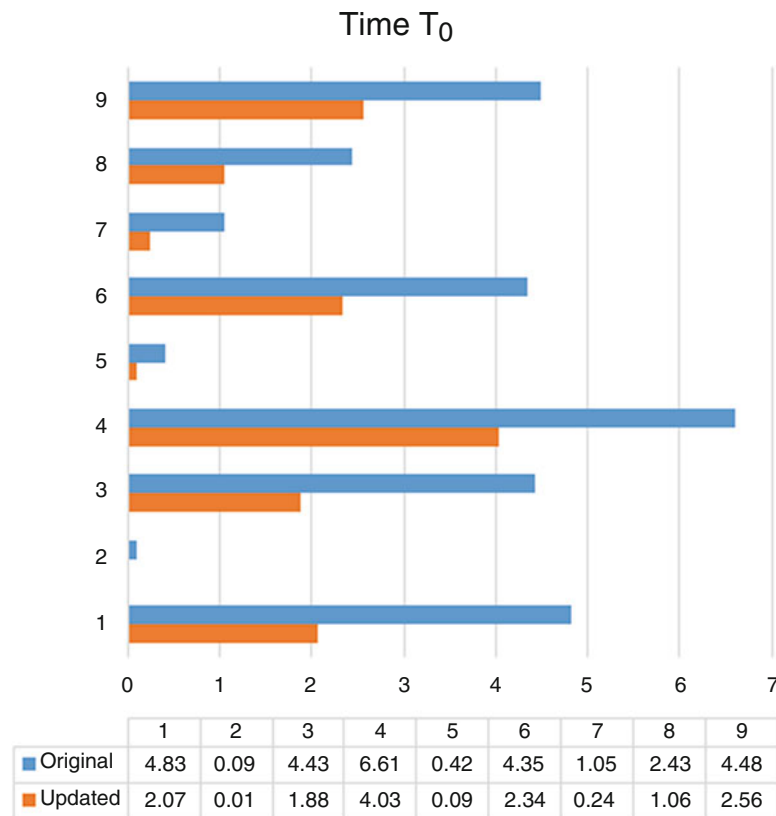
Fig. 21.10 Relative frequencies errors (*x*-axis) for each natural mode (*y*-axis) between coupled and reference model at time T_0 before (*Blue*) and after (*orange*) updating

To simulate a modification of the substructure U at the time $\overline{T}$, a lumped mass of about 0.006 kg was added at the center of the substructure U. Then, the previously obtained connection property values E_c and ρ_c are applied on the coupled system. The error percentage before and after the update is reported in Fig. 21.11 and as one can note, its reduction is very similar to the one obtained with the unmodified system. Thus the connection error can be represented in terms of mass and stiffness parameters.

Now, the analysis is repeated in terms of lumped parameters at the connection DoFs (4 for the analyzed system). In order to do that, the input parameters are set as variation of the nodal mass at the four connection points (same values). Simulating an experimental case, the two models were correlated on 10 "measured" points: 4 internal of R, 2 internal of U, 4 connections. The initial and final correlations are shown in Fig. 21.12: the updating focused on a narrower frequency range ([0–700] Hz) as at higher frequency the correlation decreases and a low correlation will negatively affect the applicability of the PC method. In Fig. 21.12, the *shape* and *amplitude* correlation coefficients [12] (respectively χ_s, χ_a) show that, after applying the obtained mass parameter, the first three natural frequencies (those in the analyzed range) are almost perfectly correlated. Note that the peaks of the green curve imply that the amplitude at the natural frequencies are not really the same, but anyway the correlation is acceptable. Furthermore these peaks can be explained by the absence of damping in the FE model and by numerical errors. The obtained variation of nodal mass is about -17.5% for each connection point. The negative value is due to the fact that the coupled model has lower natural frequencies than the reference one and consequently the higher stiffness of the latter has to be compensated.

The resulting mass error at the connection was then applied on the previously simulated modified system at time $\overline{T}$ (Fig. 21.13): the effect is almost the same and the results can be considered very good in the analyzed frequency range.

Note that if, instead of a concentrated mass, one would set the mass and stiffness properties of the connection points as input for the PC method, the procedure will be practically the same as the one performed in Virtual.Lab: in fact the PC method will update the element mass and stiffness matrices around the location of the connection DoFs.

Time T

	1	2	3	4	5	6	7	8	9
■ Original	4.8	0.07	4.44	6.59	0.42	4.35	0.87	2.43	4.51
■ Updated	2.05	0.02	1.9	4.02	0.08	2.38	0.33	1.06	2.58
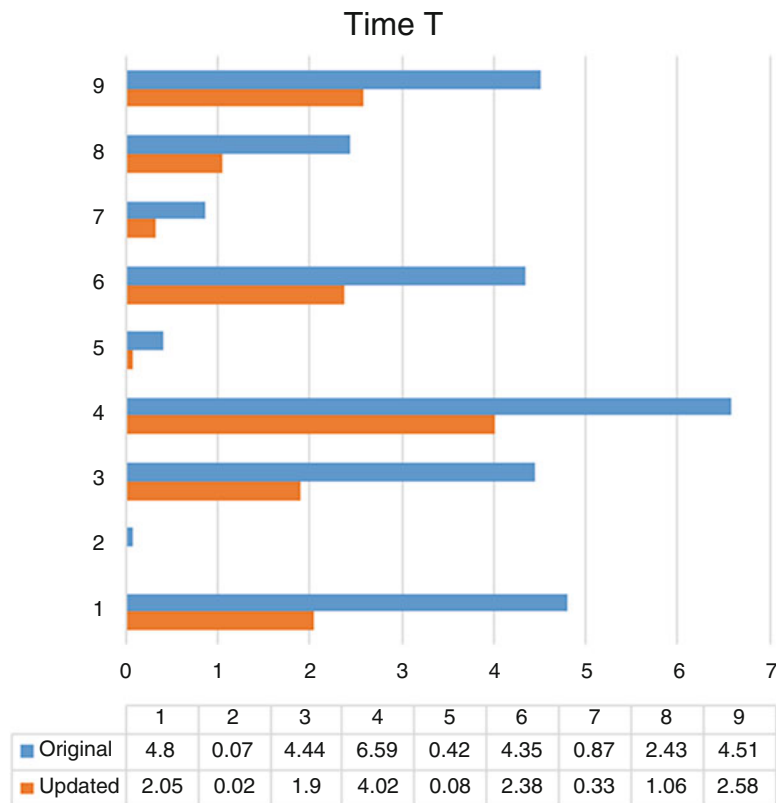
Fig. 21.11 Relative frequencies errors (*x*-axis) for each natural mode (*y*-axis) between coupled and reference model at time $\overline{T}$ before (*Blue*) and after (*red*) updating
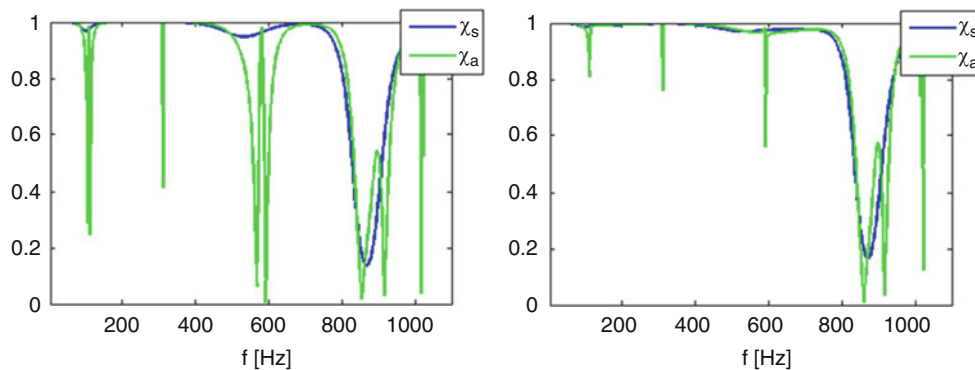
Fig. 21.12 Correlation between the reference and the coupled systems (time T_0) before (*left*) and after (*right*) updating – value of the obtained mass error: -17.5% of the nodal mass of each connection DoFs

21.4.2 Application of FCU-F

As discussed in Sect. 3.2, this method can find applicability in those cases where it is possible to measure at both sides of the connection DoFs in R and in U. In fact, considering 4 springs as shown in Fig.21.14, the connection DoFs of R and its U counterpart are not coincident as it happened for a rigid connection. The same system of beams presented in the previous section will be considered to apply the FCU-F. Four flexible connections between the substructures are defined in the FE model. Also some noise will be added to simulate an experimental case.
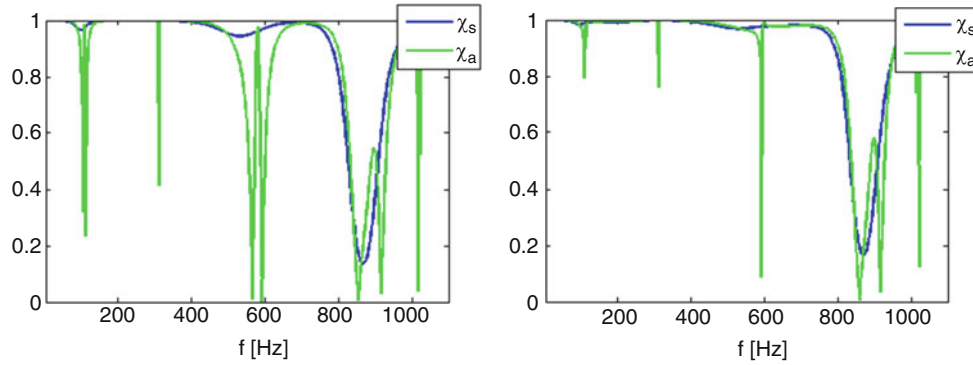
Fig. 21.13 Correlation between the reference and the coupled modified systems (time $\overline{T}$) before (*left*) and after (*center*) the application of the previously obtained mass connection error
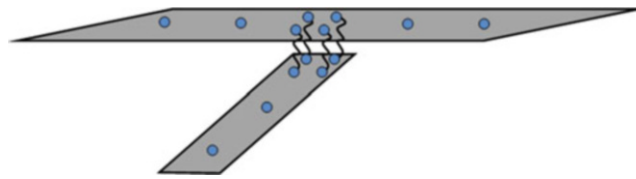
Fig. 21.14 Four flexible connections between R (8 "measured" points) and U (6 "measured" points)

The following steps are performed:

– Evaluate the FRF matrices in 'z' direction of R [8 × 8], U [6 × 6] and RU [14 × 14]. The latter, considered as the reference assembled structure, was made by connecting R and U with 4 springs with equal stiffness value $2 \cdot 10^{10} N/m$
– Evaluate Eq. (21.14) leading to a matrix with dimension [4 × 4]. By inverting it, a diagonal matrix is obtained with the values of the imposed connection stiffnesses.

In case of noisy data, additional steps are needed:

– 0.001% of complex circular noise is added to the simulated FRFs
– Elements of H_c^{-1} matrix are smoothed
– The average frequency value of each element on the diagonal of H_c^{-1} is calcualted
– Reciprocity is imposed on K_c (lower triangular matrix equal to the upper one) in order to allow the diagonalization of the matrix (in fact, for noisy data, the matrix $K_c K_c$ is not diagonal)
– The complex K_c matrix is realized using the following approach:

$$k_{real} = \text{Re}\,(k_{im}) + \text{Im}\,(k_{im}) \cdot (\text{Re}\,(k_{im})\,' \cdot \text{Re}\,(k_{im}))^{-1} \cdot \text{Re}\,(k_{im})\,' \cdot \text{Im}\,(k_{im}) \qquad (21.19)$$

– The mean value between the obtained $k_{real,ii}$ on the diagonal is calculated and substituted in each element of the diagonal (this step is only required if it assumed that all connection stiffnesses are equal)
– The resulting matrix is used in the coupling problem to evaluate RU_{coup}^{11}
– U^{11} is evaluated by decoupling R from RU_{coup}^{II}
– R and U^{11} are inserted back in Eq. 21.14 and the procedure is repeated to average out the noise

A scheme of the explained procedure is shown in Fig. 21.15.

In the considered system, to still maintain the link with the reference model presented in Fig. 21.4, a relatively high initial stiffness value for the connection spring needed to be defined. As a consequence, the method only needs to apply limited modification to this value to converge to an optimal solution. In Figs. 21.16 and 21.17, the results of the performed analysis are shown: note that, by only smoothing the data, values of the obtained K_c are not accurate and the out-of-diagonal terms have purely numerical meaning (non-uniqueness of the solution). Even if not exact, we will carry on an evaluation of these results, since our aim is to verify if this value can be applied to a modified system at time $\overline{T}$ and conquently obtain more reliable results without having to perform again a full experimental campaign. For this purpose, let us to consider the same previous modified system with an added concentrated mass at the center of the beam U. In Table 21.2, the results for the
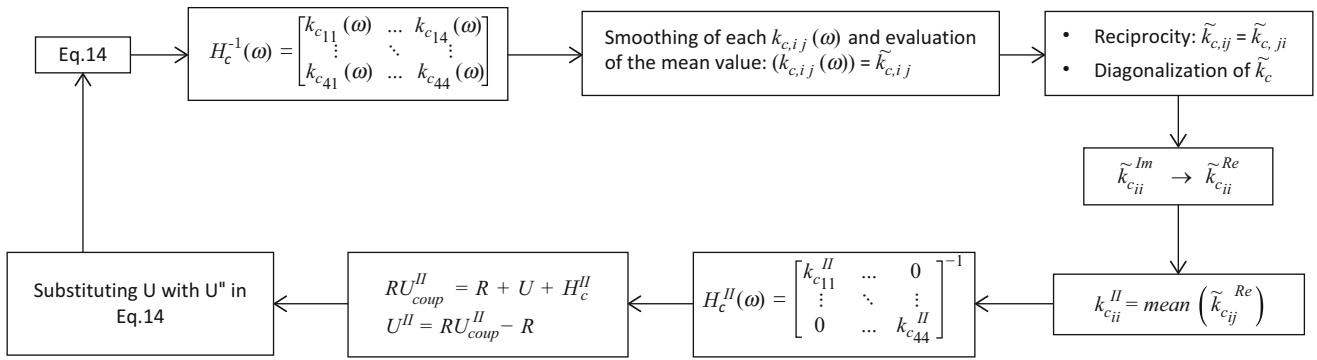
Fig. 21.15 Scheme of the FCU-F method for noisy data
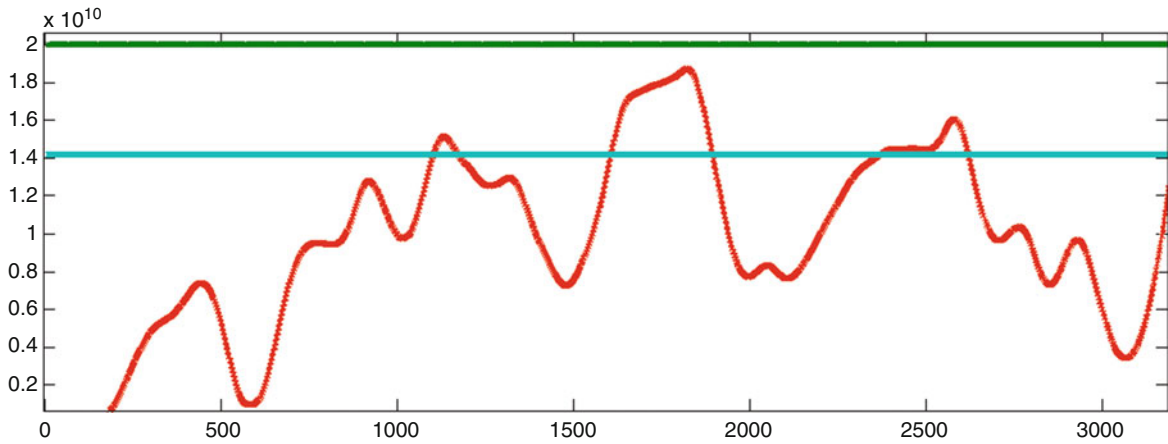
Fig. 21.16 Noise level: 0.001%. Diagonal term of the matrix k_c: smoothed (*red*), exact (*green*), FUC-F (*cyan*)
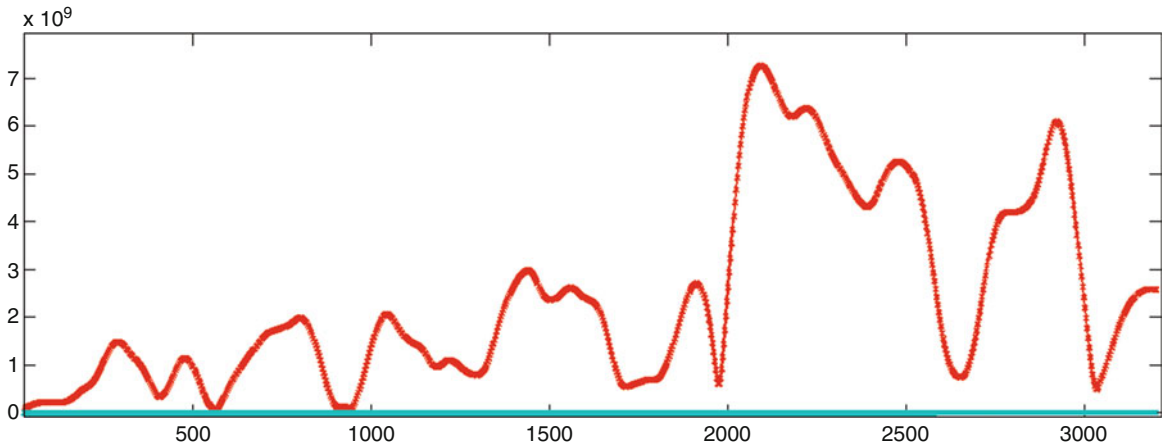
Fig. 21.17 Noise level: 0.001%. Out-of-diagonal term of the matrix k_c: smoothed (*red*), exact (*green*), FCU-F (*cyan*).

first and the modified system affected by different levels of noise are reported: the order of magnitude is always the same, but the amplitude is almost equal up to a certain level of noise. We can conclude that, for low levels of noise, the value obtained from experimental results should not change from T_0 to $\overline{T}$ and so the connection information can be used again for next substructuring cases. As a final validation of the approach, Fig. 21.18 shows the coupled FRFs using rigid and flexible connections at time T_0 (left)and $\overline{T}$ (right). In both case, in particular at higher frequencies, improved results are obtained when including flexibility at the connections. Indeed, as already mentioned, the relatively high stiffness value defined will only have a marginal effect on the lower frequencies modes compared to the assumption of rigid connection.

Table 21.2 Calculated values of $k_{c,ii}$ by applying the third method

Noise level [%]	$K_{c,ii}$ at time T_0 [N/m]	$K_{c,ii}$ at time $\overline{T}$ [N/m]
0.001	$1.397 \cdot 10^{10}$	$1.412 \cdot 10^{10}$
0.01	$6.741 \cdot 10^{9}$	$6.845 \cdot 10^{9}$
0.1	$4.523 \cdot 10^{8}$	$8.007 \cdot 10^{8}$
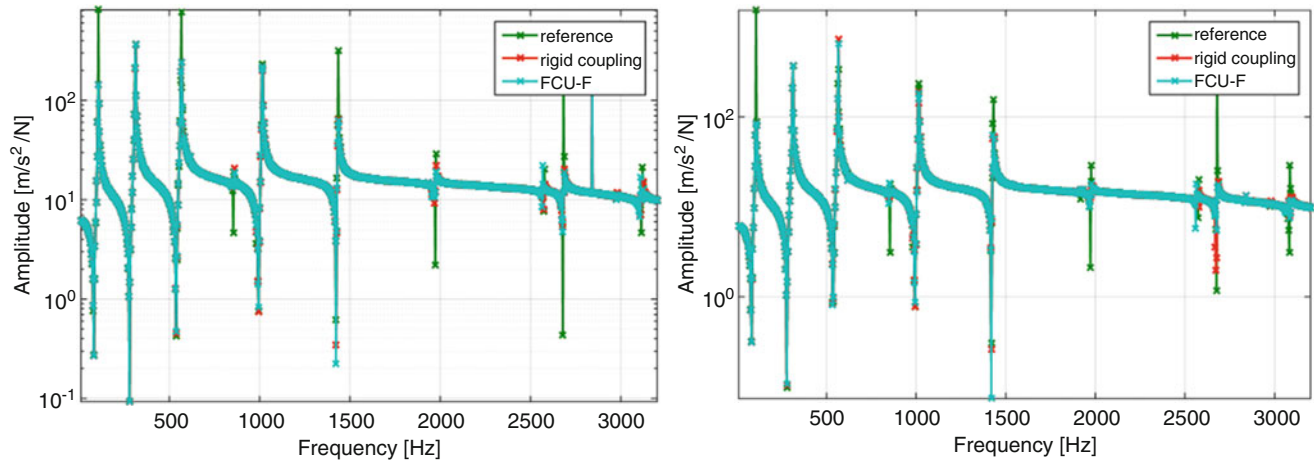
Fig. 21.18 Coupling results at time T_0 (*left*) and $\overline{T}$ (*right*) on DoF 5. Comparison between reference model, rigid connection assumption and flexible connection with stiffness derived using the FCU-F method

21.5 Conclusions

The paper proposes two iterative approaches for Dynamic Substructuring applications to compensate for typical experimental errors in measuring and/or modelling the connections. Sometimes, it is required to change one of the subsystem of the examined structure, thus one have to study how the dynamic behavior of the latter will be affected. Experimentally, by performing the coupling of two substructures one can observe some shift in frequencies with respect to the reference assembled RU. Here, two methods were proposed to find the connection uncertainties in the coupled system RU, by a comparison with the reference one. Then this information, associated to the type of connection, can be used again in following DS applications on the same system RU. The comparison between the two dynamic models find a useful way to compensate this frequency errors in term of mass and stiffness at the connection area. Of course the local modified properties cannot compensate in no case the lack of information about RDoFs. In fact at first the connection has to be reproduce as well. The analyzed system is composed by two beams and some simulations were performed by changing the subsystem U. The FCU-R method shows good results in the reported application: in fact the obtained mass connection error for the structure at the time T_0, led to the same percentage frequency difference in the analyzed range, also after changing U. Same considerations can be done for the application of the FCU-F method.

The disadvantage of these studies is that one should know at first the experimental (and also numerical, for the FCU-R) dynamic behavior of both substructures and of the assembled RU. Anyway, after this preliminary study, the connection error could be used again in other substructuring applications (by considering the same type of connection). Future developments will focus on the experimental validation of the proposed methodologies, with particular attention in the applicability of the methods on different types of connections.

References

1. Manzato, S., Napoli, C., Coppotelli, G., Fregolent, A., D'Ambrogio, W., Peeters, B.: Experimental coupling and decoupling of engineering structures using frequency-based substructuring. Dynamics of coupled structures, conference proceedings of the society for experimental mechanics series, 4, pp. 447–461 (2016)
2. De Klerk, D., Rixen, D., Voormeeren, S.N.: General framework for dynamic substructuring: history, review and classification of techniques. AIAA J. **46**(5), 1169–1181 (2008)
3. D'Ambrogio, W., Sestieri, A.: A unified approach to substructuring and structural modification problems. Shock. Vib. **11**(3), 295–309 (2004)
4. Heylen, W., Lammens, S., Sas, P.: Modal analysis theory and testing. A.5, pp. 10–20 (2007)

5. D'Ambrogio, W., Fregolent, A.: The role of interface DoFs in decoupling of substructures based on the dual domain decomposition. Mech. Syst. Signal Process. **24**(7), 2035–2048 (2010)
6. Rixen, D.J.: How measurement inaccuracies induce spurious peaks in frequency based substructuring. Proceedings of the International Modal Analysis Conference (IMAC), Jacksonville, USA (2010)
7. De Klerk, D., Rixen, D. J., Voormeeren, S. N., Pasteuning, F.: Solving the RDoF problem in experimental dynamic substructuring. Proceedings of the XXVI International Modal Analysis Conference (IMAC), Orlando, FL (2008)
8. Nicgorski, D., Avitabile, P.: Experimental issues related to frequency response measurements for frequency-based substructuring. Mech. Syst. Signal Process. **24**, 1324–1337 (2010)
9. Manzato, S., Risaliti, E., Napoli, C., Tamarozzi, T., Peeters, B.: A review of Frequency-based Substructuring methods and their applicability to Eengineering structures. Proceedings of the International Conference on Structural Engineering Dynamics (ICEDyn) 2015, Lagos, Portucal (2015)
10. D'Ambrogio, W., Fregolent, A.: Substructure decoupling without using rotational DoFs: fact or fiction? Mech. Syst. Signal Process. **72-73**, 499–512 (2016)
11. De Klerk, D., Rixen, D., De Jong, J.: The Frequency Based Substructuring (FBS) method reformulated according to the dual domain decomposition method. Proceedings of the International Modal Analysis Conference (IMAC), St. Louise, MO (2006)
12. Grafe, H.: Model updating of large structural dynamics models using measured response functions. PHD Thesis, Imperial College, London, UK (1998)
13. Arras, M., Coppotelli, G.: Finite-element structural updating using frequency response functions. J. Aircr. **52**(5), 1454–1468 (2015)
14. Barten, E., Van Der Seijs, M.V., De Klerk, D.: A complex power approach to characterise joints in experimental dynamic substructuring. Dynamics of coupled structures, conference proceedings of the society for experimental mechanics series, 1, pp. 281–296 (2014)

Chapter 22
Experimental Assessment of the Influence of Interface Geometries on Structural Dynamic Response

T. Dossogne, T.W. Jerome, D.P.T. Lancereau, S.A. Smith, M.R.W. Brake, B.R. Pacini, P. Reuß, and C.W. Schwingshackl

Abstract Jointed interfaces are sources of the greatest amount of uncertainty in the dynamics of a structural assembly. In practice, jointed connections introduce nonlinearity into a system, which is often manifested as a softening response in frequency response, exhibiting amplitude dependent damping and stiffness. Additionally, standard joints are highly susceptible to unrepeatability and variability that make meaningful prediction of the performance of a system prohibitively difficult. This high degree of uncertainty in joint structure predictions is partly due to the physical design of the interface. This paper experimentally assesses the influence of the interface geometry on both the nonlinear and uncertain aspects of jointed connections. The considered structure is the Brake-Reuß beam, which possesses a lap joint with three bolted connections, and can exhibit several different interface configurations. Five configurations with different contact areas are tested, identified, and compared, namely joints with complete contact in the interface, contact only under the pressure cones, contact under an area twice that of the pressure cones, contact only away from the pressure cones and Hertzian contact. The contact only under the pressure cone and Hertzian contact are found to behave linearly in the range of excitation used in this work. The contact area twice that of the pressure cone behaves between the complete contact and contact only under the pressure cone cases.

Keywords Bolted joints • Nonlinear vibrations • Experimental setup • Repeatability test • Lap joint • Pressure cones • Hertzian contact • Micro-slip

_____

T. Dossogne
University of Liège, 9, Allée de la Découverte B52/3, 4000, Liège, Belgium

T.W. Jerome
Graduate Program in Acoustics, The Pennsylvania State University, State College, 16801, PA, USA

Sandia National Laboratories, PO Box 5800, 87185, Albuquerque, NM, USA

D.P.T. Lancereau
Cranfield University, SN6 8LA, Shrivenham, Swindon, UK

S.A. Smith (✉)
University of Maryland, Baltimore County, 1000 Hilltop Circle, 21250, Baltimore, MD, USA

Sandia National Laboratories, PO Box 5800, 87185, Albuquerque, NM, USA
e-mail: sasmit@sandia.gov

M.R.W. Brake
Sandia National Laboratories, Albuquerque, NM, USA

William Marsh Rice University, Houston, TX, USA

B.R. Pacini
Sandia National Laboratories, PO Box 5800, 87185, Albuquerque, NM, USA

P. Reuß
Daimler AG, 70546, Stuttgart, Germany

C.W. Schwingshackl
Imperial College London, Exhibition Road, SW7 2AZ, London, UK

22.1 Introduction

Assemblies of systems that are bolted together are prevalent in many engineering applications. The ability to model and predict bolted joint behavior is of great interest, specifically for applications of high consequence, such as in defense, aerospace, and automotive engineering sectors. Such modeling and prediction of the response of bolted structures is a challenging engineering problem for several reasons, including:

- The frictional interactions within the interface of a jointed structure are not well understood, and existing models poorly capture both macroslip and microslip effects [1], unless heurculain efforts are made [2];
- The frictional characteristics of a jointed structure change over time as wear is accumulated [3–8]; and,
- The extent and evolution of the contact patch during dynamic excitation is unknown[9].

Another set of problems originates in that structures that are of the same geometric dimensions, material, and assembly process are highly variable in their behavior, exhibiting low repeatability, particularly at modal resonance. If the variability in repeatability due to the material, geometrical, and assembly constraints of the system could be minimized or understood, then models and designers would have some increased measure of predictability of the behavior of systems with bolted joints.

This research endeavors to characterize the important aspects of a system with a bolted joint in terms of repeatability, impact force, and geometric variation via interface area. Analysis of the data is performed with multiple methods to address the inherent and procedural variability of the tested systems. It is expected that some interface areas will feature more variability than others, highlighting information which may be useful to design high-performance structures and create contact models.

22.2 Interface Design

In order to assess the effects of interface geometry on the dynamics of a bolted structure, four perturbations of the Brake-Reuß beam [10, 11] were designed. The Brake-Reuß beam (BRB) (Fig. 22.1), is a 72 cm long beam that is divided into two halves joined by a three-bolt lap joint. The nominal system has a flat interface, as shown in Fig. 22.2a. This system, however, has exhibited high variability and low repeatability [11–13], and it is hypothesized that this is due to the non-uniform contact pressure across the interface. The four perturbations of this design address two different notions from recent
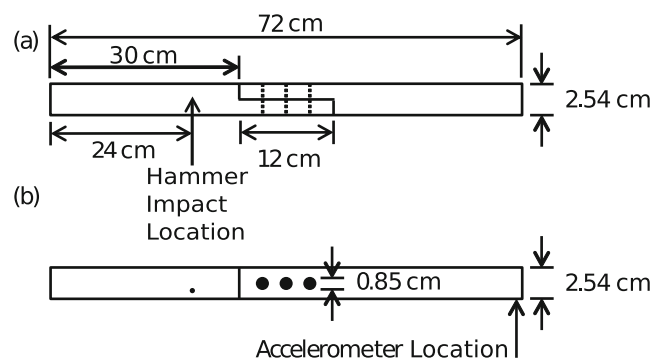
Fig. 22.1 The schematic of the Brake-Reuß beam
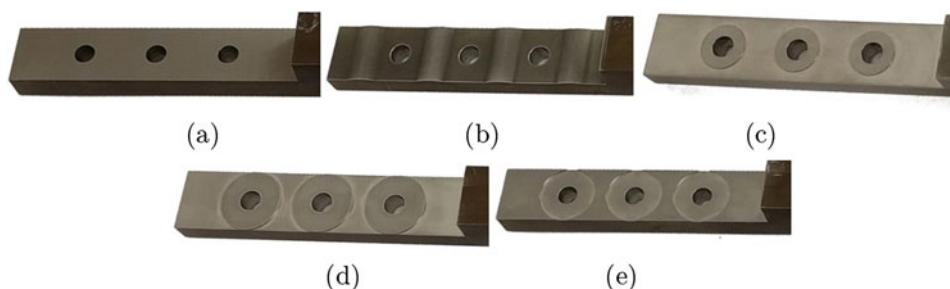
Fig. 22.2 Interface designs: (**a**) Brake-Rueß – BRB, (**b**) Hertzian contact – HRZ, (**c**) small pad – PDS, (**d**) large pad – PDL, (**e**) reverse pad – RPD

research. First, from the solid mechanics perspective, a traditional lap joint, which is a form of complete contact, is one of the worst designs possible due to the many negative qualities. Complete contacts are characterized by having a sharp edge in their profile, which results in the contact area being independent of the normal load. Additionally, the sharp edge often gives rise to singularities in the stress distributions [14]. For incomplete contact, such as Hertzian contact or contact between two cylinders, the contact area is a function of the applied normal load, and the contact pressure smoothly tends to zero as the contact edge is approached [15]. This notion led to the first BRB perturbation where a Hertzian interface was designed (Fig. 22.2b), which consists of four cylindrical bumps that are designed to not yield under the nominal bolt torques used in experiments. Recent research has indicated that most of the dissipation within a jointed interface occurs away from the pressure cones of the bolts [16–20]. Thus, the second perturbation (Fig. 22.2c, hereafter referred to as the small pad or PDS) was designed to only have contact directly under the pressure cones of the bolts. To explore the transition between the small pad interface and the nominal, flat interface, a large pad (PDL, Fig. 22.2d) was designed as a third perturbation. Additionally, the inverse of the PDL (RPD) was designed to see if this significantly exacerbated the dynamics of the system in terms of more variability and less repeatability, and is shown in Fig. 22.2e.

22.3 Experimental Setup

To investigate the effects of the interface geometry on the response of the beam, impact tests were performed. The beam was assembled using $5/16" - 24$ grade-8 steel bolts. To perform the tests, the beam was suspended on 1.7 m of bungee that was looped over an x-brace structure, crossed to help prevent beam rolling, and looped around the beam using fishing line. The supports were located approximately 5 cm in from the edges of the beam. The beam was then impacted using a PCB 086C01 Modal Impact Hammer, at the location shown in Fig. 22.1b. The beam was assembled using a torque of 20 Nm, which is lower than the recommend 36.6 Nm for the bolts used. This torque level was selected to exacerbate the nonlinear effects in lower input levels. Three different impact levels were selected, 60 N 210 N and 340 N, and each level was repeated five times. These force levels were chosen based on the experience from previous testing conducted on the BRB [21]. The response of the system was sampled at 6400 Hz with a 10 s recording time and 0.1 s pre-trigger. The response was measured for 10 s because the BRB rings for approximately 5 s and a fine frequency resolution was desired.

To assess the repeatability of the interfaces, the beam is disassembled and reassembled three times. The following procedure was used to increase the likelihood that the only change in the system is the contacts between the micro-scale disparities. The two parts of the beam were clamped between a uniform metal bar and two shorter beams with the plane of the interface perpendicular to the ground, as shown in Fig. 22.3. Due to the manufacturing process a gap is present at the edge of the beam halves in the interface, which can be seen in Fig. 22.1a. This gap can separate or close depending on the seating of the beam halves. To keep this gap constant a business card is used. The bolts are then tightened, in the order shown in Fig. 22.4, to 70% of the desired torque level and then to the full level.
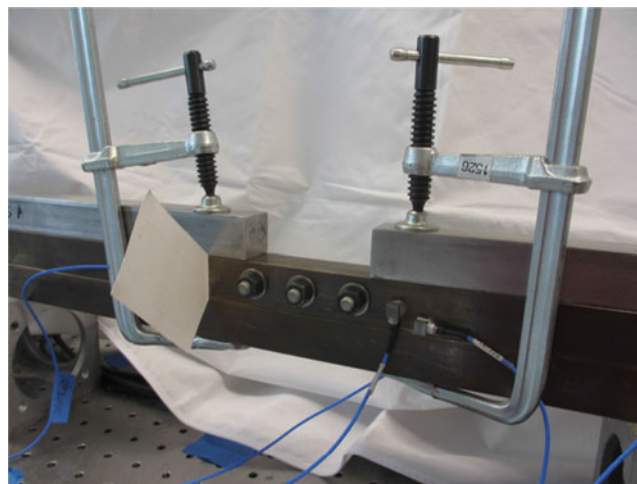
Fig. 22.3 Beam clamped for bolt tightening

Fig. 22.4 Bolt tightening for all experiments
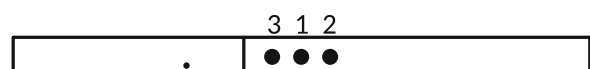
22.4 Results and Discussion

22.4.1 Pressure Film

Before any impact tests were performed, the contact area of the different interfaces were investigated using pressure film. The beam was assembled per the process outlined in the previous section except Fujifilm Prescale medium pressure film was placed in the interface in order to measure the static contact area. The bolts were then torqued and held for 2 min. The pressure film results are shown in Fig. 22.5. Note that the bottom image in all of the figures is a digitized version (done by Sensor Products INC.) of the film.

The results of the pressure films of the BRB and HRZ match with the results in [2, 22] and Fig. 22.6, respectively. The results for PDS, PDL and RPD also are expected. When the pad is smaller than the pressure cone of the bolts, the resulting contact pressure at the interface is a nearly uniform distribution. Conversely, with the larger pad the pressure distribution is observed to deviate from a uniform distribution near the edges of the outer pads, similar to the BRB. With the reversed pads, a trend similar to the large pad is observed: between the bolts acts like the HRZ, but towards the outer periphery of the interface a significant gradient in the contact pressure is observed.

Two types of interfaces can be observed in the pressure films: interfaces with sharp edges in the measured contact pressures and interfaces with large gradients in the measured contact pressures. The PDS and HRZ have what appear to be sharp edges, because the contact pressure in these interfaces saturated the pressure film. The BRB and RPD have contact pressures which fade to below 10 MPa at the edges of the interfaces. The PDL is between the two types of trends with pressure near the center of the interface being mostly saturated like the PDS and HRZ, and with the outer edges fading like the BRB and RPD. It is expected that the different interfaces will have significant impact on the nonlinear response of the beam.
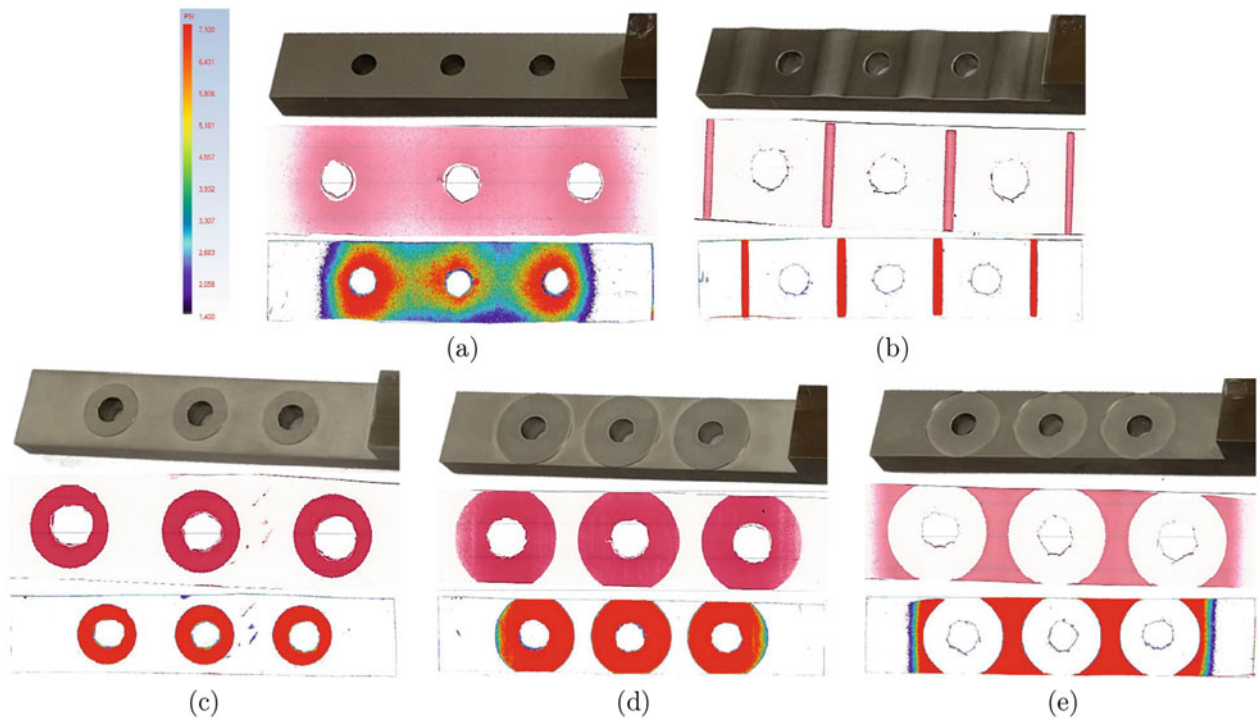
Fig. 22.5 Pressure film of (**a**) BRB, (**b**) HRZ, (**c**) PDS, (**d**) PDL, and (**e**) RPD under 20 Nm bolt torque

Fig. 22.6 Contact force from finite element simulation of the Hertzian beam (Courtesy of Robert Flicek)
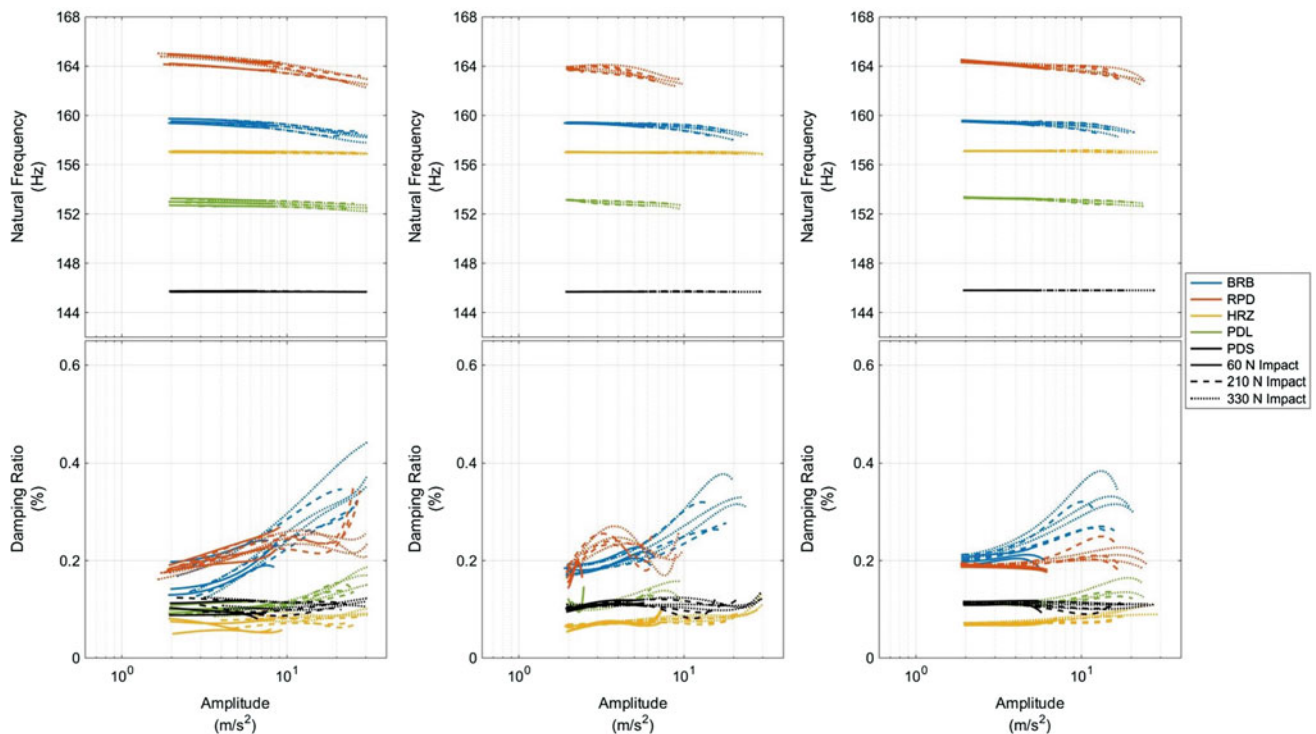
Fig. 22.7 Comparison of the different interfaces under 20 Nm torque; using (*left column*) Hilbert transform, (*center column*) direct fitting, and (*right column*) STFT

Note that for the HRZ and PDS perturbations, the pressure film became saturated. While high-level comparative conclusions could be drawn, these pressure films do not constitute an exhaustive measurement or analysis of the contact pressure distributions for the various BRBs. For a complete understanding of the contact pressure distributions, different films would need to be employed; a less sensitive pressure film should be used where the film becomes saturated and a more sensitive film in the areas where the pressure drops below 10 MPa.

22.4.2 Impact Hammer Testing Analysis

Following the measurement of the contact pressures, the hammer impact testing was conducted. The results of the impact testing were analyzed using the Hilbert transform [23], the Direct Fitting method [19, 20], and the short-time Fourier Transform (STFT) [24]. The nonlinear decay of the first bending mode of each BRB perturbation is compared in Fig. 22.7.

The RPD has the highest frequency, which could be from the mass at the interface being lower than the BRB, but the contact stiffness was not drastically changed (as opposed to the HRZ or PDS in which the contact stiffness of the interface is significantly changed while the mass is also reduced significantly). The HRZ and BRB have similar frequencies, which means that even though the contact stiffness of the HRZ maybe lower than the BRB, the removal of the material to create the HRZ interface is great enough to keep the contact stiffness-mass ratio similar. The PDS has the lowest frequency of all interfaces, and it is the most linear of all of the interfaces. Both the PDS and the HRZ interfaces have the lowest damping ratios, which indicates that redesigning the interface to have higher contact pressure reduces micro-slip, which is a large source of nonlinearity in joints. The PDL, as anticipated, shows a weaker nonlinearity than that observed in the BRB, but a stronger nonlinearity than observed in the PDS.

To assess the repeatability and variability of these systems a procedure was adopted where the dynamics of the beam were measured, the system was then disassembled, the interface was re-seated, the dynamics of the system were measured again, and the process was repeated. The frequency of the different interfaces is fairly repeatable, while the damping has large variations. The damping of systems more susceptible to changes in micro-structure (due the engagement of the disparities changing with each re-seat of the interface) of the interfaces than the frequency, which is indicated in Fig. 22.7 by the width of the measured damping responses compared to the frequency.

22.4.3 Discussion

While there is variability in the behavior of the nonlinearities for each BRB perturbation, distinctions can be made. The Brake-Reuß beam variants designed with large amounts of contact area farther from the bolt hole were less repeatable and exhibited large variability in the observed nonlinear behavior. Other observations made include:

- Interfaces with high pressure concentrations (PDS & HRZ) behaved linearly due to slip not occurring at the excitation levels achieved in this work;
- Interfaces that had more gradual pressure gradients (BRB, RPD, & PDL) behaved more nonlinearly due to micro-slip occurring in the transition zones; and,
- Damping exhibited a higher amount of variability than frequency due to the damping being more susceptible to changes in disparity contact.

An interesting result observed is that the contact of the PDL, seen in Fig. 22.5d, has characteristics of the BRB and PDS interfaces;the center pad of the PDL was saturated like the PDS, whereas a gradual pressure change was observed on the outer pads similar to the gradient of the BRB. This is mirrored in the frequency and damping variations of the PDL, seen in Fig. 22.7, were it exhibits similar nonlinear trends as the BRB at higher excitation levels, and linear trends as the PDS at lower levels. These results suggest that gradual pressure gradients and free edges are a large source of nonlinear effects in joints, while an interface in complete contact behaves linearly.

The three different techniques (Hilbert Transform, Direct Fitting, and STFT) used to analyze the impact response, have similar results for frequency and damping. Near the end of the signal the Direct Fitting and STFT start to have difficulties fitting the data for extracting damping. The main differences between the three techniques is how the data is extracted; the Hilbert Transform and Direct Fitting need the response to be filtered, and the damping is extracted by regression fitting (Hilbert Transform), exponential fitting (Direct Fitting), and the amplitude of the max Fourier coefficient (STFT).

22.5 Conclusion

The study of different interface geometries has provided insight into the possibility of designing interfaces that behave as expected, as well as having linear properties. The pressure film has proven to be a useful tool in this study to help provide insights into the dynamic behavior of the structural joint. It is found that gradual pressure gradients and free edges are a large source of nonlinear effects in joints, while an interface in complete contact behaves linearly. The two interfaces with abrupt change of contact pressure (HRZ and PDS), represent systems that have linear behavior. The three interfaces with a fading pressure distribution display nonlinear behavior. These results corroborate the hypotheses that micro-slip at the edge of the interface contact is the origin of nonlinear damping in the system. This study demonstrates that the design of the joint clearly influences the dynamic behavior of the structure.

References

1. Segalman, D.J., Gregory, D.L., Starr, M.J., Resor, B.R., Jew, M.D., Lauffer, J. P., Ames, N.M.: Handbook on Dynamics of Jointed Structures. Sandia National Laboratories, Albuquerque (2009)
2. Lacayo, R.M., Pesaresi, L., Fochler, D., Groß, J., Brake, M.R.W, Schwingshackl, C.W.: Instantaneous frequency and damping from transient ring-down data. In: IMAC XXXV A Conference and Exposition on Structural Dynamics, Garden Grove, Feb 2017
3. Müller, M., Ostermeyer, G.: A cellular automaton model to describe the three-dimensional friction and wear mechanism of Brake systems. Wear **263**(7), 1175–1188 (2007)
4. Ostermeyer, G., Müller, M.: Dynamic interaction of friction and surface topography in Brake systems. Tribol. Int. **39**(5), 370–380 (2006)
5. Müller, M., Ostermeyer, G.: Cellular automata method for macroscopic surface and friction dynamics in Brake systems. Tribol. Int. **40**(6), 942–952 (2007)
6. Bode, K., Ostermeyer, G.-P.: A comprehensive approach for the simulation of heat and heat-induced phenomena in friction materials. Wear **311**(1), 47–56 (2014)

7. Mulvihill, D., Kartal, M., Nowell, D., Hills, D.: An elastic–plastic asperity interaction model for sliding friction. Tribol. Int. **44**(12), 1679–1694 (2011)
8. Schwingshackl, C., Petrov, E., Ewins, D.: Measured and estimated friction interface parameters in a nonlinear dynamic analysis. Mech. Syst. Signal Process. **28**, 574–584 (2012)
9. Brake, M.R.W., Stark, J.G., Smith, S.A., Lancereau, T.W.J.D.P.T., Dossogne, T.: In situ measurements of contact pressure for jointed interfaces during dynamic loading experiments. In: IMAC XXXV A Conference and Exposition on Structural Dynamics, Garden Grove, Feb 2017
10. Brake, M.R.W. (ed.): The Mechanics of Jointed Structures. Springer, New York (2016)
11. Brake, M.R., Reuß, P., Segalman, D.J., Gaul, L.: Variability and repeatability of jointed structures with frictional interfaces. In: IMAC XXXII A Conference and Exposition on Structural Dynamics, Orlando, Feb 2014
12. Smith, S.A., Bilbao-Ludena, J.C., Catalfamo, S., Brake, M.R.W., Reuß, P., Schwingshackl, C.W.: The effects of boundary conditions, measurement techniques, and excitation type on measurements of the properties of mechanical joints. In: IMAC XXXII A Conference and Exposition on Structural Dynamics, Orlando, Feb 2015
13. Catalfamo, S., Smith, S.A., Morlock, F., Brake, M.R.W., Reuß, P., Schwingshackl, C.W.: Effects of experimental methods on the measurement of a nonlinear structure. In: IMAC XXXIII A Conference and Exposition on Structural Dynamics, Orlando, Feb 2016
14. Barber, J.R., Klarbring, A., Ciavarella, M.: Shakedown in frictional contact problems for the continuum. Comptes Rendus Mecanique **336**, 34–41 (2008)
15. Churchman, C., Hills, D.: General results for complete contacts subject to oscillatory shear. J. Mech. Phys. Solids **54**(6), 1186–1205 (2006)
16. Goyder, H.G.D., Ind, P., Brown, D.: Measurement of damping in bolted joints. In: ASME International Design Engineering Technical Conferences IDETC/CIE, Chicago, Aug 2012
17. Goyder, H.G.D., Ind, P., Brown, D.: Measurement of damping due to bolted joints. In: ASME International Design Engineering Technical Conferences IDETC/CIE, Portland, Aug 2013
18. Goyder, H.G.D., Ind, P., Brown, D.: Measurement of damping in a chain of bolted joints. In: ASME International Design Engineering Technical Conferences IDETC/CIE, Buffalo, Aug 2014
19. Goyder, H.G.D., Ind, P., Brown, D.: Damping in a composite beam with a joined interface. In: ASME International Design Engineering Technical Conferences IDETC/CIE, Boston, Aug 2015
20. Goyder, H.G.D., Lancereau, D.P.T., Ind, P., Brown, D.: Friction and damping associated with bolted joints: results and signal processing. In: Proceedings of the ISMA 2016 International Conference on Noise and Vibration Engineering, Leuven, Sept 2016
21. Bonney, M.S., Robertson, B.A., Schempp, F., Mignolet, M., Brake, M.R.: Experimental determination of frictional interface models. In: IMAC XXXIV A Conference and Exposition on Structural Dynamics, Orlando, Feb 2016
22. Flicek, R.C., Moore, K.J., Castelluccio, G.M., Hammetter, C., Brake, M.R.W.: Stress waves propagating through jointed connections. In: IMAC XXXIV A Conference and Exposition on Structural Dynamics, Orlando, Feb 2016
23. Sracic, M.W., Allen, M.S., Sumali, H.: Identifying the Modal Properties of Nonlinear Structures Using Measured Free Response Time Histories from a Scanning Laser Doppler Vibrometer, pp. 269–286. Springer, New York (2012)
24. Kuether, R.J., Brake, M.R.W.: Instantaneous frequency and damping from transient ring-down data. In: IMAC XXXIV A Conference and Exposition on Structural Dynamics, Orlando, Feb 2016

Chapter 23
Nonlinear Finite Element Model Updating, Part I: Experimental Techniques and Nonlinear Modal Model Parameter Extraction

Benjamin R. Pacini, Randall L. Mayes, Brian C. Owens, and Ryan A. Schultz

Abstract Linear structural dynamic models are often used to support system design and qualification. Overall, linear models provide an efficient means for conducting design studies and augmenting test data by recovering un-instrumented or un-measurable quantities (e.g. stress). Nevertheless, the use of linear models often adds significant conservatism in design and qualification programs by failing to capture critical mechanisms for energy dissipation. Unfortunately, the use of explicit nonlinear models can require unacceptably large efforts in model development and experimental characterization to account for common nonlinearities such as frictional interfaces, macro-slip, and other complex material behavior. The computational requirements are also greater by orders of magnitude. Conversely, modal models are much more computationally efficient and experimentally have shown the ability to capture typical structural nonlinearity. Thus, this work will seek to use modal nonlinear identification techniques to improve the predictive capability of a finite element structural dynamics model.

Part I of this paper discusses the experimental aspects of this work. Linear natural frequencies, damping values, and mode shapes are extracted from low excitation level testing. Subsequently, the structure is excited with high level user-defined shaker inputs. The corresponding response data are modally filtered and fit with nonlinear elements to create the nonlinear pseudo-modal model. This is then used to simulate the measured response from a high level excitation experiment which utilized a different type of input. The nonlinear model is then employed in a reduced order, generalized structural dynamics model as discussed in Part II.

Keywords Nonlinear System Identification • Nonlinear Simulation • Structural Dynamics • Modal Model • Restoring Force Surface

Abbreviations

a	Time history of the triangle function
c	Damping coefficient
f	Frequency in cycles/sec
f_c	Center frequency in cycles/sec
F	Force
F_r	Restoring force
G_{vf}	Shaker voltage to excitation force transfer function
j	Imaginary number variable
k	Stiffness coefficient
q	Modal degree of freedom
t	Time

B.R. Pacini
Sandia National Laboratories, PO Box 5800, 87185, Albuquerque, NM, USA
e-mail: brpacin@sandia.gov

R.L. Mayes (✉) • B.C. Owens • R.A. Schultz
Structural Dynamics Department, Sandia National Laboratories, P.O. Box 5800 – MS0557, Albuquerque, NM 87185, USA
e-mail: rlmayes@sandia.gov; bcowens@sandia.gov; rschult@sandia.gov

t_r	Rise time
x	Physical displacement degree of freedom
v, V	Shaker voltage, time domain and frequency domain, respectively
ζ	Modal damping ratio
ω	Frequency in radians per second
φ_{dp}	Drive point mode shape value
H	Frequency response function matrix
P	Modal response matrix
U	Known restoring force vector
Ψ	Modal filter vector
D	Subscript for desired
flm	Subscript for "first local minimum"
$\mathcal{F}$	Subscript for Fourier transform
lin	Subscript for linear
n	Subscript for natural
nl	Subscript for nonlinear
u	Subscript for updated
$+$	Moore-Penrose pseudo-inverse of a matrix

23.1 Introduction and Motivation

A large class of structural dynamic system responses are mildly nonlinear in stiffness (a few percent modal frequency change) and significantly nonlinear in damping (hundreds of percent damping ratio change) as a function of amplitude of vibration. We desire to experimentally identify such a system and then simulate the nonlinear response analytically. Such systems will typically be linear at low level excitation. At higher levels of excitation, the resonant frequencies typically decrease slightly and the apparent damping can increase more than 100%. Structures with joints typically have this softening behavior. Low-excitation-level linear models used to simulate the response may over-predict the nonlinear response by tens to hundreds of percent. Consider a frequency response function (FRF) from the hardware used in this work due to a high level and a low level impact as shown in Fig. 23.1. The low level FRF peak is almost a factor of two greater than the high level FRF peak. Occasionally, the resonant frequency will slightly increase and the apparent damping decrease as forcing amplitude increases. We desire to be able to simulate both softening and stiffening behavior.

There are two main analytical methods to capture the nonlinear behavior: local physical models and pseudo-modal models. The former are extremely computationally expensive and are prohibitively difficult to experimentally identify on a complex structure. The latter assumes the total system response of a structure is a superposition of the responses of individual modes. This allows one to study each mode individually and apply nonlinear elements in parallel with the linear spring and damper.
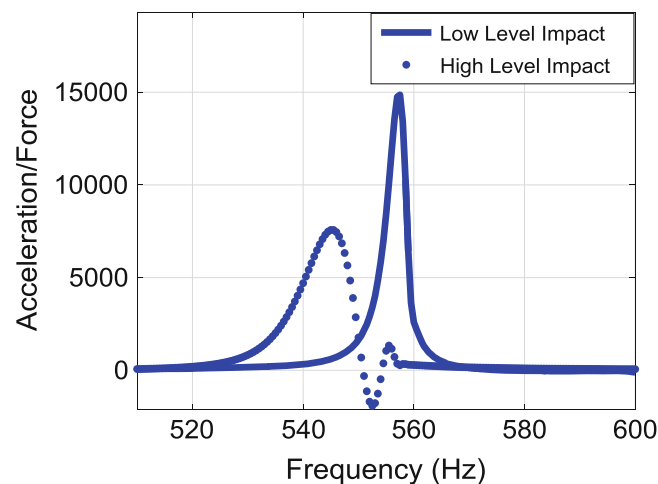
Fig. 23.1 Drive point FRF – low level vs high level impact force

Inherent in this approach is the assumption that the mode shapes do not change with response amplitude, and that the modal degrees of freedom (DOF) do not interact. The pseudo-modal approach is computationally inexpensive and methods have been developed which allow for the extraction of parameters for nonlinear models. Therefore, the pseudo modal approach is utilized for this work.

The methodology used here follows that of [1] which used the pseudo-modal model to characterize the nonlinearities of a complex structure via three different nonlinear elements/identification methodologies. The Restoring Force Surface (RFS) technique described in that work is the nonlinear model structure/identification method employed here. The approach begins with the standard modal model using a linear spring and damper for each modal mass. The spring and damper are identified in a standard low-level modal test. Then we assume that, for the nonlinear modes, nonlinear elements can be connected in parallel with the standard linear elements. Unlike the previous work using impact testing, this works shows the advantages of high level shaker tests on the nonlinear structure to provide calibration data for fitting the nonlinear parameters. The identification of these parameters is accomplished using a single modal single degree of freedom (SDOF) response created by modally filtering the measured structural responses from the high level tests. The nonlinear elements are realized by cubic polynomials for stiffness and damping as a function of response amplitude.

In Sect. 23.3 the test hardware and instrumentation is described along with the new shaker testing approach that focuses the input force on the mode of interest. The modal filtering technique used in this work is presented in Sect. 23.4. Section 23.5 describes the nonlinear model and the parameter identification processes. In Sect. 23.6 the simulation results are compared against measured high level truth data utilizing a different forcing function than the calibration data, and observations are given. Section 23.7 provides conclusions. In Part II of the paper the experimental results are incorporated into the analytical modeling framework as an update to the finite element model.

23.2   Experiments

23.2.1   Hardware Description

A solid model cross-section of the test hardware, named the Cylinder-Plate-Beam assembly (CPB), is shown in Fig. 23.2 along with the coordinate systems (CS) utilized in this work. The physical hardware is shown in Fig. 23.3. The Beam is bolted and epoxied to the Plate. The Plate-Beam is then mounted on the forward flange of the Cylinder using eight bolts. All three components are 6061 T6 aluminum. Two coordinate systems were utilized for this test: a global Cartesian coordinate system and a cylindrical coordinate system. The zero degree orientation of the cylindrical CS aligns with the global CS (i.e. $\theta = 0°$ aligns the cylindrical R+ with the Cartesian X+).

23.2.2   Test Set-Up

The CPB was softly suspended using two bungee cords to approximate a free-free boundary condition and instrumented with 10 and 100 mV/g accelerometers. Twenty-six triaxial and four uniaxial accelerometers were mounted at locations that were selected as a subset of the finite element model (FEM) nodes and minimized the condition number of the finite element mode shape matrix for the modes below 1600 Hz. By minimizing this condition number, the modal observability and independence of the mode shapes extracted from measured data were maximized.
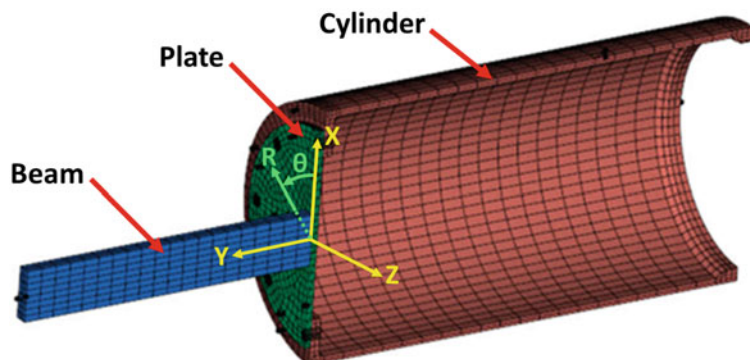
Fig. 23.2 Cylinder Plate Beam assembly full system solid model and coordinate systems
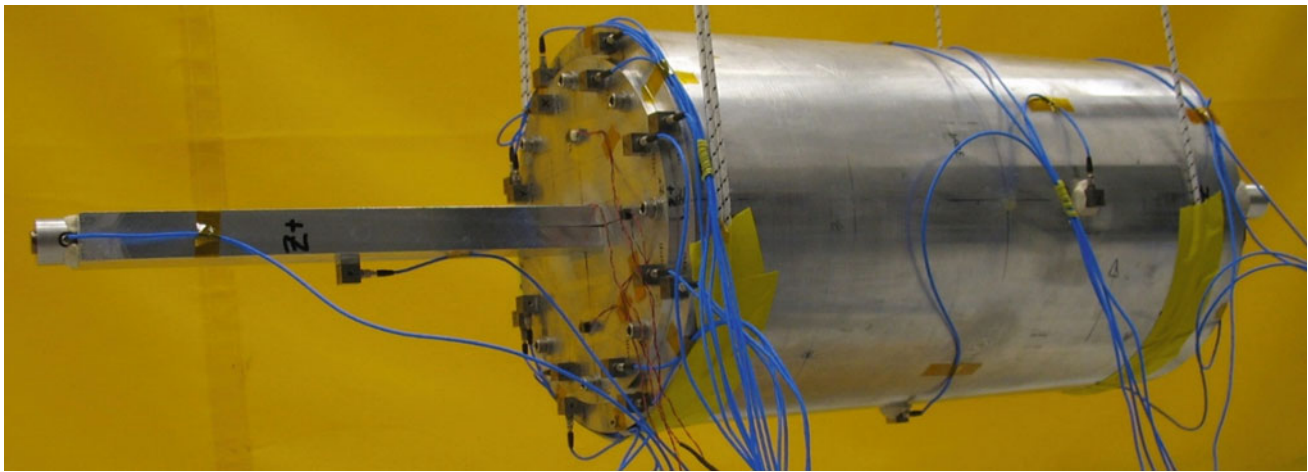
Fig. 23.3 Physical test hardware

Table 23.1 Excitation information, low-level tests

Input DOF	Description	Input type
34965R	Radial input on mid span of cylinder at 60°	Hammer
32916R	Radial input on mid span of cylinder at 30°	Hammer
53632Y	Axial input at tip of Beam	Shaker
25449Y	Axial input at aft end of cylinder at 270°	Shaker
31349Y	Axial input at aft end of cylinder at 0°	Shaker

23.2.3 Test Procedure

A series of tests were performed in this work. The first was to conduct low-level excitation tests in order to establish a linear model and collect data for developing the modal filter. Subsequently, high-level excitation tests were conducted in order to collect data for calibration of parameters for the nonlinear pseudo-modal model.

23.2.4 Extraction of the Linear Modal Model

The linear model is an essential step in this work as its mode shape matrix allows for the translation between the physical and modal domains. Additionally, the modal filter is calculated from this step (see Sect. 23.4) as well as the linear coefficients of the pseudo-modal model (see Sect. 23.5).

Low-level excitation was input at the DOFs shown in Table 23.1 in order to extract linear modal parameters (natural frequencies, damping, and shapes) of the CPB. The input force was reduced as much as possible to minimize the nonlinear response of the CPB but remain sufficiently above the noise floor. A combination of hammer impact and low-level burst random tests were used to extract the linear parameters. The Synthesize Modes And Correlate (SMAC) program by Mayes and Hensley [2] was used to extract modal parameters from each data set individually using a real modes approximation in Table 23.2. Rigid body mode shapes were calculated from solid model mass properties.

The CPB contains only metal components that are bolted together. Thus the only significant source of nonlinearity in the amplitudes achieved in this work are the joints. The only modes that exhibit detectable nonlinear response are the bending modes (7, 8, and 14) and the axial mode (11). Therefore, only these modes were selected for nonlinear modeling.

Table 23.2 Linear modal parameters[a, b]

Mode	f_n (Hz)	ζ (%cr)	Reference	Shape description
7	128	0.30	31349Y	First bend of Beam in soft direction (global X)
8	171	0.31	25449Y	First bend of Beam in stiff direction (global Z)
9	391	0.21	34965R	(2,0) ovaling of cylinder aligned with X-Z axes
10	395	0.03	34965R	(2,0) ovaling of cylinder 45° from X-Z axes
11	560	0.34	53632Y	Axial mode
12	957	0.11	34965R	(3,0) ovaling of cylinder
13	958	0.09	32916R	(3,0) ovaling of cylinder
14	978	0.23	31349Y	Second bend of Beam in soft direction (global X)

[a]Modes 7, 8,11 and 14 were considered nonlinear
[b]Rigid body modes not shown
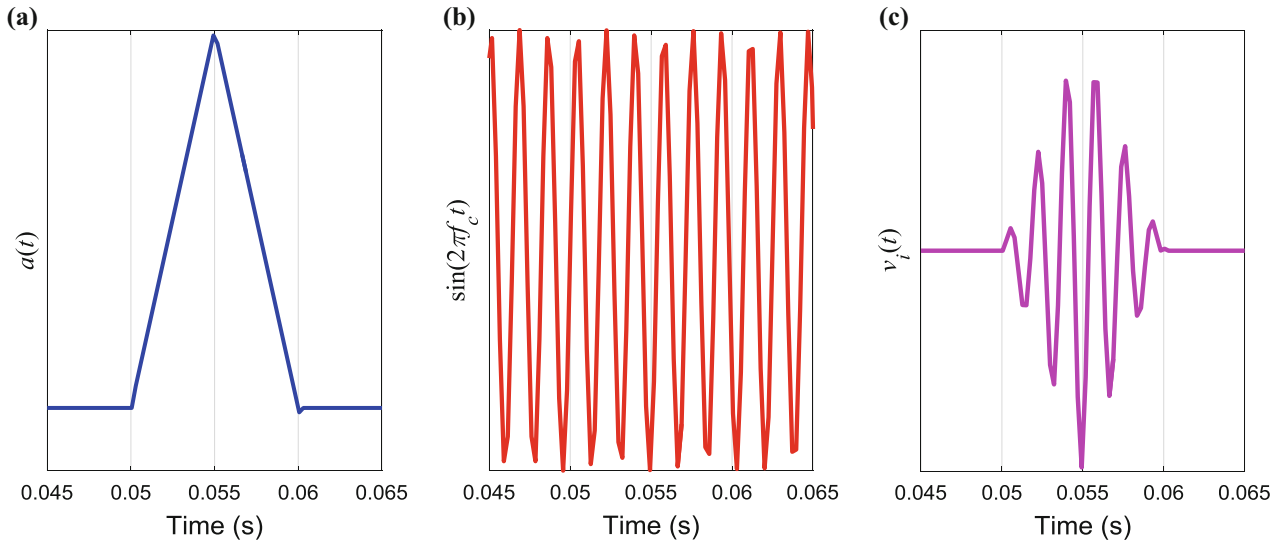
Fig. 23.4 Shaker input creation, time domain; **(a)** triangle wave $a(t)$, **(b)** sine wave $\sin(2\pi f_c t)$, and **(c)** combined signal $v_i(t)$

23.2.4.1 High Level Shaker Testing

Reference [1] utilized impact testing to extract parameters for the nonlinear models. However, impacts excite all modes at once, thus causing a large initial response which can overload accelerometers, especially the drive point. Therefore, this work employed shaker testing in order to increase the excitation amplitude of individually targeted nonlinear modes.

One method of nonlinear testing with a shaker involves a stepped-sine input with closed-loop control to maintain either constant force or response amplitude. This process is slow and difficult to practically implement due to shaker-structure interactions at resonance. Alternatively, this work developed a shaker input that is quick and simple to conduct. It also drives a targeted modal amplitude beyond that achievable by impacts which overload the drive point accelerometer.

The basic concept is to excite the structure with a sine wave at a single frequency whose amplitude is shaped by a short triangle function such that all of the input energy is concentrated near the target modal frequency.

$$v_i(t) = a(t) \sin (2\pi f_c t) \tag{23.1}$$

where $v_i(t)$ is the voltage sent to the shaker amplifier, f_c is the center frequency, and $a(t)$ is the time history of the triangle function, see Fig. 23.4.

The frequency content of $v_i(t)$ is shown in Fig. 23.5. The maximum amplitude occurs at f_c and the first local minima occurring at f_{flm} Hz above and below this value. By taking the Fourier transform of a triangle wave, the ramp up (or down) time of the triangle function, t_r, is calculated to be inversely related to f_{flm} as in the following.

$$t_r = \frac{1}{f_{flm}} \tag{23.2}$$
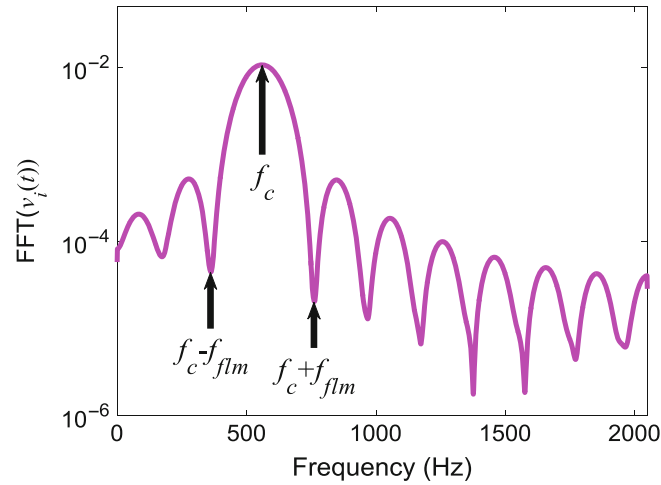
Fig. 23.5 Shaker input spectrum

Table 23.3 Shaker input parameters

Mode	f_c (Hz)	f_{flm}(Hz)
7	128	50
8	169	50
11	560	200
14	974	200

Thus, the shape of this spectrum can be specifically tailored by independently selecting the center frequency and the location of the first local minima. These values can then be used with (23.1) and (23.2) to create the voltage signal that is sent to the shaker.

In this work, f_c was selected to be the approximate linear natural frequency of the targeted mode and f_{flm} was chosen based on the target mode's linear natural frequency and damping and the proximity of nearby modes. This work did not include an exhaustive evaluation of the ramifications of various values of f_{flm}, and the values of f_{flm} for the four nonlinear modes were chosen by the authors' judgement. Table 23.3 contains the input function parameters used in the testing of all the nonlinear modes.

Exciting the structure via the shaker voltage signal described above would ideally focus the force input in a similar fashion to produce essentially a scaled version of Fig. 23.5. However, the force measured by the load cell is influenced both by the shaker input and the response of the test hardware. Thus, the force spectrum is not as smooth as the voltage spectrum and can actually have significant dips near the resonances. Since the goal of this shaker testing is to concentrate the input energy near the resonance, the shaker voltage is updated with measurements in order to maximize the response of the targeted mode. This is accomplished using the transfer function between voltage signal from (23.1) and the corresponding force measured during a test where $v_i(t)$ was the input to the shaker.

$$G_{vf}(\omega) = \frac{F(\omega)}{V_i(\omega)} \tag{23.3}$$

where $F(\omega)$ is the measured force from the experiment. A desired force spectrum, $F_D(\omega)$, can be created by scaling $V_i(\omega)$ until its minima at $f_c \pm f_{flm}$ are at approximately the same value as those in $F(\omega)$. Then, dividing $F_D(\omega)$ by the transfer function from (23.3) results in an updated shaker voltage signal spectrum, $V_u(\omega)$.

$$V_u(\omega) = \frac{F_D(\omega)}{G_{vf}(\omega)} \tag{23.4}$$

The inverse Fourier transform of $V_u(\omega)$ produces an updated time signal, $v_u(t)$, that is subsequently used as the shaker amplifier input voltage for a second test, improving the energy concentration at the targeted resonance. The nonlinear parameters for the targeted modes are extracted from the data from this second updated experiment. This process is summarized in Fig. 23.6.
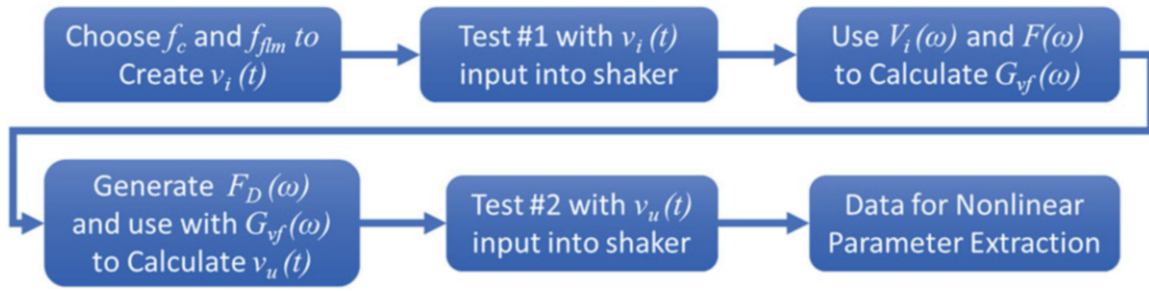
Fig. 23.6 Shaker input creation and updating flowchart
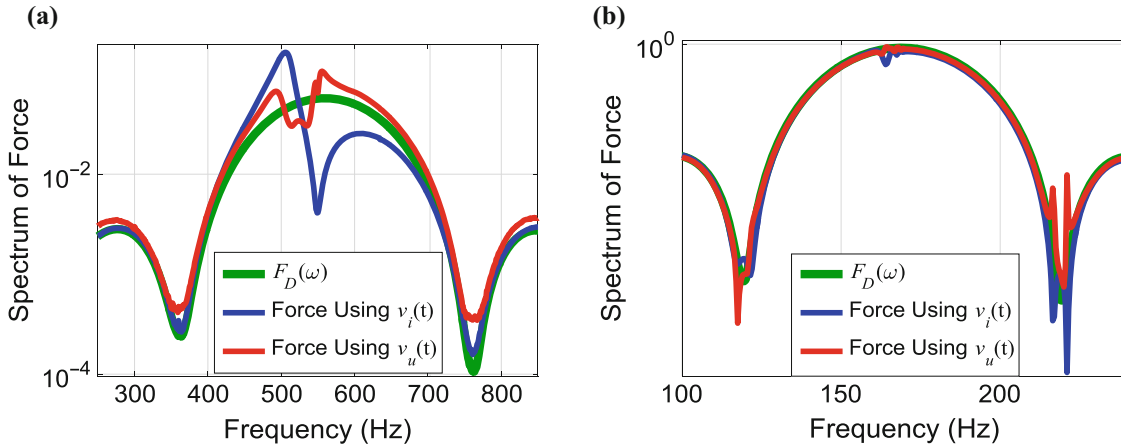
Fig. 23.7 Shaker input updating effectiveness; (a) least effective replication of desired force and (b) most effective replication of desired force

Note the transfer function is a linear operator, so this updating process has limited efficacy due to the nonlinearities in the test object. However, for this work, this updating process performed sufficiently well to concentrate the input energy at the resonance. Fig. 23.7 shows two examples of this updating process. The left plot shows an instance where the updating process made significant improvement, but still struggled to replicate the desired force spectrum. The right plot shows an example where the updating process resulted in a force spectrum very similar to the desired.

Generally, this method was able to produce higher modal responses than that achieved with a hammer without overloading the drive point or beam tip accelerometers. Fig. 23.8 shows a comparison of the maximum modal responses achieved using either shaker or hammer excitation. For modes 7 and 8, the shaker was able to excite the CPB an order of magnitude higher than the hammer before overloading the beam tip accelerometer. Conversely, for mode 14 the limiting factor for the shaker input was the stinger buckling. Overall, the shaker was found to better excite targeted modes.

23.3 Modal Filtering

To develop a nonlinear pseudo-modal model, our approach requires the structural response be separated into the individual modal responses. This requires some type of filter that can transform multiple sensor measurements into modal coordinates. Once these modal responses are calculated, the nonlinear parameters can be identified. Previous work showed that the modal filter embedded in the SMAC algorithm generally suppresses non-target modes better than other methods [1]. The following describes in greater detail the SMAC modal filter.

We desire a modal filter such that

$$\overline{\mathbf{\Psi}}^{-T} \overline{\mathbf{x}} = q_i \tag{23.5}$$
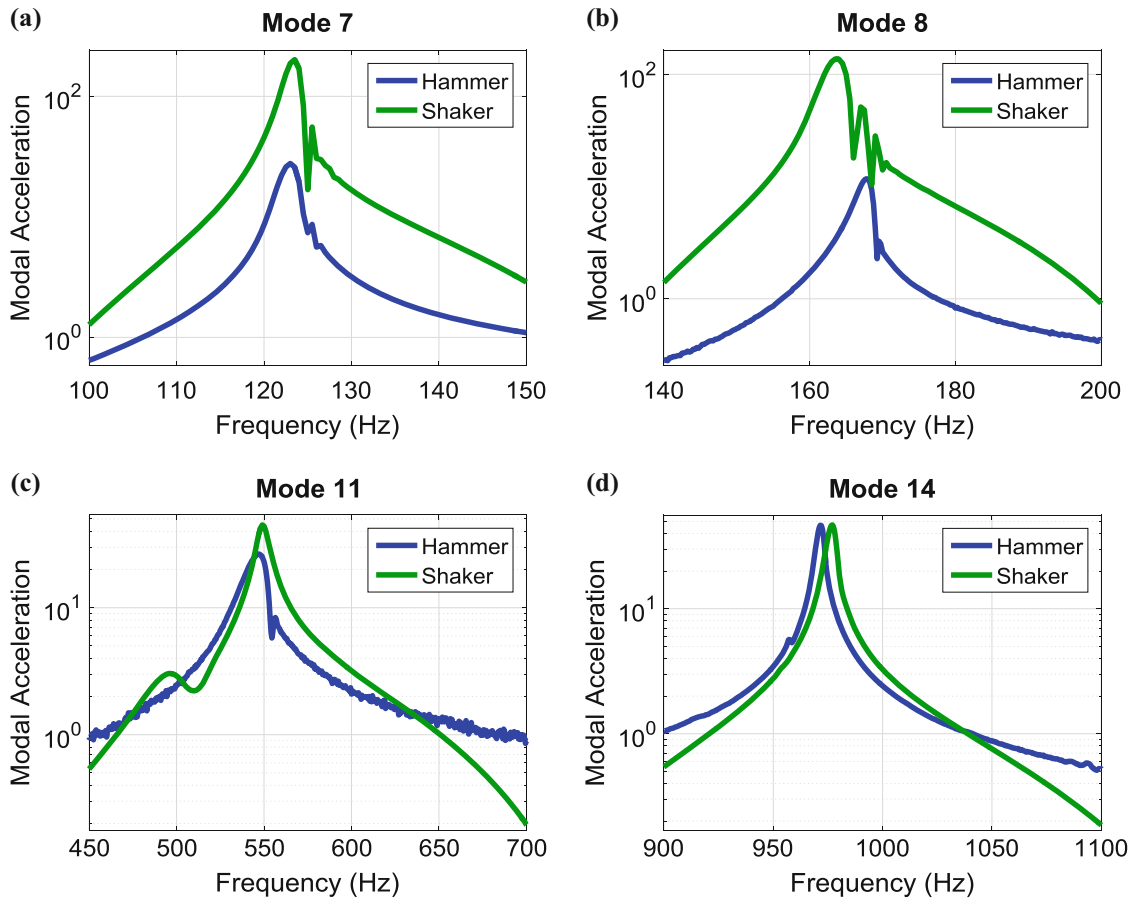
Fig. 23.8 (**a–d**) Maximum modal responses without overloading accelerometers from shaker and hammer

where q_i is the ith modal DOF, column vector $\bar{\mathbf{x}}$ contains measured responses, and $\bar{\mathbf{\Psi}}$ is the vector of weights transforming the measured responses to the modal response. The SMAC modal filter [3] obtains this vector by operating directly on the FRFs. If one employs (23.5) in the frequency domain and divides by the input force, then

$$\bar{\mathbf{\Psi}}^T \bar{\mathbf{H}}_x = H_{qi} \tag{23.6}$$

where $\bar{\mathbf{H}}_x$ is now a vector of measured FRFs and H_{qi} is an analytically calculated SDOF FRF with an estimate of the frequency and damping of the target mode and is given by

$$H_{qi} = \frac{\varphi_{dp,i}}{\omega_{ni}^2 - \omega^2 + \text{j}2\zeta_i\omega_{ni}\omega} \tag{23.7}$$

where $\varphi_{dp,i}$ is the drive point shape value for the ith mode. Columns for every frequency line of interest are included in $\bar{\mathbf{H}}_x$ and H_{qi} creating a matrix of $\mathbf{H}_x$ and a vector of the analytical FRF $\bar{\mathbf{H}}_{qi}$. Transposing (non-conjugate) and isolating the modal filter on the left side yields

$$\bar{\mathbf{\Psi}} = \mathbf{H}_x^{T+} \bar{\mathbf{H}}_{qi} \tag{23.8}$$

where the superscript $^+$ represents the pseudo-inverse. Hence, the SMAC modal filter is obtained with the measured FRFs and an analytical SDOF FRF constructed using the linear estimate of the natural frequency, damping, and drive point shape of the target mode.

23.4 Nonlinear Model

This section describes the pseudo-modal approach to capture the nonlinearities in the CPB. This approach assumes each mode can be modeled with a single degree of freedom system as a modal coordinate. Each modal degree of freedom is linked to ground with a linear spring and damper. In order to capture the nonlinearity, one adds nonlinear spring and damper elements in parallel with the linear spring and damper as seen in Fig. 23.9.

There are many methods to model/parameterize the nonlinearity. Reference [1] compares the capabilities of the Iwan, FREEVIB, and Restoring Force Surface (RFS) methods to capture the nonlinear response of the CPB in a foam-filled configuration. The RFS method is utilized for this work with the nonlinear spring and damping forces parameterized with cubic polynomials.

The RFS method has been extensively researched and refined with several permutations, see reference [4] for an extensive synopsis of the past variances and applications. The foundation of RFS is in the Newtonian equation of motion:

$$\ddot{q}(t) + F_r(q(t), \dot{q}(t)) = F(t) \tag{23.9}$$

where $F_r(q, \dot{q})$ represents the damping and stiffness forces (called the restoring forces) and $F(t)$ is the excitation force. Assuming the acceleration and excitation force are measured, then at every time instant, the restoring force is also known. We write F_r as in the following:

$$F_r(q(t), \dot{q}(t)) = c_0 \dot{q}(t) + c_1 |\dot{q}(t)| \dot{q}(t) + c_2 \dot{q}^3(t) + k_0 q(t) + k_1 |q(t)| q(t) + k_2 q^3(t) \tag{23.10}$$

where c_1, c_2, k_1, and k_2 are constants. Since c_0 and k_0 are already known from the low level modal tests (see Table 23.2), (23.9) is rearranged to

$$\begin{bmatrix} |\dot{q}| \dot{q} & \dot{q}^3 & |q| q & q^3 \end{bmatrix} \begin{bmatrix} c_1 \\ c_2 \\ k_1 \\ k_2 \end{bmatrix} = F - \ddot{q} - c_0 \dot{q} - k_0 q \tag{23.11}$$

where the time-dependency has been omitted for clarity. Equation (23.11) can be expressed as

$$\mathbf{P} \begin{bmatrix} c_1 \\ c_2 \\ k_1 \\ k_2 \end{bmatrix} = \bar{\mathbf{U}} \tag{23.12}$$

Fig. 23.9 Schematic of SDOF for RFS modal coordinate
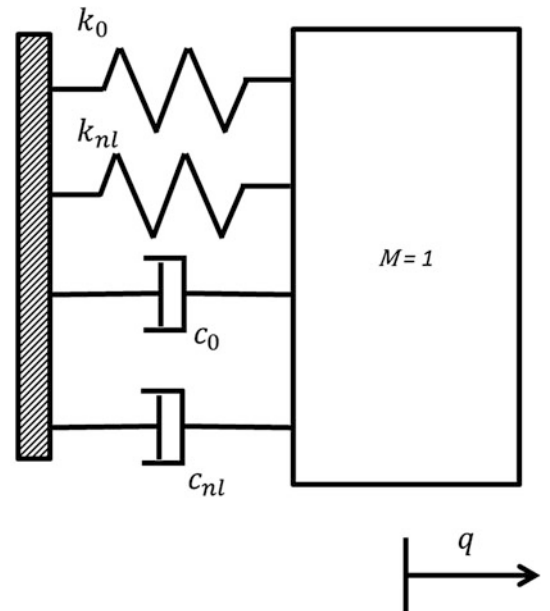
Table 23.4 Damping and stiffness coefficients

Mode	c_0	c_1	c_2	k_0	k_1	k_2
7	4.77	2.6	−1.95	6.48E + 05	−9.15E + 07	3.77E + 10
8	6.61	3.17	−3.28	1.15E + 06	−2.86E + 08	1.92E + 11
11	23.9	318	−834	1.24E + 07	−2.05E + 10	1.54E + 14
14	27.8	−188	811	3.77E + 07	−6.16E + 09	8.41E + 13

where $\mathbf{P}$ and $\overline{U}$ are processed measurements with a row for each time sample. We obtained the best results by taking the Fourier transform of $\overline{U}$ and each column of $\mathbf{P}$ giving

$$\mathbf{P_F} \begin{bmatrix} c_1 \\ c_2 \\ k_1 \\ k_2 \end{bmatrix} = \overline{\mathbf{U}}_\mathbf{F}. \tag{23.13}$$

Note that in order to yield real coefficients, $\mathbf{P_F}$ must be reconfigured to.

$$\mathbf{P_F} = \begin{bmatrix} \text{real}\,(\mathbf{P_F}) \\ \text{imaginary}\,(\mathbf{P_F}) \end{bmatrix}. \tag{23.14}$$

$\overline{\mathbf{U}}_\mathbf{F}$ must be similarly restructured. Pre-multiplying $\overline{\mathbf{U}}_\mathbf{F}$ by the pseudo-inverse of $\mathbf{P_F}$ results in the least-squares estimate for $c_1, c_2, k_1,$ and k_2 as in (23.15).

$$\begin{bmatrix} c_1 \\ c_2 \\ k_1 \\ k_2 \end{bmatrix} = \mathbf{P_F}^+ \overline{\mathbf{U}}_\mathbf{F}. \tag{23.15}$$

Note that acceleration, velocity, and displacement must all be known (estimated or measured). For this work, acceleration was obtained from the modal filtered measured accelerations and the other two states were estimated by integrating in the frequency domain.

The identification procedure described above was performed on the four identified nonlinear modes, and the results are provided in Table 23.4.

23.5 Results and Observations

To evaluate the effectiveness of the pseudo-modal model extracted as described above, a truth test was conducted where the CPB was excited from DOF 31349Y via a 0.3 s chirp (i.e. a very fast sine sweep) from 50 to 1400 Hz. This DOF was chosen since it excited three of the four nonlinear modes. The amplitude of the sweep was varied in order to maximize the response of each nonlinear mode without exceeding the maximum voltage limit of any accelerometer.

The pseudo-modal model with all 14 modes (6 rigid body, 4 linear and 4 nonlinear) was excited with simulated modal forces corresponding to the measured excitation signal from the truth test. The calculated modal responses were transformed back to the physical DOF via the linear mode shape matrix extracted from the low level test. These responses were compared against the measured data from the truth test in Figs. 23.10 and 23.11 which show the drive point response in the frequency and time domains, respectively. Note that the line labeled "Linear" is the response of a modal model which used only the linear parameters of all 14 modes.

The 31349Y drive point DOF does not excite mode 8 and thus there is no corresponding response in either of these figures. Additionally, the colored boxes in Fig. 23.11 approximately correspond to the maximum response of the indicated modes. Figs. 23.10 and 23.11 show that the nonlinear model offers an improved results over the linear model.
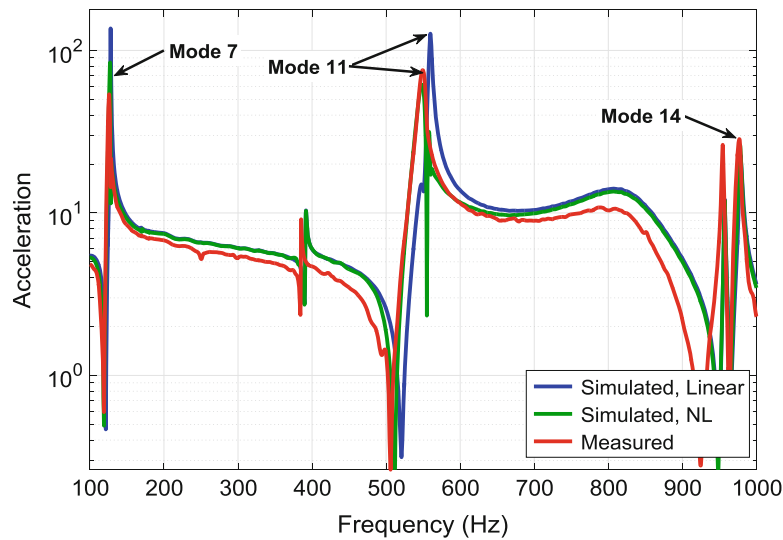
Fig. 23.10 Truth test simulation results, FFT of the drive point response for input DOF 31349Y
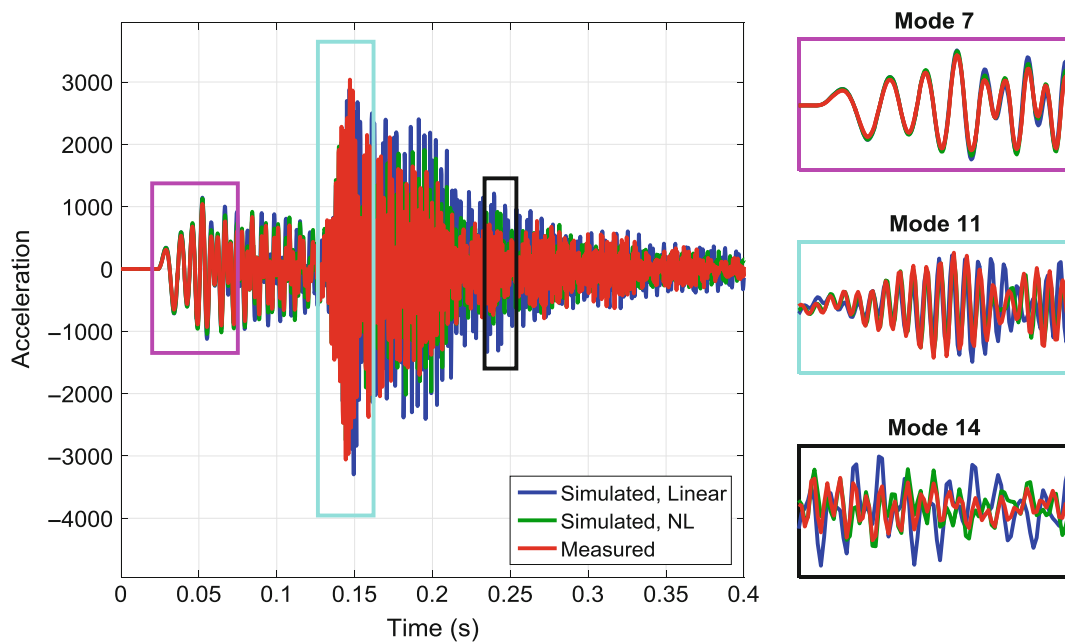
Fig. 23.11 Truth test simulation results, time domain drive point response for input DOF 31349Y

23.6   Discussion

The shaker inputs were able to drive the CPB to a much higher modal response than the hammer without overloading any accelerometers by concentrating the excitation energy near a targeted modal frequency. There are multiple benefits to this. The first is that the input spectrum can be tailored to minimize nearby resonances, enhancing the desired single mode response. The purer the modal response, the greater the accuracy of the extracted nonlinear parameters. The second advantage is that higher response amplitudes can be achieved for a given sensitivity range of accelerometers, allowing for the characterization of nonlinearities over a larger amplitude range. Thus a more accurate nonlinear model can be generated and a greater understanding of the hardware can be attained.

Although imperfect, the truth test results demonstrate that using simple cubic polynomials was an effective method for representing damping and stiffness nonlinearities of the test hardware. These models are easy to understand and were considered adequate for this work. Higher order polynomials could achieve a better fit to the measured data, but they also introduce worse conditioning for the pseudo-inverse of **P** in (23.15). The engineer may decide what polynomial order is adequate.

A disadvantageous feature of the polynomic nonlinear model is that, outside the amplitude range in which its coefficients were fit, the polynomial tends toward infinity (either positive or negative). This can cause the simulation to become unstable and give erroneous results. Therefore, the pseudo-modal with the nonlinear damping and stiffness represented by polynomials should only be used to interpolate and not for extrapolation.

23.7   Conclusions

This work showed the capability of using a pseudo-modal model to capture nonlinearities of a real structure using cubic polynomials for the stiffness and damping forces. The coefficients for these polynomials were extracted from data measured during shaker tests. A method was developed to create inputs for these shaker tests specifically tailored to concentrate the excitation energy around a target mode. This allowed for the excitation of individual modes to amplitudes greater than that achievable by impact testing while not overloading any accelerometers. Additionally, concentrating the energy around a target mode increased the efficacy of the modal filter, creating a purer modal response from which to extract nonlinear parameters. A truth test consisting of a chirp from 50 to 1400 Hz showed that the nonlinear pseudo-modal model effectively captured the nonlinear dynamics seen in the CPB and matched the measured data better than a linear model.

References

1. Mayes, R.L., Pacini, B.R, Roettgen, D. R.: A modal model to simulate typical structural dynamic nonlinearity. Presented at the 34th International Modal Analysis Conference, Orlando, FL, paper #121 January 2016
2. Hensley, Daniel P., Mayes, Randy L.: Extending SMAC to multiple references. Proceedings of the 24th International Modal Analysis Conference, Orlando, FL, pp. 220–230, January 2006
3. Mayes, R.L., Johansen, D.D.: A modal parameter extraction algorithm using best-fit reciprocal vectors. Proceedings of the 16th International Modal Analysis Conference, Santa Barbara, CA, pp. 517–521, February 1998
4. Gaëtan, K., Worden, K., Vakakisc, F.A., Golinval, J.C.: Past present, and future of nonlinear system identification in structural dynamics. Mech. Syst. Signal Process. **20**, 505–592 (2006)

Chapter 24
A Simpler Formulation for Effective Mass Calculated from Experimental Free Mode Shapes of a Test Article on a Fixture

Randall L. Mayes and Patrick S. Hunter

Abstract Effective mass for a particular mode in a particular direction is classically calculated using a combination of fixed base mode shapes, the mass matrix, and a rigid body mode shape from a finite element model. Recently, an experimental method was developed to calculate effective mass using free experimental mode shapes of a structure on a fixture (the base) along with the measured mass of the fixture and of the test article. The method required three steps. The first step involved constraining all the free modes of the fixture except one rigid body mode in the direction of interest. The second step involved calculating pseudo-modal participation factors for this case. The third step involved constraining the final fixture rigid body degree of freedom and utilizing the constraint matrices with pseudo-modal participation factors to obtain the estimate of the standard modal participation factors which can be converted to effective mass. This work provides a simpler formulation. After the constraint in step one above, the effective masses are calculated directly from the mass normalized mode shapes of the fixture. In most cases this method gives the same answer as the original approach, within experimental error. In some instances, it appears more robust with low signal to noise ratios. It also provides better physical insight as to which modes have significant effective mass in a particular direction. The new approach is illustrated by experimental example.

Keywords Effective mass • Experimental method • Modal participation factor • Fixed base modes • Drive point FRF

Abbreviations

DoF	Degree of freedom
DP	Drive point
FRF	Frequency response function
PMPF	Pseudo-modal participation factor
$H_{dp}(\omega)$	Drive point FRF at fixture after all fixture mode shapes except one are constrained
$m_{eff\,r}$	Effective modal mass for mode r
m	Mass
$\ddot{x}$	Acceleration in one Cartesian axis direction
q	Generalized coordinate
L	Reduction matrix applying the constraint to equations of motion
Φ	Mode shapes from free modal test of test article mounted on fixture
Θ	Mode shapes of test article and fixture after all fixture mode shapes except one are constrained
ζ	Modal damping ratio
η	Generalized coordinate for partially constrained system
ω	Angular frequency (radians/second)
Ψ	Mass normalized real mode shape matrix of the fixture
Γ	Eigenvectors resulting from constraint equations
b	Subscript for the base or fixture sensor DoF

R.L. Mayes (✉) • P.S. Hunter
Structural Dynamics Department, Sandia National Laboratories, P.O. Box 5800 – MS0557, Albuquerque, NM 87185, USA
e-mail: rlmayes@sandia.gov; pshunte@sandia.gov

fix   Subscript for the fixture
r   Subscript for mode number
res   Subscript for residual effective mass of all higher modes not extracted
RB   Subscript for the single rigid body mode of a partially constrained system
TA   Subscript for the test article

24.1 Introduction and Motivation

An effective mass model is a modal model that simulates response of a test article to base input in a single coordinate direction. A representation of an effective mass model is shown in Fig. 24.1. Each modal mass is scaled so that the response force of the model on the base, caused by an enforced motion of the base, accurately represents the physical force the test article would exert upon the base fixture with the same imposed motion. Another characteristic of an effective mass modal model is that the kinetic, potential and dissipated energy in the test article is reproduced accurately by the model for a given enforced base motion. When testing parts to failure, the effective mass model is useful for quantifying the failure margin over the qualification level with energy quantities that can be calculated directly from the base input accelerations that were measured. Effective mass modal models have traditionally been developed from finite element models, often times for loads analysis to make sure payloads did not overload the payload interface, for example, on a missile.

Mayes et al. [1] developed a capability to extract experimental effective mass models from a modal test of the test article on a fixture. The modal parameters of the test article/fixture assembly are constrained using the mode shapes of the fixture to obtain an estimate of the effective mass modal model for a particular direction of interest. The derivation is quite mathematical with several steps providing little physical intuition. In this work, we offer an alternative method to one of the major steps to calculate the effective masses. Although it appears to be functionally equivalent to the previous method, it provides much more physical insight by examining the base driving point frequency response function (FRF). In a recent application it appeared to be more robust to experimental mode shape errors.

24.2 Theory

The beginning of the derivation is the same as that used in the previous pseudo-modal participation factor (PMPF) approach [1], but is included for completeness. Consider a test article mounted on a fixture, or base, as represented in Fig. 24.2.

Here we consider the test article mounted to the fixture as a free structure which is typical when a structure is supported with bungee cords or foam. The modal parameters Φ, ω_r and ζ_r are extracted from an experimental modal test with modal
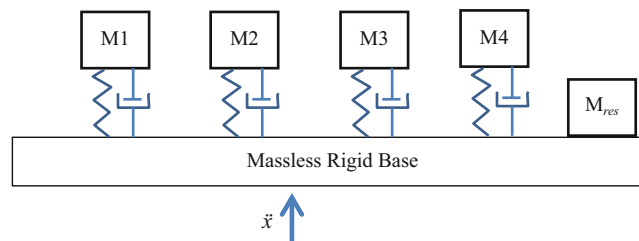
Fig. 24.1 Representation of effective mass modal model truncated to four elastic modes

Fig. 24.2 Test article on a fixture
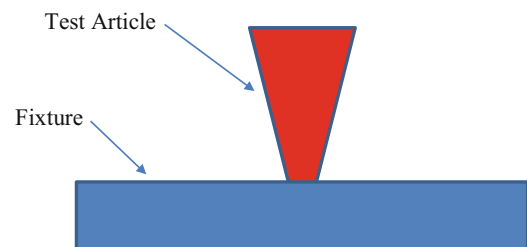
degrees of freedom (DoF) represented as q. Mass normalized mode shapes are assumed for this derivation. Here the damping matrices are neglected for convenience, but they can be handled similarly to the mass and stiffness matrices. The free vibration modal equation of motion for the tested structure and base is

$$\left[\backslash \omega_r^2 \backslash - \omega^2 I \right] \{q\} = \{0\} \tag{24.1}$$

where the stiffness is a diagonal matrix of the squares of the natural frequencies of each mode r and the mass is a diagonal identity matrix for modal DoF vector q. There are several measurements on the base, or fixture, which will be denoted as vector x_b where subscript b denotes measurement on the base. These can be estimated from the free mode shapes, Ψ, of the base (not attached to the test article) with free base modal DoF, s, as

$$\{x_b\} \approx \Phi_b \{q\} \approx \Psi \{s\} \tag{24.2}$$

This assumes that the free mode shapes of the test article provide a set of basis vectors that accurately span the space of the base motion when the test article is attached. Because fixtures are often relatively stiff and massive with respect to the test article, sometimes the Ψ mode shapes can be extracted from the obvious fixture modes in the test article/fixture modal test to save some effort. Writing the motions in terms of base modal DoF, s, gives

$$\Psi^+ \Phi_b \{q\} \approx \{s\} \tag{24.3}$$

The requirements for instrumentation of the base fixture are that it should have enough sensors to easily determine the s DoF, which means the mode shape matrix, Ψ, should be easy to invert, i.e. have a low condition number. To provide constraints robust against experimental error, we recommend having about twice as many sensors as there are active modes of the free base fixture in the frequency band of interest. For example, consider a fixture with six rigid body modes as well as one elastic mode, such as the first twisting mode of the fixture plate. In such a case, one would have seven s DoFs and approximately 14 appropriately placed sensors would be recommended on the base to give seven independent mode shapes. The appropriate s DoFs need to be aligned perfectly with the axes in which the effective masses are desired.

In the next equations, the base motions will be constrained to zero in every s direction except the rigid body direction in which the effective mass estimates are desired. For example, assume the first s DoF is associated with the direction of interest. Therefore the $s(2:n)$ displacements would be constrained to zero by taking the second through n rows of the pseudoinverse of Ψ as

$$\Psi_{2:n}^+ \Phi_b \{q\} \approx \{s_{2:n}\} = \{0\} \tag{24.4}$$

A transformation is required to enforce the constraint. Let

$$\{q\} = L \{\eta\} \tag{24.5}$$

and substitute Eq. (24.5) into Eq. (24.4) to give

$$\Psi_{2:n}^+ \Phi_b L \{\eta\} = \{0\} \tag{24.6}$$

To guarantee that Eq. (24.6) is satisfied, L is chosen in the null space so that

$$L = null \left(\Psi_{2:n}^+ \Phi_b \right) \tag{24.7}$$

Substituting Eq. (24.5) into Eq. (24.1) and pre-multiplying by the transpose of L yields

$$L^T \left[\backslash \omega_r^2 \backslash - \omega^2 I \right] L \{\eta\} = \{0\} \tag{24.8}$$

which can be solved as an eigenvalue problem to provide modal parameters for a test article on the rigid base constrained to move only in the one direction associated with s_1. These shapes will include one rigid body mode and length(q)-length(s) + 1 elastic modes. The square root of the eigenvalues from the solution of Eq. (24.8) will be the frequencies in radians/sec. If Γ
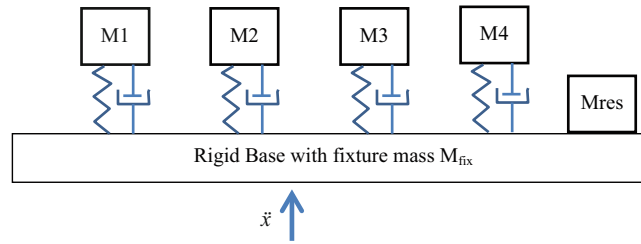
Fig. 24.3 Fixture model constrained to move only in x direction
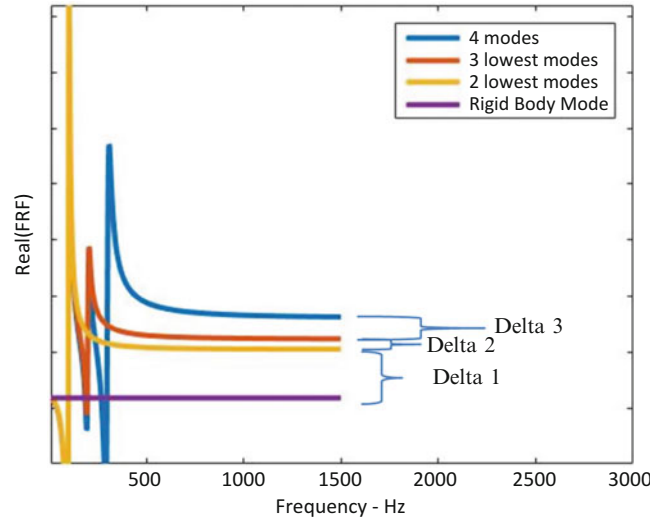
Fig. 24.4 Real part of base drive point FRF adding one mode at a time

represents the matrix of eigenvectors from solution of Eq. (24.8), the new partially constrained mode shapes of the base, Θ_b, will be

$$\Theta_b = \Phi_b \, L\Gamma. \tag{24.9}$$

Theoretically, the response of all DoF on the base should be the same in the axis aligned with the s_1 direction and zero in the remaining orthogonal axes. This gives a uni-directional model that looks like the effective mass model, except the base will have the mass of the fixture as shown in Fig. 24.3.

At this point the derivation deviates from the PMPF approach given previously [1]. Consider a force applied to the base of the model in Fig. 24.3 and the accelerance driving point FRF with mass normalized mode shapes as

$$H_{dp}(\omega) = \sum_{r=1}^{n} \frac{-\omega^2 \Theta_{br}^2}{\omega_r^2 - \omega^2 + 2j\omega\zeta_r\omega_r} \tag{24.10}$$

where Θ_{b_r} is the mode shape of the base in the x direction for mode r. Θ_{b_r} values are known from Eq. (24.9). At high frequencies in the real part of the FRF, the so-called mass lines (which are actually 1/(active mass)) are observed as modes are added to the response. At frequencies much higher than the natural frequency of one of the numbered masses in Fig. 24.3, the spring decouples the mass from the base. An example of these real valued mass lines, using the rigid body mode and three elastic modes, is given in Fig. 24.4.

The lowest amplitude mass line is associated with the one unconstrained rigid body mode (purple) and is

$$\Theta_{b\ RB}^2 = \frac{1}{m_{fix} + m_{TA}} \tag{24.11}$$

where m_{fix} is the mass of the fixture and m_{TA} is the mass of the test article. The effective mass of the first elastic mode is associated with Delta 1 in Fig. 24.4. The larger the delta, the larger the effective mass. So the first elastic mode effective mass will be

$$m_{eff\ 1} = m_{TA+fix} - \left(\Phi^2_{b\ RB} + \Phi^2_{b_1}\right)^{-1} = \left(\Phi^2_{b\ RB}\right)^{-1} - \left(\Phi^2_{b\ RB} + \Phi^2_{b_1}\right)^{-1} \tag{24.12}$$

Similarly, the effective mass for any mode, r, can be calculated as

$$m_{eff\ r} = \left(\Phi^2_{b\ RB} + \sum_{i=1}^{r-1}\Phi^2_{b_1}\right)^{-1} - \left(\Phi^2_{b\ RB} + \sum_{i=1}^{r}\Phi^2_{b_i}\right)^{-1} \tag{24.13}$$

As the mass of the fixture approaches infinity, Eq. (24.13) becomes exact, i.e. the mode shapes converge to the fixed base modes. The less massive the fixture, the more approximate is Eq. (24.13). However, for an example analytical 3 DoF system the author processed, if the mass of the fixture was more than ten times the mass of the test article, the effective mass error was less than 0.1% of the test article mass. From previous work, the accuracy of the effective mass from experimental data is not much better than 3.5% of the test article mass, so the Eq. (24.13) approximation is well within the experimental error. In all the effective mass applications the authors have worked on, the fixture mass has always been at least a factor of ten more than the test article.

The final step to estimating the effective mass model in one direction is to find the fixed base modal frequencies so that the spring stiffness (as shown in Fig. 24.3) supporting the effective masses can be calculated. The fixed base damping is also derived in this step. The process outlined in Eqs. (24.1, 24.2, 24.3, 24.4, 24.5, 24.6, 24.7, and 24.8) is repeated, though in Eq. (24.4) only the single rigid body s DoF must be constrained to zero.

As this is an experimentally based model, it should be noted that the accuracy of the mass normalized mode shapes on the fixture, the frequencies in the modal extraction, and the rigid body mode shapes are critical to an accurate estimate of the effective mass. In the upper limit, all the effective masses sum to the total mass of the test article (not including the fixture). This is a very useful check on the experimental results.

24.3 Advantages of the New Drive Point Approach

There are advantages of the new approach over the PMPF approach [1]. In the PMPF approach, the effective mass was developed from a linear combination of the pseudo-modal participation factors. The coefficient estimates were subject to errors introduced due to modal truncation for any higher modes that were not extracted. The new approach is based only on the fixture rigid body and elastic modes of interest, so it is not dependent on higher modes that are not extracted (see Fig. 24.4). For cases in which only a few modes are extracted, this should make the new approach more robust.

The second major advantage is the physical insight generated by this theory. If one has a drive point FRF near the center of gravity on the fixture, the large deltas in the real part between modes give insight as to which modes have large effective mass and which modes do not. The imaginary part of the drive point FRF will also give this similar insight, as modes with large effective mass will have larger amplitude imaginary portion peaks than modes with small amplitude peaks (assuming similar damping). The new approach is dubbed the drive point (DP) method since it is based on a drive point FRF of the system constrained to move in one axis.

24.4 Experimental Example 1

The first example comes from a structure [1] for which 28 elastic modes were extracted using the SMAC algorithm [2]. The structure is basically a 72 kg nylon beam attached to a 605 kg steel seismic mass, all suspended by soft straps yielding rigid body modes below 5 Hz. In addition to the rigid body modes, the first plate twist mode at about 1380 Hz was constrained in the s DoF of Eq. (24.4). Currently, the authors consider this the most accurate experiment they have conducted for effective mass testing. In this experiment, the effective mass errors (computed by the previous PMPF method) as compared to a validated finite element model were within about 3.5% of the total test article mass. Effective masses were calculated for the lateral soft bending direction of the beam (see Fig. 24.5).
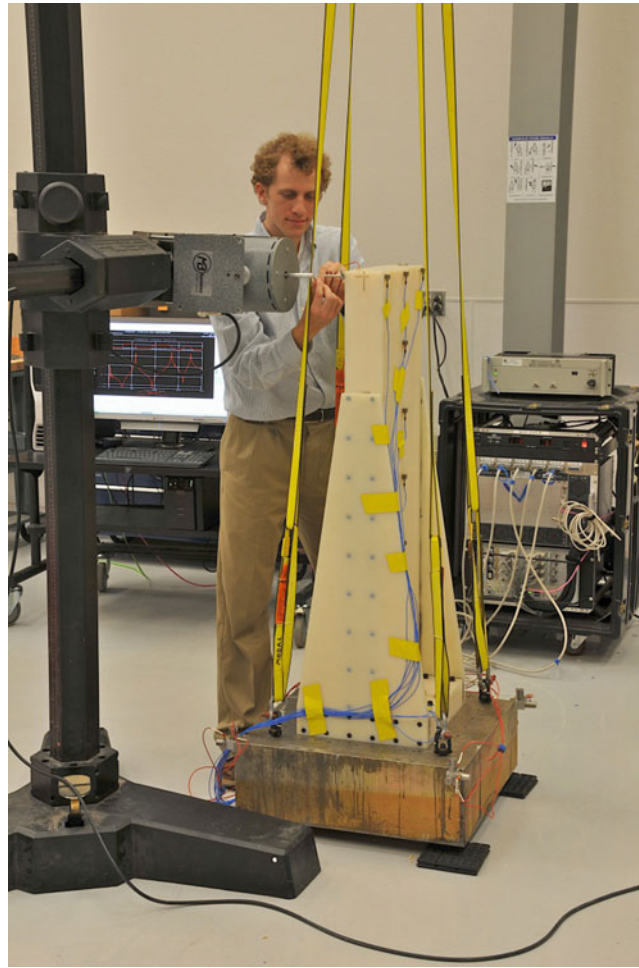
Fig. 24.5 Example 1 experimental structure for effective mass calculation

Table 24.1 Beam normalized effective masses in soft bending direction – PMPF vs new drive point theory

Fixed base test frequency (Hz)	Effective mass from PMPF	Effective mass from DP method	Difference as % of total test article mass
38	0.4152	0.4141	0.1
162	0.1870	0.1871	−0.0
393	0.0882	0.0885	−0.0
702	0.0372	0.0372	0
853	0.0036	0	0.4
1028	0.0107	0.0155	−0.5
1040	0.0031	0.0320	−2.9
1199	0.0001	0.0001	0
1301	0.0273	0.0034	2.4
1344	0.0199	0.0026	1.7
Total Mass	0.792	0.780	1.5

In Table 24.1 are provided the effective masses (normalized to 1 as the total test article mass) provided by the old PMPF method and the new DP method. All differences are less than the previously estimated worst case experimental error stated above. The final row of the table lists the sum of the effective masses, which are in good agreement for this example.

24.5 Experimental Example 2

The second example is from a project to determine effective mass from experimental data for a small component. As shown in the cut-away drawing in Fig. 24.6, the component was installed in a cavity in an aluminum fixture. The component was supported by rubber pads and held in place with a steel clamp which was secured to the fixture with cap screws. Accelerometers were placed on four of the fixture corners, several of the faces, and on the clamp. The fixture was placed on soft foam yielding rigid body modes below 30 Hz. The elastic modes were extracted using real modes in the SMAC algorithm [2]. The first unconstrained component mode was at 418 Hz and the first flexible fixture (plate twist) mode was at 3268 Hz. In addition to the rigid body modes, the plate twist mode was constrained in the s DoF of Eq. (24.4). Experimental modes were obtained and used to calculate effective masses in three orthogonal translational directions.

In Table 24.2 are provided the effective masses (normalized to 1 as the total component mass) provided by the PMPF method and the new DP method. The total effective mass is listed for each method in the last row of each section. Most of the effective mass values are consistent within 1% of the total component mass for the two methods. However, there are a few notable differences, and the sum of effective masses in the X and Y directions are more than the component mass. These issues are discussed below.

The fact that the sum of the effective masses in X and Y is more than the component mass is not physically realizable for a rigid fixture. Consider the worst case in the Y direction, where the sum of the effective mass is almost 20% greater than the component mass. There was a physical reason that led to the high effective mass estimate for the mode at 1710 Hz, which is, by itself, greater than the component mass. In the free mode shape associated with the 1710 Hz mode, there was significant Y motion of the component which also drove significant Y motion of the clamp. Therefore, the effective mass calculated at 1710 Hz included a significant percentage of the mass of the clamp as well. A rough estimate of half the mass of the active portion of the clamp participating in this mode would contribute an effective mass of 0.16 to the observed calculation. This would indicate that the effective mass of the 1710 Hz mode would be closer to 0.92 if the clamp were rigid. Although this mode had by far the most clamp motion, there was clamp motion in some of the X direction modes that would increase their effective mass as well. Since the clamp is part of the fixture, accelerometers were included on the clamp to attempt to constrain out its dynamic effects. The fixture was tested free without the component to attempt to obtain mode shapes for the clamp that could be included in the constrained s DoF of Eq. (24.4). There were three clamp modes in the empty fixture at 2161, 3776 and 3970 Hz. However, when the test article was included, these clamp modes moved to frequencies of 3276, 3969 and 4684 Hz, and their mode shapes changed significantly. When the free clamp mode shapes were included in the constraining process of Eq. (24.4), the results were disastrous with effective masses exceeding 400% of the total component mass. This suggests the free clamp mode shapes were not an adequate set of basis vectors to constrain out the true clamp motion. As such, the clamp modes were left out of the constraining process to achieve the results provided in Table 24.2.

The only large difference between the two methods was for the two modes just above 1200 Hz in the X direction. Although the effective mass sums are about the same, the individual differences are about 23% of the test article mass for those two modes, which is significant. Consider the imaginary part of the constrained driving point FRFs, H_{dp}, for each of these two modes in Fig. 24.7 below. Clearly, there is a substantial difference in their amplitudes, and correspondingly, there is an expectation for a large difference in effective mass between these two modes. For this reason, the authors believe that the
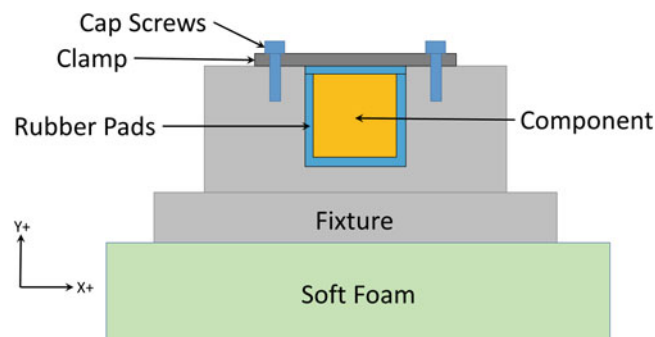
Fig. 24.6 Example 2 experimental setup for effective mass calculation

Table 24.2 Component normalized effective masses in three directions – PMPF vs new drive point theory

Fixed base frequency (Hz)	Effective mass from PMPF	Effective mass from DP method	Difference as % of total component mass
X direction			
397	0.001	0.001	0.0
644	0.111	0.105	−0.6
875	0.001	0.001	0.0
1227	0.388	0.155	−23.3
1292	0.593	0.826	23.2
1710	0.008	0.010	0.2
Total Mass	1.102	1.097	−0.5
Y direction			
397	0.000	0.000	0.0
644	0.007	0.007	0.0
875	0.095	0.089	−0.6
1227	0.007	0.006	−0.1
1292	0.011	0.009	−0.2
1710	1.076	1.079	0.3
Total Mass	1.196	1.190	−0.6
Z direction			
397	0.951	0.946	−0.5
644	0.008	0.008	0.1
875	0.000	0.000	0.0
1227	0.000	0.000	0.0
1292	0.002	0.002	0.0
1710	0.002	0.002	0.0
Total Mass	0.963	0.959	−0.5
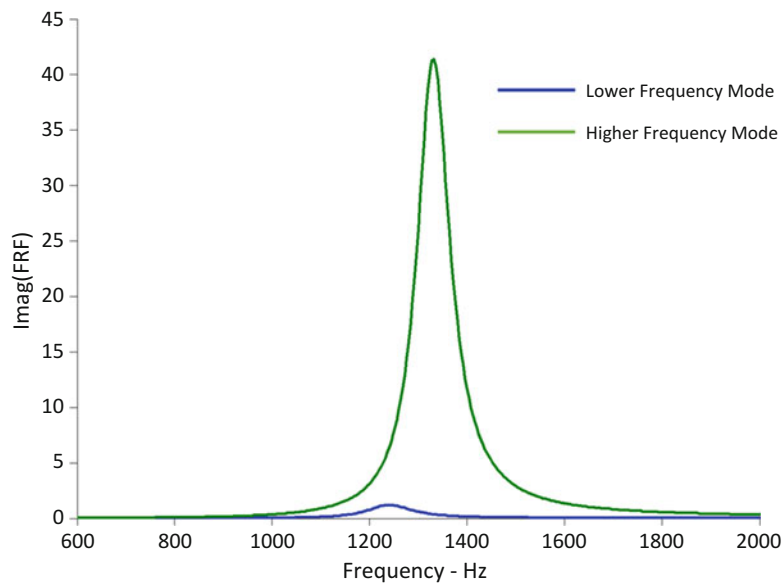
Fig. 24.7 Imaginary part of constrained drive point FRF for two modes of interest

DP estimate is more reasonable. Also, the higher mode is a translation of the component in X while the lower frequency mode is a rotation about X. It seems reasonable that the translation mode would have more effective mass in the translation direction than the rotational mode. Although this is only a single example, it may be that the DP method is demonstrating its robustness against modal truncation errors in a case where only six elastic modes of the component were extracted.

24.6   Conclusions

A revised theoretical approach, referred to as the Drive Point method, for calculating effective mass of a test article mounted on a fixture is presented with experimental examples. Effective mass experiments consist of a free modal test of the test article mounted on a fixture. When compared against the previous pseudo-modal participation factor approach on the authors' "best" previous effective mass experiment, the effective masses agreed within previously established error bounds.

The new approach provides insight from a drive point FRF at the center of gravity of the fixture, showing the large resonant responses that correspond to large effective masses for the test article. In the second experimental example, this insight was helpful in determining which approach was most appropriate where the two approaches showed significant differences. The Drive Point approach is not as prone to modal truncation error as the previous pseudo-modal participation factor approach. This is of particular advantage when there are only a few modes that can be extracted in the modal test. Although most of the effective mass estimates were nearly equivalent with the two approaches, the drive point approach appeared to give more reasonable results for X direction effective mass for two modes. This may reinforce the theoretical advantage, since the second example had many fewer modes than the first example, leading to possible modal truncation errors. In the second example, the fixture also exhibited motion of a clamp which was not able to be constrained, erroneously contributing fixture mass to some of the calculated component effective mass values.

References

1. Mayes, R.L., Schoenherr, T.F., Blecke, J., Rohe, D.P.: Efficient method of measuring effective mass of a system. Proceedings of the 31st International Modal Analysis Conference, Garden Grove, CA, February 2013, paper #194
2. Hensley, D.P., Mayes, R.L.: Extending SMAC to multiple references. Proceedings of the 24th International Modal Analysis Conference, Orlando, FL, pp. 220–230, January 2006

Chapter 25
Nonlinear Finite Element Model Updating, Part II: Implementation and Simulation

Brian C. Owens, Ryan A. Schultz, Benjamin R. Pacini, and Randall L. Mayes

Abstract Linear structural dynamic models are often used to support system design and qualification. Overall, linear models provide an efficient means for conducting design studies and augmenting test data by recovering un-instrumented or un-measurable quantities (e.g. stress). Nevertheless, the use of linear models often adds significant conservatism in design and qualification programs by failing to capture critical mechanisms for energy dissipation. Unfortunately, the use of explicit nonlinear models can require unacceptably large efforts in model development and experimental characterization to account for common nonlinearities such as frictional interfaces, macro-slip, and other complex material behavior. The computational requirements are also greater by orders of magnitude. Conversely, modal models are much more computationally efficient and experimentally have shown the ability to capture typical structural nonlinearity. Thus, this work will seek to use modal nonlinear identification techniques to improve the predictive capability of a finite element structural dynamics model.

Part I of this paper discussed experimental aspects of this work. Part II will consider use of nonlinear modal models in finite element modeling. First, the basic theory and numerical implementation is discussed. Next, the linear structural dynamic model of a configuration of interest is presented and model updating procedures are discussed. Finally, verification exercises are presented for a high level excitation using test data and simulated predictions from a structural dynamics model augmented with models obtained in nonlinear identification efforts.

Abbreviations

M	Physical mass matrix
K	Physical stiffness matrix
C	Physical damping matrix
f_n	Natural frequency in Hertz
f	Frequency in Hertz
$F(t)$	Physical force vector
Φ	Mode shape matrix
ω	Natural frequency in radians per second
ζ	Modal damping ratio
q	Modal displacement degree of freedom
$\dot{q}$	Modal velocity degree of freedom
$\ddot{q}$	Modal acceleration degree of freedom

B.C. Owens (✉) • R.A. Schultz • R.L. Mayes
Structural Dynamics Department, Sandia National Laboratories, P.O. Box 5800 – MS0557, Albuquerque, NM 87185, USA
e-mail: bcowens@sandia.gov; rschult@sandia.gov; rlmayes@sandia.gov

B.R. Pacini
Sandia National Laboratories, PO Box 5800, 87185, Albuquerque, NM, USA
e-mail: brpacin@sandia.gov

t	Time
$f(t)$	Modal force vector
$f_{nl}(q, \dot{q})$	Nonlinear restoring force vector
x	Physical displacement degree of freedom
$\dot{x}$	Physical velocity degree of freedom
$\ddot{x}$	Physical acceleration degree of freedom
σ	Stress

25.1 Introduction

Linear structural dynamics models are often used to support system design and qualification. Overall, linear models provide an efficient means for conducting design studies and augmenting test data by recovering un-instrumented or un-measurable quantities (e.g. stress). Nevertheless, the use of linear models often adds significant conservatism in design and qualification programs by failing to capture critical mechanisms for energy dissipation (e.g. joints, friction, material behavior, etc.). Unfortunately, the use of explicit nonlinear models can require unacceptably large efforts in model development and experimental characterization to account for common nonlinearities such as frictional interfaces, macro-slip, and other complex material behavior. The computational requirements are also greater by orders of magnitude.

This work uses modal nonlinear identification techniques to improve the predictive capability of structural dynamics models. Pacini and Mayes [1] have extended conventional modal testing with nonlinear system identification to develop nonlinear modal models. These experimental nonlinear models will augment linear structural dynamic finite element models allowing for the development of reduced order nonlinear structural dynamics models. A flexible, generalized framework has been created to readily accept model parameters from system identification efforts, and the predictive capability of the model is demonstrated via verification exercises. Impacts of the enhanced analysis capability are also discussed.

25.2 Modeling Theory and Framework

This section presents the basic theory as well as the numerical framework for developing the improved analysis capability that employs experimentally derived nonlinear structural dynamics models. The process of nonlinear identification during modal testing and derivation of nonlinear models will not be discussed here, but is presented in a companion paper by Pacini and Mayes [1].

Consider the classical linear structural dynamic system shown in Eq. 25.1. This equation is intended to represent a dynamic system in physical coordinates. Here M, C, and K are the physical mass, damping, and stiffness matrices respectively. Physical displacement degrees of freedom (DOFs) are present in the vector x. Physical velocity and acceleration are denoted by $\dot{x}$ and $\ddot{x}$ respectively. $F(t)$ is a generalized transient load vector that may act on any DOF of the system.

$$[M]\,\ddot{\vec{x}} + [C]\,\dot{\vec{x}} + [K]\,\vec{x} = F(t) \tag{25.1}$$

Through assumptions of linearity and modal superposition one may express the dynamic system in modal space using the relation shown in Eq. 25.2 to express the system as a collection of uncoupled, single DOF systems in as shown in Eq. 25.3. Here, Φ is the mode shape of the system and q is the modal displacement DOF. The natural frequency and damping ratio of a mode are denoted by ω_n and ζ. The modal force is denoted by $f(t)$ and is obtained through a transformation of the physical load vector.

$$\vec{x} = \Phi \vec{q} \tag{25.2}$$

$$\ddot{q} + 2\omega_n \zeta \dot{q} + \omega_n^2 q = f(t) \tag{25.3}$$

The current work augments the linear system of Eq. 25.3 with a nonlinear function f_{nl} as shown in Eq. 25.4.

$$\ddot{q} + 2\omega_n \zeta \dot{q} + \omega_n^2 q + f_{nl}(q, \dot{q}) = f(t) \tag{25.4}$$
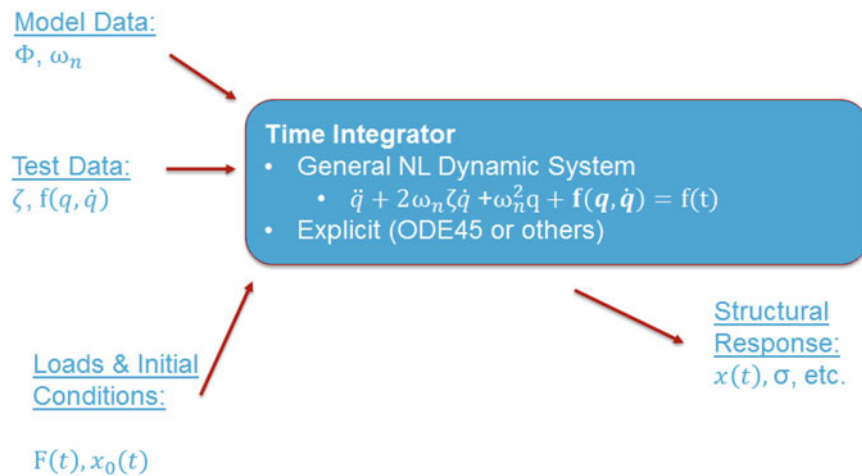
Fig. 25.1 Framework for nonlinear structural dynamics analysis

This nonlinear function restoring force, f_{nl} is obtained from experimental nonlinear identification efforts. This augmented dynamic system is readily adapted for transient analysis by common explicit time integrators such as MATLAB ODE45.

Fig. 25.1 illustrates the framework that has been developed in this work. Finite element structural dynamic modeling efforts will be used to provide linear natural frequencies and mode shapes while experimental efforts are used to characterize linear damping and nonlinear stiffness and damping. After time integration, the system can be converted back to physical space and then traditional analysis quantities of interest such as displacement, velocity, acceleration, stress, strain, and force may be recovered at any node/element in the finite element model.

25.3 Model Description and Updating

This section describes the model, linear updating, and nonlinear dynamic model. First the configuration of interest is described and details of the corresponding finite element model are given. Next, the model is updated using modal test data. Third, the specific nonlinear modal model employed in this work is presented.

25.3.1 Configuration of Interest and Finite Element Model

The hardware configuration considered in this study is a jointed structure of moderate complexity. The configuration consists of a cylinder and a simple beam attached to a plate. This configuration will be referred as the Can-Plate-Beam (CPB). CPB structural components are manufactured from 6061-T6 aluminum. The cylinder and beam/plate are connected via eight bolted joints. The jointed interface has been designed to exhibit nonlinearities. A thorough description of the hardware is given in Sect. 3 of Reference [1], but the experimental set-up and cross-section of the companion finite element model are shown in Figs. 25.2 and 25.3 respectively.

The CPB finite element model is composed primarily of 20-node hexahedral elements. The jointed connections are modeled via constraints, as this provides a greater degree of flexibility in model updating procedures such as considering the contact area in tied interfaces or specification of compliance at interfaces. The finite element model also explicitly models accelerometers via concentrated masses. These masses are offset to provide a more accurate representation of mass loading as well as a more relevant comparison between measured and predicted mode shapes.
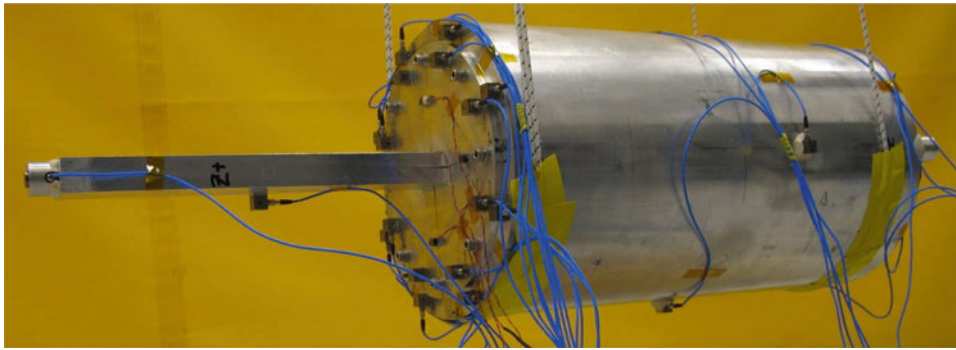
Fig. 25.2 Physical test hardware
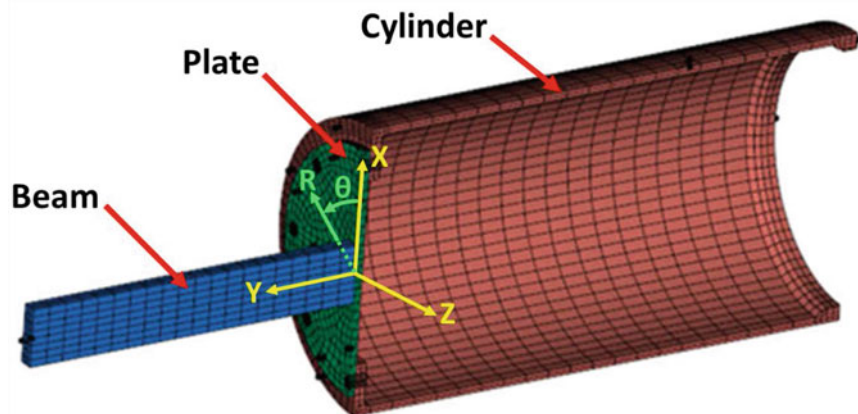
Fig. 25.3 CPB assembly full system solid model and coordinate systems

25.3.2 Linear Model Updating

First, the finite element model was updated using modal test data from low level excitation. The low-level excitation test is useful in developing an experimental linear modal model that can be used for model updating of a linear structural dynamics finite element model. Details of the linear experimental modal model are provided in Sect. 3.3 of Reference [1].

Table 25.1 presents mode frequencies, damping, and shape descriptions for modes extracted from the low-level modal testing. These modes are considered as "truth" data for model updating. Only a high level discussion of model updating will be discussed in this paper, as a detailed description of model updating procedures is beyond the scope of this work. In general, the nominal model compared reasonably well to linear modal test data. It was notable that the frequencies of the first bending modes of the beam were too stiff and the frequency of the axial mode was too soft. Parametric studies were conducted to examine the effect of cylinder Young's modulus, plate to beam tied connection area, and plate to cylinder interface constraints. Two approaches were considered for modeling the bolts between the plate and cylinder:

1. the bolts were modeled using a collection of beam and rigid bar elements (see Fig. 25.4)
2. the interface was modeled using tied constraints at discrete patches representing the bolted interface (see Fig. 25.5).

The physical beam-to-plate interface has two bolted connections along with dental cement serving as an adhesive between the contact area. Therefore, the true boundary condition at this interface is somewhat ambiguous. The bolts and adhesive were not modeled explicitly, but instead the interface was modeled through tied constraints over a discrete surface area. Ultimately, the contact area was tailored as shown in Fig. 25.6 to provide good agreement with first beam bending modes from modal test data.

The modes of the system were relatively insensitive to beam parameters considered in the beam/rigid bar modeling approach employed for the plate-to-cylinder bolted connection interfaces. Therefore, the final model employed a modified contact area and tied data which resulted in good agreement with the axial mode frequency from test data. Slight modifications (approx. +5%) was also made to the cylinder Young's modulus to obtain better agreement in ovaling modes.

Table 25.2 shows the updated model mode predictions compared to experimental data. Overall, there is good agreement between test and simulation. The most noticeable differences are in the first bending mode (soft direction) of the beam,

Table 25.1 Experimental linear modal parameters[a, b]

Mode	f_n (Hz)	ζ (%cr)	Reference DOF	Shape description
7	128	0.30	31349Y	First bend of Beam in soft direction (global X)
8	171	0.31	25449Y	First bend of Beam in stiff direction (global Z)
9	391	0.21	34965R	(2,0) ovaling of Cylinder aligned with X-Z axes
10	395	0.03	34965R	(2,0) ovaling of Cylinder 45° from X-Z axes
11	560	0.34	53632Y	Axial mode
12	957	0.11	34965R	(3,0) ovaling of Cylinder
13	958	0.09	32916R	(3,0) ovaling of Cylinder
14	978	0.23	31349Y	Second bend of Beam in soft direction (global X)

[a]Modes highlighted in green exhibited nonlinear behavior during test
[b]Rigid body modes (1–6) not shown

Fig. 25.4 Beam/rigid bar bolt interface modeling approach
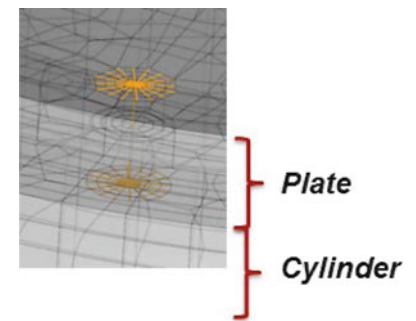
Fig. 25.5 Element "patches" used for tied constraint bolt interface modeling approach
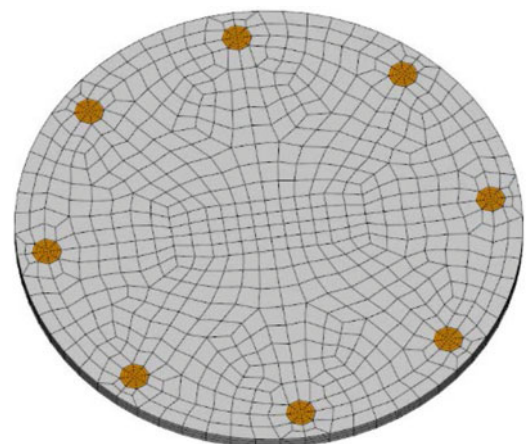
(3,0) ovaling mode, and in the second bending mode of the beam. Further model updating activities may be able to provide better agreement, but this is beyond the scope of the current work which is focused on augmenting linear structural dynamics modeling with nonlinear modal data for enhanced predictions.
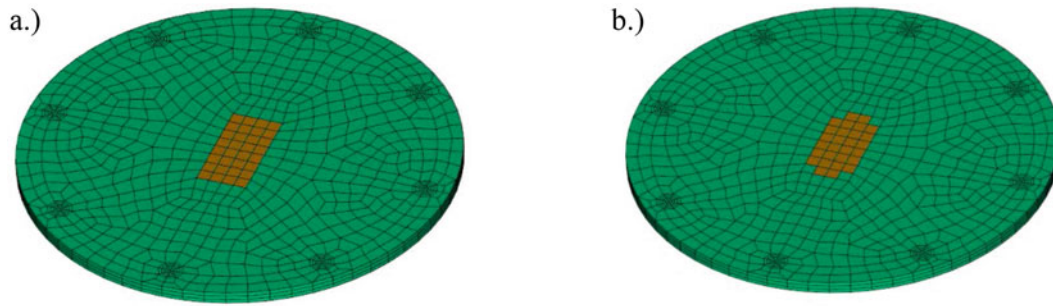
Fig. 25.6 Contact area used for tied constraint of beam to plate interface. (a) Initial tied constraint contact area. (b) Updated tied constraint contact area

Table 25.2 Comparison of experimental and simulation modes

Mode #	Test frequency (Hz)	Simulation frequency (Hz)	% Difference	Mode shape description
7	128	120	−6.3	First bend of beam in soft direction (global X)
8	171	173	1.2	First bend of beam in stiff direction (global Z)
9	391	392	0.3	(2,0) ovaling of cylinder aligned with X-Z axes
10	395	393	−0.5	(2,0) ovaling of cylinder 45° from X-Z axes
11	560	549	−2.0	Axial mode
12	957	943	−1.5	(3,0) ovaling of cylinder
13	958	913	−4.7	(3,0) ovaling of cylinder
14	978	1011	3.4	Second bend of beam in soft direction (global X)

Table 25.3 Damping and stiffness coefficients [1]

Mode	c_1	c_2	k_1	k_2
7	2.6	−1.95	−9.15E + 07	3.77E + 10
8	3.17	−3.28	−2.86E + 08	1.92E + 11
11	318	−834	−2.05E + 10	1.54E + 14
14	−188	811	−6.16E + 09	8.41E + 13

25.3.3 Nonlinear Modeling

Further modal testing was conducted at higher force input levels to drive the configuration into the nonlinear response regime. The nonlinear identification techniques discussed in Reference [1] were used to develop a nonlinear pseudo-modal model using fits for cubic stiffness and damping in the nonlinear restoring force term. The form of this modal model is shown in Eq. 25.5 and the model parameters are shown in Table 25.3. The f_{nl} term defined in Eq. 25.5 is employed in Eq. 25.4 and serves as input to the numerical framework depicted in Fig. 25.1. As noted in Table 25.1, modes 7, 8, 11, and 14 behave nonlinearly, while the other modes are predominantly linear. Therefore, nonlinear models were only developed for these modes.

$$f_{nl}\left(q(t), \dot{q}(t)\right) = c_1 \left|\dot{q}(t)\right| \dot{q}(t) + c_2 \dot{q}^3(t) + k_1 \left|q(t)\right| q(t) + k_2 q^3(t) \qquad (25.5)$$

25.4 Verification Exercise

After linear and nonlinear characterization of the CPB structure, a verification exercise was performed. The CPB was excited at a location on the flange of the cylinder in the axial (Y) direction via a 0.3 s chirp (i.e. a very fast sine sweep) from 50 to 1400 Hz. Data was recorded for 4 s. This DOF was chosen since it excited three of the four nonlinear modes. The amplitude of the sweep was varied in order to maximize the response of each nonlinear mode without exceeding the maximum voltage limit of any accelerometer. The input location and an output location on the beam tip are depicted in Fig. 25.7. The input chirp signal is depicted in Fig. 25.8.
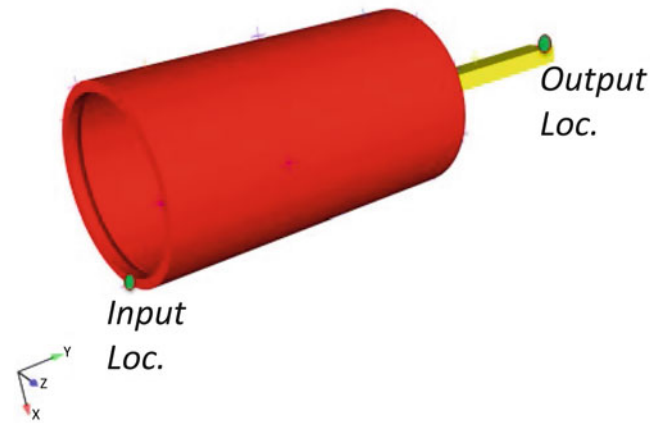
Fig. 25.7 Input and output locations considered in verification study
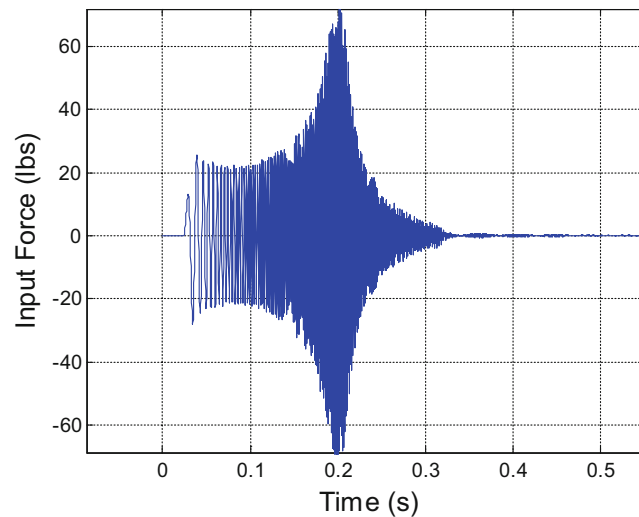
Fig. 25.8 Chirp excitation

The nonlinear framework described in Sect. 3 was used to perform a virtual experiment using the updated linear model, nonlinear modal model, and chirp excitation. This simulation employed an explicit time integration routine (ODE45) from 0 to 1 s of simulation time. The time step of this simulation was adaptively chosen by the ODE45 solver. Acceleration time history predictions were recovered at the drive point and beam tip location for comparison to experimental data. Note that only the first 1 s of the experimental data was considered in the comparison to model predictions for a more meaningful comparison. Time histories were transformed to the frequency domain via the Fast Fourier Transform (FFT). Use of the FFT allows for a succinct description of the frequency content and levels in a time series. Furthermore, environmental specifications and transfer functions are typically developed in the frequency domain.

Figure 25.9 shows acceleration FFTs of the experimental data, linear model, and nonlinear model. Overall, reasonable agreement to experimental data is observed. This level of agreement is more than sufficient for design studies and environmental specifications informed by model data. Differences in model data vs. experimental data can be attributed to error in the linear model predictions as well as differences in experimental and numerical mode shapes. It is likely that further model development could result in improved agreement, but the current level of agreement is useful for assessing the nonlinear modeling approach under development.

The axial mode is the dominant nonlinear mode of this system, and Fig. 25.10 shows a "zoomed in" FFT of this mode. It is notable that the nonlinear model simulation both captures the amplitude reduction and "softening" of the frequency. In fact, the linear model has levels approximately 2× higher than the nonlinear model. Thus, using a linear model could drive overly conservative designs (e.g. over prediction of stress response) or environmental specifications that are used for testing and qualification of a design. Furthermore, the good agreement in modal frequency for the linear axial mode and experimental data is simply due to differences in the linear axial mode observed in modal testing and that in the updated finite element model. Inspection of Table 25.2 shows the axial mode prediction is approximately 2% "soft"/low. Therefore,
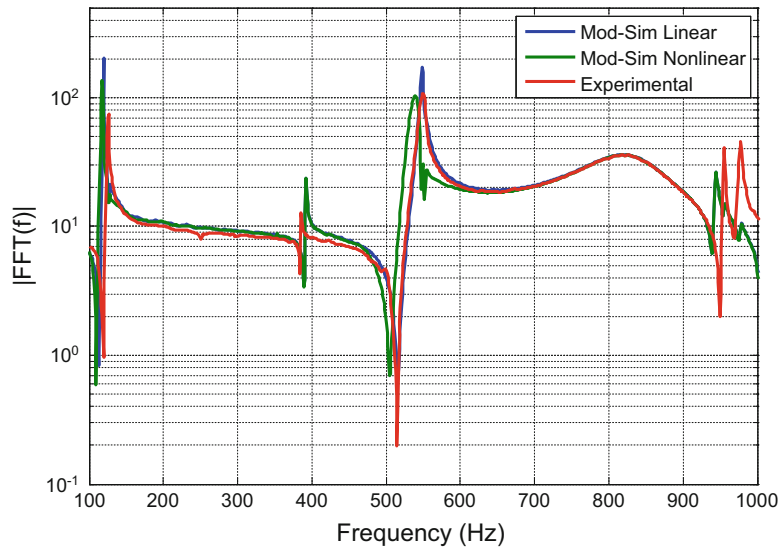
Fig. 25.9 Comparison of FFT of drive-point acceleration
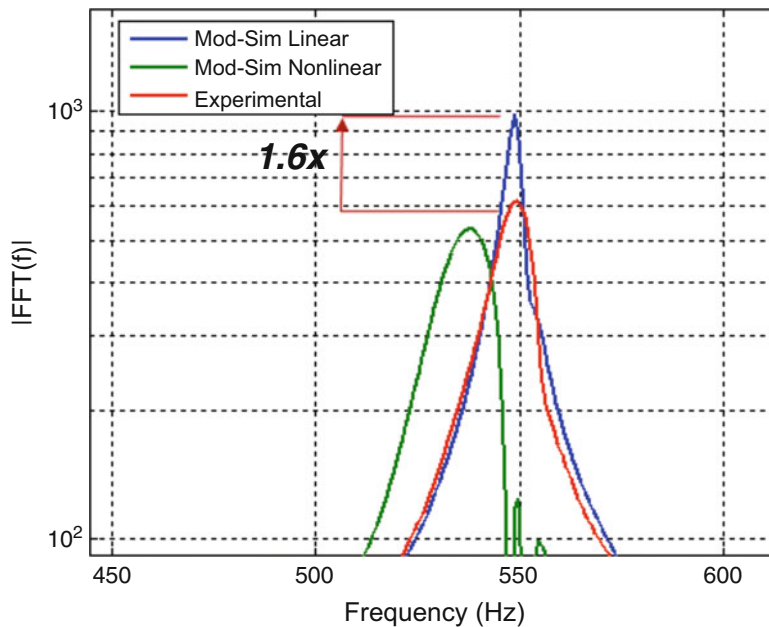
Fig. 25.10 Comparison of FFT of drive-point acceleration for axial mode

the experimental and nonlinear model "soften" at this mode due to nonlinear effects. In other words, a more accurate representation of the linear axial mode frequency would have resulted in better agreement between the nonlinear model predictions and experimental data for the axial mode FFT. The beam tip response was also examined with similar trends in verification. Therefore, these results are omitted from this paper for brevity.

Note that the secondary peak in the FFT around 550 Hz is a consequence of using the FFT on a nonlinear signal. At early times, the high level input excites nonlinearities in the axial mode, but at later times the response decays and becomes primarily linear. Since this mode has a softening behavior, this linear modal frequency appears as a "secondary peak"/irregularity at a higher frequency on the FFT.

25.5 Conclusions

This work has successfully demonstrated the ability for efficient nonlinear dynamic modeling through means of nonlinear identification methods in modal testing. Part I of this work showed the capability of using a pseudo-modal model to capture nonlinearities of a real structure using cubic polynomials for the stiffness and damping forces. Part II of this work developed a numerical framework that would accept a linear finite element structural dynamic model and augment the dynamic system with nonlinear data from test efforts. A hardware configuration of moderate complexity with nonlinear interfaces was considered and finite element model was created and updated using modal test data. The baseline dynamic system was augmented with nonlinear pseudo-modal models from experimental nonlinear identification efforts. This capability was demonstrated against an experimental verification case. The results showed good agreement in the dynamic behavior of the primary nonlinear mode of the system. Nonlinear model predictions were able to replicate frequency "softening" as well as reduction in amplitude levels associated with nonlinear effects. This improved modelling approach could significantly benefit design studies or environmental specifications informed by model data in that a more accurate representation of system dynamics would reduce conservatism in modeling efforts.

Reference

1. Pacini, B.R., Mayes, R.L., Owens, B.C., Schultz, R.A.: Nonlinear finite element model updating, Part I: experimental techniques and nonlinear modal model parameter extraction.. Presented at the 35th International Modal Analysis Conference, January 2017

Chapter 26
A Benchmark Structure for Validation of Experimental Substructuring, Transfer Path Analysis and Source Characterisation Techniques

M.V. van der Seijs, E.A. Pasma, D.D. van den Bosch, and M.W.F. Wernsen

Abstract This paper presents a practical study on popular Experimental Dynamic Substructuring topics. A series of substructures is designed of such complexity to fit in right between "real life" structures as often found in industrial applications and "academic" structures which are typically the simplest models to identify a particular phenomenon. The designed benchmark structure comprises an active side with a vibration source, a passive side and a test rig for source characterisation. The connectivity is scalable in complexity, meaning that a single-point, two-point and continuous interface can be established. Substructuring-compatible component models are obtained from impact measurements using the Virtual Point Transformation. The vibration source on the active structure is characterised on the test rig using the in-situ TPA concept. Hereafter the component TPA method is applied to simulate the response on the passive side of the coupled structure, in turn obtained using dynamic substructuring.

Keywords Dynamic substructuring • Virtual point transformation • Transfer path analysis • Blocked force • In-situ

26.1 Introduction

Dynamic Substructuring (DS), Transfer Path Analysis (TPA) and Source Characterisation (SC) are three research fields that have received tremendous attention from both science and industry. All three aim to provide practical solutions for engineering of structural vibrations and sound, with applications stretching from the automotive and aerospace industry to high-tech precision machinery and sustainable energy solutions. However, it is fair to say that the similarities between the three fields have not always been well understood [1]. This is perhaps motivated by their different origins, for instance: substructuring finds its oldest roots in numerical modelling and reduction of aerospace structures [2–5], transfer path analysis evolved hand-in-hand with automotive NVH engineering [6–10] and source characterisation emerged from fields such as vibration isolation and structure-borne sound engineering [11–15]. Only in recent years, some studies [9, 16–18] have appeared that incorporate various aspects of the three fields, while [19, 20] extend to yet other fields such as feedback control theory.

At the same time, many methods within DS, TPA and SC prove to be rather challenging to validate in the context of an industrial application. This is often due to a myriad of experimental uncertainties (signal-to-noise problems, incomparable operational/boundary conditions, presence of secondary excitation sources, etcetera) on top of the applications' inherent complexities. To avoid such uncertainties and reduce the overall complexity of a problem, studies on "academic" structures are often conducted first, such that the method's key properties present themselves as clearly identifiable and unambiguous properties. And although such studies provide an excellent basis for theory development, it remains difficult to transpose a proof of a theoretical concept to application on an industrial problem.

M.V. van der Seijs (✉) • E.A. Pasma • D.D. van den Bosch
VIBES.technology, Molengraaffsingel 14, 2629, Delft, The Netherlands
e-mail: maarten@vibestechnology.com

M.W.F. Wernsen
VIBES.technology, Molengraaffsingel 14, 2629, Delft, The Netherlands

Department of Precision and Microsystems Engineering, Delft University of Technology, Mekelweg 2, 2628CD, Delft, The Netherlands

26.1.1   Paper Goal and Outline

The goal of this paper is twofold. First, a benchmark structure is proposed of such complexity, that it fits in right between the "real-life" industrial structures on the one hand, and the limited-DoF academic examples on the other hand. Section 26.2 introduces the three benchmark substructures: an active, passive and test rig substructure. The benchmark substructures have been designed to allow for three different coupling configurations with increasing interface complexity.

The second goal of this paper is to apply concepts of DS, TPA and SC using measurements on the constructed benchmark structures. Section 26.3 presents a high-level overview of a selection of possible applications, including a virtual point transformation, coupling of substructures A and B, source characterisation of A in test assembly AR and transfer path analysis for prediction of vibrations in assembly AB.

26.2   Benchmark Design

The benchmark construction has been motivated by the desire to validate methods within the fields of experimental DS and TPA. More specifically, the aim was to experiment with methods as covered in the general framework articles on the two topics, respectively [5] and [1]. In the latter one, three types of substructures are used for theory development: an active source structure, a passive receiving structure and a test rig for source characterisation. These three substructures have formed the basis for the benchmark. Also, as the interest is in validating methods in a frequency range of 0–5000 Hz, the benchmark substructures are supposed to display sufficient dynamics (i.e. vibration modes) in this range.

26.2.1   Substructure Design

Figure 26.1 shows the three substructures. Let us introduce them one by one and briefly touch upon some design considerations:

- Substructure A is welded together from three pieces of solid aluminium (30×30 mm). It forms an evenly sided triangle and loosely resembles the character 'A', but was made asymmetric to avoid double resonance modes. It comprises a number of 10 mm diameter holes, at the corner points and along the length of the members, evenly spaced at distances of 75 mm. It hosts a vibration source (further discussed below) and can therefore represent the active source system in a TPA or SC problem. The combined weight is circa 2.5 kg.
- Substructure B is constructed from two plates of stainless steel with a solid piece of steel welded in between. The plates are produced using precise laser-cutting. Five holes are placed spanning a total distance of 300 mm, again with 75 mm spacing in between. A honeycomb-like pattern of cuts was introduced to reduce weight, as well as to provide a pattern to align sensors for an observability investigation.[1] As such, substructure B represents a receiving side into which the source vibrations of substructure A may propagate. The total weight is circa 10 kg.
- Substructure R is a collection of small identical support structures, together forming a test rig for testing of substructure A. The supports are machined from solid aluminium blocks and can be mounted on a wooden base plate. An opening in the centre was made to reduce the stiffness of the top with respect to the fixed base. The test rig R can be used to characterise the source vibrations of substructure A, for prediction of vibrations in an assembly with substructure B. The weight of each support is 670 gramme.
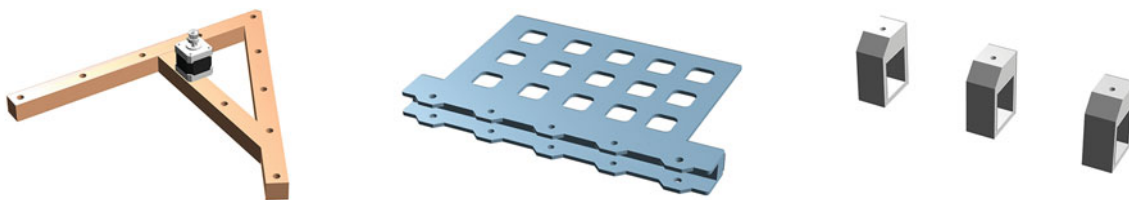
Fig. 26.1 The three benchmark substructures: active source A (*left*), passive receiver B (*centre*) and test rig parts R (*right*)

---

[1]See the paper in the proceedings of SEM IMAC 2017: *M. Wernsen et al. An indicator sensor criterion for in-situ characterisation of source vibrations*.

26.2.2 Vibration Source

For application of SC and TPA, substructure A needs to have an active vibration source. Many applied studies in this field report on difficulties with maintaining identical operational conditions throughout the various testing environments [9, 21–23]. In the definition of the benchmark, it has therefore been a key requirement to have a source that generates perfectly reproducible vibrations. Other requirements were to have a source with distinct orders, i.e. a very constant speed with a stationary excitation profile, and an excitation spectrum that renders sufficient signal-to-noise in the frequency range of interest.

The chosen vibration source is a NEMA 17 stepper motor: a typical electric motor used in 3D printing hardware. The stepper is controlled using an Arduino DUE with a Pololu A4988 stepper motor driver. It uses a PWM protocol for speed control, which can be programmed to run through various speeds. In contrast to e.g. an AC electric motor, a stepper motor has a rather 'rippled' rotational speed profile, generating a lot of motor orders, i.e. harmonics proportional to the fundamental frequency. If desired, an unbalance mass can be connected to the shaft of the motor to further amplify the vibration amplitude. The PWM signal can be connected to a tacho-pulse channel of a DAQ system, allowing for accurate speed monitoring during operational measurement.

26.2.3 Assembly Variants

The individual substructures have been designed to allow for multiple assembly configurations. Figure 26.2 shows these assemblies for AB (top) and AR (bottom). The configurations respectively represent a single coupling point, two coupling points and five coupling points, the latter resembling a continuous interface. In all cases, standard M10 bolts and nuts can be inserted to fasten the structures.

– The single-point configuration is meant to be the simplest assembly to comprehend from a structural-dynamic point of view. Although both structures comprise dozens of modes in a bandwidth of 5 kHz, one might reason that only six vibration modes can be transferred over the interface. Substructure coupling of A and B would thus imply writing an interface condition for the three translational and three rotational DoFs. The single-point configuration is well suited to investigate e.g. experimental substructure coupling and decoupling [24, 25].
– The two-point configuration roughly doubles the complexity of the assembly. Following the same reasoning, a maximum of 12 vibration modes would now be present in the vibration transfer between A and B. However, it is evident that there is interplay between the two coupling points, which deserves special attention in any application of substructuring or force identification. Indeed, the two-point coupling configuration forms a perfect basis to study phenomena related to interface conditioning, such as matrix regularisation and observability of the interface vibrations.
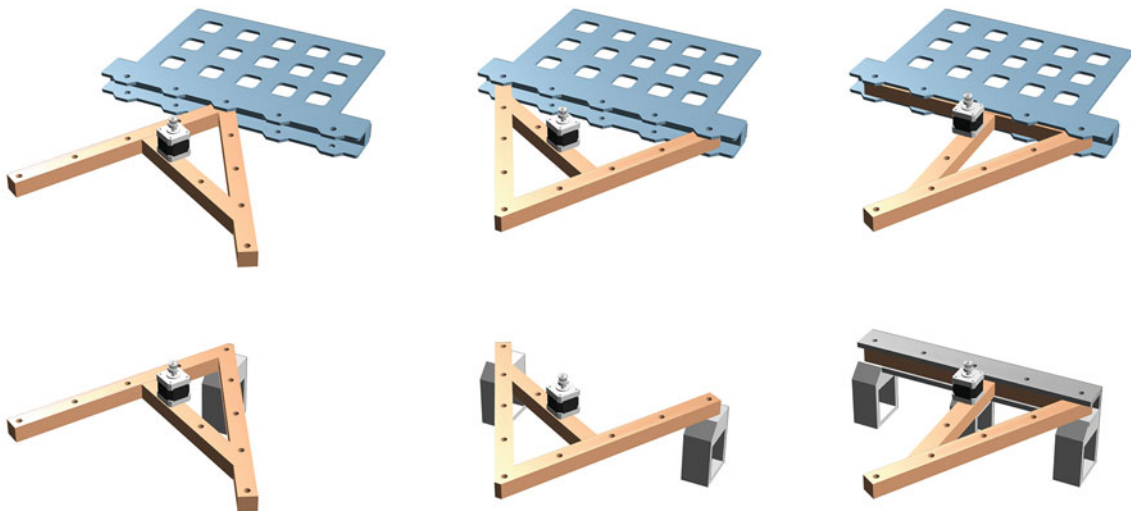
Fig. 26.2 Various configurations of the benchmark structures. *Upper row*: assemblies of A and B in 1/2/5-point configuration. *Lower row*: assemblies of A and R in 1/2-point configuration

– The five-point configuration resembles a continuous interface. In this case, it is likely that the effect of each coupling point can no longer be distinguished. Instead, the combined interface effect would probably be best considered in terms of modes. Modal substructuring techniques such as [26] can be tested on this assembly, as well the transmission simulator method [27].

The entire benchmark collection provides an abundance of data for investigation of many DS, SC and TPA topics, which shall be the topic of the next section.

26.3 Applications

The coming sections provide a high-level overview of some experimental applications. Examples are shown of experimental modelling using virtual point transformation, dynamic substructuring, source characterisation and transfer path analysis. In order not to dwell in theory, the derivations and equations have been kept to a minimum. Reference is made to original literature for the interested reader.

For the purpose of this study, an extended range of assemblies has been subjected to impact hammer and operational measurements. Figure 26.3 shows two of those assemblies: AB in single-point and AR in two-point coupling configuration. All separate substructures and the assemblies AB have been measured in free-floating conditions, i.e. suspended by soft springs. The assemblies AR have been mounted onto a wooden base plate, in turn resting on a test table on air springs.

26.3.1 Experimental Modelling

Experimental modelling can be understood as the art of obtaining a structural-dynamic model (such as FRFs) from measurements [18, 28, 29]. It constitutes a fundamental step in experimental substructuring, but also finds application in component transfer path analysis. This section briefly discusses how a nodal FRF model can be obtained from impact hammer measurements, demonstrated for experimental modelling of substructures A and B.

26.3.1.1 Short Theory of the Virtual Point Transformation

Typically, experimentally obtained models lack a common interface which allows for substructure coupling. In the numerical domain, nodes provide this common interface, as a direct result of FE modelling (sometimes after remeshing or a node collocation technique [30]). The Virtual Point Transformation [29] introduces such nodes in experimentally obtained models.

(a)   (b)
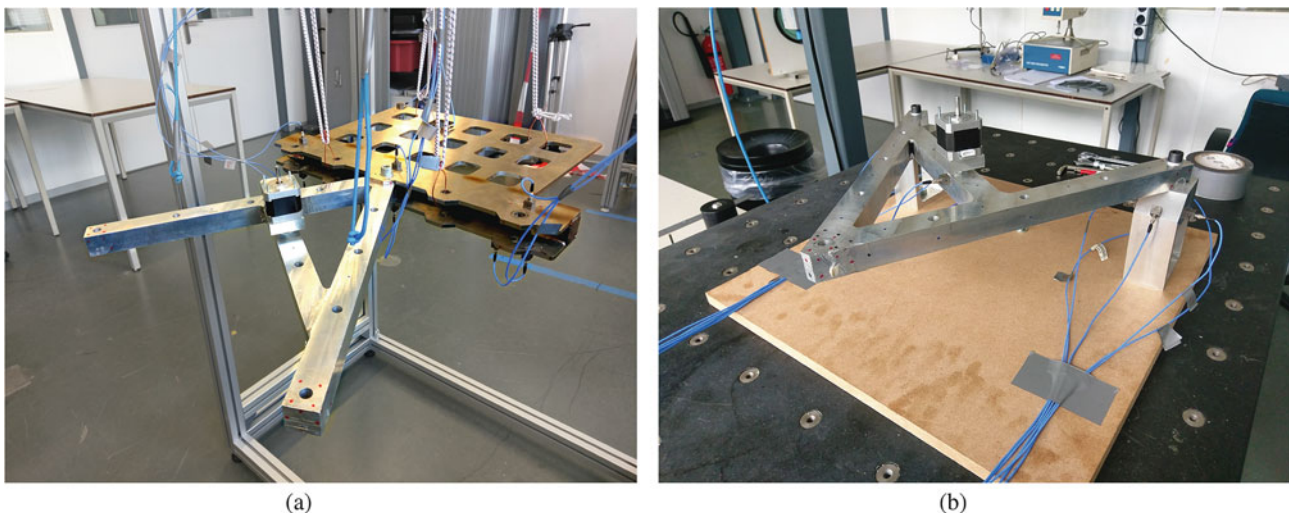
Fig. 26.3 Two test configurations. (**a**) Assembly AB in the single-point coupling configuration, free-floating suspended by soft springs. (**b**) Assembly AR in the two-point coupling configuration, mounted to a wooden base plate resting on a test table

The main idea is to choose a point on or near a physical interface of a substructure that can be made compatible with the other (experimental or numerical) substructure to couple. All measured displacements **u** and forces **f** around the interface can be transformed to this virtual point, resulting in a 6-DoF 'nodal' description consisting of virtual translations/rotations **q** and forces/moments **m**:

$$\text{Displacements:} \quad \mathbf{u} = \mathbf{R_u q} \quad \Longrightarrow \quad \mathbf{q} = (\mathbf{R_u})^+ \mathbf{u} \qquad \mathbf{R_u} \in \mathbb{R}^{n \times 6} \tag{26.1a}$$

$$\text{Forces:} \quad \mathbf{m} = \mathbf{R_f^T f} \quad \Longrightarrow \quad \mathbf{f} = \left(\mathbf{R_f^T}\right)^+ \mathbf{m} \qquad \mathbf{R_f} \in \mathbb{R}^{m \times 6} \tag{26.1b}$$

The two transformations allow to compute a 6×6 virtual point FRF matrix $\mathbf{Y_{qm}}(\omega)$ from a measured $n \times m$ matrix $\mathbf{Y}(\omega)$. This can easily be set up for each coupling point, building a experimental 'super-element' that is compatible for substructuring with other models:

$$\text{Measured FRFs:} \quad \mathbf{u} = \mathbf{Yf} \tag{26.2a}$$

$$\text{Virtual point FRFs:} \quad \mathbf{q} = (\mathbf{R_u})^+ \mathbf{Y} \left(\mathbf{R_f^T}\right)^+ \mathbf{m} \quad \Longrightarrow \quad \mathbf{q} = \mathbf{Y_{qm} m} \tag{26.2b}$$

One underlying assumption of this transformation is that the measured substructures behave rigidly in the vicinity of this interface in the frequency range of interest [29]. This assumption and other criteria will be discussed next.

26.3.1.2 FRF Measurement

All substructure FRFs have been obtained by impact hammer testing. Figure 26.4 depicts how hammer impact points (red arrows) and tri-axial accelerometers (grey cubes) have been positioned and oriented on substructures A and B. Besides some internal points, the main interest for both substructures are the three coupling points. Each coupling point has been instrumented by 3 tri-axial accelerometers of type PCB 356B21. To determine forces and moments, 16 impact hammer positions are chosen per coupling point. Altogether, this results in sufficient overdetermination of the virtual point transformations.

26.3.1.3 FRF Consistency

In order to evaluate the above assumption on rigidity and obtain insight in the contribution of single force impacts or displacements to the VP dynamics, several consistency checks can be done. With a consistency check, the experimentally obtained results are first transformed to the virtual point and then expanded (or projected) back on the original measured DoFs [18, 29]. The difference in the original response and the projected response provides inside on how much residual
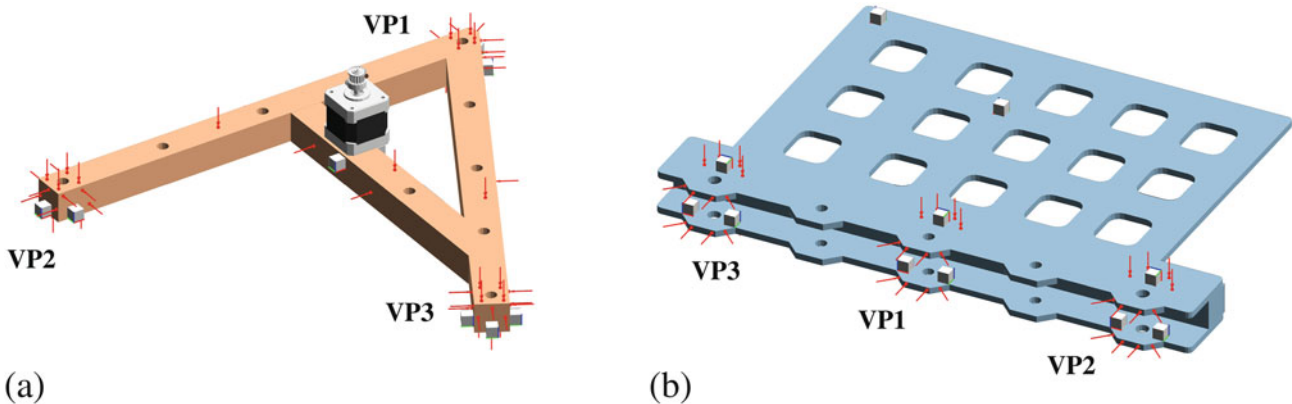
Fig. 26.4 Acceleration sensors (indicated by *grey cubes*) and impact locations (*red arrows*) visualised on the substructures. (**a**) Substructure A. The three coupling points are each instrumented by 3 tri-axial accelerometers and 16 impact points. (**b**) Substructure B. The three coupling points are each instrumented by 3 tri-axial accelerometers and 16 impact points; 2 additional sensors register target responses in the structure
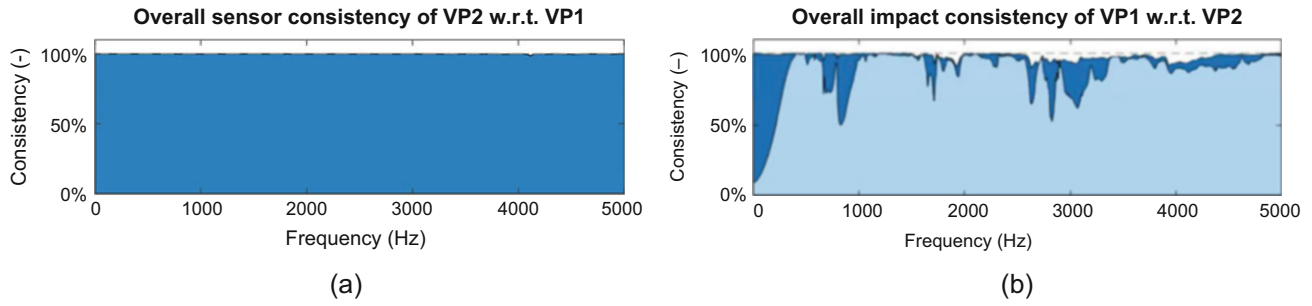
Fig. 26.5 Sensor and impact consistency checks for substructure A. (**a**) Overall sensor consistency of 9 sensor channels around VP2 with respect to excitations around VP1. (**b**) Overall impact consistency of 16 (*light blue*) and 13 (*blue*) impacts out of 16 around VP1 with respect to responses around VP2

dynamics (interface flexibility) has been neglected with the virtual point transformation. More practically, this technique is used to evaluate the contribution of single measured DoFs to the transformed VP dynamics. This can be used to find erroneous definitions of sensor and impact positions or directions in the transformation, or discard 'bad impacts'[2] from the transformation.

Let us illustrate the various consistency checks for substructure A. Figure 26.5a shows the overall sensor consistency of VP2 for excitations around VP1. This operation takes the accelerances of all 9 sensors channels (FRF matrix rows) around VP2 (**u**) for a combination of hammer impacts (FRF matrix columns) around VP1, transforms these to the virtual point **q** and expands the accelerances back to their original sensor channels ($\tilde{\mathbf{u}}$). The score of 100% over the full bandwidth of 5000 Hz indicates that all sensor channels are perfectly consistent, i.e. $\tilde{\mathbf{u}} = \mathbf{u}$. This is obvious as the region between the three sensors is very stiff; values below 100% would probably indicate incorrect placement of a sensor.

Figure 26.5b shows the overall impact consistency for VP1 with respect to responses around VP2. The light-blue area was computed for all 16 impact points, which is clearly not optimal. Looking into the specific impact consistency for each 16 impacts, three impacts had significant lower score than average. By discarding these 3 from the set of 16, the full 6-DoF set of virtual point forces/moments can still be determined. The dark-blue area was computed for the optimised set, clearly showing an improved overall impact consistency.

26.3.1.4 FRF Reciprocity

The VP transformation allows to validate reciprocity of the obtained virtual point FRFs, as computed by Eq. (26.2b). Note that this is possible as the VP displacements (i.e. linear and rotational accelerations) are perfectly 'vectorially associated' with the corresponding VP loads (i.e. forces and moments). In other words, the virtual point FRFs behave as if they were computed for nodes of an FE model.

Figure 26.6 shows two typical virtual point FRFs: response VP2Y over force VP3Y of substructure A (left) and response VP2Z over force VP3Z of substructure B (right). The FRFs reciprocal FRFs are displayed in red. It can be observed that reciprocity is indeed satisfied, especially up to 2 kHz.

26.3.2 Dynamic Substructuring

Now that VP transformed FRFs are available for substructure A and B, both structures are coupled using the LM-FBS algorithm [5, 31]. To do so, the substructure FRF matrices of A and B are put in block-diagonal form and an appropriate Boolean matrix **B** is written (not discussed here):

$$\tilde{\mathbf{Y}} = \mathbf{Y} - \mathbf{Y}\mathbf{B}^T \left(\mathbf{B}\mathbf{Y}\mathbf{B}^T\right)^{-1} \mathbf{B}\mathbf{Y} \qquad \mathbf{Y} \triangleq \begin{bmatrix} \mathbf{Y}^A & \mathbf{0} \\ \mathbf{0} & \mathbf{Y}^B \end{bmatrix} \tag{26.3}$$

---

[2]Bad impacts can for instance be caused by a low impact energy in the frequency range of interest, low signal-to noise ratio, poor reachability with an impact hammer due to geometric constraints, double pulses, etcetera.
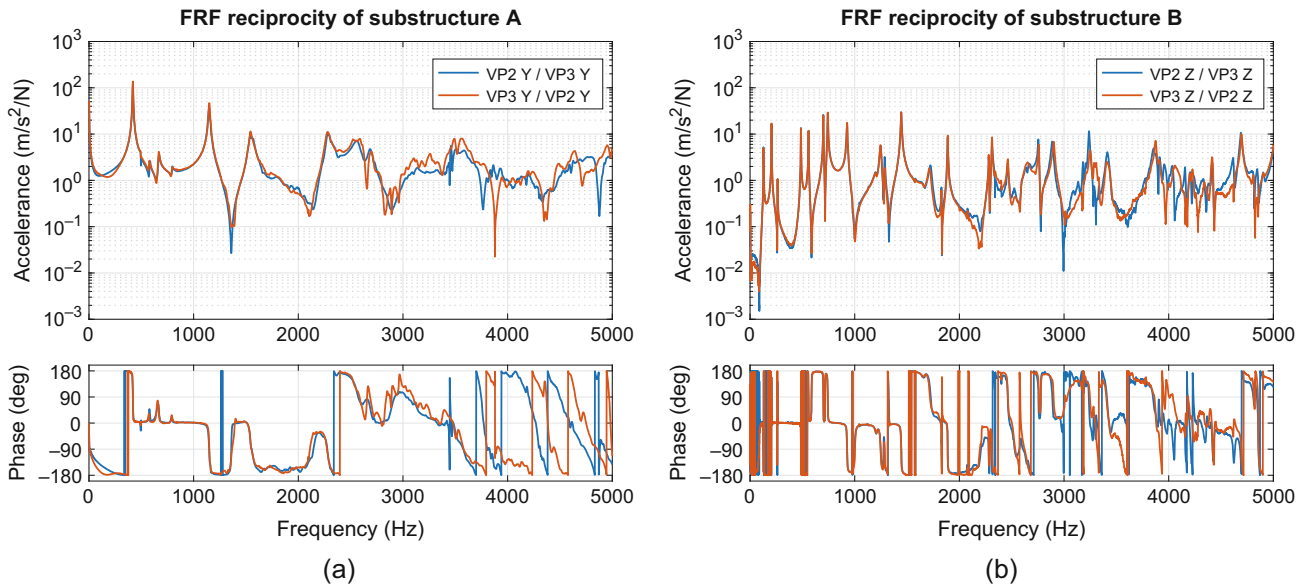
Fig. 26.6 Reciprocity of the virtual point FRFs of the experimental models of substructure A and B. (**a**) Substructure A: Y-direction of VP2 to VP3 and its reciprocal. (**b**) Substructure B: Z-direction of VP2 to VP3 and its reciprocal
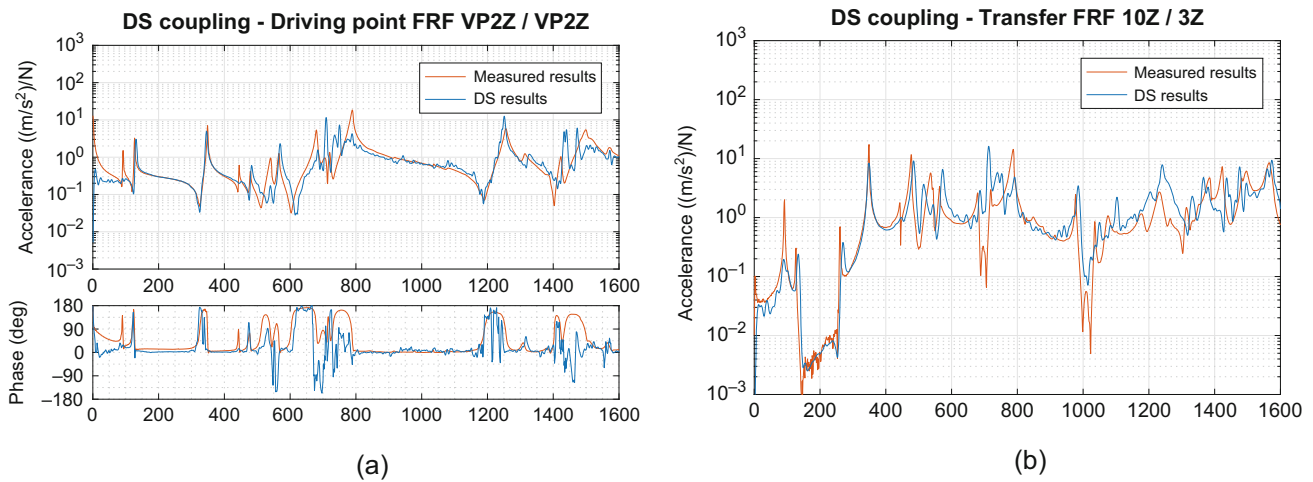
Fig. 26.7 Application of dynamic substructuring: assembled FRFs of AB (*blue*) in two-point coupling configuration, compared against the validation measurement (*red*). (**a**) Driving-point FRF for VP3 in Z-direction. (**b**) Transfer FRF for an internal impact point on A to an internal acceleration response on B, both in Z-direction

The two-point coupling configuration is considered, which means that coupling is performed by requiring strict coordinate compatibility and force equilibrium for the FRFs of virtual points 2 and 3. We now focus on the frequency range of 0–1600 Hz.

Some results of the substructured FRFs of AB are depicted in Fig. 26.7. First in Fig. 26.7a, a driving point FRF on the coupling interface is shown, namely for VP2 in Z-direction. The phase is shown as well to assess the passivity[3] of the FRF. Figure 26.7b shows a transfer FRF from an internal force impact point on structure A to an acceleration response internally on structure B. Both points are not part of a coupling VP, hence the transfer FRF is realised by coupling over the interface. The substructured FRFs (blue) are compared the measured FRFs of the coupled structure AB.

---

[3]For an accelerance driving point FRF, the phase should be bounded by 0 and $+180°$.

The first substructuring results, although not perfect yet, are by all means encouraging. It can be seen how resonance frequencies are created at roughly the right frequencies. The phase around anti-resonances is not fully stable, however the overall amplitude of the FRFs match quite well. Note that no filtering or processing has been applied to the measured FRF data, except for transformation to virtual points.

26.3.3 In-Situ Source Characterisation

To characterise the active vibrations of source structure A, the in-situ characterisation method is used [15]. This method describes the source structure using 'blocked forces' on its interfaces (as if the component were connected to a fully rigid boundary) by measuring operational responses on a connected receiver structure. More specifically, this method is able to characterise a source structure in an assembly, with the resulting characterisation being a property of the source structure only rather than being a property of the combined assembly. Because this characterisation is a source-inherent property, the obtained blocked forces are transferable to other receiving structures. Therefore, in theory, the source may be characterised in the original assembly (e.g. AB) or on a test rig with different dynamic properties (e.g. AR). This paper shows examples of both variants.

The in-situ source characterisation method comprises three steps. Here, it is discussed for the test rig variant; for more explanation of the notation and terminology used, see [1].

1. Operational measurement of the source structure A mounted to a test rig R where indicator responses $\mathbf{u}_4$ on test rig R are measured (see the test setup in Fig. 26.3b);
2. FRF measurement of the combined structure AR, more specifically from force inputs at the interface $\mathbf{f}_2$ to the indicator responses on the test rig $\mathbf{u}_4$. Here it is key that the DoFs $\mathbf{u}_4$ are the same set as with the operational measurement;
3. Characterisation of the active source by means of a matrix-inverse operation, resulting in blocked forces for each operational measurement cycle:

$$\mathbf{f}_2^{\text{eq}} = \left(\mathbf{Y}_{42}^{\text{AR}}\right)^{+} \mathbf{u}_4 \tag{26.4}$$

where $\mathbf{f}_2^{\text{eq}}$ denotes the blocked forces representing the source structure, $\mathbf{u}_4$ the measured operational responses of step 1 and $\mathbf{Y}_{42}^{\text{AR}}$ the FRFs of the source on test rig measured in step 2.

Note that if a virtual point transformation to a 6-DoF description is done on the force input side of the FRF matrix (i.e. the columns of $\mathbf{Y}_{42}$ relate to forces and moments in virtual point format), the resulting blocked forces $\mathbf{f}_2^{\text{eq}}$ will also present themselves in this form, making them easily transferable to other structures. In other words, one would obtain a source characterisation comprising three forces and three moments per coupling point, instead of a series of only translational forces.

The source vibrations of the active structure A have been characterised in the original 'target' assembly with passive side B *and* on the test rig structure R. Hence, the two in-situ characterisations yield two sets of 12 blocked forces/moments: 6 for each coupling point. These sets are used for vibration prediction in target assembly AB, which is presented in the next section.

26.3.4 Component-Based Transfer Path Analysis

For the purpose of virtual noise and vibration prediction (sometimes called Virtual Acoustic Prototyping, [32]), component Transfer Path Analysis is applied on the benchmark data. The advantage of component TPA is the ability to predict target response levels $\mathbf{u}_3$ in/on a passive structure B using an independent source characterisation (i.e. blocked forces) of a source A.

The governing equation of component TPA is as follows:

$$\mathbf{u}_3 = \mathbf{Y}_{32}^{\text{AB}} \mathbf{f}_2^{\text{eq}} \tag{26.5}$$

where $\mathbf{f}_2^{\text{eq}}$ is a set of equivalent/blocked forces for instance obtained by Eq. (26.4) and $\mathbf{Y}_{32}^{\text{AB}}$ the FRF matrix of assembly AB from the interfaces to the responses of interest $\mathbf{u}_3$ (sometimes called Noise Transfer Functions). Combining this with Dynamic Substructuring, one can predict the vibration levels as described above without ever physically assembling structures A
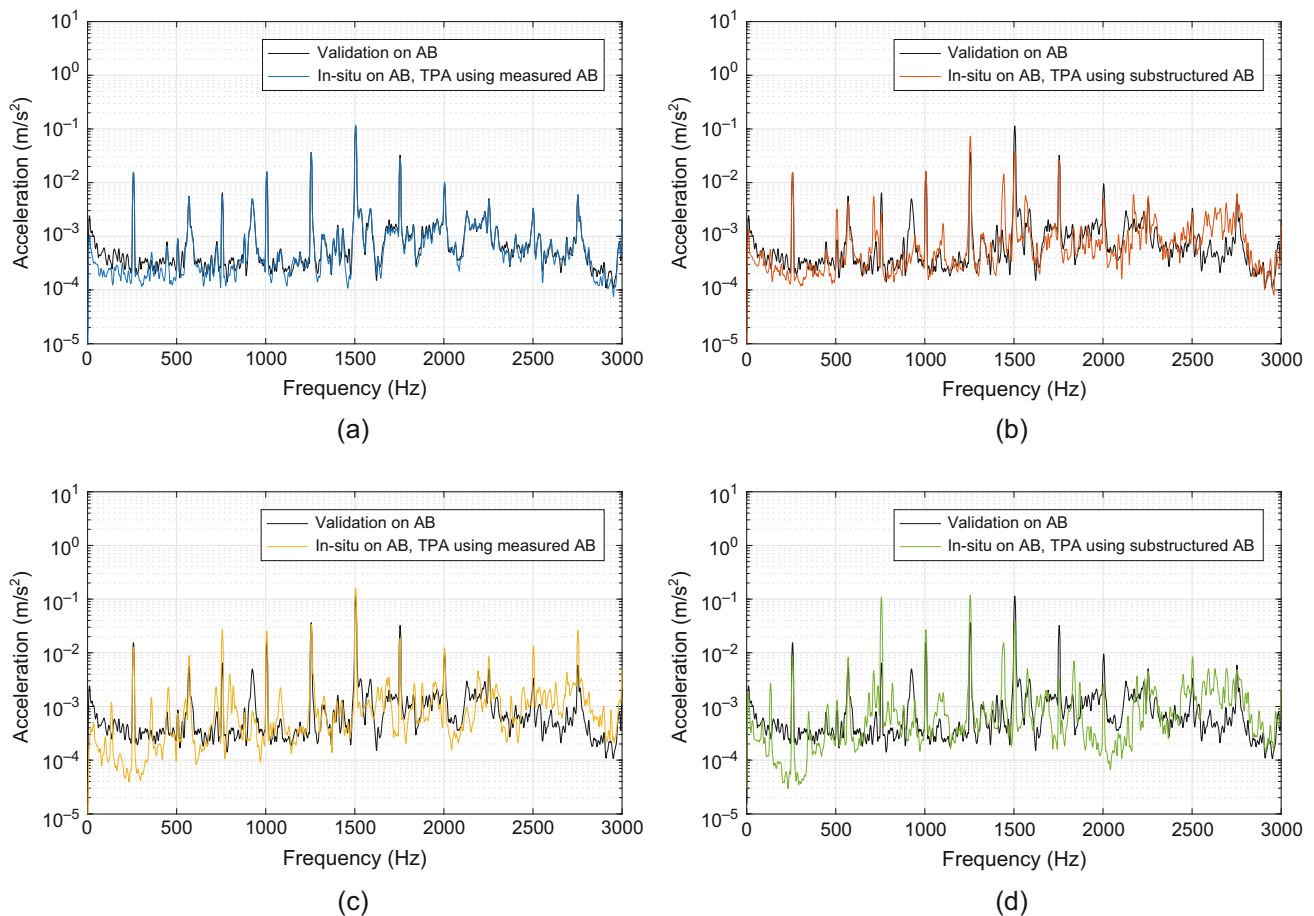
Fig. 26.8 Four results of in-situ source characterisation and TPA prediction (*blue/red/yellow/green*), all compared to a validation measurement in structure AB (*black*). (**a**) In-situ on AB, TPA prediction using measured FRFs of AB. (**b**) In-situ on AB, TPA prediction using substructured FRFs of AB. (**c**) In-situ on AR, TPA prediction using measured FRFs of AB. (**d**) In-situ on AR, TPA prediction using substructured FRFs of AB

and B [16]. In practice, this allows for a separation in development process, since two parties are able to work on their own structures A and B and an interface is provided in terms of blocked forces, possibly in the format of Virtual Point forces and moments.

Four results of component TPA are shown in Fig. 26.8, namely for source characterisation in AB (top) and AR (bottom) and for component TPA using a measured set of FRFs of AB (left) and substructured FRFs obtained by coupling of A and B (right). A validation response measurement is added for comparison, which is identical for all four plots. Remind that all characterisations are expressed in virtual point blocked forces and moments, i.e. 12 DoFs in total.

The first result in Fig. 26.8a constitutes the most literal application of in-situ TPA: the source is characterised in the original assembly AB, after which the virtual point blocked forces and moments are applied to the same assembly. Near identical results are obtained, especially at the peaks corresponding to the actual signal (source vibration orders) of the stepper motor. Figure 26.8b shows an application of the same blocked forces to the substructured FRFs of assembly AB. Most peaks are well approximated, which may be considered a very good result considering the various substructure FRF measurements involved (A, B and AB). Note that this approach goes into the direction of virtual vibration prototyping, which heavily relies on the virtual point transformation to provide common interfaces between the various measurements.

The results of Fig. 26.8c, d present similar results as above, yet for source characterisations calculated from operational measurements on the test rig. The imposed challenge here is that the test rig structure R possesses very different dynamic properties than B, resulting in totally different operational indicator responses ($\mathbf{u}_4^{AR}$) than in the original assembly ($\mathbf{u}_4^{AB}$). It is thus interesting to investigate if a source characterisation can be determined that renders similar responses on another passive side, i.e. is *transferable* to arbitrary assemblies.

Figure 26.8c on the left depicts the test rig characterisation applied to the measured FRF of AB. The results are encouraging, as many peaks that exceed the signal noise floor find roughly the right order of magnitude. The noise floor,

indeed, has been a limiting factor in this measurement, as the signal on the test rig sensors hardly exceeded the noise level. Finally, Fig. 26.8d shows what might be considered the holy grail of component TPA: a characterisation of source vibrations on a test rig, applied to an experimental model of the target assembly obtained using dynamic substructuring. This indeed constitutes a novelty in experimental DS and TPA, and shall be a direction for further investigation.

26.4 Conclusions and Outlook

In this paper, a series of benchmark substructures has been presented for method development and validation in the field of DS, TPA and SC. The three benchmark substructures can be connected in several ways, which makes the complexity of the interface problem adjustable to a one-point, two-point or continuous connection. Several applications have been shown to validate methods of experimental modelling, virtual point transformation, dynamic substructuring and source characterisation. Many more validations can be done, which is topic of further research at VIBES.technology.

References

1. van der Seijs, M.V., de Klerk, D., Rixen, D.J.: General framework for transfer path analysis: history, theory and classification of techniques. Mech. Syst. Signal Process. **68–69**, 217–244 (2016). doi:10.1016/j.ymssp.2015.08.004
2. Hurty, W.C.: Vibrations of structural systems by component mode synthesis. J .Eng. Mech. Div. **86**(4), 51–70 (1960)
3. Craig, R.R.J., Bampton, M.C.C.: Coupling of substructures using component mode synthesis. AIAA J. **6**(7), 1313–1319 (1968). doi:10.2514/3.2947
4. Rubin, S.: Improved component-mode representation for structural dynamic analysis. AIAA J. **13**(8), 995–1006 (1975). doi:10.2514/3.60497
5. de Klerk, D., Rixen, D.J., Voormeeren, S.N.: General framework for dynamic substructuring: history, review and classifcation of techniques. AIAA J. **46**(8), 1169–1181 (2008). doi:10.2514/1.33274
6. Plunt, J.: Finding and fixing vehicle NVH problems with transfer path analysis. Sound Vib. **39**(11), 12–16 (2005)
7. van der Auweraer, H., Mas, P., Dom, S., Vecchio, A., Janssens, K., van de Ponseele, P.: Transfer path analysis in the critical path of vehicle refinement: the role of fast, hybrid and operational path analysis. Technical report 2007-01-2352, SAE technical paper (2007). doi:10.4271/2007-01-2352
8. Sjövall, P.: Identification and Synthesis of Components for Vibration Transfer Path Analysis. Chalmers University of Technology, Gothenburg (2007)
9. de Klerk, D.: Dynamic response characterization of complex systems through operational identification and dynamic substructuring. Ph.D. thesis, Delft University of Technology (2009)
10. Scheuren, J., Lohrmann, M.: Transfer path analysis – experiences, expectations and perspectives. In: International Noise and Vibration Colloquium. SAE Brazil, Sao Paulo (2014)
11. Mondot, J.M., Petersson, B.A.T.: Characterization of structure-borne sound sources: the source descriptor and the coupling function. J. Sound Vib. **114**(3), 507–518 (1987). doi:10.1016/S0022-460X(87)80020-2
12. Petersson, B.A.T., Gibbs, B.M.: Use of the source descriptor concept in studies of multi-point and multi-directional vibrational sources. J. Sound Vib. **168**(1), 157–176 (1993). doi:10.1006/jsvi.1993.1367
13. ISO Technical Committee 43/Subcommittee 1/Workgroup 22 (ISO/TC43/SC1/WG22): Acoustics – characterization of sources of structure-borne sound with respect to sound radiation from connected structures – measurement of velocity at the contact points of machinery when resiliently mounted, ISO 9611, International Standards Organisation (1996)
14. Moorhouse, A.T.: On the characteristic power of structure-borne sound sources. J. Sound Vib. **248**(3), 441–459 (2001). doi:10.1006/jsvi.2001.3797
15. Moorhouse, A.T., Elliott, A.S., Evans, T.A.: In situ measurement of the blocked force of structure-borne sound sources. J. Sound Vib. **325**(4–5), 679–685 (2009). doi:10.1016/j.jsv.2009.04.035
16. Rixen, D.J., Boogaard, A., van der Seijs, M.V., van Schothorst, G., van der Poel, T.: Vibration source description in substructuring: a theoretical depiction. Mech. Syst. Signal Process. **60–61**, 498–511 (2015). doi:10.1016/j.ymssp.2015.01.024
17. Madsen, M.B.: Electrical power assisted steering – dynamic source strength characteristic and vehicle NVH prediction. Master's thesis, University of Southern Denmark (2014)
18. van der Seijs, M.V.: Experimental dynamic substructuring: analysis and design strategies for vehicle development. Ph.D. thesis, Delft University of Technology (2016). doi:10.4233/uuid:28b31294-8d53-49eb-b108-284b63edf670
19. Botelho, R.M., Christenson, R.E.: Mathematical equivalence between dynamic substructuring and feedback control theory. In: Dynamics of Coupled Structures. Proceedings of the 33rd IMAC, A Conference and Exposition on Structural Dynamics, vol. 4, chapter 3, pp. 31–40. Springer, New York (2015). doi:10.1007/978-3-319-15209-7_4
20. Franco, J.A., Botelho, R.M., Christenson, R.E.: Controls based hybrid sub-structuring approach to transfer path analysis. In: Dynamics of Coupled Structures. Proceedings of the 34rd IMAC, A Conference and Exposition on Structural Dynamics, vol. 4, chapter 3, pp. 15–24. Springer, New York (2016). doi:10.1007/978-3-319-29763-7_3
21. Elliott, A.S., Moorhouse, A.T., Huntley, T., Tate, S.: In-situ source path contribution analysis of structure borne road noise. J. Sound Vib. **332**(24), 6276–6295 (2013). doi:10.1016/j.jsv.2013.05.031

22. van der Seijs, M.V., Pasma, E.A., de Klerk, D., Rixen, D.J.: A comparison of two component TPA approaches for steering gear noise prediction. In: Dynamics of Coupled Structures. Proceedings of the 33rd IMAC, A Conference and Exposition on Structural Dynamics, vol. 4, chapter 7, pp. 71–79. Springer, New York (2015). doi:10.1007/978-3-319-15209-7_7

23. Lennström, D., Olsson, M., Wullens, F., Nykänen, A.: Validation of the blocked force method for various boundary conditions for automotive source characterization. Appl. Acoust. **102**, 108–119 (2016). doi:10.1016/j.apacoust.2015.08.019

24. D'Ambrogio, W., Fregolent, A.: Decoupling procedures in the general framework of frequency based substructuring. In: Proceedings of the XXVII International Modal Analysis Conference (IMAC), Orlando. Society for Experimental Mechanics, Bethel (2009)

25. Voormeeren, S., Rixen, D.: A family of substructure decoupling techniques based on a dual assembly approach. Mech. Syst. Signal Process. **27**(18), 379 (2012). doi:10.1016/j.ymssp.2011.07.028

26. Allen, M., Mayes, R., Bergman, E.: Experimental modal substructuring to couple and uncouple substructures with flexible fixtures and multi-point connections. J. Sound Vib. **329**(23), 4891–4906 (2010). doi:10.1016/j.jsv.2010.06.007

27. Mayes, R.L., Rohe, D.P.: Coupling experimental and analytical substructures with a continuous connection using the transmission simulator method. In: Topics in Experimental Dynamic Substructuring. Proceedings of the 31st IMAC, A Conference on Structural Dynamics, vol. 2, chapter 10, pp. 123–135. Springer, New York (2013). doi:10.1007/978-1-4614-6540-9_10

28. Wikipedia, Dynamic substructuring – Wikipedia, the free encyclopedia (2016). Accessed July 2016

29. van der Seijs, M.V., van den Bosch, D.D., Rixen, D.J., de Klerk, D.: An improved methodology for the virtual point transformation of measured frequency response functions in dynamic substructuring. In: Papadrakakis, M., Papadopoulos, V., Plevris, V. (eds.) 4th ECCOMAS Thematic Conference on Computational Methods in Structural Dynamics and Earthquake Engineering (COMPDYN), Kos Island, pp. 4334–4347 (2013). doi:10.13140/RG.2.1.2715.3126

30. Voormeeren, S.N.: Dynamic substructuring methodologies for integrated dynamic analysis of wind turbines. Ph.D. thesis, Delft University of Technology (2012). doi:10.4233/uuid:f45f0548-d5ec-46aa-be7e-7f1c2b57590d

31. de Klerk, D., Rixen, D., de Jong, J.: The frequency based substructuring method reformulated according to the dual domain decomposition method. In: Proceedings of the XXIV International Modal Analysis Conference (IMAC), St. Louis. Society for Experimental Mechanics, Bethel (2006)

32. Moorhouse, A.T., Seiffert, G.: Characterisation of an airborne sound source for use in a virtual acoustic prototype. J. Sound Vib. **296**(1–2), 334–352 (2006). doi:10.1016/j.jsv.2006.03.017

Chapter 27
Nonlinear Modal Substructuring of Panel and Stiffener Assemblies via Characteristic Constraint Modes

Joseph D. Schoneman, Matthew S. Allen, and Robert J. Kuether

Abstract Thin beams and panels subjected to large loadings will behave nonlinearly due to membrane stretch effects as they approach deflections on the order of their thickness; this behavior can be efficiently and accurately modeled using nonlinear reduced order models based on the structure's linear normal modes. However, the complexity of such reduced order models grows cubically with the number of linear modes in the basis set, making complicated geometries prohibitively expensive to compute. Component mode synthesis techniques may be used to reduce this cost by assembling a set of smaller nonlinear subcomponent models, each of which can be more quickly computed than a nonlinear model of the entire structure. Since geometric nonlinearity is heavily dependent on each structure's boundary conditions, however, subcomponents of an assembly which are constrained only at their interfaces – such as panels mounted to an underlying frame – prove difficult to treat using existing nonlinear modeling techniques. This work uses Craig-Bampton dynamic substructuring combined with characteristic constraint modes for interface reduction to examine the challenges associated with panel and frame assemblies, with a simple example motivating a discussion of current solutions and future challenges.

Keywords Nonlinear reduced order models • Dynamic substructuring • Characteristic constraint modes

27.1 Motivation

Linear analysis techniques form the foundation of modern structural dynamics. Most structures behave linearly at low levels of dynamic excitation, but certain high performance applications require low mass designs to withstand high environmental loads, causing responses in the nonlinear regime. It has long been possible to compute the response of geometrically nonlinear structures in finite element (FE) software, but the computational cost is orders of magnitude higher than that for linear analysis of the same structure. State-of-the-art FE software combined with high performance computing clusters allow multi-physics simulations with extremely complicated models – millions of degrees of freedom – to be performed in a reasonable amount of time: several hours to several days, depending on the model complexity and physics involved. This capability is extremely powerful, but such analysis times still limit the amount of design insight which can be obtained from a model. For applications requiring hundreds or thousands of analyses, such as optimization studies or Monte Carlo uncertainty quantification, day-long simulation times are not acceptable.

Specific motivating cases include skin panels of hypersonic vehicles [1], which undergo severe thermoacoustic loadings at cruising speeds in excess of Mach 5, as well as the ducted engine assemblies of stealth aircraft, where jet exhaust impinges directly on the structure. More recently, the spaceflight companies Blue Origin and Space Exploration Technologies Corporation have demonstrated the recovery of suborbital and first-stage orbital boosters, respectively. As each company moves forward with plans to land even larger stages, high-amplitude response of thin-walled booster structures may be a subject of increasing interest. Geometric nonlinearity is also significant in the analysis of joined-wing concepts [2] and in the behavior of extremely lightweight space structures such as solar sails [3]. Another application of interest is the "digital twin"

J.D. Schoneman (✉)
ATA Engineering, Huntsville, AL, USA
e-mail: joe.schoneman@ata-e.com

M.S. Allen
Department of Engineering Physics, University of Wisconsin, Madison, WI 53706, USA
e-mail: matt.allen@wisc.edu

R.J. Kuether
Sandia National Laboratories, Albuquerque, NM, USA
e-mail: rjkueth@sandia.gov

concept under examination by the United States Air Force, which proposes the simulation of an entire aircraft over its flight history in near-realtime [4]. Full-order coupled simulation of the thermal, aerodynamic, and nonlinear structural physics of an aircraft is still barely (if at all) feasible, let alone achievable in real-time.

27.1.1 Nonlinear Reduced Order Models

For these and other scenarios in which rapid analysis of a structure is required, reduced order models (ROMs) are a common solution. A subset of basis vectors is used to model the structure's dynamics in a reduced space. When the full order structural model is treated as linear, the system's eigenvectors have unique properties that allow the equations of motion to be decoupled and solved analytically in either the time or frequency domain. This results in a reduction of the model by truncating the number of modes used to superpose the response. In the nonlinear case, numerical integration is the only generally applicable method to obtain a solution for a structure's equations of motion. In this scenario, reducing the order of a model is of even greater interest, as it dramatically reduces the cost of integration. The complication lies in accurately representing the nonlinear behavior of the full-order model in the reduced space, a task which is not straightforward to accomplish in comparison to linear structures. Proper model reduction of nonlinear systems is domain-dependent and closely linked to the type of nonlinearity being modeled. In this work, large-deflection nonlinearities of thin structures are considered; the nonlinearity of interest arises when the bending of a beam or plate couples into membrane stretching along the axis of the structure.

The earliest known presentation of large-deflection nonlinear reduced order modeling (NLROM) techniques is that by Nash [5] in 1977, with other early work in the field put forward by Segalman and Dorhmann [6, 7], McEwan [8], and Muravyov and Rizzi [9]. A review of work in the field was performed by Mignolet et al. [10] in 2013. Nonlinearities are usually represented as a series of quadratic and cubic terms in the modal coordinates, which are often obtained by leveraging the nonlinear analysis capabilities of commercial finite element software. A low-order subset of linear modes is selected for inclusion in the NLROM basis; a series of nonlinear static finite element analyses then characterizes the nonlinear effects of membrane stretching. Forces (deflections) are applied in the shapes of a selected modal basis, and the resulting deflections (forces) from the finite element analysis are used to determine suitable coefficients for nonlinear terms in the NLROM. The technique used for this study is given by Gordon and Hollkamp [1, 11]. In those works, nonlinear model reduction of a single structure was performed, but in this paper, the model reduction techniques are performed on individual components which are later assembled. Models generated using the former, more conventional approach are referred to here as "monolithic NLROMs" and will be used to validate the substructured NLROMs created in Sect. 27.4.3.

27.1.2 Component Mode Synthesis

For complicated structural assemblies, submodels of each component are often created independently and later assembled to form a model of the full assembly. The Craig-Bampton (CB) technique [12], with fixed-interface (FI) modes to model internal deformations and constraint modes to model boundary deformations, is an extremely common method for so-called component mode synthesis (CMS), although many other techniques exist. In the linear case, substructuring approaches are often used to enable the reuse of repeated components in an assembly, to couple numerical finite element models (FEMs) with experimentally-obtained representations of complex components, or to pass structural models between organizations without exposing proprietary design information. While such motivations are important, the key objective in this work is to use nonlinear CMS in order to obtain NLROMs that would be infeasible to construct directly from the assembled model. The computational cost of constructing an NLROM grows cubically with the number of basis vectors retained. Models containing several tens of modes become unwieldy to construct, and models containing as few as a hundred modes require so many static load cases that the NLROM is not competitive with full-order time integration, particularly when validation time and the process of selecting NLROM basis vectors is factored in.

If an assembly can be represented using a collection of lower-order NLROMs, then the computation requirements become quite reasonable. Kuether [13–15] demonstrated the application of nonlinear CMS techniques using several examples, most notably a pair of plates pinned about their edges and joined at a common edge, as shown in Fig. 27.1a. This assembly is a simplification of a more realistic model for an aircraft skin, where thin skin panels are supported by an underlying frame composed of stringers and longerons. In many applications, fixed or pinned boundary conditions may not be sufficiently accurate to model these structures adequately. Unfortunately, several challenges arise when attempting to construct a
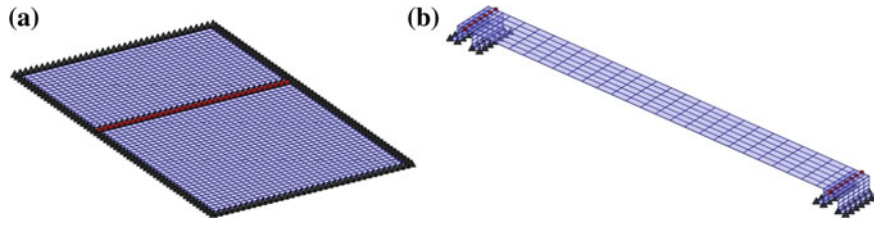
Fig. 27.1 (**a**) Two-panel model examined by Kuether [15]; note that each panel is fully constrained in its unassembled state. (**b**) Assembled beam/stiffener model studied here; the beam component is free-free when unassembled. In both images, *black triangles* denote boundary conditions while *red squares* denote coupling points

component NLROM of a skin panel that is supported by stiffeners: not only does the free-free nature of the panel in its unassembled state cause challenges for obtaining static FE solutions, but the nonlinearity in each component is largely dependent on the stiffness of its supporting structure. To accurately model component nonlinearities, this boundary stiffness must be adequately accounted for.

This paper extends Kuether's work by examining a truncated panel section mounted on two stiffeners, shown in Fig. 27.1b – perhaps the simplest example which will demonstrate the relevant difficulties. The underlying theory for linear and nonlinear component mode synthesis is outlined in Sects. 27.2 and 27.3 before moving on to the case study in Sect. 27.4.

27.2 Linear Component Mode Synthesis

The theoretical development of Craig-Bampton component mode synthesis [12] is quite mature and not presented here. The characteristic constraint (CC) mode concept is a more recent development [16], but is also omitted for brevity; only a description of each component's reduced model is provided. The system of interest consists of n components and a total of N degrees of freedom (DOF). The jth component is represented in full-order form by the undamped equation of motion (27.1)

$$\mathbf{M}^j\ddot{\mathbf{x}}^j + \mathbf{K}^j\mathbf{x}^j = \mathbf{f}^j \tag{27.1}$$

with mass matrix $\mathbf{M}^j$, stiffness matrix $\mathbf{K}^j$, forcing vector $\mathbf{f}^j$, and physical displacement vector $\mathbf{x}^j$ with N^j degrees of freedom. The double-overdot operator refers to the second derivative of each element with respect to time. Damping is omitted from this formulation; however, linear damping terms may easily be included. A variety of methods exist to calculate damping, but the most common rely on estimation or measurement of a damping ratio ζ for each mode. In the substructuring context, the damping ratios of each component may be estimated individually and assembled to obtain a system damping matrix, or the damping may be added using modes of the full assembly. Since the validation metric used here (described in Sect. 27.3.6) operates on the conservative model of the structure, no further consideration is given to damping.

The Craig-Bampton CMS technique reduces the order of equation (27.1) while placing it in a form amenable to substructuring with other components in the system. The system-level use of CC modes further reduces the order of the model by performing a secondary modal reduction on the assembled boundary degrees of freedom of the structure. First, the jth component's displacements are represented in Craig-Bampton form by

$$\begin{Bmatrix} \mathbf{x}_i^j \\ \mathbf{x}_b^j \end{Bmatrix} = \begin{bmatrix} \boldsymbol{\Psi}_{ik}^j & \boldsymbol{\Psi}_{ib}^j \\ \mathbf{0}_{bk}^j & \mathbf{I}_{bb}^j \end{bmatrix} \begin{Bmatrix} \mathbf{q}_k^j \\ \mathbf{x}_b^j \end{Bmatrix} = \mathbf{T}_{CB}^j \begin{Bmatrix} \mathbf{q}_k^j \\ \mathbf{x}_b^j \end{Bmatrix} \tag{27.2}$$

where the internal degrees of freedom $\mathbf{x}_i^j$ are modeled with a combination of k fixed interface modes $\boldsymbol{\Psi}_{ik}^j$ and constraint modes $\boldsymbol{\Psi}_{ib}^j$ with corresponding modal amplitudes $\mathbf{q}_k^j$ and boundary degrees of freedom $\mathbf{x}_b^j$. Once each component model is available, the structure is assembled; however, a large number of boundary DOF will still be present if the components feature large component boundaries. The characteristic constraint modal reduction is used to alleviate this issue. At the assembly level, the Craig-Bampton degrees of freedom are expressed as

$$\begin{Bmatrix} \mathbf{q}_{\hat{k}} \\ \mathbf{q}_{\hat{b}} \end{Bmatrix} = \begin{bmatrix} \mathbf{I}_{\hat{k}\hat{k}} & \mathbf{0}_{\hat{k}C} \\ \mathbf{0}_{C\hat{k}} & \hat{\boldsymbol{\Psi}}_{CC} \end{bmatrix} \begin{Bmatrix} \mathbf{q}_{\hat{k}} \\ \mathbf{q}_{CC} \end{Bmatrix} \tag{27.3}$$

where $\mathbf{q}_{\hat{k}}$ is the collection of FI modal amplitudes, $\mathbf{q}_{\hat{b}}$ is the set of boundary DOF, $\hat{\mathbf{\Psi}}_{CC}$ is the CC modal matrix and $\mathbf{q}_{CC}$ is the CC amplitude vector. To make use of this transformation using nonlinear reduced order models, the global CC modes must be "localized" to each component; the boundary DOF of the jth component are denoted in terms of the CC modal matrix by $\mathbf{x}_b^j = \{\hat{\mathbf{\Psi}}_{CC}\}^j \mathbf{q}_{CC}$. This leads to a component-level model in terms of the FI and CC modes,

$$\begin{Bmatrix} \mathbf{x}_i^j \\ \mathbf{x}_b^j \end{Bmatrix} = \begin{bmatrix} \mathbf{\Psi}_{ik}^j & \mathbf{\Psi}_{ib}^j \{\hat{\mathbf{\Psi}}_{CC}\}^j \\ \mathbf{0}_{bk}^j & \{\hat{\mathbf{\Psi}}_{CC}\}^j \end{bmatrix} \begin{Bmatrix} \mathbf{q}_k^j \\ \mathbf{q}_{CC} \end{Bmatrix} \tag{27.4}$$

This transformation matrix can be used as a basis for generating nonlinear reduced order models, as described below.

27.3 Extension to Geometrically Nonlinear Structures

The substructuring approach is now extended to admit geometrically nonlinear restoring forces. An explanation of the implicit condensation and expansion (ICE) method [1, 11] as implemented in this work is presented. The assembly procedure itself follows, along with a discussion on the use of alternative basis vectors to represent the nonlinear restoring force vector.

27.3.1 Component-Level Nonlinearity

Consider the application of the aforementioned substructuring techniques to structures involving nonlinear forces. Each conservative component equation of motion is now

$$\mathbf{M}^j \ddot{\mathbf{x}}^j + \mathbf{K}^j \mathbf{x}^j + \mathbf{f}_{nl}^j(\mathbf{x}^j) = \mathbf{f}^j \tag{27.5}$$

with $\mathbf{f}_{nl}^j(\mathbf{x}^j)$ a nonlinear restoring force vector associated with the geometric nonlinearity of the system. Given a modal reduction matrix and corresponding set of generalized coordinates $\mathbf{x}^j = \mathbf{\Phi}^j \mathbf{q}^j$, where $\mathbf{\Phi}^j$ is a matrix of FI and component-localized CC modes and $\mathbf{q}^j$ are their modal coordinates, the reduced system becomes

$$\bar{\mathbf{M}}^j \ddot{\mathbf{q}}^j + \bar{\mathbf{K}}^j \mathbf{q}^j + \boldsymbol{\theta}^j(\mathbf{q}^j) = \bar{\mathbf{f}}^j \tag{27.6}$$

The transformed load vector is $\bar{\mathbf{f}}^j = (\mathbf{\Phi}^j)^T \mathbf{f}^j$ and the reduced system matrices are $\bar{\mathbf{M}}^j = (\mathbf{\Phi}^j)^T \mathbf{M}^j (\mathbf{\Phi}^j)$ and $\bar{\mathbf{K}}^j = (\mathbf{\Phi}^j)^T \mathbf{K}^j (\mathbf{\Phi}^j)$. For Craig-Bampton models using characteristic constraint modes, $\mathbf{\Phi}^j$ will contain the component's fixed-interface modes along with the local partition of the system's characteristic constraint modes; in this case the reduced mass matrix will not be diagonal. The component stiffness matrix is not necessarily diagonalized by the local partition of system CC modes, but the block corresponding to the FI modes will at least be diagonal.

The nonlinear force, when transformed to the modal domain, becomes $\boldsymbol{\theta}^j(\mathbf{q}^j) = (\mathbf{\Phi}^j)^T \mathbf{f}_{nl}^j(\mathbf{\Phi}^j \mathbf{q}^j)$. The physical-coordinate form of this force, $\mathbf{f}_{nl}^j$, is never actually considered. Instead, the rth term in the nonlinear modal restoring force vector is known to take the form

$$\theta_r^j(q_1^j, q_2^j, \ldots, q_m^j) = \sum_{i=1}^m \sum_{k=1}^m B_r^j(i, k) q_i^j q_k^j + \sum_{i=1}^m \sum_{k=1}^m \sum_{l=1}^m A_r^j(i, j, k) q_i^j q_k^j q_l^j \tag{27.7}$$

The summation index m indicates the number of basis vectors in $\mathbf{\Phi}^j$. The arrays A_r^j and B_r^j contain quadratic and cubic stiffness coefficients of the nonlinear model; specification of these coefficients provides complete determination of the NLROM. Two key approaches exist to perform this task; the ICE method [17] is used here, although the enforced displacement technique [9] is also popular. Using ICE, a series of static loads are applied to the full order model, each one a linear combination of the basis vectors in $\mathbf{\Phi}^j$. These are pre-multiplied by the stiffness matrix to better isolate individual modes. Hence, the vectors $\mathbf{f}_A$, used to identify cubic stiffness coefficients, and $\mathbf{f}_B$, used to identify quadratic stiffness coefficients, are defined in terms of basis vectors of index r, s, and v as

$$\mathbf{f}_A = \frac{1}{3}\mathbf{K}^j\left[f_r\{\mathbf{\Phi}^j\}_r + f_s\{\mathbf{\Phi}^j\}_s + f_v\{\mathbf{\Phi}^j\}_v\right]$$

$$\mathbf{f}_B = \frac{1}{2}\mathbf{K}^j\left[f_r\{\mathbf{\Phi}^j\}_r + f_s\{\mathbf{\Phi}^j\}_s\right]$$

(27.8)

with a separate load scaling term f_r, f_s, and f_v for each mode in the basis. The indices r, s, and v need not be unique, and the fractional factors are included so that loadings including, for example, three instances of the rth mode, will have an effective scaling factor of f_r rather than $3f_r$. Selection of these load scaling terms is critical for an accurate fit of the nonlinear coefficients, since weak loadings will not sufficiently exercise the structural nonlinearities, but strong loadings will lead to convergence issues in the FEA solution. Kuether et al. [18] showed that an effective rule for selecting force amplitudes is to scale them such that the nonlinear static FE solution deflects 15–20% less (more) than a purely linear static solution due to the hardening (softening) characteristic of the nonlinearity. Loads pushing the linear model of the structure to a one thickness displacement often satisfy this criterion. Thus, the load scaling factors can be defined using the thickness h, a deflection scaling factor α_r, and the set of single-mode loadings. For the rth mode,

$$\mathbf{K}^j\mathbf{x}^j = f_r\mathbf{K}^j\{\mathbf{\Phi}^j\}_r$$

$$\alpha_r h = \max|\mathbf{x}^j| = \max|f_r\{\mathbf{\Phi}^j\}_r|$$

$$f_r = \frac{\alpha_r h}{\max|\{\mathbf{\Phi}^j\}_r|}$$

The resulting nonlinear deflection for each single-mode load case with the load scaling factor f_r can be compared to the value $\alpha_r h$, and α_r adjusted as needed until the linear/nonlinear ratio approaches 0.8 or 1.2.

Once the scaling factors are determined, a full set of load cases is generated and supplied to a nonlinear FEA code. The required number of load cases to specify all of the A_r^j and B_r^j coefficients has a cubic order of growth; the exact count can be determined from

$$2m + \frac{2m!}{(m-2)!} + \frac{4m!}{3(m-3)!} = \frac{2}{3}(2m^3 - 3m^2 + 4m)$$

(27.9)

27.3.2 Nash's Form of Nonlinear Restoring Force

The polynomial expression (27.7) is an explicit description of the nonlinear restoring force on a mode-by-mode basis, but a more compact representation is available due to Nash [5]. By defining the quadratic and cubic nonlinear force vectors as

$$\boldsymbol{\beta}^j(\mathbf{q}^j) \Rightarrow \beta_r^j(\mathbf{q}^j) = \sum_{i=1}^m \sum_{k=1}^m B_r^j(i,k)q_i^j q_k^j$$

$$\boldsymbol{\alpha}^j(\mathbf{q}^j) \Rightarrow \alpha_r^j(\mathbf{q}^j) = \sum_{i=1}^m \sum_{k=1}^m \sum_{l=1}^m A_r^j(i,j,k)q_i^j q_k^j q_l^j$$

and taking the Jacobian of each so that $\mathbf{N}_1^j(\mathbf{q}^j) = \nabla\boldsymbol{\beta}^j(\mathbf{q}^j)$ and $\mathbf{N}_2^j(\mathbf{q}^j) = \nabla\boldsymbol{\alpha}^j(\mathbf{q}^j)$, the component equation of motion can be written

$$\bar{\mathbf{M}}^j\ddot{\mathbf{q}}^j + \left[\bar{\mathbf{K}}^j + \frac{1}{2}\mathbf{N}_1^j(\mathbf{q}^j) + \frac{1}{3}\mathbf{N}_2^j(\mathbf{q}^j)\right]\mathbf{q}^j = \mathbf{0}$$

which is a form amenable to assembly within a substructure of multiple components.

27.3.3 Assembly of Craig-Bampton/Characteristic Constraint Substructures

To proceed with actual assembly of the nonlinear forces, we must apply a procedure which differs somewhat from the linear assembly process. The full assembly equations of motion are

$$\hat{\mathbf{M}}_{CC}\ddot{\hat{\mathbf{q}}}_{CC} + \left[\hat{\mathbf{K}}_{CC} + \frac{1}{2}\hat{\mathbf{N}}_1(\hat{\mathbf{q}}_{CC}) + \frac{1}{3}\hat{\mathbf{N}}_2(\hat{\mathbf{q}}_{CC})\right]\hat{\mathbf{q}}_{CC} = \hat{\mathbf{f}}_{CC} \tag{27.10}$$

in which $\hat{\mathbf{N}}_1(\hat{\mathbf{q}}_{CC})$ are $\hat{\mathbf{N}}_2(\hat{\mathbf{q}}_{CC})$ the assembled nonlinear Jacobian matrices which we seek. Recall that the system degrees of freedom are written in terms of the component FI modal amplitudes $\mathbf{q}_k^j$ and the global CC modal amplitudes $\mathbf{q}_{CC}$,

$$\hat{\mathbf{q}}_{CC} = \begin{Bmatrix} \mathbf{q}_k^1 \\ \mathbf{q}_k^2 \\ \vdots \\ \mathbf{q}_k^n \\ \mathbf{q}_{CC} \end{Bmatrix}$$

Each characteristic constraint mode will enter the displacements of all components in the assembly. An "unassembled" vector of FI/CC coordinates can also be written:

$$\hat{\mathbf{q}}_{CC,u} = \begin{Bmatrix} \mathbf{q}_k^1 \\ \mathbf{q}_{CC} \\ \mathbf{q}_k^2 \\ \mathbf{q}_{CC} \\ \vdots \\ \mathbf{q}_k^n \\ \mathbf{q}_{CC} \end{Bmatrix} = \begin{Bmatrix} \mathbf{q}^1 \\ \mathbf{q}^2 \\ \vdots \\ \mathbf{q}^n \end{Bmatrix}$$

The assembled and unassembled coordinate vectors are related by $\hat{\mathbf{q}}_{CC} = \mathbf{L}_{CC}\hat{\mathbf{q}}_{CC,u}$. $\mathbf{L}_{CC}$ is an assembly matrix operating in the FI/CC domain, and can be constructed easily since all fixed interface modes are independent of each other and all characteristic constraint modes are constrained. This assembly matrix provides a framework for assembling the nonlinear restoring forces of each component. Similar to assembly of the linear system matrices, unassembled Jacobian matrices are block diagonal in terms of the component Jacobians,

$$\hat{\mathbf{N}}_{1,u}(\hat{\mathbf{q}}_{CC,u}) = \begin{bmatrix} \mathbf{N}_1^1(\mathbf{q}^1) & & & \\ & \mathbf{N}_1^2(\mathbf{q}^2) & & \\ & & \ddots & \\ & & & \mathbf{N}_1^n(\mathbf{q}^n) \end{bmatrix} \quad \hat{\mathbf{N}}_{2,u}(\hat{\mathbf{q}}_{CC,u}) = \begin{bmatrix} \mathbf{N}_2^1(\mathbf{q}^1) & & & \\ & \mathbf{N}_2^2(\mathbf{q}^2) & & \\ & & \ddots & \\ & & & \mathbf{N}_2^n(\mathbf{q}^n) \end{bmatrix} \tag{27.11}$$

The assembled Jacobian matrices are written

$$\hat{\mathbf{N}}_1(\hat{\mathbf{q}}_{CC}) = \mathbf{L}_{CC}^T\hat{\mathbf{N}}_{1,u}(\mathbf{L}_{CC}\hat{\mathbf{q}}_{CC,u})\mathbf{L}_{CC}$$
$$\hat{\mathbf{N}}_2(\hat{\mathbf{q}}_{CC}) = \mathbf{L}_{CC}^T\hat{\mathbf{N}}_{2,u}(\mathbf{L}_{CC}\hat{\mathbf{q}}_{CC,u})\mathbf{L}_{CC} \tag{27.12}$$

27.3.4 Basis Vectors of the Nonlinear Restoring Force

Finally, the component transformation matrix $\mathbf{\Phi}^j$ corresponding to the FI/CC mode coordinates $\mathbf{q}^j$ must be specified. A natural choice for the basis transformation is the set of FI and CC vectors, as shown in equation (27.4), so that

$$\mathbf{\Phi}^j = \begin{bmatrix} \mathbf{\Psi}^j_{ik} & \mathbf{\Psi}^j_{ib}\{\hat{\mathbf{\Psi}}_{CC}\}^j \\ \mathbf{0}^j_{bk} & \{\hat{\mathbf{\Psi}}_{CC}\}^j \end{bmatrix} \tag{27.13}$$

With this selection made, the overall process for computing and assembling an NLROM is summarized as follows:

- After the FI/CC substructuring procedure, partition the characteristic mode matrix and supply $\mathbf{\Phi}^j$ to each component.
- Set the load scaling factors f_r so that each single-mode load case, having the shape $\mathbf{K}^j\{\mathbf{\Phi}^j\}_r$, yields a nonlinear static deflection which differs from a linear static prediction by 15–20%. Linear displacements of one thickness provide a good starting point.
- Compute all possible permutations of the load cases from equation (27.8), supply as static loads to a nonlinear FEA program, and curve-fit coefficients of the NLROM according to equation (27.7). Each NLROM is now available at the component level.
- The nonlinear restoring force is assembled at each timestep for simulation. Each component NLROM is supplied with the FI and CC displacements $\mathbf{q}^j$ to compute the component Jacobian matrices; these are then assembled using equation (27.12) and supplied to the equations of motion (27.10) to advance the system state.

Note from the last point that a nonlinear model of the full system is never explicitly created. A full assembly procedure could be accomplished with the aid of symbolic algebra software; however, such an approach is not taken in this work.

27.3.5 Nonlinear Force Definition with Alternative Basis Vectors

A critical aspect of the ICE algorithm is the process used to estimate modal displacements resulting from the nonlinear deflections obtained from FEA software. Suppose the matrix of displacements, obtained from an FE code, is denoted by $\mathbf{Y}$. When the usual approach is used [17] so that the load basis $\mathbf{\Phi}^j$ is orthogonal through the stiffness matrix, so that $(\mathbf{\Phi}^j)^T\mathbf{K}^j\mathbf{\Phi}^j = \mathbf{\Lambda}$ where $\mathbf{\Lambda}$ is a diagonal matrix with nonzero determinant, a left pseudo-inverse of $\mathbf{\Phi}^j$ can be written so that $[\mathbf{\Lambda}^{-1}(\mathbf{\Phi}^j)^T\mathbf{K}^j]\mathbf{\Phi}^j = \mathbf{I}$ and the modal displacements associated with the loading are $\mathbf{q}^j = [\mathbf{\Lambda}^{-1}(\mathbf{\Phi}^j)^T\mathbf{K}^j]\mathbf{Y}$.[1]

Unfortunately, orthogonality cannot be guaranteed for the basis vectors used here, which involve partitions of the system CC modes to individual components. As such, MATLAB's *pinv* routine was used generate a Moore-Penrose pseudo-inverse of $\mathbf{\Phi}^j$ to estimate modal amplitudes from the nonlinear FE results. It may be the case that $\mathbf{\Phi}^j$ is poorly conditioned – the localized CC modes may very closely resemble FI modes of that component, for instance – which causes difficulty in finding an accurate solution for the modal amplitudes. When the modal coefficients for a given set of forces cannot be accurately estimated, the least squares routine used to construct equation (27.7) does not provide accurate estimates of the nonlinear restoring force coefficients, and the resulting NLROM is inaccurate or even unstable.

To circumvent this issue, alternate sets of basis vectors can be used in the static curve fit procedure. These sets should still span the subspace described by the FI and localized CC modes, but display orthogonality with respect to each other for better conditioning and more accurate estimation of the modal response amplitudes. Two decomposition strategies are immediately obvious: the singular value decomposition (SVD) and the QR decomposition. The former method seems attractive due to its natural sorting of basis vectors by singular value. However, it turns out that the singular values tend to be inversely proportional to the natural frequency, so that the SVD prioritizes the relatively unimportant high-frequency deformations over the low-frequency modes that are of interest in creating NLROMs. As such, only the QR decomposition is used to obtain an orthogonal basis of the FI/CC subspace. With this method, the initial matrix $\mathbf{\Phi}^j$ can be written

$$\mathbf{\Phi}^j = \mathbf{Q}^j\mathbf{R}^j = \begin{bmatrix} \mathbf{Q}^j_1 & \mathbf{Q}^j_2 \end{bmatrix} \begin{bmatrix} \mathbf{R}^j_1 \\ \mathbf{0} \end{bmatrix} \tag{27.14}$$

---

[1] If the $\mathbf{\Phi}^j$ is orthogonal through the mass matrix $\mathbf{M}^j$, then $\mathbf{q}^j = (\mathbf{\Phi}^j)^T\mathbf{M}^j\mathbf{Y}$. This is not the case when a Craig-Bampton transformation is used.

so that

$$\mathbf{x}^j = \mathbf{\Phi}^j \mathbf{q}^j = \mathbf{Q}_1^j \mathbf{R}_1^j \mathbf{q}^j$$

where $\mathbf{Q}_1^j$ is orthogonal and $\mathbf{R}_1^j$ is upper triangular. Writing the amplitudes as $\mathbf{\eta}^j = \mathbf{R}_1^j \mathbf{q}^j$, the transformed basis vectors are contained in $\mathbf{Q}_1^j$:

$$\mathbf{x}^j = \mathbf{Q}_1^j \mathbf{\eta}^j$$

Static loads can be applied in the shape of the basis vectors of $\mathbf{Q}_1^j$ and used to evaluate the nonlinear restoring force coefficients in terms of those shapes. No matter whether the nonlinear force is represented using FI/CC coordinates or via the QR decomposition, the full assembly is still integrated using the FI/CC coordinates. At each timestep, each component's nonlinear restoring force is computed by

- Transforming from FI/CC coordinates to decomposition coordinates using $\mathbf{\eta}^j = \mathbf{\Gamma}^j \mathbf{q}^j$ (with $\mathbf{\Gamma}^j$ corresponding to either $\mathbf{\Gamma}_{SVD}^j$ or $\mathbf{\Gamma}_{QR}^j$).
- Using the identified coefficients to compute Jacobian matrices in the decomposed space; $\tilde{\mathbf{N}}_1^j(\mathbf{\eta}^j)$ and $\tilde{\mathbf{N}}_2^j(\mathbf{\eta}^j)$, with overtilde denoting that these matrices do not operate on FI/CC coordinates.
- Transforming the component Jacobian matrices back to FI/CC space as shown in equation (27.15)

$$\mathbf{N}_1^j(\mathbf{q}^j) = (\mathbf{\Gamma}^j)^T \tilde{\mathbf{N}}_1^j(\mathbf{\eta}^j) \mathbf{\Gamma}^j$$
$$\mathbf{N}_2^j(\mathbf{q}^j) = (\mathbf{\Gamma}^j)^T \tilde{\mathbf{N}}_2^j(\mathbf{\eta}^j) \mathbf{\Gamma}^j$$

(27.15)

The linear model of each component remains in the untransformed FI/CC space. Once each component's nonlinear restoring force is evaluated, assembly proceeds as usual via equation (27.12).

27.3.6 Nonlinear Normal Modes for Model Validation

To validate the NLROMs constructed in Sect. 27.4, the nonlinear normal mode (NNM) concept is applied to check for dynamic equivalence of the full-order and reduced models. Two main definitions of the NNM exist. The first, due to Rosenberg [19], defines an NNM as a *vibration in unison* of a system. This can be interpreted as a straightforward generalization of linear normal modes to nonlinear systems; however, it is not rigorously applicable to damped structures. To discuss NNMs in the context of nonconservative systems, Shaw and Pierre define a nonlinear normal mode as an invariant manifold in phase space [20]. Periodic orbits which begin in this manifold remain in it for all time.

The definition used in this work is a slight modification of Rosenberg's, advanced by Kerschen et al. [21] The requirement for vibration in unison is relaxed so that an NNM is a *not-necessarily synchronous periodic motion* of the conservative system. Removing the requirement for synchronous motion admits the possibility of internal resonances – periodic solutions in which modes interact when their frequencies reach integer ratios – as NNMs, and is also useful when pursuing numerical computation of nonlinear modes.

For use with generally applicable algorithms for the numerical continuation of periodic solutions, the nonlinear equations of motion (27.6) are recast into homogeneous state-space form,

$$\dot{\mathbf{z}} = \mathbf{g}(\mathbf{z})$$

(27.16)

where the state vector is $\mathbf{z} = [\mathbf{q}^T \; \dot{\mathbf{q}}^T]^T$ and the state function is

$$\mathbf{g}(\mathbf{z}) = \left\{ \begin{matrix} \dot{\mathbf{q}} \\ -(\bar{\mathbf{M}}^j)^{-1}(\bar{\mathbf{K}}^j \mathbf{q}^j + \mathbf{\theta}^j(\mathbf{q}^j)) \end{matrix} \right\}$$

To emphasize the dependence of the solution on the initial conditions $\mathbf{z}_0$, solutions at a time t are written as $\mathbf{z}(t, \mathbf{z}_0)$. Then, a two-point boundary problem is solved using a periodicity condition,

$$\mathbf{H}(\mathbf{z}_0, T) = \mathbf{z}(T, \mathbf{z}_0) - \mathbf{z}_0$$

(27.17)

H is referred to as a *shooting function* and, when driven to zero for a minimal period T, the resulting state vector $\mathbf{z}_0$ corresponds to the initial condition of an NNM of the system. In this work, numerical computation of NNMs was performed using the *NNMcont* MATLAB package, available from the University of Liège website[2] and described by Peeters et al. [22].

Once an NNM is computed from a particular model, its dynamics are compared to the full-order model using a "periodicity" metric. Given any point along the frequency-energy curve, the initial conditions $\mathbf{z}_0$ and period T can be supplied to an FEM and integrated directly. The resulting output, designated $\mathbf{z}_{FE}$, can then be used to obtain a "periodicity error" condition ϵ, defined as

$$\epsilon = \frac{||\mathbf{z}_0 - \mathbf{z}_{FE}||}{||\mathbf{z}_0||} \tag{27.18}$$

with values on the order of 1% generally taken as acceptable.

27.4 Case Study

The example structure used here, shown in Fig. 27.1b, was conceived to meet several requirements while maintaining a minimum level of complexity:

- Contain at least three components, to expose any effects related to multiple boundary interfaces.
- Use a configuration similar to the panel/stiffener construction used on many aircraft.
- Contain a sufficient number of interface DOF suitable for reduction using CC modes.
- Exhibit strong nonlinear effects in only the "beam" portion of the model.
- Specify no boundary conditions on the "beam" portion in its unassembled state.

This last item turns out to be the most critical, since the geometric nonlinearity of thin beams and panels is intimately related to the boundary conditions of those structures. Further, the ICE method of NLROM generation is not directly applicable to free-free structures. These difficulties are discussed in Sect. 27.4.3. First, an overview of the model and its linear representation is presented.

27.4.1 Structural Model and Linear Substructuring

Two separate assemblies are investigated below. While both have the same general form and use identical structural properties for the beam component, the stiffener thicknesses are modified in each case to obtain slightly different linear dynamic behavior and markedly different nonlinear behavior. The two assemblies are referred to as "soft" and "stiff" in accordance with the different stiffener thicknesses. Structural, material, and mesh properties of the FEM are summarized in Tables 27.1 and 27.2.

Table 27.1 Material and structural properties of the truncated beam/stiffener assembly components

Part	Young's modulus [MPa]	Density [kg/m³]	Thickness [mm]
Panel	71,000	2,700	1.5
Stiffener [soft]			
Stiffener [stiff]			4.0
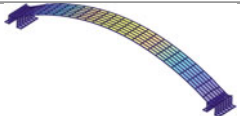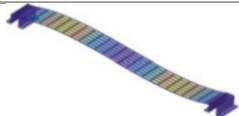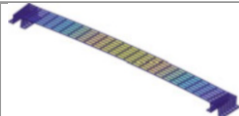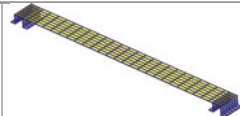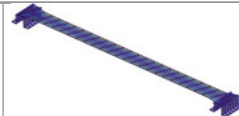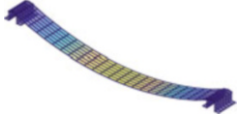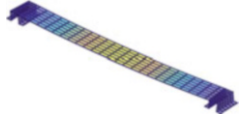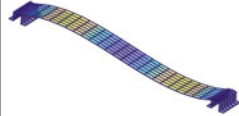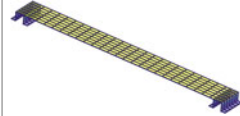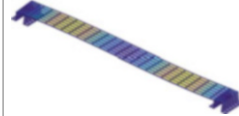
Table 27.2 Mesh properties of the truncated beam/stiffener assembly components

Part	Nodes	S4R elements	DOF
Panel	182	150	1,092
Stiffener [soft]	105	84	630
Stiffener [stiff]			
Assembly	392	318	2,352

[2]URL: http://www.ltas-vis.ulg.ac.be/cmsms/index.php?page=nnm
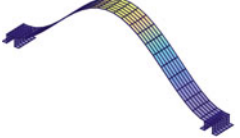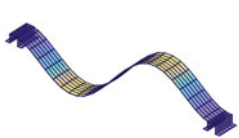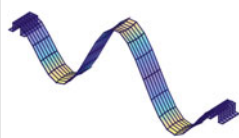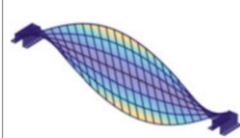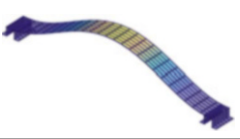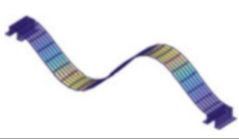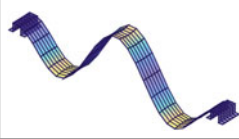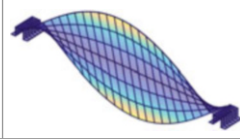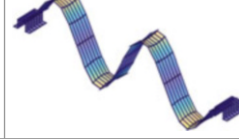
Table 27.3 Characteristic constraint modes of the "soft" (*top*) and "stiff" (*bottom*) assembled models

Soft component (1.5 mm thickness)				
Mode 1: 199.6 Hz	Mode 2: 512.2 Hz	Mode 3: 945.8 Hz	Mode 4: 1.091 kHz	Mode 5: 1.49 kHz
Stiff component (4 mm thickness)				
Mode 1: 730.0 Hz	Mode 2: 1.58 kHz	Mode 3: 1.95 kHz	Mode 4: 3.86 kHz	Mode 5: 4.46 kHz

Table 27.4 Vibration modes of the assembled model, computed with the fixed-interface and characteristic constraint modes shown in Tables 27.5, 27.6, and 27.3

Soft component (1.5 mm thickness)				
Mode 1: 31.9 Hz	Mode 2: 88.5 Hz	Mode 3: 176.0 Hz	Mode 4: 197.2 Hz	Mode 5: 296.0 Hz
Stiff component (4 mm thickness)				
Mode 1: 32.2 Hz	Mode 2: 89.6 Hz	Mode 3: 178.0 Hz	Mode 4: 198.6 Hz	Mode 5: 299.7 Hz

Five fixed interface modes were retained for the beam and each stiffener; these are shown, along with their corresponding frequencies, in "Appendix". Even though the stiffener modes are at very high frequencies and begin to push the spatial limitations of the coarse mesh, including five FI modes in each stiffener is necessary to obtain more than a handful of modes for the full assembly. Five CC modes were retained for each model and are shown in Table 27.3. CC mode 1 of each structure is similar to a pinned bending mode – note that the frequency of "soft" CC mode 1 is roughly one quarter the frequency of the "stiff" counterpart. CC mode 4 in each structure is a vertical displacement of the panel on its supports, with the soft structure also showing a rotational displacement of the panel in CC mode 5. By inspection, the most critical modes for panel nonlinearity are CC mode 1 on both structures, mode 2 on the soft structure, and mode 3 on the stiff structure.

Modes of the assembled system are shown in Table 27.4. Modal assurance criterion (MAC) and frequency error checks are provided in "Appendix" and demonstrate that the first five modes of the assembly are comparable to their counterparts from the full-order model. Frequency errors remain below 0.1% for the first five modes of each structure, after which the substructured models immediately lose all accuracy. This results in a frequency range of validity up to 300 Hz, which is sufficient for the nonlinear model desired. The Craig-Bampton substructuring method reduces each model from 2,352 to 99 total degrees of freedom, 84 of which are boundary DOF. Attempting to specify a beam NLROM with 89 basis vectors (5 FI modes and 84 constraint modes) would require an untenable 776,384 load cases. By introducing the secondary CC mode reduction, the 84 boundary DOF can be represented using only 5 CC modes, for a total of 20 DOF in the assembly. This means that only 10 basis vectors are required for the panel NLROM, resulting in a much more manageable 1,160 load cases for NLROM specification. It turns out that not all of the FI and CC modes need be included in the model to obtain an accurate first NNM, leading to further reductions in the load case requirements.
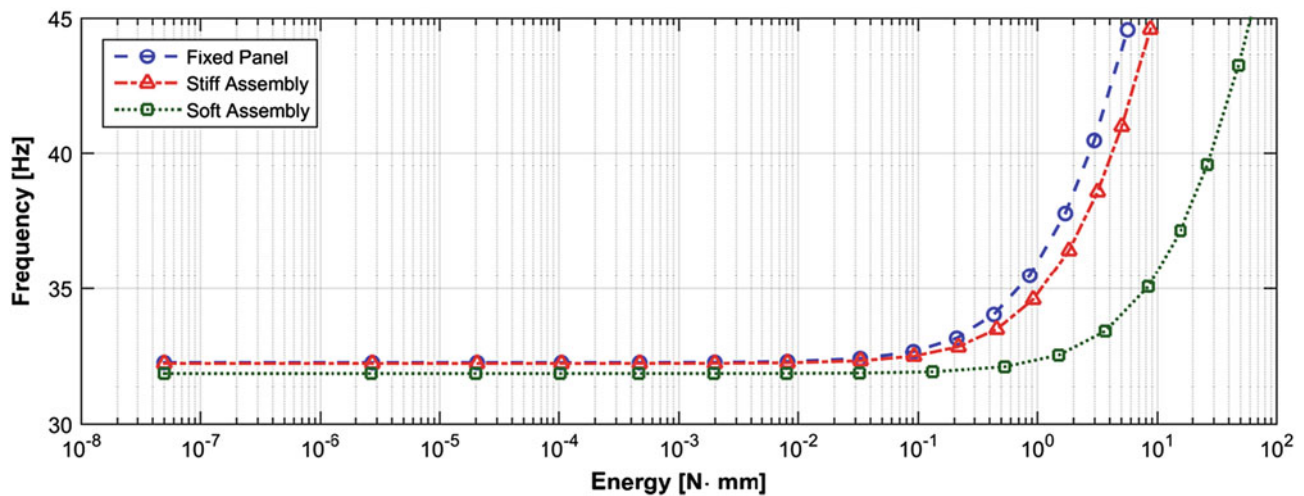
Fig. 27.2   Truth NNMs of the soft and stiff assemblies along with a fully-fixed FEA model of the panel only

27.4.2   Reference Nonlinear Model

Before constructing substructured reduced-order models of the assembly, monolithic NLROMs were formed to serve as truth models of the system's nonlinear dynamics. Reduced order models using mode 1 only, modes 1–3, and modes 1–5 were constructed and used to compute the first nonlinear normal mode of each assembly; the resulting NNM backbones for all three NLROMs lie nearly atop one another, as shown in "Appendix", Figs. 27.9 and 27.10. For reference, an NNM corresponding to a fully-constrained NLROM of the panel only is plotted in Fig. 27.2 along with each assembly's five-mode NLROM, demonstrating that the clamped boundary conditions significantly affect nonlinear behavior of the structure. The stiff model and fully clamped model have nearly identical linear natural frequencies, indicating that the stiff assembly approximates a "built-in" set of boundary conditions. The soft assembly has a somewhat lower linear natural frequency and displays significantly less nonlinear stiffening – the frequency shift effects do not appear until higher energy levels, and the frequency increases more slowly than the other two models. These three NNM curves are used during inspection of the substructured NLROM results below to better understand the behavior of each assembled model.

27.4.3   Nonlinear Substructuring

Nonlinear substructuring is conducted on the assumption that only the panel component need be treated as nonlinear, reducing the number of required load cases to specify each NLROM; this assumption is justified based on the extreme natural frequencies of the stiffeners relative to the panel and assembly modes. Only a subset of the lowest FI and CC modes are used to specify the NLROMs, further reducing the number of load cases required for the model.

The key difficulty associated with this model lies in the panel's lack of boundary conditions in its unassembled state. Immediately this raises an issue with the nonlinear static FEA solutions that must be obtained, since baseline static solvers cannot handle free-free structures. "Inertia relief" (IR) procedures, which allow a static solution by applying forces to eliminate rigid body motion of the structure [23], can overcome this limitation. Unfortunately, the use of IR with the ICE method is not yet well understood. Further, there is a more critical problem to be overcome: physically, nonlinearity of the panel will be dominated by its interaction with the supports, a fact that would not be addressed by using an IR solution procedure. The panel's FI modes correspond to an unphysical infinite stiffness at the boundaries, while the CC modes are associated with the stiffness of the assembly, statically reduced to the set of boundary nodes. A single, consistent set of boundary conditions must be selected for use in the nonlinear, static FEA routine. Using fully-fixed boundary conditions on FI mode load cases and statically reduced boundary conditions on CC modes is not straightforward, since the modal displacements are inherently coupled and their stiffness coefficients must be estimated in concert with each other.
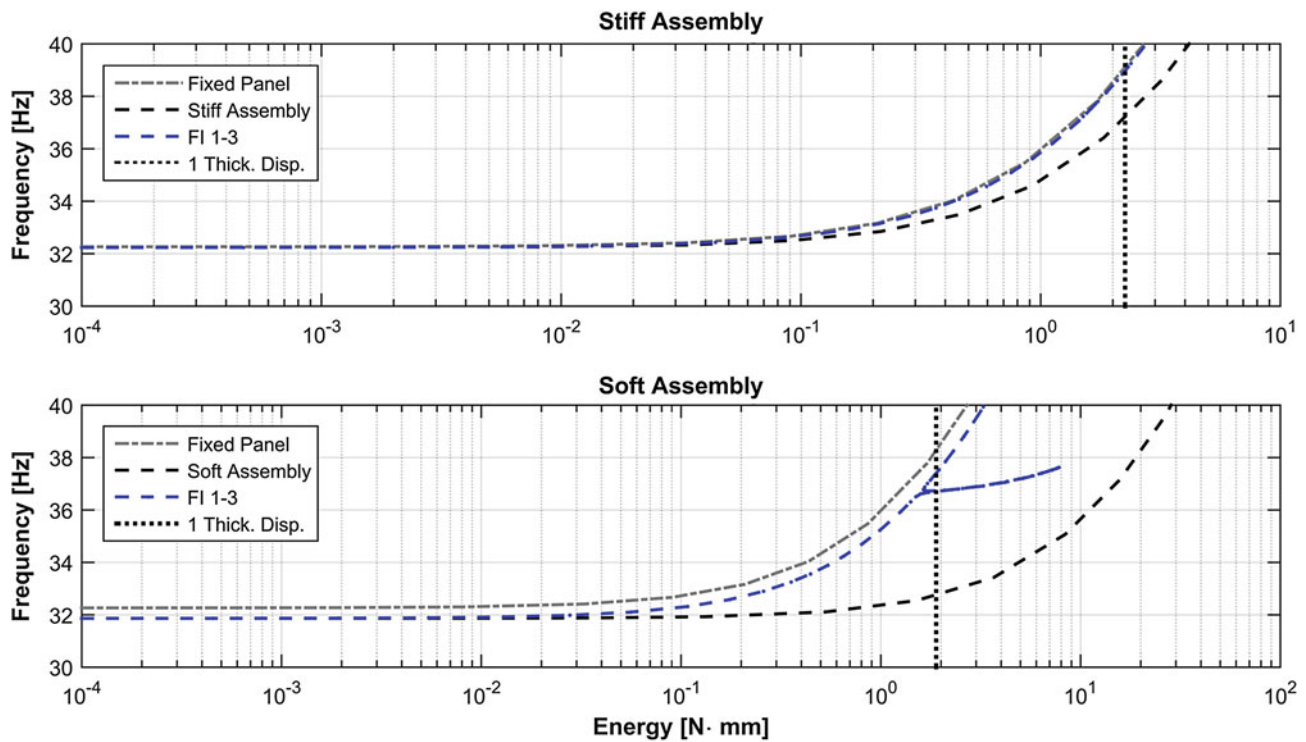
Fig. 27.3 NNMs computed from substructured NLROMs using only fixed interface modes as a basis for the nonlinear forces and fully-fixed boundary conditions for the ICE load cases

27.4.4 Fixed Interface/Characteristic Constraint Mode Basis

With these considerations in mind, it is clear that some combination of alternate procedures must be devised to properly handle the panel in this example. Using the natural basis of FI/CC modes, three possible solutions, listed below, were examined. Once NLROMs were computed using each method, NNMs emanating from the first linear normal mode of each assembly were obtained and compared with the reference modes of Fig. 27.2 to assess the accuracy of the nonlinear models.

- To illustrate the issues caused by inaccurate boundary conditions, an NLROM was constructed using only the fixed-interface modes with fully constrained boundary conditions. The first three panel FI modes were used to construct each NLROM; NNMs resulting from this technique are shown in Fig. 27.3.
- NLROMs were constructed using both FI and CC modes with an approximation of the linear assembly stiffness applied to the boundaries of the panel. This approximation was achieved by statically reducing the assembly stiffness to each boundary DOF on the panel and applying the resulting stiffness values as a set of grounded springs at each degree of freedom. Along with the first three panel FI modes, the first assembly CC mode was included for a pair of NLROMs. The resulting NNMs are shown in Fig. 27.4.
- Finally, loads were applied to the panel within a full FEM of the assembly. This is referred to as an in situ technique and is described in further detail below. The resulting NNMs are shown in Fig. 27.5. Again, these NLROMs used a combination of the first three panel FI modes and the first CC mode as a basis set.

27.4.4.1 Fully Fixed Boundary Conditions

Nonlinear normal modes from the fully fixed case (Fig. 27.3) show NNM backbones tracking closely with the panel-only backbones, indicating that the nonlinear stiffnesses are not determined appropriately when the panel boundaries are fully fixed. Since the linear substructuring is still accurate, the NNM backbone of the soft assembly maintains the correct linear natural frequency at low amplitudes, but ends up tracking the fixed panel's frequency behavior at higher energies. These results are exactly what should be expected from the ICE method, since in neither case is the panel's nonlinear stiffness
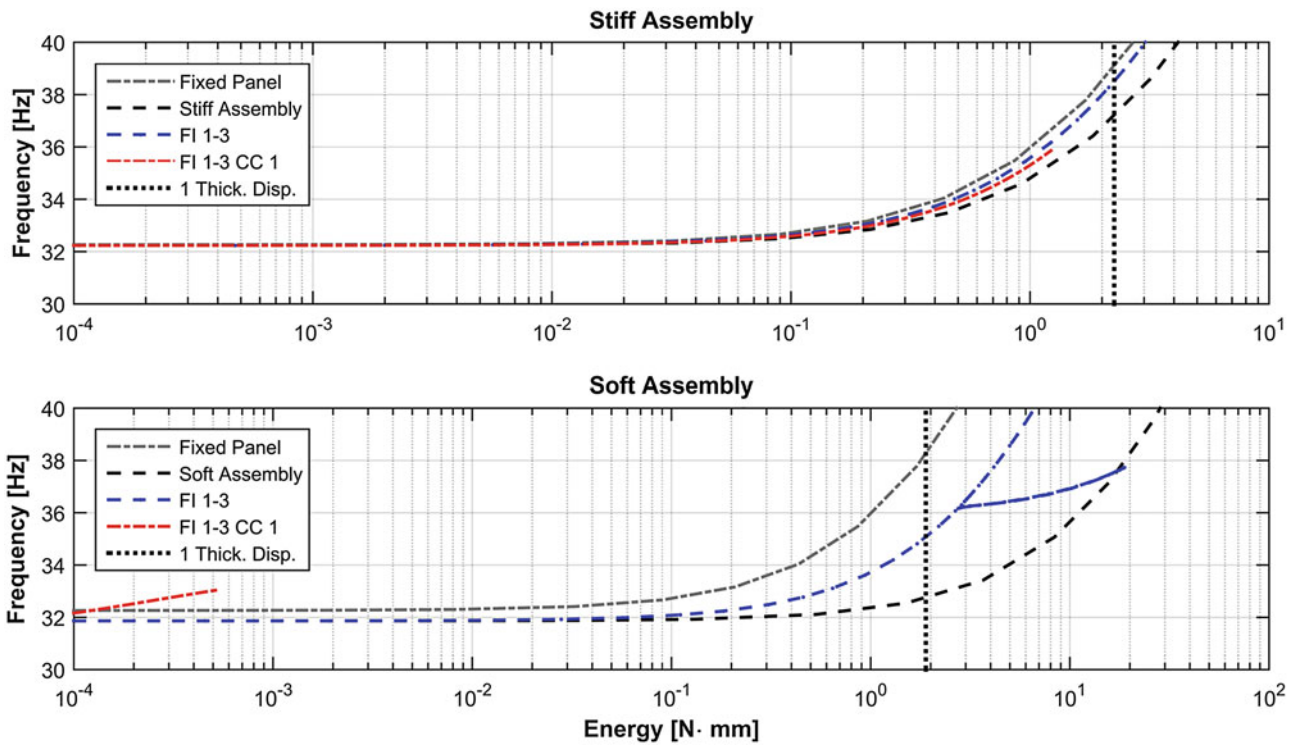
Fig. 27.4 NNMs computed from substructured NLROMs using FI and CC modes as a basis for the nonlinear forces, with grounded springs applied at the boundaries according to linear, static reduction. In both cases, including CC mode 1 led to a poor nonlinear fit and spurious/non-convergent NNM backbones
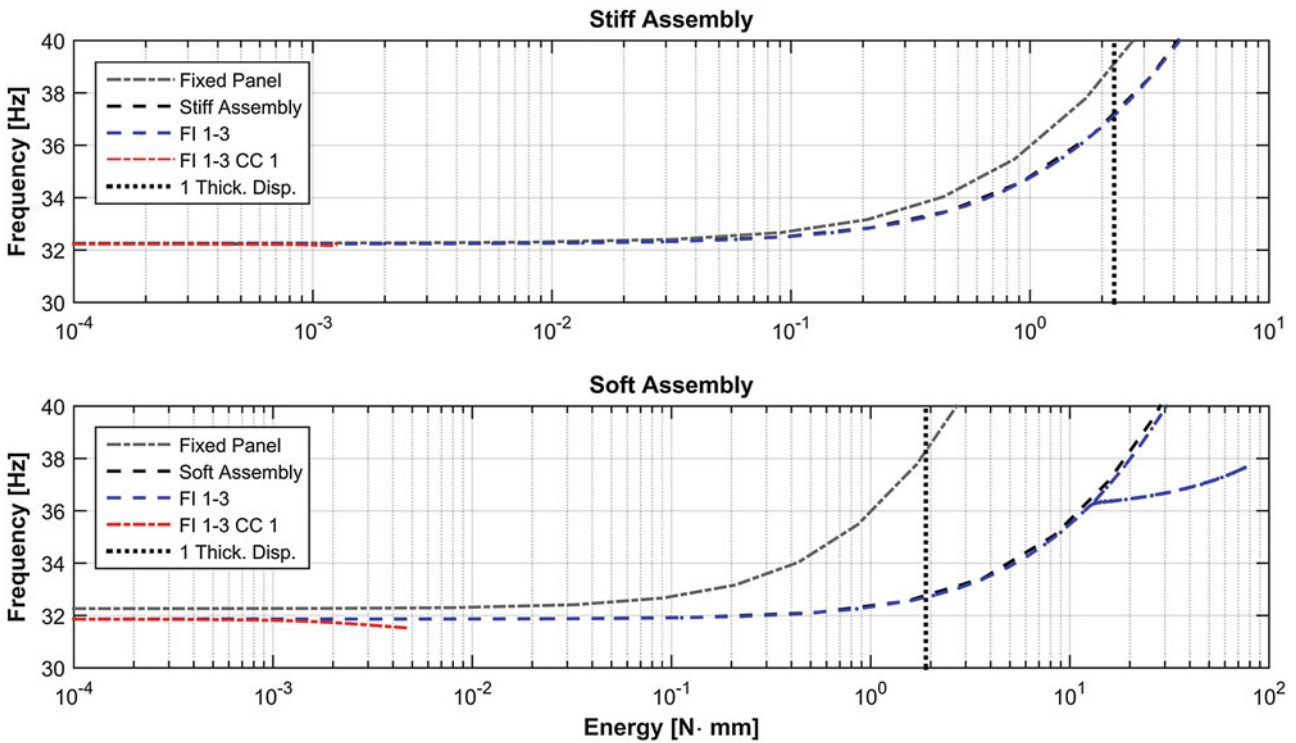
Fig. 27.5 NNMs computed from substructured NLROMs using FI and CC modes as a basis for the nonlinear forces and the in situ finite element technique to provide accurate boundary stiffness. In both cases, including CC mode 1 led to a poor nonlinear fit and spurious/non-convergent NNM backbone

affected by the underlying stiffness of its boundaries – the FI modes of the panel are identical in both assemblies. Including characteristic CC in the force basis would at least provide some measure of differentiation between the two models; as discussed earlier, however, the CC modes cannot be included if the boundary nodes are fixed, and it is not possible to apply load combinations with FI and CC force vectors if disparate boundary conditions are used on the two subsets of modes. The fixed set of boundary conditions cannot be used to compute component NLROMs for this model.

27.4.4.2 Linear, Statically Reduced Boundary Conditions

For this case (Fig. 27.4), NNMs associated with the FI-only models show slight softening relative to the fully fixed panel but are still quite far from the desired truth backbones. Additionally, the NNMs computed from the combined FI/CC basis set do not converge well, with both models failing well before reaching a displacement level of one thickness. Addressing the first issue, the linear approximation to the boundary conditions is clearly insufficiently accurate to produce valid NLROMs using implicit condensation. This is surprising, given that the stiffeners do not undergo large deformations compared to the deformations of the panel, but there is little to be done. Note that the linear approximation includes a static reduction to each individual degree of freedom at the boundary; it remains an open question whether retaining coupling between boundary DOF will lead to an accurate NLROM. This procedure was not attempted due to the difficulty involved in specifying arbitrary stiffness matrices at the boundaries of the FEM. It may also be the case that the boundary stiffness experienced by each node, rather than stiffness coupling between nodes, dominates membrane stretching in the panel. In this case it is the linear boundary approximation itself, rather than the static reduction, that is at fault for the poor models.

27.4.4.3 In Situ Boundary Conditions

The results above show that a linear approximation to the component boundary conditions is not sufficiently accurate for use with the implicit condensation method. Rather than attempting to formulate more esoteric representations for the boundary stiffness, it is convenient to simply refer to the most accurate possible representation: A full-order FEM of the assembly, which provides a limiting case for the utility of nonlinear substructuring given the most accurate possible component boundaries. The procedure is straightforward: ICE load cases are applied to the subset of DOF corresponding to the component of interest in the FEM, while the remaining DOF are left unloaded. The resulting displacements of that DOF subset are extracted and used in the NLROM construction procedure as per usual, and coefficients of the NLROM are specified in the usual manner. Since it takes place within the full-order model of the assembly, this approach is referred to as the in situ substructuring method. The procedure may initially seem indistinguishable from the construction of a monolithic NLROM of the assembly; it is critical to realize that the loads in this instance are being applied only to single components, as opposed to the monolithic approach which uses modes of the entire assembly. Practically speaking, this still dramatically reduces the number of load cases required to specify an NLROM, as discussed in Sect. 27.5.

Sets of modes identical to those from Fig. 27.4 were used with the in situ procedure and backbones of the first NNM were again generated, with the resulting curves shown in Fig. 27.5. As one would hope, the NNM backbones of the substructured models finally lie close to those of their respective assemblies. The stiff structure shows nearly perfect agreement, although a slight discrepancy and unexpected internal resonance are visible in the NNM backbone of the soft structure. Again, however, models including the first CC mode do not converge to appreciable energy levels.

27.4.5 QR-Transformed Basis Vectors

The non-convergence of NLROMs including CC modes is a result of the similarity between the structure's first characteristic constraint mode and the beam's first fixed interface mode. The former, with some rotation allowed at the beam interface, resembles a pinned beam mode; the latter is a fully clamped beam mode. Forces applied to the full-order FEM in these mode shapes result in displacements which are difficult to distinguish from each other. As a result, the data matrix used to specify NLROM coefficients is poorly conditioned, and an inaccurate NLROM results.

The QR-transformed basis alleviates this issue by providing an orthogonal set of vectors to use for load case specification. While the FI modes are largely unaffected by the QR decomposition, each CC mode is altered by removing any components that are parallel to any of the fixed interface modes. As a result, the FEM displacements can be reliably distinguished from each other, and deformations at the component interface can be included in the basis.
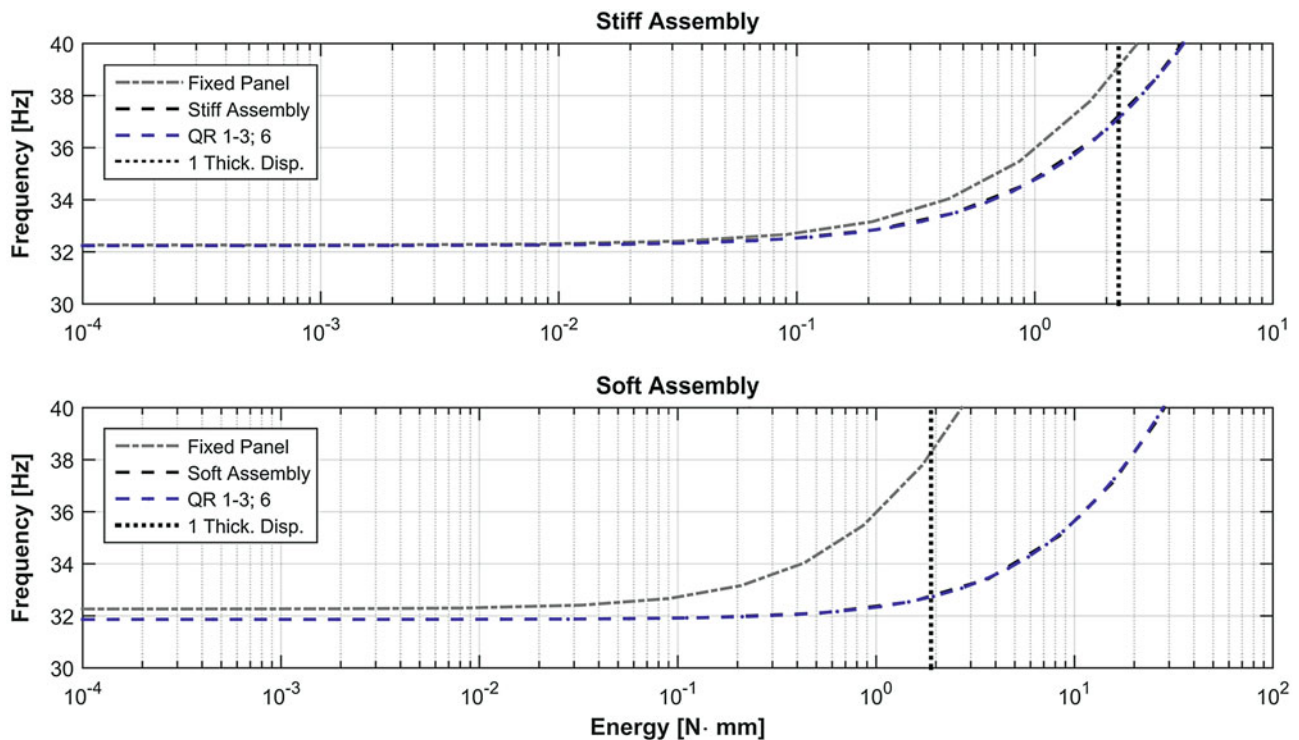
Fig. 27.6 NNMs computed from substructured NLROMs using vectors from a QR factorization of the FI and CC modeset. Including QR mode 6, corresponding to the component of CC mode 1 which was orthogonal to the FI modes, led to a more accurate NNM for the soft system

The NLROMs computed from the QR basis not only converge to suitable energy levels but are more accurate than their counterparts computed with the FI modes only. The resulting backbones of NNM 1 from the QR basis NLROMs are shown in Fig. 27.6. The models shown here use QR modes 1, 2, 3, and 6; these correspond to FI modes 1, 2, and 3, along with the remnant of CC mode 1, which was orthogonal to FI mode 1. The backbone of the stiff structure was already indistinguishable from that of its corresponding assembly NLROM, but the soft assembly backbone has now shifted directly onto the truth curve. Though the difference is slight, the shift is still significant: in a more sophisticated model, omission of constraint deformations could alter the nonlinear dynamics to a much greater extent. For this assembly, only the alternate QR basis was suitable for constructing an NLROM using the implicit condensation procedure.

27.5   Discussion and Future Prospects

The panel/stiffener model examined here demonstrated two main challenges that are not encountered in assemblies with fixed-boundary nonlinear components. First, since the key panel component was not constrained in the unassembled state, loads could not be arbitrarily applied to the panel without somehow modifying the boundary conditions. Attempts to model the structure's boundary conditions using linear, statically reduced stiffnesses – grounding springs at each DOF – yielded inaccurate nonlinear models. An important future step is to investigate a fully coupled boundary stiffness at the interface, rather than the single DOF static reduction procedure that was used here. Moving beyond the linear, statically reduced approximation, an in situ technique which simply used a full-order FEM of the assembly to describe the component boundary's static behavior during the implicit condensation procedure proved successful.

A second difficulty arose in attempting to include both fixed interface and characteristic constraint modes in the NLROM force basis. The deformations spanned by the first three FI modes and first CC mode were required for an accurate NLROM; however, all models using these four basis vectors led to poor curve fits, due to the similarities between FI and CC mode 1. It is critical to note that, even though the FI and CC modes are nearly orthogonal to each other through the component stiffness matrix, the resulting deformations from a nonlinear static solution are not necessarily well differentiated. As a result, mixing the FI and CC modes led to higher displacement residuals and poor nonlinear coefficient fits.

The alternate basis examined in Sect. 27.4.5 was the key to circumventing this issue. Performing a QR factorization of the FI/CC modeset of interest allowed nonlinear force basis resulting in a good coefficient fit to be obtained. Since it allowed inclusion of displacements associated with boundary motion, this basis provided a more accurate NLROM for the assembly on soft supports (the stiff-support version was not noticeably affected). It may be the case that, for panels mounted on stiffeners, force vectors obtained from low-frequency FI and CC modes yield similar displacements. If so, use of an alternate basis such as that obtained from a QR factorization will be critical to obtaining accurate NLROMs of these assemblies.

A remaining question to be addressed is whether a more modular procedure can be devised to take the place of the in situ construction process. Component modularity is a key benefit of linear substructuring techniques, allowing manufacturers to share models without exposing proprietary technical parameters. The heavily coupled nature of nonlinear structures, however, makes it unlikely that full component modularity can be achieved with nonlinear CMS. A more pressing reason for the desire for modularity is based not simply on convenience, but on accuracy of the resulting NLROMs. The case study in this paper contained only a single component exhibiting nonlinearity. When multiple nonlinear components are present in close proximity to each other, loads applied to one component will induce displacements in neighboring parts; it is possible and indeed likely that these displacements will contaminate the nonlinear coefficients obtained for the component of interest. For this reason, the in situ procedure with implicit condensation and expansion used here is not yet fully mature or generally applicable to arbitrary assemblies.

The question of efficiency also bears discussion, although it is of less immediate concern. While resorting to a full-order FEM in order to obtain a component NLROM is by no means desirable, it is not a disqualifying requirement. The key benefit of a substructuring approach in specifying NLROMs is the reduction in load cases required to construct a model. Due to the cubic order of growth of these load cases, complicated, built-up geometries which require tens of modes to model quickly become prohibitive. Figure 27.7 illustrates this principle.

Consider a model which requires 30 modes in the nonlinear basis. A total of 34,280 load cases are required to specify this NLROM. Were the model split into nine nonlinear components, a slightly reduced number of load cases (29,736) would be necessary if each component required 14 modes. Should each component's nonlinear basis be reduced to 10 modes, 10,440 load cases would be needed; at 5 modes, the count drops to 1,160. Even if each of these load cases were run on the full-order FEM, a dramatic savings in construction time would be achieved.
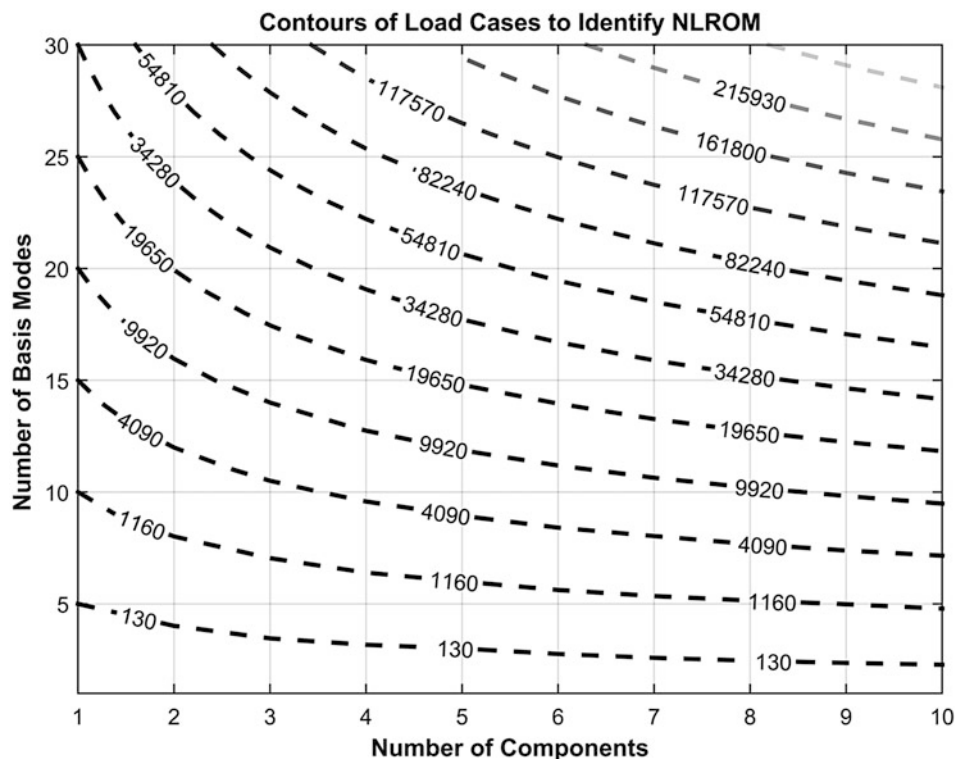
Fig. 27.7 Contours of required load cases to specify an ICE NLROM as a function of component count and number of basis modes per component. Contours correspond to single-component models at multiples of five basis modes

This work has demonstrated the feasibility of applying CMS methods to panel/stiffener assemblies, along with the challenges associated with such a relatively simple extension of prior work. An in situ method involving the full-order assembly finite element model was proposed and demonstrated along with the use of alternate basis vectors to specify nonlinear restoring forces. The collection of techniques was sufficient to model an assembly with a single nonlinear component, but further examination along these lines must be conducted before the methods can be generalized to complex models at an industrial scale.

Appendix

Various details related to the linear models of the substructure components are given below. Retained fixed interface modes of the panel are given in Table 27.5.

Retained fixed interface modes of the hat stiffeners for soft and stiff assemblies are shown in Table 27.6.
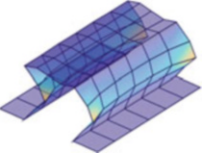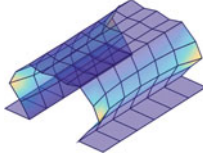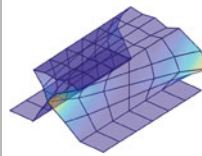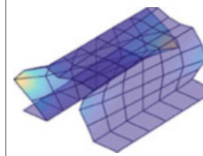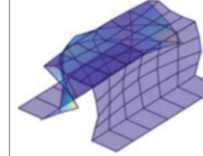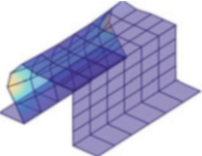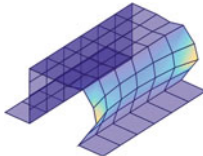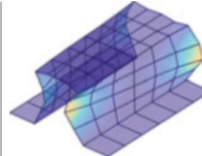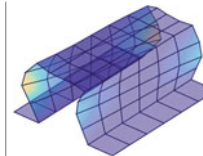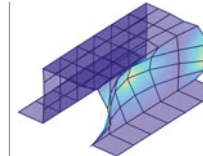
A modal assurance criterion (MAC) check, along with corresponding frequency errors, between the substructured model and its full-order FEA counterpart is given in Fig. 27.8.

Nonlinear normal modes generated using various NLROMs of each assembly, along with the resultant periodicity errors from each model, are shown in Figs. 27.9 and 27.10 for the stiff and soft assemblies, respectively.

Table 27.5 Retained fixed interface modes of the panel

| Mode 1: 32.3 Hz | Mode 2: 89.7 Hz | Mode 3: 178.2 Hz | Mode 4: 198.6 Hz | Mode 5: 300.0 Hz |

Table 27.6 Retained fixed interface modes of the "soft" (top) and "stiff" (bottom) stiffeners

Soft component (1.5 mm thickness)

| Mode 1: 20.2 kHz | Mode 2: 20.2 kHz | Mode 3: 20.4 kHz | Mode 4: 20.4 kHz | Mode 5: 21.9 kHz |

Stiff component (4 mm thickness)

| Mode 1: 40.6 kHz | Mode 2: 40.6 kHz | Mode 3: 40.8 kHz | Mode 4: 40.8 kHz | Mode 5: 43.8 kHz |
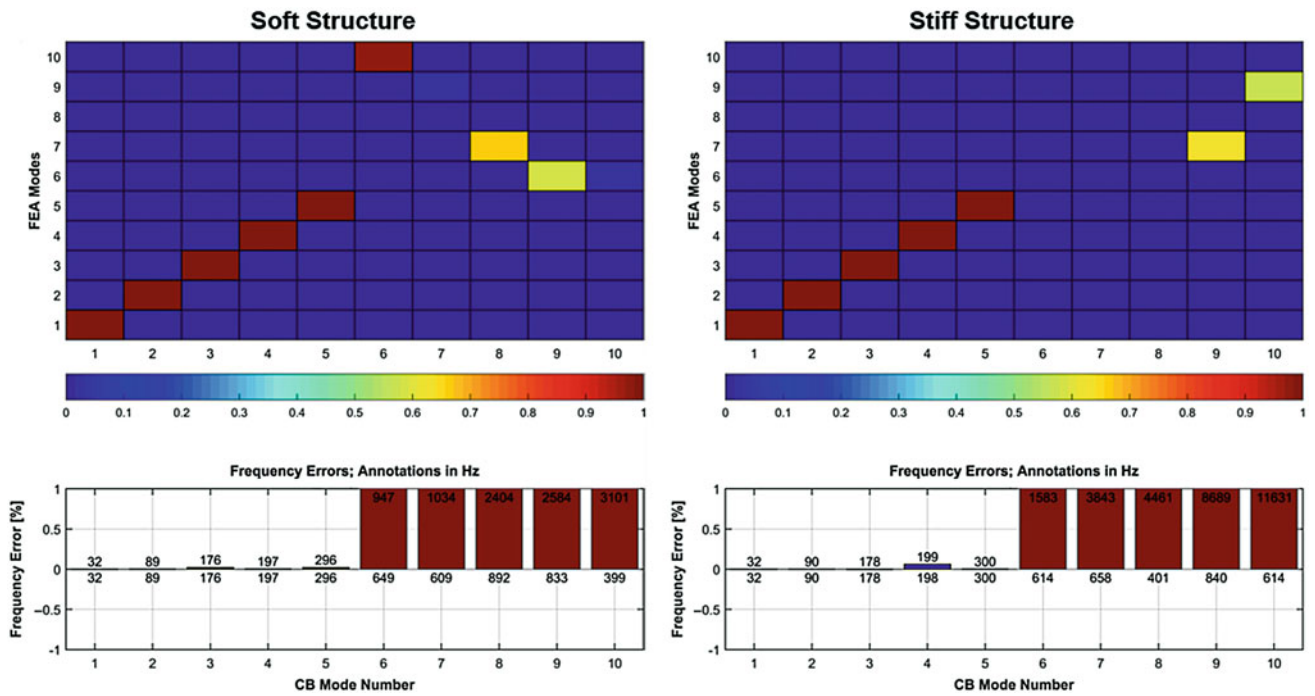
Fig. 27.8 (*Top*): Cross-MAC between full-order FEA truth modes and substructure modes. (*Bottom*): Frequency errors between truth and substructure modes, based on matching MAC value; frequency values along the horizontal axis are full-order values while those adjacent to error bars are the substructured values
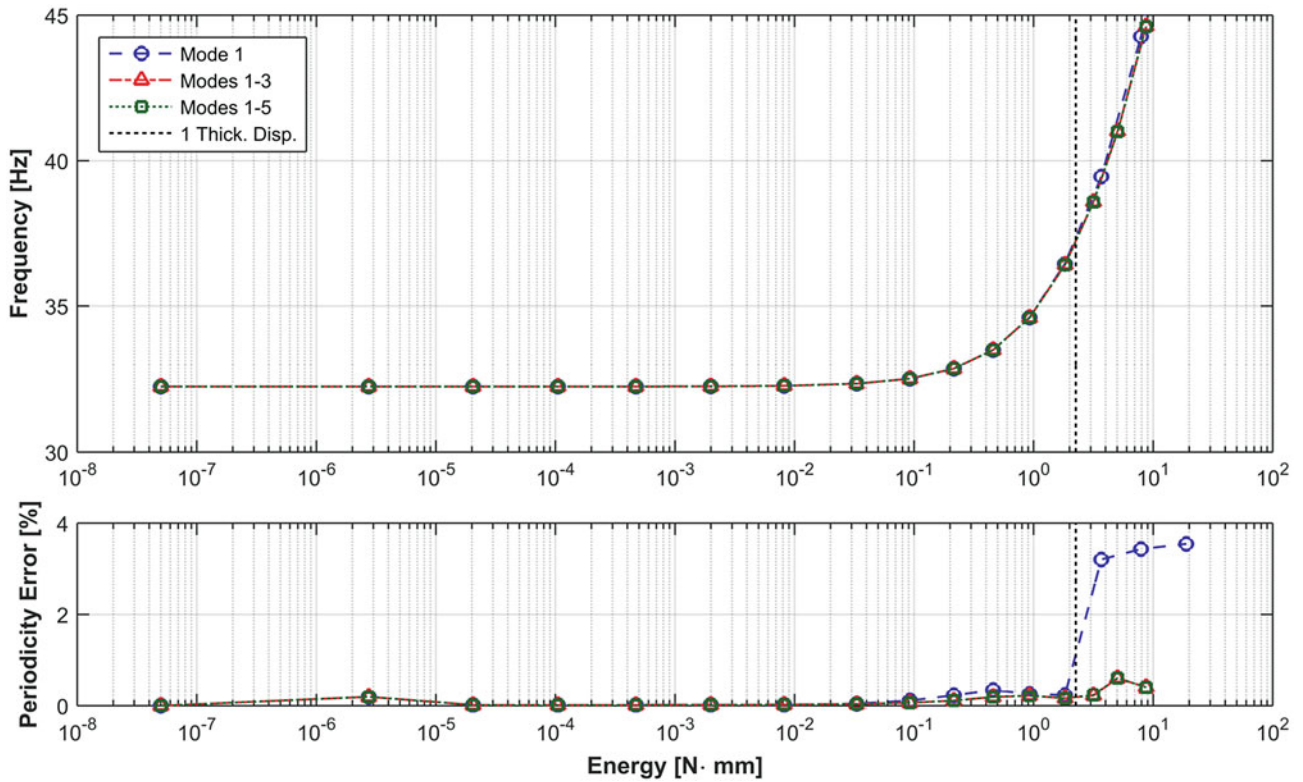
Fig. 27.9 (*Top*) NNMs computed using one, three, and five-mode ROMs of a fully assembled FEA model with "stiff" supports. (*Bottom*) Periodicity errors associated with each computed backbone curve
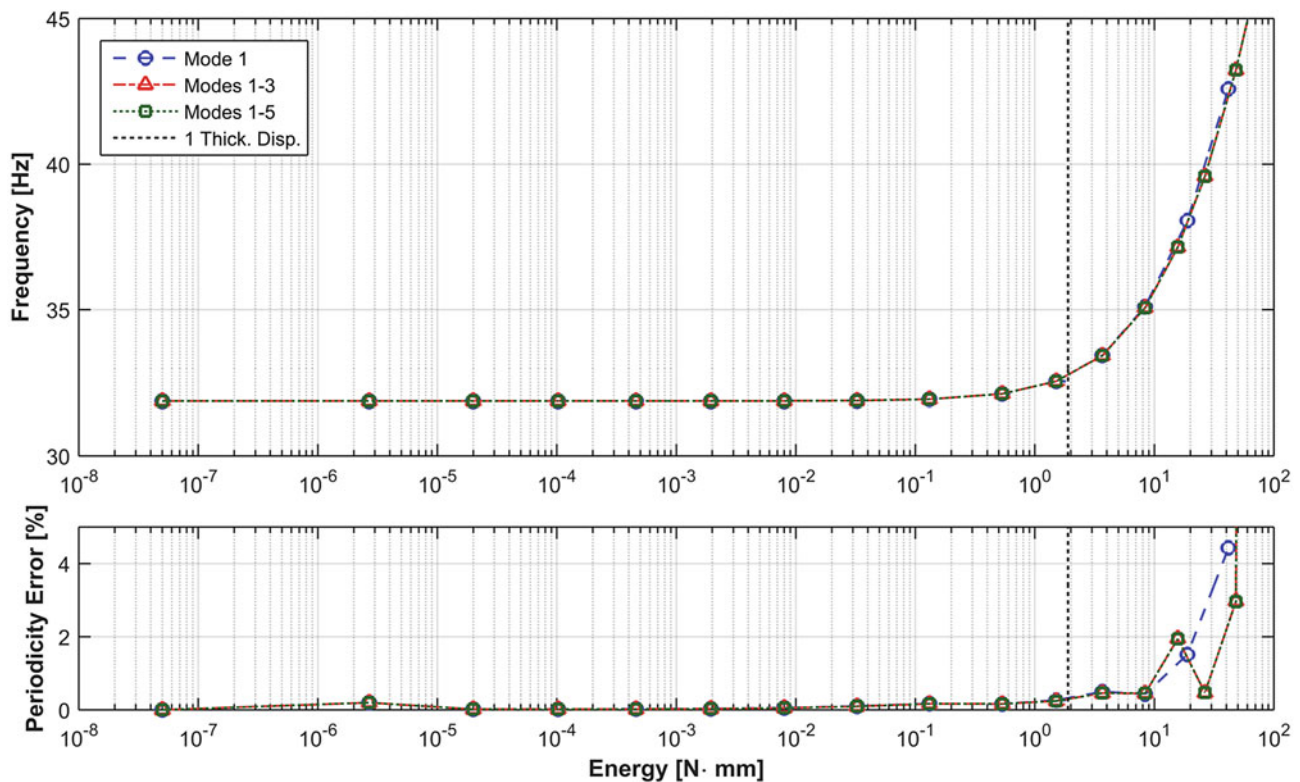
Fig. 27.10 (*Top*) NNMs computed using one, three, and five-mode ROMs of a fully assembled FEA model with "soft" supports. (*Bottom*) Periodicity errors associated with each computed backbone curve

References

1. Gordon, R.W., Hollkamp, J.J.: Reduced-order models for acoustic response prediction. Technical report. AFRL-RBWP-TR-2011-3040, Air Force Research Laboratory (2011)
2. Teunisse, N., Tiso, P., Demasi, L., Cavallaro, R.: Computational reduced order methods for structurally nonlinear joined wings. In: 56th AIAA/ASCE/AHS/ASC Structures, Structural Dynamics, and Materials Conference, Kissimmee, Jan 2015
3. Wang, J., Tzikang, C., Sleight, D.W., Tessler, A.: Simulating nonlinear deformations of solar sail membranes using explicit time integration. In: 45th AIAA/ASCE/AHS/ASC Structures, Structural Dynamics, and Materials Conference, Palm Springs, Mar 2004
4. Tuegel, E.J., Ingraffea, A.R., Eason, T.G., Spottswood, M.S.: Reengineering aircraft structural life prediction using a digital twin. Int. J. Aerosp. Eng. **2011**, 1–14 (2011)
5. Nash, M.: Nonlinear structural dynamics by finite element modal synthesis. Ph.D. thesis, Department of Aeronautics, Imperial College (1977)
6. Segalman, D.J., Dohrmann, C.R.: Method for calculating the dynamics of rotating flexible structures, Part 1: derivation. J. Vib. Acoust. Trans. ASME **118**, 313–317 (1996)
7. Segalman, D.J., Dohrmann, C.R.: Method for calculating the dynamics of rotating flexible structures, Part 2: example calculations. J. Vib. Acoust. Trans. ASME **118**, 318–322 (1996)
8. McEwan, M.I., Wright, J., Cooper, J.E., Leung, A.Y.T.: A combined modal/finite element analysis technique for the dynamic response of a non-linear beam to harmonic excitation. J. Sound Vib. **243**, 601–624 (2001)
9. Muravyov, A.A., Rizzi, S.A.: Determination of nonlinear stiffness with application to random vibration of geometrically nonlinear structures. Comput. Struct. **81**, 1513–1523 (2003)
10. Mignolet, M.P., Przekop, A., Rizzi, S.A., Spottswood, S.M.: A review of indirect/non-intrusive reduced order modeling of nonlinear geometric structures. J. Sound Vib. **332**, 2437–2460 (2013)
11. Hollkamp, J.J., Gordon, R.W., Spottswood, S.M.: Nonlinear modal models for sonic fatigue response prediction: a comparison of methods. J. Sound Vib. **284**, 1145–1163 (2005)
12. Bampton, M.C., Craig, R.R., Jr.: Coupling of substructures for dynamic analyses. AIAA J. **6**(7), 1313–1319 (1968)
13. Kuether, R.J., Allen, M.S.: Substructuring with nonlinear reduced order models and interface reduction with characteristic constraint modes. In: 55th AIAA/ASME/ASCE/AHS/ASC Structures, Structural Dynamics, and Materials Conference, National Harbor (2014)
14. Kuether, R.J.: Nonlinear modal substructuring of geometrically nonlinear finite element models. Ph.D. thesis, University of Wisconsin – Madison (2014)
15. Kuether, R.J., Allen, M.S., Hollkamp, J.J.: Modal substructuring of geometrically nonlinear finite-element models. AIAA J. **54**(2), 691–702 (2015)
16. Castanier, M.P., Tan, Y.-C., Pierre, C.: Characteristic constraint modes for component mode synthesis. AIAA J. **39**(6), 1182–1187 (2001)

17. Hollkamp, J.J., Gordon, R.W.: Reduced-order models for nonlinear response prediction: implicit condensation and expansion. J. Sound Vib. **318**, 1139–1153 (2008)
18. Allen, M.S., Kuether, R.J., Deaner, B., Sracic, M.W.: A numerical continuation method to compute nonlinear normal modes using modal reduction. In: 53rd AIAA/ASCE/AHS/ASC Structures, Structural Dynamics, and Materials Conference, Honolulu (2012)
19. Rosenberg, R.M.: Normal modes of nonlinear dual-mode systems. J. Appl. Mech. 27(2), 263–268 (1960)
20. Shaw, S., Pierre, C.: Normal modes for non-linear vibratory systems. J. Sound Vib. **164**(1), 85–124 (1993)
21. Kerschen, G., Peeters, M., Golinval, J., Vakakis, A.F.: Nonlinear normal modes, part I: a useful framework for the structural dynamicist. Mech. Syst. Signal Process. **23**(1), 170–194 (2009)
22. Peeters, M., Viguié, R., Sérandour, G., Kerschen, G., Golinval, J.-C.: Nonlinear normal modes, Part II: toward a practical computation using numerical continuation techniques. Mech. Syst. Signal Process. **23**(1), 195–216 (2009)
23. Abaqus Theory Manual. Abaqus version 2012. Dassault Systemes/Simulia, Johnston (2012)

Chapter 28
Experimental Evaluation of Multi-functional Nonlinear Floor Isolation Systems

P. Scott Harvey, Nisal Halaba Arachchige Senarathna, and Corey D. Casey

Abstract Acceleration-sensitive equipment housed inside of buildings is susceptible to damage from strong floor motions of the primary structure produced by earthquakes. Floor isolation systems (FISs) represent an effective strategy to protect such equipment from these motions by decoupling the equipment from the primary structure. However, even the most effective isolation systems are incapable of protecting equipment from building collapse in the event of strong ground shaking. This study experimentally explores the use of a novel multi-functional FIS capable of mitigating both equipment accelerations and facility drifts by passively adapting to achieve desired building-system performance. For low intensity disturbances, the system functions like a traditional isolation system, but for high intensity events, impacts in the isolation system act to increase the coupling between the primary structure and the FIS, pumping energy like a vibro-impact absorber. A scale experimental model, consisting of a three-story frame and an isolated mass, is used to demonstrate and evaluate the design methodology via shake table tests. The dynamic properties of the experimental model are identified, and the isolator's displacement capacity and the disturbance frequency and amplitude provide the parametric variation. The performance of the multi-functional FIS was established and is described in this study.

Keywords Seismic isolation • Vibration isolation • Vibration absorption • Vibro-impact • Multi-functional

28.1 Introduction and Background

Performance-based seismic design of buildings aims to ensure structural integrity, immediate occupancy, and operational performance levels following an earthquake. Critical facilities must remain functional during and after major earthquakes for the public welfare and safety [1]. However, the functionality of these critical facilities is not dictated by the primary building structure's integrity alone, but instead must also consider damages to the building contents [2]. Damage to building contents typically occurs at lower levels of shaking intensity than structural damage. To protect sensitive equipment, vibration isolation is widely used for individual pieces of equipment [3, 4] and floors within buildings [5–7]. The majority of research to date has focused on the development and evaluation of the floor or equipment isolation systems alone without incorporating interactions with the primary building structure. This work incorporates these interactions and aims to demonstrate that these interactions can be synergistic to the overall building system performance.

By isolating a portion of the floor mass, floor isolation systems (FISs) can be designed to behave as dynamic vibration absorbers (or tuned mass dampers), which are passive energy dissipation devices that can reduce the response (drift) of the primary structure to which they are attached [8]. However, this requires the FIS to be *tuned* to the primary structure's natural period, negating the equipment isolation performance of the system. Unlike conventional vibration absorbers, nonlinear energy sinks rely on essential nonlinear restoring forces to transfer energy from lower modes to higher modes of the system [9]. *Vibro-impact dampers* have been shown to be superior to their linear counterparts [9].

The proposed approach takes advantage of the fact that FISs have limited displacement capacities, which if exceeded results in impacts, much like a vibro-impact damper. The disturbance intensity at which impacts are realized depends on the displacement capacity of the FIS, which can be tuned to achieve the desired building system performance. In so doing, the FIS may exhibit two distinct functions depending on the seismic disturbance intensity: (i) equipment protection via isolation from harsh floor motions and (ii) primary structure protection via nonlinear energy transfer from the building to the FIS. This novel adaptive passive seismic protective technique is experimentally assessed in this study.

P.S. Harvey (✉) • N. Halaba Arachchige Senarathna • C.D. Casey
School of Civil Engineering & Environmental Science, University of Oklahoma, 202 W. Boyd Street, 73019, Norman, OK, USA
e-mail: harvey@ou.edu

Fig. 28.1 Photos of experimental setup: (**a**) three-story structure and (**b**) floor isolation system

28.2 Experimental Setup and Characterization

This study aims to experimentally demonstrate the multi-functional FIS concept. As such a three-story primary structure with an attached secondary system was fabricated. The model three-story structure is shown in Fig. 28.1a. The structure has an overall height of 2.44 m equally distributed between the three stories, with floor masses of approximately 102 kg. The columns are 19.05-mm-diameter steel rods with 710.5 mm of clearance between each floor. Free response tests were conducted to determine the structure's natural frequencies, which were measured to be 2.527, 7.373, and 10.71 Hz. These values closely match the predicted values assuming a shear-type structural model. The secondary (isolation) system is comprised of two 8.2-kg steel plates supported by a linear bearing. Springs attached to the linear bearing carriage act to recenter the system. Brackets are mounted on either side of the carriage to restrain its motion, acting as displacement limits. The isolation system is installed on the second floor of the structure. The combined primary structure plus secondary system is mounted on a uniaxial shake table capable of reproducing harmonic and seismic base excitations.

The experimental setup described here is currently being subjected to a series of tests to assess its performance in terms of both isolation and vibration absorption. The experimental protocol includes monotone base excitations of varying frequency and amplitude. Frequencies explored are near the primary structures natural frequency in the range of 1.5–3.5 Hz. The excitation amplitude is varied to explore a range of responses. There exists a critical excitation amplitude that induces impacts in the secondary system, below which the combined system behaves linearly and above which the system enters a nonlinear regime with impacts. Presently, the impact interface (i.e., stiffness, energy dissipation, coefficient of restitution, etc.) are being tuned to achieve improved performance. Isolation performance is quantified by the ratio of the peak absolute acceleration of the isolated blocks to the peak absolute acceleration of the floor to which it is attached (second floor). Vibration absorption performance is quantified by the reduction in the total drift of the structure with and without the secondary system attached. The results of this experimental study will shed light on the benefits and drawbacks of the proposed approach.

References

1. Shi, Y., Kurata, M., Nakashima, M.: Disorder and damage of base-isolated medical facilities when subjected to near-fault and long-period ground motions. Earthq. Eng. Struct. Dyn. **43**(11), 1683–1701 (2014)
2. Konstantinidis, D., Nikfar, F.: Seismic response of sliding equipment and contents in base-isolated buildings subjected to broadband ground motions. Earthq. Eng. Struct. Dyn. **44**(6), 865–887 (2015)
3. Harvey, Jr., P.S., Gavin, H.P.: The nonholonomic and chaotic nature of a rolling isolation system. J. Sound Vib. **332**, 3535–3551 (2012)
4. Demetriades, G.F., Constantinou, M.C., Reinhorn, A.M.: Study of wire rope systems for seismic protection of equipment in buildings. Eng. Struct. **15**, 321–334 (1993)
5. Lu, L.-Y., Lee, T.-Y., Juang, S.-Y., Yeh, S.-W.: Polynomial friction pendulum isolators (PFPIs) for building floor isolation: an experimental and theoretical study. Eng. Struct. **56**, 970–982 (2013)

6. Liu, S., Warn, G.P.: Seismic performance and sensitivity of floor isolation systems in steel plate shear wall structures. Eng. Struct. **42**, 115–126 (2012)
7. Jia, G., Gidaris, I., Taflanidis, A.A., Mavroeidis, G.P.: Reliability-based assessement/design of floor isolation systems. Eng. Struct. **78**, 41–56 (2014)
8. Matta, E., De Stefano, A.: Robust design of mass-uncertain rolling-pendulum TMDs for the seismic protection of buildings. Mech. Syst. Signal Process. **23**, 127–147 (2009)
9. Nucera, F., McFarland, D.M., Bergman, L.A., Vakakis, A.F.: Application of broadband nonlinear targeted energy transfers for seismic mitigation of a shear frame: computational results. J. Sound Vib. **329**, 2973–2994 (2010)

Chapter 29
Variability of Dynamic Response in Jointed Structures

D. Di Maio, Z. Mitha, J.V. Paul, and X. Chi

Abstract This study focuses on the variability of the dynamic response of jointed structures. It is well known that the dynamic response of joints is prone to variability issues when they are open and closed again. This paper will present one numerical example and two experimental ones on different type of structures used for studying this issue of variability. The numerical example will focus on parameters such as torque magnitude and contact area. The analysis, which is linear, will present the changes of natural frequency caused by the variation of these two parameters. The experimental examples will focus on parameters like torque magnitude, torque sequence and number of assembling. Both natural frequency and damping changes will be measured from a number of repeated sequences and analysed using statistical methods.

Keywords Variability • Repeatability • Jointed structures • Dynamic response

29.1 Introduction

This research work focuses on the variability of dynamic response for jointed structures. Joints are convenient for assembling and maintenaning complex engineering machines. This research is focused on the issues related to the variability of the dynamic response when joints are opened and closed several times, which happens in any regular maintenance. This concept of variability is coined by the term "repeatability", where manufacturers attempt to maximise the repeatability of a structure in order to minimise the variability.

Joints are not always modelled because of the excessive time requirement and computational effort needed. The simplest solution to this problem, is to fully join the parts together assuming no relative motion. Hence the calculation of natural frequencies will be limited within a theoretical model, as the variability caused by this relative motion will be limited. This relative motion can be determined by several parameters such as torque, contact area, material type, bolting sequence and several others. Hence from an experimental view point several parameters can be investigated, whereas from a numerical one this number can be smaller. The major restriction is caused by the nonlinear dynamic behaviour of the contact conditions, which the modern FE solver cannot tackle yet. This brief overview shows how complex joints can be. Furthermore, studies on variability are very limited due to their time consuming nature and so literature is scarce. Instead, much research is carried out on establishing laws for the dynamic behaviour of jointed structures since it is a nonlinear phenomenon that is much more appealing to the scientific community [1–3] and [4]. Nevertheless, the variability of dynamic response in flexible structures might be more sensitive for certain response modes than others and, therefore, any nonlinearity associated to that variability is more challenging as well as fundamental to study.

This work will present one numerical work and two experimental ones. Natural frequencies were calculated and measured in all the three test cases; the loss factor was measured in the experimental test case. The numerical work was focussed on two parameters such as bolt preload and the contact area designed for the assembly of the two parts. The experimental works focussed on several parameters such as torque level, bolting sequence, number of number of repetitions. Tests were carried out under linear response conditions so as to be able to calculate the natural frequency and damping loss factor by modal analysis. The large amount of data was processed by statistical methods in order to capture the standard deviation from the mean value calculated from several repetitions.


D. Di Maio (✉) • Z. Mitha • J.V. Paul • X. Chi

Department of Mechanical Engineering, University of Bristol, University walk, BS8 1TR, Bristol, UK

e-mail: dario.dimaio@bristol.ac.uk

29.2 Test Structures and Setup

Two different test structures were designed and made for this experimental work, as shown in Fig. 29.1a, c. These structures were freely suspended and a shaker was attached to one of the extremities. Due to the continuous disassembly and reassembly of the structures, it was decided to attach the shaker in such a way that would minimise setup difficulties. The solution applied in these cases was to have a powerful permanent magnet installed at the force gauge so as to bond the shaker to the structures by a magnetic force. Some repeatability checks were carried out in order to assure the correct force transmission every time the gauge was disconnected; this is shown in Sect. 29.4.1. The level of the excitation forces were set to a low amplitude so as to avoid any activation of nonlinearities. The test setup is shown in Fig. 29.2.

Regarding the FE model used for the numerical work some information about the meshing dimension are provided; ABAQUS software was used for this piece of work. Firstly the element shape of the mesh for all the following tests is tetrahedral as it was impossible to perform accurate meshes if a hexahedral element shape was used on a structure
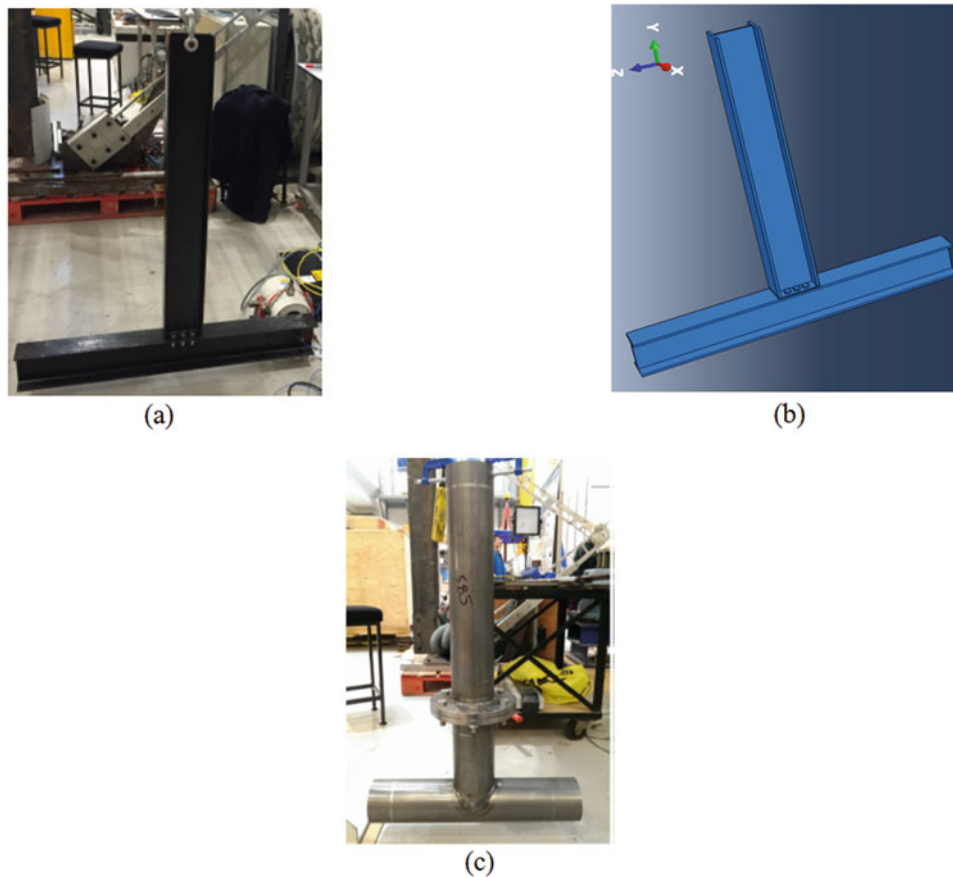
Fig. 29.1 Test structures. (**a**) I-beam in T shape assembly. (**b**) FEM of the type (**a**). (**c**) Pipes with bolted flanges
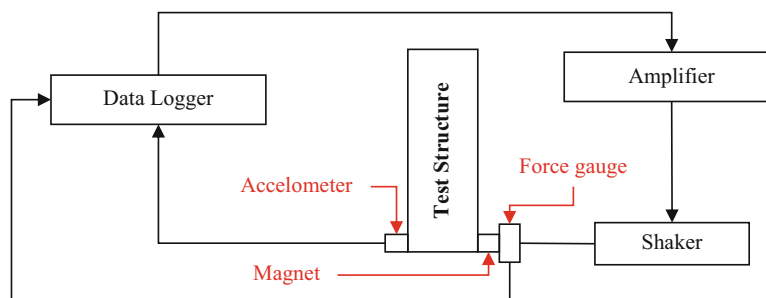
Fig. 29.2 Test setup

with complicated geometry, especially when circular patterns were involved. The element size was determined from mesh convergence, which is 8 mm globally with minimum size control factor 0.01 of the global element size. The element size for bolts is auto-calculated 3.4 mm with 0.1 minimum size control factor by ABAQUS.

Measurements were made up to 1 kHz within which several modes were available for the down selection. Instead, the FE analysis was carried out using the first six mode shapes. The next sections will present some of the results obtained from each test case studied and discussion will be provided to the test case studied.

29.3 FE Analysis of I-Beam in T Shape Assembly

The mode shapes for the structure were calculated and presented in Fig. 29.3. These modes were used for calculating the new natural frequencies where a parameter, such as the bolt preload, was used instead of the fully constrained conditions. This section will present four cases where the preload, the size of the contact area, the size of the bolt body and the size of the bolt head were changed for simulating the new natural frequencies of six mode shapes.

Figure 29.4 shows the effect of the bolt preload on the natural frequencies of the six mode shapes. The largest preload was set to 500kN and the smallest 1 N. As expected some modes were minimally affected by these changes but other ones were more sensitive.

Figure 29.5 shows the effect of the size of the bolt head diameter on the natural frequency. For this case the bolt preload was set up to 20kN. Most of the modes were insensitive to these changes, but Mode 4 was highly responsive.
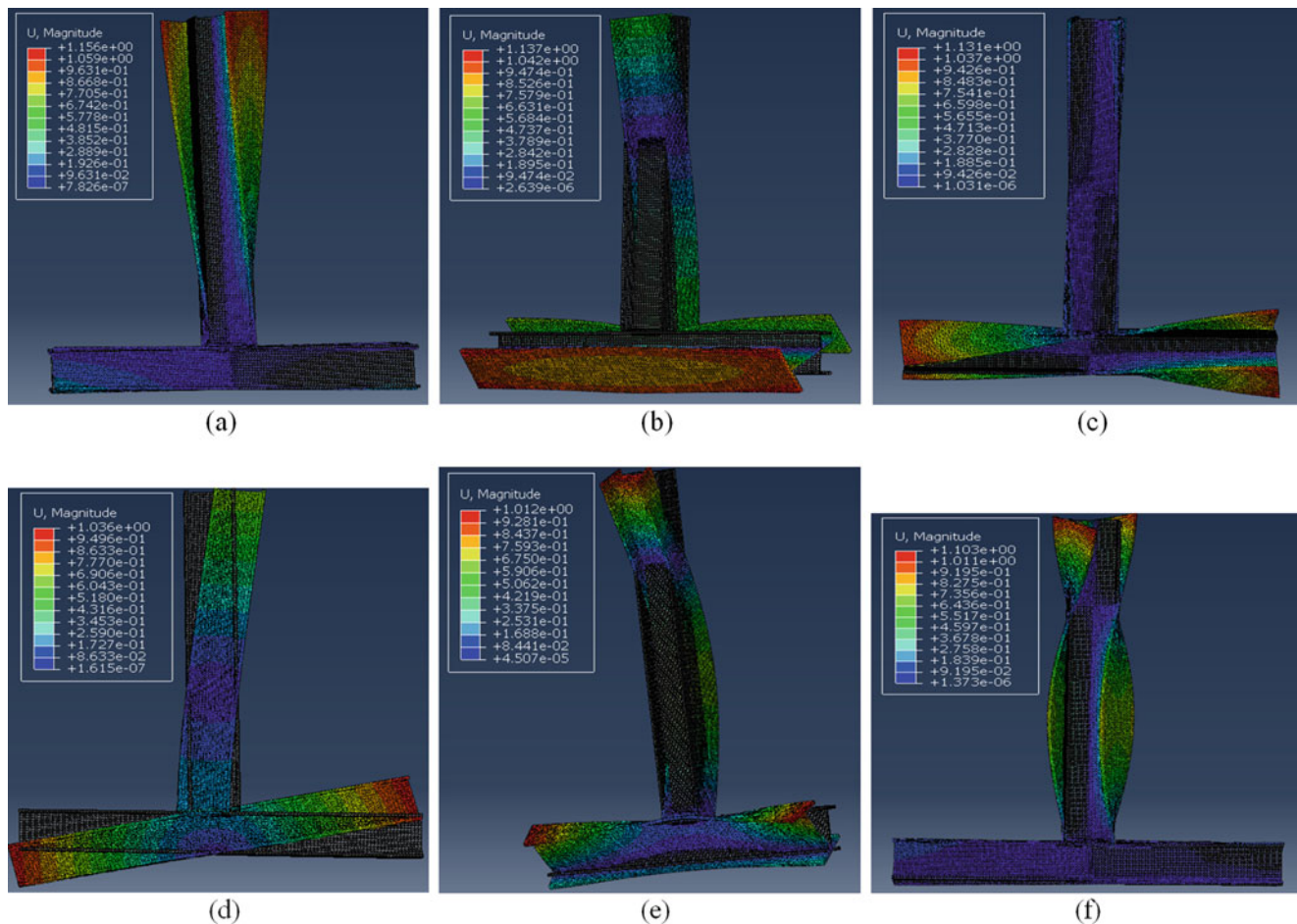
Fig. 29.3 Mode shapes and natural frequencies of the test structure. (**a**) Mode at 67.5 Hz. (**b**) Mode at 98.2 Hz. (**c**) Mode at 124.2 Hz. (**d**) Mode at 144.2 Hz. (**e**) Mode at 244.1 Hz. (**f**) Mode at 320.4 Hz
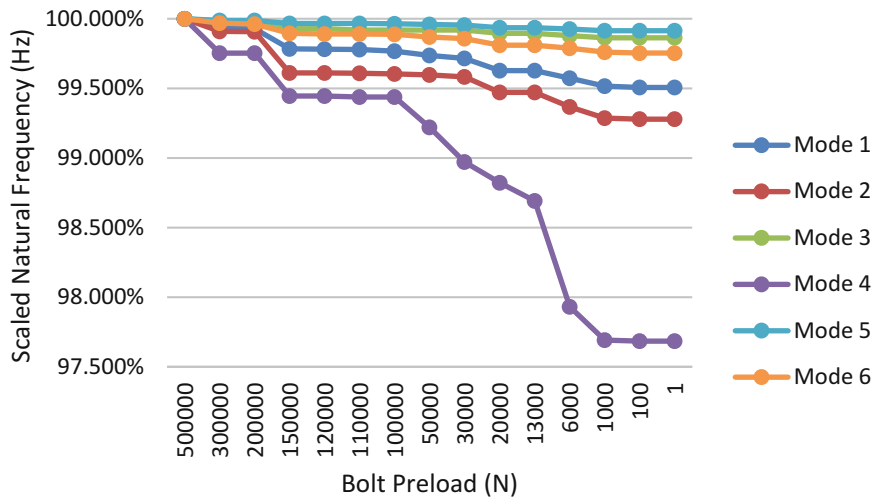
Fig. 29.4 Effect of bolt preload on the natural frequency
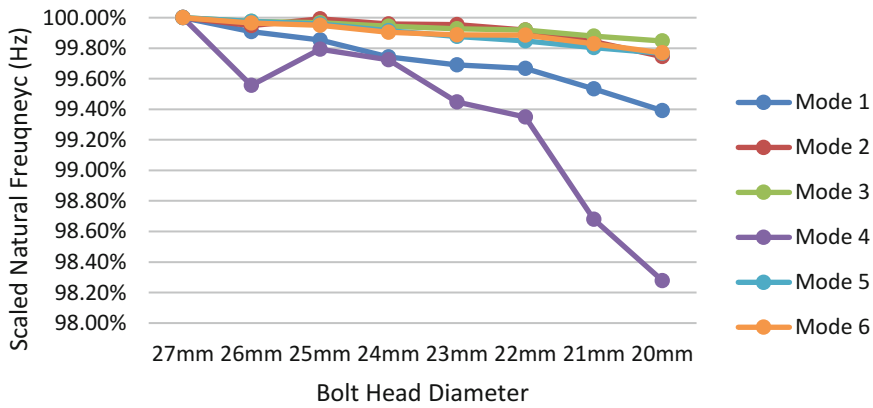
Fig. 29.5 Effect of the size of the bolt head diameter on the natural frequency
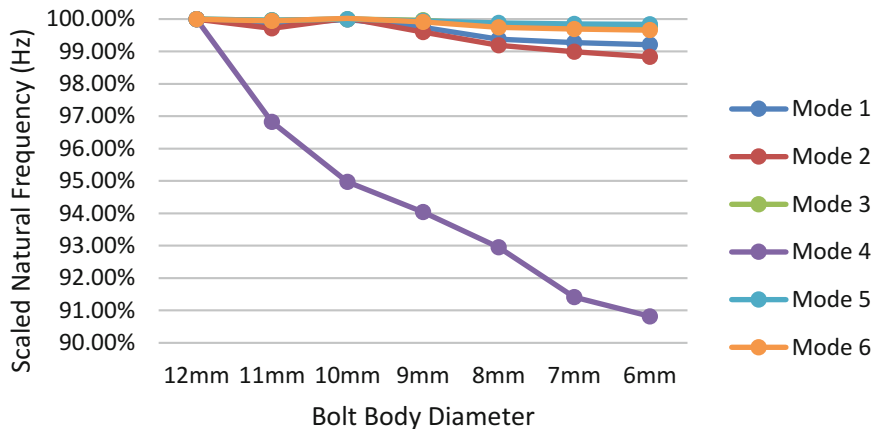

Fig. 29.6 Effect of the size of the bolt body on the natural frequency

Figure 29.6 shows the effect of the size of the bolt body on the natural frequency. Even for this case the bolt preload was set up to 20kN. Despite most of the modes being insensitive to this parameter, Mode 4 once again shows the highest relative frequency shift.
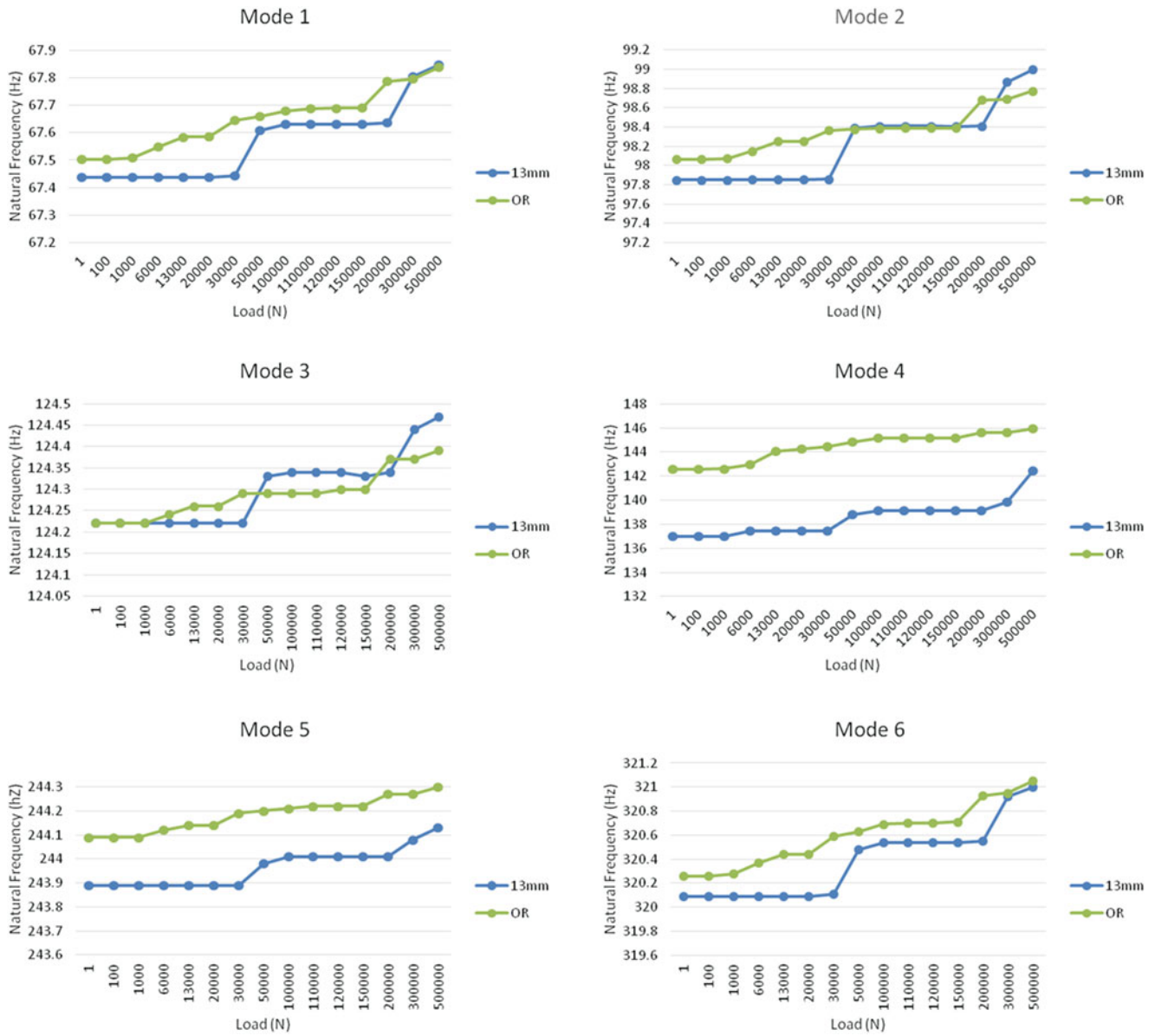
Fig. 29.7 Effect of the size of the contact area on the natural frequency

Finally, Fig. 29.7 shows the effect of the size of the contact area on natural frequency for all modes. One set of tests are presented here, where the diameter of the bolted holes being cut was set to13 mm. For each structure with a varying contact area, a full preload test was performed. The results were then compared to the data from the preload tests of the original structure (referred to as "OR" within the legend).

These FE analyses showed that Mode 4 was the most sensitive to the variation of the parameters, as presented in Figs. 29.4, 29.5, and 29.6. However, the reduction of contact area showed a different relationship where all modes were fairly insensitive to any preload used for the bolt. This seems to suggest that the reduced contact area generates more local stiffness which in turns makes the natural frequency less variable. This set of examples shows how much an improved level modelling adds important value to the study of the variability of the dynamic response.

29.4 Experimental Works

This section will report the two experimental cases by presenting the most interesting data analysis.

29.4.1 Bolted Flange Joints (BFJs)

Bolted Flange Joints (BFJs) are used nearly in all industrial piping systems including in oil and gas plants which are considered as high-risk facilities. These connections represent leak relevant positions, where a single failure may lead to catastrophic damage. Hence, the correct functioning of BFJs is required to ensure the overall performance of such facilities and to avoid possible accidents. Recent studies have shown a high vulnerability of piping systems and their components, including joints, to seismic and non-seismic vibrations (such as those induced by rotating machinery). Pipeline failures account for the majority of oil-field disasters that have led to destruction of lives and environment. Hence, there is a pressing need to better understand the dynamics of bolted flanges. Figure 29.1c shows the test structure, which is made of two pipes connected by bolted flanges. Six M16 bolts were used to connect the two flanges. Four mode shapes were selected for the experimental testing (Fig. 29.8).
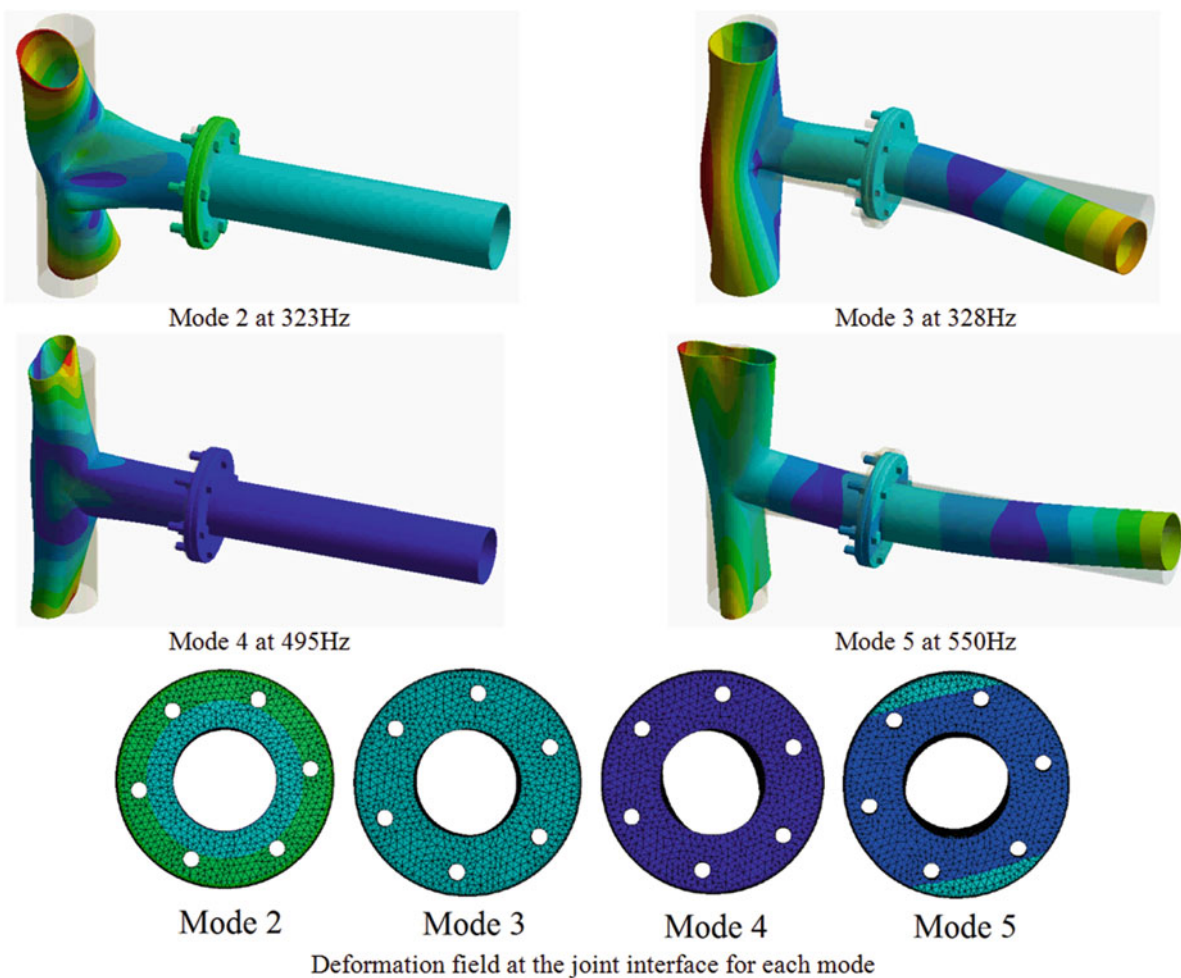
Fig. 29.8 Mode shapes and flange deformation

A series of tests were performed to study the variations in natural frequency and damping where certain parameters that influence the dynamics of the joints were varied. Three parameters were determined to be of interest:

1. Bolt preload
2. Tightening sequence
3. Differential torque

These tests were performed to quantify the sensitivity of the modes to each of these parameters and to determine how they affect the repeatability of the modal parameters.

All measurements are prone to systematic errors which can be environmental changes or imprecise calibrated measurement instruments. Repeated measurements do not reduce systematic error and hence care must be taken to avoid it. In addition to this, there can also be random errors that are caused by unknown changes in the experiment and are hence inherently unpredictable. A series of tests were performed to quantify the error in both natural frequency and loss factor. The structure was bolted with a preload of 10 Nm. This value of torque was chosen as the joint seems to induce the least repeatability at lower preloads. After each test, the structure was detached from the shaker and accelerometer, taken off the bungee cables and then re-attached so as to simulate all the previous experimental conditions except for the disassembly of the joints. These observations, presented in Fig. 29.9, give weight to the assumption that the errors caused by changes in the environment or variations in the suspension of the structure are insignificant compared to the effect that changes in the joint interface has on the modal properties of the structure.

In this section, the effect of bolt-preload on the modal parameters of the pipe section is investigated. The structure was repeatedly detached and assembled to perform a series of tests. The preload torque was varied through 10, 20 and 30 Nm for different series of tests. The natural frequency and damping were estimated from the inherent FRFs obtained (Figs. 29.10 and 29.11).
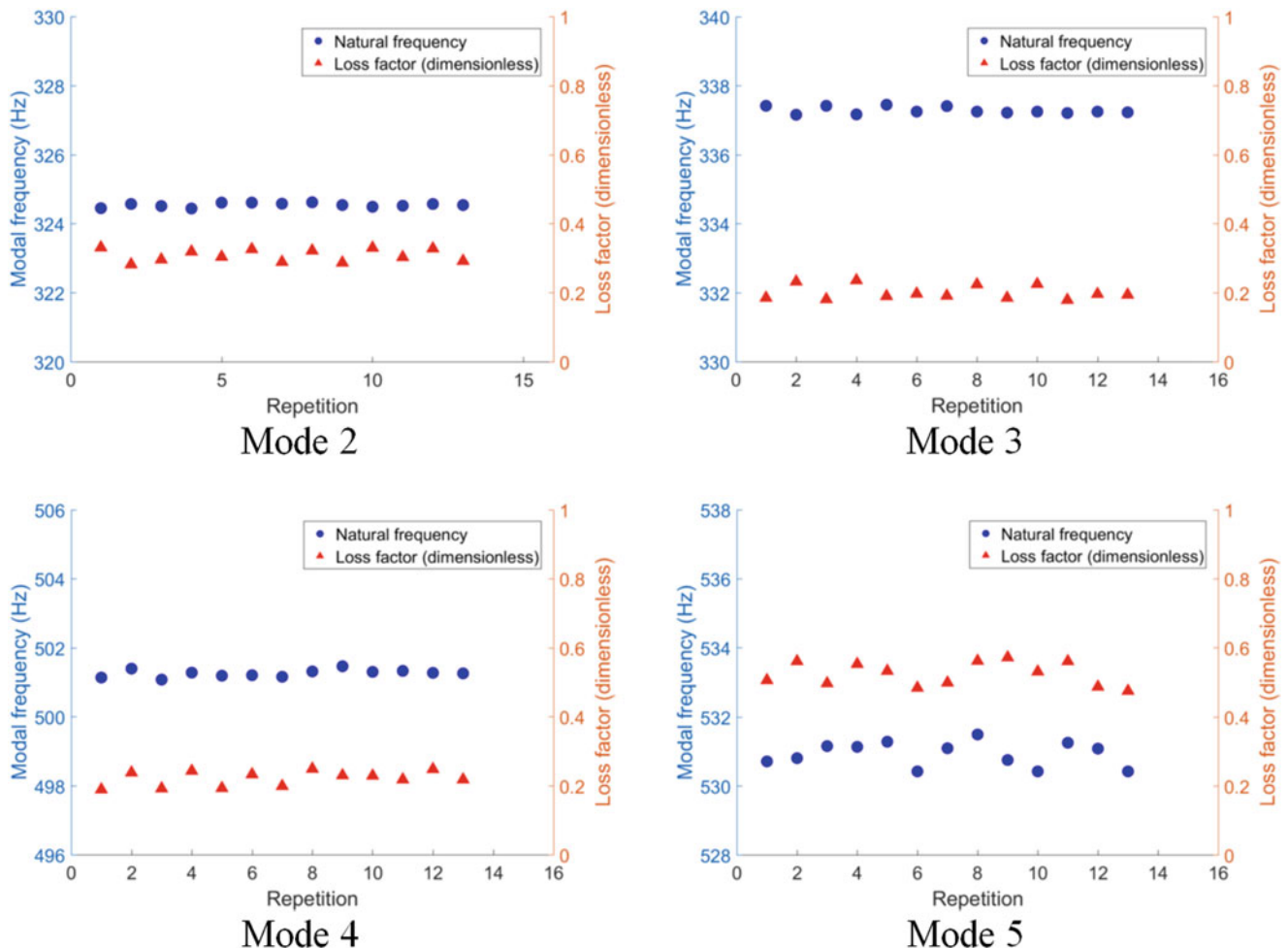

Fig. 29.9 Scatter plots of modal data for error analysis

In this section, the effect of bolt tightening sequence on the modal parameters of the pipe section is investigated. The structure was repeatedly detached and assembled to perform a series of tests. The bolt preload was kept constant at 10 Nm, since the scattering of data points was maximum at low bolt-preloads (as seen in previous section) and any trends in data are easier to spot. The natural frequency and damping were estimated from the inherent FRFs obtained (Fig. 29.12).

In this section, the variation of the modal parameters of the pipe section when combinations of bolt preloads were applied on the joint, is explored. The structure was repeatedly detached and assembled to perform a series of tests. The tightening sequence was kept constant for all the tests. The natural frequency and damping were estimated from the inherent FRFs obtained (Figs. 29.13 and 29.14).

This section presents a study of the repeatability of the modal behaviour of a bolted flange when various parameters that affect the contact condition of the joint were changed. Three parameters and their effects were explored – bolt preload, torque sequence and torque configuration, respectively. The results from the experimental analysis show that the mode-shape and the stress distribution at the flange interface play a critical role in the variability of modal parameters. Also it is noticed that repeatability of modal behaviour varies from mode to mode and from parameter to parameter. Some modes exhibited greater sensitivity to certain parameters than others. Numerical analysis revealed that Modes 2 and 5 have non-uniform stress distribution at the joint interface. This corresponded well with the large scattering of modal data and non-repeatability of the modal dynamics for these two modes. When the overall torque on the flange is increased, the joint becomes rigid and the variability in natural frequency and loss factor decreases.
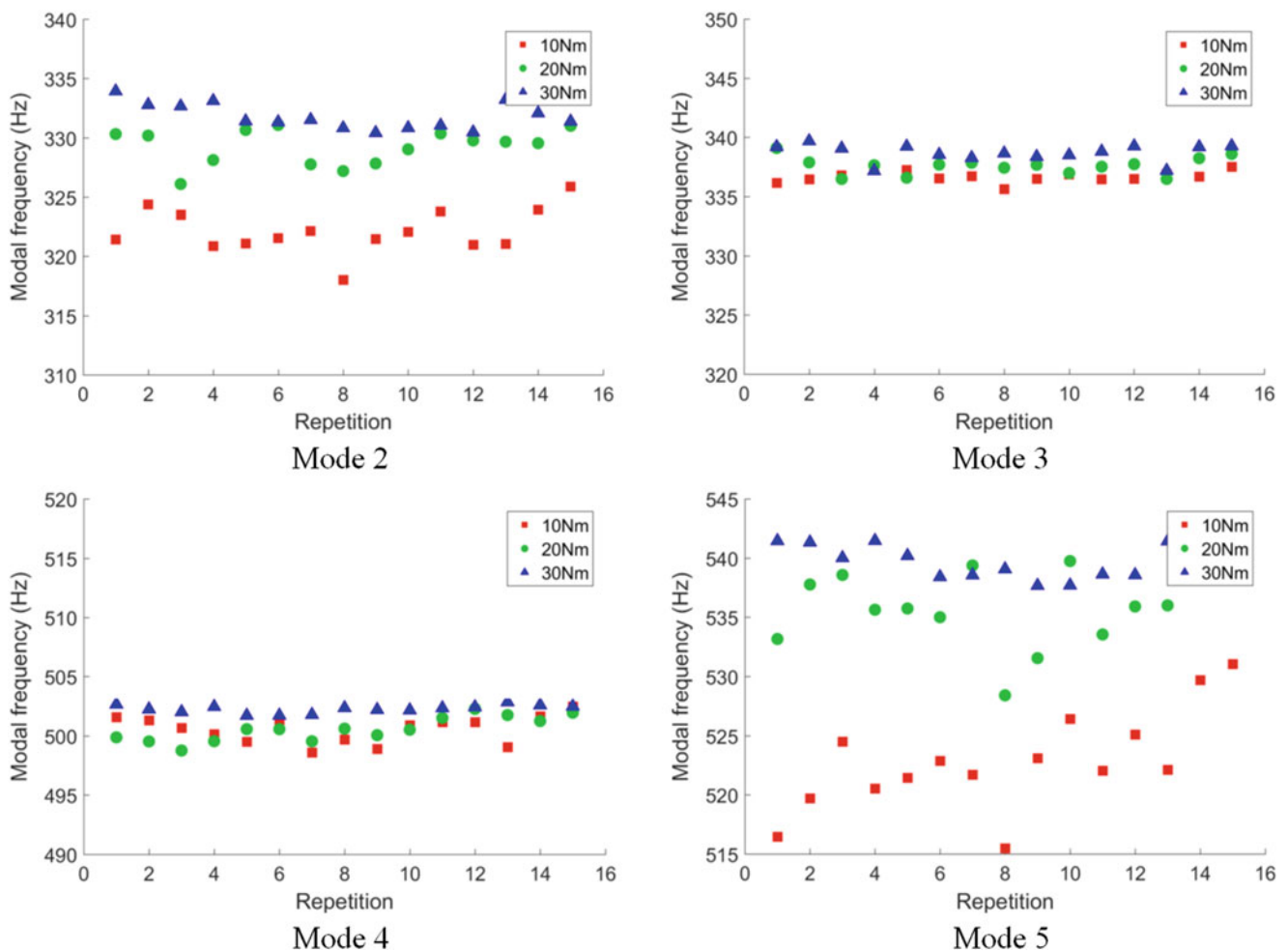

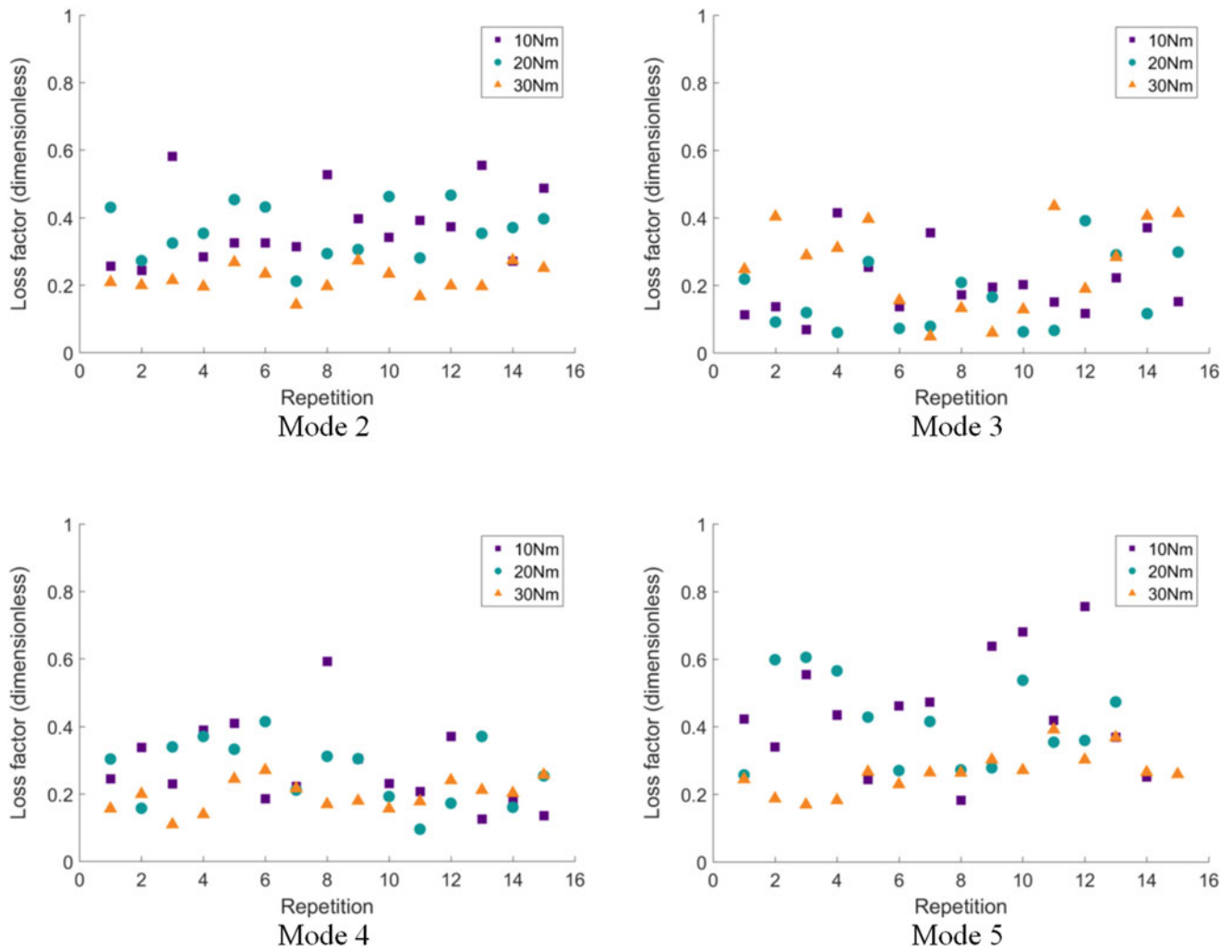**Fig. 29.10** Variability of the natural frequency and loss factor
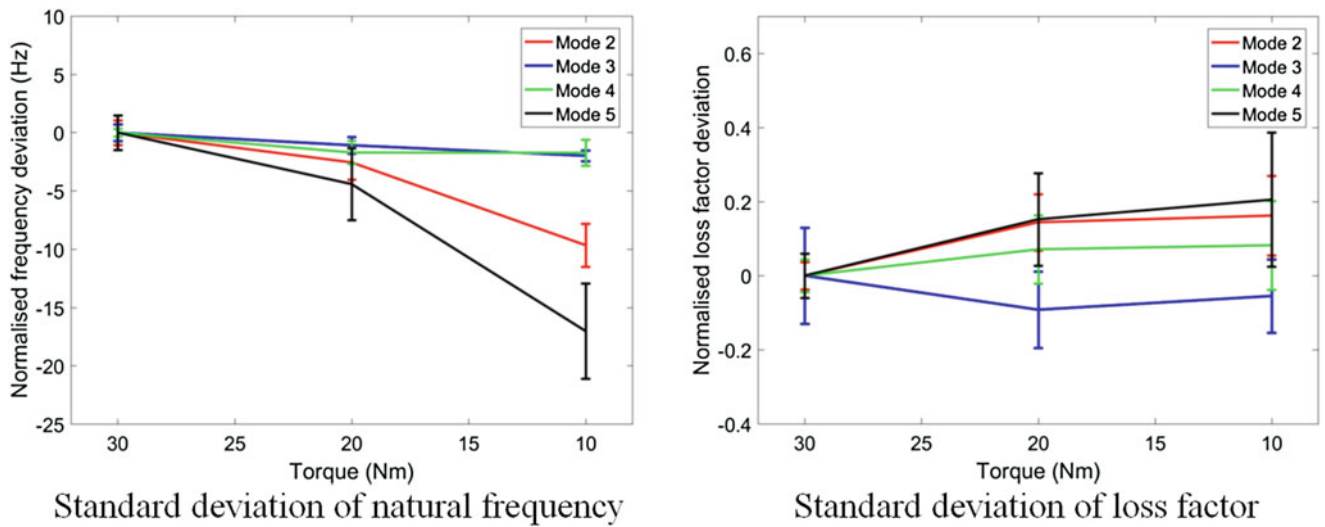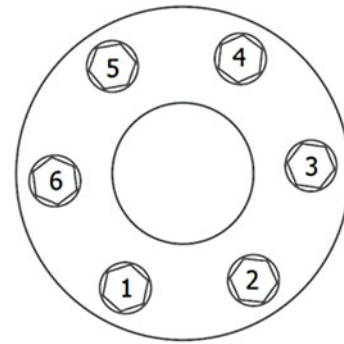
Fig. 29.10 (continued)
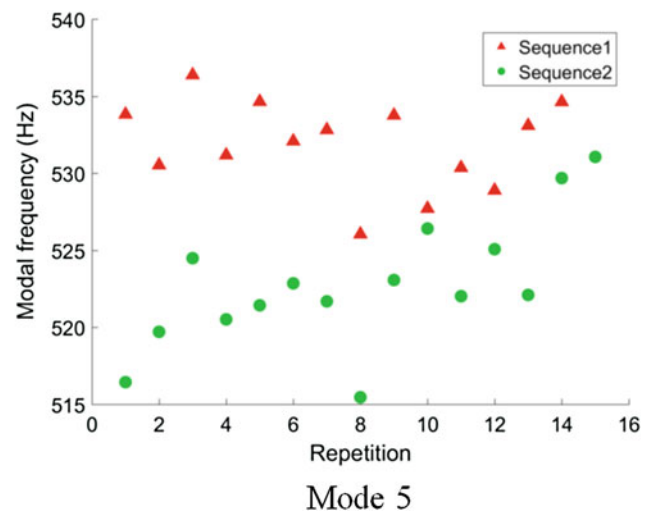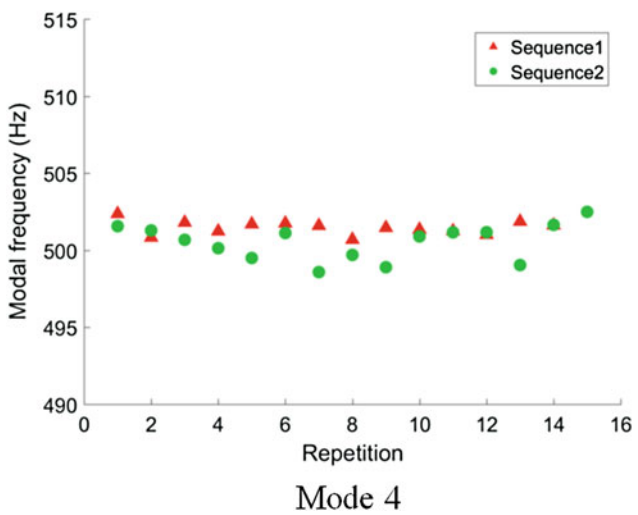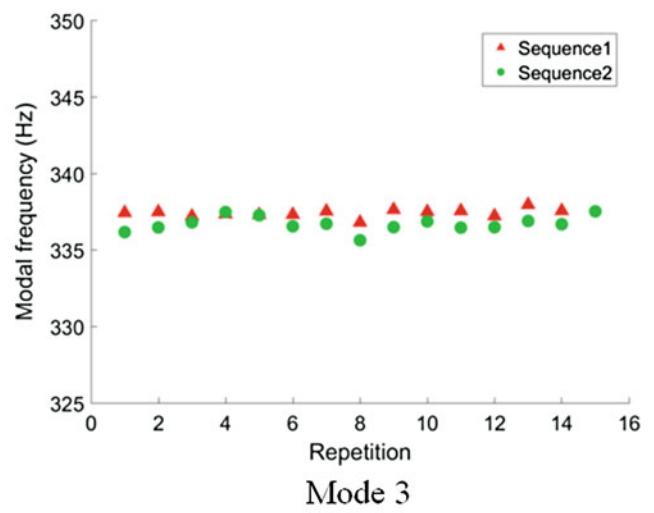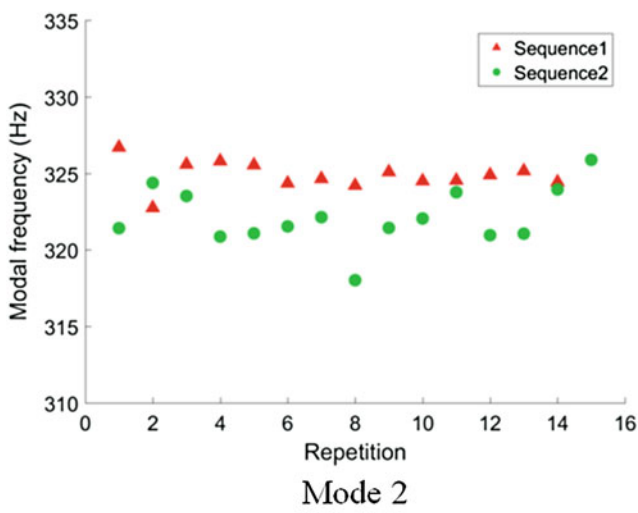

Fig. 29.11 Standard Deviation
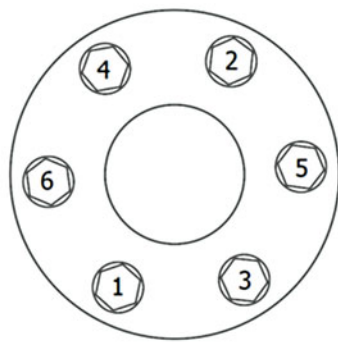
Fig. 29.12 Two bolt-tightening sequences used for the natural frequency and loss factor analysis
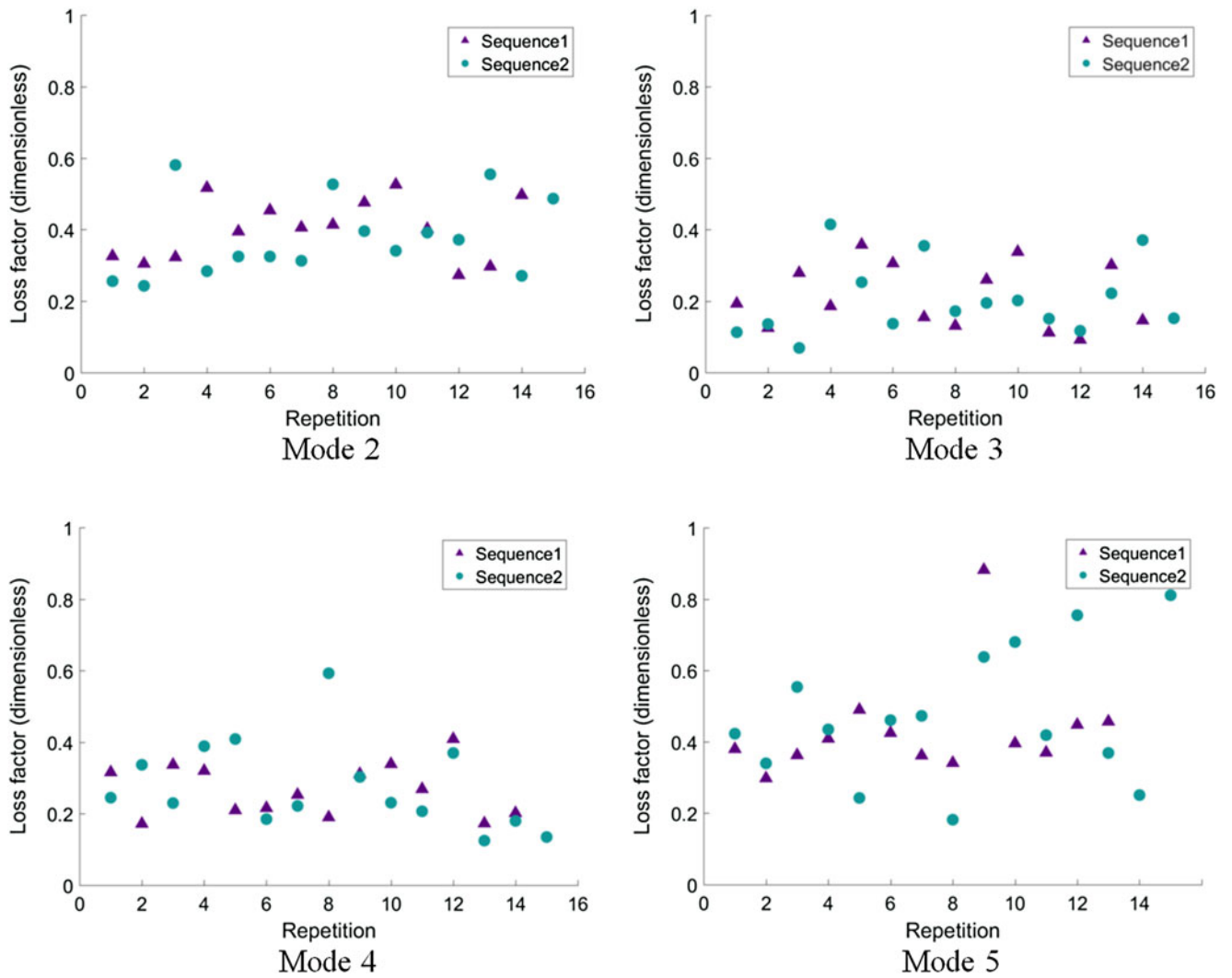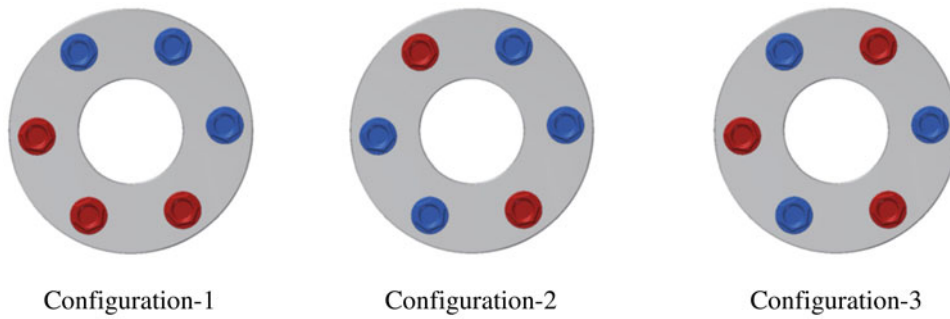
Fig. 29.12 (continued)

Fig. 29.13 Three different combinations of low and high bolt pre-loads used for analysis (*Red* bolts are torqued to 20 Nm while *Blue* bolts are torqued to 10 Nm)

29.4.2 I-Beam in T Shape Assembly

A T-shaped assembly was chosen to evaluate the construction of a beam to column connection. This involved the horizontal I-beam cross section being jointed to the side of the vertical I-beam. In order to make this possible, an extra interface was needed to bolt the I-beams together. Therefore an end plate, composed of mild steel, was welded to the horizontal I-beam face. This would then be bolted to the vertical I-beam with six M12 bolts, as shown in Fig. 29.1a. Once the structure was prepared, two modes were selected for testing, one at 220 Hz and other at 750 Hz. The structure was then disassembled and reassembled 15 times for each of the five torque settings while measurements of natural frequency and damping were taken.

Examination of Fig. 29.15a, b shows all the data values gathered for Mode 1. Clearly there is a large spread of data, most notably in Fig. 29.15a, where several data points occurred around 235 Hz while the majority were found at 220 Hz. These outliers at 235 Hz appeared for all torque settings, regardless of their value. This disparity between values at 220 Hz and 235 Hz seems to suggest systematic error as the natural frequency of structure should not theoretically change by such a large amount for all torque values. The most likely explanation is that the mode is highly sensitive to testing. This explanation agrees with data in Fig. 29.16a where no clear outliers occurred for Mode 2, despite data being measured for the exact same samples. As a result, these outliers for natural frequencies and their corresponding loss factors, were ignored from further analysis, as they would unfairly affect the mean and standard deviations calculated for comparison and as shown in Fig. 29.15c–f.

The correlation coefficient, ρ, shows a value close to 1 for Fig. 29.15c, suggesting a positive correlation between torque preload and natural frequency. Furthermore, the correlation of determination, R^2, is also close to 1 indicating a linear
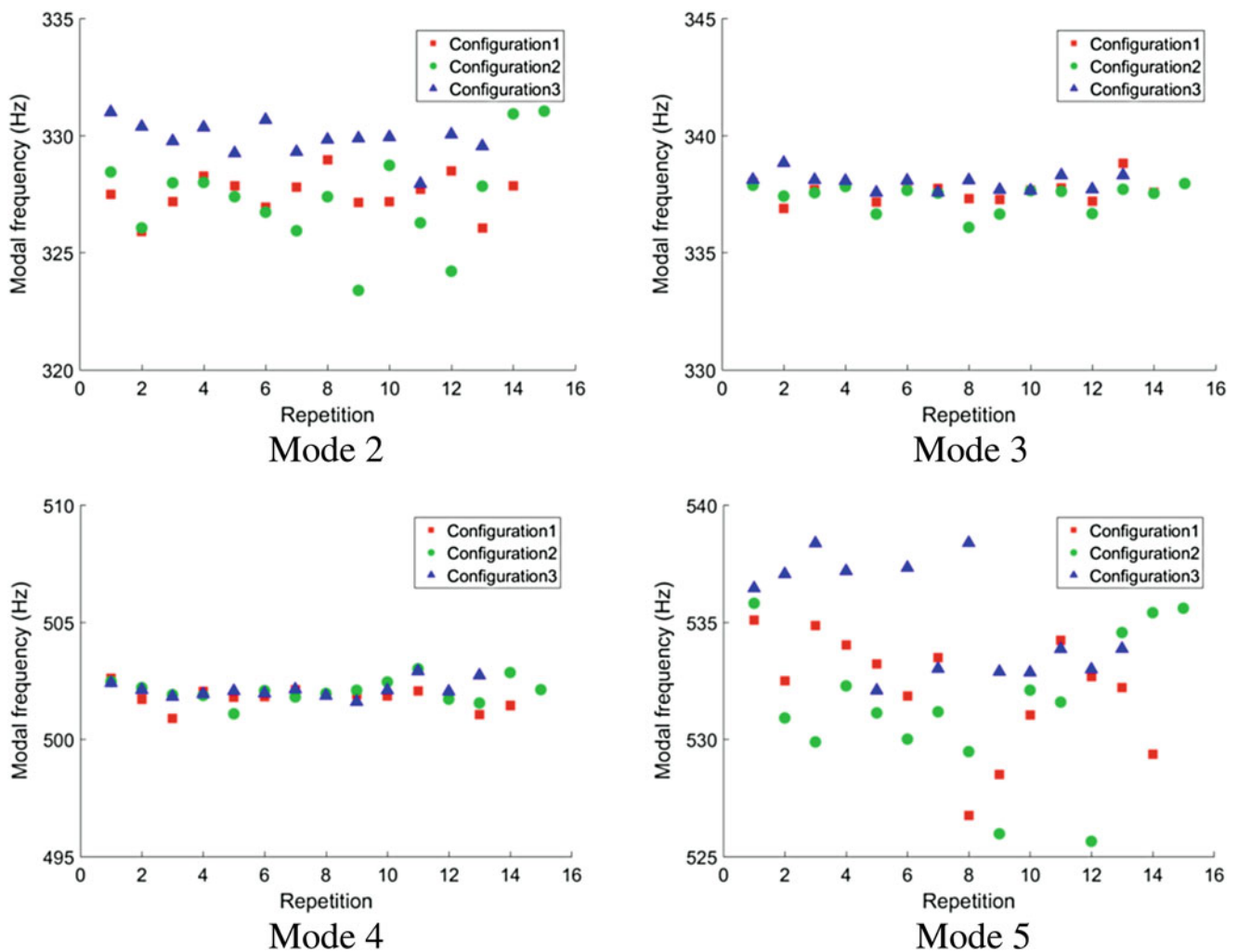

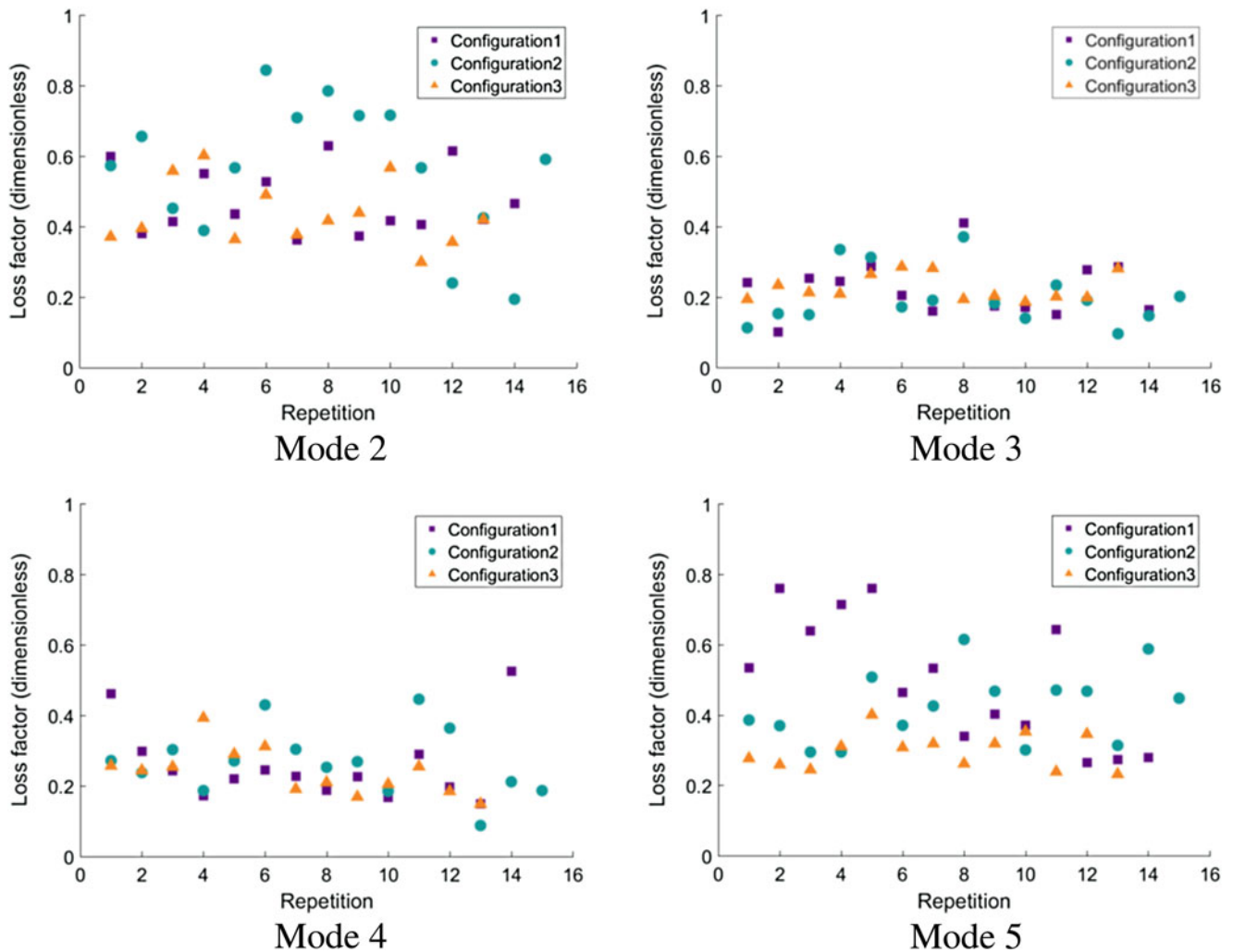**Fig. 29.14** Natural frequency and loss factor variability

Fig. 29.14 (continued)

relationship between the two variables. This is consistent with dynamic theory, as the higher the torque preload, the more stiff the structure and therefore the higher the natural frequency. Figure 29.15d shows a similar linear relationship between torque and loss factor, except it is in the negative direction shown by its correlation coefficient close to −1. Given that loss factor is a representation of mechanical damping, the higher the torque preload, the stiffer the structure, the less energy is dissipated by the system and therefore the lower the mechanical damping and loss factor of the mode. Given the linear relationships of both natural frequency and loss factor to torque, this behaviour is validated by dynamic theory.

Figure 29.15e, f show how the standard deviation changes with constant torque preload. Standard deviation is a measure of repeatability as the higher the standard deviation of a sample, the larger its spread in data and hence the less repeatable it is. Both graphs have a negative correlation coefficient of −0.9655 and −0.9484 respectively, indicating that the standard deviations of natural frequency and loss factor decrease with torque. Therefore the repeatability of the structure increases with torque preload. As a bolted surface becomes tighter and more rigid, the ability of the structure to twist, turn or displace in any manner reduces; as a result it is not surprising that this trend is observed. The R^2 value of Fig. 29.15e means that 93.21% of the variance in natural frequency standard deviation can be explained by a linear relationship between the torque and standard deviation. Although a linear relationship could explain the trend in repeatability, visually it seems more likely that the repeatability is increasing at a greater rate between torques, as the gradient of the line plot becomes steeper and steeper. Given that only 4 data points are plotted, it is hard to be certain of this, but a linear relationship for repeatability also seems to be unsupported by Fig. 29.15f, where the R^2 value is less than 0.9 and visually there is a considerable jump in the standard deviation of loss factor between 20 and 40 Nm. Therefore there does not seem to be a linear relationship between repeatability and modal behaviour. As mentioned, both sets of data do suggest that repeatability increases with

torque preload, but it is not clear in what fashion or whether a predictable model can be suggested by these results. For this particular mode, it does appear that the repeatability of natural frequency increases at a greater rate between torques indicating that torque preload should be set to 60 Nm or higher in order to maximise repeatability. For loss factor, a decrease of 43.9% in standard deviation was observed between 20 and 40 Nm, suggesting a torque preload of 40 Nm or higher should be used to maximise repeatability.

All the experimental data for Mode 2 is plotted in Fig. 29.16a, b. Unlike Mode 1, both loss factor and natural frequency appear to have no outliers and a relatively smaller spread in data values. From the onset, this suggests that the mode is relatively stable with a high level of repeatability. The lack of outliers means that all data points are valid for statistical analysis. Further examination is therefore needed to determine if any trends can be used to model repeatability.

Figure 29.16c, d show how the mean natural frequency and mean loss factor of Mode 2 vary with constant torque preload. Figure 29.16c has a ρ value of 0.9994 indicating a strong positive correlation between torque preload and natural frequency. Furthermore, its R^2 value of 0.9988 suggests a linear relationship between the two variables. These results conform to vibration theory where the higher the torque preload, the stiffer the structure and the higher its natural frequencies. Figure 29.16d has a ρ value of -0.9870 showing a negative correlation between loss factor and torque preload. Similarly a high R^2 value of 0.9742 was calculated, suggesting a linear relationship between the two variables. This is also consistent with vibration theory as the higher the torque preload, the less energy dissipated during vibration and the lower the loss factor.
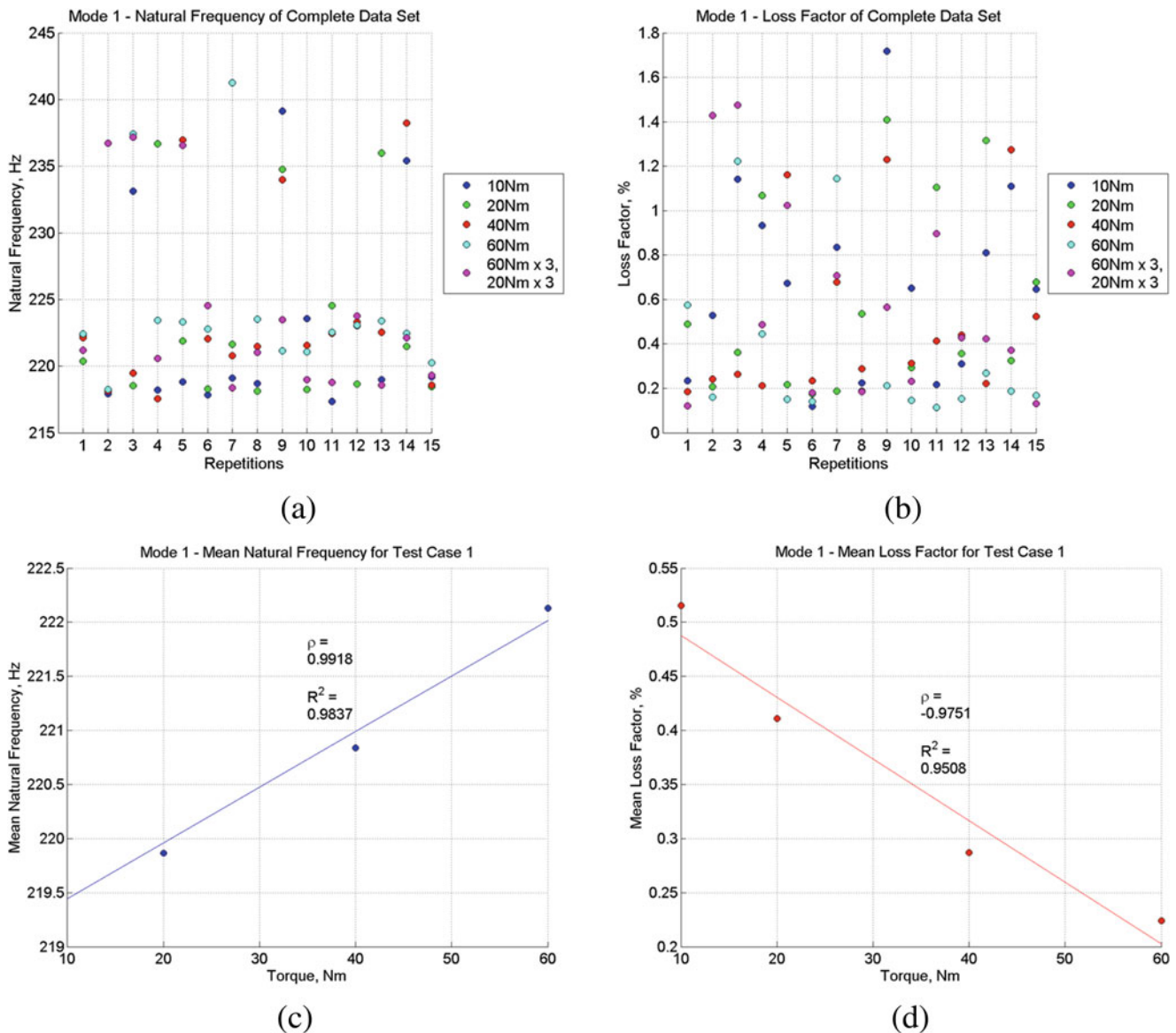

(a)

(b)

(c)

(d)

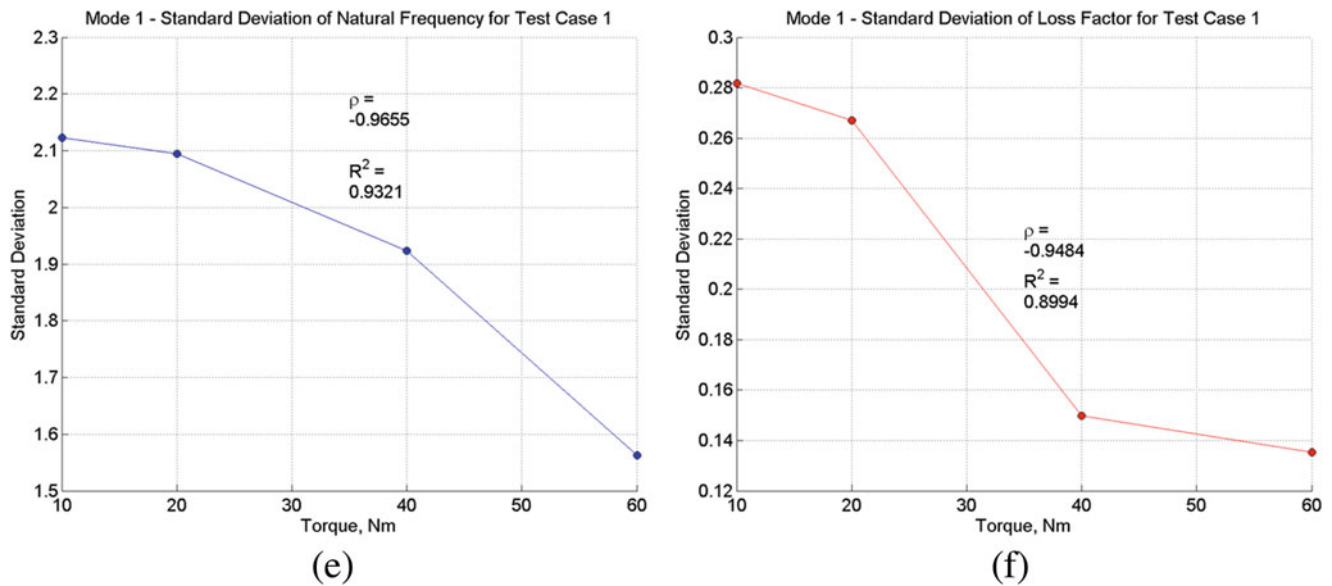**Fig. 29.15** Natural frequency and damping for mode at 220 Hz

Fig. 29.15 (continued)

Understanding how the standard deviation of the natural frequency and loss factor change is vital to understanding how repeatability changes, as the smaller the spread in data, the more repeatable the modal behaviour. This is illustrated by Fig. 29.16e, f where both standard deviations of the natural frequency and the loss factor change with torque preload. Visually both have similar shapes and correlation coefficients (-0.7124 & -0.7797) suggesting a relationship between modal properties and torque preload i.e. the repeatability of both natural frequency and loss factor decrease in tandem with torque preload. It is unsurprising that the correlation coefficient is negative because the higher the torque preload, the tighter the bolts, the more rigid and secure the structure, and less likely it is to deviate from its standard modal behaviour. The R^2 values of both graphs are relatively low suggesting that a linear relationship between repeatability and torque preload does not exist. Both do show dramatic jumps in standard deviation between 10 and 20 Nm. This indicates that the repeatability of mode increases significantly between these torque values and that a minimum of 20 Nm should be used in order to increase repeatability. Although the R^2 values indicate a non-linear model for repeatability, if one were to disregard the data points at 10 Nm and focus on the torque preloads onwards, visually a linear relationship would be reasonable to suggest for both natural frequency and loss factor. This means that repeatability could increase after a particular torque (20 Nm in this case) and then follow a linear relationship in terms of further increase. By disregarding 10 Nm and calculating the R^2 values for the data points at 20, 40 and 60 Nm, one can see if a linear relationship does exist between repeatability and modal behaviour from 20 Nm onwards. A value of 0.7826 for natural frequency and 0.9967 for loss factor was produced. This new R^2 value for loss factor suggests a linear relationship as it is close to 1, while the new R^2 value for natural frequency suggests the opposite as it is relatively low. Given that both contradict each other, it is inconclusive whether repeatability can be modelled to be linear from a point onwards.

29.5 Discussion of the Results

This work presented two types of structures usually designed in mechanical engineering. The simplicity of the assembly posed a question about the effect of the bolted joints on the variability of the dynamic response. The work is split in two parts, one numerical and one experimental. The joints presented in here are not usually modelled in practice where components are often bonded together. This design choice is simple and makes the model faster to run simulations. Instead, from a practical view point, maintenance aims at disassembling and reassembling the joints numerous time. Hence, the questions are about (i) what happens if they are modelled and (ii) how repeatable is the dynamic response if the joint is opened and closed several times.

The numerical work was focused on four parameters (preload, the size of the contact area, the size of the bolt body and the size of the bolt head), two of which are more relevant since the bolt head and body diameters are standardized and hardly changeable. The FE analysis is also based on linear response conditions. The change in the preload has shown that some

modes are more sensitive than others, in particular Mode 4, to the changes applied. Mode 1 and Mode 2 were also sensitive to this parameter variation. By looking at the mode shapes it is possible to infer that Mode 4 seems to stress the bolt because of the in-plane bending with a large inertia created by the motion of the two beams; so the bolts take most of the load. Similar observation could be drawn by looking at Modes 1 and 2. However, in this case Mode 1 is the least sensitive and this is probably due to the torsional mode of the up-right beam. Interestingly, when the contact areas between the bolted parts were reduced and the preload was again varied between 1 N and 500,000 N, the natural frequencies of the modes become less variable than before. This can be explained due to the increased pressure distribution and therefore higher local contact stiffness.

The experimental work was conducted under low level of excitation forces so as to measure linear responses. It is well known that joints show typical nonlinear responses but these were not taken into account at this stage. So, the work was confined to the understanding of the variation of natural frequency and loss factor due to the opening and closing of the joints. Four modes were analysed for the pipe assembly whereas only two modes for the I-beam assembly. It is also clear from the experimental examples that some response modes are more sensitive than others. This evident for the jointed pipe in Sect. 29.4.1 which shows that Modes 3 and 4 are insensitive to the assembly operation while the others produce much
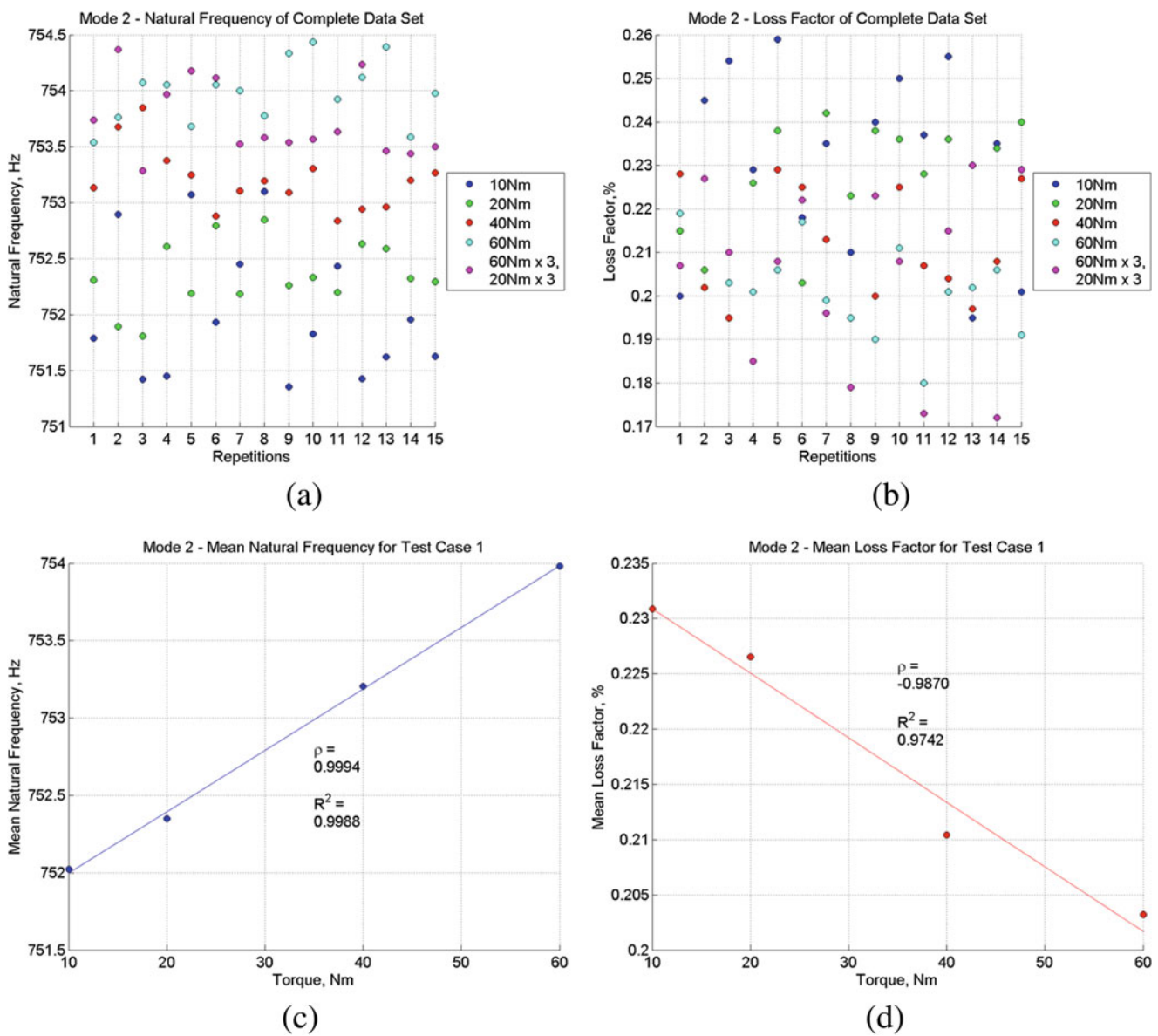

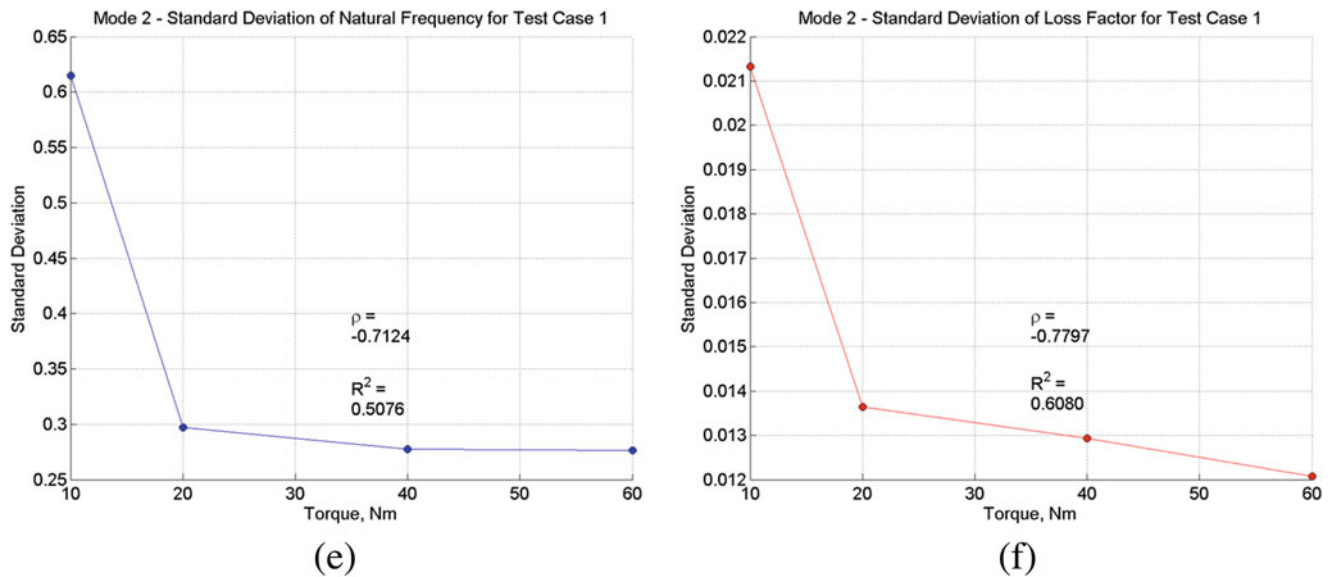Fig. 29.16 Natural frequency and damping for mode at 750 Hz

Fig. 29.16 (continued)

higher variability in both frequency and damping. The experimental outcome could be partially expected by inspection of the deformation of the flange as shown in Fig. 29.8. In this Figure it is possible to see that Modes 3 and 4 present the least deformation of the flanged area and so joints would be the least exercised during the vibration loading; hence the higher level of repeatability. Similarly, but less evident, it is presented for the I-beams in Sect. 29.4.2. There, two modes were analysed and Mode 1 showed a poorer standard deviation of the natural frequencies as shown in Fig. 29.15e, than Mode 2 as presented in Fig. 29.16e. Both show that an increased torque level makes the natural frequency of the assembly increasingly less variable. In both experimental cases the damping loss factors present significant scatter, in some cases more bounded but in others highly variable. This was somehow expected since a number of factors can influence the variance of the loss factor, which is not just due to the jointed areas, for example the method of suspension can play an important contribution.

29.6 Conclusions

This paper presented a research work on the variability of dynamic response of jointed structures. The aim was not to investigate the nonlinear dynamics of joints but, instead, to observe how variable both natural frequency and loss factor are when the joint is open and closed several times. Assembled structures are maintained and it is common to open and close joints. The major challenge is given by the large variability of both frequency and damping this will create a level of aleatory uncertainty. It is possible to say from an experimental point of view that some response modes presented less variability to the assembly procedure that other modes investigated. The true physics is not identified but an explanation can be given by saying that level of deformation of the jointed interfaces is smaller for some modes than for others. Whichever contact stiffness at the interface and any consequent stick-slip condition that follows will be mode dependent and so some modes will be less sensitive to those conditions and thus resulting in less variable natural frequency.

References

1. Ma, X., Bergman, L., Vakakis, A.: Identification of bolted joints through laser vibrometry. J. Sound Vib. **246**(3), 441–460 (2001)
2. Ouyang, H., Oldfield, M.J., Mottershead, J.E.: Experimental and theoretical studies of a bolted joint excited by a torsional dynamic load. Int. J. Mech. Sci. **48**(12), 1447–1455 (2006)
3. Gregory, D. L. et al, "Experimental Investigations of an Inclined Lap-Type Bolted Joint". http://prod.sandia.gov/techlib/access-control.cgi/2003/031193.pdf
4. Segalman DJ, et al. Handbook on Dynamics of Jointed Structures. http://prod.sandia.gov/techlib/access-control.cgi/2009/094164.pdf (2009)

Chapter 30
Predicting the Dynamics of Flexible Space Payloads Under Different Boundary Conditions Through Substructure Decoupling

Walter D'Ambrogio and Annalisa Fregolent

Abstract Flexible space payloads, such as solar panels or array antennas for space applications, can be attached to the body of the satellite using different types of joints. To predict the dynamic behaviour of such structures under different boundary conditions, it is convenient to start from their dynamic behaviour in free-free conditions. In fact, the effect of different boundary conditions, such as additional constraints or appended structures, can be taken into account starting from the frequency response functions in free-free conditions. In this situation, they would exhibit rigid body modes at zero frequency. To experimentally simulate free-free boundary conditions, flexible supports such as soft springs are typically used: with such arrangement, rigid body modes occur at low non-zero frequencies. Since flexible space payloads exhibit the first flexible modes at very low frequencies, the two sets of modes become coupled and the low frequency dynamics of the free-free structure cannot be estimated directly from measurements. To overcome this problem, substructure decoupling can be used, that allows to identify the dynamics of a substructure (i.e. the free-free panel) after measuring the FRFs on the complete structure (i.e. the panel with the supports) and from a dynamic model of the residual substructure (i.e. the supporting structure). Subsequently, the effect of additional boundary conditions can be predicted using an FRF condensation procedure. The procedure is tested on a reduced scale model of a space solar panel.

Keywords Low frequency flexible modes • Freely supported structures • Substructure decoupling • Experimental dynamic substructuring

30.1 Introduction

The goal of this paper is to investigate the possibility of sequentially applying substructure decoupling [1, 2] and constraint addition to the identification of compliant space structures, such as solar panels or array antennas for space applications, under different boundary conditions. Such structures are large thin structures, with the first flexible modes occurring at very low frequencies. They can be attached to the body of the satellite using different types of joints. To predict the dynamic behaviour of such structures under different boundary conditions, it is convenient to start from their dynamic behaviour in free-free conditions. In fact, the effect of different boundary conditions, such as additional constraints or appended structures, can be taken into account starting from the frequency response functions in free-free conditions. In this situation, they would exhibit rigid body modes at zero frequency.

To experimentally simulate free-free boundary conditions, flexible mounts such as soft springs are typically used: with such arrangement, rigid body modes occur at low but non-zero frequencies. Since compliant structures exhibit the first flexible modes at very low frequencies, the two sets of modes become coupled, and measured FRFs do not describe correctly the low frequency dynamics of the free-free structure.

Instead of using raw measurements, the effect of the supports on the measured FRFs can be removed by using substructure decoupling. It consists in the identification of a dynamic model of a structural subsystem, starting from an experimental dynamic model (e.g. FRFs) of the assembled structure and from a dynamic model of a known portion of it (the so-called residual substructure). The structure mounted on the supports plays the role of the assembled structure, whilst the supports alone are the residual substructure. The dynamics of the free-free structure can be finally reconstructed after measuring the

---

W. D'Ambrogio (✉)

Dipartimento di Ingegneria Industriale e dell'Informazione e di Economia, Università dell'Aquila, Via G. Gronchi, 18, I-67100, L'Aquila, Italy
e-mail: walter.dambrogio@univaq.it

A. Fregolent

Dipartimento di Ingegneria Meccanica e Aerospaziale, Università di Roma La Sapienza, Via Eudossiana 18, I 00184, Rome, Italy
e-mail: annalisa.fregolent@uniroma1.it

FRFs on the assembled structure and, if necessary, on the supports. Since the effect of the supports is going to be removed, one could use stiffer supports than those typically used to simulate free boundary conditions [3], thus making easier the test rig realization procedure. However, when using stiffer supports, the FRF level in the low frequency range decreases and so does the signal to noise ratio [4]. Therefore, the supports should be quite soft. Finally, the FRFs of the structure under different boundary conditions, such as additional kinematic constraints, can be predicted using an FRF condensation procedure detailed in Sect. 30.2.2 and similar to dynamic condensation. The procedure is tested on a reduced scale model of a space solar panel using different support conditions.

30.2   Theoretical Background

30.2.1   Decoupling Technique

Substructure decoupling represents a special case of experimental dynamic substructuring [5, 6]. A dynamic model of a substructure is identified, starting from an experimental dynamic model (e.g. FRFs) of the assembled structure RU and from a dynamic model of a known portion of it (the so-called residual substructure R). The unknown substructure U (N_U DoFs) is joined to the residual substructure R (N_R DoFs) by n_c coupling DoFs. The degrees of freedom of the assembled structure (N_{RU} DoFs) can be partitioned into coupling DoFs (c), internal DoFs of substructure U (u) and internal DoFs of substructure R (r).

Several assembly techniques can be used, e.g. dual assembly [1, 2] and hybrid assembly [7]. Using dual assembly, the predicted FRF matrix of the unknown substructure U is:

$$
\begin{aligned}
\mathbf{H}^{\mathbf{U}} = {} & \begin{bmatrix} \mathbf{H}^{\mathbf{RU}} & \mathbf{0} \\ \mathbf{0} & -\mathbf{H}^{\mathbf{R}} \end{bmatrix} - \begin{bmatrix} \mathbf{H}^{\mathbf{RU}} & \mathbf{0} \\ \mathbf{0} & -\mathbf{H}^{\mathbf{R}} \end{bmatrix} \begin{bmatrix} \mathbf{B}_{\mathbf{E}}^{\mathbf{RU}^{T}} \\ \mathbf{B}_{\mathbf{E}}^{\mathbf{R}^{T}} \end{bmatrix} \times \\
& \times \left(\begin{bmatrix} \mathbf{B}_{\mathbf{C}}^{\mathbf{RU}} & \mathbf{B}_{\mathbf{C}}^{\mathbf{R}} \end{bmatrix} \begin{bmatrix} \mathbf{H}^{\mathbf{RU}} & \mathbf{0} \\ \mathbf{0} & -\mathbf{H}^{\mathbf{R}} \end{bmatrix} \begin{bmatrix} \mathbf{B}_{\mathbf{E}}^{\mathbf{RU}^{T}} \\ \mathbf{B}_{\mathbf{E}}^{\mathbf{R}^{T}} \end{bmatrix} \right)^{+} \times \\
& \times \begin{bmatrix} \mathbf{B}_{\mathbf{C}}^{\mathbf{RU}} & \mathbf{B}_{\mathbf{C}}^{\mathbf{R}} \end{bmatrix} \begin{bmatrix} \mathbf{H}^{\mathbf{RU}} & \mathbf{0} \\ \mathbf{0} & -\mathbf{H}^{\mathbf{R}} \end{bmatrix}
\end{aligned}
\tag{30.1}
$$

where $\mathbf{H}^{\mathbf{RU}}$ and $\mathbf{H}^{\mathbf{R}}$ are the FRF matrices of the assembled structure RU and of the residual substructure R, $\mathbf{B_C} = [\mathbf{B}_{\mathbf{C}}^{\mathbf{RU}} \quad \mathbf{B}_{\mathbf{C}}^{\mathbf{R}}]$ and $\mathbf{B_E} = [\mathbf{B}_{\mathbf{E}}^{\mathbf{RU}} \quad \mathbf{B}_{\mathbf{E}}^{\mathbf{R}}]$ are signed Boolean matrices used to enforce compatibility and equilibrium at interface DoFs, and the symbol $^{+}$ denotes the generalized inverse.

As stated in [1], with the dual assembly, the rows and the columns of $\mathbf{H}^{\mathbf{U}}$ corresponding to compatibility and equilibrium DoFs appear twice. Obviously, only independent entries are retained.

30.2.2   Effect of Additional Constraints

If the dynamic behaviour of a given structure is known through its FRF matrix $\mathbf{H}$, the effect of additional kinematic constraints can be easily considered through an FRF condensation procedure similar to dynamic condensation. DoFs can be partitioned into unconstrained DoFs (master set M) and constrained DoFs (slave set S). It is assumed that the known displacement of the constrained DoFs is zero, i.e. $\mathbf{u_S} = \mathbf{0_S}$. It is also assumed that the applied forces $\mathbf{f_M}$ on the unconstrained DoFs are known. Therefore, the following relation can be written:

$$
\begin{bmatrix} \mathbf{H_{MM}} & \mathbf{H_{MS}} \\ \mathbf{H_{SM}} & \mathbf{H_{SS}} \end{bmatrix} \begin{bmatrix} \mathbf{f_M} \\ \mathbf{f_S} \end{bmatrix} = \begin{bmatrix} \mathbf{u_M} \\ \mathbf{0_S} \end{bmatrix}
\tag{30.2}
$$

By isolating the second row of the Eq. (30.2), it is obtained:

$$\mathbf{H_{SM}f_M + H_{SS}f_S = 0_S} \tag{30.3}$$

from which the constraint reactions $\mathbf{f_S}$ are:

$$\mathbf{f_S = -\left(H_{SS}\right)^{-1}H_{SM}f_M} \tag{30.4}$$

By back substituting $\mathbf{f_S}$ in the first row of Eq. (30.2), it is obtained:

$$\left[\mathbf{H_{MM} - H_{MS}\left(H_{SS}\right)^{-1}H_{SM}}\right]\mathbf{f_M = u_M} \quad \Rightarrow \quad \mathbf{H^C f_M = u_M} \tag{30.5}$$

where

$$\mathbf{H^C = H_{MM} - H_{MS}\left(H_{SS}\right)^{-1}H_{SM}} \tag{30.6}$$

represents the FRF matrix of the structure with additional kinematic constraints.

30.2.3 Sequential Application of Substructure Decoupling and Constraint Addition

In order to predict the dynamics of flexible space payloads under different boundary conditions, the following procedure can be applied:

- the FRFs $\mathbf{H^{RU}}$ of the structure of interest mounted on flexible supports (assembled structure) are obtained (measured);
- the FRFs $\mathbf{H^U}$ of the structure of interest in free-free conditions (i.e. after removing the effect of flexible supports) are identified using substructure decoupling;
- the FRFs $\mathbf{H^C}$ of the structure of interest under different boundary conditions (additional kinematic constraints) are obtained using the FRF condensation procedure, Eq. (30.6), on the FRFs $\mathbf{H^U}$ in free-free conditions:

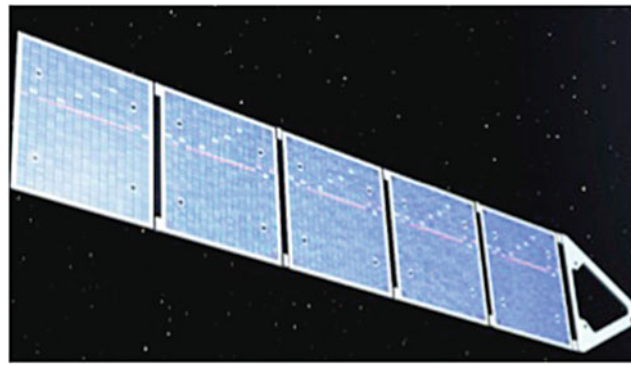$$\mathbf{H^C = H_{MM}^U - H_{MS}^U\left(H_{SS}^U\right)^{-1}H_{SM}^U} \tag{30.7}$$

30.3 Full Scale Structure and Reduced Scale Model

The full scale structure is the solar panel on satellite Sentinel-I. The spacecraft and the solar panel are shown in Figs. 30.1 and 30.2. The size of the solar panel is $7.36 \times 1.73 \times 0.024$ m.
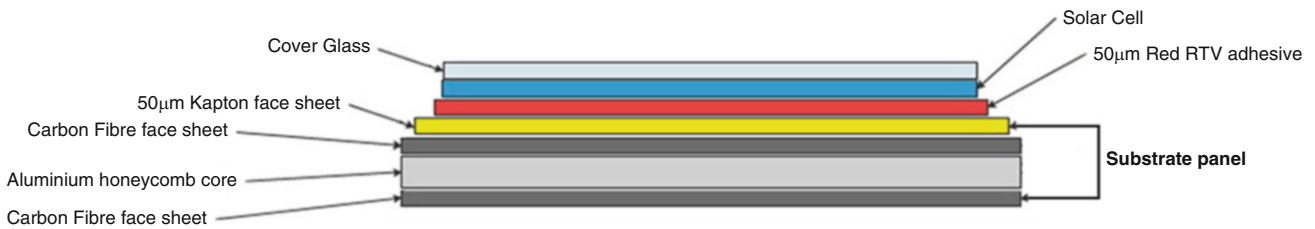
The cross section characteristics of the solar panel are quite complex as shown in Fig. 30.3. An FE model of the full scale structure is built to determine reference natural frequencies and mode shapes. Due to the large size of the solar panel and
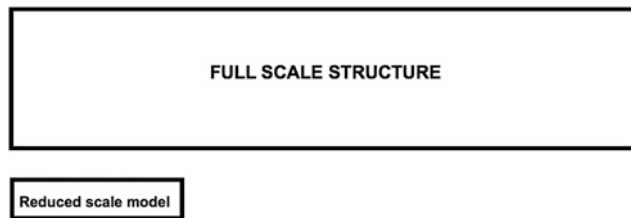

Fig. 30.1 Satellite Sentinel-I

Fig. 30.2 Solar panel on satellite Sentinel-I

Fig. 30.3 Cross section characteristics of solar panel

Fig. 30.4 Comparison between the full scale structure and the reduced scale model

Table 30.1 Comparison between natural frequencies of the two models (B = bending; T = torsional)

Mode	Full scale model [Hz]	Reduced scale model [Hz]	Error [%]
1B	3.88	3.90	0.52
1T	9.70	9.38	−3.30
2B	10.72	10.82	0.93
2T	20.00	19.47	−2.65
3B	21.01	21.35	1.62
3T	31.46	30.92	−1.72
4B	34.63	35.46	2.40
4T	44.54	44.31	−0.52

to the limited availability and high cost of the materials used to build such systems, the experimental analysis is carried out on an aluminum scale model. The reduced scale model should have a dynamic behavior very close to that of the true solar panel, and specifically very similar natural frequencies and mode shapes.

The aspect ratio (length over width) of the full scale panel is about 4. To avoid possible inversions of natural frequencies corresponding to different mode shapes (e.g. flexural and torsional), the aspect ratio of the reduced scale model is kept around the same value. The thickness is selected so as to minimize the natural frequency error. The size of the reduced scale model is 2.00 × 0.50 × 0.003 m. A visual comparison between the full scale structure and the reduced scale model is shown in Fig. 30.4.

The natural frequencies of the full and reduced scale models are compared in Table 30.1, showing that the scale reduction is acceptable.

30.4   Simulated Results

30.4.1   Decoupling

In view of the application of decoupling techniques to the identification of the free dynamics of the panel, a fixture to support the panel and to connect it to the ground is also designed.

A very simple choice is to support the panel with four soft springs (see Fig. 30.5), such that the frequency of the first rigid body mode of the panel be lower than that of the first flexible mode of the panel. The springs are non symmetrically located on four points: point 1 is 430 mm from the left edge and 20 mm from the bottom edge; point 2 is 430 mm from the left edge and 30 mm from the top edge; point 3 is 370 mm from the right edge and 30 mm from the top edge; point 4 is 370 mm from the right edge and 20 mm from the bottom edge.

By using four commercial springs, with stiffness $k = 720 \, \text{N/m}$, and considering that the mass of the panel is 8.13 kg, a natural frequency of the heave mode of about 3 Hz is obtained which is lower than the first bending mode at 3.9 Hz. An advantage of using springs with known stiffness instead of a more complicated supporting structure, is that the FRFs of the residual substructure (springs) needs not to be measured. Furthermore, the predicted FRF matrix of the unknown substructure can be explicitly found by considering that the receptance matrix of the residual substructure is:

$$\mathbf{H^R} = \begin{bmatrix} 1/k & 0 & 0 & 0 \\ 0 & 1/k & 0 & 0 \\ 0 & 0 & 1/k & 0 \\ 0 & 0 & 0 & 1/k \end{bmatrix} \tag{30.8}$$

and, by assuming that two internal DoFs of substructure U are measured, the matrices used to enforce compatibility and equilibrium at the four interface DoFs are:

$$\mathbf{B_C^{RU}} = \mathbf{B_E^{RU}} = [\mathbf{I_4} \quad \mathbf{O}_{4,2}] \qquad \mathbf{B_C^R} = \mathbf{B_E^R} = -\mathbf{I_4} \tag{30.9}$$

where $\mathbf{I}_n$ is the $n \times n$ identity matrix and $\mathbf{O}_{n,m}$ is the $n \times m$ matrix of zeros, being m the number of internal DOFs of substructure U. From Eq. (30.1), after some algebraic manipulations, it is found:

$$\mathbf{H^U} = \begin{bmatrix} \mathbf{H^{RU}} - \mathbf{H^{RU}} \mathbf{B_E^{RU}}^T (\hat{\mathbf{H}}^{RU} - \mathbf{H^R})^{-1} \mathbf{B_C^{RU}} \mathbf{H^{RU}} & -\mathbf{H^{RU}} \mathbf{B_E^{RU}}^T (\hat{\mathbf{H}}^{RU} - \mathbf{H^R})^{-1} \mathbf{H^R} \\ -\mathbf{H^R} (\hat{\mathbf{H}}^{RU} - \mathbf{H^R})^{-1} \mathbf{B_C^{RU}} \mathbf{H^{RU}} & -\mathbf{H^R} - \mathbf{H^R} (\hat{\mathbf{H}}^{RU} - \mathbf{H^R})^{-1} \mathbf{H^R} \end{bmatrix} \tag{30.10}$$

where $\hat{\mathbf{H}}^{RU} = \mathbf{B_C^{RU}} \mathbf{H^{RU}} \mathbf{B_E^{RU}}$ is a 4×4 matrix that represents the FRF of the assembled system at the interface DoFs.
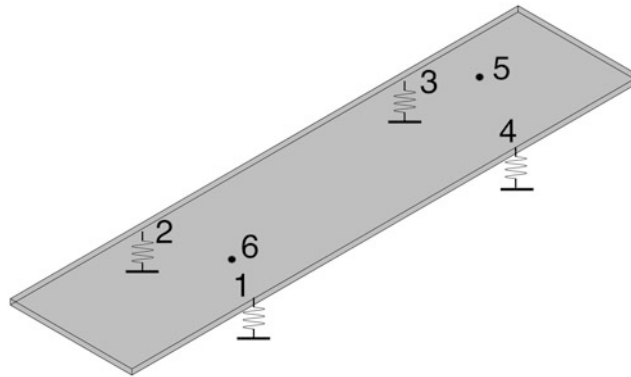
Fig. 30.5   Panel supported by four springs

To check the feasibility of the idea, an FE model of the assembled structure is built, from which numerical Frequency Response Functions (FRFs) to be used for decoupling are obtained.

To simulate the effect of noise on the FRFs, a random perturbation is generated and it is added to the FRFs $\hat{H}_{rs}$ computed from the FE model of the assembled structure:

$$H_{rs}(\omega_k) = \hat{H}_{rs}(\omega_k) + N_{rs}(\omega_k)\,\sigma_{rs}\,p \tag{30.11}$$

where:

- $N_{rs}(\omega_k)$ is the Fourier transform of a band limited white noise $n_{rs}(t)$ having zero mean and unit standard deviation, obtained by low-pass filtering, in the frequency band of interest, a broad band white noise $w_{rs}(t)$;
- σ_{rs} is an estimate of the standard deviation of the response at DoF r to a unit excitation at DoF s (i.e. H_{rs});
- p represents the noise level, i.e. $p = 0.05$ stands for 5% noise.

Since the FRFs of the residual substructure are computed from the known stiffness of the four springs, no noise should be added to such FRFs.

First, the decoupling procedure is applied using noise free FRFs. The FRF predicted on point 5 of the unknown substructure is shown in Fig. 30.6 in the frequency range 0–50 Hz, to highlight the low frequency behaviour. As expected, it is completely superimposed to the reference FRF provided by the FE model, showing that the procedure is carried out correctly.

The decoupling procedure is then applied using FRFs polluted with 3% noise (the noise level is referred to the RMS value of the FRF in the frequency band of interest 0–150 Hz). A typical noise polluted FRF is compared with a noise free FRF in Fig. 30.7. The effect of noise is mostly visible for low values of the FRF.
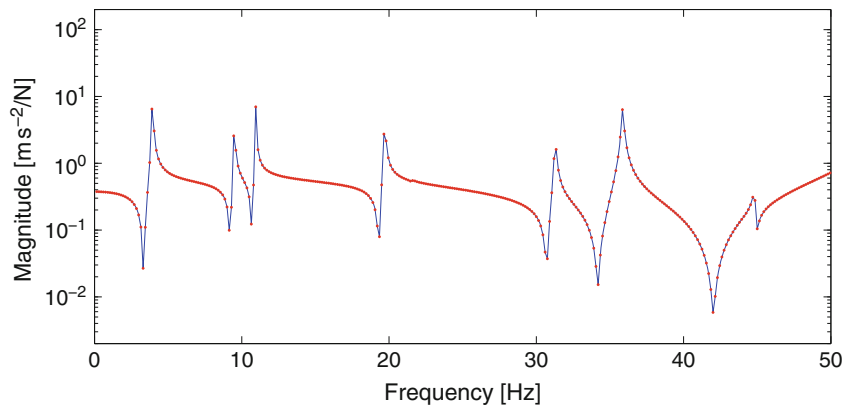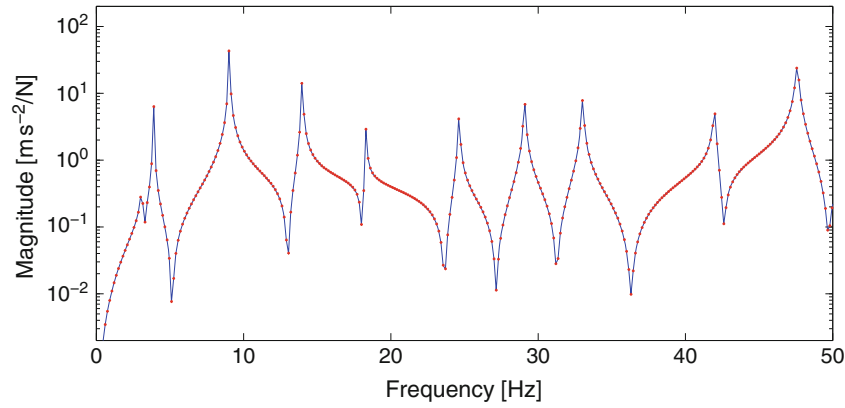

Fig. 30.6 $H^U_{5z,5z}$: true (—), predicted using noise free FRFs ($***$)
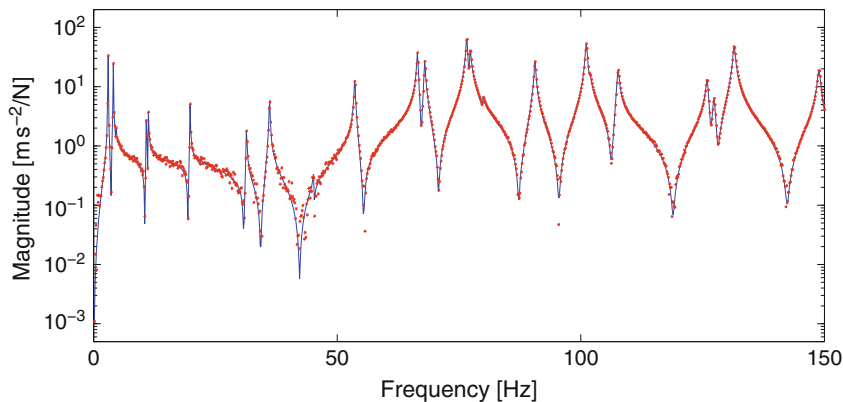
Fig. 30.7 $H^{RU}_{5z,5z}$: noise free (—), 3% noise ($***$)
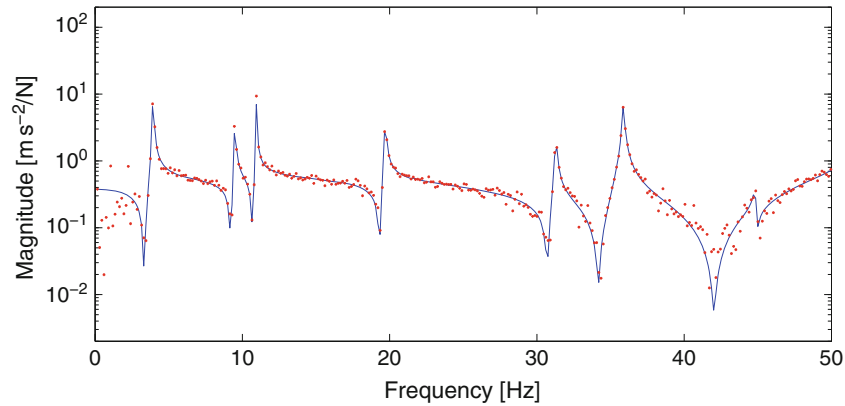
Fig. 30.8 $H^U_{5z,5z}$: true (—), predicted using 3% noise ($***$)

Fig. 30.9 $H^C_{5z,5z}$: true (—), predicted using noise free FRFs($***$)

The FRF predicted on point 5 of the unknown substructure, from FRFs of the assembled structure polluted with 3% noise, is shown in Fig. 30.8. The very low frequency range shows some scatter but the first natural frequency of the unknown substructure is correctly identified.

It is expected that similar or even harder difficulties can be encountered when using experimental data.

30.4.2 Addition of Constraints

Starting from the FRFs of the free-free panel obtained in the previous section using substructure decoupling, the effect of additional constraints is predicted using the FRF condensation procedure.

Results obtained by blocking DoFs $2z$, $3z$, $4z$ are shown. Therefore, master DoFs are $1z$, $5z$, $6z$. True FRFs of the panel with DoFs $2z$, $3z$, $4z$ blocked are computed using an FE model.

The FRF predicted on point 5 of the additionally constrained structure starting from noise free FRFs is shown in Fig. 30.9. As expected, it is completely superimposed to the true FRF showing that the procedure works correctly.

The FRF predicted on point 5 of the additionally constrained structure starting from FRFs polluted with 3% noise is shown in Fig. 30.10. As expected, noise in the starting FRFs gets amplified during each step of the procedure: first, at the end of the decoupling procedure used to obtain the FRFs of the free structure; then, at the end of the procedure used to add kinematic constraints. The effect is a significant amount of scatter below 10 Hz that completely hides the first resonance peak which is probably close to a nodal line of the first mode.
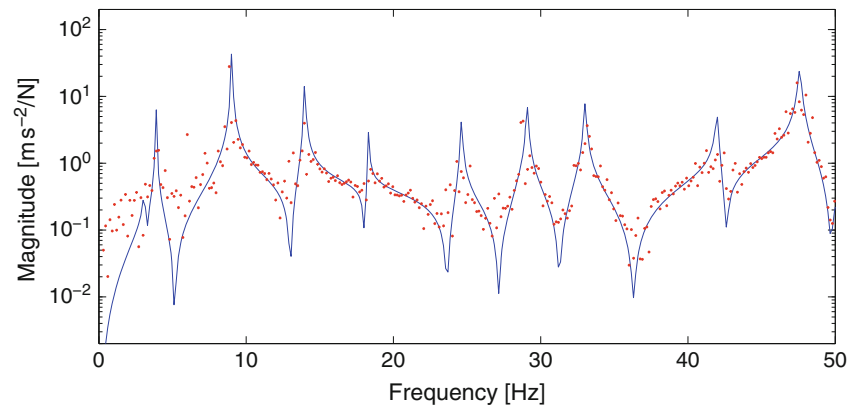
Fig. 30.10 $H^C_{5z,5z}$: true (—), predicted using 3% noise (∗∗∗)
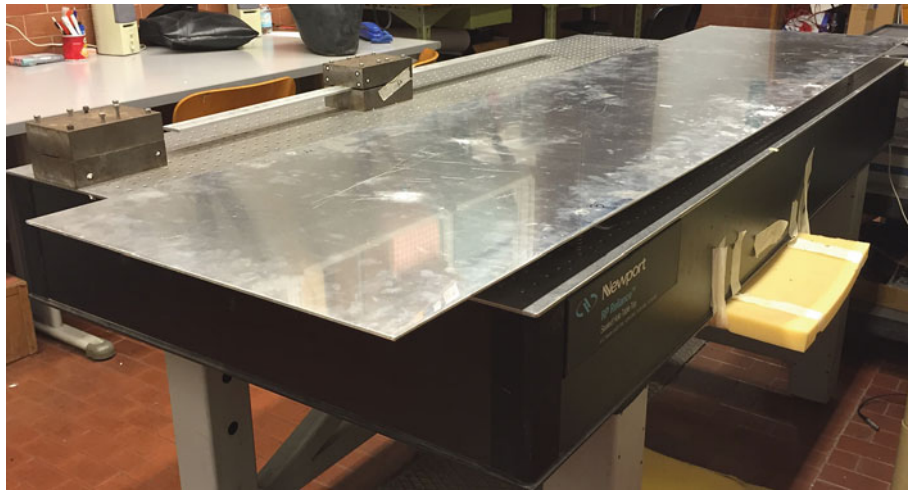
Fig. 30.11 Reduced scale model of the space solar panel

30.5   Further Developments and Conclusions

An experimental demonstration of the proposed procedure is planned in the near future. To this aim, a reduced scale model of the space solar panel is built, see Fig. 30.11, and it is laid down on soft springs. It will be subjected to laboratory tests to obtain the experimental FRFs to be used for substructure decoupling and for adding different boundary conditions.

In this paper, the sequential application of substructure decoupling and constraint addition, in order to predict the dynamics of very flexible structures under different boundary conditions, is tested using simulated data. Using noise free data, the procedure provides correct results, i.e. the same FRFs obtained by an FE model with additional constraints. Using noise polluted data, results of substructure decoupling are still acceptable whilst results after adding constraints show a more significant scatter due to error amplification that occurs at each stage of the procedure.

References

1. D'Ambrogio, W., Fregolent, A.: The role of interface DoFs in decoupling of substructures based on the dual domain decomposition. Mech. Syst. Signal Process. **24**(7), 2035–2048 (2010)
2. Voormeeren, S.N., Rixen, D.J.: A family of substructure decoupling techniques based on a dual assembly approach. Mech. Syst. Signal Process. **27**, 379–396 (2012)

3. D'Ambrogio, W., Di Nucci, N., Fregolent, A.: Experimental identification of flexible space payloads by substructure decoupling. In: Proceedings of 34th IMAC, Orlando, Jan 2016
4. D'Ambrogio, W., Fregolent, A.: Ground test identification of pliable space structures by decoupling techniques. In: Sas, P., Moens, D., van de Walle, A. (eds.) Proceedings of ISMA 2016 – International Conference on Noise and Vibration Engineering, Leuven, Sept 2016, pp. 2161–2168 (2016)
5. Jetmundsen, B., Bielawa, R., Flannelly, W.: Generalised frequency domain substructure synthesis. J. Am. Helicopter Soc. **33**(1), 55–64 (1988)
6. de Klerk, D., Rixen, D.J., Voormeeren, S.: General framework for dynamic substructuring: history, review, and classification of techniques. AIAA J. **46**(5), 1169–1181 (2008)
7. D'Ambrogio, W., Fregolent, A.: Inverse dynamic substructuring using direct hybrid assembly in the frequency domain. Mech. Syst. Signal Process. **45**(2), 360–377 (2014)

Chapter 31
Evolutionary Identification of Block-Structured Systems

M. Schoukens and K. Worden

Abstract The identification of a nonlinear model often involves a significant amount of user interaction. The proposed SADE evolutionary algorithm-based identification approach for block-structured systems reduces this user interaction to a minimum. This is illustrated in this paper for the Wiener-Hammerstein class of systems. On top of this, most of the assumptions and limitations on the considered Wiener-Hammerstein system class can be omitted compared to the popular BLA and correlation based approaches. The developed identification algorithm is applied on the 2009 Wiener-Hammerstein benchmark to illustrate its good performance.

Keywords Wiener-Hammerstein • Block-Oriented • Nonlinear Systems • System Identification • Evolutionary Algorithms

31.1 Introduction

Nonlinear models are becoming more and more important nowadays to obtain a better insight in the behaviour of the system under test, to compensate for a potential nonlinear behaviour, or to improve control performance. One of the more popular nonlinear model structures is the block-oriented model [1]. Block-oriented nonlinear models are quite simple to understand and easy to use, due to the separation of the nonlinear dynamic behaviour into linear time invariant (LTI) dynamics and static nonlinearities. The Wiener-Hammerstein system class can be seen as a generalisation of the popular Wiener and Hammerstein system classes. A Wiener-Hammerstein system is a block oriented system where the static nonlinearity is sandwiched in between two LTI blocks (see Fig. 31.1).

The problem of identifying a Wiener-Hammerstein system is challenging since the nonlinear subsystem is inaccessible from both the input and the output. A variety of Wiener-Hammerstein identification methods have been developed over the last years using different approaches. Two nonparametric methods are described in [2, 3] using carefully designed input signals, Volterra (and tensor decomposition) based approaches are presented in [4–6], and some methods use evolutionary algorithms [7–9] to solve the nonlinear optimisation problem. A wide range of approaches use the Best Linear Approximation (BLA) [10, 11], or a similar correlation analysis, as a starting point for the algorithm, e.g. [3, 8, 12–16]. The interest in the Wiener-Hammerstein identification problem is also illustrated by the two Wiener-Hammerstein benchmarks that are available online [17, 18].

This paper proposes to use the SADE evolutionary algorithm optimisation approach [19, 20] to tackle the Wiener-Hammerstein identification problem in a user-friendly way. The SADE algorithm has proven its robustness already in the past on the identification of hysteretic systems [21, 22]. The proposed identification algorithm requires very little user interaction. On top of this, most of the assumptions and limitations on the system class can be omitted compared to the BLA and correlation based approaches.

The proposed evolutionary approach is very different from the one reported in [8], where the evolutionary optimisation is used only for the pole-zero allocation problem reported in [13]. The approaches that are presented in [7, 9] are more similar to the method presented in this paper. However, [7] only considers the problem where the LTI blocks are represented by a

M. Schoukens
Department of ELEC, Vrije Universiteit Brussel, Pleinlaan 2, B-1050, Brussels, Belgium

K. Worden (✉)
Dynamics Research Group, Department of Mechanical Engineering, University of Sheffield, Mappin Street, S1 3JD, Sheffield, UK
e-mail: k.worden@sheffield.ac.uk
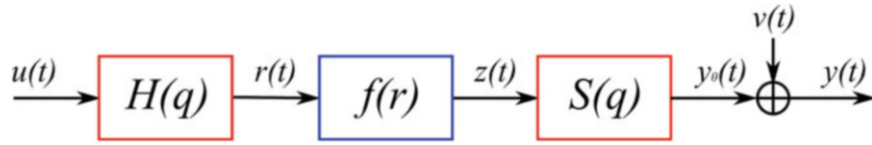
Fig. 31.1 A Wiener-Hammerstein system consists of a static nonlinear block f(r) sandwiched in between two LTI blocks $H(q)$ and $S(q)$

FIR model, and a simplified differential evolution algorithm is used. The method presented in [9] uses a biosocial culture algorithm. It is comparable to the approach presented here, although it requires more hyperparameters to be selected by the user.

The remainder of the paper introduces the Wiener-Hammerstein identification problem (Sect. 31.2), discusses the evolutionary algorithm-based identification method (Sect. 31.3) and illustrates the effectiveness of the method in Sect. 31.4 on the 2009 Wiener-Hammerstein benchmark that was studied at the IFAC SYSID conference in 2009 [17].

31.2 Problem Formulation

Wiener-Hammerstein systems consist of a static nonlinear block that is sandwiched in between two LTI blocks (Fig. 31.1). The output $y(t)$ of a Wiener-Hammerstein system is given by:

$$y(t) = S(q) \left[f \left(H(q) \left[u(t) \right] \right) \right] + v(t), \tag{31.1}$$

where $u(t)$ is the known input signal, and $v(t)$ is an unknown additive disturbance with a finite variance acting on the output only. It is assumed that the input $u(t)$ is persistently exciting the system under test. The system blocks $H(q)$, $S(q)$ and $f(r)$ are given by:

$$H(q) = \frac{D(q)}{C(q)} = \frac{d_0 + d_1 q^{-1} + \ldots + d_{n_d} q^{-n_d}}{c_0 + c_1 q^{-1} + \ldots + c_{n_c} q^{-n_c}}, \tag{31.2}$$

$$S(q) = \frac{B(q)}{A(q)} = \frac{b_0 + b_1 q^{-1} + \ldots + b_{n_b} q^{-n_b}}{a_0 + a_1 q^{-1} + \ldots + a_{n_a} q^{-n_a}}, \tag{31.3}$$

$$f(r(t)) = \sum_{j=0}^{n_w} w_j f_j(r(t)), \tag{31.4}$$

where q^{-1} denotes the backwards shift operator, and f_j forms a set of nonlinear basis functions. Without limitation, it is assumed in the remainder of the paper that these nonlinear basis functions are given by $f_j(r) = r^j$. Note that the method itself is not limited to a nonlinearity that is given by a nonlinear basis function expansion. Other nonlinearity representations, such as neural networks, could also be used in combination with the SADE optimisation based approach.

The Wiener-Hammerstein structure is subject to some identifiabilty issues since only the signals $u(t)$ and $y(t)$ are known. A gain exchange is possible in between the two LTI and the static nonlinear blocks. Also a delay exchange is possible in between the two LTI blocks. To obtain a unique model representation, the first nonzero coefficients (the nonzero coefficients belonging to the lowest power of q^{-1}) of $D(q)$, $C(q)$, $B(q)$, $A(q)$ are set to zero, and all the full-sample delays are allocated to the LTI subsystem $H(q)$.

As a result, assuming that a_0, b_0, c_0 and d_0 are equal to units, the unknown parameter vector to estimate is given by:

$$\theta = \begin{bmatrix} a_1 & \ldots & a_{n_a} & b_1 & \ldots & b_{n_b} & c_1 & \ldots & c_{n_c} & d_1 & \ldots & d_{n_d} & w_0 & \ldots & w_{n_w} \end{bmatrix} \tag{31.5}$$

The model orders n_a, n_b, n_c, n_d and n_w are set here by the user, although they could be determined by cross-validation in a free machine learning approach.

31.3 Evolutionary Algorithm-Based Identification

31.3.1 SADE Algorithm

As it is often natural to frame system identification problems directly in terms of optimisation, it is thus natural to take advantage of the state of the art in optimisation. For some time now, evolutionary algorithms (EAs) have provided a powerful and versatile approach to optimisation and have therefore proved useful for SI. EAs began with the basic Genetic Algorithm (GA) and even the simplest form of that algorithm proved useful for SI; an early example of using a GA for the identification of Bouc-Wen hysteretic systems can be found in [21]. However, once real-parameter evolutionary schemes like Differential Evolution (DE) emerged [23], it quickly became clear that they offered major advantages for SI. The first application of DE for the Bouc-Wen model appeared in [24]. As in all evolutionary optimisation procedures, a population of possible solutions (here, the vector of parameter estimates), is iterated in such a way that succeeding generations of the population contain better solutions to the problem in accordance with the Darwinian principle of 'survival of the fittest'. The problem is framed here as a minimisation problem with a least squares cost function defined as:

$$V(\theta) = \frac{1}{N} \sum_{t=1}^{N} (y(t) - \hat{y}(t, \theta))^2 , \tag{31.6}$$

where N is the total number of samples in the estimation record, and $y(t, \theta)$ is the modeled output given by Eq. (31.1) using the parameter set θ.

The standard DE algorithm of reference [23] attempts to transform a randomly generated initial population of parameter vectors into an optimal solution through repeated cycles of evolutionary operations, in this case: *mutation*, *crossover* and *selection*. In order to assess the suitability of a certain solution, a cost or fitness function is needed; the cost function in Eq. (31.6) is the one used here. Figure 31.2 shows a schematic for the DE procedure for evolving between populations. The following process is repeated with each vector within the current population being taken as a *target vector*; each of these vectors has an associated cost taken from Eq. (31.6). Each target vector is pitted against a *trial vector* in a competition which results in the vector with lowest cost advancing to the next generation.

The mutation procedure used in basic DE proceeds as follows. Two vectors A and B are randomly chosen from the current population to form a vector differential $A - B$. A *mutated* vector is then obtained by adding this differential, multiplied by a scaling factor F, to a further randomly chosen vector C to give the overall expression for the mutated vector: $C + F(A - B)$. The scaling factor, F, is often found have an optimal value between 0.4 and 1.0.

The *trial vector* is the child of two vectors: the target vector and the mutated vector, and is obtained via a crossover process; in this work uniform crossover is used. Uniform crossover decides which of the two parent vectors contributes to each chromosome of the trial vector by a series of $D - 1$ binomial experiments. Each experiment is mediated by a crossover parameter C_r (where $0 \leq C_r \leq 1$). If a random number generated from the uniform distribution on [0,1] is greater than C_r, the trial vector takes its parameter from the target vector, otherwise the parameter comes from the mutated vector.

This process of evolving through the generations is repeated until the population becomes dominated by only a few low cost solutions, any of which would be suitable. Like the vast majority of optimisation algorithms, convergence to the global minimum is not guaranteed; however, one of the benefits of the evolutionary approach is that it more resistant to finding a local minimum.

A potential weakness of the standard implementation of the DE algorithm as described above is that it requires the prior specification of a number of *hyperparameters* (parameters which need to be specified before the algorithm can run). Apart from the population size, maximum number of iterations etc., the algorithm needs a priori specification of the scaling factor F and crossover probability C_r. The values used in [24] were chosen on the basis of trial and error; however, they are not guaranteed to work as well in all situations and an algorithm which establishes 'optimum' values for these parameters during the course of the evolution is clearly desirable. Such an algorithm is available in the form of the Self-Adaptive Differential Evolution (SADE) algorithm [19, 20]; the description and implementation of the algorithm here largely follows [20].

The development of the SADE algorithm begins with the observation that Storn and Price, the originators of DE, arrived at five possible strategies for the mutation operation [25]:

1. *rand1*: $M = A + F(B - C)$
2. *best1*: $M = X^* + F(B - C)$
3. *current-to-best*: $M = T + F(X^* - T) + F(B - C)$
4. *best2*: $M = X^* + F(A - B) + F(C - D)$
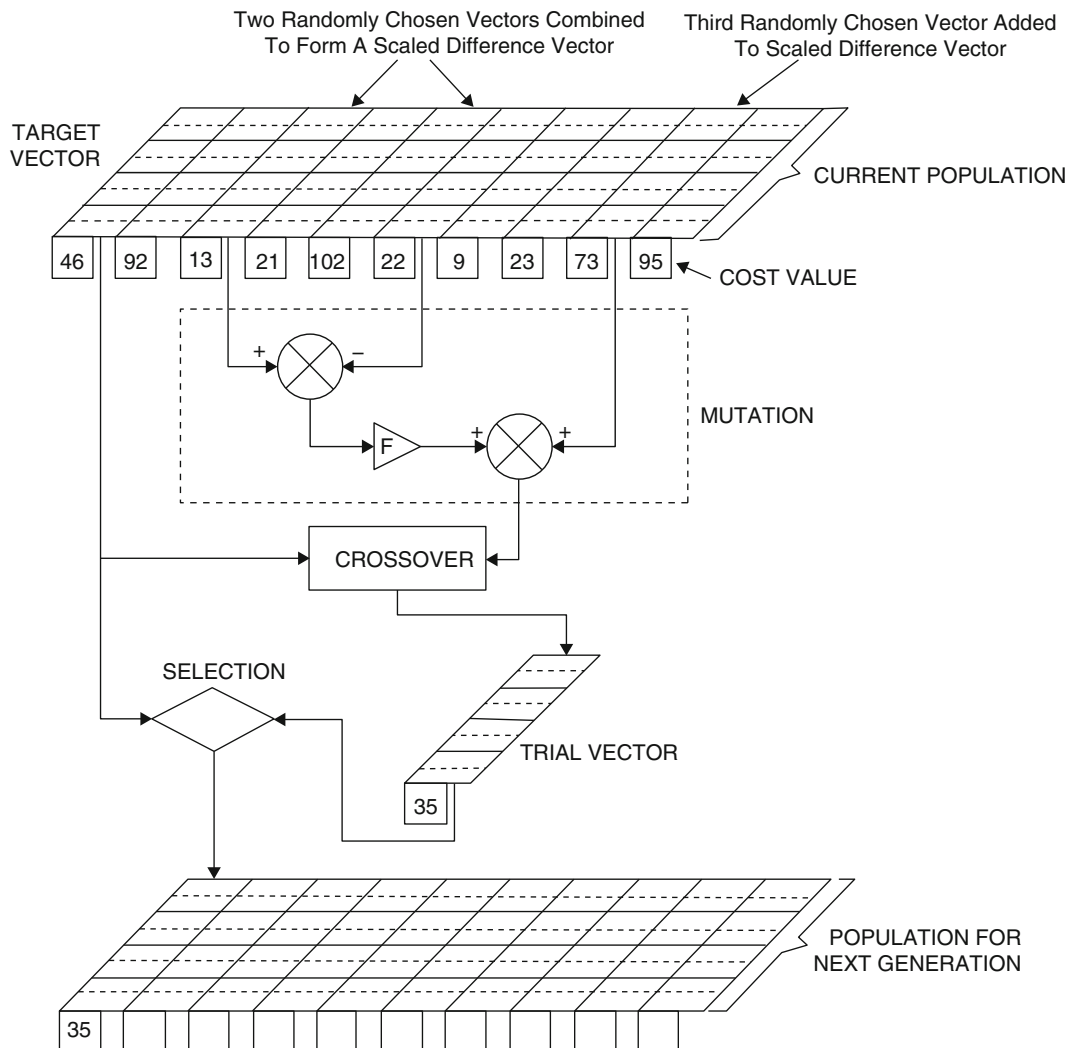5. *rand2*: $M = A + F(B - C) + F(D - E)$

Fig. 31.2 Schematic for the standard DE algorithm

where T is the current trial vector, X^* is the vector with (currently) best cost and (A, B, C, D, E) are randomly-chosen vectors in the population distinct from T. F is a standard (positive) scaling factor. The SADE algorithm also uses multiple variants of the mutation algorithm as above; however these are restricted to the following four:

1. *rand1*
2. *current-to-best2*: $M = T + F(X^* - T) + F(A - B) + F(C - D)$
3. *rand2*
4. *current-to-rand*: $M = T + K(A - T) + F(B - C)$

In the strategy *current-to-rand*, K is defined as a coefficient of combination and would generally be assumed in the range $[-0.5, 1.5]$; however, in the implementation of [20] and the one used here, the prescription $K = F$ is used to essentially restrict the number of tunable parameters. The SADE algorithm uses the standard crossover approach, except that at least one crossover is forced in each operation on the vectors. If mutation moves a parameter outside its allowed (predefined) bounds, it is pinned to the boundary. Selection is performed exactly as in DE; if the trial vector has smaller (or equal) cost to the target, it replaces the target in the next generation.

The adaption strategy must now be defined. First, a set of probabilities are defined: $\{p_1, p_2, p_3, p_4\}$, which are the probabilities that a given mutation strategy will be used in forming a trial vector. These probabilities are initialised to be all equal to 0.25. When a trial vector is formed during SADE, a roulette wheel selection is used to choose the mutation strategy on the basis of the probabilities (initially, all equal). At the end of a given generation, the numbers of trial vectors successfully surviving to the next generation from each strategy are recorded as: $\{s_1, s_2, s_3, s_4\}$; the numbers of trial vectors

from each strategy which are discarded are recorded as: $\{d_1, d_2, d_3, d_4\}$. At the beginning of a SADE run, the survival and discard numbers are established over the first generations, this interval is called the *learning period* (and is another example of a hyperparameter). At the end of the learning period, the strategy probabilities are updated by,

$$p_i = \frac{s_i}{s_i + d_i} \tag{31.7}$$

After the learning period, the probabilities are updated every generation but using survival and discard numbers established over a moving window of the last N_L generations. The algorithm thus adapts the preferred mutation strategies. SADE also incorporates adaption or variation on the hyperparameters F and C_r. The scaling factor F mediates the convergence speed of the algorithm, with large values being appropriate to global search early in a run and small values being consistent with local search later in the run. The implementation of SADE used here largely follows [19] and differs only in one major aspect, concerning the adaption of F. Adaption of the parameter C_r is based on accumulated experience of the successful values for the parameter over the run. It is assumed that the crossover probability for a trial is normally distributed about a mean $\overline{C}_r$ with standard deviation 0.1. At initiation, the parameter C_r is set to 0.5 to give equal likelihood of each parent contributing a chromosome. The crossover probabilities are then held fixed for each population index for a certain number of generations and then resampled. In a rather similar manner to the adaption of the strategy probabilities, the C_r values for trial vectors successfully passing to the next generation are recorded over a certain greater number of generations and their mean value is adopted as the next $\overline{C}_r$. The record of successful trials is cleared at this point in order to avoid long-term memory effects. The version of the algorithm here adapts F in essentially the same manner as C_r but uses the Gaussian $N(0.5, 0.3)$ for the initial distribution. At this point, the reader might legitimately argue that SADE has simply replaced one set of hyperparameters (F, C_r) with another (duration of the learning period etc.). In fact, because DE and SADE are heuristic algorithms, there is no analytical counter to this argument. However, the transition to SADE is justified by the fact that the algorithm appears to be very robust with respect to the new hyperparameters.

From an SI point of view there are a number of advantages to the evolutionary approaches. First of all, in general, EAs are quite resistant to stalling in local minima because they use a (potentially large) population of possible solutions. Specific to SI problems, EAs offer the advantages that they work just as well for problems which are nonlinear in the parameters or have hidden or latent variables; one only needs measurements of any states which appear in the cost function. Of course, there are disadvantages too; the algorithms can be slow, depending on the computational cost of the objective function and, because the algorithms are fundamentally heuristic, there is no recourse to mathematics in order to prove theorems on parameter bias etc.

31.3.2 Initialisation

At the start of the SADE algorithm a random initial population is generated. This population is generated here such that the LTI subsystems $H(q)$ and $S(q)$ are stable, and such that the parameters θ are limited within a given parameter range. The algorithm is implemented such that the parameters remain within that range during the optimisation.

31.4 Wiener-Hammerstein Benchmark Results

31.4.1 Benchmark Setup

A detailed description of the benchmark is given in [17]. The benchmark data are generated from a Wiener-Hammerstein nonlinear electronic circuit, as shown in Fig. 31.3. The first LTI block is a third order Chebyshev low-pass filter with 0.5 dB ripple and a cut-off frequency at 4.4 kHz. The second LTI block is a third order inverse Chebyshev low-pass filter with a -40 dB stop band starting at 5 kHz. The static nonlinearity is a one-sided saturation implemented as a resistor-diode network. The system is excited by low-pass filtered Gaussian noise, with cut-off frequency set at 10 kHz. The input and output signals are measured with a sampling frequency equal to 51.2 kHz.

The benchmark setup is chosen as an illustration since a good comparison with other identification methods is possible using this system. A wide range of results on the 2009 Wiener-Hammerstein benchmark are reported in [26].
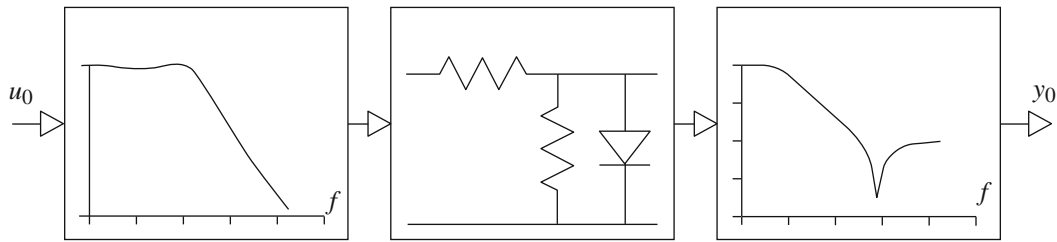
Fig. 31.3 Wiener-Hammerstein benchmark system

Table 31.1 Settings of the SADE optimisation algorithm

Population size	1600
Generation number	5000
Parameter range	$[-55]$
Update generation number	100
Mean update generation number	100
Strategy learning period	100

Table 31.2 Results on the 2009 Wiener-Hammerstein benchmark

| Run number	1	2	3	4	5	6	7	8	9	10
Estimation error rms (mV)	8.7	8.7	25.6	8.7	8.8	8.7	8.7	8.7	8.7	8.7
Estimation error mean (mV)	1.40	1.40	−1.81	1.40	1.43	1.40	1.40	1.40	1.40	1.40
Estimation error std (mV)	8.6	8.6	25.6	8.6	8.7	8.6	8.6	8.6	8.6	8.6
Validation error rms (mV)	9.3	9.3	32.0	9.3	9.5	9.3	9.3	9.3	9.3	9.3
Validation error mean (mV)	−0.33	−0.33	−0.50	−0.33	−0.36	−0.33	−0.33	−0.33	−0.33	−0.33
Validation error std (mV)	9.3	9.3	32.0	9.3	9.4	9.3	9.3	9.3	9.3	9.3

31.4.2 Model Estimation

The estimation of the model is performed on a small set of the available estimation data, only samples 4901–6000 are considered. The model orders n_a, n_b, n_c, n_d are set equal to 3, the static nonlinearity is estimated as a third degree polynomial. This results in a total of 16 free parameters to estimate.

The SADE algorithm is set to use a population size of 1600 and runs for 5000 iterations. The parameter values are limited to the range $[-5, 5]$, the exact settings of the SADE algorithm can be found in Table 31.1. To test the robustness of the proposed algorithm, ten different runs of the algorithm are made, each starting from a new, randomly generated, initial population.

31.4.3 Validation Results

The validation estimation results are reported in Table 31.2, as requested in [17] the root mean square error (RMSE) is used as the error criterion. The obtained RMSE is comparable with the one obtained by other Wiener-Hammerstein identification methods using a third-order polynomial static nonlinearity [26]. The time-domain validation output and the obtained model error are shown in Fig. 31.4. Note that the peaks in the error suggests that a further improvement of the RMSE can be expected if a higher order polynomial nonlinearity, or another nonlinearity structure is considered. Note that the proposed approach converges in 8 out of the 10 cases to the same minimum. Run number 5 is very near to this minimum, and after a closer inspection it turned out that this particular run was not yet fully converged to its minimum. Run number 3 got stuck in a local minimum.
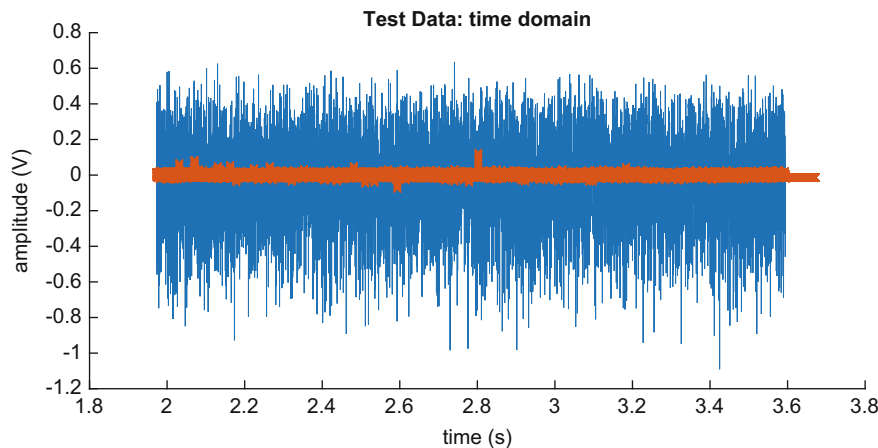
Fig. 31.4 Time-domain representation of the measured validation output (*blue*) and the model error (*red*)

31.5 Conclusions

This paper illustrates how evolutionary algorithms in general, and the SADE algorithm in particular, offer a robust and user-friendly optimisation tool for the identification of block-oriented structures. The Wiener-Hammerstein structure is studied in detail in this paper, however, one can expect to obtain similar results on other model structures.

The SADE evolutionary algorithm used in this paper requires almost no user interaction. It is known to be quite robust with respect to the setting of the hyperparameters. The main downside of the evolutionary algorithms is the rather heavy computational load.

References

1. Giri, F., Bai, E.W. (eds.): Block-Oriented Nonlinear System Identification. Volume 404 of Lecture Notes in Control and Information Sciences. Springer, Berlin/Heidelberg (2010)
2. Vandersteen, G., Rolain, Y., Schoukens, J.: Non-parametric estimation of the frequency-response functions of the linear blocks of a Wiener-Hammerstein model. Automatica **33**(7), 1351–1355 (1997)
3. Tiels, K., Schoukens, M., Schoukens, J.: Initial estimates for Wiener-Hammerstein models using phase-coupled multisines. Automatica **60**, 201–209 (2015)
4. Weiss, M., Evans, C., Rees, D.: Identification of nonlinear cascade systems using paired multisine signals. IEEE Trans. Instrum. Meas. **47**(1), 332–336 (1998)
5. Tan, A.H., Godfrey, K.: Identification of Wiener-Hammerstein models using linear interpolation in the frequency domain (LIFRED). IEEE Trans. Instrum. Meas. **51**(3), 509–521 (2002)
6. Ben Ahmed, Z., Favier, G., Derbel, N.: Tensor-based methods for Wiener-Hammerstein system identification. In: 10th International Multiconference on Systems, Signals Devices (SSD), 2013, Niagara Falls, pp. 1–6, Mar 2013
7. Dewhirst, O.P., Simpson, D.M., Angarita, N., Allen, R., Newland, P.L.: Wiener-Hammerstein parameter estimation using differential evolution: application to limb reflex dynamics. In: International Conference on Bio-inspired Systems and Signal Processing, Valencia, pp. 271–276 (2010)
8. Schoukens, M., Vandersteen, G., Rolain, Y., Ferranti, F.: Fast identification of Wiener-Hammerstein systems using discrete optimization. IET Electron. Lett. **50**(25), 1942–1944 (2014)
9. Naitali, A., Giri, F.: Wiener-Hammerstein system identification – an evolutionary approach. Int. J. Syst. Sci. **47**(1), 45–61 (2016)
10. Pintelon, R., Schoukens, J.: System Identification: A Frequency Domain Approach, 2nd edn. Wiley/IEEE Press, Hoboken (2012)
11. Schoukens, J., Vaes, M., Pintelon, R.: Linear system identification in a nonlinear setting: nonparametric analysis of the nonlinear distortions and their impact on the best linear approximation. IEEE Control Syst. **36**(3), 38–69 (2016)
12. Billings, S.A., Fakhouri, S.Y.: Identification of a class of nonlinear systems using correlation analysis. Proc. Inst. Electr. Eng. **125**(7), 691–697 (1978)

13. Sjöberg, J., Lauwers, L., Schoukens, J.: Identification of Wiener-Hammerstein models: two algorithms based on the best split of a linear model applied to the SYSID'09 benchmark problem. Control Eng. Pract. **20**(11), 1119–1125 (2012)
14. Schoukens, M., Pintelon, R., Rolain, Y.: Identification of Wiener-Hammerstein systems by a nonparametric separation of the best linear approximation. Automatica **50**(2), 628–634 (2014)
15. Vanbeylen, L.: A fractional approach to identify Wiener-Hammerstein systems. Automatica **50**(3), 903–909 (2014)
16. Giordano, G., Sjöberg, J.: A time-domain fractional approach for Wiener-Hammerstein systems identification. In: 17th IFAC Symposium on System Identification SYSID 2015, Beijing, vol. 48, no. 28, pp. 1232–1237 (2015)
17. Schoukens, J., Suykens, J.A.K., Ljung, L.: Wiener-Hammerstein benchmark. In: 15th IFAC Symposium on System Identification (SYSID), Saint-Malo, July 2009
18. Schoukens, M., Noël, J.P.: Wiener-Hammerstein benchmark with process noise. In: Workshop on Nonlinear System Identification Benchmarks, Brussels, pp. 15–19, Apr 2016
19. Qin, A.K., Suganthan, P.N.: Self-adaptive differential evolution algorithm for numerical optimization. In: 2005 IEEE Congress on Evolutionary Computation, Edinburgh, pp. 1785–1791 (2005)
20. Huang, V.L., Qin A.K., Suganthan, P.N.: Self-adaptive differential evolution algorithm for constrained real-parameter optimization. In: IEEE Congress on Evolutionary Computation, Vancouver, pp. 17–24 (2006)
21. Deacon, B.P., Worden, K.: Identification of hysteretic systems using genetic algorithms. In: Proceedings of EUROMECH – 2nd European Nonlinear Oscillations Conference, Prague, pp. 55–58 (1996)
22. Worden, K., Manson, G.: On the identification of hysteretic systems. Part I: fitness landscapes and evolutionary identification. Mech. Syst. Signal Process. **29**(0), 201–212 (2012)
23. Price, K., Storn, R.: Differential evolution – a simple and efficient heuristic for global optimization over continuous spaces. J. Glob. Optim. **11**(4), 341–359 (1997)
24. Kyprianou, A., Worden, K., Panet, M.: Identification of hysteretic systems using the differential evolution algorithm. J. Sound Vib. **248**(2), 289–314 (2001)
25. Storn, R., Price, K.: Technical report. http://www.icsi.berkeley.edu/~storn/code.html. Accessed 27 oct 2009
26. Marconato, A., Schoukens, M., Rolain, Y., Schoukens, J.: Study of the effective number of parameters in nonlinear identification benchmarks. In: 52nd IEEE Conference on Decision and Control, Florence, pp. 4308–4313, Dec 2013,

Chapter 32
Modal Analysis of Transmission Line Cables

Nilson Barbieri, Marcos José Mannala, Renato Barbieri, Mayara Kelly Tenório Calado, and Gabriel de Sant'Anna Vitor Barbieri

Abstract The objective of this work is validate a mathematical model (Finite Element Method) for dynamic simulation of transmission lines cables to different mechanical loads. For better electrical and structural purposes were tested three different types of new cables available on the market, Tern (CAA), 1120 and 6201 (alloy) with variable mechanical loads (between 15 and 35% of rupture stress). The dynamic tests were performed on a test bench of transmission line components using an impact hammer system for excitation and five accelerometers to obtain the vibrational data. The dynamic tests used samples with 35 and 54 m long with different mechanical tensile loads. Mathematical models (linear and nonlinear) obtained by the Finite Element Method were used to obtain the corresponding numerical modal data. The results showed that the linear model has great errors when the cable is large and low mechanical traction were used (errors in the order of 16%). The nonlinear model shows better agreement between the numerical and experimental results (errors in the order of 2.5%).The numerical results obtained using the non-linear model showed good agreement with experimental data for all the mechanical tensile variation range used and for three different types of cable.

Keywords Transmission line cable • Modal analysis • FEM • Nonlinear model

32.1 Introduction

The dynamics of electric transmission line cables has been studied for many years, because the induced mechanical vibrations can cause damage not only to the cables, but also the structures and accessories installed on the lines. These vibrations can oscillate structures and components and are most commonly induced by the wind. The main consequence is the appearance of damage by fatigue of the aluminium wires, often in preceding points to their insertions in the suspension brackets or anchor due to the additional alternating voltages to those provided for in the project. Thus, the useful life of the line is related to the vibrations and the level of its amplitude and frequency. In conventional transmission lines, one or more Stockbridge dampers are installed on the conductor in order to minimize the amplitudes of vibrations caused by wind. This problem has been studied in various parts of the world with solutions and applications of the most varied possible. This has allowed the increase in the size of the cables and the mechanical loading of these lines with a consequent increase in energy transportation and life of drivers and accessories. Therefore, it is also considered, the constant need to improve the design tools, simulation and validation of computational models [1–3], aimed in the first instance, the reduction of costs of new projects and operational changes in existing lines.

N. Barbieri (✉)
Programa de Pós-Graduação em Engenharia Mecânica, Pontifícia Universidade Católica do Paraná (PUCPR), Curitiba, Brazil

Universidade Tecnológica Federal do Paraná (UTFPR), Curitiba, Brazil
e-mail: nilson.barbieri@pucpr.br

M.J. Mannala
Institutos LACTEC, Curitiba, Brazil

R. Barbieri
Faculdade de Engenharia de Joinville-FEJ, Joinville, Brazil

M.K.T. Calado • G. de Sant'Anna Vitor Barbieri
Programa de Pós-Graduação em Engenharia Mecânica, Pontifícia Universidade Católica do Paraná (PUCPR), Curitiba, Brazil

32.2 Results

Figure 32.1 gives an overview of the bench used for modal testing. In the figure is shown a cable with a Stockbridge damper attached in the same.

The sensors used to obtain the vibrational data for the three types of cables are accelerometers PCB model 352C33 and 338C04. The external force was applied by impact hammer PCBI 291M55 at a distance of 0.5 m from the end. The accelerometers were placed at positions L/16, L/8, L/4, 3L/8 and L/2 in the sample of length L. The rational fraction polynomial method (RFPM) is used to experimental modal analysis. Figure 32.2 shows the curves of variation of the natural frequency of the first five vibration modes with respect to the cable mechanical tensile load. As expected, the values of the natural frequencies increase with increasing tensile load. The increases are higher for higher modes.

Figure 32.3 shows variations of frequencies of the first five modes obtained experimentally by linear numerical model and non-linear numerical model. It can be seen that the first mode presents some differences at low tensile loads. The differences are more pronounced using the linear model.

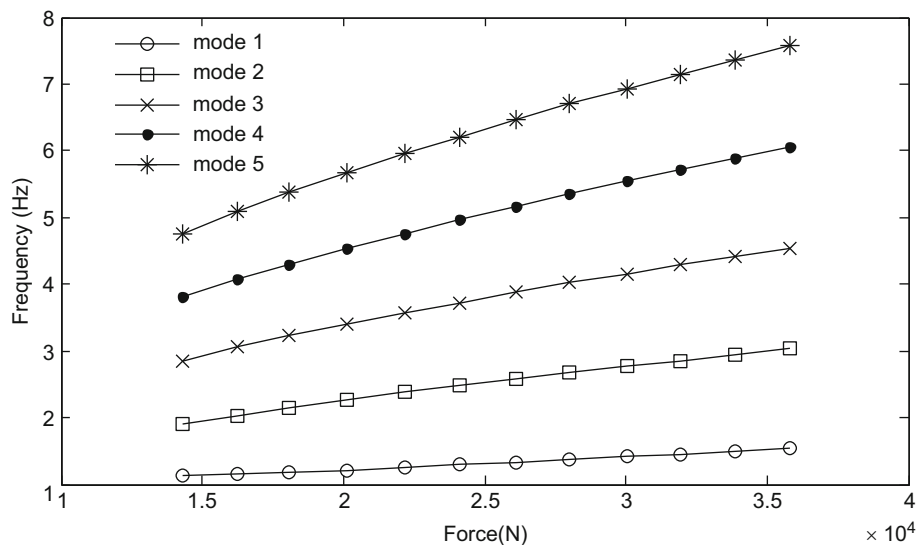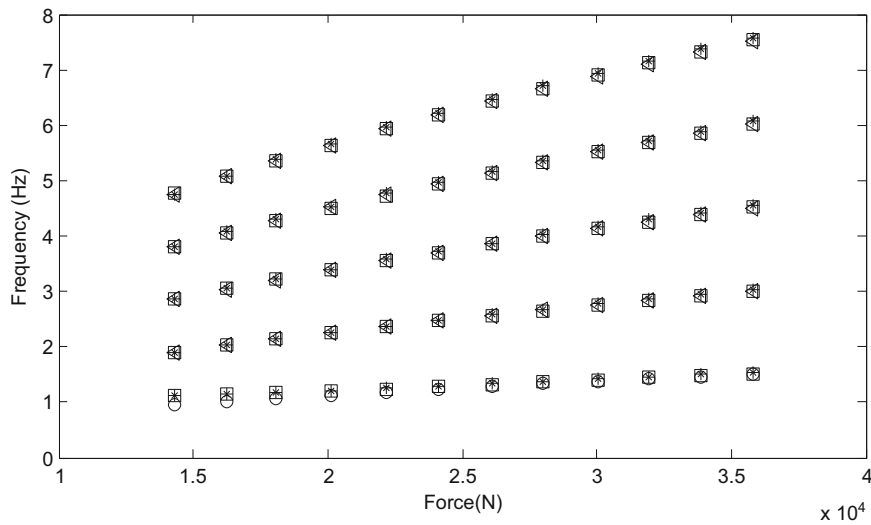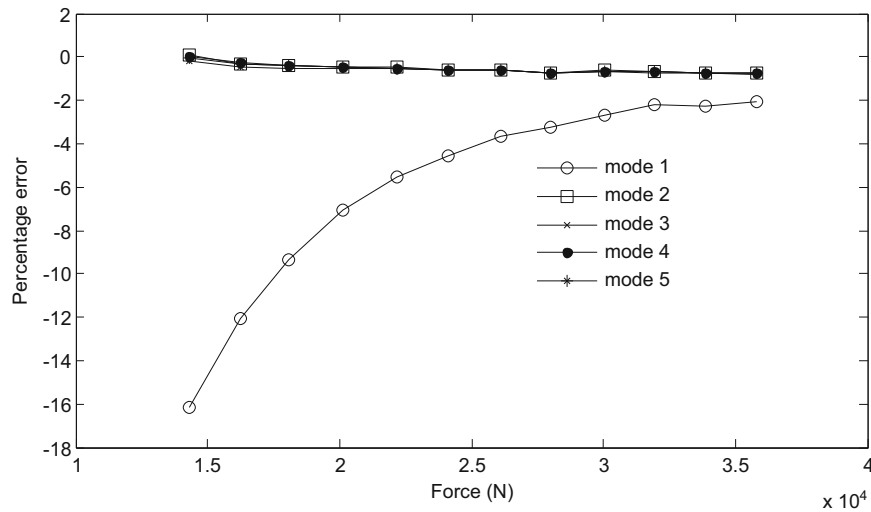**Fig. 32.1** Transmission line cable test bench

Fig. 32.2 Variation of natural frequencies with mechanical tensile load

Fig. 32.3 Variation of natural frequencies with mechanical tensile load (* experimental data; □ nonlinear FEM model; ○ linear FEM model)

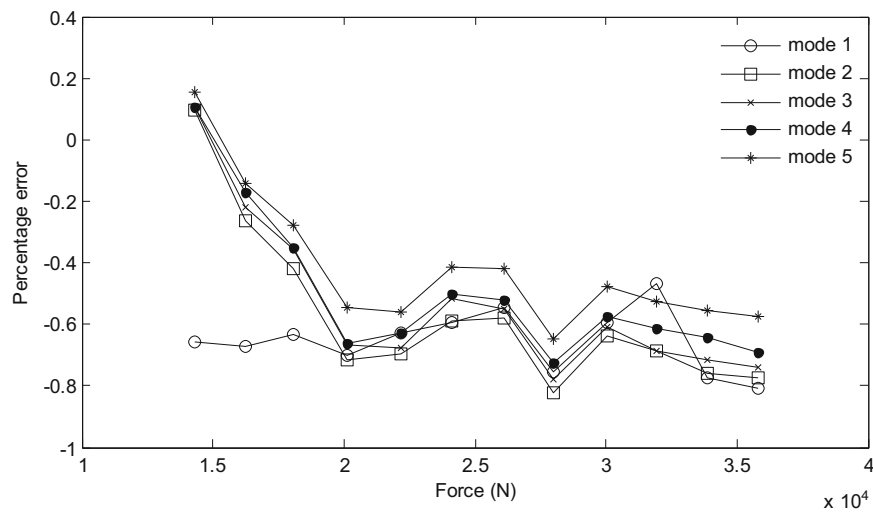**Fig. 32.4** Variation of natural frequencies using linear numerical model

Figure 32.4 shows the percentage error of the values of natural frequencies of the first five modes of vibration taking into account the numerical values obtained by linear model. The experimental values were considered as reference values. It is noted errors in the order of 16% for the first vibrate mode at low loads of mechanical traction and with increasing mechanical load the errors decrease.

Figure 32.5 shows the percentage error obtained using non-linear numerical model. Note in this case that the maximum error is of the order of 0.8%, ie the non-linear model has a much better fit to the linear model.

The results shown in Figs. 32.2, 32.3, 32.4, and 32.5 refer to TERN CAA cable. The results for the other two cables maintained the same behavior with variations in the errors between the experimental and numerical values.

32.3   Conclusions

In this work, it was noted that the linear model for dynamic analysis conductor cable provides good results only for high mechanical cable loads, which is not commonly used in practice. The linear model also shows good results for small samples length.

Fig. 32.5 Variation of natural frequencies using nonlinear numerical model

For samples of great length (over 30 m) nonlinear model presents better results than linear models mainly for low mechanical loads. This fact is evidenced by analyzing the behavior of first vibration mode.

We used three different cables for dynamic analysis and it was noted that the largest percentage error of the numerical values of the natural frequency of the first vibrate mode using non-linear models was around 2.5% for low mechanical loads and the error for the linear model was in order of 16%.

References

1. Barbieri, N., Souza Jr., O. H., Barbieri, R.: Dynamical analysis of transmission line cables. Part 1 – linear theory. Mech. Syst. Signal Process. **18**(3), 659–669 (2004)
2. Barbieri, N., Souza Jr., O. H., Barbieri, R.: Dynamical analysis of transmission line cables. Part 2 – damping estimation. Mech. Syst. Signal Process. **18**(3), 671–681 (2004)
3. Barbieri, N., Souza Jr., O. H., Barbieri, R.: Dynamical analysis of transmission line cables. Part 3 – nonlinear theory. Mech. Syst. Signal Process. **22**, 992–1007 (2008)